Pascal Laugier
Guillaume Haïat *Editors*

Bone Quantitative Ultrasound

Springer

Bone Quantitative Ultrasound

Pascal Laugier • Guillaume Haïat
Editors

Bone Quantitative Ultrasound

Springer

Editors
Pascal Laugier
Université Pierre et Marie Curie
CNRS
Laboratoire d'Imagerie Parametrique
15, rue de L'Ecole de Medecine
75006 Paris
France
pascal.laugier@upmc.fr

Guillaume Haïat
CNRS
B2OA UMR 7052
10, avenue de Verdun
75010 Paris
France
guillaume.haiat@univ-paris-est.fr

ISBN 978-94-007-0016-1 e-ISBN 978-94-007-0017-8
DOI 10.1007/978-94-007-0017-8
Springer Dordrecht Heidelberg London New York

Contents

Introduction vii
Pascal Laugier and Guillaume Haïat

1 Bone Overview 1
David Mitton, Christian Roux, and Pascal Laugier

2 Introduction to the Physics of Ultrasound 29
Pascal Laugier and Guillaume Haïat

3 Quantitative Ultrasound Instrumentation for Bone In Vivo Characterization 47
Pascal Laugier

4 Clinical Applications 73
Reinhard Barkmann and Claus-C. Glüer

5 Poromechanical Models 83
Michal Pakula, Mariusz Kaczmarek, and Frederic Padilla

6 Scattering by Trabecular Bone 123
Frédéric Padilla and Keith Wear

7 Guided Waves in Cortical Bone 147
Maryline Talmant, Josquin Foiret, and Jean-Gabriel Minonzio

8 Numerical Methods for Ultrasonic Bone Characterization 181
Emmanuel Bossy and Quentin Grimal

9 Homogenization Theories and Inverse Problems 229
Robert P. Gilbert, Ana Vasilic, and Sandra Ilic

10 Linear Acoustics of Trabecular Bone 265
Janne P. Karjalainen, Ossi Riekkinen, Juha Töyräs, and Jukka S. Jurvelin

11 The Fast and Slow Wave Propagation in Cancellous Bone: Experiments and Simulations 291
Atsushi Hosokawa, Yoshiki Nagatani, and Mami Matsukawa

12 Phase Velocity of Cancellous Bone: Negative Dispersion Arising from Fast and Slow Waves, Interference, Diffraction, and Phase Cancellation at Piezoelectric Receiving Elements 319
Christian C. Anderson, Adam Q. Bauer, Karen R. Marutyan, Mark R. Holland, Michal Pakula, G. Larry Bretthorst, Pascal Laugier, and James G. Miller

13 Linear Ultrasonic Properties of Cortical Bone: In Vitro Studies 331
Guillaume Haïat

14 Ultrasonic Monitoring of Fracture Healing 361
Vasilios C. Protopappas, Maria G. Vavva, Konstantinos N. Malizos, Demos Polyzos, and Dimitrios I. Fotiadis

15 Nonlinear Acoustics for Non-invasive Assessment of Bone Micro-damage 381
Marie Muller and Guillaume Renaud

16 Microscopic Elastic Properties 409
Kay Raum

17 Ultrasonic Computed Tomography 441
Philippe Lasaygues, Régine Guillermin, and Jean-Pierre Lefebvre

Index 461

Introduction

Pascal Laugier and Guillaume Haïat

Ask yourself what makes the strength of a building such as the Eiffel tower, i.e., its ability to withstand bending and shearing forces of the wind. The quantity of scrap used to build it? The intrinsic strength of each iron beam? The structure (i.e., size, shape, orientation of the beams, overall shape of the building)? All these factors contribute to the strength would answer the engineer. The Eiffel tower was surprisingly inspired by the work in early 1850s of the anatomist Hermann von Meyer on the anatomy of the femur (thighbone). Like engineers who control the integrity and the strength of buildings (towers, bridges), physicians scrutinize the strength of our bones, specifically to detect fragile bones and identify subjects at fracture risk and in need for treatment.

Fragile bones are commonly, but not exclusively, encountered in a disease called osteoporosis characterized by a decrease in bone mass and structural and material deterioration of bone, leading to increased susceptibility to fractures. Osteoporosis is most common in women after menopause, but may also develop in men, and may occur in anyone in the presence of particular hormonal disorders and other chronic diseases or as a result of medications. Osteoporosis may significantly affect life expectancy and quality of life. Osteoporosis is a major public health threat with extremely high costs to health care systems. Approximately one in two women and one in four men over age 50 will have an osteoporosis related fracture in their remaining lifetime. The costs measure in billions of dollars annually and these numbers are expected to increase, with as many as 6.3 million hip fractures predicted annually, around the world, by 2050. Clinicians and researchers alike are emphasizing the importance of early detection of osteoporosis and fracture prevention.

Today, X-ray measured bone mass serves as a surrogate for bone fragility, but fails to take into account other important aspects like material strength or microstructure. Mechanical waves such as ultrasound are intrinsically suited to probe

P. Laugier (✉)
Université Pierre et Marie Curie, CNRS, Laboratoire d'Imagerie Parametrique,
15, rue de L'Ecole de Medecine, 75006 Paris, France
e-mail: pascal.laugier@upmc.fr

G. Haïat
CNRS, B2OA UMR 7052, 10, avenue de Verdun, 75010 Paris, France
e-mail: guillaume.haiat@univ-paris-est.fr

mechanical properties and may perhaps have the best chances of all modalities to yield non-invasively an improved estimation of bone fragility combined with advantages like lack of ionizing radiation and cost-effectiveness.

Although the clinical potential of ultrasound for the investigation of bone fragility was recognized as early as in the 1950s where an ultrasound method was described for monitoring fracture healing [1], ultrasound was used episodically to investigate bone properties until the 1990s. The reason why ultrasound techniques were not used before this date was because of immature technology and poor understanding of the interaction mechanisms between ultrasound and bone. In 1984, Chris Langton et al. took a step forward by discovering that the transmission of ultrasound through the heel could discriminate osteoporotic from non-osteoporotic women [2]. He demonstrated that the heel of osteoporotic patients could transmit ultrasound waves with less attenuation than that of age-matched normal subjects. Since then many advances have been achieved and a variety of different sophisticated technologies capable of measuring different skeletal sites such as the heel, fingers, wrist, leg or hip have been introduced and evaluated. The evidence that ultrasound is a valid (radiation free and inexpensive) method for fracture risk assessment is first class. Several devices received FDA approval that further opened the door to clinical acceptance and use. Bone ultrasound technology, termed QUS (Quantitative Ultrasound), gained a place in the armamentarium of modalities used to assess the skeleton.

While the concept of measuring attenuation and velocity of ultrasound in bone has changed little since its inception, technology has evolved. Quantitative ultrasound imaging of the skeleton was first applied to image the heel [3]. Technological advances have provided clinicians with smaller, lighter, and portable equipment such as an inexpensive device operated with four AAA batteries [4].

An important limitation of QUS today is their limited access to peripheral skeletal sites only. One of the most significant recent technological advances is the new QUS scanner developed for direct assessment of skeletal properties at the proximal femur (hip) [5]. For X-ray based techniques, measurements directly at the main osteoporotic fracture sites have proved to be superior to measurements in the peripheral skeleton. It is reasonable to also expect better hip fracture risk prediction for QUS assessment at the proximal femur compared to the heel. However, the complexity of the anatomy and the presence of soft tissues make measurements at this site quite challenging.

More recently, the emphasis of innovative QUS basic research has shifted towards cortical long bone measurements, such as the tibia (leg) or the radius (forearm). Like tube or pipelines inspected by non destructive ultrasonic testing methods, long bones can be probed by ultrasound waves produced in response to an impact (the ultrasound impulse) transmitted by a source to the bone through soft tissues. Interestingly, long bones support the propagation of different kind of waves, such as surface or guided waves, which contain relevant information on micro-structural and material properties. Judicious choice of propagation modes over a suitable frequency range can be achieved and subsequent measurements of their velocities can reflect distinct aspects of bone quality [6], hoping that they would appropriately

reflect the bone quality status at the main fracture sites (e.g., hip or spine) and its changes associated with disease or treatment.

QUS techniques could find widespread clinical use to predict bone fragility not only in osteoporotic patients, but also in a wider context of bone diseases in female, male and pediatric populations. For example, preliminary studies suggest that this technique may be a useful method of assessing changes in bone health in preterm infants for whom X-ray technologies are unsuitable. An ultrasound wearable system for remote monitoring of the healing process in fractured long bones has also been reported [7].

QUS techniques and implementations have been introduced into clinical practice despite the fact that the interpretation of QUS data is hampered by the structural complexity of bone. Interaction mechanisms between ultrasound and bone are still poorly understood. Modeling can be seen as a major need in order to drive future experiments, to optimize measurements, to integrate multiscale knowledge, and to relate QUS variables to relevant bone biomechanical properties. Ultrasound propagation through bone is complex. It may involve different wave types, each with its own propagation characteristics. An accurate interpretation of ultrasound measurement results requires first a detailed understanding of ultrasound propagation with clear identification of the different waves and their exact propagation paths. The complex and multiscale nature of bone significantly complicates the task of solving equations, though.

Recently developed computer simulation tools offer a fertile alternative to intractable theoretical formulations. Computer simulation will likely have its greatest impact by allowing the researcher to visualize the propagation of ultrasound through the complex three-dimensional bone structures and by providing insight into the interaction mechanisms between ultrasound and bone. Simulators and computers may well become the primary tool for investigators to answer questions such as: how is the wave transmitted through the bone, what is the path followed by the wave? How does it interact with bone? What kind of wave is propagating? Computer simulations have been applied to the problem of transmission through pieces of spongy bone (such as that found in the femur at the hip), and along or across long cortical bones such as the radius [8–10]. In every case, the computer simulations provided valuable insight into the properties (e.g., nature and pathway) of the propagating waves. Computer simulation therefore resembles experiments in a virtual laboratory with independent control over each bone parameter. Virtual scenarios of osteoporosis for instance can be easily implemented and used to form a comprehensive understanding of bone ultrasonic properties and their relation to bone biomechanical competence [11], help validate or refute theoretical approaches, and probe new experimental configurations.

Although the methodology for assessing bone properties using ultrasound is much less developed to date than with X-rays, the potential of ultrasound extends far beyond the currently available techniques and is largely unexploited. Many new areas of investigation are in preliminary stages, though. Most active research is carried out in QUS to develop new measurement modes, access to the central skeleton (hip), exploit multiple propagation modes or extend the frequency range of the

measurements. All these new developments should result in new QUS variables and systems able to provide information on material or structural properties other than density and ultimately on osteoporotic fracture risk.

Quantitative ultrasound (QUS) of bone is a relatively recent research field. The research community is steadily growing, with interdisciplinary branches in acoustics, medical imaging, biomechanics, biomedical engineering, applied mathematics, bone biology and clinical sciences, resulting in significant achievements in new ultrasound technologies to measure bone and develop models to elucidate the interaction and the propagation of ultrasonic waves in complex bone structures. The present book will offer the most recent experimental results and theoretical concepts developed so far and would be intended for researchers, graduate or undergraduate students, engineers and clinicians who are involved in the field.

The **first chapter** is intended for readers who do not have a background in bone biomechanics. It gives a description of bone, highlighting the complex and hierarchical structure of bone, pointing to bone properties that determine bone strength. Then basic definitions and concepts of biomechanics are given. The clinical context (osteoporosis) in which quantitative ultrasound (QUS) has been developed is described. The first chapter can be skipped by readers who have a good knowledge of bone biomechanics. The **second chapter** offers an ultrasound overview which is intended for readers who do not have a background in the physics of ultrasound and may be skipped by those readers who already have a good knowledge of ultrasound wave propagation. Basic definitions of acoustics and equations of ultrasound wave propagation in homogeneous media are given. The **third chapter** is devoted to the generic measurement and signal processing methods implemented in bone clinical ultrasound devices. The section describes the devices, their practical use and clinical performance measures. The potential of QUS for a clinical application in osteoporosis management, the status today and its future perspectives are described in Chap. 4.

Chapters 4 to 9 cover the physical principles of ultrasound propagation in heterogeneous media such as bone and the interaction between an ultrasound wave and bone structures. Our goal is to give the reader an extensive view of the interaction mechanisms as an aid to understand the QUS potential and the types of variables that can be determined by QUS in order to characterize bone strength. The propagation of sound in bone, bone marrow and surrounding soft tissue is still subject of intensive research and a unique conclusive theory does not exists yet. Ultrasonic wave propagation in cancellous bone and cortical bone obeys different theories. For example, the Biot theory modeling bone as a poroelastic medium and the theory of scattering have been extensively used to describe wave propagation in cancellous bone, whereas propagation in cortical bone falls in the scope of guided waves theories. In these chapters, we intend to present in details the models that are used to solve the direct problem and strategies that are currently developed to solve the inverse problem. These developments will include analytical theories (Biot theory of poroelasticity, theory of scattering, guided wave theory) and numerical approaches that have grown exponentially in recent years. We assume that the reader is familiar with the theory of elastic wave propagation in homogeneous media as well as with

the underlying physical concepts of elastic wave interaction with heterogeneous media. This part of the book covers many advanced physical and mathematical concepts used to model ultrasound propagation in bone. Also, in order to differentiate the numerous variables used in ultrasound measurements it is important to better understand the complexity of the underlying physical concepts.

Chapters 10 to 14 review research findings of in vitro and in vivo ultrasound studies of bone and highlights some useful concepts that may lead to a better insight into the relationships between characteristics of ultrasound propagation and bone properties. This part of the book refers as much as possible to the theoretical developments presented in Chaps. 4–9. Clinically available QUS techniques rely on the quantitative measurement of linear acoustic parameters. Therefore much of the discussion is dedicated to these parameters (e.g., attenuation, speed of sound, backscatter coefficient) and to their relationship to bone mechanical and structural properties. The goal is to highlight the foundations for the clinical use of QUS technologies for fracture risk prediction and bone status assessment. Chapter 14 presents the state of the art and provides an extensive review of studies in the literature dealing with bone healing monitoring by ultrasonic means.

Intensive research is ongoing in many different areas of applications of ultrasound to characterize bone. The three last chapters (**15 to 17**) cover these cutting-edge researches (non-linear ultrasonics, ultrasound tomography, and acoustic microscopy) although they are still at an early development stage. The goal is to give a flavour of new areas of investigation that are currently investigated with the aim of measuring a variety of material and structural properties at several descriptive levels of bone structure from the tissue to the organ level.

References

1. I. M. Siegel, G. T. Anast, and T. Fields, "The determination of fracture healing by measurement of sound velocity across the fracture site," *Surg Gynecol Obstet* **107**, 327–332 (1958).
2. C. M. Langton, S. B. Palmer, and S. W. Porter, "The measurement of broadband ultrasonic attenuation in cancellous bone," *Eng Med* **13**, 89–91 (1984).
3. P. Laugier, B. Fournier, and G. Berger, "Ultrasound parametric imaging of the calcaneus: in vivo results with a new device," *Calcif Tissue Int* **58**, 326–331 (1996).
4. J. J. Kaufman, G. Luoc, D. Conroyd, W. A. Johnsone, R. L. Altmane, and R. S. Siffert, "New ultrasound system for bone assessment," presented at Medical Imaging, San Diego (2004).
5. R. Barkmann, S. Dencks, P. Laugier, F. Padilla, K. Brixen, J. Ryg, A. Seekamp, L. Mahlke, A. Bremer, M. Heller, and C. C. Glüer, "Femur ultrasound (FemUS) – first clinical results on hip fracture discrimination and estimation of femoral BMD," *Osteoporos Int* **21**, 969–976 (2010).
6. A. Tatarinov, N. Sarvazyan, and A. Sarvazyan, "Use of multiple acoustic wave modes for assessment of long bones: model study," *Ultrasonics* **43**, 672–680 (2005).
7. V. C. Protopappas, D. A. Baga, D. I. Fotiadis, A. C. Likas, A. A. Papachristos, and K. N. Malizos, "An ultrasound wearable system for the monitoring and acceleration of fracture healing in long bones," *IEEE Trans Biomed Eng* **52**, 1597–1608 (2005).
8. E. Bossy, F. Padilla, F. Peyrin, and P. Laugier, "Three-dimensional simulation of ultrasound propagation through trabecular bone structures measured by synchrotron microtomography," *Phys Med Biol* **50**, 545–556 (2005).

9. E. Bossy, M. Talmant, and P. Laugier, "Three-dimensional simulations of ultrasonic axial transmission velocity measurement on cortical bone models," *J Acoust Soc Am* **115**, 2314–2324 (2004).
10. J. Grondin, Q. Grimal, K. Engelke, and P. Laugier, "Potential of QUS to assess cortical bone geometry at the hip: a model based study," *Ultrasound Med Biol* **36**, 656–666 (2010).
11. G. Haïat, F. Padilla, F. Peyrin, and P. Laugier, "Variation of ultrasonic parameters with microstructure and material properties of trabecular bone: a 3D model simulation," *J Bone Miner Res* **22**, 665–674 (2007).

Chapter 1
Bone Overview

David Mitton, Christian Roux, and Pascal Laugier

Abstract This chapter is intended for readers who do not have a background in bone biomechanics. It gives a description of bone, highlighting its complex and hierarchical structure, starting at the macroscopic scale from an entire bone, such as the femur, down to the nanoscopic scale and its basic components: the collagen fibers and the mineral crystals. Then, some definitions and concepts of biomechanics are given in relation to the hierarchical structure of bone. The goal is to define the main parameters that can be used to assess bone mechanical competence. Some mechanical features are accessible using the quantitative ultrasound (QUS) technologies that are presented in subsequent chapters. Finally, the clinical context in which QUS has been developed is described. Diagnosis and follow-up of osteoporosis is a major public health problem in which QUS can play a role.

Keywords Anisotropy · Biomechanics · Bone mineral density · Bulk modulus · Canaliculi · Cancellous bone · Collagen fibers · Cortical bone · Damage · Densitometry · Density · Diagnosis · Elastic coefficient · Elasticity · Failure load · Fatigue · Fracture risk · Haversian canal · Isotropy · Lamellae · Microarchitecture · Microcracks · Crystals · Multi-scale · Osteoblasts · Osteoclasts · Osteocytes · Osteon · Osteoporosis · Poisson's coefficient · Porosity · Rigidity · Shear modulus · Strain · Strength · Stress · Toughness · Trabeculae · Viscoelasticity · Young's modulus

D. Mitton (✉)
Université Lyon 1, F-69622, Lyon, France; INRETS, UMR_T9406, LBMC
e-mail: david.mitton@inrets.fr

C. Roux
Université Paris-Descartes, Faculté de Médecine, Hopital Cochin, Paris, France
e-mail: christian roux@cch.ap-hop-paris.fr

P. Laugier
Université Pierre et Marie Curie, CNRS, Laboratoire d'Imagerie Parametrique,
15, rue de L'Ecole de Medecine, 75006 Paris, France
e-mail: pascal.laugier@upmc.fr

P. Laugier and G. Haïat (eds.), *Bone Quantitative Ultrasound*,
DOI 10.1007/978-94-007-0017-8_1,

1.1 Introduction

This chapter gives an overview of the basic knowledge necessary to study bone biomechanics. First of all, we shall describe the different types of bone tissue and the hierarchical structure of bone that is extending over multiple scales. This structural organisation will serve as a link to introduce the different biomechanical parameters, such as elasticity, strength and toughness. These are standard parameters to estimate bone structural or material properties. They are useful to assess the mechanical competence of bone considered as a structure (e.g., a whole femur) or as a material (e.g., a cylindrical specimen of cortical bone). Bone quantitative ultrasound has been developed in the context of osteoporosis. The main features of this disease and the diagnosis needs will be discussed to provide the reader with a better knowledge of bone properties that are of particular interest in this pathology. More specifically, the target of any diagnostic tool is the accurate prediction of fracture risk. Fracture risk is related to various factors such as (i) bone strength which is related to the intrinsic components (collagen fibers, bone crystals and cells activity) and to the hierarchical organisation of bone, and (ii) bone loading which depends on body weight, muscles activity and risk of fall.

1.2 Bone Description

1.2.1 What Is Bone?

Bone has three main functions: (1) sustaining loads from external actions (gravity) or from muscular insertion (movement), (2) a metabolic activity and (3) a protection role of vital organs (this is for example the case of the thorax and the skull). As bone strength *in vivo* assessment is the main topic of this book, we focus in the following on bone mechanical behaviour.

Bone is a living material. Bone evolves during life according to different factors having an effect on bone physiology or biology (physical activities, nutrition, hormones and medications). Bones adapt their shape and structure to their environment and especially to their mechanical environment. One illustration of bone adaptation is the bone loss occurring during exposure to microgravity [1]. This effect was observed for the astronauts in human space flights. The measurement sites in the load-bearing lower skeleton showed higher losses than the spine and arms [2]. The opposite effect could be observed in case of intensive physical activity. For example, an *in vivo* experiment was performed on dog to induce locally mechanical loading using a hydraulic bone chamber [3]. The authors found a 600% increase in the Young's modulus (see definition in Sect. 1.3) of the loaded bone tissue. These examples illustrate the bone adaptation to mechanical loading. This was conceptualized by Wolff's law in 1892 [4] stating that mechanical stress was responsible for determining the architecture of bone. These adaptations of bone to the mechanical

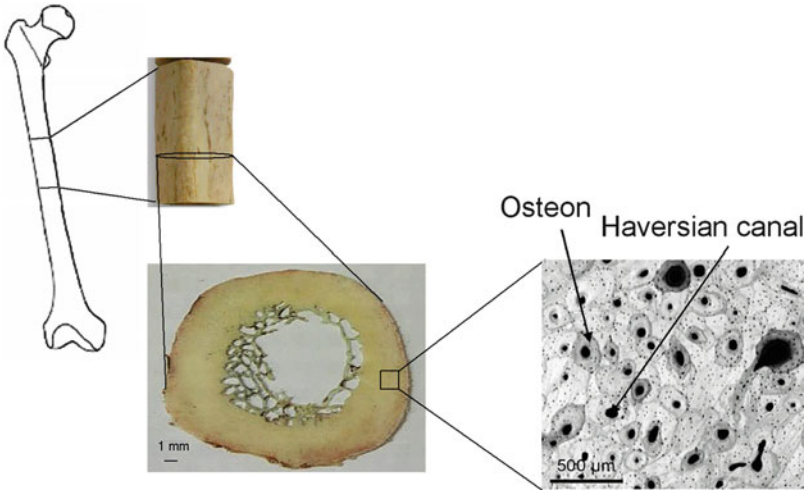

Fig. 1.1 Multilevel organization of cortical bone. Form *left to right*: mid-diaphysis of a femur; cross section at the mid-diaphysis illustrating the outer cortical shell and the inner cancellous bone compartment at the periphery of the medullary canal; scanning acoustic microscopy of cortical bone showing the osteons, haversian canals and osteocytes lacunae (*black dots*), scales are indicative

environment can be easily observed for other biological tissues. For example, the effect of physical activity is faster and more visible on the muscular tissue.

Bone is composed of two main components:

- Cortical (or compact) bone that composes the external envelope of all bones (long bones such as femur or tibia, short bones such as vertebra or calcaneus and flat bones such as the skull). Cortical bone presents a dense structure of low porosity (typical porosity is of a few % to 15%) that seems compact at the macroscopic level.
- Cancellous (or trabecular) bone found in the inner parts of bones. Cancellous bone looks like a highly porous sponge with a three-dimensional (3-D) structure made of connected plates and/or rods, called trabeculae. *In vivo* the cavities formed by the trabeculae network are filled with bone marrow. These two bone types are illustrated by Figs. 1.1 and 1.2.

1.2.2 Multi-scale Description

Bone is a hierarchical structure that extends over several organization levels. This hierarchical structure results in the exceptional mechanical competence of bone. Bone is a composite material containing about 70% mineral (hydroxyapatite), 22% proteins (type I collagen) and 8% water by weight [5]. Bone organisation depends on different levels, leading to a hierarchical structure (Fig. 1.3).

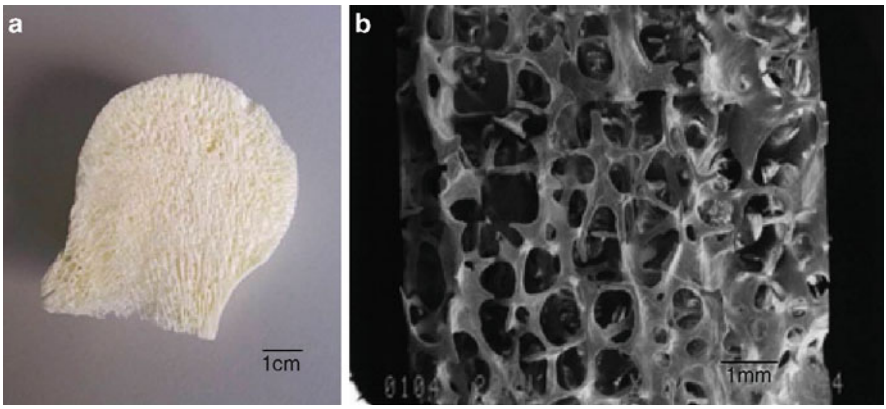

Fig. 1.2 Defatted cancellous bone specimens. (**a**) Half femoral head showing the macroscopic architecture of cancellous bone, (**b**) scanning electron microscopy images of vertebral cancellous bone specimen illustrating rod and plate connective elements

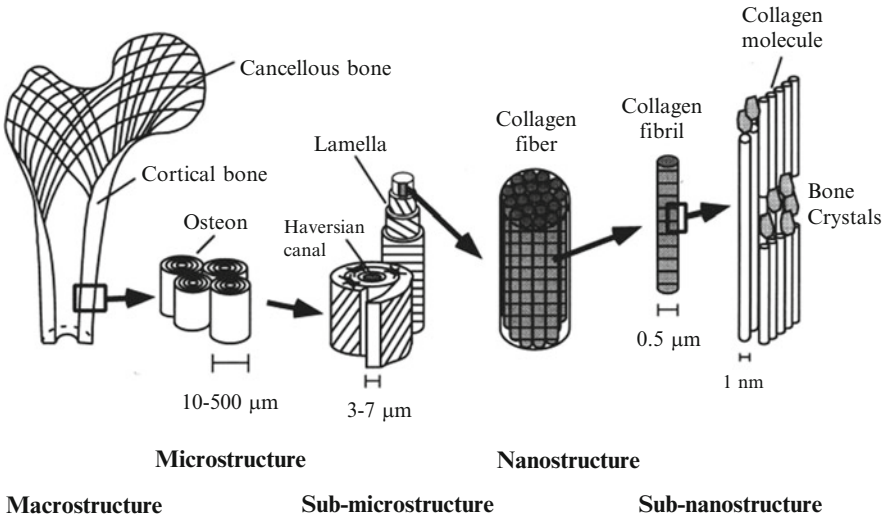

Fig. 1.3 Hierarchical structural organisation of bone (Reprinted from [6], copyright 1998, with permission from Elsevier)

As shown in Fig. 1.3 bone organisation is complex and depends on the analysed level.

Starting at the nanoscale with basic constituents (collagen and hydroxyapatite), bone is made of collagen molecules which are organised in fibrils. Fibrils are themselves arranged in fibers. The crystals, aligned with the fibers, are located in the interfibrillar spaces. Mineralized fibers are aligned to form bone lamellae of typical

thickness of a few micrometers. The orientation of the fibers depends on the lamellae and may change within lamellar sublayers. This organisation was described as the twisted plywood structure [7].

The osteon constitutes the bone structural unit (BSU) in cortical bone. An osteon is a cylindrical structure (100–300 μm in diameter) [8] consisting of several concentric lamellae surrounding a Haversian canal. The Haversian canals encompass the blood vessels and nerves. The interstitial tissue which is between osteons represents the remnants of osteons after remodeling. It can be identified as irregular lamellar structures that lack a central Haversian canal. At the periphery of each osteon, and separating it from adjacent osteons or from interstitial tissue, is a cement line which is less mineralized and rich in proteoglycans. In cancellous bone, trabeculae of thickness around 100 μm are composed of aligned bone packets.

This hierarchical structure of bone also includes porosity at various scales. For cortical bone the largest porosity is due to resorption cavities and Haversian canals (20–100 μm indiameter). A smaller scale porosity is related the Volkmann canals (network connecting the Haversian canals and perpendicular to them) and to the osteocytes lacunae and canaliculi of a few μm to less than 1μm in diameter.

1.2.3 Bone Remodelling

The bone evolution over time is due to its cells activity. In addition to the tissue matrix (collagen fibers and bone crystals) bone contains various types of cell: osteoblasts, osteoclasts and osteocytes. Remodelling is the replacement of old bone tissue by new bone tissue. Remodelling occurs in childhood to insure bone growth and bone shaping, in the adult skeleton to maintain bone mass, to adapt the skeleton to the loads or to repair microcracks. Bone remodelling is also involved in fracture healing. Bone cells act successively during the remodelling process. First of all the osteoclasts remove old bone (resorption). Then the osteoblats add new bone (remodelling). After mineralization osteoblasts become osteocytes and remain in the mineralised bone matrix. The new bone tissue which is not mineralized at the beginning of the remodelling process is called osteoid. For cortical bone the remodelling process occurs along tunnels and creates osteons. For cancellous bone the remodelling process takes place at the surface of the trabeculae. A comprehensive description of the resorption/remodelling process can be found in the referenced papers [9, 10].

Even if the exact mechanism inducing bone remodelling is not perfectly known at the present time, it is hypothesized that osteocytes and canaliculi act as mecanotransducers to activate bone remodelling.

Two types of bone can be identified according to the pattern of collagen forming the osteoid: woven bone is characterized by an irregular apposition of collagen fibres and lamellar bone is characterized by a regular parallel alignment of collagen into lamellae sublayers. Woven bone appears when osteoblasts produce osteoid rapidly.

In adults, woven bone is formed during fracture healing. Following a fracture, woven bone is remodelled and lamellar bone is deposited. Normally all bone in healthy mature human adults is lamellar bone.

1.3 Bone Biomechanics

This section will define the various parameters used to assess the mechanical competence of bone from the organ level to the microscopic scale. In addition to the macroscopic and microscopic levels described in Fig. 1.1, the mesoscopic level will be introduced for the study of bone biomechanics. The mesoscopic level corresponds to the millimetric scale (e.g. calibrated specimens of few millimetres for each dimension). To describe bone mechanical competence various terms must be defined. They are sometimes not properly used. For example, strength is different from elasticity. To better explain such mechanical characteristics, the hierarchical structure of bone will be taken as a guideline.

From a mechanical point of view, a distinction is usually made between structural and material properties. As an example, the Eiffel Tower is a structure, the steel composing the tower is a material. The same distinction can be done in bone biomechanics. The femur is a structure. Its mechanical competence is influenced by its shape and size. At the macroscopic level, cortical or cancellous bone can be seen as materials composing the femur. Parameters independent of the geometry (shape and size) can be assessed using calibrated specimens. At the mesoscopic level cancellous bone is a structure composed of trabecular tissue (material).

The analysis of the biomechanical properties will be conducted according to the different scales.

1.3.1 Rigidity and Failure Load at the Macroscopic Level

Let us consider the upper extremity of the femur loaded in a single stance phase configuration. This configuration mimicks the monopodal loading. This loading condition can be reproduced *ex vivo* on a testing machine. From this specific experiment, the load applied to simulate a single stance phase configuration and the corresponding displacement can be measured. The load-displacement curve is plotted from such measurements (Fig. 1.4). The rigidity (R) can be assessed from the linear part of the curve:

$$R = \frac{F}{\Delta l} \text{ in N/mm} \tag{1.1}$$

F is the load (in N) and Δl the displacement (in mm).

The rigidity assesses the capability of the bone to withstand a loading. The rigidity evaluates the elasticity of a complex shape (such as an entire bone or a portion of bone, in this example the proximal femur).

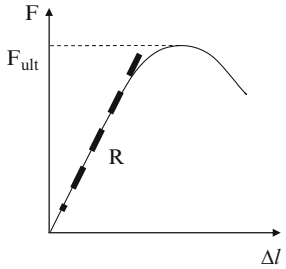

Fig. 1.4 Load-displacement curve, ultimate load (F_{ult}) and rigidity (R)

Table 1.1 Rigidity and ultimate load of different human bones

	Rigidity Mean (SD) {Range}	Ultimate load (N) Mean (SD) {Range}
Femur		
Single stance phase loading	–	5568 (1597) [12], {4937–16948} [13], 9039 (3412)[a] [14]
Lateral loading	–	4000 {1100–8700} [15], 2586 (1146)[a] [14]
Vertebra		
Compression	–	{2602–5802} [16]
Anterior bending	3109 (1234) (N/m) [17]	{630–2970} [18], 2098 (815) [17]
Radius (Distal third diaphysis)		
Compression	–	12946 (3644) [19]

[a]Data obtained on 40 paired femurs

The ultimate response of the structure is defined by the ultimate load (failure load) which corresponds to the maximum of the load-displacement curve (Fig. 1.4). These parameters depend on the geometry of the bone. The bigger the bone is the higher the rigidity and the failure load are.

In daily life, the loads applied on the skeleton are not only compressive loads. Bending or torsion can also be observed. Most of the time, these loadings are combined. However, to evaluate the rigidity and ultimate load of a specific entire bone, biomechanical experiments are performed either in compression, in tension, in bending or in torsion. At the macroscopic level on entire bone (such as the femur) bending and torsion experiments will give global response in terms of rigidity and ultimate load.

Table 1.1 shows the variability of the data that were obtained on different anatomical sites at the level of the organ (proximal femur, vertebra, distal third of the radius). Among several factors of variability, the data are influenced by the age of the subject. As an example the mean femoral strength in lateral loading configuration is 7200 ± 1090 N for young subjects (33 years old in average) and 3440 ± 1330 N for elderly subjects (74 years old in average) [11].

1.3.2 Elasticity, Strength and Damage at the Mesoscopic Level

To evaluate the mechanical response of bone at the mesoscopic level, it is necessary to define calibrated specimens (parallelepiped, cubic or cylindrical). Thus the parameters issued from such an approach are independent of the geometry of the sample (size and shape) in contrast to the mechanical properties assessed on whole bone. To keep the example of the femur, the cortical or cancellous bone specimens can be cut from the femur. Experiments performed on such specimens lead to the derivation of mechanical properties. The following relationships can be applied assuming homogeneity and linear elasticity. The homogeneity is a valid assumption when considering the bone tissue at the mesoscopic level. In the specific case of cancellous bone it is necessary to have sample of at least 5 mm in each dimension [20].

1.3.2.1 Stress

The stress (σ) is assessed from the measurement of the load (F) applied to a given area (A) (Fig. 1.5):

$$\sigma = \frac{F}{A} \text{in MPa } (\text{N/mm}^2) \tag{1.2}$$

1.3.2.2 Strain

The strain (ε) can be computed from the ratio of the measured displacement (Δl) and the initial specimen length (l_o) (Fig. 1.6). This definition is only valid for small strains (under 5%) [8]. This limit is compatible with the values measured on bone.

$$\varepsilon = \frac{\Delta l}{l_o} \tag{1.3}$$

From such parameters, it is possible to plot the stress-strain curve (e.g. in the longitudinal axis of a long bone) (Fig. 1.7).

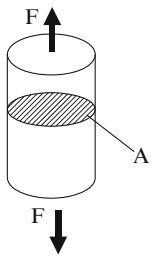

Fig. 1.5 Schematic representation of a specimen subjected to a tension load (F) on an area (A)

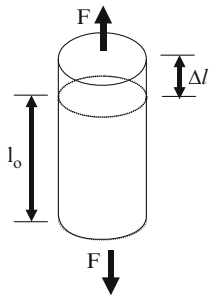

Fig. 1.6 Schematic representation of the displacement (Δl) under a tension load (F) for a specimen of initial length (l_o)

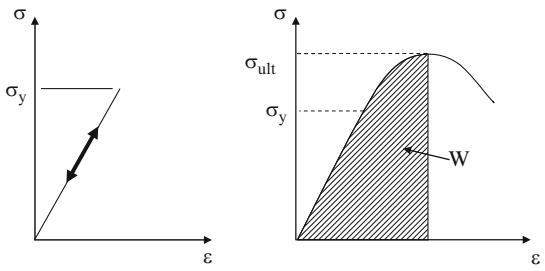

Fig. 1.7 Stress-strain curves. On the *left* the curve represents the elastic behavior up to the yield stress (σ_y) (*the double arrow* represents the loading and unloading). On the *right* is a typical stress-strain curve extending above the ultimate stress (σ_{ult}) the area under the curve represent the energy until failure (W)

1.3.2.3 Elasticity

If the material after loading returns to the initial position (Fig. 1.7, *left*), the material presents an elastic behaviour. The yield point corresponds to the end of the elastic domain and is defined by the yield stress (σ_y).

The material elasticity is defined by the Young's modulus or modulus of elasticity (E) which can be assessed as the slope of the linear part of the stress-strain curve.

$$E = \frac{\sigma}{\varepsilon} \text{ in MPa } (\text{N/mm}^2) \tag{1.4}$$

1.3.2.4 Poisson's Coefficient

When a specimen is submitted to a uniaxial loading (compression or tension) it respectively expands or shrinks in the orthogonal directions (Fig. 1.8). The Poisson's ratio (ν) is defined by Eq. 1.5.

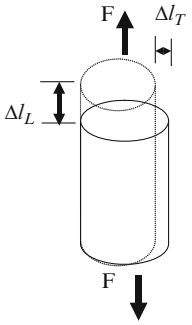

Fig. 1.8 Schematic representation of the displacements along two orthogonal directions (Δl_T: transverse displacement, Δl_L: longitudinal displacement) for a specimen submitted to tensile test

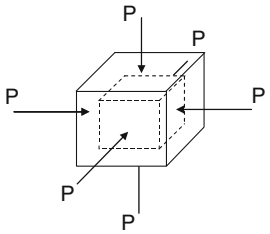

Fig. 1.9 Illustration of uniform compression

$$\nu = -\frac{\frac{\Delta l_T}{l_{0_T}}}{\frac{\Delta l_L}{l_{0_L}}} = -\frac{\varepsilon_T}{\varepsilon_L} \tag{1.5}$$

1.3.2.5 Bulk Modulus

The bulk modulus (K) of an isotropic material (see the isotropy-anisotropy paragraph for definition) measures its resistance to uniform compression (i.e., uniform load applied in all directions) (Fig. 1.9).

$$K = -V\frac{\partial P}{\partial V} \text{ in MPa} \tag{1.6}$$

where P is pressure, V is volume, and $\frac{\partial P}{\partial V}$ denotes the partial derivative of pressure with respect to volume.

The bulk modulus is linked to the Young's modulus (E) and the Poisson's ratio (ν) by the following relationship [21]:

$$K = \frac{E}{3(1-2\nu)} \text{ in MPa} \tag{1.7}$$

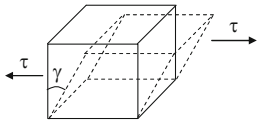

Fig. 1.10 Representation of the shear deformation of a cubic specimen submitted to shear stress (τ)

1.3.2.6 Shear Modulus

The shear modulus (G) is defined as the ratio of the shear stress (τ) and the shear strain (γ) (Fig. 1.10). γ is equivalent to the tangent of the angle in the hypothesis of small displacements.

$$G = \frac{\tau}{\gamma} \text{ in MPa} \tag{1.8}$$

The shear modulus is related to the Young's modulus and the Poisson's ratio [21]:

$$G = \frac{E}{2(1+\nu)} \text{ in MPa} \tag{1.9}$$

1.3.2.7 Isotropy – Anisotropy

Isotropy is the property of being directionally independent. A material is anisotropic when its mechanical properties vary according to the direction of analysis. In first approximation, cortical and cancellous bones can be considered orthotropic, which means that the properties differ according to orthogonal directions.

Several factors contribute to the mechanical anisotropy of bone. These include the orientation of the BSU and of the Haversian porous network, the orientation of the lamellae and the alignment of collagen fibers and hydroxyapatite crystals. In hierarchical structures like bone, the anisotropy depends on the observational level.

1.3.2.8 Elastic Coefficients

The mechanical response of an anisotropic material depends on the direction of loading. The previous relationships regarding elasticity were given for one direction. By generalization, the linear elastic constitutive law becomes:

$$C_{ij} = \frac{\sigma_i}{\varepsilon_j} \text{ in MPa} \tag{1.10}$$

C is the stiffness tensor and C_{ij} are the elastic coefficients.

In the case of orthotropy, the stiffness tensor contains nine independent coefficients and can be written:

$$[C] = \begin{bmatrix} C_{11} & C_{12} & C_{13} & 0 & 0 & 0 \\ C_{12} & C_{22} & C_{23} & 0 & 0 & 0 \\ C_{13} & C_{23} & C_{33} & 0 & 0 & 0 \\ 0 & 0 & 0 & C_{44} & 0 & 0 \\ 0 & 0 & 0 & 0 & C_{55} & 0 \\ 0 & 0 & 0 & 0 & 0 & C_{66} \end{bmatrix} \tag{1.11}$$

Conversely, strain can be expressed as a function of stress. This leads to an expression of the compliance tensor (inverse of the stiffness tensor) which is usually expressed as a function of engineering constants (the Young's moduli (E_i), the Poisson's ratios (ν_{ij}) and the shear moduli (G_{ij})) and is written as [8]:

$$\begin{bmatrix} \varepsilon_{11} \\ \varepsilon_{22} \\ \varepsilon_{33} \\ 2\varepsilon_{23} \\ 2\varepsilon_{13} \\ 2\varepsilon_{12} \end{bmatrix} = \begin{bmatrix} \frac{1}{E_1} & -\frac{\nu_{12}}{E_1} & -\frac{\nu_{13}}{E_1} & 0 & 0 & 0 \\ -\frac{\nu_{21}}{E_2} & \frac{1}{E_2} & -\frac{\nu_{23}}{E_2} & 0 & 0 & 0 \\ -\frac{\nu_{31}}{E_3} & -\frac{\nu_{32}}{E_3} & \frac{1}{E_3} & 0 & 0 & 0 \\ 0 & 0 & 0 & \frac{1}{G_{23}} & 0 & 0 \\ 0 & 0 & 0 & 0 & \frac{1}{G_{13}} & 0 \\ 0 & 0 & 0 & 0 & 0 & \frac{1}{G_{12}} \end{bmatrix} \begin{bmatrix} \sigma_{11} \\ \sigma_{22} \\ \sigma_{33} \\ \sigma_{23} \\ \sigma_{13} \\ \sigma_{12} \end{bmatrix} \tag{1.12}$$

The first six coefficients in the upper left part of the matrix are related to compression loadings and the last three in the bottom right diagonal are linked to shear loadings.

1.3.2.9 Viscoelasticity

Viscoelasticity of a material leads to energy dissipation. Contrary to an elastic material which releases all the energy it receives, a viscoelastic material does not release all the input energy. The energy dissipation leads to a hysteretic behavior where the stress-strain curve during unloading is different from the stress-strain curve during loading. This phenomenon is illustrated in Fig. 1.11 and corresponds to the area between the loading and unloading curve. As for most of biological tissues, viscoelasticity is observed for bone.

As a consequence of viscoelasticity, a different mechanical response is recorded according to the loading speed. It must be noted that conventional mechanical tests (compression, tension, bending, shear and torsion) are often performed under quasi-static loading conditions whereas ultrasound measurements correspond to

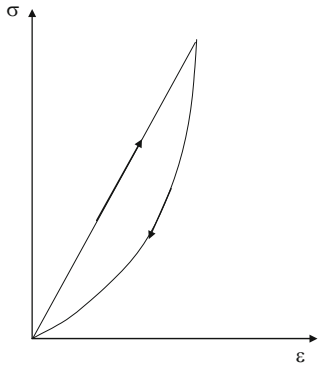

Fig. 1.11 Loading-unloading cycle (hysteresis loop) of the stress-strain curve, below the yield stress. The area between the two *curves* represents the dissipative energy

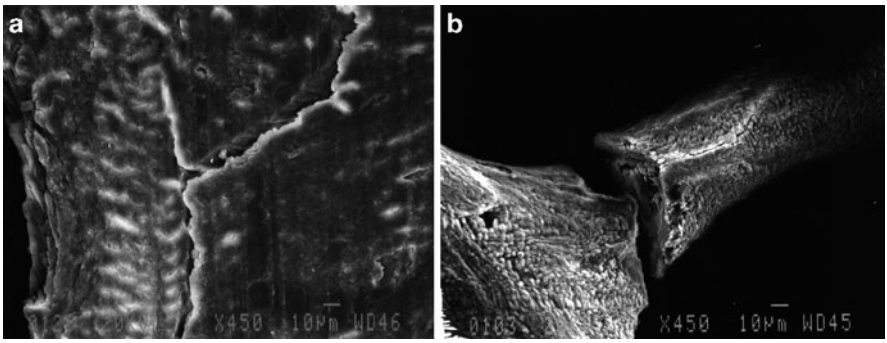

Fig. 1.12 Scanning electron microscopy images of loaded trabeculae, (**a**) microcrack, (**b**) broken trabecula

dynamic mechanical testing with high strain rate. This difference is important when comparing the data obtained by both methods.

1.3.2.10 Strength

The strength of a material is its ability to withstand an applied stress without failure. The ultimate stress gives a quantification of the ultimate strength.

1.3.2.11 Damage

Damage is a degradation of the material. Figure 1.12 shows microcracks and failure of two different loaded bone trabeculae (see Chap. 15 for details on the use of ultrasound to investigate damage in bone tissue).

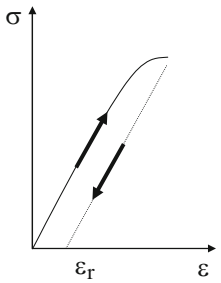

Fig. 1.13 Loading-unloading cycle above the yield stress, with residual strain (ε_r)

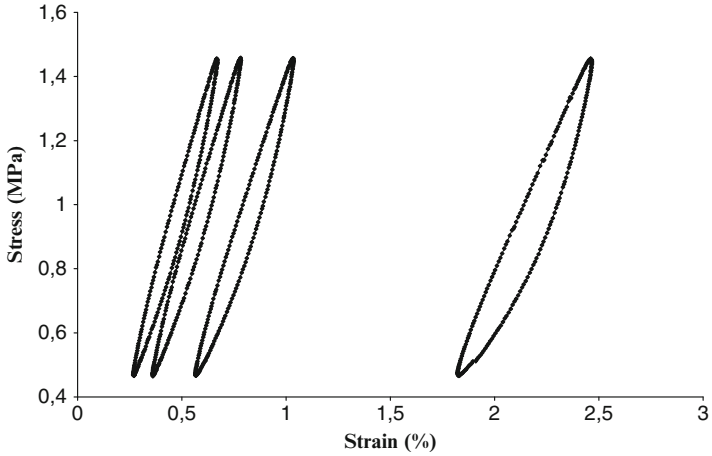

Fig. 1.14 Typical diagram of the evolution of the stress-strain curves recorded during a fatigue test. The first cycle on the *left* corresponds to the first cycle of the fatigue test conducted on a cancellous bone specimen, the last cycle on the *right* corresponds to 900th cycles

Bone damage occurs:

– When loading above the yield stress. Unloading leads to residual strain (ε_r) (Fig. 1.13)

Above the yield point, the behaviour is related to the plastic domain. In case of unloading the material will not return to the initial state and will present a residual strain. The residual strain is related to the damage induced in the material.

– In fatigue, loading under the yield point during a certain amount of time will lead to damage accumulation in the specimen (Fig. 1.14).

Damage can be assessed by the computation of the Young's modulus at the initial state and subsequently for the following loading cycles. The damage is noted D and is computed by:

$$D = 1 - \frac{E_n}{E_o} \tag{1.13}$$

where E_0 is the Young's modulus at the initial step and E_n is the Young's modulus for the current loading cycle.

1.3.2.12 Toughness

The toughness of a material is the capability of bone tissue to absorb energy during the failure process. It can be assessed from the computation of the energy until failure which is the area under the stress-strain curve up to failure (Fig. 1.7). Fracture mechanics approaches are usually employed. Two parameters are commonly used for assessing fracture toughness: critical stress intensity factor $(K_c \; in \; MPa.\sqrt{m})$ and critical strain energy release rate $(G_c \; in \; J.m^{-2})$, respectively. The former characterizes the stress intensity around the crack tip, whereas the latter is related to the surface energy of the newly formed crack surfaces [22].

Orders of magnitude of the main parameters that can be assessed for both cortical and cancellous bones at the mesoscopic level are presented in Table 1.2. The large variability is due to differences in measurement protocols and to intra or inter-subject variability.

Table 1.2 Mechanical properties of human bone at the mesoscopic level (cortical and cancellous bone)

	Cortical bone Mean (SD) {Range}	Cancellous bone Mean (SD) {Range}
Elasticity		
Young's modulus (longitudinal, E_L) (MPa)	Femoral diaphysis: 14300 (400) in tension, 11800 (360) in compression [23] 17400[b] [8]	Vertebra: 138 (83)[a] Femoral head: 417 (85) [24]
Young's modulus (transverse, E_T) (MPa)	9600[b] [8]	Vertebra {16–100}[a]
Poisson's coefficient (ν)	Femur: 0.22–0.42 [25]	Proximal femur: 0.3 [26]
Shear modulus (G) (MPa)	3510[b] [8]	Femoral head: {100–500} [27]
Strength		
Ultimate stress (MPa)	Femoral diaphysis: 53.8 (20.3) in tension, 106.4 (29.4) in compression [23]	Vertebra: 1.6 (0.9)[a] Femoral head: 9.6 (2.4) [24]
Toughness		
Critical stress intensity factor (K_c) ($MPa.\sqrt{m}$)	Humeral diaphysis: 2.06 (0.2) [28]	Femoral head: {0.1–1} [29]

[a] Mitton, unpublished data
[b] Anatomical site non defined

1.3.3 Elasticity at the Microscopic Level

Young's modulus can also be assessed at a microscopic level. Apart from acoustic microscopy that will be detailed in Chap. 16, bone tissue micro-elastic properties can be assessed with three methods: (1) traditional mechanical testing (compression, tension and three or four-point bending), (2) micro-computed tomography (μCT) image-based finite-element models and (3) nanoindentation.

1. Traditional mechanical testing already mentioned at the macro- or mesoscopic scales have been adapted to test small specimens. More details can be found in the references [8, 30]. At the microscopic scale, the difficulties are related to the small size of the samples that can be prepared from human bones (cortical thickness at some anatomical sites is less than 1 mm and trabeculae thickness is around 100 μm).
2. To overcome these limits the Young's modulus of bone tissues (cortical and trabecular) can be assessed by an inverse method using micro finite element modelling and biomechanical experiments. Such method is based on imaging such as high resolution computed tomography [31–33]. The tissue Young's modulus is obtained by an optimization routine that matches both the experimental and simulated displacement of the specimen for a given load.
3. Nanoindentation uses a diamond indenter to load and unload a material. The Young's modulus can be derived from the unloading curve [34] (Fig. 1.15).

Table 1.3 shows the variability of the Young's modulus according the anatomical site, the measuring methods. Nanoindentation can assess the spatial heterogeneity of the elastic properties for osteons $(22.5 \pm 1.3\text{GPa})$ and for interstitial lamellae (25.8 ± 0.7) [34] or within lamellae [35].

1.3.4 Synthesis

It is important to note that a large number of investigators have reported a strong linear relationship between the Young's modulus and the ultimate compressive

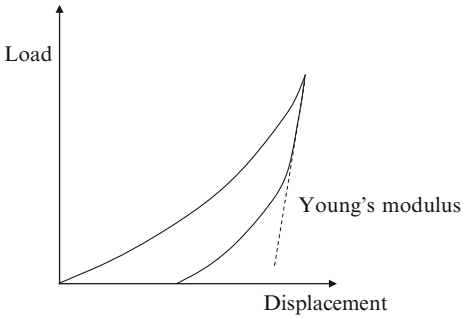

Fig. 1.15 Typical load-displacement curve for a nanoindention test. The Young's modulus is derived from the slope of the *upper* portion of the unloading curve

Table 1.3 Elastic properties of human bone tissue at the microscopic level (cortical and cancellous tissues)

	Values in GPa, mean (SD) {Range}	
Young's modulus	Cortical tissue	Cancellous tissue
Tensile test (tibia)	18.6 (3.5) [36]	10.4 (3.5) [36]
Three-point bending (iliac crest)	4.89 [37]	3.81 [37]
Three-point bending (tibia)	5.44 (1.25) [38]	4.59 (1.60) [38]
µCT image-based finite element models (proximal tibia)	–	{2.23–10.1} [31]
µCT image-based finite element models (vertebra)	–	5.7 (1.6) [39]
CT image-based finite element models (98 µm pixel size) (radius)	16 (1.8) [19]	–
Nanoindentation (femur)	20.02 (0.27) [40] 25.0 (4.3) [41]	18.14 (1.7) (distal epiphysis) [40] 6.9 (4.3) (neck) [41]

µCT: micro computed tomography

strength [24, 42]. Moreover, there is also an extremely tight correlation between the Young's modulus and the bending strength [43]. Thus, Young's modulus can be used as a surrogate for bone strength. The measurement of the ultrasound propagation velocity (see Chap. 13) that is directly related to the bone stiffness (or to the Young's modulus) can also be used as a surrogate measurement for bone strength.

The orders of magnitude of the main mechanical parameters are summarized in Tables 1.1–1.3. The important variability is due to various factors, including intra and inter-subjects differences, skeletal sites and experimental protocols. In particular, the macro or mesoscopic mechanical properties (ultimate strength, toughness, fatigue strength) of cancellous and cortical bones decrease with age [44–46]. These modifications are related to an increased porosity and cancellous bone micro-architecture degradation. At the microscopic level the elastic properties are not affected by aging [47]. However collagen crosslinking, collagen fibers orientation, their interaction with bone crystals and water content are modified by aging and are correlated with toughness reduction for cortical bone [22, 48].

To summarise, the influences of the bone composition and structure on its mechanical properties are the following [49]:

1. The porosity modifies Young's modulus independently of density
2. Microcracks weaken cortical bone tissue and contribute to increased susceptibility to fracture
3. The collagen fibrils provide tensile strength and toughness
4. The crystalline structure provides compressive strength and brittleness

1.4 Densitometric and Morphological Parameters

The main densitometric and morphological parameters affecting the mechanical competence of bone are listed Table 1.4. The preferred techniques to measure these characteristics are indicated below.

At the macroscopic scale, the quantitative analysis includes the assessment of bone mineral density and morphology:

– Bone mineral density (BMD) corresponds to the density of the mineral phase of the bone. This density can be measured with X-ray absorptiometry techniques. The mineral phase alone contributes to the images. Because the amount of mineral is normalized by the total area or total volume occupied by the bone, BMD does not represent the true density but rather is an apparent density. BMD can be assessed *in vivo* using imaging techniques such as:

  - Dual X-ray absorptiometry (DXA): DXA is the gold standard method in clinics for densitometry measurements. A DXA image is a 2D projection of the segment of interest (Fig. 1.16) where both cancellous and cortical bone are superimposed. Thus the density is obtained in g/cm^2 and refers to areal bone mineral density (BMD_a) [50].
  - X-ray quantitative computed tomography (QCT): a certain number of cross-sections of the anatomical site are reconstructed from QCT acquisitions. Volumetric density (g/cm^3) (BMD) is derived from volumetric (or three-dimensional, 3-D) measurements performed using QCT, enabling differentiation between cortical and cancellous bone densities.

Extensive details on the techniques and the parameters that can be derived from such methods can be found in the International Commission on Radiation Units and Measurements (ICRU) bone densitometry report [50].

Table 1.4 Main bone structural features determining bone strength, according to physical scale (From [67])

Scale (m)	Bone characteristics
$>10^{-2}$	**Macrostructure**
	Bone densities
	Whole bone morphology (size and shape)
10^{-2}–10^{-3}	**Mesoscopic scale** (apparent and real densities)
10^{-6}–10^{-3}	**Microstructure** (porosity, cortical thickness, trabecular number and spacing, structural anisotropy)
10^{-9}–10^{-6}	**Sub-microstructure** (microcracks)
	Nanostructure (collagen fibers)
$<10^{-9}$	**Sub-nanostructure** (hydroxyapatite crystals)

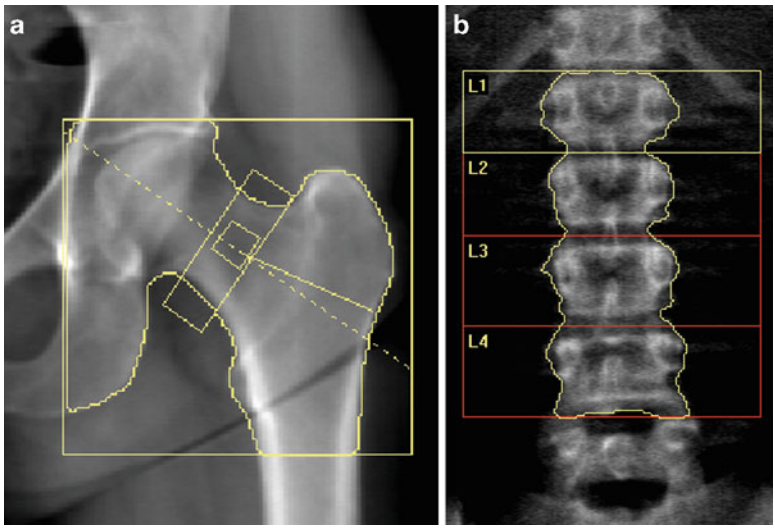

Fig. 1.16 Dual-X-ray Absorptiometry (DXA) images and areas of interest for bone mineral density measurement (**a**) hip and (**b**) lumbar spine

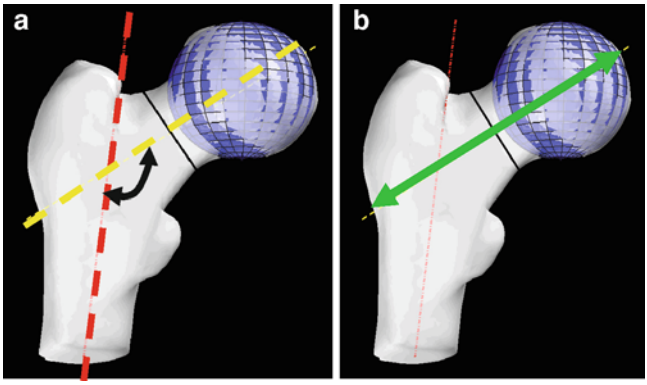

Fig. 1.17 Example of femoral geometric features derived from 3-D model issued from biplanar radiography (**a**) neck shaft angle and (**b**) the femoral neck axis length

– Geometric features (e.g. in the case of the proximal femur: neck shaft angle, femoral neck axis length, cortical thickness of the femoral neck) (Fig. 1.17) can be derived either using plain radiographic or DXA projection images with potential bias due to projection, or in 3-D using biplanar radiography [51, 52] or computed tomography [53].

At the mesoscopic scale, bone density can be measured in small bone specimens of a few millimetres in each dimension by weighting the specimens and by dividing

bone mass by the volume defined by the external dimensions. This density is an apparent density (ρ_{app}). When the considered volume is the volume of bone tissue alone, excluding the bone marrow cavities, the density represents the actual density of the bone tissue (ρ_{real}). The bone volume can be obtained applying Archimede's principle and using Eq. 1.14:

$$\rho_{real} = \frac{M_{air}}{M_{air} - M_{water}} \rho_{water} \text{ in g/cm}^3 \tag{1.14}$$

with M_{air} the specimen weight in the air, M_{water} the specimen weight in water and ρ_{water} the water density.

Both the apparent and the actual densities are expressed in g/cm^3. Using this method, the weight of the bone specimens accounts for the total weight of collagen fibers and hydroxyapatite crystals.

Mineral density and micro-architectural parameters can be assessed at the microscopic scale:

- Bone density can be determined using high resolution imaging techniques such as microradiography [54] and synchrotron-radiation micro computed tomodensitometry ($\text{SR} - \mu\text{CT}$). Because the resolution allows separating the tissue from the cavities, the density is the true mineral density of the tissue, and is often referred to as the degree of mineralization (g/cm^3). The heterogeneity of the mineralization is illustrated in Fig. 1.18.
- Micro-architectural parameters of cortical bone (cortical thickness, porosity) and trabecular bone (e.g., trabecular number Tb.N, trabecular thickness Tb.Th, trabecular separation Tb.Sp, connectivity and structural anisotropy) can be assessed *in vitro* from 2-D cross-sectional histomorphometry [55] or in 3-D using high resolution imaging modalities. The first approaches using micro-computed

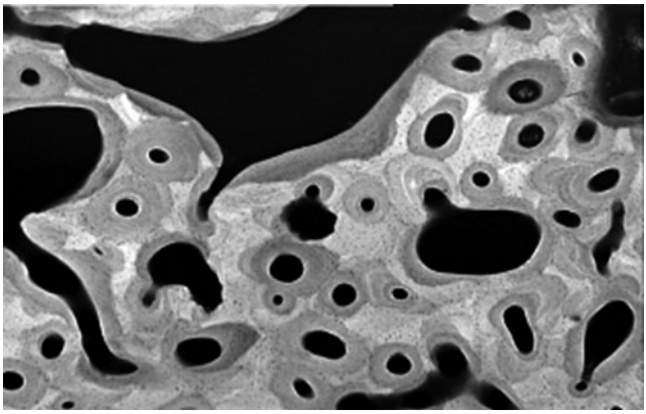

Fig. 1.18 Microradiograph of a $100 \pm 1\,\mu$m-thick section illustrating the heterogeneity of the mineralization in the various bone structural units. The *darker* is the young bone and the *brighter* is the interstitial old bone. (Reprinted from [54], copyright 2008, with permission from Elsevier)

Fig. 1.19 3-D image (High-Resolution Peripheral Quantitative Computed Tomography) of radius, *top* view (Courtesy of S. Boutroy, INSERM U831 Lyon, France)

tomography (μCT) were proposed in the beginning of the 1990s [56, 57]. Improvement in the resolution of clinically available imaging systems such as high resolution peripheral quantitative computed tomography (HR pQCT) [58, 59] (Fig. 1.19) or high-resolution magnetic resonance imaging (HR-MRI) [60, 61] has enabled *in vivo* assessment of bone micro-architecture. Bone micro-architecture can also be assessed indirectly using texture analysis from high resolution radiography [62].

– Microcracks (few microns in width and around 100 μm in length) can be quantitatively assessed using histomorphometric techniques [63, 64] and more recently X-ray μCT or synchrotron micro-computed tomography (SR − μCT) [65] leading to the 3-D representation of microcracks.

At the nano scale, the bone tissue can be examined by synchrotron radiation techniques that have been reviewed by Peyrin [66]. For example, spectroscopic techniques such as X-ray fluorescence and Fourier Transform Infra Red spectroscopy may be implemented with synchrotron source to obtain chemical information on bone tissue. X-ray diffraction and small-angle X-ray scattering are complementary diffraction techniques to characterize hydroxyapatite crystals and mineral particles in terms of their orientation, shape and thickness [66].

1.5 Osteoporosis

1.5.1 Definition

Osteoporosis is a skeletal disease in which the density and quality of bone are reduced, leading to weakness of the skeleton and increased risk of fracture, particularly of the spine, wrist, hip, pelvis and arm [68]. Bone quality encompasses a number of bone tissue properties, beyond density, that govern mechanical resistance

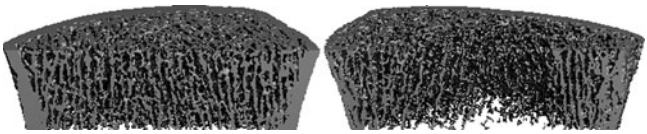

Fig. 1.20 3-D high-resolution peripheral quantitative computed tomography images of tibia from healthy premenopausal (*left*) and severe osteoporotic postmenopausal (*right*) women. Osteoporosis induces an increased porosity and a reduced thickness of the cortical shell and disruption in the trabecular network (Courtesy of S. Boutroy, INSERM U831 Lyon, France)

such as bone geometry, cortical properties, trabecular micro-architecture, bone tissue mineralization, quality of collagen and hydroxyapatite crystals, and presence of microcracks [62]. The main cause of osteoporosis is hormonal deficiency, and thus the most frequent disease is post menopausal osteoporosis.

Figure 1.20 illustrates the deterioration of cancellous bone microstructure and reduction of bone mass that leads to bone fragility.

1.5.2 Epidemiology

Osteoporosis is considered as a major public health problem due to the number and consequences of fractures. At least 40% of post menopausal women [69] over the age of 50 and 15–30% of men [70] will sustain one or more fragility fractures in their remaining lifetime. By comparison, the risk is 10% for breast cancer and 46% for cardio-vascular diseases [71, 72].

Because of the increase in the number of frail elderly patients, the world-wide number of hip fractures is projected to increase dramatically in the next decades [73]. An expanding part of the health-care system costs is dedicated to osteoporosis.

1.5.3 Diagnosis

Osteoporosis diagnosis in clinical practice relies today on areal bone mineral density (BMD_a) measurements at the hip or lumbar spine [74]. The diagnosis of osteoporosis is based on the T-score [50] concept. The T-score denotes the difference between a measured value x of an individual subject and the mean value from a healthy young reference population (denoted by index Y) normalized by the standard deviation SD_r of the reference population distribution:

$$T = \frac{x - \bar{x}_r(age = age_Y)}{SD_r(age = age_Y)} \tag{1.15}$$

The World Health Organisation (WHO) [75] definition uses BMD_a to categorize a subject into one of four groups (Table 1.5).

Table 1.5 T-score values according to four groups of subjects. BMD_a is the areal Bone Mineral Density assessed by dual X-ray absorptiometry

Normal	BMD_a T-score ≥ -1.0
Low bone mass or osteopenia	$-1.0 > BMD_a$ T-score > -2.5
Osteoporosis	$-2.5 \geq BMD_a$ T-score
Established osteoporosis	$-2.5 \geq BMD_a$ T-score and at least one osteoporotic fracture

However a substantial overlap exists between the BMD_a values of non-fractured and fractured patients [76], confirming that bone factors beyond BMD_a have an impact on fracture risk.

In addition to BMD assessment, clinical risk factors assessment is mandatory to select patients with the highest risk of fracture who should receive the highest priority for treatment. A tool to calculate the individual 10-year risk of fracture is now available: the FRAX® [77]. It is based on factors such as age, sex, weight, height and clinical risk factors which include previous fragility fractures, premature menopause, parental history of hip fracture, current tobacco smoking, long-term use of glucocorticoids, rheumatoid arthritis, and other causes of secondary osteoporosis. Treatments are now available for osteoporosis, which have shown in studies of appropriate methodology that they are able to decrease the risk of fractures [78]. Most of these treatments increase bone density, but this increase does not fully explain the anti fracture effect. Thus treatments have also positive effect on non-quantitative parameters of bone.

The currently accepted definition of osteoporosis considering that not only bone mass is affected but that factors of bone quality are also deteriorated strongly suggests the need for complementary methods to assess fracture risk *in vivo*.

Quantitative ultrasound (QUS) technologies have augmented the armamentarium of bone assessment technologies in the 1990s [79], but they are not yet widely accepted, partly because of technical immaturity and partly because of lack of standardization between different technical approaches and among various manufacturers. Recently, progress in patient-specific finite element analysis has been proposed as an effective means of direct assessment of patient-specific skeletal risk factors. Regarding the skeletal risk factors, it is important to distinguish bone strength and the amount of load applied on a specific bone. Keaveny and Bouxsein have evaluated the load-to-strength ratio called Φ [80]. When Φ is greater than a critical value (the biomechanical fracture threshold), fracture is more likely to occur. Strength can be determined by patient-specific QCT-based finite element analysis [81–84]. Patient-specific finite element models take into account the individual macroscopic geometry and bone density. To improve the strength predictability *in vivo* there is a need for a better estimation of cancellous and cortical bone mechanical properties (elasticity and ultimate strength) using non-destructive methods. Besides, up to now the main limit to use the Φ ratio is the estimation of patient-specific loads applied on a specific bone. It is still based on important hypotheses (especially for muscular loading) and is still not sufficiently

subject-specific. Researches are under way to be able to assess accurate subject-specific loads. In a near future, such an approach should complement clinical risk factors analysis.

1.6 Conclusion

In current clinical practice the quantification of bone mechanical competence or strength is mainly related to the measurement of bone mineral density. However as this was shown in this chapter, the bone biomechanics (elasticity and strength) is related to other specific features beyond density, such as elementary components of the tissue and the hierarchical structure of bone.

Moreover in the context of osteoporosis there is a need for patient-specific quantitative data to improve fracture risk prediction. Multi-scale modelling approach is under way in the international research community (e.g. the Osteoporotic Virtual Physiological Human project (VPHOP) [85]) and should probably offer in a near future improved risk fracture assessment.

As part of this initiative, quantitative ultrasounds are good candidate for assessing subject-specific properties because they are non-destructive, radiation free and make use of elastic waves that are inherently sensitive to architectural and mechanical features of the propagation medium. The following chapters will present the most recent researches on quantitative ultrasound.

Acknowledgments The authors would like to acknowledge Catherine Verdu (INSA Lyon) who performed the scanning electron microscopy images.

References

1. T. F. Lang, "What do we know about fracture risk in long-duration spaceflight?," J Musculoskelet Neuronal Interact **6**(4), 319–321 (2006).
2. A. LeBlanc, V. Schneider, L. Shackelford, S. West, V. Oganov, A. Bakulin, and L. Voronin, "Bone mineral and lean tissue loss after long duration space flight," J Musculoskelet Neuronal Interact **1**(2), 157–160 (2000).
3. R. E. Guldberg, N. J. Caldwell, X. E. Guo, R. W. Goulet, S. J. Hollister, and S. A. Goldstein, "Mechanical stimulation of tissue repair in the hydraulic bone chamber," J Bone Miner Res **12**(8), 1295–1302 (1997).
4. R. Huiskes, "The law of adaptative bone remodeling: a case for crying newton?," *in Recent advances in human biology-Bone structure and remodeling*, A. Odgaard and H. Weinans, eds. (World Scientific, Singapore-New Jersey-London-Hong Kong 1995), pp. 137–145.
5. P. Augat and S. Schorlemmer, "The role of cortical bone and its microstructure in bone strength," Age Ageing **35** (Suppl 2), ii27–ii31 (2006).
6. J. Y. Rho, L. Kuhn-Spearing, and P. Zioupos, "Mechanical properties and the hierarchical structure of bone," Med Eng Phys **20**(2), 92–102 (1998).
7. M. M. Giraud-Guille, "Twisted plywood architecture of collagen fibrils in human compact bone osteons," Calcif Tissue Int **42**(3), 167–180 (1988).
8. S. Cowin, ed., *Bone mechanics handbook* (CRC Press, Boca Raton, FL, 2001).

9. D. B. Burr and R. B. Martin, "Errors in bone remodeling: toward a unified theory of metabolic bone disease," Am J Anat **186**(2), 186–216 (1989).
10. E. Seeman, "Bone modeling and remodeling," Crit Rev Eukaryot Gene Expr **19**(3), 219–233 (2009).
11. M. L. Bouxsein, A. C. Courtney, and W. C. Haynes, "Ultrasound and densitometry of the calcaneus correlates with the failure load of cadaveric femurs," Calcif Tissue Int **56**, 99–103 (1995).
12. A. Le Bras, S. Kolta, P. Soubrane, W. Skalli, C. Roux, and D. Mitton, "Assessment of femoral neck strength by 3-dimensional X-ray absorptiometry," J Clin Densitom **9**(4), 425–430 (2006).
13. M. D. Smith, D. D. Cody, S. A. Goldstein, A. M. Cooperman, L. S. Matthews, and M. J. Flynn, "Proximal femoral bone density and its correlation to fracture load and hip-screw penetration load," Clin Orthop Relat Res **283**, 244–251 (1992).
14. L. Duchemin, W. Skalli, V. Topouchian, M. Benissa, and D. Mitton, "Femoral fracture load and failure energy in two loading configurations: an *in vitro* study," presented at the European Orthopaedic Research Society, Bologna, 2006.
15. P. H. Nicholson, G. Lowet, X. G. Cheng, S. Boonen, G. van der Perre, and J. Dequeker, "Assessment of the strength of the proximal femur *in vitro*: relationship with ultrasonic measurements of the calcaneus," Bone **20**(3), 219–224 (1997).
16. M. A. Haidekker, R. Andresen, and H. J. Werner, "Relationship between structural parameters, bone mineral density and fracture load in lumbar vertebrae, based on high-resolution computed tomography, quantitative computed tomography and compression tests," Osteoporos Int **9**(5), 433–440 (1999).
17. E. Sapin, F. Chan, C. Ayoub, C. Roux, W. Skalli, and D. Mitton, "Anterior bending on whole vertebrae using controlled boundary conditions for model validation," J Musculoskelet Res **12**(2), 71–76 (2009).
18. J. M. Buckley, L. Cheng, K. Loo, C. Slyfield, and Z. Xu, "Quantitative computed tomography-based predictions of vertebral strength in anterior bending," Spine (Phila Pa 1976) **32**(9), 1019–1027 (2007).
19. M. R. Bosisio, M. Talmant, W. Skalli, P. Laugier, and D. Mitton, "Apparent Young's modulus of human radius using inverse finite-element method," J Biomech **40**(9), 2022–2028 (2007).
20. R. J. S. Brown, "Connection between formation factor for electrical resistivity and fluid-solid coupling factor in Biot's equations for acoustic waves in fluid filled with porous media," Geophysics **45**, 1269–1275 (1980).
21. J. Lemaitre and J. L. Chaboche, *Mécanique des matériaux solides* (Dunod, Paris, 2004).
22. X. Wang and S. Puram, "The toughness of cortical bone and its relationship with age," Ann Biomed Eng **32**(1), 123–135 (2004).
23. L. Duchemin, V. Bousson, C. Raossanaly, C. Bergot, J. D. Laredo, W. Skalli, and D. Mitton, "Prediction of mechanical properties of cortical bone by quantitative computed tomography," Med Eng Phys **30**(3), 321–328 (2008).
24. D. Mitton, J. Rappeneau, and R. Bardonnet, "Effect of a supercritical CO2 based treatment on mechanical properties of human cancellous bone," Eur J Orthop Surg Traumatol **15**(4), 264–269 (2005).
25. R. B. Ashman, S. C. Cowin, W. C. Van Buskirk, and J. C. Rice, "A continuous wave technique for the measurement of the elastic properties of cortical bone," J Biomech **17**, 349–361 (1984).
26. E. Verhulp, B. van Rietbergen, and R. Huiskes, "Comparison of micro-level and continuum-level voxel models of the proximal femur," J Biomech **39**(16), 2951–2957 (2006).
27. K. Bruyere Garnier, R. Dumas, C. Rumelhart, and M. E. Arlot, "Mechanical characterization in shear of human femoral cancellous bone: torsion and shear tests," Med Eng Phys **21**(9), 641–649 (1999).
28. R. K. Nalla, J. J. Kruzic, and R. O. Ritchie, "On the origin of the toughness of mineralized tissue: microcracking or crack bridging?," Bone **34**(5), 790–798 (2004).
29. R. B. Cook and P. Zioupos, "The fracture toughness of cancellous bone," J Biomech **42**(13), 2054–2060 (2009).
30. C. H. Turner and D. B. Burr, "Basic biomechanical measurements of bone: a tutorial," Bone **14**(4), 595–608 (1993).

31. B. van Rietbergen, H. Weinans, R. Huiskes, and A. Odgaard, "A new method to determine trabecular bone elastic properties and loading using micromechanical finite-element models," J Biomech **28**(1), 69–81 (1995).
32. A. J. Ladd, J. H. Kinney, D. L. Haupt, and S. A. Goldstein, "Finite-element modeling of trabecular bone: comparison with mechanical testing and determination of tissue modulus," J Orthop Res **16**(5), 622–628 (1998).
33. H. Follet, F. Peyrin, E. Vidal-Salle, A. Bonnassie, C. Rumelhart, and P. J. Meunier, "Intrinsic mechanical properties of trabecular calcaneus determined by finite-element models using 3D synchrotron microtomography," J Biomech **40**(10), 2174–2183 (2007).
34. J. Y. Rho, T. Y. Tsui, and G. M. Pharr, "Elastic properties of human cortical and trabecular lamellar bone measured by nanoindentation," Biomaterials. **18**(20), 1325–1330. (1997).
35. H. S. Gupta, U. Stachewicz, W. Wagermaier, P. Roschger, H. D. Wagner, and P. Fratzl, "Mechanical modulation at the lamellar level in osteonal bone," J Mater Res **21**(8), 1913–1921 (2006).
36. J. Y. Rho, R. B. Ashman, and C. H. Turner, "Young's modulus of trabecular and cortical bone material: ultrasonic and microtensile measurements," J Biomech **26**(2), 111–119 (1993).
37. J. L. Kuhn, S. A. Goldstein, K. Choi, M. London, L. A. Feldkamp, and L. S. Matthews, "Comparison of the trabecular and cortical tissue moduli from human iliac crests," J Orthop Res **7**(6), 876–884 (1989).
38. K. Choi, J. L. Kuhn, M. J. Ciarelli, and S. A. Goldstein, "The elastic moduli of human subchondral, trabecular, and cortical bone tissue and the size-dependency of cortical bone modulus," J Biomech **23**(11), 1103–1113 (1990).
39. F. J. Hou, S. M. Lang, S. J. Hoshaw, D. A. Reimann, and D. P. Fyhrie, "Human vertebral body apparent and hard tissue stiffness," J Biomech **31**(11), 1009–1015 (1998).
40. C. H. Turner, J. Rho, Y. Takano, T. Y. Tsui, and G. M. Pharr, "The elastic properties of trabecular and cortical bone tissues are similar: results from two microscopic measurement techniques," J Biomech. **32**(4), 437–441 (1999).
41. P. K. Zysset, X. E. Guo, C. E. Hoffler, K. E. Moore, and S. A. Goldstein, "Elastic modulus and hardness of cortical and trabecular bone lamellae measured by nanoindentation in the human femur," J Biomech **32**(10), 1005–1012 (1999).
42. S. A. Goldstein, D. L. Wilson, D. A. Sonstegard, and L. S. Matthews, "The mechanical properties of human tibial trabecular bone as a function of metaphyseal location," J Biomech **16**(12), 965–969 (1983).
43. J. D. Currey, "What determines the bending strength of compact bone?," J Exp Biol **202**(Pt 18), 2495–2503 (1999).
44. R. W. McCalden, J. A. McGeough, M. B. Barker, and C. M. Court-Brown, "Age-related changes in the tensile properties of cortical bone. The relative importance of changes in porosity, mineralization, and microstructure," J Bone Joint Surg Am **75**(8), 1193–1205 (1993).
45. R. W. McCalden, J. A. McGeough, and C. M. Court-Brown, "Age-related changes in the compressive strength of cancellous bone. The relative importance of changes in density and trabecular architecture," J Bone Joint Surg Am **79**(3), 421–427 (1997).
46. T. Diab, K. W. Condon, D. B. Burr, and D. Vashishth, "Age-related change in the damage morphology of human cortical bone and its role in bone fragility," Bone **38**(3), 427–431 (2006).
47. C. E. Hoffler, K. E. Moore, K. Kozloff, P. K. Zysset, and S. A. Goldstein, "Age, gender, and bone lamellae elastic moduli," J Orthop Res **18**(3), 432–437 (2000).
48. J. S. Nyman, A. Roy, J. H. Tyler, R. L. Acuna, H. J. Gayle, and X. Wang, "Age-related factors affecting the postyield energy dissipation of human cortical bone," J Orthop Res **25**(5), 646–655 (2007).
49. D. Mitton, "Cortical bone composition and biomechanical implications," Osteoporo Int **19**, 853–855 (2008).
50. W. Kalender, K. Engelke, T. P. Fuerst, C.-C. Glüer, P. Laugier, and J. Shepherd, "Quantitative aspects of bone densitometry (ICRU Report 81)," J ICRU **9**(1), 1–130 (2009).
51. A. Le Bras, S. Laporte, V. Bousson, D. Mitton, J. A. De Guise, J. D. Laredo, and W. Skalli, "3D reconstruction of the proximal femur with low-dose digital stereoradiography," Comput Aided Surg **9**(3), 51–57 (2004).

52. G. Haiat, F. Padilla, R. Barkmann, S. Kolta, C. Latremouille, C. C. Glüer, and P. Laugier, "In vitro speed of sound measurement at intact human femur specimens," Ultrasound Med Biol **31**(7), 987–996 (2005).
53. F. Jenson, F. Padilla, V. Bousson, C. Bergot, J. D. Laredo, and P. Laugier, "In vitro ultrasonic characterization of human cancellous femoral bone using transmission and backscatter measurements: relationships to bone mineral density," J Acoust Soc Am **119**(1), 654–663 (2006).
54. G. Boivin, Y. Bala, A. Doublier, D. Farlay, L. G. Ste-Marie, P. J. Meunier, and P. D. Delmas, "The role of mineralization and organic matrix in the microhardness of bone tissue from controls and osteoporotic patients," Bone **43**(3), 532–538 (2008).
55. A. M. Parfitt, M. K. Drezner, F. H. Glorieux, J. A. Kanis, H. Malluche, P. J. Meunier, S. M. Ott, and R. R. Recker, "Bone histomorphometry: standardization of nomenclature, symbols, and units. Report of the ASBMR Histomorphometry Nomenclature Committee," J Bone Miner Res **2**(6), 595–610 (1987).
56. J. L. Kuhn, S. A. Goldstein, L. A. Feldkamp, R. W. Goulet, and G. Jesion, "Evaluation of a microcomputed tomography system to study trabecular bone structure," J Orthop Res **8**(6), 833–842 (1990).
57. P. Ruegsegger, B. Koller, and R. Muller, "A microtomographic system for the nondestructive evaluation of bone architecture," Calcif Tissue Int **58**(1), 24–29 (1996).
58. A. Laib, H. J. Hauselmann, and P. Ruegsegger, "In vivo high resolution 3D-QCT of the human forearm," Technol Health Care **6**(5–6), 329–337 (1998).
59. S. Boutroy, M. L. Bouxsein, F. Munoz, and P. D. Delmas, "In vivo assessment of trabecular bone microarchitecture by high-resolution peripheral quantitative computed tomography," J Clin Endocrinol Metab **90**(12), 6508–6515. Epub 2005 Sep 6527 (2005).
60. S. Majumdar and H. K. Genant, "A review of the recent advances in magnetic resonance imaging in the assessment of osteoporosis," Osteoporos Int **5**(2), 79–92 (1995).
61. H. W. Chung, F. W. Wehrli, J. L. Williams, S. D. Kugelmass, and S. L. Wehrli, "Quantitative analysis of trabecular microstructure by 400 MHz nuclear magnetic resonance imaging," J Bone Miner Res **10**(5), 803–811 (1995).
62. L. Pothuaud, C. L. Benhamou, P. Porion, E. Lespessailles, R. Harba, and P. Levitz, "Fractal dimension of trabecular bone projection texture is related to three-dimensional microarchitecture," J Bone Miner Res **15**(4), 691–699 (2000).
63. D. B. Burr and M. Hooser, "Alterations to the en bloc basic fuchsin staining protocol for the demonstration of microdamage produced *in vivo*," Bone **17**(4), 431–433 (1995).
64. R. D. Chapurlat, P. Garnero, G. Breart, P. J. Meunier, and P. D. Delmas, "Serum type I collagen breakdown product (serum CTX) predicts hip fracture risk in elderly women: the EPIDOS study," Bone **27**(2), 283–286 (2000).
65. A. Larrue, A. Rattner, N. Laroche, L. Vico, and F. Peyrin, "Feasibility of micro-crack detection in human trabecular bone images from 3D synchrotron microtomography," Conf Proc IEEE Eng Med Biol Soc **2007**, 3918–3921 (2007).
66. G. Haïat, F. Padilla, M. Svrcekova, Y. Chevalier, D. Pahr, F. Peyrin, P. Laugier, and P. Zysset, "Relationship between ultrasonic parameters and apparent trabecular bone elastic modulus: a numerical approach," J Biomech **42**(13), 2033–2039 (2009).
67. C. J. Hernandez and T. M. Keaveny, "A biomechanical perspective on bone quality," Bone **39**(6), 1173–1181 (2006).
68. IOF, "Osteoporosis in the Workplace: the social, economic and human costs of osteoporosis on employees, employers and governments" (2002).
69. L. J. Melton, III, E. A. Chrischilles, C. Cooper, A. W. Lane, and B. L. Riggs, "Perspective. How many women have osteoporosis?," J Bone Miner Res **7**(9), 1005–1010 (1992).
70. A. Randell, P. N. Sambrook, T. V. Nguyen, H. Lapsley, G. Jones, P. J. Kelly, and J. A. Eisman, "Direct clinical and welfare costs of osteoporotic fractures in elderly men and women," Osteoporos Int **5**(6), 427–432 (1995).
71. S. R. Cummings, D. B. Karpf, F. Harris, H. K. Genant, K. Ensrud, A. Z. LaCroix, and D. M. Black, "Improvement in spine bone density and reduction in risk of vertebral fractures during treatment with antiresorptive drugs," Am J Med **112**(4), 281–289 (2002).

72. O. Johnell, J. A. Kanis, A. Oden, I. Sernbo, I. Redlund-Johnell, C. Petterson, C. De Laet, and B. Jonsson, "Mortality after osteoporotic fractures," Osteoporos Int **15**(1), 38–42 (2004).
73. B. Gullberg, O. Johnell, and J. A. Kanis, "World-wide projections for hip fracture," Osteoporos Int **7**(5), 407–413 (1997).
74. C. C. Gluer, S. R. Cummings, D. C. Bauer, K. Stone, A. Pressman, A. Mathur, and H. K. Genant, "Osteoporosis: association of recent fractures with quantitative US findings," Radiology **199**(3), 725–732 (1996).
75. WHO, "Assessment of osteoporotic fracture risk and its application to screening for postmenopausal osteoporosis," (World Health Organization, Geneva, 1994).
76. S. C. Schuit, M. van der Klift, A. E. Weel, C. E. de Laet, H. Burger, E. Seeman, A. Hofman, A. G. Uitterlinden, J. P. van Leeuwen, and H. A. Pols, "Fracture incidence and association with bone mineral density in elderly men and women: the Rotterdam Study," Bone **34**(1), 195–202 (2004).
77. J. A. Kanis, N. Burlet, C. Cooper, P. D. Delmas, J. Y. Reginster, F. Borgstrom, and R. Rizzoli, "European guidance for the diagnosis and management of osteoporosis in postmenopausal women," Osteoporos Int **19**(4), 399–428 (2008).
78. P. J. Meunier, C. Roux, S. Ortolani, M. Diaz-Curiel, J. Compston, P. Marquis, C. Cormier, G. Isaia, J. Badurski, J. D. Wark, J. Collette, and J. Y. Reginster, "Effects of long-term strontium ranelate treatment on vertebral fracture risk in postmenopausal women with osteoporosis," Osteoporos Int **20**(10), 1663–1673 (2009).
79. P. Laugier, "Instrumentation for *in vivo* ultrasonic characterization of bone strength," IEEE Trans Ultrason Ferroelectr Freq Control **55**(6), 1179–1196 (2008).
80. T. M. Keaveny and M. L. Bouxsein, "Theoretical implications of the biomechanical fracture threshold," J Bone Miner Res **23**(10), 1541–1547 (2008).
81. J. H. Keyak, S. A. Rossi, K. A. Jones, and H. B. Skinner, "Prediction of femoral fracture load using automated finite element modeling," J Biomech **31**(2), 125–133 (1998).
82. L. Duchemin, D. Mitton, E. Jolivet, V. Bousson, J. D. Laredo, and W. Skalli, "An anatomical subject-specific FE-model for hip fracture load prediction," Comput Methods Biomech Biomed Engin **11**(2), 105–111 (2008).
83. E. Schileo, F. Taddei, L. Cristofolini, and M. Viceconti, "Subject-specific finite element models implementing a maximum principal strain criterion are able to estimate failure risk and fracture location on human femurs tested *in vitro*," J Biomech **41**(2), 356–367 (2008).
84. T. M. Keaveny, P. F. Hoffmann, M. Singh, L. Palermo, J. P. Bilezikian, S. L. Greenspan, and D. M. Black, "Femoral bone strength and its relation to cortical and trabecular changes after treatment with PTH, alendronate, and their combination as assessed by finite element analysis of quantitative CT scans," J Bone Miner Res **23**(12), 1974–1982 (2008).
85. R. Thiel, K. A. Stroetmann, V. N. Stroetmann, and M. Viceconti, "Designing a socio-economic assessment method for integrative biomedical research: the Osteoporotic Virtual Physiological Human project," Stud Health Technol Inform **150**, 876–880 (2009).

Chapter 2
Introduction to the Physics of Ultrasound

Pascal Laugier and Guillaume Haïat

Abstract From an acoustical point of view, bone is a complex medium as it is heterogeneous, anisotropic and viscoelastic. This chapter reviews the basic notions of physical acoustics which are necessary to tackle the problem of the ultrasonic propagation in bone, in the perspective of the application of quantitative ultrasound (QUS) techniques to bone characterization. The first section introduces the basic phenomena related to the field of medical ultrasound. Basic description of wave propagation is introduced. Mechanical bases are necessary to understand the elastodynamic nature of the interaction between bone and ultrasound. The physical determinants of the speed of sound of the different types of waves corresponding to the propagation in a liquid and in a solid are considered. The effects of boundary conditions (guided waves) are also detailed. The second section describes the physical interaction between an ultrasonic wave and bone tissue, by introducing reflection/refraction, attenuation and scattering phenomena.

Keywords Absorption · Anisotropy · Attenuation · Compression wave · Diffraction · Elastic modulus · Elastic solid · Group velocity · Guided wave · Impedance · Kramers Krönig · Lamb waves · Phase velocity · Poisson's ratio · Reflection · Refraction · Scattering · Shear wave · Snell's law · Speckle · Speed of sound · Stiffness · Strain · Stress · Young's modulus

2.1 Fundamentals of Ultrasound

In analogy to visible and ultraviolet light, the terms sound and ultrasound are used to describe the propagation of a mechanical perturbation in different frequency ranges. Ultrasound corresponds to a mechanical wave propagating at frequencies

P. Laugier (✉)
Université Pierre et Marie Curie, CNRS, Laboratoire d'Imagerie Parametrique,
15, rue de L'Ecole de Medecine, 75006 Paris, France
e-mail: pascal.laugier@upmc.fr

G. Haïat
CNRS, B2OA UMR 7052, 10, avenue de Verdun, 75010 Paris, France
e-mail: guillaume.haiat@univ-paris-est.fr

P. Laugier and G. Haïat (eds.), *Bone Quantitative Ultrasound*,
DOI 10.1007/978-94-007-0017-8_2,

above the range of human hearing (conventionally 20 kHz). Ultrasound and sound waves propagate in fluids (gases and liquids) and solids. The mechanical perturbation provokes tiny disturbances of the medium particles from their resting position. These disturbances induce a displacement of these particles and are transmitted step by step to other parts of the medium. The interaction between the particles can be schematically described using a mechanical spring analogy. In particular the wave propagation depends on the intrinsic elastic properties of the medium as well as on its mass density. For tiny perturbations (linear propagation regime), no mass is transported as the wave propagates from point to point: the medium as a whole remains stationary. In depth analysis of some aspects of non-linear propagation regimes will be provided in Chap. 15.

Perfect fluids (i.e. non viscous) support bulk compression waves only, which are characterized by density changes of the medium in which the particles oscillate in the longitudinal direction or the direction of wave propagation. Thus, bulk compression waves correspond to longitudinal waves. Moreover, bulk compression elastic waves can also propagate in solids. However, in solids unlike in fluids, a shearing strain produced at some point can be transmitted to adjacent layers by the strong binding between particles. This mechanism generates transverse waves also called bulk shear waves, for which the particle motion is perpendicular to the direction of propagation in the case of isotropic solids (refer to subsection 1.5.3 for the anisotropic case).

Biological soft tissues are viscoelastic solids, where both bulk compression and shear waves can propagate. However, typically, in soft tissues, ultrasound bulk shear waves are usually neglected because shear waves are highly attenuated at ultrasonic frequencies. However, in hard tissues like bone, both compression and shear waves must be considered.

The reader will find in what follows basic descriptions of elementary aspects of the physics of ultrasound. However, the aim of the authors only consists in introducing the basic description of fundamental phenomena involved in ultrasonic characterization of bone. Readers interested in deeper and more complete description of the acoustics of wave are referred to dedicated books [1–4].

2.1.1 Frequency–Period–Wavelength

As known from basic physics the characteristic variables describing the propagation of a monochromatic wave in time and space are frequency f or period T and wavelength λ given by:

$$\lambda = \frac{c}{f} = cT, \tag{2.1}$$

where c is the wave propagation velocity (also termed sound velocity or speed of sound). Typical diagnostic ultrasound devices employ frequencies in the range of 2–15 MHz. In contrast, due to the frequency dependence of ultrasound attenuation and to high attenuation values in bone, lower frequencies in the range of 250 kHz to

1.25 MHz are used in bone clinical devices, although higher frequencies have been tested experimentally, for example to investigate cancellous bone micro-structure [5] or to measure microelastic properties of cortical bone [6].

In cortical bone a typical sound velocity of $4000\,\mathrm{m}\cdot\mathrm{s}^{-1}$ results in a wavelength of 16 mm at 250 kHz and of 4 mm at 1.0 MHz. A representative value of sound velocity in cancellous bone of the human calcaneus is $1500\,\mathrm{m}\cdot\mathrm{s}^{-1}$ resulting in a wavelength of 3.1 mm at 500 kHz.

2.1.2 Phase Velocity–Group Velocity

Two fundamentally different sound velocities can be distinguished. Phase velocity corresponds to the propagation velocity of a given phase that is of a single frequency component of a periodic wave. A propagating medium is said to be dispersive if the phase velocity is a function of frequency or wavelength, which is the case for example in all attenuating media. This means that the different frequencies contained in the signal do not propagate at a constant velocity, which derive from the linearity and causality principles (see Chap. 12). Group velocity corresponds physically to the velocity at which energy or information is conveyed along the direction of propagation. In the case of a dispersive medium, the group velocity may differ from the phase velocity. It is important to be aware of velocity dispersion because it potentially affects the accuracy of speed of sound measurements [7–10]. Note that the attenuation coefficient and velocity dispersion are related through the Kramers-Krönig relationships [11, 12].

2.1.3 Notion of Stress

A stress is defined by a force per unit area applied to a given medium. Any stress applied to a solid can be expressed as a combination of pure compression and pure shear stresses [1]. If the solid is anisotropic the combination of compression and shear stresses can be described in terms of a stress matrix (also called stress tensor). In contrast, fluids only support pure compression stress, which is called pressure. A compression wave propagating in fluids or in isotropic solid media produces compressions and expansions, which causes pressure changes. The instantaneous value of the total pressure minus the ambient pressure is then called acoustic pressure or simply sound pressure. In contrast, shear wave causes shear stress.

We shall assume that the stress can be expressed in one-dimensional form and that therefore the waves are either purely longitudinal or purely transversal. This approach allows for a much simpler (but correct) description of the propagation phenomena. The description adopted for isotropic media can then be modified to take into account bone anisotropy (see for example Chap. 8).

2.1.4 Acoustic Impedance

During the propagation of an acoustic wave in a fluid, the particles of the medium are subject to displacements around their resting positions. The velocity of these displacements is called acoustic particle velocity and noted v. Thus, the particle velocity is the speed of motion of the particles due to the sound wave, it must be distinguished from the sound velocities defined in Sect. 1.2. For plane waves in a lossless medium (non-attenuating medium), the sound pressure p and particle velocity v are related to each other following :

$$p = \rho c v = Z v, \tag{2.2}$$

where ρ is the mass density of the medium at rest, and $Z = \rho \cdot c$ is called specific acoustic impedance.

2.1.5 Acoustic Intensity

The energy transported in an ultrasound wave is usually characterized by an acoustic intensity I defined as the energy transmitted per unit time (usually 1 s) and per unit area (usually $1\,\mathrm{cm}^2$) in the direction normal to the considered area. In the field of medical ultrasound, intensity is measured in $\mathrm{W}\cdot\mathrm{cm}^{-2}$. In the far field of an unfocused transducer where the wave front can be considered as a planar wave or at the focus of a focused transducer, the intensity of a monochromatic wave is related to the sound pressure as follows:

$$I = \frac{p^2}{2Z}. \tag{2.3}$$

2.1.6 Determinant of the Speed of Sound

In the linear propagation regime (tiny perturbation or small wave amplitude) speed of sound is a characteristic of the medium. It is independent from the wave amplitude and can be determined from the material and geometrical properties of the medium. To account for wave type, for example bulk compression, bulk shear, surface, or guided wave specific differences in c, the generalized concept of an effective elastic modulus M_e and an effective mass density ρ_e can be introduced [13]. The effective elastic modulus is related to elastic and geometrical characteristics of the medium, which determine the stiffness with respect to a given type of wave. The effective mass density is related to the inertia of the propagating medium. Following this concept c is expressed as:

$$c = \sqrt{\frac{M_e}{\rho_e}}. \tag{2.4}$$

A common correction in realistic systems is that speed of sound can also depend on the amplitude of the wave, leading to a nonlinear wave propagation (Chap. 15).

2.1.6.1 Case of a Fluid

In fluids, M_e is given by the adiabatic bulk modulus of elasticity K, the reciprocal of the adiabatic compressibility χ. The effective mass density ρ_e is the mass density of the fluid. The propagating waves are pure compression waves. K physically corresponds to the force opposing compression of the fluid. Compressibility is the relative change in volume when the pressure changes by one unit. A fluid model is generally adopted to describe waves at ultrasonic frequencies in soft tissue.

Of interest is the temperature dependence of c. Speed of sound in water is $1482\,\mathrm{m}\cdot\mathrm{s}^{-1}$ at 20°C. Between 20°C and 37°C it increases with a temperature coefficient of about $2.5\,\mathrm{m}\cdot\mathrm{s}^{-1}\cdot{}^{\circ}\mathrm{C}^{-1}$ [14]. As soft tissues are largely composed of water, it is not surprising that their speed of sound also increases with temperature. Fat is the exception. Speed of sound in fat decreases when temperature increases [15]. The observed temperature dependent decrease of c of trabecular bone marrow is also likely due to the influence of fat, an important component of bone marrow [16].

2.1.6.2 Case of an Infinite Isotropic Homogeneous Elastic Solids

For solids, M_e is given by a combination of the elastic properties. In general, this combination can be expressed using the different components of the elastic stiffness tensor (or matrix), noted c_{ij} and called stiffness coefficients. The stiffness coefficients are defined by the linear coefficients of proportionality between the different components of the stress and strain matrixes [17]. An isotropic homogeneous elastic solid can be equivalently described by:

- Two stiffness coefficients c_{11} and c_{12}
- The Lamé coefficients λ (bulk modulus, not to be confused with the wavelength) and μ (shear modulus)
- Two engineering constants such as E (Young's modulus) and ν (Poisson's ratio)

The Lamé coefficients (λ, μ) can be expressed as a function of the stiffness coefficients (c_{11}, c_{12}) or as a function of the engineering constants (E, ν). Similarly, the stiffness coefficients are related to the engineering constants. The full derivation of the wave propagation equation in anisotropic elastic solids is out of the scope of this chapter. Readers can find a comprehensive description in many classical textbooks, for example [1,2,17]. We only indicate in the following the principle of derivation of the wave propagation equation for the case of an isotropic linear elastic solid. Three equations are necessary to obtain the linear propagation equation in an isotropic solid. The first equation, corresponding to the constitutive law (Hooke's law) of the isotropic material considered, expresses the general relationship existing between

stress and strain in a perfectly elastic solid:

$$\sigma = \lambda \cdot tr(\varepsilon) + 2\mu\varepsilon, \tag{2.5}$$

where σ denotes the stress tensor, ε the strain tensor and tr(ε) is the trace of ε. The second equation corresponds to the equation of motion and is given by:

$$\rho \frac{\partial^2 u}{\partial t^2} = div(\sigma), \tag{2.6}$$

where ρ denotes the mass density of the solid, u denotes the elementary particle displacement vector and *div* the divergence operator ($div = \frac{\partial}{dx} + \frac{\partial}{dy} + \frac{\partial}{dz}$).

The last equation relates the strain tensor with the displacement field and is given by:

$$\varepsilon = \frac{1}{2}(grad(u) +^T grad(u)), \tag{2.7}$$

where grad indicates the gradient tensor and $^{\mathrm{T}}$ indicates the transpose operation. By combining Eqs. 2.5–2.7 and considering respectively the case where the particle displacement is parallel and perpendicular to the direction of propagation, the wave propagation equations corresponding to the case of a longitudinal and shear wave mode are obtained and are given respectively by:

$$\rho \frac{\partial^2 u}{\partial t^2} = (\lambda + 2\mu) \cdot \Delta u \text{ and } \rho \frac{\partial^2 u}{\partial t^2} = \mu \cdot \Delta u \tag{2.8}$$

where Δ denotes the Laplacian operator: $\Delta = \frac{\partial^2}{dx^2} + \frac{\partial^2}{dy^2} + \frac{\partial^2}{dz^2}$.

In summary, in an infinite isotropic homogeneous solid body, in which the propagating wave does not interact with the boundary of the medium, the longitudinal and shear (transversal) propagation velocity c_l and $c_s$are given by [1]:

$$c_l = \sqrt{\frac{\lambda + 2\mu}{\rho}} = \sqrt{\frac{c_{11}}{\rho}} = \sqrt{\frac{E(1-\nu)}{\rho(1+\nu)(1-2\nu)}} \tag{2.9}$$

and

$$c_s = \sqrt{\frac{\mu}{\rho}} = \sqrt{\frac{c_{11} - c_{12}}{2\rho}} = \sqrt{\frac{E}{\rho(1+\nu)}} \tag{2.10}$$

2.1.6.3 Infinite Anisotropic Homogeneous Elastic Solids

In homogeneous anisotropic media, the elastic properties depend on the direction of propagation of the acoustical wave. For example, in crystalline materials, the elastic properties (and thus the sound velocities) depend on the orientation of the crystalline directions relative to the direction of propagation. In this case, M_e

depends on the direction of propagation, wave polarization (the direction of particle displacement with respect to propagation direction) and crystal class of symmetry. For an arbitrary direction in a crystal, three wave types can generally propagate: one quasi-longitudinal and two quasi-transverse waves. However, there are special directions called symmetry axes along which pure longitudinal or shear waves propagate. Details of the relationships between sound velocity and elastic coefficients for infinite anisotropic elastic solids are beyond the scope of this chapter and can be found in reference books on elastic waves in solids [1–3].

For cortical bone the general degree of anisotropy is that of orthotropic material symmetry [18], which is characterized by nine independent stiffness coefficients. A simplified model of a transverse isotropic elastic solid medium, which reduces the number of independent coefficients of the stiffness matrix to five, has also been considered [19–23]. The directional dependence of engineering elastic moduli such as E or σ can then be derived from the stiffness coefficients. These assumptions about bone symmetry were used successfully in studying in vitro ultrasound propagation along the various symmetry axes of cortical bone specimens [18, 21, 24, 25].

2.1.6.4 Finite Homogeneous Elastic Solids

Equations 2.9 and 2.10 were introduced for unbounded media assuming that the wavelength λ is much smaller than the smallest sample dimension. In the opposite case (e.g., when the propagation medium is thin compared to λ), multiple reflections, mode conversions and interferences of longitudinal and shear waves from the sample boundaries occur. These phenomena create a wave guide character of the sound propagation within boundaries of the considered medium. In this case, sound perturbations can be represented as superposition of resonant guided wave modes (so-called eigen modes).

Guided wave modes which exist in plates are known as Lamb waves, which are complex waves traveling through the entire plate. Different families of Lamb wave modes can be distinguished including symmetrical modes (in-phase displacements of opposite plate surfaces) and asymmetrical or flexural modes (anti-phase displacements of opposite plate surfaces), as shown in Fig. 2.1.

Guided wave modes have been described for rods [3] as well as for tubes [26]. Guided wave modes are always dispersive, which means that their phase velocities are function of the wavelength (or frequency) and of the layer thickness.

Fig. 2.1 Illustration of symmetrical and asymmetrical guided wave modes propagating through the entire thickness of a plate

In addition, phase velocity is also function of the elastic properties and density of the medium [27].

The wave guide character of the sound propagation has been evidenced for cortical bone in the 0.25–2 MHz frequency range. In this case, cortical bone can be modeled as a plate-like (2-D description) or a tube-like (3-D description) layered medium [27, 28].

A particular case of guided wave is the extensional or bar wave in a thin rod, a configuration which has been used to measure the properties of cortical bone. Under the assumption that the cross-sectional dimensions of the rod (in the case of a cylindrical rod, its diameter) are much smaller than λ, only a longitudinal stress component can be considered along the propagation direction of the rod. In this case, the speed of sound c is given by [13]:

$$c = \sqrt{\frac{E}{\rho}} \Leftrightarrow E = \rho\, c^2 \tag{2.11}$$

For in vivo measurements purposes, guided waves in cortical bone can be excited from the surrounding soft tissues using an incident beam at a specific angle [28]. If a wave is guided by the bone cortex with a phase velocity greater than that of the compression wave of the surrounding soft tissues, the energy propagating in the bone cortex can leak into the soft tissue. Thus, power is continuously radiated into the soft tissues, the guided wave mode can be detected and its velocity measured with sensors placed at its surface. A comprehensive review of guided waves used to investigate cortical bone is given in Chap. 7.

2.1.6.5 Inhomogeneous Elastic Solids

In the sections above, the sound wave propagation was restricted to homogeneous elastic solids. However, bone is highly heterogeneous at different scales, and can be described by a composite and poroelastic material. The derivation of M_e for composite or poroelastic materials may be rather complex and requires cumbersome theoretical developments. Moreover, due to the important difference in porosity and structure between cortical and trabecular bone, the analysis of ultrasound propagation may require different theoretical frameworks for these two types of bone structures.

As the medium is no longer homogeneous but rather a mixture of several components such as collagen fibers, hydroxyapatite crystals, water, non-collagen substance and marrow, which are all characterized by different elastic coefficients, it remains difficult to simply determine M_e. Replacing the actual material by a homogenized material is the best we can expect. M_e can then be determined assuming that λ is much larger than d, where d is the characteristic size of the structural heterogeneities such as, for example, osteons, Haversian canals, osteocytes, lacunae, apatite crystals and collagen fibers. At the scale of the wavelength, the medium can then be considered homogeneous and therefore Eqs. 2.9 and 2.10 can be applied using the

homogenized stiffness coefficients. The effective elastic modulus and the effective mass density can be derived from experiments or theoretical models. Different multiscale homogenization approaches [20, 29–32] have been developed to determine a homogenized value for M_e, which is the only way to practically estimate the material properties at the scale of λ.

The porosity of human cortical bone is rather low and the pore size ($\sim$50 to 100 µm) is smaller than typical wavelengths (>1 mm). Therefore, the aforementioned homogenization theories can be applied and cortical bone can be modeled as a mono-phase homogeneous medium (rather than a two-phase medium) in regard to the ultrasonic propagation. Therefore, ultrasound propagation at diagnostic frequencies (around 1 MHz) in cortical bone can be described at first approximation by the propagation in an anisotropic homogeneous medium (see Chap. 13).

In contrast, such an assumption is not valid for cancellous bone where porosity values are rather high. The pore size ($\sim$500 to 1000 µm) is comparable to the wavelength (1.5 mm at 500 kHz). The elasticity of such a poroelastic structure then intrinsically depends on the structure of the bone. Several theoretical concepts considering poroelasticity such as Biot's theory [33–39] and Schoenberg's theory for multilayered media [40–44] have been applied to describe ultrasound propagation in cancellous bone. These models will be detailed in Chap. 5.

2.2 Tissue Interaction

2.2.1 Specular Reflection and Refraction

As known from basic physics, reflection and refraction occur at the boundary between two media with different characteristic acoustic impedances or different speeds of sound. If the surface is smooth compared to the wavelength, specular reflections occur whereas for rough surfaces, reflections are diffuse [45]. Specular reflection forms the basis of pulse-echo ultrasonic imaging (echography) and contributes to image formation displaying organ boundaries. It is convenient to distinguish fluid–fluid interfaces such as the discontinuity between two soft tissues, which is the typical model for diagnostic clinical ultrasound, and fluid-solid interfaces, which represent more realistically the boundary between soft tissue and cortical bone. The interaction between ultrasound and cancellous bone is more complicated. It can best be described by scattering phenomena, which will be discussed in Sect. 2.3. In what follows, we shall assume that the incident wave is a plane wave in the fluid for the sake of simplicity.[1]

[1] Any kind of wave may be decomposed in a sum of planar waves.

2.2.1.1 Fluid–Fluid Interface

If a plane wave impinges on a smooth plane interface (i.e. under the assumption of specular reflection), a reflected and a transmitted wave will be generated (see Fig. 2.2a). As only longitudinal waves can exist in a fluid, the refracted and reflected waves are also longitudinal. According to Snell's law, (i) the reflection angle θ_1 is equal to the angle of the incident wave and (ii) the transmitted wave is refracted away from the direction of the incident wave θ_1 at a refraction angle θ_2 given by:

$$\frac{\sin\theta_2}{c_2} = \frac{\sin\theta_1}{c_1}, \tag{2.12}$$

where and c_1 and c_2 are the sound velocities of the first and second medium.

For normal incidence ($\theta_1 = 0^\circ$), the reflected and transmitted waves are also normal to the interface. The ratio of the reflected to the incident acoustic pressure amplitude is called amplitude reflection coefficient r. The ratio of the transmitted to the incident acoustic amplitude is called amplitude transmission coefficient t. Coefficients t and r are given by:

$$r = \frac{Z_1 - Z_2}{Z_1 + Z_2} \quad t = \frac{2Z_2}{Z_1 + Z_2}. \tag{2.13}$$

Similarly intensity reflection (R) and transmission coefficients (T) are defined by the ratio of the reflected to the incident acoustic intensity and the ratio of the transmitted to the incident acoustic amplitude, respectively:

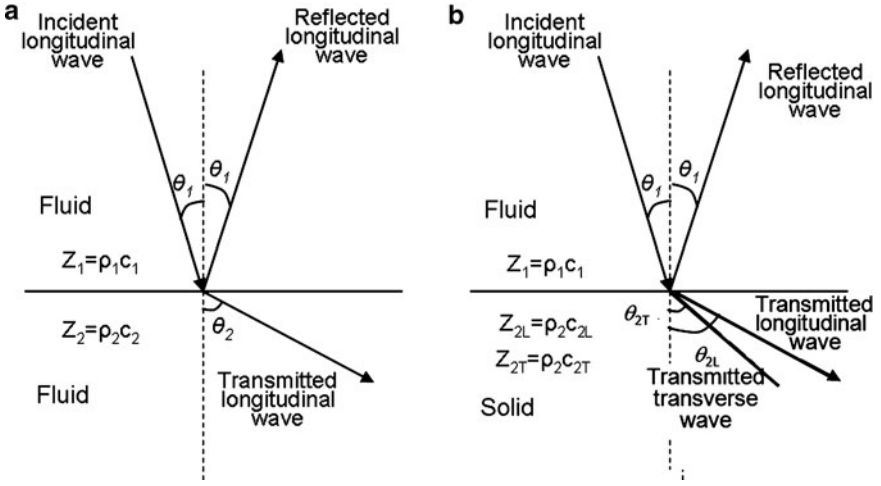

Fig. 2.2 Reflection and refraction at the boundary (**a**) between two fluid media and (**b**) between a fluid and a solid medium

Table 2.1 Typical values for sound velocity, characteristic acoustic impedance, and attenuation (see next section) in different biological tissues for temperatures in the range between 20°C and 37°C. These values are only indicative of the order of magnitude, due to dramatic biological variability

Tissue	Ultrasound propagation velocity c $(m \cdot s^{-1})$	Characteristic acoustic impedance Z $(kg \cdot s^{-1} \cdot m^{-2})$	Slope of the attenuation coefficient $(dB \cdot cm^{-1} \cdot MHz^{-1})$
Water (20°C)	1480	1.48×10^6	[a]
Cancellous bone	1450–1800	$1.54 \times 10^6 - 2.2 \times 10^6$	10–40
Cortical bone	3000–4000	$4 \times 10^6 - 8 \times 10^6$	1–10
Fat	1450	1.38×10^6	0.8
Muscle	1550–1630	$1.65 \times 10^6 - 1.74 \times 10^6$	0.5–1.5
Skin	1600	1.7×10^6	2–4

[a] The attenuation in water exhibits a quadratic variation with frequency f. Its attenuation coefficient in $dB \cdot cm^{-1}$ is $\alpha(f) = 0.002f^2$

$$R = \left(\frac{Z_1 - Z_2}{Z_1 + Z_2}\right)^2 \quad T = \frac{4Z_1Z_2}{(Z_1 + Z_2)^2}. \tag{2.14}$$

where Z_1 and Z_2 are the characteristic acoustic impedances of the first and second medium for longitudinal waves, respectively. One can verify that $T + R = 1$, which corresponds to the conservation of energy equation (in the lossless case). The amount of energy in the reflected wave depends on the impedance discontinuity of the two media. The greater the difference, the greater is the reflected energy.

Table 2.1 shows the different values of sound velocity, of acoustic impedance, and of the slope of the attenuation coefficient as a function of frequency for selected tissues playing a part in bone QUS evaluation. As can be seen, for soft tissues Z differs only slightly from that of water. In case of small impedance discontinuities (e.g., such as between two soft tissues), the reflected beam typically carries less than 1% of the incident energy and 99% or more of the incident energy is transmitted through the interface. Because of relatively small velocity changes in various soft tissues, refraction is generally not a serious problem.

2.2.1.2 Fluid–Solid Interface

In the case where the second medium is a solid such as cortical bone, Eq. 2.13 represents the ideal case for normal incidence and serves as guidelines to determine the reflected and transmitted energies. When ultrasound strikes a cortical bone interface at normal incidence, approximately 25–50% of the incident energy is transferred to the reflected wave and only 75–50% to the refracted longitudinal wave.

For oblique incidence the refracted longitudinal plane wave in the solid is partially converted into a shear wave, and two refracted beams exist, as shown in

Fig. 2.2b. For oblique incidence Snell's law must be generalized to [1]:

$$\frac{\sin(\theta_1)}{c_1} = \frac{\sin(\theta_{2L})}{c_{2L}} = \frac{\sin(\theta_{2T})}{c_{2T}}, \tag{2.15}$$

where subscripts 2L and 2T refer respectively to the refracted longitudinal and shear waves in the solid medium (e.g., bone). As longitudinal waves in solids propagate most of the time with a greater sound speed than in fluids, the refraction angle θ_{2L} is larger than the angle of incidence θ_I. When θ_I is higher than a certain value θ_c, total internal reflection occurs and the longitudinal wave is no longer transmitted into the solid. The refracted wave is termed evanescent as it travels parallel to the interface and decays exponentially from the boundary. The corresponding incident angle θ_c is termed the first critical angle and is given by:

$$\sin(\theta_c) = \frac{c_1}{c_{2L}}. \tag{2.16}$$

The value of longitudinal wave velocity in cortical bone stands in the range 3500–4200 $\mathrm{m \cdot s^{-1}}$ (see Chap. 13), which gives typical values of θ_c between 20° and 25°.

If the velocity of the shear wave in the solid is also greater than the velocity of the longitudinal wave in the fluid then analogously there is a second critical angle at which the shear refracted beam propagates along the surface. Actually, the propagation of sound waves in solids is even more complicated and several critical angles may exist [1, 17]. The measurement of critical angles is the basis of ultrasound critical-angle reflectometry (UCR), which has been used to characterize bone in vitro as well as in vivo [46–48]. In UCR, the sound velocities of the longitudinal and the shear waves in cortical bone can directly be determined from θ_c according to Snell's law if the speed of sound of the surrounding fluid (or soft tissue) is known precisely.

2.2.2 Attenuation

Two main mechanisms contribute to ultrasound attenuation: absorption and scattering. Different mechanisms are responsible for absorption phenomena (thermal conductance effects, chemical effects, viscous effects, non linearity ...). So far, the phenomena responsible for ultrasound absorption in biological tissues have not been completely understood. In liquids (respectively homogeneous solids), the viscous (respectively viscoelastic) forces between neighboring particles moving with different velocities are major sources of acoustic wave absorption. For example, viscous losses may explain sound wave absorption in water where attenuation varies with the square of the frequency. However, this model of viscosity (quadratic dependence of the attenuation coefficient versus frequency) does not explain experimental mea-

surements of absorption in soft biological tissues as well as in bone in the diagnostic frequency range.

Other models hypothesized that a significant fraction of the absorption of longitudinal waves in soft tissues involves a spectrum of relaxation mechanisms at the macromolecular scale of proteins [49] or potentially thermal transport phenomena arising from temperature gradients in the medium [50]. In the frequency range where characteristic relaxation times are close to the wave time period, a quasi-linear variation of the attenuation coefficient with frequency can be observed.

Attenuation differs substantially between fluid-like soft tissues and porous media such as bone, in which (i) viscous friction effects due to the relative motion of marrow and solid frame, (ii) scattering of the ultrasonic wave by bone heterogeneity and (iii) longitudinal to shear mode conversion contribute significantly. The mechanisms of scattering will be presented in the next section. Acoustic attenuation in cancellous bone is usually almost one order of magnitude higher than in cortical bone. This is likely due to the large bone surface-to-volume ratio, which reinforces scattering, mode conversion and viscous friction. Recent studies suggest that loss mechanisms such as mode conversion, that is the transformation of longitudinal waves into shear waves (and subsequent absorption of these shear waves) occurring at the surface of the scattering particles, may be a significant contributor to the overall attenuation in bone in the diagnostic frequency range [51, 52].

Further important factors that contribute to the total wave intensity attenuation as it propagates through a complex medium such as a limb composed of several layers of different media (surrounding soft tissues, bone, marrow) are diffraction, reflection and refraction. Due to diffraction phenomena, the acoustic beam emitted from a planar (unfocused) transducer will increase its diameter as the wave propagates and the intensity will decrease with increasing distance from the source. Reflection and refraction losses at tissue interfaces according to Eq. 2.13 depend on the impedance mismatch at the interfaces. In general, overall ultrasound attenuation is characterized by the following exponential decrease of the pressure amplitude p and of the amplitude of the acoustic intensity I with the traveling distance z:

$$p = p_0 e^{-\alpha z} \text{ and } I = I_0 e^{-2\alpha z} \tag{2.17}$$

where p_0 and I_0 are the pressure and intensity at $z = 0$, respectively. The quantity α (expressed in cm^{-1}) is the pressure frequency-dependent attenuation coefficient. The factor 2 in the exponential term of the intensity equation results from transforming pressure into intensity, as intensity is proportional to the square of pressure. In biomedical ultrasonics, the commonly used units for α and for its slope when plotted versus frequency are $\text{dB} \cdot \text{cm}^{-1}$ and $\text{dB} \cdot \text{cm}^{-1} \cdot \text{MHz}^{-1}$, respectively. The unit conversion cm^{-1} to $\text{dB} \cdot \text{cm}^{-1}$ writes [53]:

$$\alpha[dB \cdot cm^{-1}] = \frac{1}{z} \cdot 10 \ln \frac{I_0}{I} = 8.686 \alpha[cm^{-1}] \tag{2.18}$$

Some authors use α as the intensity frequency-dependent attenuation coefficient ($I = I_0 e^{-\alpha z}$). Then, the conversion to dB results in $\alpha[\mathrm{dB \cdot cm^{-1}}] = 4.343\alpha[\mathrm{cm^{-1}}]$.

2.2.3 Tissue Penetration

It has been shown experimentally that ultrasound attenuation in biological tissues varies approximately linearly with frequency [54]. The linear dependency has been documented for soft tissues over a broad frequency range from 1 to 50 MHz and also for cancellous bone in a limited frequency range of 0.2–2 MHz [55–59]. Since attenuation in tissues increases with frequency, the price paid for using shorter wavelengths (that is for improving spatial resolution) is an increase in attenuation, which limits the possible penetration depth due to the sensitivity of the sensor. For most soft tissues, values of the slope of the attenuation coefficient versus frequency are approximately comprised in the range $0.5–1.0\,\mathrm{dB \cdot cm^{-1} \cdot MHz^{-1}}$ (see Table 2.1). In bone, the slope of the attenuation coefficient is one or two orders of magnitude higher than in soft tissues. Hence, lower frequencies (around 0.5–1 MHz) are commonly used for skeletal investigations.

2.2.4 Scattering

Scattering phenomena result from the interaction between a primary ultrasonic wave and the boundaries of particles (inhomogeneities) if their physical properties such as density or elasticity are different from those of the surrounding medium. In this case, the oscillatory movement of the scatterer is different from that of the surrounding medium, which leads to the emission of a secondary wave denoted scattered wave.

The scattering regime of a single particle depends on the ratio between its dimension and λ. If λ is much smaller than the size of the heterogeneity, specular reflection obeying the usual laws of reflection occurs (see Eq. 2.13). In contrast, a scattered wave is created if the dimensions of the heterogeneities are comparable to or lower than the wavelength. The scattering problem of light and sound by small scatterers was first solved by Lord Rayleigh [60] and is therefore called Rayleigh scattering. For scatterers much smaller than the wavelength, the intensity of the scattered waves is proportional to the fourth power of the frequency of the incident wave. It is also proportional to the sixth power of the size of the scatterers, i.e., to the square of its volume [61]. The case of scatterers with larger sizes or sizes comparable to the wavelength involves more complicated calculations [61].

The scattered intensity from soft tissue is generally considerably smaller than the specularly reflected intensity from organ boundaries. However, similar to specular reflection, such scattering events are of primary importance for image formation and for assessing micro-structural properties of the medium such as scatterer size of scatterer number density. In ultrasound images of soft tissues, scattering causes the grainy aspect or echostructure, also denoted speckle.

In soft tissue, the density and compressibility of scatterers are close to those of the surrounding medium. Thus the contribution of scattering to overall attenuation is relatively small. At low MHz frequencies, attenuation by scattering in soft tissue is typically 10–15% of the total attenuation [62]. In contrast, scattering is likely to be an important attenuation mechanism in bone. Although scattering from bone has received less attention than attenuation and sound velocity, its study is important because it may explain mechanisms responsible for attenuation [51] and for velocity dispersion [63]. Ultrasonic scattering predominantly occurs in cancellous bone in comparison to cortical bone. Cancellous bone can be considered as a highly inhomogeneous scattering medium: a soft tissue-like medium, i.e. bone marrow, containing a solid matrix, i.e. mineralized collagen of interconnected trabecular elements with a mean thickness ranging from 50 to 150 µm. Trabeculae are likely candidates for scattering sites due to the high contrast in acoustic properties between mineralized tissue and marrow [64]. Various scattering models for trabecular bone have been proposed and will be extensively presented in Chap. 6.

References

1. D. Royer and E. Dieulesaint, *Elastic Waves in Solids I* (Springer, New York, 2000).
2. B. A. Auld, *Acoustic Fields and Waves in Solids* (Krieger Pub Co, New York, 1990).
3. J. D. Achenbach, *Wave Propagation in Elastic Solids* (Elsevier, Amsterdam, 1973).
4. S. Temkin, *Elements of Acoustics* (John Wiley & Sons Inc, New York, 1981).
5. M. A. Hakulinen, J. S. Day, J. Toyras, H. Weinans, and J. S. Jurvelin, "Ultrasonic characterization of human trabecular bone microstructure," Phys Med Biol. **51**(6), 1633–1648 (2006).
6. K. Raum, "Microelastic imaging of bone," IEEE Trans Ultrason Ferroelectr Freq Control **55**(7), 1417–1431 (2008).
7. G. Haïat, F. Padilla, R. Barkmann, S. Dencks, U. Moser, C.-C. Glüer, and P. Laugier, "Optimal prediction of bone mineral density with ultrasonic measurements in excised human femur," Calcif Tissue Int **77**(3) (2005).
8. G. Haïat, F. Padilla, R. O. Cleveland, and P. Laugier, "Effects of frequency-dependent attenuation and velocity dispersion on in vitro ultrasound velocity measurements in intact human femur specimens," IEEE Trans Ultrason Ferroelectr Freq Control **53**(1), 39–51 (2006).
9. K. A. Wear, "The effects of frequency-dependant attenuation and dispersion on sound speed measurements: applications in human trabecular bone," IEEE Trans Ultrason Ferroelectr Freq Control **47**(1), 265–273 (2000).
10. K. A. Wear, "A numerical method to predict the effects of frequency-dependent attenuation and dispersion on speed of sound estimates in cancellous bone," J Acoust Soc Am **109**(3), 1213–1218 (2001).
11. M. O'Donnell, E. T. Jaynes, and J. G. Miller, "General relationships between ultrasonic attenuation and dispersion," J Acoust Soc Am **63**(6) (1978).
12. M. O'Donnell, E. T. Jaynes, and J. G. Miller, "Kramers-Kronig relationship between ultrasonic attenuation and phase velocity," J Acoust Soc Am **69**(3), 696–701 (1981).
13. V. Shutilov, *Fundamental Physics of Ultrasound* (Gordon and Breach, New York, 1988).
14. N. Bilaniuk and G. S. K. Wong, "Speed of sound in pure wateras a function of temperature," J Acoust Soc Am **93**(3), 1609–1612 (1993).
15. S. A. Goss, R. L. Johnston, and F. Dunn, "Comprehensive compilation of empirical ultrasonic properties of mammalian tissues," J Acoust Soc Am **64**(2), 423–457 (1978).
16. P. H. Nicholson and M. L. Bouxsein, "Effect of temperature on ultrasonic properties of the calcaneus in situ," Osteoporos Int **13**(11), 888–892 (2002).

17. G. S. Kino, *Acoustic Waves: Devised Imaging and Analog Signal* (Prentice Hall, Englewood Cliffs, 1987).
18. R. B. Ashman, S. C. Cowin, W. C. Van Buskirk, and J. C. Rice, "A continuous wave technique for the mesurement of the elastic properties of cortical bone," J Biomech **17**, 349–361 (1984).
19. J. L. Katz, "Anisotropy of Young's modulus of bone," Nature **283**, 106–107 (1980).
20. P. J. Arnoux, J. Bonnoit, P. Chabrand, M. Jean, and M. Pithioux, "Numerical damage models using a structural approach: application in bones and ligaments," Eur Phys J Appl Phys **17**, 65–73 (2002).
21. H. S. Yoon and J. L. Katz, "Ultrasonic wave propagation inhuman cortical bone - II. Measurements of elastic properties and microhardness," J Biomech **9**, 459–464 (1976).
22. G. Haiat, S. Naili, Q. Grimal, M. Talmant, C. Desceliers, and C. Soize, "Influence of a gradient of material properties on ultrasonic wave propagation in cortical bone: application to axial transmission," J Acoust Soc Am. **125**(6), 4043–4052 (2009).
23. E. Bossy, M. Talmant, and P. Laugier, "Three-dimensional simulations of ultrasonic axial transmission velocity measurement on cortical bone models," J Acoust Soc Am **115**(5 Pt 1), 2314–2324 (2004).
24. S. B. Lang, "Ultrasonic method for measuring elastic coefficients of bone and results on fresh and dried bovine bones," IEEE T Bio-med Eng **BME-17**(2), 101–105 (1970).
25. L. Serpe and J. Y. Rho, "The nonlinear transition period of broadband ultrasonic attenuation as bone density varies," J Biomech **29**, 963–966 (1996).
26. D. Gazis, "Three-dimensional investigation of the propagation of waves in hollow circular cylinders.II. Numerical Results," J Acoust Soc Am **31**(5), 573–578 (1959).
27. I. Viktorov, *Rayleigh and Lamb Waves* (Plenum, New York, 1967).
28. P. Moilanen, "Ultrasonic guided waves in bone," IEEE Trans Ultrason Ferroelectr Freq Control **55**(6), 1277–1286 (2008).
29. C. Hellmich and F. J. Ulm, "Micromechanical model for ultrastructural stiffness of mineralized tissues," J Eng Mech **128**(8), 898–908 (2002).
30. J. M. Crolet, B. Aoubiza, and A. Meunier, "Compact bone: numerical simulation of mechanical characteristics," J Biomech **26**(6), 677–687 (1993).
31. B. Aoubiza, J. M. Crolet, and A. Meunier, "On the mechanical characterization of compact bone structure using the homogenization theory," J Biomech **29**(12), 1539–1547 (1996).
32. C. Hellmisch and F. J. Ulm, "Micromechanical Model for Ultrastructural Stiffness of Mineralized Tissues," J Eng Mech **128**(8), 898–908 (2002).
33. A. Hosokawa, "Simulation of ultrasound propagation through bovine cancellous bone using elastic and Biot's finite-difference time-domain methods," J Acoust Soc Am **118**(3 Pt 1), 1782–1789 (2005).
34. A. Hosokawa and T. Otani, "Acoustic anisotropy in bovine cancellous bone," J Acoust Soc Am **103**(5), 2718–2722 (1998).
35. Z. E. Fellah, J. Y. Chapelon, S. Berger, W. Lauriks, and C. Depollier, "Ultrasonic wave propagation in human cancellous bone: application of Biot theory," J Acoust Soc Am **116**(1), 61–73 (2004).
36. E. R. Hughes, T. G. Leighton, G. W. Petley, P. R. White, and R. C. Chivers, "Estimation of critical and viscous frequencies for Biot theory in cancellous bone," Ultrasonics **41**(5), 365–368 (2003).
37. K. I. Lee, H. S. Roh, and S. W. Yoon, "Correlations between acoustic properties and bone density in bovine cancellous bone from 0.5 to 2 MHz," J Acoust Soc Am **113**(5), 2933–2938 (2003).
38. K. A. Wear, A. Laib, A. P. Stuber, and J. C. Reynolds, "Comparison of measurements of phase velocity in human calcaneus to Biot theory," J Acoust Soc Am **117**(5), 3319–3324 (2005).
39. J. L. Williams, "Ultrasonic wave propagation in cancellous and cortical bone: Prediction of experimental results by Biot's theory," J Acoust Soc Am **91**(2), 1106–1112 (1992).
40. E. R. Hubbuck, T. G. Leighton, P. R. White, and G. W. Petley, "A stratified model for ultrasonic propagation in cancellous bone," presented at the Joint meeting of the 16th International Congress on Acoustics and the 135th Meeting of the Acoustical Society of America, Seattle, Washington, June 20–26, 1998.

41. E. R. Hughes, T. G. Leighton, G. W. Petley, and P. R. White, "Ultrasonic propagation in cancellous bone: a new stratified model," Ultrasound Med Biol. **25**(5), 811–821 (1999).
42. W. Lin, Y. X. Qin, and C. Rubin, "Ultrasonic wave propagation in trabecular bone predicted by the stratified model," Ann Biomed Eng **29**(9), 781–790 (2001).
43. F. Padilla and P. Laugier, "Phase and group velocities of fast and slow compressional waves in trabecular bone," J Acoust Soc Am **108**(4), 1949–1952 (2000).
44. K. A. Wear, "A stratified model to predict dispersion in trabecular bone," IEEE Trans Ultrason Ferroelectr Freq Control **48**(4), 1079–1083 (2001).
45. A. Ishimaru, *Wave Propagation and Scattering in Random Media* (Wiley, NewYork, 1999).
46. P. P. Antich, J. A. Anderson, R. B. Ashman, J. E. Dowdey, J. Gonzales, R. C. Murry, J. E. Zerwekh, and C. Y. Pak, "Measurement of mechanical properties of bone material in vitro by ultrasound reflection: methodology and comparison with ultrasound transmission," J Bone Miner Res **6**(4), 417–426 (1991).
47. P. P. Antich, C. Y. C. Pak, J. Gonzales, J. A. Anderson, R. B. Ashman, K. Sakhaee, and C. Rubin, "Measurement of intrinsic bone quality in vivo by reflection ultrasound: correction of impaired quality with slow-release sodium fluoride and calcium citrate," J Bone Miner Res **8**(3), 301–311 (1993).
48. S. S. Mehta, P. P. Antich, M. M. Daphtary, D. G. Bronson, and E. Richer, "Bone material ultrasound velocity is predictive of whole bone strength," Ultrasound Med Biol **27**(6), 861–867 (2001).
49. J. C. Bamber, *Physical Principles of Medical Ultrasonics* (John Wiley & Sons, Chichester, UK, 1986).
50. K. S. Peat and R. Kirby, "Acoustic wave motion along a narrow cylindrical duct in the presence of an axial mean flow and temperature gradient," J Acoust Soc Am **107**(4), 1859–1867 (2000).
51. E. Bossy, F. Padilla, F. Peyrin, and P. Laugier, "Three-dimensional simulation of ultrasound propagation through trabecular bone structures measured by synchrotron microtomography," Phys Med Biol **50**(23), 5545–5556 (2005).
52. K. A. Wear, "Mechanisms for attenuation in cancellous-bone-mimicking phantoms.," IEEE Trans Ultrason Ferroelectr Freq Control **55**(11), 2418–2425 (2008).
53. T. L. Szabo, *Diagnostic Ultrasound*, Academic press series on biomedical engineering (Elsevier Academic Press, London, UK, 2004).
54. K. T. Dussik and D. J. Fritch, "Determination of sound attenuation and sound velocity in the structure constituting the joints, and of the ultrasonic field distribution with the joints of living tissues and anatomical preparations, both in normal and pathological conditions" (1956).
55. S. Chaffaï, F. Padilla, G. Berger, and P. Laugier, "In vitro measurement of the frequency-dependent attenuation in cancellous bone between 0.2–2.0 MHz," J Acoust Soc Am **108**, 1281–1289 (2000).
56. S. Han, J. Rho, J. Medige, and I. Ziv, "Ultrasound velocity and broadband attenuation over a wide range of bone mineral density," Osteoporosis Int **6**, 291–296 (1996).
57. C. M. Langton, S. B. Palmer, and S. W. Porter, "The measurement of broadband ultrasonic attenuation in cancellous bone," Eng Med. **13**(2), 89–91 (1984).
58. R. Strelitzki and J. A. Evans, "Diffraction and interface losses in broadband ultrasound attenuation measurements of the calcaneus," Physiol Meas **19**, 197–204 (1998).
59. K. A. Wear, "Ultrasonic attenuation in human calcaneus from 0.2 to 1.7 MHz," IEEE Trans Ultrason Ferroelectr Freq Control **48**(2), 602–608 (2001).
60. J. W. S. Rayleigh and R. B. Lindsay, *Theory of Sound* (Macmillan, London, UK, 1878).
61. P. Morse and K. Ingard, *Theoretical Acoustics* (Princetown University Press, Princetown, NJ, 1986).
62. J. C. Bamber, "Ultrasonic properties of tissue," in *Ultrasound in medicine*, F. A. Duck, A. C. Baker, and A. C. Starritt, eds. (Institute of Physics Publishing, Bristol, UK, 1998).
63. G. Haiat, A. Lhemery, F. Renaud, F. Padilla, P. Laugier, and S. Naili, "Velocity dispersion in trabecular bone: influence of multiple scattering and of absorption," J Acoust Soc Am **124**(6), 4047–4058 (2008).
64. K. A. Wear, "Frequency dependence of ultrasonic backscatter from human trabecular bone: theory and experiment," J Acoust Soc Am **106**(6), 3659–3664 (1999).

Chapter 3
Quantitative Ultrasound Instrumentation for Bone In Vivo Characterization

Pascal Laugier

Abstract Although it has been over 20 years since the first recorded use of quantitative ultrasound (QUS) technology to predict bone strength, the field has not yet reached its maturity. Among several QUS technologies available to measure cortical or cancellous bone sites, at least some of them have demonstrated potential to predict fracture risk in a number of clinical circumstances, with an equivalent efficiency compared to X-ray densitometry techniques, with the advantages of being non-ionizing, inexpensive, portable, highly acceptable to patients and repeatable. In this chapter, we review instrumental developments that have led to in vivo applications of bone QUS. While several proposals have been made for practical clinical use, there are a number of critical issues that still need to be addressed, such as quality control and standardization. On the other side, although still at an early stage of development, recent QUS approaches to assess bone quality factors seem very promising. These include guided waves to assess mechanical and structural properties of long cortical bones or new QUS technologies adapted to measure the central skeleton (hip). New data acquisition and signal processing procedures are prone to reveal bone properties beyond bone mineral quantity and to provide a more accurate assessment of bone strength.

Keywords Attenuation · Axial transmission · Bidirectional axial transmission · Bone quality · Bone strength · BUA · Calcaneus · Circumferential waves · Densitometry · Diffraction · Femur · Forearm · Fracture risk · Heel · Hip · Phalanges · Phase cancellation · QUS imaging · Radius · SOS · Tibia · Transverse transmission · Velocity dispersion

P. Laugier (✉)
Université Pierre et Marie Curie, CNRS, Laboratoire d'Imagerie Parametrique,
15, rue de L'Ecole de Medecine, 75006 Paris, France
e-mail: pascal.laugier@upmc.fr

P. Laugier and G. Haïat (eds.), *Bone Quantitative Ultrasound*,
DOI 10.1007/978-94-007-0017-8_3,

3.1 Introduction

Gold standard methods for the in vivo assessment of bone strength and of its clinical counterpart, the risk of fracture, are based on X-ray based bone mineral density (BMD) measurements [1]. While BMD is an important predictor of bone strength, additional factors are required to explain strength more accurately. These include tissue-intrinsic material properties and bone structure. Because ultrasound wave characteristics are closely linked to the material and structural properties of the propagation medium, ultrasound is appropriate to probe bone biomechanical strength.

In the past 20 years the field has produced a diversity of innovative ultrasound technological developments targeting in vivo characterization of bone strength.

The first clinical application to bone of ultrasound waves was described in the late 1950s for monitoring fracture healing at the tibia [2]. The introduction of quantitative ultrasound (QUS) methods in the field of osteoporosis followed the study published in 1984 by Langton et al. [3] demonstrating that the slope of the frequency-dependent attenuation at the calcaneus could discriminate osteoporotic from non-osteoporotic patients. This led to the opening of a new research and development area known as bone QUS. Many advances have been achieved during the last 20 years and a variety of different sophisticated technologies have been introduced to assess in vivo the skeletal status by providing measurements of ultrasonic parameters of cancellous bone or cortical bone sites such as the calcaneus [3], fingers phalanges [4], radius [5, 6], tibia [7] and proximal femur [8]. The absence of exposure to ionizing radiation, the portability and the modest cost of the machines are appealing factors of QUS devices. The main clinical field of application is fracture risk prediction for osteroporosis, although many other bone pathological conditions may benefit from ultrasound measurements. For example, fracture healing can be monitored using QUS axial transmission measurements as detailed in Chap. 14. The clinical validation for fracture risk prediction and the acceptance among clinicians is however not identical for all devices. Only heel QUS measures are proven to predict hip fractures and all osteoporotic fractures with similar relative risk as other central X-ray based bone density measurements [9–11].

This chapter is an introduction to the different devices that have been developed for in vivo assessment of skeletal status. It is common to classify the different approaches into two classes of devices which differ by their specific transducers arrangement. The transverse transmission techniques (Sect. 3.2), using a pair of transducers facing each other placed on each side of a skeletal site, provide estimates of the speed of sound $(\mathrm{SOS}, \mathrm{m\ s^{-1}})$ and frequency-dependent attenuation also termed in the QUS field broadband ultrasonic attenuation (BUA, dB/MHz). Modern axial transmission techniques (Sect. 3.3), directly inherited from the seminal work on fracture healing, use a specific measurement configuration in which the transducers are aligned along the bone axis to generate and measure guided waves in the cortical layer of long bone diaphysis. Because bone is a highly attenuating medium, most investigations use the transmission of low frequencies from 100 kHz to 2.0 MHz which is substantially lower than the clinical frequencies used in conventional ultrasonography of soft tissues. Other in vivo approaches based on

ultrasound reflection [12–17] or backscatter [18–20] are still confined to research work and will not be presented in this chapter. Some of these research aspects are covered in different chapters (Chaps. 6 and 10). Aspects such as modeling of ultrasound propagation (Chap. 8), in vitro experimental measurements (Chaps. 10–13) and clinical performances (Chap. 4) are covered by other chapters and thus are not addressed here.

3.2 Transverse Transmission

The transverse transmission technique uses two piezoelectric transducers, a transmitter and a receiver, placed on opposite sides of the skeletal site to be measured. While the calcaneus (heel bone) is the preferred skeletal site, the method has been applied for a while to the measurement at the finger phalanxes. More recently, devices has been introduced to measure the ultradistal radius at the forearm [6, 21] or the proximal femur at the hip [8, 22, 23].

Principles of measurements have been detailed in previous publications [24–26] and are only briefly recalled here for the sake of completeness.

3.2.1 Principles of Transverse Transmission Measurements

Assuming that the system response and the propagation are linear, the propagation characteristics such as attenuation and velocity are obtained using the well known substitution technique, illustrated in Fig. 3.1a and b. The signal transmitted through the skeletal site in response to a broadband ultrasonic excitation is compared to the signal transmitted through a reference medium such as water of known attenuation (α_{ref}) and speed of sound (c_{ref}). The frequency-dependent attenuation is obtained from the spectral analysis of the two signals shown in Fig. 3.1c, typically using a Fast Fourier Transform algorithm. The amplitude spectrum (Fig. 3.1d) of the received waveform that has propagated through the reference medium is given by:

$$\begin{aligned} A^{ref}(f) &= A_0(f)\,U^{ref}(f) \quad \text{with} \\ U^{ref}(f) &= A_d^{ref}(f)\,e^{-2i\pi f\frac{L}{c_{ref}}} \end{aligned} \tag{3.1}$$

$A_0(f)$ is the instrumentation transfer function describing the amplitude spectrum of the electrical input signal and the transfer functions of the transmitting and receiving transducers and of the electronics. The transfer function $U^{ref}(f)$ characterizes the ultrasound pulse propagation in the reference material. Its exponential term describes the propagation of a harmonic plane wave of wavelength λ_{ref}. The propagation depends on the frequency, the acoustic properties of the medium and the geometrical properties of the transmitting and receiving transducers. L is the distance between transmitter and receiver. $A_d^{ref}(f)$ is the transfer function of the

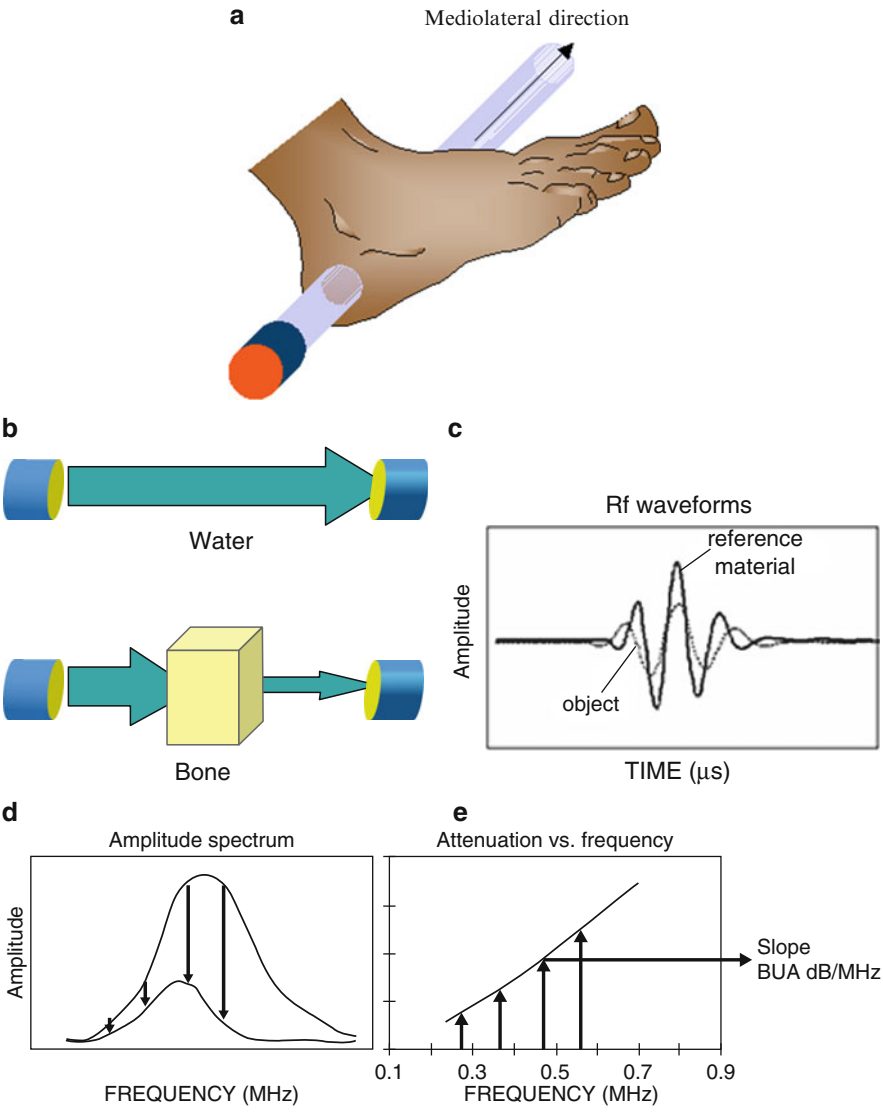

Fig. 3.1 Principles of transverse transmission at the heel (**a**): placement of transducers in the mediolateral direction, (**b**) and (**c**): substitution principle, example of radiofrequency traces recorded in water (*solid line*) and through the heel (*dashed line*) (**d**) amplitude spectra of the reference signal (*solid line*) and of the signal transmitted through the heel (*dashed line*) (**e**): frequency dependent attenuation

diffraction effect [24, 27], which cannot be described in details within the scope of this chapter. Typically water is used as reference material. In this case the ultrasonic attenuation at frequencies lower than 1 MHz, which are normally used in bone quantitative ultrasound, can be neglected.

After the initial reference measurement, a second measurement is performed on skeletal site to be investigated, that is the ultrasound propagates for example along a water-bone-water path. The amplitude spectrum of the received waveform is then given by:

$$A(f) = A_0(f)\,T(f)\,U(f) \quad \text{with}$$
$$U(f) = A_d(f)\; e^{-2i\pi f\left(\frac{L-l}{c_{ref}}+\frac{l}{c(f)}\right)}\; e^{-\alpha(f)l} \tag{3.2}$$

$T(f)$ is the product of the transmission coefficient for the reference material-sample and sample-reference material interfaces. The first exponential term of the transfer function $U(f)$ again describes the propagation of a harmonic plane wave. The term $e^{-\alpha(f)l}$ accounts for the attenuation of the skeletal part of a thickness l replacing an equivalent thickness of the reference material. $c(f)$ is the speed of sound in bone that may be frequency-dependent and $\alpha(f)$ is the frequency-dependent attenuation coefficient of the sample. $A_d(f)$ as before is the diffraction transfer function.

3.2.1.1 Frequency-Dependent Attenuation

The apparent frequency-dependent attenuation, that is the signal loss, is defined on a logarithmic scale as follows:

$$\hat{\alpha}(f)\,l = \ln\frac{|A^{ref}(f)|}{|A(f)|}, \tag{3.3}$$

where $\hat{\alpha}(f)$ is the measured apparent attenuation coefficient. Using Eqs. 3.2 and 3.3, it can be written as:

$$\hat{\alpha}(f)\,l = \alpha(f)\,l + \ln\frac{|A_d^{ref}(f)|}{|A_d(f)|} - \ln|T(f)| \tag{3.4}$$

where $|x|$ is the amplitude of a complex number x. In the frequency range used to make in vivo measurements of the human calcaneus, the ultrasonic attenuation varies quasi-linearly with frequency [28, 29] (Fig. 3.1e). The slope of a linear regression fit to $\hat{\alpha}(f)\,l$ in the frequency range of approximately 0.2–0.6 MHz yields the BUA value.

The extraction of an unbiased attenuation slope from the empirically determined signal loss in Eq. 3.3 assumes that (i) the effect of diffraction $(\ln|A_d^{ref}(f)| - \ln|A_d(f)|)$ is small and can be neglected [24, 30], (ii) transmission losses $(\ln|T(f)|)$ are independent of frequency (the effect of interface losses on the attenuation curve is a simple vertical offset which does not affect the slope estimate) [31] and (iii) phase cancellation effects are negligible, which is the case if the sample thickness and speed of sound across the ultrasonic beam profile are uniform. Overlapping of fast and slow waves may also cause phase cancellation [32–34]

(see Chap. 12) but is usually not a concern for in vivo measurements, at least at the heel. The measurements yield total loss through the intervening tissues in the beam, i.e., bone and surrounding soft tissues. The effect of the latter is generally neglected [25]. Not many devices actually provide an estimate of the bone thickness. Therefore the slope of the frequency-dependent attenuation (BUA) rather than the slope of the attenuation coefficient (i.e., normalized BUA by thickness) is measured.

3.2.1.2 Speed of Sound

Two principal approaches have been used to measure SOS. The first one assumes that c is frequency-independent and uses simple time domain methods. c is simply calculated from the difference of two time-of-flight (TOF) measurements one of the signal transmitted through the reference material alone and the other from the signal transmitted through the reference material and skeletal site:

$$\begin{aligned} &\text{reference material :} && TOF^{ref} = \frac{L}{c_{ref}} \\ &\text{reference material and sample :} && TOF = \frac{L-l}{c_{ref}} + \frac{l}{c} \\ &\text{difference signal :} && \Delta TOF = \frac{l}{c} - \frac{l}{c_{ref}} \end{aligned} \tag{3.5}$$

$$c = \frac{1}{\frac{1}{c_{ref}} + \frac{\Delta TOF}{l}} \tag{3.6}$$

If measurements are taken using probes in direct contact to the skin equation Eq. 3.6 reduces to:

$$c = \frac{l}{TOF} \tag{3.7}$$

Various criteria are used to estimate TOF, for example the first arrival point, the first zero-crossing point, or a fixed threshold on the rising front of the received electrical signal (see Fig. 3.2). Frequency-dependent attenuation and velocity dispersion are acknowledged sources of bias when measuring velocity in the time

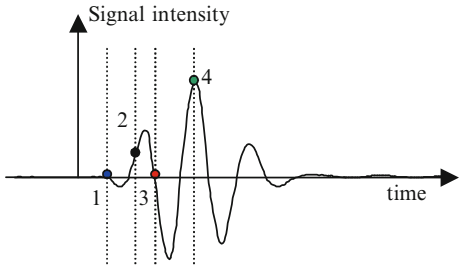

Fig. 3.2 Variation of criteria used to measure time of flight: (1) first apparent deviation from baseline, (2) fixed threshold, (3) first zero-crossing, (4) maximum

domain [24, 35–38]. As the signal is distorted while propagating through bone, the envelope of the received signal may differ considerably from the reference signal [38, 39]. Ambiguities in time-domain methods for velocity measurements in cancellous bone were reported by several investigators [36–38]. For example, velocity variations from one zero crossing to the next one for a calcaneus with BUA of 20 $\mathrm{dB} \cdot \mathrm{cm}^{-1} \cdot \mathrm{MHz}^{-1}$ can be of the order of $30\,\mathrm{m} \cdot \mathrm{s}^{-1}$ [40], which is considerable compared to the difference between fractured and unfractured women [41]. This effect is a function of the frequency-dependent attenuation [42].

Because there is no consensus on a standardized protocol for velocity determinations in bone, the comparison or pooling of measurements obtained from different devices is particularly difficult. Wear has suggested a numerical method to compute corrections for previously acquired SOS, to improve standardization in bone sonometry and to overcome discrepancies in SOS estimates due to transit-time marker location, but such a method has not been implemented yet in practice [43]. As discussed for BUA, the thickness l of the skeletal site must be known and the impact of soft tissue must be neglected.

In the second approach, a frequency-dependent $c(f)$ is estimated from the phase $\phi(f)$ of the complex ratio of the spectra given in Eqs. 3.1 and 3.2:

$$\phi(f) = \mathrm{atan}\left[\frac{A(f)}{A^{ref}(f)}\right] = 2\pi l f\left(\frac{1}{c_{ref}} - \frac{1}{c(f)}\right) \tag{3.8}$$

Arctangent routines only provide principal phase values between $-\pi$ and π, termed the wrapped phase. For a continuous phase spectrum values at modulo 2π are required. These values are determined by appropriately adding or subtracting multiples of 2π to the principal value until the discontinuities induced by the modulo 2π operation are removed. The unwrapped phase $\phi_u(f)$ is:

$$\phi_u(f) = \phi(f) \pm 2k\pi, \tag{3.9}$$

where k is an integer. Due to the limited bandwidth of the transducer the phase is known only within an integer multiple of 2π. The constant $2k\pi$ accounts for this phase ambiguity. A more accurate velocity estimate can be obtained using the y-axis intercept (zero-frequency) of $\phi_u(f)$, which can be derived from the least square fit to the data. If for example there is a 2π-error in the phase the calculated intercept will be close to -2π. In this case, the correct phase is obtained by adding 2π. Using Eq. 3.9 in which the measured phase $\phi(f)$ is replaced by the unwrapped phase $\phi_u(f)$, the phase velocity can be calculated as follows:

$$c(f) = \frac{1}{\frac{1}{c_{ref}} - \frac{\phi_u(f)}{2\pi f l}}. \tag{3.10}$$

In some devices, different sets of ultrasound parameters are reported, although they are still reflecting either attenuation or time-of-flight. These include for example mean frequency (estimated using zero crossing analysis), envelope velocity, relative

pulse width and the relative energy, which measures the total amount of energy transmitted through the heel, relative to the known reference or input signal [44].

3.2.2 Heel Devices

QUS measurements at the heel use broadband transducers, either planar or focused, with a center frequency of 0.5 MHz. Frequency dependent parameters are obtained in the frequency bandwidth 0.2–0.6 MHz approximately.

3.2.2.1 Water-Based Devices

The first clinical devices were water-based devices. The heel is immersed between two transducers with a fixed or adjustable distance. Depending on the device, the water bath is either at room temperature or temperature-controlled. As temperature strongly influences ultrasonic variables, temperature control is preferable to ensure lower precision errors. When temperature control is not possible, software procedures are sometimes implemented allowing for some compensation of temperature-related variations of sound velocity. An additional output variable provided by several devices is an empirically defined linear combination of BUA and SOS. Because of opposite temperature-related trends of BUA and SOS, the effect of temperature variations tends to cancel out in linear combinations [45].

3.2.2.2 Dry Contact Devices

Water-based devices tend to be replaced by dry contact technology because of easier portability and better hygiene. Dry QUS systems contain two broadband ultrasound transducers positioned by springs or motors on each side of the heel to maintain constant pressure in direct contact with the patient's skin. Dry contact systems incorporate soft flexible elastomer coupling pads or water-filled bladders on the ultrasound transducers to accommodate irregular limb surfaces and to ensure good contact without discomfort. A water-based gel is required for obtaining ultrasonic coupling between the transducers or the pads and the patient's skin. Most of the devices use proprietary algorithms to measure QUS parameters, heel thickness, or the thickness of bone. Compared to wet-systems, in dry systems there is reduced control over the measurement environment such as temperature stability.

3.2.2.3 Fixed Versus Moving Transducers

Most heel QUS devices use fixed flat-surface unfocused transducers. Thus, BUA and SOS are measured in a fixed region relative to the device coordinate system. Consequently anatomical inter-individual variability may result in different bone

areas being measured in different individuals. This also potentially limits long-term precision in repeated measurements on the same subjects. Several solutions have been proposed to overcome this problem, such as movable transducers that can be automatically positioned relative to some anatomical landmark.

In one device, a laser beam positioner selects the volume of interest relative to the centre of the external malleolus. Another dry scanning system uses quasi point source transducers with wide transmission angles and a hemispherical contact surface rather than flat-surface unfocused transducers. The transducers are pushed inwardly toward each other by springs. The hemispherical contact surfaces enable the transducers to move smoothly across the heel surface without losing contact. The total scanning area includes the back and bottom edges of the heel bone. At the start of a scan, the device searches for the plantar and posterior acoustic edges. Appropriate signal processing of the received waveform allows detecting the proximity to an edge of the calcaneus. According to the manufacturer a measure of the relative proportion of high versus low frequency energy is an indication of the proximity to a bone edge. The transducers then move to a predetermined location to scan a region of approximately 1 cm^2. This procedure enables the device to place the target region in an anatomically analogous location on every subject's bone regardless of the varying amount of soft tissue. BUA results are calculated for the selected region of interest.

3.2.2.4 Imaging Devices

For QUS imaging the ultrasound beam is scanned either mechanically or electronically with respect to the bone. One of several analysis regions of interest (ROI) may be defined relative to anatomical landmarks of the bone or to topological features of the obtained image. Average values can be calculated by averaging QUS parameters within this region of interest (ROI). Typically size, form and ROI location are operator adjustable. However, a manual ROI determination increases precision errors thus automatic ROI positioning is preferable. For example, in the calcaneus some devices use the region of lowest attenuation in the greater tuberosity [46] to automatically place a circular ROI in the posterior part of the calcaneus (Fig. 3.3).

Further substantial technological progress have been achieved with waterless contact QUS imaging. One commercially available device uses two fixed transducers with a water-based gel for acoustic coupling: one single large transducer that transmits a plane wave through the heel and on the receiving side a 590 multi-element 2D array. This array employs an active focusing sub-aperture in order to form a focused received ultrasound beam in the calcaneus mid-plane. Scanning of the active focusing sub-aperture is performed electronically over the whole matrix surface. The transducers are encased in thermo-regulated water balloons made of compliant silicone membranes to accommodate different heel shapes, to establish direct contact with the patient's skin, and to keep the foot dry. A pump allows for membrane inflation to conform closely to the patient's foot and to provide large-area imaging through a temperature-controlled medium. The device instantly provides a

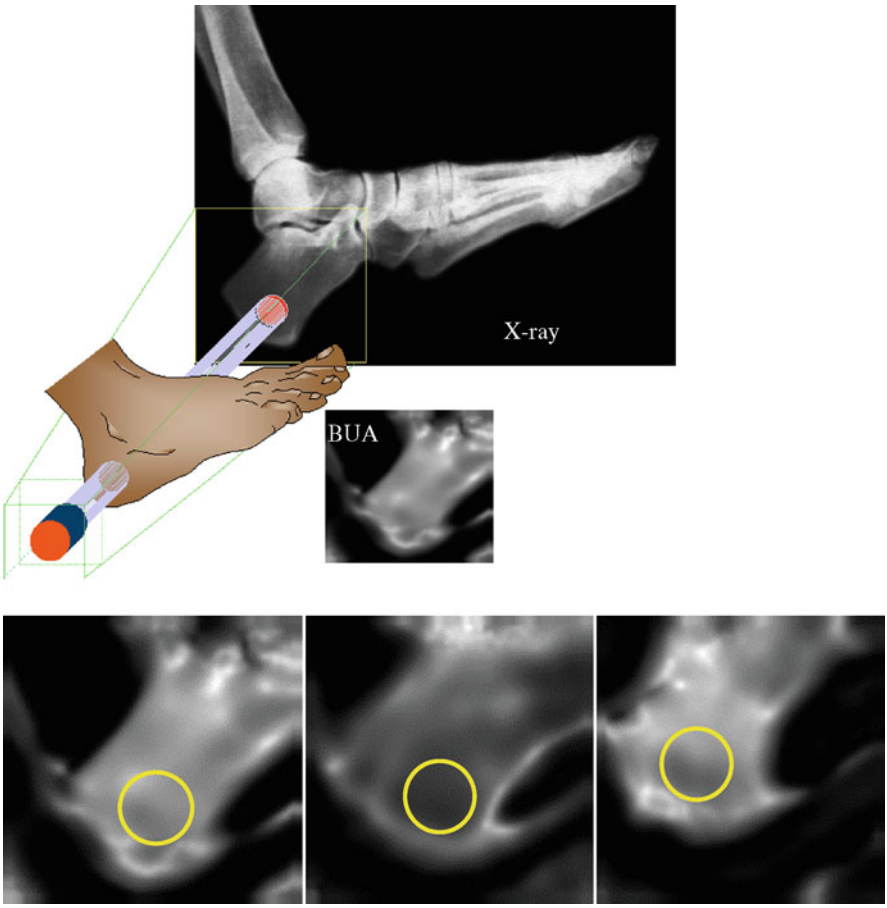

Fig. 3.3 *Top*: Illustration of transverse transmission at the heel. Comparison for a given subject between the BUA image and standard plain X-ray radiography of the heel. *Bottom*: BUA images of the heel from three different subjects with automatically positioned circular ROI. Typical characteristics of a BUA image are: Field of view: $60 \times 60\,\text{mm}^2$, pixel size: $1\,\text{mm}^2$

real time preview of the calcaneus. This eliminates "blind" measurements and permits heel positioning adjustments prior to the quantitative assessment [47]. Another substantially different prototype device for waterless contact QUS imaging using two 2D arrays of transducers and permitting beam focusing at both the transmit and receive stages has also been described [48].

3.2.3 Finger Phalanges Device

One commercial device measures the amplitude-dependent speed of sound (Ad-SOS) at the distal metaphysis of the first phalanx of fingers I–IV. Measurements

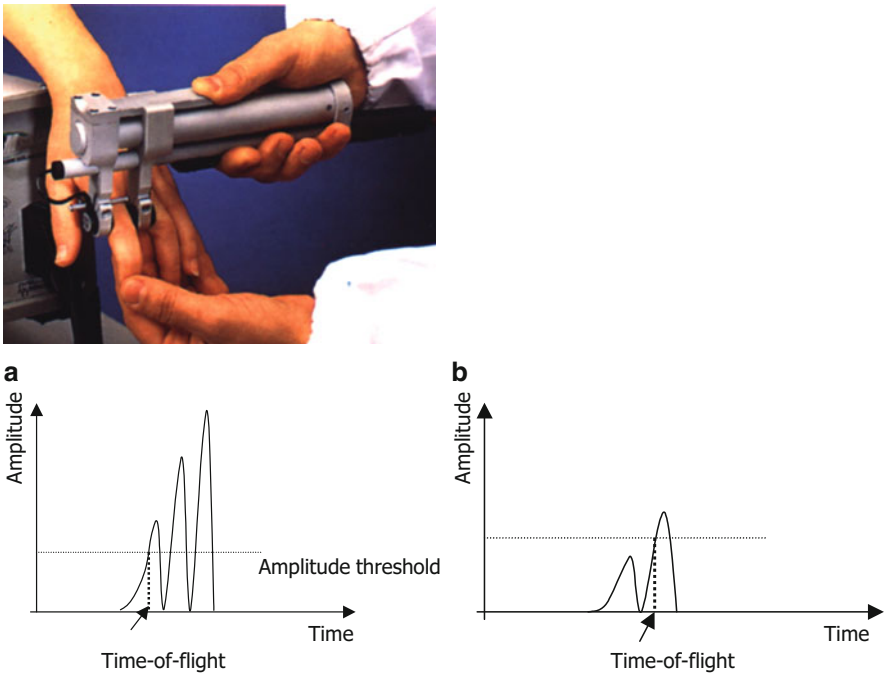

Fig. 3.4 *Top*: Illustration of transverse transmission measurement at the finger phalanges. *Bottom*: Schematic illustration of the signal recorded in (**a**) a normal postmenopausal woman and (**b**) in an osteoporotic postmenopausal woman

are carried out on each of the four phalanges and results are averaged. The instrument is equipped with two 12 mm diameter, 1.25 MHz plane transducers mounted on an electronic caliper that measures the distance between the probes (Fig. 3.4). The probes are positioned on the mediolateral surfaces of the distal metaphysis of the phalanx using the phalanx condyle as reference point. Coupling is achieved with a standard ultrasound gel. The probe positioning is slightly varied until the optimum signal (defined in terms of number of peaks and the amplitude of the peaks, following manufacturer recommendations) is recorded, then Ad-SOS is measured.

With this device, which measures the finger phalanges, TOF is defined as the time between the emitted pulse and the first part of the signal that is above a predetermined amplitude threshold (Fig. 3.4). Thus TOF depends on the signal amplitude relative to the predetermined threshold: the higher the signal amplitude, the shorter the time of flight [49]. The velocity measured with this technique is amplitude-related and has been termed amplitude-dependent speed of sound (Ad-SOS). In osteoporotic bone, significant attenuation is observed and the amplitude of the first signal is too small to trigger the read out electronics. Compared to normal bone, such attenuation results in later signal detection and longer time of flight. In the phalanx, curved propagation occurs [50] due to circumferential guided waves. In

this case the exact propagation path length is unknown. Using the finger thickness rather than the exact path length l in Eq. 3.3 results in an apparent speed of sound rather than in an accurate velocity estimate.

The interaction of a plane incident wave with the phalanx generates multiple pathways. A phalange can be considered as a hollow tube consisting mainly of cortical bone surrounding the medullary canal filled with cancellous bone to some extent and bone marrow, which is a fluid-like medium. The incident wavefront is partly refracted as a longitudinal wave propagating through the cortex along a curved pathway, while another pathway originates in the longitudinal wave transmitted at normal incidence through the medullary canal [50–52]. Because speed of sound in cortical bone is much higher than in soft tissue the first part of the received signal corresponds to a fast curved pathway through the cortex [50], while the wave transmitted through the medullary canal arrives later. Finally, mode conversion or multiple wave reflections occurs on interfaces and creates multiple additional late arriving waves at the receiver. Several delayed and interfering components contribute to the signal received after crossing the phalanx. The extraction of Ad-SOS yields information related to the fastest part of the transmitted signal, only. Time intervals between signals following different pathways and relative signal amplitudes are influenced by material properties and by the bone morphology (cortical cross-sectional area, area of the medullary canal, cortical thickness) [50, 53].

Enhanced signal analysis has been tested for the phalanx and several parameters derived from the ultrasonic trace were derived such as the fast wave amplitude, number of peaks, signal dynamic, bone transmission time, growth trend of the peaks amplitude and other signal features. Several studies have pointed out the value of some of these parameters to reveal information on structural features of bone [50, 54]. For example, Barkmann et al. [50] in a study performed in human phalanges have found that cross-sectional cortical area, medullary canal area, and relative cortical area could be estimated from speed of sound and wave amplitude. A different parameter, the ultrasound bone profile index (UBPI), resulting from such enhanced signal analysis has been reported in literature. It is based on a combination of selected features of the ultrasonic signal specifically related to bone structural properties. It is processed in a statistical approach to express the probability of fracture incidence to provide automatic computer assisted analysis [55].

3.2.4 Forearm Device

A device to measure the ultradistal radius at the forearm in transverse transmission has been developed (Fig. 3.5) [21]. The approach is based on the modelization of propagation in cancellous bone using Biot's theory (see Chaps. 5 and 11) which predicts two distinct longitudinal waves denoted as fast and slow waves [56,57]. The distal radius at 4% of forearm length, a site with high volume fraction of cancellous bone, is set between a pair of confocally aligned broadband focused transducers (diameter of 20 mm with a concave active area and a focal point of 40 mm, 1 MHz-center frequency) through water filled bags.

Fig. 3.5 Illustration of transverse transmission measurements at the forearm (Courtesy of Isao Mano, OYO Electric CO., LTD.)

Both transducers are moved simultaneously during scanning. The ultrasonic beam is scanned in a raster pattern through the measurement site using a two-axis scanning mechanism. Two scans are necessary. During the first scan, the transmitted ultrasonic signals are recorded at intervals of 2 mm in both X-Y directions over a scanning area of $28 \times 28\,\mathrm{mm}^2$. The principal interest of this first scan is to determine the second scan position for ultrasonic measurements. The overall amplitude of the transmitted signals is analyzed to obtain a local attenuation distribution of the measurement site. The measured attenuation levels are converted into a color variation and the local attenuation distribution is displayed as a pseudo-bone density image of the measurement site (mapping of the distal radius, the distal ulna and some parts of the palm). The local distribution of the propagation speed of the overall transmitted signals is also displayed as a SOS image. These two images, together with the measured values of attenuation and SOS, are used to confirm the bone geometry of the measurement site and to determine the second scanning position, where bone density and elasticity of cancellous bone are measured.

During this second scan (area of $4 \times 4\,\mathrm{mm}^2$), measurements are performed at intervals of 1 mm both in the transmission and echo modes. The transmitted signals include both the fast and slow waves. Transmitted signals are analyzed to measure the amplitudes and the propagation times (time of flight) of both the fast and slow waves. The echo signals are analyzed to obtain the soft tissue thickness and the bone thickness in mm. Several bone properties are estimated from the combination of transmission and reflection measurements following the model extensively reported in [6,21,58]. These included bone mass (bone mineral density $(\mathrm{mg/cm}^3)$) and bone volume fraction BV/TV (%) of cancellous bone, thickness of cortical bone (mm), and elastic constant of cancellous bone (GPa). Ultrasound properties are estimated based on a model and must therefore be considered as "apparent" bone properties. The good correlation between in vivo estimated bone density and that obtained from site matched peripheral computed tomography measurements suggest a good reliability of the developed system. However, the clinical usefulness of the combined estimation of density and stiffness has yet to be validated.

3.2.5 Hip Device

A limitation of the previously described devices is their application to peripheral sites of the skeleton only. Site specific density measurements have the highest predictive power, in particular for the proximal femur. Osteoporotic fractures of the femur cause high costs and considerable mortality. Technological developments have recently been undertaken to adapt transverse transmission techniques to perform measurements directly at the hip in order to obtain a higher sensitivity to hip fracture risk prediction [8, 22, 23].

Apart the size and specific design of the prototype adapted to measure the hip, the measurement principles are similar to those of heel devices. The FemUS prototype device developed by Barkmann et al. [22, 23] comprises two ultrasound transducers of 600 kHz center frequency mounted opposite to each other on a C-arm in a distance of 50 cm. Both transducers are able to transmit and receive ultrasonic waves. The C-arm can be moved in two linear directions. Additionally, it can be rotated around two axes. All movements are driven by stepper motors and are controlled by a PC. For better ultrasound coupling the transducers are submerged in a temperature-controlled water bath. A recess in the water bath allows positioning the patient who is lying on a table between the transducers. Inflatable water filled membranes are used to establish smooth contact between the water bath that contains the transducers and the patient's skin avoiding air along the sound path of the ultrasound beam.

The proximal femur at the hip is more irregularly shaped compared to the calcaneus (a more or less parallelepipedic shaped bone) and surrounded by a large amount of soft tissue. Ultrasound propagation through the hip is more complex than through the calcaneus and the received signal may result from the combination of multiple waves transmitted through different pathways in different parts of the bone. Different wave components with different shape and phase may interfere, resulting in a complex signal. In particular, circumferential waves guided by the cortical shell may interfere with waves transmitted directly through the trabecular compartment [59]. Therefore, more sophisticated signal processing techniques are requested to extract the ultrasonic parameters from hip QUS measurements [60, 61].

3.3 Axial Transmission

In axial transmission techniques that were initially developed in the 1950s to study fracture healing of cortical bone, a transmitter and a receiver were used to measure the sound speed along the cortical bone layer parallel to its long axis. The transducers are placed on the skin and measure the arrival time of the wave which propagates along the bone axis and arrives at the receiver first. In contrast to transverse transmission techniques, which require a transducer to be placed on each side of the bone, the transducer set-up is much easier in axial transmission, which therefore may be applied to a greater number of skeletal sites.

3.3.1 Principles of Axial Transmission Measurements

Several axial transmission devices have been developed. Although all axial transmission approaches are based on the same basic measurement principles, different waves may contribute to the measured signal. The signals obtained at the receivers are the combination of all waves propagating axially along the long axis of the bone (see Chap. 7). In the early development of the technique, attention was focused in analyzing the signals in time domain and in determining the velocity of the first arriving signal, denoted FAS. The time-of-flight (TOF) of the FAS is measured and the velocity is calculated from either the transmitter-receiver distance divided by TOF or by dividing the distance between two receivers by the corresponding difference in TOF of the signal. The time criterion used to measure TOF is not always clearly specified by the manufacturers, although an early time point in the FAS is presumably used to avoid inaccuracies in time determination due to interference of FAS with later arriving signals. In some devices, speed of sound is derived from the slope of the curve of TOF versus d_{ER}, the transmitter-receiver distance, as the position of the receiver is moved stepwise along the interface [62–64] (Fig. 3.6). It was found in several clinical studies that FAS velocity discriminates healthy subjects from osteoporotic patients [5, 65–68].

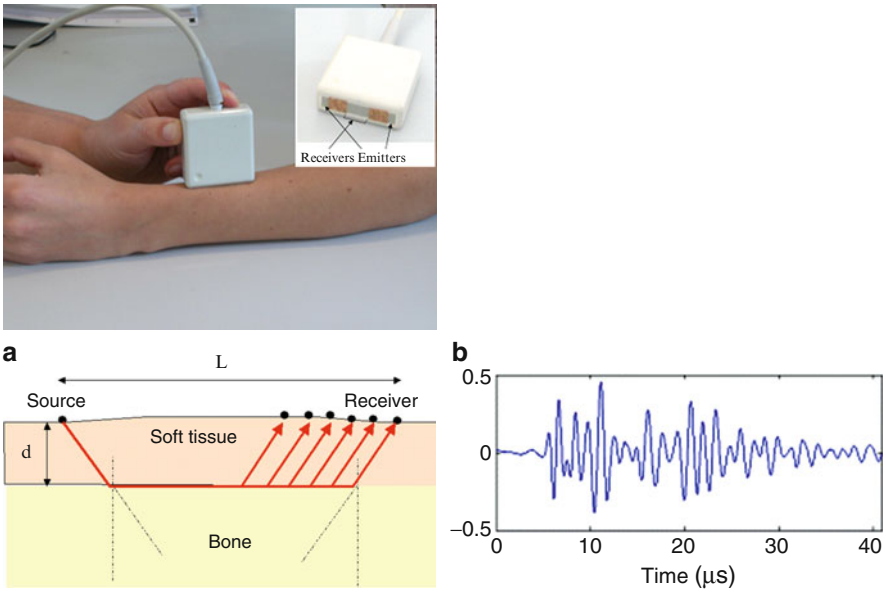

Fig. 3.6 Illustration of axial transmission at the forearm. *Top*: ultrasonic probe for bidirectional axial transmission measurements. The front layer of the probe is shown on the insert. Two emitting zones are placed at the extremities of the probe. The receiving zone is central. *Bottom* (**a**) principle of axial transmission and signal acquisition using a receiver array; (**b**) typical signal acquired on the radius in vivo

The FAS can be seen as a guided S_0 wave in the low frequency regime (i.e., low cortical thickness-to-wavelength ratio) and as a lateral compression wave in the high frequency regime (i.e., high cortical thickness-to-wavelength ratio) [69]. As these two modes of acoustic waves are differentially sensitive to the mechanical and structural properties of cortical bone, it has been suggested to separate these two modes in the receive signal by making measurements at two frequencies. A dual-frequency axial transmission prototype has been described, in which measurements are conducted at 0.1 and 1.0 MHz [70].

The possibility of measuring wave modes other than the first arriving signal in cortical bone has been investigated recently [71–74], suggesting that such measurements could yield additional diagnostic information of the material and geometric properties of bone [75]. An energetic slower signal component arriving after the FAS has been observed [76] and shown in vitro to be consistent with the antisymmetric guided wave (A0, plate model) or the fundamental flexural tube mode (F11, tube model) [77]. This mode is especially sensitive to the cortical bone thickness. Thus, if correctly identified and extracted by appropriate signal analysis, it may be suitable for data inversion processes [77]. More details can be found in the reference [78] and in Chap. 7. Signal processing techniques were proposed to isolate this signal component and to measure its phase velocity. These include the group velocity filtering technique proposed by Moilanen and coworkers [71,78] and the singular value decomposition proposed in Sasso et al. [73,79]. The research strategy is now to extract and characterize multiple propagation modes from a single acquisition dataset using arrays of transducers [80].

Details on the physical interpretation of the measured signals and their relationships to several bone characteristics (e.g., cortical thickness, porosity, mineralization) can be found in Chap. 7.

3.3.2 Axial Transmission Devices

Several devices have been designed to measure the SOS of ultrasonic waves axially transmitted along cortical bone. A first instrument was introduced to measure the longitudinal transmission of an acoustic 250 kHz pulse along the cortical layer of the mid-tibia [7] defined as the mid-point between the distal apex of the medial malleolus and the distal aspect of the patella. The probe is placed parallel to the longitudinal axis of the bone (see Fig. 3.6). The transducers are coupled to the skin through standard ultrasound gel. The transit time of a pulse along a defined 50 mm distance is measured. The probe is moved back and forth across the tibial surface and velocity readings are continuously recorded. The resultant velocity is an average of the five highest percent readings during the scan.

Multi-site axial transmission was introduced commercially as the direct successor to tibial axial transmission. Similar to tibial axial transmission, the fundamental physical principle behind multi-site axial transmission is the measurement of SOS at approximately 1.25 MHz instead at 250 kHz. Basic measurement principles are

identical in both techniques, but different waves may be involved in the fastest part of the signal due to the significant difference in the operating frequency. The main advantage of a multi site device is the possibility of measuring skeletal sites which may be more relevant for fracture risk prediction than the tibia. Currently, the preferred anatomic site for multi-site axial transmission is the distal one-third radius, although other peripheral sites have been investigated as well [5, 65, 68]. In one of these devices that is commercially available, the transit time of a center frequency pulse (1.25 MHz) along a defined distance between transmitter and receiver is measured. The probe contains four transducers; a transducer pair and a receiver pair. In order to increase the amplitude of the transmitted and received signals, the transducers are mounted at an angle close to the critical angle relative to the surface of the probe.

The four ultrasonic transducers are used for a determination of acoustic soft tissue velocity and to compensate changes in the tissue thickness along the bone. Both factors severely impact on the trueness of the ultrasound propagation measurement through bone. Although the exact algorithm used by the manufacturer remains undisclosed, one may reasonably assume that several ultrasonic recordings are performed by combining direct transmission or reflection between different transmitters and receivers, so that several acoustic pathways involving soft tissue path portions of the same length and variable bone path length may be analyzed. Thus processing different signal propagation times yields the signal propagation time in a cortical portion.

To avoid the measurement technique to be operator-dependent, specific scanning methodologies were developed that must be followed carefully to obtain reproducible results. For a distal radius measurement the arm is marked at the midpoint between the elbow and the tip of the third finger. The probe is positioned adjacent to the mark on the proximal side. A gel is applied to the probe to ensure proper ultrasound coupling. A measurement is performed by placing the probe parallel to the longitudinal axis of the bone. A scan is performed by moving the probe face circumferentially around the bone. A minimum of 150–200 discrete velocity readings are recorded. Time of flight is measured for each trace. During scanning, SOS is determined in many different positions with a pulse repetition frequency of about 0.1 Hz to yield an SOS profile of the bone.

Every single sequence of the ultrasonic transmission and reception is validated using proprietary procedures. The resulting velocity is an average of the 5% highest readings. Measurement quality is ensured by requiring three consistent scan cycles to obtain an SOS result. The three SOS values are checked for consistency and quality. If an outlier value is detected the user is requested to perform a fourth and sometimes even a fifth cycle in order to obtain three statistically consistent SOS values (i.e., the coefficient of variation must not exceed a predetermined threshold, typically 1% or 1.5%). Under normal conditions the entire measurement takes between 1 and 2 min.

The device offers a family of small hand-held probes designed to measure various skeletal sites under different soft tissue thickness conditions. The smallest probes can be used to measure skeletal sites where the layer of covering soft tissue is the

thinnest such as the finger phalanxes, while the larger probes are dedicated for skeletal sites covered by a thicker layer of soft tissue such as the distal one-third radius. Still some patients cannot be measured due to thick soft tissue [68]. A minimum distance must separate the source from the receiver to observe the lateral wave or the guided modes. This has important implications for clinical measurements in patients and probably explains why this axial transmission implementation fails in some patients. Weiss et al. reported that in a study of 1610 women measuring the radius failed in about 0.6% [68].

Bossy et al. have developed a bi-directional axial transmission probe (1 MHz) (Fig. 3.6) in which an ultrasonic pulse is transmitted along the bone surface in two opposite directions from two sources placed at both ends of a distinct group of receivers [81]. A simple combination of the time delays derived from waves propagating in opposite directions efficiently corrects automatically for soft tissue [81].

In the approaches described above, the time-of-flight of the FAS is measured and used to calculate velocity. Other axial transmission prototypes devices have been described based on a different approach, which is to use low frequencies and, in some cases, special transducers or coupling conditions, in order to excite and measure guided waves propagating in the bone at relatively low velocities. One such device uses 200 kHz broadband transducers [63] and another uses specially-designed 110 kHz needle transducers [82, 83]. A comprehensive review of these approaches has been given by Moilanen [78].

3.4 Discussion and Conclusion

QUS technologies have been developed and adapted to measure mostly peripheral skeletal sites such as the heel, forearm or hand phalanges, and recently the central skeleton at the hip. QUS techniques have found widespread clinical use to predict bone fragility not only in osteoporotic patients, but also in a wider context of bone diseases in female, male and pediatric populations [9, 84–87]. Preliminary studies suggest that this technique may be a useful method of assessing changes in bone health in preterm infants for whom dual energy X-ray absorptiometry is unsuitable for such settings [88]. An ultrasound wearable system for remote monitoring of the healing process in fractured long bones has also been reported [72].

For a given class of devices, e.g., transverse transmission or axial transmission, most implementations are based on similar physical principles despite some technology diversity. However, the propagating characteristics may vary depending on the skeletal site (cancellous bone versus cortical bone) and the technical implementation (e.g., interrogating frequencies). The measured signals with various technologies are thus differently affected by different bone material or structural properties.

A consensus has been reached stating that QUS properties (BUA, SOS) of cancellous bone are a good surrogates measures of site-matched bone mineral density (BMD): evidences of strong positive linear relationships between BUA and SOS with BMD were obtained both in vitro ($r^2 \sim 0.70$–0.95) [26, 39, 89–94] and in vivo

($r^2 \sim 0.60$–0.80) [95, 96]. Building on these results, some heel devices provide an output variable termed estimated heel BMD measured in $g \cdot cm^{-2}$ [97]. The limited impact of cancellous bone microarchitecture on ultrasound values measured uniaxially in transmission [92] prompted a search for other ultrasound parameters, such as backscatter [98, 99] or reflection [100–102] that may reflect bone microarchitecture or the intrinsic quality of bone tissue.

Axial transmission SOS reflects both structural and intrinsic material properties of cortical bone. Experimental studies on excised human radii demonstrated the sensitivity of the velocity of the FAS (SOS_{FAS}) to porosity and degree of mineralization [103] and also to intrinsic elastic properties [104]. Up to 84% of the variability of SOS_{FAS} is explained with a combination of cortical thickness, porosity and acoustic impedance reflecting intrinsic stiffness [104]. While SOS_{FAS} correlates weakly with cortical thickness and moderately with BMD, the velocity of the energetic slower signal component arriving after the FAS (consistent with the antisymmetric guided wave A0) correlates moderately with cortical thickness but weakly with BMD [64, 105]. This result obtained in vitro on radius samples has suggested that a multimodal approach in which several propagating modes are characterized would be appropriate to yield a more complete view of cortical bone status. Sophisticated axial transmission approaches are currently explored in which multiple propagation modes are identified and their propagation velocity are characterized with the ultimate goal to extract several indicators on various components of bone strength.

Even for a class of devices, such as, for example, heel transverse transmission, differences exist in hardware, transducer design, analysis regions, signal processing algorithms. Systems also vary with respect to data acquisition procedures, coupling, and output variables. So far there is no standardization among manufacturers. Due to the lack of standardization, different technical implementations cause substantial differences in QUS variables values between different commercial devices. Until there is an accepted standard for ultrasound measurement, the results obtained with one device cannot be directly compared to those from another, even though both claim to deliver the same measurements such as BUA or SOS at the heel or SOS at the radius. The multitude of modalities, techniques, and implementations is confusing for the clinician who needs support in clinical decisions. Obviously this requires clear definitions of measured quantities and standardization of acquisition and analysis routines. From a clinical perspective, a comparison of the diagnostic potential across different techniques and modalities is required. From a technical perspective, the development of quality standards and cross-calibrations of QUS scanners is necessary, so that results from different devices can be compared.

The potential of ultrasound extends far beyond the currently available techniques and is largely unexploited. Most active research is carried out in QUS to develop new measurement modes (e.g., scattering, see Chap. 6), exploit multiple propagation modes (see Chap. 7) and assess microdamage (Chap. 15). All these new developments should result in new QUS variables and systems able to provide information on material or structural properties other than density, and ultimately on bone fragility and fracture risk.

References

1. C. Simonelli, R. A. Adler, G. M. Blake, J. P. Caudill, A. Khan, E. Leib, M. Maricic, J. C. Prior, S. R. Eis, C. Rosen, and D. L. Kendler, "Dual-Energy X-Ray Absorptiometry Technical issues: the 2007 ISCD Official Positions," J Clin Densitom ***11***(1), 109–122 (2008).
2. I. Siegel, G. T. Anast, and T. Melds, "The determination of fracture healing by measurement of sound velocity across the fracture site," Surg Gynecol Obste, ***107***(3), 327–332 (1958).
3. C. M. Langton, S. B. Palmer, and S. W. Porter, "The measurement of broadband ultrasonic attenuation in cancellous bone," Eng Med ***13***(2), 89–91 (1984).
4. K. E. Fredfeldt, "Sound velocity in the middle phalanges of the human hand," Acta Radiol Diagn ***27***, 95–96 (1986).
5. D. Hans, S. Srivastav, C. Singal, R. Barkmann, C. Njeh, E. Kantorovich, et al., "Does combining the results from multiple bone sites measured by a new quantitative ultrasound device improve discrimination of hip fracture?," J Bone Miner Res ***14***, 644–651 (1999).
6. T. Otani, I. Mano, T. Tsujimoto, T. Yamamoto, R. Teshima, and H. Naka, "Estimation of in vivo cancellous bone elasticity," Jap J Appl Phys ***48***, 07GK05-01-07GK05-05 (2009).
7. A. J. Foldes, A. Rimon, D. D. Keinan, and M. M. Popovtzer, "Quantitative ultrasound of the tibia: a novel approach assessment of bone status," Bone ***17***(4), 363–367 (1995).
8. R. Barkmann, P. Laugier, U. Moser, S. Dencks, M. Klausner, F. Padilla, G. Haiat, M. Heller, and C. C. Glüer, "In vivo measurements of ultrasound transmission through the human proximal femur," Ultrasound Med Biol ***34***(7), 1186–1190 (2008).
9. C. C. Glüer, R. Eastell, D. M. Reid, D. Felsenberg, C. Roux, R. Barkmann, W. Timm, T. Blenk, G. Armbrecht, A. Stewart, J. Clowes, F. E. Thomasius, and S. Kolta, "Association of five quantitative ultrasound devices and bone densitometry with osteoporotic vertebral fractures in a population-based sample: the OPUS Study," J Bone Miner Res ***19***(5), 782–793 (2004).
10. M. A. Krieg, R. Barkmann, S. Gonnelli, A. Stewart, D. C. Bauer, L. Del Rio Barquero, J. J. Kaufman, R. Lorenc, P. D. Miller, W. P. Olszynski, C. Poiana, A. M. Schott, E. M. Lewiecki, and D. Hans, "Quantitative ultrasound in the management of osteoporosis: the 2007 ISCD Official Positions," J Clin Densitom ***11***(1), 163–187 (2008).
11. F. Marin, J. Gonzalez-Macias, A. Diez-Perez, S. Palma, and M. Delgado-Rodriguez, "Relationship between bone quantitative ultrasound and fractures: a meta-analysis," J Bone Miner Res ***21***(7), 1126–1135 (2006).
12. P. P. Antich, J. A. Anderson, R. B. Ashman, J. E. Dowdey, J. Gonzales, R. Murry, J. Zerwekh, and C. Y. C. Pak, "Measurement of mechanical properties of bone material in vitro by ultrasound reflection: Methodology and comparison with ultrasound transmission," J Bone Miner Res ***6***(4), 417–426 (1991).
13. P. P. Antich, C. Y. C. Pak, J. Gonzales, J. A. Anderson, R. B. Ashman, K. Sakhaee, and C. Rubin, "Measurement of intrinsic bone quality in vivo by reflection ultrasound: correction of impaired quality with slow-release sodium fluoride and calcium citrate," J Bone Miner Res ***8***(3), 301–311 (1993).
14. J. E. Zerwekh, P. P. Antich, S. Mehta, K. Sakhaee, F. Gottschalk, and C. Y. Pak, "Reflection ultrasound velocities and histomorphometric and connectivity analyses: correlations and effect of slow-release sodium fluoride," J Bone Miner Res ***12***(12), 2068–2075 (1997).
15. E. Richer, M. A. Lewis, C. V. Odvina, M. A. Vazquez, B. J. Smith, R. D. Peterson, J. R. Poindexter, P. P. Antich, and C. Y. Pak, "Reduction in normalized bone elasticity following long-term bisphosphonate treatment as measured by ultrasound critical angle reflectometry," Osteoporos Int ***16***(11), 1384–1392. Epub 2005 Feb 1322 (2005).
16. S. Mehta and P. Antich, "Measurement of shear-wave velocity by ultrasound critical-angle reflectometry," Ultrasound Med Biol ***23***(7), 1123–1126 (1997).
17. S. Mehta, S, O. K. Oz, and P. P. Antich, "Bone elasticity and ultrasound velocity are affected by subtle changes in the organic matrix.," J Bone Miner Res ***13***(1), 114–121 (1998).
18. B. S. Garra, M. Locher, S. Felker, and K. A. Wear, "Measurements of ultrasonic backscattered spectral centroid shift from spine in vivo: methodology and preliminary results," Ultrasound Med Biol ***35***(1), 165–168 (2009).

19. C. Roux, V. Roberjot, R. Porcher, S. Kolta, M. Dougados, and P. Laugier, "Ultrasonic backscatter and transmission parameters at the os calcis in postmenopausal osteoporosis," J Bone Miner Res ***16***(7), 1353–1362 (2001).
20. K. A. Wear and B. S. Garra, "Assessment of bone density using ultrasonic backscatter," Ultrasound Med Biol ***24***(5), 689–695 (1998).
21. I. Mano, K. Horii, S. Takai, T. Suzaki, H. Nagaoka, and T. Otani, "Development of novel ul-trasonic bone densitometry using acoustic parameters of cancellous bone for fast and slow waves," Jpn J Appl Phys ***45***, 4700–4702 (2006).
22. R. Barkmann, S. Dencks, P. Laugier, F. Padilla, K. Brixen, J. Ryg, A. Seekamp, L. Mahlke, A. Bremer, M. Heller, and C. C. Glüer, "Femur ultrasound (FemUS)-first clinical results on hip fracture discrimination and estimation of femoral BMD," Osteoporos Int ***21***(6), 969–976 (2010).
23. R. Barkmann, P. Laugier, U. Moser, S. Dencks, M. Klausner, F. Padilla, G. Haïat, and C. C. Glüer, "A device for in vivo measurements of quantitative ultrasound variables at the human proximal femur," IEEE Trans Ultrason Ferroelectr Freq Control ***55***(6), 1197–1204 (2008).
24. P. Droin, G. Berger, and P. Laugier, "Dispersion of acoustic waves in cancellous bone," IEEE Trans Ultrasonics Ferroelectr Freq Control ***45***, 581–592 (1998).
25. P. Laugier, "Instrumentation for in vivo assessment of bone strength," IEEE Trans Ultrason Ferroelectr Freq Control ***55***(6), 1179–1196 (2008).
26. P. Laugier, P. Droin, A. M. Laval-Jeantet, and G. Berger, "In vitro assessment of the relationship between acoustic properties and bone mass density of the calcaneus by comparison of ultrasound parametric imaging and QCT," Bone ***20***, 157–165 (1997).
27. J. J. Kaufman, W. Xu, A. E. Chiabrera, and R. S. Siffert, "Diffraction effects in insertion mode estimation of ultrasound group velocity," IEEE Trans Ultrason Ferroelectr Freq Control ***42***, 232–242 (1995).
28. S. Chaffaï, F. Padilla, G. Berger, and P. Laugier, "In vitro measurement of the frequency-dependent attenuation in cancellous bone between 0.2-2.0 MHz," J Acoust Soc Am ***108***, 1281–1289 (2000).
29. K. A. Wear, "Ultrasonic attenuation in human calcaneus from 0.2 to 1.7 MHz," IEEE Trans Ultrason Ferroelectr Freq Control ***48***(2), 602–608 (2001).
30. W. Xu and J. J. Kaufman, "Diffraction correction methods for insertion ultrasound attenuation estimation," IEEE Trans Biomed Eng ***40***(6), 563–570 (1993).
31. R. Strelitzki and J. A. Evans, "Diffraction and interface losses in broadband ultrasound attenuation measurements of the calcaneus," Physiol Meas ***19***, 197–204 (1998).
32. C. C. Anderson, K. R. Marutyan, M. R. Holland, K. A. Wear, and J. G. Miller, "Interference between wave modes may contribute to the apparent negative dispersion observed in cancellous bone," J Acoust Soc Am ***124***(3), 1781–1789 (2008).
33. A. Q. Bauer, K. R. Marutyan, M. R. Holland, and J. G. Miller, "Negative dispersion in bone: the role of interference in measurements of the apparent phase velocity of two temporally overlapping signals," J Acoust Soc Am ***123***(4), 2407–2414 (2008).
34. K. R. Marutyan, M. R. Holland, and J. G. Miller, "Anomalous negative dispersion in bone can result from the interference of fast and slow waves," J Acoust Soc Am ***120***(5 Pt 1), EL55–61 (2006).
35. V. M. Merkulova, "Accuracy of the pulse method for measuring the attenuation and velocity of ultrasound," Sov Phys Acoust ***12***, 411–467 (1967).
36. P. H. F. Nicholson, G. Lowet, C. M. Langton, J. Dequeker, and G. Van der Perre, "A comparison of time-domain and frequency domain approaches to ultrasonic velocity measurement in trabecular bone," Phys Med Biol ***41***, 2421–2435 (1996).
37. R. Strelitzki and J. A. Evans, "On the measurement of the velocity of ultrasound in the os calcis using short pulses," Eur J Ultrasound ***4***, 205–213 (1996).
38. K. Wear, "The effects of frequency-dependent attenuation and dispersion on sound speed measurements: applications in human trabecular bone," IEEE Trans Ultrason Ferroelectr Freq Control ***47***(1), 265–273 (2000).

39. G. Haiat, F. Padilla, R. Barkmann, S. Dencks, U. Moser, C. C. Gluer, and P. Laugier, "Optimal prediction of bone mineral density with ultrasonic measurements in excised human femur," Calcif Tissue Int ***77***(3), 186–192 (2005).
40. K. A. Wear, "A numerical method to predict the effects of frequency-dependent attenuation and dispersion on speed of sound estimates in cancellous bone," J Acoust Soc Am ***109***(3), 1213–1218 (2001).
41. D. Hans, P. Dargent-Moline, A. M. Schott, J. L. Sebert, C. Cormier, P. O. Kotski, P. D. Delmas, J. M. Pouilles, G. Breart, and P. J. Meunier, "Ultrasonographic heel measurements to predict hip fracture in elderly women: the Epidos prospective study," Lancet ***348***(9026), 511–514 (1996).
42. G. Haiat, F. Padilla, R. O. Cleveland, and P. Laugier, "Effects of frequency-dependent attenuation and velocity dispersion on in vitro ultrasound velocity measurements in intact human femur specimens," IEEE Trans Ultrason Ferroelectr Freq Control ***53***(1), 39–51 (2006).
43. K. A. Wear, "method for improved standardization of in vivo calcaneal time-domain speed-of-sound measurements," IEEE Trans Ultrason Ferroelectr Freq Control ***55***(7), 1473–1479 (2008).
44. J. J. Kaufman, G. Luoc, D. Conroyd, W. A. Johnsone, R. L. Altmane, and R. S. Siffert, "New ultrasound system for bone assessment," presented at the Medical Imaging, San Diego, 2004.
45. R. Morris, R. Mazess, J. Trempe, and J. Hanson, "Stiffness compensates for temperature variation in ultra-sound densitometry," J Bone Miner Res 12(S1), S388 (1997).
46. B. Fournier, C. Chappard, C. Roux, G. Berger, and P. Laugier, "Quantitative ultrasound imaging at the calcaneus using an automatic region of interest," Osteoporos Int ***7***, 363–369 (1997).
47. C. Cepollaro, S. Gonnelli, A. Montagnani, C. Caffarelli, A. Cadirni, S. Martini, and R. Nuti, "In Vivo Performance Evaluation of the Achilles Insight QUS Device," J Clin Densitom ***8***(3), 341–346 (2005).
48. M. A. Gomez, M. Defontaine, B. Giraudeau, E. Camus, L. Colin, P. Laugier, and F. Patat, "In vivo performance of a matrix-based quantitative ultrasound imaging device dedicated to calcaneus investigation," Ultrasound Med Biol ***28***(10), 1285–1293 (2002).
49. C. F. Njeh, D. Hans, T. Fuerst, C. C. Glüer, and H. K. Genant, Quantitative Ultrasound: assesment of osteoporosis and bone status (Martin Dunitz, London, 1999).
50. R. Barkmann, S. Lüsse, B. Stampa, S. Sakata, M. Heller, and C.-C. Glüer, "Assessment of the geometry of human finger phalanges using quantitative ultrasound in vivo," Osteoporosis International ***11***, 745–755 (2000).
51. C. M. Langton, C. M. Riggs, and G. P. Evans, "Pathway of ultrasound waves in the equine third metacarpal bone," J Biomed Eng ***13***(113–118) (1991).
52. R. McCartney and L. Jeffcott, "Combined 2.25 MHz ultrasound velocity and bone mineral density measurements in the equine metacarpus and their in vivo applications.," Med Biol Eng Comput ***25***, 620–626 (1897).
53. S. Sakata, R. Barkmann, E. M. Lochmuller, M. Heller, and C. C. Gluer, "Assessing bone status beyond BMD: evaluation of bone geometry and porosity by quantitative ultrasound of human finger phalanges," J Bone Miner Res ***19***(6), 924–930. Epub 2004 Jan 2027 (2004).
54. R. Cadossi, F. de Terlizzi, V. Cane, M. Fini, and C. Wuster, "Assessment of bone architecture with ultrasonometry: experimental and clinical experience," Horm Res ***54***(Suppl 1), 9–18 (2000).
55. C. Wüster, C. Albanese, D. De Aloysio, F. Duboeuf, M. Gambacciani, S. Gonnelli, C. Glüer, D. Hans, J. Joly, J. Reginster, F. De Terlizzi, and R. Cadossi, "Phalangeal osteosonogrammetry study: age-related changes, diagnostic sensitivity, and discrimination power. The Phalangeal Osteosonogrammetry Study Group," J Bone Miner Res ***15***(8), 1603–1614 (2000).
56. Z. E. Fellah, J. Y. Chapelon, S. Berger, W. Lauriks, and C. Depollier, "Ultrasonic wave propagation in human cancellous bone: application of Biot theory," J Acoust Soc Am ***116***(1), 61–73 (2004).
57. A. Hosokawa and T. Otani, "Ultrasonic wave propagation in bovine cancellous bone," J Acoust Soc Am ***101***(1), 1–5 (1997).
58. T. Otani, "Quantitative estimation of bone density and bone quality using acoustic parameters of cancellous bone for fast and slow waves," Jpn J Appl Phys ***44***, 4578–4582 (2005).

59. J. Grondin, Q. Grimal, K. Engelke, and P. Laugier, "Potential of QUS to assess cortical bone geometry at the hip: a model based study," Ultrasound Med Biol ***36***(4), 656–666 (2010).
60. S. Dencks, R. Barkmann, F. Padilla, G. Haïat, P. Laugier, and C. C. Glüer, "Wavelet-based signal processing of in vitro ultrasonic measurements at the proximal femur," Ultrasound Med Biol ***33***(6), 970–980 (2007).
61. S. Dencks, R. Barkmann, F. Padilla, P. Laugier, G. Schmitz, and C. C. Glüer, "Model-based estimation of quantitative ultrasound variables at the proximal femur," IEEE Trans Ultrason Ferroelectr Freq Control ***55***(6), 1304–1315 (2008).
62. G. Lowet and G. Van der Perre, "Ultrasound velocity measurement in long bones: measurement method and simulation of ultrasound wave propagation," J Biomech ***29***(10), 1255–1262 (1996).
63. P. Moilanen, P. H. Nicholson, T. Karkkainen, Q. Wang, J. Timonen, and S. Cheng, "Assessment of the tibia using ultrasonic guided waves in pubertal girls," Osteoporos Int ***14***(12), 1020–1027. Epub 2003 Oct 1015 (2003).
64. M. Muller, P. Moilanen, E. Bossy, P. Nicholson, V. Kilappa, J. Timonen, M. Talmant, S. Cheng, and P. Laugier, "Comparison of three ultrasonic axial transmission methods for bone assessment," Ultrasound Med Biol ***31***(5), 633–642 (2005).
65. R. Barkmann, E. Kantorovich, C. Singal, D. Hans, H. Genant, M. Heller, and C. Glüer, "A new method for quantitative ultrasound measurements at multiple skeletal sites," J Clin Densitom ***3***, 1–7 (2000).
66. C. Njeh, I. Saeed, M. Grigorian, D. L. Kendler, B. Fan, J. Shepherd, M. McClung, W. M. Drake, and H. K. Genant, "Assessment of bone status using speed of sound at multiple anatomical sites," Ultrasound Med Biol ***10***, 1337–1345 (2001).
67. M. Talmant, S. Kolta, C. Roux, D. Haguenauer, I. Vedel, B. Cassou, E. Bossy, and P. Laugier, "In vivo performance evaluation of bi-directional ultrasonic axial transmission for cortical bone assessment," Ultrasound Med Biol ***35***(6), 912–919 (2009).
68. M. Weiss, A. Ben-Shlomo, H. P., and S. Ish-Shalom, "Discrimination of proximal hip fracture by quantitative ultrasound measurement at the radius," Osteoporos Int ***11***, 411–416 (2000).
69. E. Bossy, M. Talmant, and P. Laugier, "Effect of bone cortical thickness on velocity measurements using ultrasonic axial transmission: a 2D simulation study," J Acoust Soc Am ***112***(1), 297–307 (2002).
70. A. Sarvazyan, A. Tatarinov, V. Egorov, S. Airapetian, V. Kurtenok, and C. J. J. Gatt, "Application of the dual-frequency ultrasonometer for osteoporosis detection," Ultrasonics ***49***(3), 331–337 (2009).
71. P. Moilanen, P. H. Nicholson, V. Kilappa, S. Cheng, and J. Timonen, "Measuring guided waves in long bones: modeling and experiments in free and immersed plates," Ultrasound Med Biol ***32***(5), 709–719 (2006).
72. V. C. Protopappas, I. C. Kourtis, L. C. Kourtis, K. N. Malizos, C. V. Massalas, and D. I. Fotiadis, "Three-dimensional finite element modeling of guided ultrasound wave propagation in intact and healing long bones," J Acoust Soc Am ***121***(6), 3907–3921 (2007).
73. M. Sasso, G. Haiat, M. Talmant, P. Laugier, and S. Naili, "SVD-based algorithm for axial transmission ultrasound technique application to cortical bone characterization," IEEE Trans Ultrason Ferroelectr Freq Control ***55***(6), 1328–1332 (2008).
74. D. Ta, W. Wang, Y. Wang, L. H. Le, and Y. Zhou, "Measurement of the dispersion and attenuation of cylindrical ultrasonic guided waves in long bone," Ultrasound Med Biol ***35***(4), 641–652 (2009).
75. P. Moilanen, V. Kilappa, P. H. Nicholson, J. Timonen, and S. Cheng, "Thickness sensitivity of ultrasound velocity in long bone phantoms," Ultrasound Med Biol ***30***(11), 1517–1521. (2004).
76. P. Nicholson, P. Moilanen, T. Kärkkäinen, J. Timonen, and S. Cheng, "Guided ultrasonic waves in long bones: modelling, experiment and in vivo application," Physiol Meas ***23***, 755–768 (2002).
77. P. Moilanen, P. H. Nicholson, V. Kilappa, S. Cheng, and Timonen, J., "Assessment of the cortical bone thickness using ultrasonic guided waves: modelling and in vitro study," Ultrasound Med Biol ***33***(2), 254–262 (2007).

78. P. Moilanen, "Ultrasonic guided waves in bone," IEEE Trans Ultrason Ferroelectr Freq Control ***55***(6), 1277–1286 (2008).
79. M. Sasso, M. Talmant, G. Haiat, S. Naili, and P. Laugier, "Analysis of the most energetic low frequency arrival in axially transmitted signals in cortical bone," IEEE Trans Ultrason Ferroelectr Freq Control ***56***(11), 2463–2470 (2009).
80. J. G. Minonzio, M. Talmant, and P. Laugier, "Guided waves analysis using multi-emitters and multi-receivers arrays: decomposition of the transmission matrix," J Acoust Soc Am ***127***(5), 2913–2919 (2010).
81. E. Bossy, M. Talmant, M. Defontaine, F. Patat, and P. Laugier, "Bidirectional axial transmission can improve accuracy and precision of ultrasonic velocity measurement in cortical bone: a validation on test materials," IEEE Trans Ultrason Ferroelectr Freq Control ***51***(1), 71–79 (2004).
82. F. Lefebvre, Y. Deblock, P. Campistron, D. Ahite, and J. J. Fabre, "Development of a new ultrasonic technique for bone and biomaterials in vitro characterization," J Biomed Mater Res ***63***(4), 441–446 (2002).
83. H. Jansons, A. Tatarinov, V. Dzenis, and A. Kregers, "Constructional peculiarities of the human tibia defined by reference to ultrasound measurement data," Biomaterials ***5***, 221–226 (1984).
84. J. Huopio, H. Kroger, R. Honkanen, J. Jurvelin, S. Saarikoski, and E. Alhava, "Calcaneal ultrasound predicts early postmenopausal fractures as well as axial BMD. A prospective study of 422 women," Osteoporos Int ***15***(3), 190–195 (2004).
85. K. T. Khaw, J. Reeve, R. Luben, S. Bingham, A. Welch, N. Wareham, S. Oakes, and N. Day, "Prediction of total and hip fracture risk in men and women by quantitative ultrasound of the calcaneus: EPIC-Norfolk prospective population study," Lancet ***363***(9404), 197–202 (2004).
86. X. P. Liao, W. L. Zhang, J. He, J. H. Sun, and P. Huang, "Bone measurements of infants in the first 3 months of life by quantitative ultrasound: the influence of gestational age, season, and postnatal age," Pediatr Radiol ***35***(9), 847–853 (2005).
87. A. Stewart, V. Kumar, and D. M. Reid, "Long-term fracture prediction by DXA and QUS: a 10-year prospective study," J Bone Miner Res ***21***(3), 413–418. Epub 2005 Dec 2019 (2006).
88. H. McDevitt and S. F. Ahmed, "Quantitative ultrasound assessment of bone health in the neonate," Neonatology ***91***(1), 2–11 (2007).
89. G. Haiat, F. Padilla, R. Barkmann, S. Kolta, C. Latremouille, C. C. Gluer, and P. Laugier, "In vitro speed of sound measurement at intact human femur specimens," Ultrasound Med Biol ***31***(7), 987–996 (2005).
90. F. Jenson, F. Padilla, V. Bousson, C. Bergot, J. D. Laredo, and L. P., "In vitro ultrasonic characterization of human cancellous femoral bone using transmission and backscatter measurements: relationships to bone mineral density," J Acoust Soc Am ***119***(1), 654–663 (2006).
91. C. M. Langton, C. F. Njeh, R. Hodgskinson, and J. D. Currey, "Prediction of mechanical properties of the human calcaneus by broadband ultrasonic attenuation," Bone ***18***(6), 495–503 (1996).
92. P. H. Nicholson, R. Müller, G. Lowet, X. G. Cheng, T. Hildebrand, P. Rüegseger, G. van der Perre, J. Dequeker, and S. Boonen, "Do quantitative ultrasound measurement reflect structure independently of density in human vertebral cancellous bone," Bone ***23***(5), 425–431 (1998).
93. C. F. Njeh, R. Hodgskinson, J. D. Currey, and C. M. Langton, "Orthogonal relationships between ultrasonic velocity and material properties of bovine cancellous bone," Med Eng Phys ***18***(5), 373–381 (1996).
94. K. Wear, A. Stuber, and J. C. Reynolds, "Relationships of ultrasonic backscatter with ultrasonic attenuation, sound speed and bone mineral density in human calcaneus," Ultrasound Med Biol ***26***(8), 1311–1316 (2000).
95. C. Chappard, P. Laugier, B. Fournier, C. Roux, and G. Berger, "Assessment of the relationship between broadband ultrasound attenuation and bone mineral density at the calcaneus using BUA imaging and DXA," Osteoporos Int ***7***, 316–322 (1997).
96. J. Toyras, M. T. Nieminen, H. Kroger, and J. S. Jurvelin, "Bone mineral density, ultrasound velocity, and broadband attenuation predict mechanical properties of trabecular bone differently," Bone ***31***(4), 503–507 (2002).

97. "http://www.hologic.com/prod-bd/pdf/broch-sahara.pdf."
98. F. Padilla, F. Jenson, and P. Laugier, "Estimation of trabecular thickness using ultrasound ultrasonic baclkscatter," Ultrasonic Imaging ***28***, 3–22 (2006).
99. K. A. Wear, "Ultrasonic scattering from cancellous bone: a review," IEEE Trans Ultrason Ferroelectr Freq Control ***55***(7), 1432–1441 (2008).
100. J. P. Karjalainen, J. Töyräs, O. Riekkinen, M. Hakulinen, and J. S. Jurvelin, "Ultrasound backscatter imaging provides frequency-dependent information on structure, composition and mechanical properties of human trabecular bone," Ultrasound Med Biol ***35***(8), 1376–1384 (2009).
101. O. Riekkinen, M. A. Hakulinen, M. J. Lammi, J. S. Jurvelin, A. Kallioniemi, and J. Töyräs, "Acoustic properties of trabecular bone–relationships to tissue composition," Ultrasound Med Biol ***33***(9), 1438–1444 (2007).
102. O. Riekkinen, M. A. Hakulinen, J. Töyräs, and J. S. Jurvelin, "Spatial variation of acoustic properties is related with mechanical properties of trabecular bone," Phys Med Biol ***52***(23), 6961–6968 (2007).
103. E. Bossy, M. Talmant, F. Peyrin, L. Akrout, P. Cloetens, and P. Laugier, "An in vitro study of the ultrasonic axial transmission technique at the radius: 1-MHz velocity measurements are sensitive to both mineralization and intracortical porosity," J Bone Miner Res ***19***(9), 1548–1556. Epub 2004 Jun 1542 (2004).
104. K. Raum, I. Leguerney, F. Chandelier, E. Bossy, M. Talmant, A. Saied, F. Peyrin, and P. Laugier, "Bone microstructure and elastic tissue properties are reflected in QUS axial transmission measurements," Ultrasound Med Biol ***31***(9), 1225–1235 (2005).
105. M. Muller, D. Mitton, P. Moilanen, V. Bousson, M. Talmant, and P. Laugier, "Prediction of bone mechanical properties using QUS and pQCT: study of the human distal radius," Med Eng Phys ***30***(6), 761–767 (2008).

Chapter 4
Clinical Applications

Reinhard Barkmann and Claus-C. Glüer

Abstract Quantitative Ultrasound (QUS) methods measure aspects of bone strength which are associated with the fragility of the bone. It has been proven that QUS (at least for some devices measuring at the heel bone) can predict osteoporotic fractures in elderly women with a predictive power similar to that of the recommended method DXA, which measures x-ray attenuation in the mineral phase of the bone to calculate a bone mineral density. However, the use of QUS in clinical practice is still uncertain. Unsolved quality assurance issues, the diversity of the approaches and the unanswered question, if patients with low QUS results will most likely profit from a therapy still limit the prospects of the method for widespread clinical use. Nevertheless, QUS has the potential for a clinical application. Advantages over DXA are the smaller size and lower price of the devices and the lack of ionizing radiation. Once the mentioned problems will be solved, QUS could become an important part in osteoporosis management, at least in rural environments and less-developed countries with limited access to DXA.

Keywords Diagnosis · Fracture risk · Monitoring · Osteoporosis · Quality control · Treatment

4.1 Introduction

Most guidelines for the management of osteoporosis recommend Dual X-ray Absorptiometry (DXA) measurements for the diagnosis of osteoporosis and as part of the diagnostic procedure for the assessment of the osteoporotic fracture risk and treatment initiation. DXA is a method measuring x-ray attenuation in the mineral phase of the bone to calculate a bone mineral density (BMD). Special purpose DXA

R. Barkmann (✉) and C.-C. Glüer
Arbeitsgruppe Medizinische Physik, Klinik für Diagnostische Radiologie,
Universitätsklinikum Schleswig-Holstein, Kiel, Germany
e-mail: barkmann@rad.uni-kiel.de; glueer@rad.uni-kiel.de

P. Laugier and G. Haïat (eds.), *Bone Quantitative Ultrasound*,
DOI 10.1007/978-94-007-0017-8_4,

devices are relative large and expensive, and access is limited in rural environments and less-developed countries. Quantitative Ultrasound (QUS) methods also measure aspects of bone strength which are associated with the fragility of the bone [1, 2]. Several prospective and cross-sectional studies have been published proving that QUS (at least for some devices acting in transverse transmission at the heel bone) can predict osteoporotic fractures in elderly women with a predictive power similar to that of DXA [3, 4].

QUS has advantages over DXA. The devices are inexpensive and transportable and the method is free of ionizing radiation [5, 6]. Despite of the fact that the ability of QUS to predict osteoporotic fracture risk is well established, its use in clinical practice is still uncertain. Unsolved quality assurance issues, the diversity of the approaches and the unanswered question, if patients with low QUS results will most likely profit from a therapy still limit the prospects of the method for widespread clinical use [7, 8].

We will describe the potential of QUS for a clinical application in osteoporosis management, the status today and its future perspectives.

4.2 QUS for Fracture Risk Assessment

The best studies with regard to the clinical application of QUS describe the estimation of osteoporotic fracture risk. It has been shown in cross-sectional and prospective studies, that the power of transverse transmission QUS of the heel is comparable to DXA of the hip or spine with regard to the estimation of osteoporotic fracture risk [4]. This holds true for vertebral and hip fractures as well as for the global fracture risk. However, the differences between different QUS technologies have to be taken into account, and even if different devices use the same method they may perform differently because of technological implementation details. Available data clearly demonstrate strong and consistent predictive power for fracture risk for several different QUS devices measuring at the heel bone while the performance of QUS devices measuring at other skeletal sites is poorer.

In a consensus statement the International Society for Clinical Densitometry (ISCD) has summarized the performance of heel QUS devices in comparison with DXA with regard to prospective studies for the prediction of osteoporotic fractures in postmenopausal women [4]. Relative risks or hazard ratios for hip fractures range between 1.9 and 2.5 for the Achilles and the Sahara devices, for vertebral fractures between 1.6 and 2.3 for the Achilles device and between 1.3 and 1.7 for non vertebral clinical fractures for the Achilles and the Sahara devices. In the mean time the Achilles was replaced by a successor model, the Achilles InSight [9]. Total hip or femur neck BMD measurements by DXA showed a similar performance.

In a study comparing the performance of four heel QUS devices and one device measuring the phalanges in transverse transmission the heel devices (Achilles, DTU-one, QUS-2 and UBIS 5000) were predictors of hip and vertebral fractures at least as well as central DXA [10]. The phalanges QUS DBM Sonic failed to predict

hip and vertebral fractures in concordance with another study [11] and showed modest predictive power for osteoporotic fractures of any type.

From these data it is evident that validated heel QUS devices predict osteoporotic fractures in postmenopausal women and in men over the age of 65 (shown for hip and all non vertebral fractures) independently and as well as central DXA BMD [4].

4.3 Diagnosis of Osteoporosis

Osteoporosis is defined as a 'disease characterized by low bone mass and microarchitectural deterioration of bone tissue leading to enhanced bone fragility and a consequent increase in fracture risk' [12]. In order to introduce a quantitative measure of osteoporosis the World Health Organization (WHO) proposed BMD measurements using DXA in postmenopausal Caucasian women. The BMD value of an individual patient is expressed in terms of the number of standard deviations from the mean BMD of a healthy young-adult reference population, commonly referred to as the T-score [13]. Osteoporosis has been defined by a T-score of -2.5 or less based on BMD measurements applied to the hip and lumbar spine (the radius is no longer considered an adequate measurement site for diagnostic purposes). However, it is not possible to apply the WHO criteria to other technologies and other skeletal sites and it cannot simply be used for QUS. DXA and different QUS approaches may show very different age-related declines [14–16]. Consequently, the number of subjects who fall below the T-score $= -2.5$ threshold will vary and different percentages of subjects will be identified as osteoporotic. For different QUS devices the prevalence of 60 year old women with a T-score below -2.5 varies from 4% to 50% [4]. By using device and variable specific thresholds it seems as if this problem can be overcome, because these thresholds could be chosen appropriate so that the same number of patients would be classified as osteoporotic. However, the correlation between peripherally measured QUS variables and axial BMD is moderate and a strong mismatching would occur, e.g. a considerable number of patients would be classified as osteoporotic by one method but not by the other and vice versa (Fig. 4.1). One has to conclude that peripheral QUS cannot be used to diagnose osteoporosis as long as DXA remains the gold standard for diagnosis. However, one should keep in mind that the diagnosis of osteoporosis is only indirect, i.e. by means of exclusion of other causes of bone loss. Moreover, in a different definition of osteoporosis put forward by an NIH panel [17] the key criterion for osteoporosis is reduced bone strength, not reduced bone density. According to this definition, DXA and other methods such as QUS could be used to identify subjects with the diagnosis of osteoporosis. However one should note that there is no consensus how this could be done in clinical practice. Moreover, different methods would identify different patients as being osteoporotic and this would create confusion in clinical practice. Therefore, for the time being, DXA remains the only accepted method for diagnosis of osteoporosis.

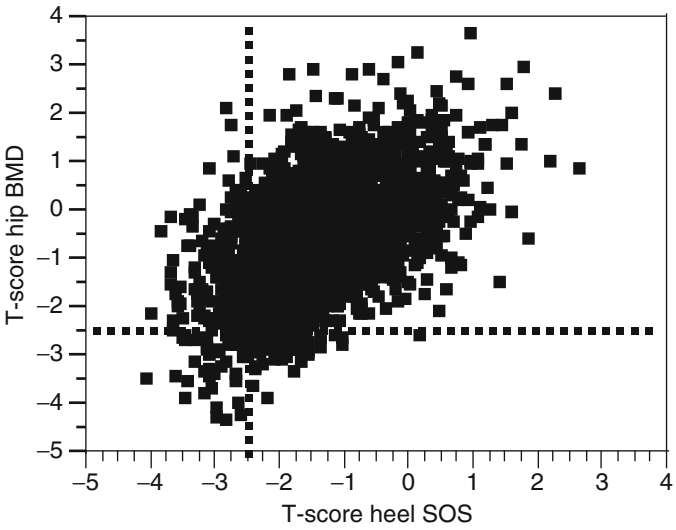

Fig. 4.1 Correlation between total hip BMD and calcaneus SOS. *The dotted lines* mark the osteoporosis thresholds for both variables. Only in the *lower left rectangle* the same patients are classified as osteoporotic by both methods. In the *lower right* and *upper left rectangle* a considerable amount of patients are misclassified (Data from the OPUS study [18])

4.4 Treatment Initiation

Because QUS cannot be used to diagnose osteoporosis it is not clear whether QUS can be used to initiate a treatment. For peripheral DXA a triaging approach has been suggested, applying technique-specific thresholds to classify patients according to their risk of osteoporosis [19]. In this approach a technique-specific upper BMD threshold was defined identifying women without osteoporosis at a level of specificity of 90% – these patients do not require treatment. Women with a BMD below a technique-specific lower threshold are classified as osteoporotic at a level of sensitivity of 90% and should be treated without a further central DXA measurement. For women with a result between these thresholds the diagnosis is unclear and a central DXA measurement should be performed additionally. This approach could also be applied to QUS-variables. However, QUS and central DXA results correlated only at a level of approximately R^2 of 0.2–0.4 [20, 21]. In its recent position with regard to QUS the ISCD has calculated these numbers for two QUS devices concluding that 56% of the women have QUS results between the two thresholds and thus would still require an additional DXA measurement but for the remaining 44% a QUS result would be sufficient. This number could be enhanced if QUS approaches with stronger correlation to central DXA could be developed. First measurements with an experimental device for femur QUS measurements show a stronger correlation of $R^2 = 0.7$ with hip BMD [22] and the number of patients

who would not have to be referred to a DXA measurement increases to 90%. This device, while not yet available for clinical use shows the potential of site-specific QUS approaches, specifically for measurements at the hip.

Despite of their moderate correlation QUS and central BMD have similar power to predict osteoporotic fractures. Not exactly the same patients are classified as osteoporotic, nevertheless, low results in BMD and QUS both are associated with a high fracture risk. But the question still remains, if patients, who are identified by QUS as having a high fracture risk, will profit from a therapy, i.e. will benefit from a significant reduction in fracture risk. For DXA osteoporosis treatment agents reduce vertebral fracture risk by about 50–70% and appendicular fracture risk by about 30% [23, 24]. Currently, there are no studies showing similar reductions for QUS, because usually patients for pharmaceutical treatment studies were selected by low axial DXA results. Measured at the same site, heel QUS and BMD are strongly correlated [8], which shows that at trabecular sites QUS and DXA predominantly measure the same aspects of bone strength. Therefore, it is unlikely that studies in future will show performance for heel QUS inferior to that established for axial DXA.

Recently, in national and international guidelines for osteoporosis management the paradigm for treatment recommendation was changed. Instead of the WHO criterion the level of fracture risk based on age, lifestyle, clinical risk factors and a quantitative measure (usually DXA) is proposed to derive an intervention threshold [4]. In the future, a similar approach might be applicable based on QUS results as a quantitative measure [25, 26].

4.5 Monitoring Treatment with QUS

In general, peripheral skeletal sites are less sensitive to treatment induced changes compared to axial sites, specifically measurements at the spine. This is disadvantageous for QUS methods, which are only applicable at peripheral sites (unless their precision would be better than the precision of axial methods like DXA, which so far is not the case). The picture gets more complicated because different QUS methods exist. There are only few studies dealing with the effect of pharmaceutical treatment on QUS results, showing no clear evidence that QUS is useful for treatment monitoring [27–30]. Best performance has been shown for QUS at the heel, which shows a similar pattern as axial DXA in patients treated with antiresorptive drugs [4]. This may be due to the fact that both the calcaneus and the vertebral bodies largely consist of highly responsive trabecular bone. Up to date only few studies have been published for QUS devices and for most of them longitudinal sensitivity, i.e. the ratio between responsiveness and precision was better for DXA of the spine than for peripheral QUS [4]. Since responsiveness cannot be altered the goal should be to improve the precision of QUS approaches to maximize longitudinal sensitivity.

4.6 Quality Control

An important issue for clinical utility is the establishment of sufficient quality control procedures. These include monitoring of the stability of the devices as well as guidelines for the handling of error sources.

For QUS measurement errors can emerge from wrong positioning, inadequate consideration of the impact of soft tissue properties or inadequate coupling between transducers and the skin of the patients. To achieve sufficient accuracy anatomically consistent regions of the bone must be measured with QUS. The use of an imaging system may help to overcome positioning errors by placing a ROI on the image [31, 32]. The prevention of measurement errors due to incorrect positioning is of great importance for the individual subject. Creation of an image also permits the documentation of the correct positioning by the operator and the validity of the measurement, issues that are particularly relevant for longitudinal follow-up.

QUS variables are influenced by the properties of all materials being penetrated by the ultrasound beam. For example, the thickness and the temperature of the skin and of subcutaneous tissue have an impact on the propagation of the wave. Variations in the heel thickness change SOS due to the changes in the bone-to-soft-tissue-ratio along the ultrasound pathway. Compared to gel-coupled devices, for water-based systems a smaller effect can be anticipated because the acoustical parameters of oedema and water are quite similar [33, 34]. The temperatures of the fatty layers around the calcaneus affect particularly the SOS variable [33]. This is considered to be the strongest error source. Warming up of the foot prior to the measurement could be one recommendation; definition of a procedure of correcting the QUS results using a foot temperature measurement might also or further enhance the performance.

The achievement of a good quality transmission of the ultrasonic beam into the body by using a coupling gel or liquid is essential. In systems using water as coupling medium air bubbles in the water and variations in water temperature represent potential error sources which can be avoided by adding surfactants and using temperature control. In gel-coupled systems, errors may be caused by the temperature-dependence and aging of coupling pads [33].

Monitoring the performance and stability of the devices by regular quality control measurements using appropriate phantoms is a precondition for the assessment of good measurement quality. A phantom should emulate the in vivo measurement as much as possible in terms of geometry and acoustic properties. This can best be achieved with an anthropomorphic phantom. Factors affecting the stability like temperature variations also have to be considered. Presently, there are no universally accepted QUS phantoms, only “manufacturer specific” non-anthropomorphic phantoms. However, it is unknown to what extent changes in phantom results reflect true changes in vivo and if such devices can be used for the calibration of the system. Although some attempts have been made to build reliable phantoms [35–38] this issue has not yet been solved satisfying.

4.7 Summary

There is strong evidence that (at least some) QUS methods can be used to predict osteoporotic fractures as well as central DXA. The most promising approach for the clinical use of QUS seems to be the estimation of the osteoporotic fracture risk by combing a QUS-measurement of the calcaneus (using a validated device) with clinical risk factors. Once it has been shown that patients with low QUS results profit from a therapy as well as patients with low DXA results this procedure might obviate the need to obtain DXA results in all patients considered for treatment. In the mean time, quality assurance concepts should be improved, including optimized QUS phantoms, stringent quality control procedures and guidelines for handling of error sources and training of the users.

References

1. M. L. Bouxsein, B. S. Coan, and S. C. Lee, "Prediction of the strength of the elderly proximal femur by bone mineral density and quantitative ultrasound measurements of the heel and tibia," Bone **25**(1), 49–54 (1999).
2. E. M. Lochmüller, R. Müller, V. Kuhn, C. A. Lill, and F. Eckstein, "Can novel clinical densitometric techniques replace or improve DXA in predicting bone strength in osteoporosis at the hip and other skeletal sites?," J Bone Miner Res **18**(5), 906–912 (2003).
3. F. Marin, J. Gonzalez-Macias, A. Diez-Perez, S. Palma, and M. Delgado-Rodriguez, "Relationship between bone quantitative ultrasound and fractures: a meta-analysis," J Bone Miner Res **21**(7), 1126–1135 (2006).
4. M. A. Krieg, R. Barkmann, S. Gonnelli, A. Stewart, D. C. Bauer, L. Del Rio Barquero, J. J. Kaufman, R. Lorenc, P. D. Miller, W. P. Olszynski, C. Poiana, A. M. Schott, E. M. Lewiecki, and D. Hans, "Quantitative ultrasound in the management of osteoporosis: the 2007 ISCD Official Positions," J Clin Densitom **11**(1), 163–187 (2008).
5. R. Barkmann, "Quantitative Ultrasound," in *Radiology of Osteoporosis*, 2nd edn. S. Grampp, ed. (Springer, Heidelberg, 2008), pp. 163–173.
6. C. F. Njeh, D. Hans, T. Fuerst, C. C. Glüer, and H. K. Genant, *Quantitative Ultrasound: Assessment of Osteoporosis and Bone Status* (Martin Dunitz, London, 1999).
7. C. C. Gluer, "Quantitative Ultrasound – it is time to focus research efforts," Bone **40**(1), 9–13 (2007).
8. R. S. Siffert and J. J. Kaufman, "Ultrasonic bone assessment: "the time has come," Bone **40**(1), 5–8 (2007).
9. C. Cepollaro, S. Gonnelli, A. Montagnani, C. Caffarelli, A. Cadirni, S. Martini, and R. Nuti, "In vivo performance evaluation of the Achilles Insight QUS device," J Clin Densitom **8**(3), 341–346 (2005).
10. C. C. Gluer, R. Barkmann, T. Blenk, A. Stewart, S. Kolta, J. Finigan, C. Graeff, J. Von der Gablentz, I. Eastell, D. M. Reid, C. Roux, and D. Felsenberg, "Quantitative ultrasound predicts incident vertebral and hip fractures at least as strongly as DXA: the OPUS study," J Bone Miner Res **22**, S21–S21 (2007).
11. M. A. Krieg, J. Cornuz, C. Ruffieux, G. Van Melle, D. Buche, M. A. Dambacher, D. Hans, F. Hartl, H. J. Hauselmann, M. Kraenzlin, K. Lippuner, M. Neff, P. Pancaldi, R. Rizzoli, F. Tanzi, R. Theiler, A. Tyndall, C. Wimpfheimer, and P. Burckhardt, "Prediction of hip fracture risk by quantitative ultrasound in more than 7000 Swiss women $>$ or $=$ 70 years of age: comparison of three technologically different bone ultrasound devices in the SEMOF study," J Bone Miner Res **21**(9), 1457–1463 (2006).

12. "Consensus development conference: diagnosis, prophylaxis, and treatment of osteoporosis," Am J Med **94**(6), 646–650 (1993).
13. C. Simonelli, R. A. Adler, G. M. Blake, J. P. Caudill, A. Khan, E. Leib, M. Maricic, J. C. Prior, S. R. Eis, C. Rosen, and D. L. Kendler, "Dual-Energy X-Ray Absorptiometry Technical issues: the 2007 ISCD Official Positions," J Clin Densitom **11**(1), 109–122 (2008).
14. M. L. Frost, G. M. Blake, and I. Fogelman, "Can the WHO criteria for diagnosing osteoporosis be applied to calcaneal quantitative ultrasound?," Osteoporos Int **11**(4), 321–330 (2000).
15. K. G. Faulkner, E. von Stetten, and P. Miller, "Discordance in patient classification using T-scores," J Clin Densitom **2**(3), 343–350 (1999).
16. D. Hans, R. Rizzoli, D. Thiebaud, K. Lippuner, S. Allaoua, L. Genton, F. Luzuy, M. A. Krieg, P. Jaeger, and D. O. Slosman, "Reference data in a Swiss population. Discordance in patient classification using T-scores among calcaneum, spine, and femur," J Clin Densitom **4**(4), 291–298 (2001).
17. NIH, "Osteoporosis prevention, diagnosis, and therapy," JAMA **285**(6), 785–795 (2001).
18. C. C. Glüer, R. Eastell, D. M. Reid, D. Felsenberg, C. Roux, R. Barkmann, W. Timm, T. Blenk, G. Armbrecht, A. Stewart, J. Clowes, F. E. Thomasius, and S. Kolta, "Association of five quantitative ultrasound devices and bone densitometry with osteoporotic vertebral fractures in a population-based sample: the OPUS Study," J Bone Miner Res **19**(5), 782–793 (2004).
19. G. M. Blake, D. J. Chinn, S. A. Steel, R. Patel, E. Panayiotou, J. Thorpe, and J. N. Fordham, "A list of device-specific thresholds for the clinical interpretation of peripheral x-ray absorptiometry examinations," Osteoporos Int **16**(12), 2149–2156 (2005).
20. K. G. Faulkner, M. R. McClung, L. J. Coleman, and E. Kingston-Sandahl, "Quantitative ultrasound of the heel: correlation with densitometric measurements at different skeletal sites," Osteoporos Int **4**(1), 42–47 (1994).
21. L. Rosenthall, A. Tenenhouse, and J. Caminis, "A correlative study of ultrasound calcaneal and dual-energy X-ray absorptiometry bone measurements of the lumbar spine and femur in 1000 women," Eur J Nucl Med **22**(5), 402–406 (1995).
22. R. Barkmann, S. Dencks, P. Laugier, F. Padilla, K. Brixen, J. Ryg, A. Seekamp, L. Mahlke, A. Bremer, M. Heller, and C. C. Gluer, "Femur ultrasound (FemUS)-first clinical results on hip fracture discrimination and estimation of femoral BMD," Osteoporos Int (2009).
23. J. A. Kanis, N. Burlet, C. Cooper, P. D. Delmas, J. Y. Reginster, F. Borgstrom, and R. Rizzoli, "European guidance for the diagnosis and management of osteoporosis in postmenopausal women," Osteoporos Int **19**(4), 399–428 (2008).
24. S. Boonen, R. F. Laan, I. P. Barton, and N. B. Watts, "Effect of osteoporosis treatments on risk of non-vertebral fractures: review and meta-analysis of intention-to-treat studies," Osteoporos Int **16**(10), 1291–1298 (2005).
25. D. Hans, C. Durosier, J. A. Kanis, H. Johansson, A. M. Schott-Pethelaz, and M. A. Krieg, "Assessment of the 10-year probability of osteoporotic hip fracture combining clinical risk factors and heel bone ultrasound: the EPISEM prospective cohort of 12,958 elderly women," J Bone Miner Res **23**(7), 1045–1051 (2008).
26. A. Moayyeri, S. Kaptoge, N. Dalzell, S. Bingham, R. N. Luben, N. J. Wareham, J. Reeve, and K. T. Khaw, "Is QUS or DXA better for predicting the 10-year absolute risk of fracture?," J Bone Miner Res **24**(7), 1319–1325 (2009).
27. S. Gonnelli, C. Cepollaro, A. Montagnani, S. Martini, L. Gennari, M. Mangeri, and C. Gennari, "Heel ultrasonography in monitoring alendronate therapy: a four-year longitudinal study," Osteoporos Int **13**(5), 415–421 (2002).
28. S. Gonnelli, G. Martini, C. Caffarelli, S. Salvadori, A. Cadirni, A. Montagnani, and R. Nuti, "Teriparatide's effects on quantitative ultrasound parameters and bone density in women with established osteoporosis," Osteoporos Int **17**(10), 1524–1531 (2006).
29. M. A. Krieg, A. F. Jacquet, M. Bremgartner, S. Cuttelod, D. Thiebaud, and P. Burckhardt, "Effect of supplementation with vitamin D3 and calcium on quantitative ultrasound of bone in elderly institutionalized women: a longitudinal study," Osteoporos Int **9**(6), 483–488 (1999).
30. M. L. Frost, G. M. Blake, and I. Fogelman, "Changes in QUS and BMD measurements with antiresorptive therapy: a two-year longitudinal study," Calcif Tissue Int **69**(3), 138–146 (2001).

31. D. Hans, A. M. Schott, M. E. Arlot, E. Sornay, P. D. Delmas, and P. J. Meunier, "Influence of anthropometric parameters on ultrasound measurements of Os calcis," Osteoporos Int **5**(5), 371–376 (1995).
32. S. Cheng, C. F. Njeh, B. Fan, X. Cheng, D. Hans, L. Wang, T. Fuerst, and H. K. Genant, "Influence of region of interest and bone size on calcaneal BMD: implications for the accuracy of quantitative ultrasound assessments at the calcaneus," Br J Radiol **75**(889), 59–68 (2002).
33. M. A. Paggiosi, A. Blumsohn, R. Barkmann, and R. Eastell, "Effect of temperature on the longitudinal variability of quantitative ultrasound variables," J Clin Densitom **8**(4), 436–444 (2005).
34. M. Iki, E. Kajita, S. Mitamura, H. Nishino, T. Yamagami, and N. Nagahama, "Precision of quantitative ultrasound measurement of the heel bone and effects of ambient temperature on the parameters," Osteoporos Int **10**(6), 462–467 (1999).
35. W. D. Evans, E. A. Jones, and G. M. Owen, "Factors affecting the in vivo precision of broadband ultrasonic attenuation," Phys Med Biol **40**(1), 137–151 (1995).
36. P. O. Kotzki, D. Buyck, D. Hans, E. Thomas, F. Bonnel, F. Favier, P. J. Meunier, and M. Rossi, "Influence of fat on ultrasound measurements of the os calcis," Calcif Tissue Int **54**(2), 91–95 (1994).
37. C. Chappard, E. Camus, F. Lefebvre, G. Guillot, J. Bittoun, G. Berger, and P. Laugier, "Evaluation of error bounds on calcaneal speed of sound caused by surrounding soft tissue," J Clin Densitom **3**(2), 121–131 (2000).
38. A. Johansen and M. D. Stone, "The effect of ankle oedema on bone ultrasound assessment at the heel," Osteoporos Int **7**(1), 44–47 (1997).

Chapter 5
Poromechanical Models

Michal Pakula, Mariusz Kaczmarek, and Frederic Padilla

Abstract This chapter reviews the Biot's model for predicting propagation of ultrasonic waves in cancellous bone. A presentation of the general theory, including recent developments in the field of poroelastic modelling is proposed. These include micro-inhomogeneity in the fluid flow, thermal conduction effects, macroscopic viscous stresses and micro-poromechanical models such as the multi-layer model. Studies comparing empirical results with predictions from different versions of the Biot's model are reviewed, and the relevance of these models is discussed. A parametric analysis is performed to illustrate the strong sensitivity of the theoretical predictions to the input parameters.

Keywords Attenuation coefficient · Biot-Allard model · Biot's theory · Biot-Willis elastic constants · Characteristic size of pore space · Darcy flow · Dynamic coupling · Fast wave · Interaction force · Johnson-Koplik-Dashen model · Modified Biot-Attenborough model · Multi-layer model · Permeability · Phase velocity · Poro-elasticity · Poromechanical modelling · Porosity · Schoenberg model · Slip effect · Slow wave · Squirt flow · Tortuosity · Two-phase model · Velocity dispersion · Viscous characteristic length · Viscous coupling

M. Pakula (✉) and M. Kaczmarek
Institute of Mechanics and Applied Computer Science, Kazimierz Wielki University in Bydgoszcz, Poland
e-mail: michalp@ukw.edu.pl; mkk@ukw.edu.pl

F. Padilla
Université Pierre et Marie Curie, CNRS, Laboratoire d'Imagerie Parametrique, UMR 7623, Paris, France
and
University of Michigan Medical Center, Department of Radiology, Ann Arbor, MI, USA
e-mail: fpadilla@umich.edu

P. Laugier and G. Haïat (eds.), *Bone Quantitative Ultrasound*,
DOI 10.1007/978-94-007-0017-8_5,

5.1 Introduction

Cancellous bone is a porous medium, composed of connected solid trabeculae (the solid frame or skeleton) filled with marrow (the saturating fluid). For *in vitro* experiments, marrow is frequently replaced by water. This is why numerous attempts have been made to model ultrasonic wave propagation in cancellous bones using the Biot's theory [1–3], the most fundamental and well known model of wave propagation in porous media. Since the original Biot's theory is not yet validated for trabecular bones more recent developments in the field of poroelastic modelling (e.g. some micromechanical models like the multi-layer model) are also considered.

Macroscopic two-phase modelling of wave propagation in fluid saturated porous materials, particularly bones, is based on the concept of superimposed interacting continua to describe the solid phase, or skeleton (with its organic and mineral components), and the fluid phase (marrow). The field of modelling known as poromechanics takes into account the porous and permeable nature of cancellous bones, assuming that the skeleton and pore fluid can carry loads and that the fluid can be transported in the pore space as illustrated by the Fig. 5.1. Moreover, in contrast to single phase theories, the structure of the skeleton can be described in poromechanics by parameters characteristics of the inertial, elastic and viscous properties of the two phases. The poromechanical approach predicts specific features in the types of wave modes, in the mechanisms of dispersion and attenuation, and in the forms of interaction at bone boundaries, some of which were indeed observed in experimental study of cancellous bones.

This chapter reviews the application of the original Biot's theory and its more recent developments to model the ultrasonic propagation in fluid saturated cancellous bones.

In a first part, the theoretical formulation of the Biot's model is presented. The original Biot's model equations are given as well as its subsequent developments based on more general theories like the theory of mixtures [4, 5] and on modelling techniques such as upscaling methods [6–8]. This presentation is not limited to the models already applied to predict wave propagation in bones. It also describes

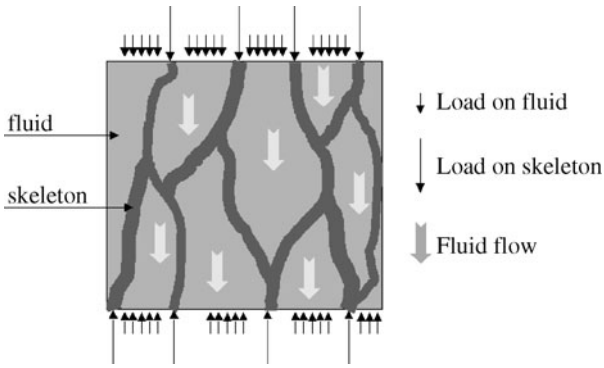

Fig. 5.1 Schematic illustration of a loaded piece of bone along with transport of fluid

additional effects which were introduced in other domains like earth sciences, acoustics or materials sciences [9–11], and which could potentially play a significant role during propagation in bones.

The second part of the chapter is a review of the studies comparing empirical results obtained in cancellous bones with predictions from different versions of the Biot's model. This review is followed by a sensitivity analysis of the theoretical predictions to variations in the input parameters, which illustrates the difficulty of use of poromechanics models due to the potentially large number of unknowns and the large inter-specimens variability in bones.

5.2 Biot Theory

5.2.1 Balance Equations

The reader may refer to Chap. 2 for the basic knowledge on wave propagation, which is necessary to understand this chapter. Assuming that the pore fluid is homogeneous (partial saturation or composition of immiscible fluids are not considered) and that there is no mass exchange between the fluid and the skeleton, the general form of the balance equations for mass and linear momentum for the phase α (with $\alpha = s$ for solid skeleton or f for fluid) can be written as:

$$\begin{aligned} &\frac{d^\alpha}{dt}\rho^\alpha + \rho^\alpha \nabla \cdot \mathbf{v}^\alpha = 0 \\ &\rho^\alpha \frac{d^\alpha}{dt}\mathbf{v}^\alpha - \nabla \cdot \mathbf{T}^\alpha - \rho^\alpha \mathbf{g}^\alpha = \mathbf{R}^\alpha \end{aligned} \tag{5.1}$$

where, $\rho^\alpha, \mathbf{v}^\alpha$ are the macroscopic mass density and velocity vector, $\mathbf{T}^\alpha$ denotes average stress tensor, $\mathbf{g}^\alpha$ is the density of body forces, and $\mathbf{R}^\alpha$ stands for the interaction force or linear momentum exchange. The interaction forces and the operator of material time derivative satisfy the following relationships:

$$\begin{aligned} \mathbf{R}^s &= -\mathbf{R}^f, \\ \frac{d^\alpha}{dt} &= \frac{\partial}{\partial t} + \mathbf{v}^\alpha \cdot \nabla. \end{aligned}$$

When the stress tensors are symmetric, body forces are insignificant, and effects requiring energy balance and additional degrees of freedom, e.g. related to changes of porosity, are negligible the linearized two-phase model of wave propagation can then be based on the two equations of linear momentum for the solid and the fluid phases:

$$\begin{aligned} &\rho^s \frac{\partial}{\partial t}\mathbf{v}^s - \nabla \cdot \mathbf{T}^s = \mathbf{R}^s \\ &\rho^f \frac{\partial}{\partial t}\mathbf{v}^f - \nabla \cdot \mathbf{T}^f = \mathbf{R}^f \end{aligned} \tag{5.2}$$

Taking into account the porosity of the material ϕ (defined as the ratio of the pore volume over the total volume of the sample), the macroscopic mass densities and stress tensors of the phases can be expressed by the following intrinsic averages:

$$\rho^s = (1-\phi)\bar{\rho}^s, \quad \rho^f = \phi\bar{\rho}^f$$
$$\mathbf{T}^s = (1-\phi)\overline{\mathbf{T}}^s, \quad \mathbf{T}^f = \phi\overline{\mathbf{T}}^f$$

where $\bar{\rho}^s, \bar{\rho}^f$ are the intrinsic mass densities of the solid and the fluid phase, and $\overline{\mathbf{T}}^s, \overline{\mathbf{T}}^f$ are the appropriate intrinsic stress tensors.

5.2.2 Boundary Conditions

Modeling the interaction of waves with boundaries (including wave's reflection and transmission) or the generation of surface waves requires the use of boundary conditions. Usually, these conditions refer to the interfaces (contacts) between the fluid filled porous material and another fluid, an impermeable solid or another fluid saturated porous medium [12]. In general, conditions of continuity of volumetric flux and total stresses and/or pressure are required.

The condition of continuity of volumetric flux (derived from the continuity of mass flux) determined on both sides of the interface (denoted by $+$ and $-$) is

$$(\tilde{\mathbf{v}}^+ - \tilde{\mathbf{v}}^-) \cdot \mathbf{n} = 0 \tag{5.3}$$

where $\tilde{\mathbf{v}}$ is the vector of volumetric flux and $\mathbf{n}$ denotes the normal unit vector to the interface. While for single phase materials the vector of volumetric flux is equal to the velocity, in the case of a porous medium it reads

$$\tilde{\mathbf{v}} = (1-\phi)\mathbf{v}^s + \phi\mathbf{v}^f.$$

If a porous medium is in a contact with another porous medium or a solid, the equality of the normal components of the velocities of solids is also required.

The condition of continuity of normal and tangential components of total stress can be written as

$$[(\mathbf{T}^+ - \mathbf{T}^-) \cdot \mathbf{n}] \cdot \mathbf{n} = 0$$
$$[(\mathbf{T}^+ - \mathbf{T}^-) \cdot \mathbf{n}] \cdot \boldsymbol{\tau} = 0 \tag{5.4}$$

where $\boldsymbol{\tau}$ is the tangential unit vector. The total stress $\mathbf{T}$ for single phase materials is identical with the appropriate stress tensor for solid or fluid, but for saturated porous materials, it is the sum of the stress tensors of the two phases:

$$\mathbf{T} = \mathbf{T}^s + \mathbf{T}^f.$$

If at the boundary there is a contact between fluids (an ambient fluid and the fluid in the pores), the continuity of pressure is additionally required, i.e.

$$p^+ - p^- = 0$$

where p denotes the pore pressure or the pressure in the free fluid.

Modeling the interaction of waves with a boundary of porous material which leads to generation of surface waves requires the stress free boundary conditions:

$$(\mathbf{T}\cdot\mathbf{n})\cdot\mathbf{n} = 0, \quad (\mathbf{T}\cdot\mathbf{n})\cdot\boldsymbol{\tau} = 0, \quad p = 0 \tag{5.5}$$

More general conditions including dissipation, slip effect or frequency dependence can also be considered [12–15].

5.2.3 Constitutive Equations

The specific properties of the materials are described within constitutive models. In the case of poromechanics, the model usually constitutes equations for stress tensors $\mathbf{T}^\alpha$ and interaction forces $\mathbf{R}^\alpha$.

5.2.3.1 Isotropic Case

Assuming an isotropic porous material fully saturated, with an elastic skeleton, Biot [1] postulated that:

$$\begin{aligned}\mathbf{T}^s &= 2N\boldsymbol{\varepsilon}^s + (A\theta^{\mathrm{s}} + \mathrm{Q}\theta^f)\mathbf{I}\\ \mathbf{T}^f &= (\mathrm{Q}\theta^{\mathrm{s}} + \mathrm{R}\theta^f)\mathbf{I}\end{aligned} \tag{5.6}$$

where

$$\theta^\alpha = tr\boldsymbol{\varepsilon}^\alpha$$

are the dilatations, $\boldsymbol{\varepsilon}^\alpha$ the strain tensors, and N, A, Q, R elasticity constants. It should be noticed that the above model neglects viscous components in stress tensors (and as a result in surface forces), and assumes spatially uniform porosity. If the material constituting the skeleton is microscopically homogeneous, the elasticity constants A, Q and R can be related to physically well defined and measurable parameters of the porous medium: the porosity (ϕ), the bulk modulus of the solid material and of the fluid (K_s, K_f), and the bulk modulus of the drained skeleton (K_b). These constants are given by:

$$\begin{aligned}A &= \frac{(1-\phi)\left(1-\phi-\frac{K_b}{K_s}\right)K_s + \phi\frac{K_s}{K_f}K_b}{1-\phi-\frac{K_b}{K_s}+\phi\frac{K_s}{K_f}} + \frac{4}{3}N\\ Q &= \frac{\phi\left(1-\phi-\frac{K_b}{K_s}\right)K_s}{1-\phi-\frac{K_b}{K_s}+\phi\frac{K_s}{K_f}}, \quad R = \frac{\phi^2 K_s}{1-\phi-\frac{K_b}{K_s}+\phi\frac{K_s}{K_f}}\end{aligned} \tag{5.7}$$

The form of the interaction force proposed by Biot [1] includes viscous and dynamic couplings, proportional to relative velocities and relative accelerations of phases, respectively:

$$\mathbf{R}^s = -\mathbf{R}^f = b(\mathbf{v}^f - \mathbf{v}^s) + c\frac{\partial}{\partial t}(\mathbf{v}^f - \mathbf{v}^s) \tag{5.8}$$

In the simplest case (low frequency range [1]) the coefficients b and c define the intensity of viscous and dynamic interaction forces. The coefficient b is approximated assuming a quasistatic flow (Darcy's flow), while the coefficient c is derived assuming a flow of ideal fluid. They can be written as:

$$b = b_0 = \frac{\eta}{\kappa}\phi^2, \quad c = c_0 = \rho^f(\alpha - 1) \tag{5.9}$$

where η is the viscosity of fluid and κ and α are parameters describing structure of the porous material called permeability and tortuosity. The last two parameters are a measure of the viscous and inertial interactions between phases in the case of a linear quasistatic flow and in the case of a flow of ideal fluid, respectively.

A better approximation of the interaction forces $\mathbf{R}^s$ and $\mathbf{R}^f$ can be found by taking into account the fact that transient spatial distribution of microscopic velocities and accelerations of the two phases (particularly fluid) depend not only on the viscosity and pore structure, but also on the frequency. This fact led Biot [2] to consider the relation (Eq. 5.8) for simple shapes of pores (infinite slit and circular channels) with axes parallel to the direction of wave propagation, and to introduce a complex, frequency and structure dependent correction to the parameter b_0. The equivalent model can be formulated by scaling the parameters b and c appearing in Eq. 5.8 by two real, frequency and structure dependent functions φ and ψ:

$$b = \varphi b_0, \quad c = \psi c_0 \tag{5.10}$$

In the case of circular pores, these two functions can be written as [2]

$$\begin{aligned} \varphi &= \mathrm{Re}\left\{\frac{\Omega J_1(\Omega)}{4J_2(\Omega)}\right\} \\ \psi &= 1 - \frac{\eta\phi}{\omega\bar{\rho}^f\kappa(\alpha-1)}\mathrm{Im}\left\{\frac{\Omega J_1(\Omega)}{4J_2(\Omega)}\right\} \end{aligned} \tag{5.11}$$

where $\Omega = \sqrt{i\frac{\omega d^2\bar{\rho}^f}{\eta}}$, d denotes the characteristic size of pores, J_1, and J_2 are Bessel functions of the first kind, $i = \sqrt{-1}$, $\omega = 2\pi f$ and f is frequency.

5.2.3.2 Transverse Isotropy Case

Modeling the mechanical and structural anisotropy of bones for the case of transverse isotropy can be done by postulating appropriate constitutive relationships for

stress tensors and interaction forces, and by assuming that the other properties of the material are not affected by anisotropy. Assuming that the symmetry is around the z axis, the components of the stress tensors for transverse isotropy are [3, 16]:

$$\begin{aligned}
T_{xx}^s &= 2N\varepsilon_{xx}^s + A(\varepsilon_{\mathrm{xx}}^{\mathrm{s}} + \varepsilon_{\mathrm{yy}}^s) + F\varepsilon_{zz}^s + M\theta^f \\
T_{yy}^s &= 2N\varepsilon_{yy}^s + A(\varepsilon_{\mathrm{xx}}^{\mathrm{s}} + \varepsilon_{yy}^s) + F\varepsilon_{zz}^s + M\theta^f \\
T_{zz}^s &= C\varepsilon_{zz}^s + F(\varepsilon_{\mathrm{xx}}^{\mathrm{s}} + \varepsilon_{yy}^s) + Q\theta^f \\
T_{xy}^s &= 2N\varepsilon_{xy}^s, T_{xz}^s = L\varepsilon_{xz}^s, T_{yz}^s = L\varepsilon_{yz}^s \\
T^f &= [M(\varepsilon_{\mathrm{xx}}^{\mathrm{s}} + \varepsilon_{yy}^s) + Q\varepsilon_{zz}^s + R\theta^f]
\end{aligned} \tag{5.12}$$

where *N, A, F, M, C, Q, L* and *R* are elasticity constants. Since there are no simple relationships between the above anisotropic elasticity constants and elasticity parameters of phases and porosity, like Eq. 5.7, the constants must be identified throughout indirect techniques dedicated for anisotropic cases [17]. The appropriate relations for the interaction forces are:

$$\begin{aligned}
R_x^s &= b_t(v_x^f - v_x^s) + c_t\frac{\partial}{\partial t}(v_x^f - v_x^s) \\
R_y^s &= b_t(v_y^f - v_y^s) + c_t\frac{\partial}{\partial t}(v_y^f - v_y^s) \\
R_z^s &= b_z(v_z^f - v_z^s) + c_z\frac{\partial}{\partial t}(v_z^f - v_z^s)
\end{aligned} \tag{5.13}$$

where $b_t(= b_x = b_y)$, b_z, $c_t(= c_x = c_y)$ and c_z are the components of the tensor coefficients of viscous and dynamic interaction forces ($\mathbf{R}^s = -\mathbf{R}^f$) for the considered symmetry.

5.2.4 Wave Equations and Dispersion Relationships

If the operation of divergence is performed on the combined Eqs. 5.2, 5.6, 5.8 and the properties of the operator $\nabla\cdot$ are used, the following system of wave equations for longitudinal waves can be obtained:

$$\begin{aligned}
&\rho^s\frac{\partial^2}{\partial t^2}\theta^s - (2N+A)\nabla^2\theta^s - Q\nabla^2\theta^f - b\frac{\partial}{\partial t}(\theta^f - \theta^s) - c\frac{\partial^2}{\partial t^2}(\theta^f - \theta^s) = 0 \\
&\rho^f\frac{\partial^2}{\partial t^2}\theta^f - Q\nabla^2\theta^s - R\nabla^2\theta^f + b\frac{\partial}{\partial t}(\theta^f - \theta^s) + c\frac{\partial^2}{\partial t^2}(\theta^f - \theta^s) = 0
\end{aligned} \tag{5.14}$$

Using *curl* ($\nabla\times$) operator on the system of combined Eqs. 5.2, 5.6 and 5.8 leads to the wave equations for distorsional or shear waves:

$$\begin{aligned}
&\rho^s \frac{\partial^2}{\partial t^2}\boldsymbol{\Omega}^s - N\nabla^2\boldsymbol{\Omega}^s - b\frac{\partial}{\partial t}(\boldsymbol{\Omega}^f - \boldsymbol{\Omega}^s) - c\frac{\partial^2}{\partial t^2}(\boldsymbol{\Omega}^f - \boldsymbol{\Omega}^s) = 0 \\
&\rho^f \frac{\partial^2}{\partial t^2}\boldsymbol{\Omega}^f + b\frac{\partial}{\partial t}(\boldsymbol{\Omega}^f - \boldsymbol{\Omega}^s) + c\frac{\partial^2}{\partial t^2}(\boldsymbol{\Omega}^f - \boldsymbol{\Omega}^s) = 0
\end{aligned} \tag{5.15}$$

where $\boldsymbol{\Omega}^\alpha = \frac{1}{2}\nabla\times\mathbf{u}^\alpha$ are rotation vectors.

The solutions of the systems of wave Eqs. 5.14 and 5.15 for plane harmonic dilatational and shear waves propagating in direction x can be found in the forms:

$$\begin{aligned}
&E^\alpha = C^\alpha \exp[i(kx+\omega t)] \\
&\Omega^\alpha = D^\alpha \exp[i(lx+\omega t)], \quad \alpha = s, f
\end{aligned} \tag{5.16}$$

where Ω^α are the components of $\boldsymbol{\Omega}^\alpha$ in direction x, k and l are the wave numbers of longitudinal and shear waves, ω denotes angular frequency and C^α and D^α are constants. Introduction of the solutions (5.16) into wave Eqs. 5.14 and 5.15 leads to a system of homogeneous algebraic equations for the constants C^α and D^α. The solutions of this system of equations are not trivial if the determinants of the systems are equal to zero. This last condition leads to the dispersion relations for longitudinal waves:

$$k^4 A_1 - k^2\omega^2 A_2 + \omega^4 A_3 = 0 \tag{5.17}$$

and for shear waves:

$$l^2 A_4 - \omega^2 A_3 = 0 \tag{5.18}$$

where

$$\begin{aligned}
A_1 &= (2N+A)R - Q^2, \\
A_2 &= (2N+A+R+2Q)\left(c - \frac{i}{\omega}b\right) + \rho^s R + \rho^f(2N+A) \\
A_3 &= \rho^s\rho^f + (\rho^s+\rho^f)\left(c - \frac{i}{\omega}b\right) \\
A_4 &= N\left[\rho^f + c - \frac{i}{\omega}(\rho^s+\rho^f)b\right]
\end{aligned} \tag{5.19}$$

Finding the solutions of Eqs. 5.17 and 5.18 with respect to k and l respectively, with positive real components of the wave numbers, shows that two longitudinal waves and a single shear wave may propagate in the material. The phase velocities of the fast and slow longitudinal waves (denoted with indices 1 and 2) are:

$$v_{1/2} = \frac{\omega}{\mathrm{Re}(k_{1/2})}$$

while the phase velocity of the shear wave is:

$$v_s = \frac{\omega}{\mathrm{Re}(l)}.$$

The corresponding attenuation coefficients are:

$$\alpha_{1/2} = \mathrm{Im}(k_{1/2})$$

for the longitudinal waves, and

$$\alpha_s = \mathrm{Im}(l)$$

for the shear wave.

5.2.5 Extensions of Poromechanical Modelling

Since the introduction of Biot's model of wave propagation in 1956 [1, 2] for fluid saturated elastic and isotropic porous materials, many modifications (extensions) have appeared in the literature. In 1962, Biot published a paper [3] in which he generalized the model to take into account anisotropy, viscoelasticity and dissipation in the solid. Numbers of other papers have appeared later in which additional physical effects were discussed. Most of these proposed extensions of the Biot's model are reviewed in the following sections.

5.2.5.1 Contributions of Micro-Inhomogeneity of Fluid Flow

One development of Biot's poroelasticity is related to the incorporation of the effects of micro-heterogeneity in the motion of the phases, particularly in the fluid velocity field. This effect was already introduced by Biot [1] but limited to the geometry of a single channel of constant size which axis is parallel to the direction of propagation of the waves. More advanced models [2, 16, 18–24] take into account various directions and different sizes of channels, with flows along channels, squirt flows (flow perpendicular to the direction of the flow in the channel), and microscopic effects related to fluid slip at the interface between the solid skeleton and the fluid. These three effects are illustrated in Fig. 5.2.

Corrections for the viscous and dynamic components of the interaction forces have been proposed, to take into account the deviation from steady state flow approximation (Darcy flow) and ideal fluid flow approximations. They are based on a representation of the pore space as a system of circular straight channels of random

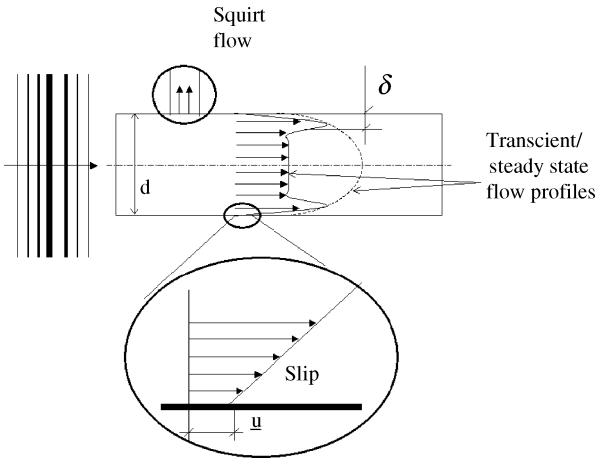

Fig. 5.2 Microscopic effects in pores considered in poromechanics

diameters and directions [20]. For the parameters φ and ψ (Eq. 5.11), these corrections take the form:

$$\varphi = \mathrm{Re}\left\{\sqrt{1-\frac{4i\alpha^2\kappa^2\omega\bar{\rho}^f}{\eta\phi^2\Lambda^2}}\right\}$$
$$\psi = \mathrm{Re}\left\{1+\frac{i\eta\phi}{\omega\bar{\rho}^f\kappa(\alpha-1)}\sqrt{1-\frac{4i\alpha^2\kappa^2\omega\bar{\rho}^f}{\eta\phi^2\Lambda^2}}\right\} \tag{5.20}$$

where Λ is a characteristic size of pore space, a measure of the dynamically connected pores [20, 25, 26].

The same effects, without assumption of harmonic motion, can be derived by considering the history dependence of the interaction forces, or by using a representation of the interaction forces based on partial time derivatives of relative velocity [27].

Transient heterogeneity of microscopic field of pressure, e.g. due to different pore size distribution and various microscopic deformations of the skeleton, results in flow of fluid in directions different from the directions of the channels (exchange of fluid between different pores). To model this effect within a two-phase approach, a complex factor which multiplies the Biot's constitutive equation for stress in fluid (5.6) was proposed [18, 19]:

$$\mathbf{T}^f = \underline{\mathrm{K}}(\omega, r)(\mathrm{Q}\theta^{\mathrm{s}} + \mathrm{R}\theta^f)\mathbf{I} \tag{5.21}$$

where $\underline{\mathrm{K}}$ is a complex function, which depends on the frequency ω and on the characteristic dimension of squirt flow r. The meaning of the squirt flow for

modeling waves in bones has not been evaluated yet. Finding its role could be possible by following the methodology developed for rocks [18, 19], i.e. by considering appropriate microscopic structures with channels perpendicular to the wave propagation direction, and by modeling the transient flow through them.

The presence of slip or jump of microscopic tangential velocity at the interface between fluid and solid has been considered as potentially influencing the macroscopic interaction force. It has been proposed to incorporate this effect through further corrections of the parameter introduced by Biot to represent the influence of flow heterogeneity on viscous interaction forces [24]. In the present formulation it is equivalent to a modification of the parameters φ and ψ, including their dependence on average slip velocity.

5.2.5.2 Dissipation Due to the Thermal Conduction in the Fluid

Local temperature changes due to compression and expansion of phases and associated heat conduction are sources of dissipation of wave energy. This phenomenon was modeled in a macroscopic two-phase approach by Lee et al. [21, 22] by taking into consideration its part in the fluid phase, through a complex density of fluid in Eq. 5.2 and a compressibility parameter R in the constitutive Eq. 5.6. This model also includes three additional parameters, which according to Lee et al. represent contributions to local temperature changes from the nonrigid porous frame. Although it has been found that experimental data can be better fitted with this modified model when the parameters are adjusted accordingly, part of these phenomenological additional parameters do not have clear physical meaning. This makes difficult an assessment of the robustness of the model.

5.2.5.3 Model Including Macroscopic Viscous Stresses

Viscous properties of fluid and/or solid phase in the poromechanical models of wave propagation can be included through constitutive functions for macroscopic stresses and interaction forces. The basic constitutive model for macroscopic stress tensors of poromechanics takes into account the elastic components and neglects viscous contributions, both in fluid and solid phase. For propagation of waves in low and medium permeability materials, this assumption seems to be justified because the main dissipation and dispersion mechanism comes then from the viscous interaction force. In high permeability materials, like trabecular bones, the assumption may not be adequate and one should consider then the two-phase constitutive model which incorporates viscous components in the macroscopic stress tensors [3, 23]. This model can be formulated by replacing elasticity parameters in constitutive Eqs. 5.6 by frequency dependent operators or complex frequency dependent functions.

5.2.5.4 Micro-Poromechanical Models

Micro-poromechanical models using simplified description of the geometry of the structure are used when the input parameters required by the Biot's model can not be measured. The most commonly used is the so-called Schonberg's model [28] of alternating fluid and solid layers. This model is a generalization of the theory proposed by Rytov [29] and Brekhowskih [30], who considered plane wave propagation in layered media at normal incidence or along the layers. Schoenberg analyzed wave propagation at arbitrary incidence angle with respect to the orientation of the layered structure. He found exact analytical solutions, namely solutions which are valid at all frequencies, wavenumbers and angles of incidence. For all the propagation angles, except when the propagation direction is perpendicular to the layers, two modes are predicted: a fast wave, for which the motions in the solid and fluid layers are in phase, and a slow wave, for which these motions are 180° out of phase [28]. The reader can refer to Chap. 11 for a description of the experiments carried out to investigate the behavior of the fast and slow wave modes. The theory has been verified experimentally using ultrasonic technique by Plona et al. [31, 32]. Immersion experiments were performed in the frequency range 0.2–2 MHz on systems composed of water/Plexiglas and water/aluminum parallel layers. Both the single wave propagating normal to the layers and the two waves propagating parallel to the layers were observed.

Such micro-poromechanical models, and especially the Schonberg's model [28], lead to a better understanding of the Biot's model in the long wavelength regime. In particular, they give insights into the relative role of fluid flow inhomogeneity during propagation in fluid saturated porous elastic media.

5.3 Review of the Application of Biot Theory to Propagation Through Cancellous Bone

Ultrasonic wave propagation in fluid-saturated cancellous bone has been interpreted in terms of Biot's model [1–3] with varying degrees of success. The application of Biot's theory for modelling wave propagation in cancellous bone was reviewed by Haire and Langton [33] in 1999. Following that, more or less sophisticated modifications of Biot's model have been used, aimed to accurately describe the interaction mechanisms arising at the fluid (marrow) – solid (bone matrix) interface, or to account for additional effects influencing wave propagation. These models have been reviewed in the previous sections.

This section is devoted to a review of the experimental and theoretical results available in the literature, in order to discuss the relevance of the models to predict accurately the observed phenomena. As it will be seen, one of the major difficulties in the use of these models lies in the large number of input parameters required, describing properties (elastic, inertial, viscous) of both phases.

5.3.1 Experimental Observation of Fast and Slow Waves in Cancellous Bone

One of the most discussed features of the Biot's theory has been the presence in the signals transmitted through the cancellous bone of two pulses associated with two longitudinal waves, known as fast and slow waves.

Indeed, the poroelastic nature of cancellous bone has been confirmed by a few authors who reported the observation of two compressional wave modes. Two waves were measured *in vitro* in bovine [21, 22, 34–41] and in human [41–47] cancellous bone specimens obtained from various anatomic sites (femoral neck, femoral head, distal epiphysis of femur, proximal ends of tibia).

The difficulty of observation of the two waves in the time domain may be attributed to microstructural features of the specimens, the most important being the anisotropy. Hosokawa and Otani [36] found that if the wave propagates along the main orientation of the trabecular network, then two separate waves were observed. As the relative angle between the ultrasonic beam and the orientation of trabecular network increases (from 0° to 60°) the amplitude of the slow wave decreases (from 0 to −15 dB) [36]. Therefore, for high angles, the slow wave amplitude, even when present, is too small to be detected [36]. Based on these results, Hosokawa and Otani concluded that the slow wave in cancellous bone is effectively generated by the relative motion of the fluid and the solid, in the case where the wave propagates along the main direction of alignment of the trabeculae.

These findings were confirmed experimentally in bovine cancellous bones [37] and the results were examined in the light of the stratified model [37, 48]. It was found that an idealized model of highly oriented trabecular bone structure predicted closely the values of the speed of sound of the two waves when the propagation direction was parallel to the main orientation of the trabeculae [37]. When the propagation direction was not parallel to the main orientation of the trabeculae, a potential time overlap of the two associated pulses, and a decrease in slow wave amplitude were found [48].

The influence of the anisotropy on the conditions of observation of both compressional waves was confirmed by Haiat et al. [49–51] using three-dimensional finite-difference time-domain simulations in human femoral trabecular microstructures (see Chap. 7 for more details). The authors predicted that both waves would overlap in time domain for a direction of propagation perpendicular to the main trabecular orientation and would be separated when these two directions are parallel, for specimens with a high degree of anisotropy.

Density can also play a role in the condition of observation of the two waves by influencing the relative amplitudes of the two waves. This was confirmed experimentally [47].

Combined effects of anisotropy and density may explain why in many ultrasonic studies of cancellous bones, apparently only one longitudinal wave is observed [52–54]. Based on a pure velocity criterion, one could assume that the wave observed is a 'fast' wave according to the Biot's model, since its velocity is larger than the velocity in the saturating fluid. This statement has however to be

qualified. Considering for example the case of *in vivo* measurement at the calcaneus [55], where the propagation direction is orthogonal to the main orientation direction of the trabeculae, it is likely that the observed waveform is composed of overlapping fast and slow waves. As a result the estimated velocity may have values higher than the velocity in the fluid filling pores, while most of the energy is conveyed by the wave propagating mainly in the fluid (especially for the high porosity specimens). The effect of overlapping pulses on the estimation of velocity will be discussed in more details in Sect. 5.3.3.1 and in Chap. 12.

Another factor potentially influential for the generation of the two modes is the presence, *in vivo*, of the cortical shell surrounding the trabecular bone. It is important to note that all the reported *in vitro* observations of the two modes were obtained on pure trabecular bones specimens, after removal of the cortical endplates. In geophysics, free fluid transfer between the porous medium and the embedding fluid has been shown to be important for the generation of the two waves [56–58]. But the influence of the cortical endplates on the generation of the fast and slow waves has not yet been studied in cancellous bones.

In vivo, the clinical ultrasonic devices currently used to characterize cancellous bone perform measurements at the calcaneum (the heel bone). Measurements are performed in a medio-lateral direction, and the propagation direction is perpendicular to the main direction of orientation of the trabeculae. The presence of the cortical endplates, in addition to the effect of anisotropy, may explain why only one wave is measured.

To date, only one study reported the observation of two waves *in vivo* [46, 59]. Measurements were made at the distal end of the radius, where trabecular bone can be found. The device is composed of a pair of coaxially and confocally aligned broadband focused ultrasonic transducers (1 MHz centre frequency, 20 mm in diameter, focal length of 40 mm) [46, 59]. The authors of this study assumed that the two waves observed in cancellous bone correspond to the fast and slow waves predicted by Biot's theory. In contrast to the *in vitro* cases, the wave is assumed to be transmitted to the cancellous bone *via* the cortical shell, resulting in a propagation of the incident energy mostly carried along the trabeculae. The results were then interpreted in the framework of the Biot's theory, however the exact nature of the two waves has not been confirmed yet. In particular, the cortical shell may guide the propagation of circumferential waves [60, 61], which may arrive before the wave transmitted through the medulary canal.

5.3.2 Parameters of the Biot's Models

One of the critical points for the use of Biot's models is to obtain realistic values of the parameters (a dozen input parameters in the isotropic case), describing the physical characteristics of the propagating medium. These parameters can be measured. Nevertheless, due to the complexity of such measurements, the model has been most of the time applied by using input parameters found in different literature

Table 5.1 Input parameters for calculations of the Biot's model. The exponent n is required to estimate the Biot–Willis [74] elastic constants (P, Q, and R). In the case of Fellah et al. [43,45], data for the sample M2 were chosen. Opt.: Value obtained using optimization; m: marrow; w: water; b.f.: bovine femur; h.f.: human femur; h.c.: human calcaneus

Parameters		Hosokawa and Otani [35] b.f.	Fellah et al. [43] h.f.	Wear et al. [52] h.c.	Sebaa et al. [45] h.f.	Pakula et al. [62] h.f.
Bulk modulus of fluid (GPa)	K_f	$2^{(m)}$	$2.28^{(w)}$	$2.2^{(w)}$	$2.28^{(w)}$	$2.25^{(w)}$
Young modulus of solid phase (GPa)	E_s	22	–	8.3	13	13
Poisson ratio of solid phase	v_s	0.32	–	0.3	0.3	0.3
Bulk modulus of solid phase (GPa)	K_s	$20.37^{(1)}$	20	$6.9^{(1)}$	$10.8^{(1)}$	$10.8^{(1)}$
Porosity	f_v	0.79	0.77	0.79	0.79	0.79
Exponent	n	$1.46^{(Opt.)}$	–	$1.75^{(Opt.)}$	–	–
Young Modulus of trabecular frame (GPa)	E_b	$2.25^{(2)}$	–	$0.54^{(2)}$	$2.47^{(Opt.)}$	–
Poisson ratio of trabecular frame	ν_b	0.32	–	0.23	$0.25^{(Opt.)}$	0.24
Bulk modulus of solid frame (GPa)	K_b	$2.08^{(3)}$	4	$0.33^{(3)}$	$1.64^{(3)}$	0.67
Shear modulus of solid frame (GPa)	N	0.85	1.7	0.22	0.99	0.42
Tortuosity	α	1.06	1.01	1.06	1.05	1.5
Permeability ($10^{-6}\,cm^2$)	κ	200	–	–	–	3.6
Viscous characteristic length (μm)	Λ	–	2.7	–	10.12	55.6
Fluid density (kg/m^3)	ρ_f	930	1000	1000	1000	1000
Fluid viscosity (Pa.s)	η	1.5	10^{-3}	10^{-3}	10^{-3}	10^{-3}
Solid density (kg/m^3)	ρ_s	1960	1960	1800	1990	1800

(1) Calculated using the formula $K_s = E_s/(3(1-2v_s))$;
(2) Calculated using the formula $E_b = E_s(1-f_v)^n$;
(3) Calculated using the formula $K_b = E_b/(3(1-2v_b))$;
(4) Calculated using the formula $N = E_b/(2(1+v_b))$.

sources (often from different materials), or estimated from experimental data by optimization procedures. Table 5.1 reports parameters values used by different authors to compute the model predictions.

Porosity can be calculated from 3-D micro-computed tomography (μCT) [52, 62, 63] or measured using Archimede's principle [35, 52, 54]. Typical values of porosity for human cancellous bones range from 55% to 95%, depending on the anatomical site and bone status.

Permeability, which is a measure of the ability of a fluid to filter through a porous medium, has been measured in both human and bovine cancellous bones. In human bones, reported values span over three order of magnitude [62, 64–66] ranging from 0.08×10^{-6} to $10.15 \times 10^{-6}\,cm^2$ in human femur [62]. Permeability has been found

to be correlated to porosity [62,64–66] and to be strongly influenced by the relative orientation between the flow direction and the principal orientation of trabecular network [66]. Animal bones were found to be more permeable than human bones [64], mainly because of their bigger pore size.

Only a few papers have reported tortuosity values for human cancellous bones. Tortuosity has been measured using electrical spectroscopy [54, 62], wave reflectometry [42–45] or estimated from the porosity [35,36,52,53]. Values ranging from 1.01 to 1.5 were reported.

The elastic properties of bone tissue, which are requested to estimate the macroscopic elastic properties of the saturated porous frame, can be measured using atomic force microscopy [67], nanoidentation [68] or acoustical microscopy [69,70] (see Chap. 16). Then, micromechanical models, e.g. [9,71,72], are used to calculate the values of the bulk and shear modulus of the solid frame [38,62].

Numerous authors [35, 36, 52–54] have used a power law to relate the Young modulus of trabecular frame (E_b) to the intrinsic Young's modulus of the solid phase (E_s) and to the bone volume fraction (1-porosity). This power law is based on a simplified cellular model of porous structures of bones proposed by Gibson [73]. Assuming known the Young's modulus of the solid phase (E_s), the unknown parameter of this power law (the exponent of the power law n) is estimated by fitting the predictions of Biot's model to the fast wave velocity over a range of porosity. Some authors [52] used both E_s and n as fitting parameters.

Gibson derived analytically that the exponent n has a value of 1 when the material is loaded along the direction of trabecular alignment and a value comprised between 2 and 3 in the transverse directions [73]. For bovine cancellous bones, Williams [53] estimated a value of $n = 1.23$ for bovine tibia for the direction of wave propagation along the major trabecular alignment. Hosokawa and Otani [35] reported that the values of the exponent n are function of the trabecular alignment for the specimens obtained form distal epiphysis of bovine femoral bone. They estimated a value of $n = 2.14$ for propagation in the perpendicular direction to the predominant trabecular orientation, and a value of $n = 1.46$ for the parallel direction [35]. Wear et al. [52] found $n = 1.75$ for human calcaneus measured in mediolateral (or lateromedial) direction. Wear et al. [52] explained the differences between their results and the results obtained by Williams [53] and Hosokawa and Otani [36] in terms of different organization of trabecular network of bovine and human bones, namely that the organization of trabeculae may not be as consistent in the human calcaneus as bovine tibia and femur. This method to estimate the Young's modulus of the skeleton frame is relatively simple and do not require independent measurements of bulk and shear moduli of the cancellous structure. The drawback is that it relies on an idealized cellular description of the micro-architecture.

Finally, the characteristics of the marrow, a fluid-like mixture of red (hematopoietic) and yellow (fatty) marrow [75, 76], namely its density and viscosity, have been so far taken from the literature. Most of the study has been performed with water-saturated skeleton frame [21, 22, 27, 37, 39, 41–45, 47, 48, 52–54, 77–82] i.e. assuming a very low viscosity of 10^{-3} Pa.s. Use of water saturated specimens is motivated by practical reasons such as preservation, specimen manipulation, and

ease of experimentation in water. A few studies dealt with marrow saturated specimens [35, 36, 39, 82–84]. Viscosity in marrow is several orders of magnitude higher than in water [85, 86].

Pakula et al. [62] provided systematic measurements of almost all of the input parameters required by the Biot's theory for a statistically representative group of human bones (35 specimens), obtained from a single skeletal site (proximal femur). They concluded that the values of those parameters may vary significantly from one specimen to another, even when they came from the same anatomical location. The results enlightened the difficulty to use Biot's theory for modeling wave propagation in cancellous bone, implying the necessity of individual evaluation of these input parameters. This necessity arises from the important expected variations of these parameters from one specimen to another, potentially due to variations in mechanical properties of the skeleton frame or in structural anisotropy. Therefore the question arises of the sensitivity of the Biot's model to these input parameters, to their variability as well as to their measurement errors. This question will be treated in Sect. 5.4.

5.3.3 Predictions of Phase Velocity and Attenuation Coefficient

In the studies in which both the fast and the slow waves have been measured, similar general trends have been reported concerning the relationships of wave parameters (velocity, attenuation) with frequency and density. We will first summarize these experimental findings, and then discuss the predictions of these experimental observations by different poro-elastic models.

5.3.3.1 Experimental Findings

Relationship Between the Velocities of Fast and Slow Waves and Bone Volume Fraction

Fast wave velocity was found to be positively correlated to bone volume fraction [35, 36, 41, 53, 81, 87] in bovine and sheep specimens from different anatomical origins [35, 41, 53, 81, 87], and in human calcaneus [52].

The measured values of the phase velocity of the fast wave for bovine tibia varied from 2500 to 3400 m/s for bone volume fraction ranging from 0.1 to 0.3 [53], while for bovine femoral specimens it varied from 2200 to 2700 m/s for bone volume fraction ranging from 0.05 to 0.3 [35, 36]. For the highest bone volume fractions (0.3–0.8) in bovine tibia, fast wave velocity varies from 2400 to 3800 m/s [81].

Similar trends were obtained in human calcaneus [52] in a representative group of 53 specimens. The range of bone volume fraction (0.02–0.14) was considerably narrower than in bovine cancellous bone studies, and the fast wave velocity varied insignificantly from 1475 to 1570 m/s. A slight non-linear trend in the relationship with porosity was reported [52].

In human femoral bone specimens, the fast wave velocity measured along the main direction of alignment of the trabeculae was found to increase from 2100 to 2900 m/s, when the bone volume fraction increased from 0.1 to 0.4 [47].

In most of the studies the velocity of the slow wave was found to be independent of the porosity [35, 36, 41, 47] and its value close to the propagation speed in the in the fluid filling pores (marrow or water). However, one study reported a positive linear correlation of the slow wave velocity (ranging from 1150 to 1450 m/s) with porosity [41] ($R^2 = 0.26$, $p < 10^{-3}$).

Relationship Between the Attenuation (Amplitudes) of Fast and Slow Waves and Bone Volume Fraction

The attenuation of the fast wave has been reported to be negatively correlated with bone volume fraction [35,36,41,54,80,87,88]. Moreover, a nonlinear (parabolic) dependence of the attenuation of the fast wave with respect to porosity has been found. The maximum values were measured for porosities of 65–70% [54] and 60% [87]. The parabolic behavior of the slope of the attenuation coefficient of fast wave for bovine and human specimens as a function porosity was also observed by Cardoso et al. [41] for the porosity values ranging from 60% to 92%. The maximum value ($140\,\mathrm{dB}\,(\mathrm{cm\,MHz})^{-1}$) was measured for a porosity of 75%.

In contrast, a positive linear behavior was observed for the frequency slope of attenuation of the slow wave (range of observed values 15–40 dB $(\mathrm{cm} \cdot \mathrm{MHz})^{-1}$; $R^2 = 0.15$, $p < 10^{-2}$).

The relatives amplitudes of both waves change with bone volume fraction. At low bone volume fraction, the amplitude of the fast wave remains much lower than that of the slow wave. When the bone volume fraction increases the amplitudes of fast and slow wave become equal. This result indicates that the properties of the fast waves are strongly related to the solid part of cancellous bone, whereas the slow wave properties depend more on the fluid part [35, 36, 41–45, 51].

Dependence of Fast and Slow Waves Amplitudes on Anisotropy

Structural anisotropy of bovine cancellous bone had been found to impact the experimental observation of two longitudinal waves in the material.

When the angle between the propagation direction and the main orientation of trabecular alignment decreases, the amplitude of the slow wave increases and become higher than the amplitude of the fast wave [36]. Currently such behavior, that has never been observed in classical porous material like rocks, is interpreted in terms of boundary effect which appears at the fluid/bone surface [54]. Due to the very high porosity of cancellous bone, the amount of energy which is presumably transferred from the fluid as a fast wave is much smaller than the amount converted into a slow wave. This may lead to the apparent higher attenuation of the fast wave than the slow wave [43].

Dependence of Fast and Slow Waves Velocities on Anisotropy

The effect of the anisotropy on waves velocities was reported in many different studies [35–37, 41, 47, 48, 53, 89].

It was demonstrated that the wave velocity is dependent on the propagation direction with respect to the main direction of alignment of the trabeculae, showing a maximum fast wave velocity when the direction of propagation is parallel to the main direction of orientation of the trabeculae [36, 90]. In bovine specimens, the fast wave velocity was found to decrease with insonation angle, from around 2800–3200 m/s at 0° to between 2000–2200 m/s at 60° [90], and from 2500 m/s at 0° to 1800 m/s at 90° [36]. The 0° denotes propagation parallel to the trabeculae and 90° a propagation perpendicular to the trabeculae. By contrast, the slow wave velocity, for those angles where it was observed, remained close to the propagation speed in the fluid filling pores.

Interestingly, it was reported that the specimens in which the two waves could be observed did not exhibit statistically higher apparent density than the rest of the specimens, but did exhibit statistically higher acoustic anisotropy ratio [47].

Negative Dispersion of Wave Velocity

Although there is a general consensus on the fact that bone attenuates both longitudinal waves in a manner that is approximately linear with frequency [21,35,41,91,92], there is considerable variation in the behavior of the frequency dependence of phase velocity (dispersion) among bone samples. In studies where two longitudinal waves were clearly observed and were analyzed separately, a positive dispersion (increasing phase velocity with increasing frequency) of both waves was reported [35].

Nevertheless, in studies in which a single transmitted waveform was observed, positive dispersion was reported only in approximately 10–20% of the measured sites [93, 94], and a number of studies have reported negative dispersion *in vitro* [93–96] and *in vivo* [55]. This negative velocity dispersion has been found to be intriguing, because the attenuation coefficient typically raised quasi-linearly with frequency, which, together with a negative velocity dispersion, is inconsistent with the causality-imposed Kramers–Kronig relations [97] (see Chap. 12 for in depth discussion on the possible origins of negative velocity dispersion in cancellous bone).

5.3.3.2 Comparison of Predictions with Experiments

Comparison of the Biot's model predictions with experimental data was published by many authors [21, 22, 27, 33, 35–40, 42–45, 47–49, 52–54, 62, 78, 80, 88–90, 98, 99] with varying degrees of success. In the following subsections the most relevant results will be presented and summarized.

It is noteworthy that in several studies, like [35,36] and [21,22,40,53,54,99,100], some of the parameters requested by the Biot's model (e.g. the exponent n, used to relate the Young modulus of trabecular frame to the intrinsic mechanical properties of the skeleton and to the bone volume fraction, see Sect. 5.3.2), were obtained by fitting theoretical predictions to the experimental results. Therefore the agreement obtained between theoretical predictions and experimental data does not necessarily mean that the Biot model is valid, unless some independent estimates of the input parameters can be provided by other techniques.

Prediction of Wave Velocities

The first comparison of the Biot's model predictions with experimental data was published by McKelvie [80], who reported that the measured frequency dependence of the phase velocity was not correctly predicted by the Biot theory, particularly for the higher bone volume fractions.

In the studies published after the paper of McKelvie [80], some of the parameters requested by the Biot's model were obtained by fitting theoretical predictions to experimental results. The agreement reported between predictions of wave velocities by the Biot's model and the experimental data was then good [35, 36, 53, 54, 81].

Using a similar fitting approach, it was also shown that the Biot's model predicted reasonably well the experimental dependence of phase velocity on porosity (Root mean square error $= 15.8\,\mathrm{m/s}$), and even the slight non-linear trend in the relationship [52].

An excellent agreement between predicted and measured phase velocities was obtained [21, 22, 40] by using the Modified Biot-Attenborough model [101] (MBA) in 12 cancellous bone specimens from the proximal ends of one bovine tibia. In particular, the MBA model was able to predict the experimental slight negative dispersion of the phase velocity.

Compared with the Biot's model, the MBA model introduces a set of new phenomenological parameters describing the thermo-mechanical coupling. These parameters do not have clear physical meaning and are therefore difficult to link to measurable quantities. They were estimated by fitting the experimental data, namely wave velocity, attenuation and effective impedance of the porous medium, with the porosity. This model therefore requires an *a priori* knowledge of the porosity dependence of the experimental data.

The general conclusion is that there is a reasonably good agreement for waves velocity between Biot's predictions and experimental data, as long as some of the parameters necessary for the computations of the model are adjusted to fit the experimental results. As discussed previously, this is not *per se* a demonstration of the validity of the model, which would need independent estimates of these input parameters.

Prediction of Wave Attenuation and Amplitudes

The different Biot's models have lead to various degree of success in the prediction of attenuation. The Biot's model was found to predict qualitatively the right order of magnitude of the frequency dependent attenuation of the fast wave in human calcaneus specimens [80], although the full range of experimental values observed in this set of specimens was not predicted. On the other hand, the same model gave prediction of waves amplitudes much lower than the measured ones in bovine specimens [35, 36]. In this last study [36], an argument was made that discrepancy between the theory and the experiments for attenuation coefficients might be due to a partial replacement of marrow by water which penetrated the pores of cancellous bone during the saturation, leading to additional physical mechanisms of attenuation not included in the Biot theory.

Identically, the Biot's theory modified by Johnson-Koplik-Dashen (JKD) proved to be unsuccessful when the concept of dynamic tortuosity [20] was used. It lead to absolute values of attenuation considerably lower than the experimental ones, although the predicted frequency dependence of the attenuation was found to be similar to the experimental one [54]. This suggested again that physical mechanisms not included in the Biot-JKD model might play an important role in attenuation. These mechanisms lead to additional losses due to reflections at the flat surfaces of the bone specimens, diffraction, scattering, and phase cancellation. Interestingly this model predicted that the attenuation coefficient of the fast wave plotted vs. porosity would exhibit nonlinear behavior, having its maximum for porosities comprised between 65% and 70%, in agreement with previous experimental observations [41,54,87,102]. This is however difficult to confirm experimentally, because the porosities of human cancellous bones range typically from 75% to 95%, and only the decreasing portion of the curve is normally seen [54].

On the other hand, when the Biot-JKD model was used to introduce the viscous exchange between fluid and solid structure, the model predicted very well the experimental signals transmitted through three human femoral cancellous bone specimens of highly oriented structure and high porosities [42,43]. The same Biot-JKD model was also used to solve an inverse problem, i.e. to extract parameters of the model (Young's modulus and Poisson ratio of the skeletal frame, porosity, dynamic tortuosity and viscous characteristic length) from experimental data [44,45]. The values obtained by the optimization procedure on the experimental data were found to be close to the values measured on air-saturated specimens, by independent techniques developed for characterization of air-saturated porous materials [43, 103–105], at the exception of the viscous characteristic lengths.

As for the prediction of the velocity, the modified Biot-Attenborough model [101] (MBA) proved to give excellent predictions of the attenuation [21,22,40]: The MBA model was able to predict the linear dependence of attenuation as a function of frequency, as well as the nonlinear relationship of porosity with attenuation and with the slope of a linear fit of the attenuation versus frequency (BUA).

To summarize, it seems that some of the Biot's models (JKD with viscous exchange, MBA) allow quantitative predictions of attenuation [21, 22, 40, 42, 43].

However, as in the case of the prediction of the velocity, it should be noted that these models are used within a model-fitting approach, in which parameters are adjusted in order to fit the experimental observations. The relevance of the values of the adjusted parameters is questionable, or at least might be valid only for the very small selected set of specimens used in these studies. This is especially the case for the MBA model, in which some of the parameters fitted do not have a clear physical meaning.

Prediction of the Effects of Anisotropy

Most of the studies have examined the anisotropic solid structure as a factor influencing the existence of the fast and slow waves in cancellous bone [36, 37, 41, 47, 48, 51, 53, 90]. One Can Distinguish Three Approaches.

The first one uses the Biot's model for isotropic homogeneous porous material and introduces anisotropy through an adjustable parameter (the exponent n), which relates the Young's modulus of trabecular framework with the intrinsic Young's modulus of the bone tissue and the volume fraction of bone (c.f. Table 5.1, Sect. 5.3.2). Following Williams [53] and Hosokawa and Otani [35, 36] the values for the exponent n are determined by fitting the prediction of the fast wave velocity as a function of porosity to its experimental values. The values for the exponent n may vary from 2.14 [36] for bovine femoral distal epiphysis with propagation perpendicular to the predominant trabecular orientation, to 1.23 [53] and 1.46 [36] for propagation in the parallel direction. The value $n = 1.75$ found in human calcaneus is explained by a less regular organization of the trabeculae network in human calcaneus compared to bovine femur or tibia.

The second approach consists in introducing angle dependent parameters in the Biot's model. Expressions were proposed for the anisotropic tortuosity and for the angle dependent Young's modulus [90]. Such method improved the agreement between theory and experiment for fast wave velocity at low angles, but degraded it at high angles [90]. In another study, a phenomenological expression for the tortuosity, being porosity and angle dependent [98], was derived from data obtained at audiofrequencies in air-filled bone replicas. These angle-dependent structural properties of cancellous bone were introduced into the Biot–Allard model [106]. It was suggested that such an approach might be useful to give further insight into the factors that have the most important influence on the angle-dependency of wave speeds and attenuation in cancellous bone [98]. The effect of the anisotropy of the bone structure was also examined within the Biot-Attenborough model [21], by introducing an angle dependent parameter "s1" (c.f. Sects. 5.2.5.2 and 5.3.2).

Finally, the third approach analyses the effect of the anisotropic trabecular structure in the light of the stratified models. A multilayer model of porous bone was used to compute the group velocity and relative arrival times of the two longitudinals waves as a function of the propagation angle [37, 48]. It was found that when the refraction angle increases, the energy of the slow wave is refracted from the phase propagation direction, and that for a refraction angle greater than 40°, the slow

wave may not be observed due to the overlapping of the fast and slow waves signals. These analytical results concerning the existence of two compressional waves vs. the orientation of trabecular network obtained by different authors [36, 37, 48] were confirmed by computational simulations [51]. A stratified-Biot model was also used in order to model the angle dependent ultrasonic properties of the bone material [37]. This model linked the merits of two models: Biot's model, which includes viscous effects and the Schoenberg (stratified) model, which includes the anisotropic properties of the material. In comparison to the results obtained when only the Schoenberg's model was applied [37], the newly developed model improved the predictions of the fast wave velocity at high propagation angles. The multilayered model [37] was also extended to simulate the attenuation due to the reflection and transmission at the fluid/cancellous bone (modeled as a stratified medium composed on an ideal fluid and an elastic solid) boundary for the case where the incident wave enters normally to the layers [87], i.e. for the case where one longitudinal wave exist. The predicted influence of the apparent density of bone on the wave velocity and attenuation was found to be correlated ($R = -0.93$) with experimental data obtained on sheep femoral condyles [87]. However, although the predicted frequency dependence of the attenuation coefficient was consistent with the experimental one, the absolute values of the predicted attenuations were found to be approximately the half of the measured ones. That may be attributed to the important role of absorption in the bone material (not considered in this study). Accordingly to the stratified model, the bone boundary plays an important role in the wave attenuation in cancellous bone, potentially as important as absorption in bone [87].

To summarize, the structural anisotropy of cancellous bone was introduced in the Biot's model in simplified ways. As anticipated, the theoretical predictions of the Biot's model including angle dependent parameters or simplified anisotropic structure reflect better the experimental observations than the Biot's model for isotropic material.

In order to introduce a more fundamental approach to model the mechanical and structural anisotropy of cancellous bones, it is necessary to postulate appropriate constitutive relationships for stress tensors and interaction forces (like those proposed in the Sect. 5.2.3.2 for the case of transverse isotropy). However, such approach requires more parameters to be measured by independent techniques and thus its potential usefulness is doubtful.

Predictions of Negative Dispersion of Wave Velocity

One of the most convincing explanation to interpret the apparent anomalous negative velocity dispersion is that interfering wave modes similar to those observed in bone could contribute to the observed negative dispersion (see Chap. 12 for more details) [97]. Numerical simulations and experiments have shown evidence that a mixed waveform composed of two interfering pulses can exhibit negative dispersion when it is analyzed conventionally under the assumption that only one wave is present. The importance of these findings in the context of ultrasonic studies of

cancellous bones is that such effect is observed even when little or no visual evidence of interference exists in the time-domain data [97].

Another source of negative dispersion may come from scattering. In particular, when the propagation direction is normal to the main orientation direction of the trabeculaes, it has been suggested that scattering effect may explain the negative dispersion [107].

Although the stratified-like models may also explain many empirical observations negative dispersion of phase velocity in cancellous bones [108], they are too dependent upon assumed values for material and structural properties to be of much practical value [108].

5.3.3.3 Effect of the Saturating Fluid

While *in vivo*, the pores of cancellous bones are filled with a fluid-like mixture of red (hematopoietic) and yellow (fatty) marrow [75, 76], in the *in vitro* experiments marrow is usually removed and replaced with water [84]. *In vitro* studies of water-saturated bone specimens are motivated by practical reasons such as preservation, specimen preparation, and ease of experimentation in water. In addition, because marrow composition is known to vary with age, skeletal site, and health condition [75], replacing marrow with water is beneficial for reducing the variability of the results and for accurately determining the relationships between QUS variables and structural and material bone properties.

Comparison of sound velocity and attenuation coefficient measurements for marrow- and water-saturated bones has been investigated, but inconsistent results have been reported. For example, the presence of water in the pores instead of marrow has been reported to have a significant impact on SOS (m/s) and on the slope of the frequency dependent attenuation, experimentally in human femur [85] and human calcaneus specimens [84], and numerically in finite difference time domain simulations of wave propagation [109]. In contrast, other groups reported no significant difference in the frequency slope of the attenuation coefficient as well as in the phase velocity when marrow was replaced with water in human calcaneus specimens both experimentally [79, 82, 110] and numerically [83]. Reasons for these inconsistencies have not been investigated in detail. There may be several reasons caused by experimental imprecision, differences in structure of investigated bone samples (e.g. bone volume fraction and trabecular orientation), and/or in signal processing procedures.

The effect of saturating fluid on the wave parameters was investigated in details by Pakula et al. [82] with the goal of evaluating its contribution to velocity dispersion, absorption, and scattering mechanisms. They found insignificant the role of the fluid properties (neither viscous nor elastic) on attenuation coefficient. Specifically, the fact that no difference in attenuation could be observed between marrow-filled and water-filled specimens contradicts Biot's predictions in which attenuation is expected to be much larger with a highly viscous filling fluid (like marrow) compared to a filling fluid with low viscosity (like water). These results point to the serious

limitations of Biot modeling of cancellous bone. These experimental studies led the authors to conjuncture that the longitudinal-to-shear scattering, together with absorption in the solid phase, are the main candidates to be the sources for attenuation. They also reported the differences observed in phase velocities for cancellous bones saturated with fluids of varying elastic properties. These results suggested that the effect of inherent individual variability in marrow on the measured QUS properties can be important, and may be particularly important during *in vivo* studies.

Nicholson and Bouxsein [84] investigated the relationships between QUS measurements and bone mineral density (BMD) for marrow and water saturated human cancellous bone specimens from the calcaneus. They found that QUS measurements in marrow-saturated specimens correlated weaker with BMD than did corresponding measurements in water saturated specimens. The authors justified this result by the inter-specimen marrow heterogeneity and concluded, as later confirmed by Pakula et al. [82], that the potential impact of marrow should be considered when interpreting clinical QUS measurements.

5.4 Sensitivity of the Biot's Model to Selected Parameters

To illustrate the influence of input selected parameters (i.e. tortuosity, fluid viscosity and permeability) of Biot's theory on the models outputs the results of parametric studies using Biot model are presented in this section (for the input parameters taken from own experimental studies, see Table 5.1 – last column). Then, the results of the sensitivity analysis are discussed, and the model suitability for description of ultrasonic wave propagation in cancellous bone is discussed in the light of the most cited results existing in the literature. The computations were performed using as input parameters the (average) values measured during a systematic study of 35 human femoral cancellous bones [62]. The parametric studies refer to parameters which role is not evident within the Biot's model because their values for cancellous bone cannot be easily identified. The three mostly used versions of Biot model to predict ultrasonic wave propagation in cancellous bones are compared. The calculations are performed for these three mostly used versions, which where described in details in Sect. 5.2:

- The Biot model for low frequencies [1], where the Poiseuille flow approximation in the pores during the wave propagation is satisfied (B_LF).
- The Biot model for high frequencies [2] (B_HF), which takes into account heterogeneity of the microscopic fluid flow during the wave propagation. The correction was proposed by Biot for the structures composed of parallel tubes of the same diameter filled with viscous fluid, and for a system of fluid and solid layers. The model is valid up to a frequency at which the wavelengths become of the order of the pore size.
- The Biot model modified by Johnson, Koplik and Dashen [20], which includes the concept of dynamic tortuosity (B_JKD).

5.4.1 *Influence of the Tortuosity and of the Saturating Fluid on the Wave Parameters*

In order to evaluate the role of the fluid viscosity on the wave parameters, predictions of the models for marrow ($\eta_m = 1\,\mathrm{Pa}\cdot\mathrm{s}$) and water ($\eta_w = 0.001\,\mathrm{Pa}\cdot\mathrm{s}$) saturated cancellous bone are presented in Figs. 5.3 and 5.4 for two values of tortuosity.

At high tortuosity ($\alpha = 1.5$, average value measured in Pakula et al. [62]), see Fig. 5.3, a higher viscosity of the fluid (marrow) leads to a higher dispersion and lower values of the velocities of both longitudinal waves. When the frequency increases, the phase velocity curves tend to reach the values obtained for water. Similarly, the attenuation dramatically increases for marrow filled bones in comparison with water filled material. For the slow wave, the level of attenuation reaches 100 dB/cm.

At low tortuosity ($\alpha = 1.05$), the values of phase velocity are slightly higher than at high tortuosity. In the case of the attenuation coefficient, particularly of the fast wave (Fig. 5.4b), a significant increase of the absolute level and of the slope is observed. The slow wave attenuation is slightly lower than for higher tortuosity.

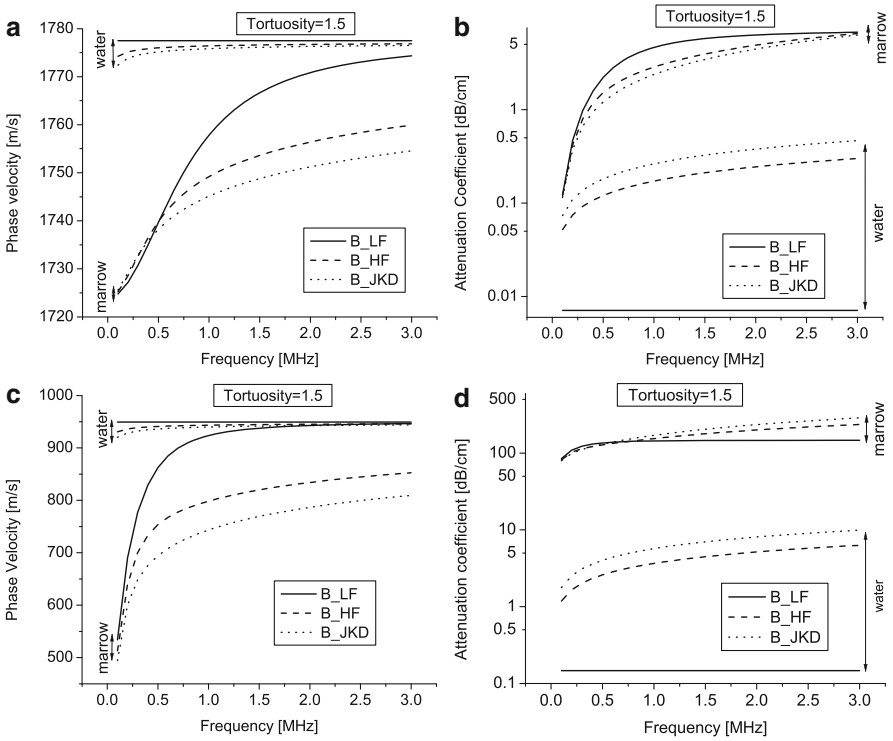

Fig. 5.3 Comparison of the predictions for phase velocity of *fast* (**a**) and *slow* (**c**) waves and attenuation coefficient of *fast* (**b**) and of *slow* (**d**) waves. Models: B_LF–Biot's for low frequency range [1], B_HF Biot's for high frequency range [2] and B_JKD–Biot's with viscodynamic correction introduced by Johnson et al. [20] Tortuosity = 1.5

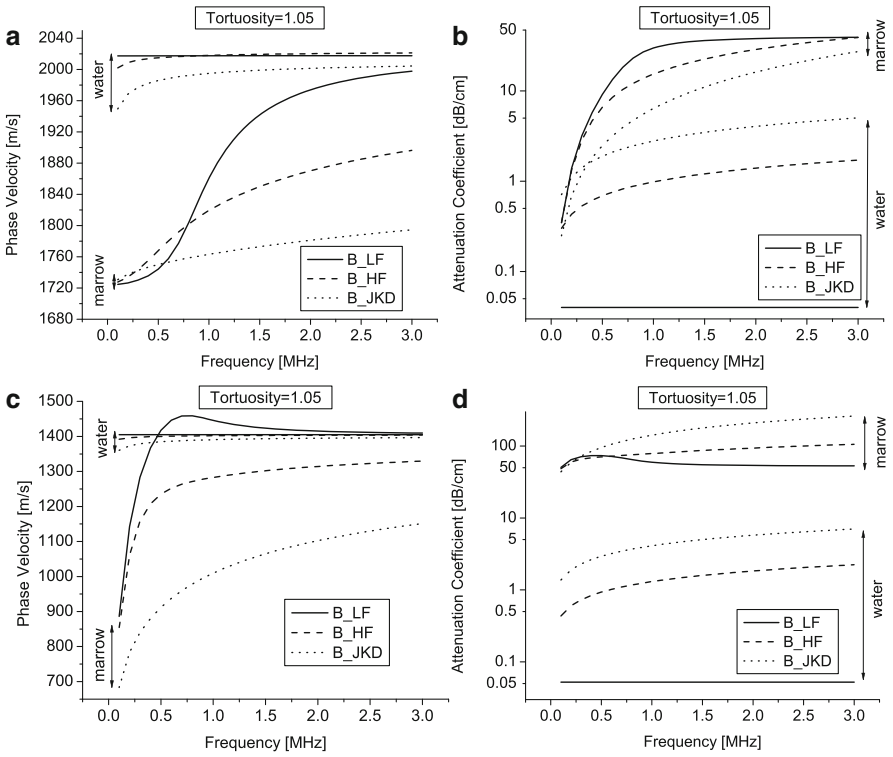

Fig. 5.4 Comparison of the predictions of the phase velocity of *fast* (**a**) and *slow* (**c**) waves and of the attenuation coefficient of *fast* (**b**) and of *slow* (**d**) waves. Models: B_LF–Biot's for low frequency range [1], B_HF Biot's for high frequency range [2] and B_JKD–Biot's with viscodynamic correction introduced by Johnson et al. [20] Tortuosity = 1.05

The computations show that the wave parameters (particularly the attenuation coefficient of both waves) strongly depend on the fluid viscosity. Such expected behavior results from the viscous-like mechanism of friction at the fluid/solid interphase included in the Biot's models. The models predictions prove also a significant role of tortuosity, which may lead to an increase of fast wave attenuation when tortuosity decreases.

Ambiguous ultrasonic results were reported in the literature for cancellous bones saturated with marrow and water: some authors reported differences between marrow and water saturated bones [84, 85, 109] while the others reported opposite conclusions [79, 82, 83, 110]. It is interesting to note that the reported experimental differences in attenuation and speed of sound between marrow and water saturated specimens are much smaller that those resulting from the computations of the Biot's models with different viscosities. It seems therefore that the current versions of the model do not describe appropriately the physical mechanisms associated with the fluid viscosity. Especially for low tortuosity and marrow as the saturating fluid, the three models seem to overestimate the attenuation when compared to typical values of attenuation measured. Another possibility is that the model describes

appropriately the physical mechanisms associated with the fluid viscosity, but that the contribution of this mechanism to total attenuation is minor compared to other physical mechanisms not accounted for by the model. Further theoretical studies taking into account for example the viscoelastic properties of the solid phase could be helpful to discriminate which of the physical mechanism mostly influence the wave attenuation.

5.4.2 *Parametric Analysis of the Reflection/Transmission Coefficients*

Another factor which may lead to the attenuation of the wave energy transmitted through bones is the conversion of the incident wave energy into reflected and transmitted waves. Usually, for ultrasonic studies of cancellous bones, the incident wave originates from a fluid, and the fast and slow waves are generated at the fluid/ saturated cancellous bone boundary.

Figure 5.5 presents the stress (pressure) transmission coefficients of the fast and the slow waves at the boundary fluid/fluid saturated bone as a function of the frequency for normal incidence. The computations were performed for the same models as in Sect. 5.4.1, the same tortuosities, and for cancellous bones saturated with marrow and water.

For relatively high tortuosity ($\alpha = 1.5$), the presence of marrow in pores does not influence significantly the transmission coefficients. The changes of transmission coefficients over the whole analyzed frequency range are smaller than 10%.

In the case of low tortuosity, a relative inversion of the values of transmission coefficients takes place in bones saturated with water (the transmission coefficient of the fast wave becomes smaller than for the slow wave around 1 MHz). In the case of marrow filled bones, such an inversion is also predicted by the B_LF model.

Figures 5.6 and 5.7 show the transmission coefficients of fast, slow and shear waves as well as the reflection coefficient at the boundary fluid/ fluid saturated bone as a function of the incident angle at 1 MHz. The calculations were performed for the three versions of Biot models for the two different fluids (marrow and water) and for two different tortuosities.

The coefficients change slightly when the angle of incidence varies between 0 and 40°. For angles higher than 40°, the variations of the transmissions coefficients become much more important. This finding demonstrates that the variations of the transmission coefficient have to be taken into account when the incidence angle deviates from the normal. This is particularly important when the effect of the anisotropy on the attenuation coefficient is studied by rotating a slice of cancellous bone. Variations of the transmission coefficient might then be a confounding factor if not corrected for.

These calculations were performed assuming that the incident wave impinges the pure cancellous bone (like in most of *in vitro* studies), while during *in vivo* examination (e.g. at the calcaneus) cancellous bone is surrounded by a cortical shell.

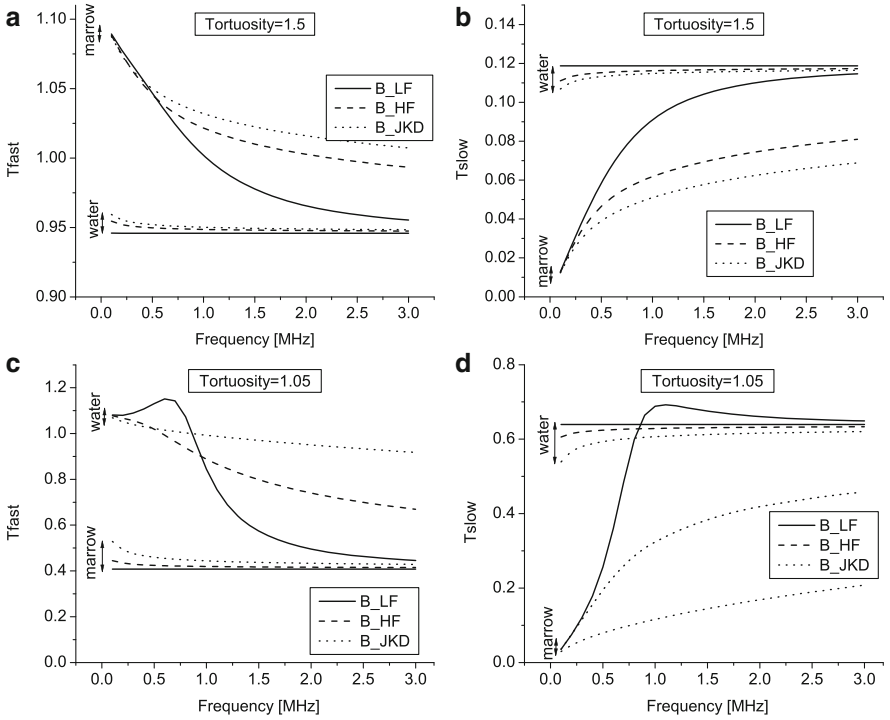

Fig. 5.5 Stress (pressure) transmission coefficients as a function of frequency for a high tortuosity specimen (*top*) and low tortuosity specimen (*bottom*), for *fast* (*Tfast*) and *slow* wave (*Tslow*), through the boundary fluid/fluid saturated bone at normal incidence. Models: Biot low frequency range model (B_LF) [2], Biot high frequency range model (B_HF) [111] and Biot's with viscodynamic correction introduced by Johnson et al. [20]

The effect of the cortical shell on the anisotropy of the transmission coefficient has now to be studied to know it is necessary to compensate for variations in incidence angle if any, during *in vivo* measurement.

5.4.3 *Influence of the Tortuosity, the Permeability and the Viscosity on the Viscodynamic Correction Functions*

In Sect. 5.2.5 were presented additional physical effects, which were not included in the Biot's paper for low frequency range [1] and which may be relevant to model wave propagation in cancellous bones. One of the most important is related to the heterogeneity of fluid flow during propagation.

In Fig. 5.8, the frequency dependences of the viscodynamic corrections proposed by Biot for the high frequency range (B_HF) [2] and by Johnson, Koplik

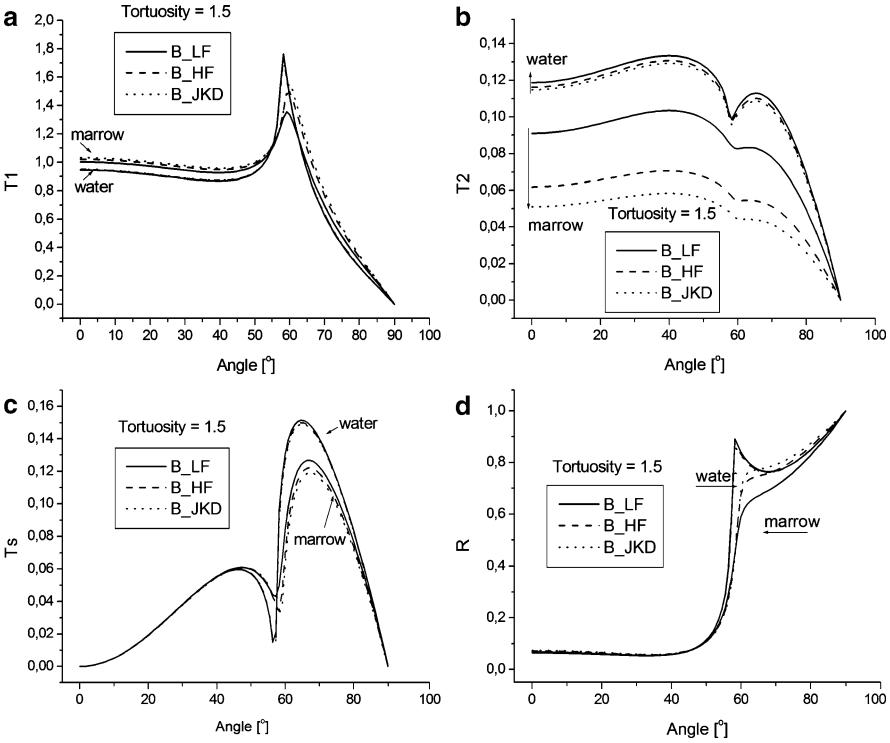

Fig. 5.6 Reflection (**d**) and transmission coefficients of the *fast* (**a**), *slow* (**b**) and *shear* (**c**) waves as a function of the incidence angle on a fluid/ fluid saturated bone boundary for a high tortuosity specimen (alpha = 1.5). Models: Biot low frequency range model (B_LF) [1], Biot high frequency range model (B_HF) [2] and Biot's with viscodynamic correction introduced by Johnson et al. [20] Calculations are performed at 1 MHz

and Dashen [20] (B_JKD) are depicted. The functions are plotted for two values of tortuosity, permeability and viscous characteristic length (Λ). The most important finding is that the functions corresponding to the B_JKD model highly increase when the values of the tortuosity and Λ decreases. This can be attributed to the fact that the B_JDK corrections have been derived for a randomly oriented system of channel [20], while the B_HF corrections were calculated based on a system of parallel channels [2]. The latter model of structure of pore space seems to be better to characterize low tortuosity materials while the B_JKD model leads to extremely high values of correction functions.

Figure 5.8 shows that the role of the different viscodynamic corrections is particularly important for the attenuation of the fast wave if the bones have low tortuosities. Therefore, both the absolute values and the slope of the attenuation coefficient depend strongly on the type of model applied.

The different behaviors of the correction functions on input parameters are an important point to consider. Both the Biot high frequency model B_HF and the Biot

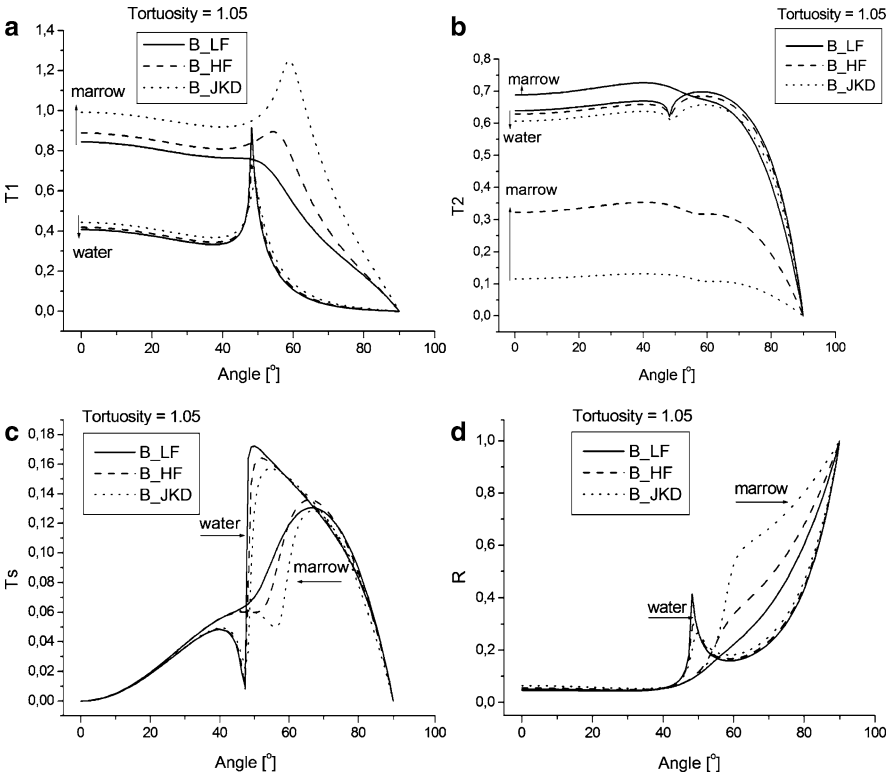

Fig. 5.7 Reflection (**d**) and transmission coefficients of the *fast* (**a**), *slow* (**b**) and *shear* (**c**) waves as a function of the incidence angle at the fluid/ fluid saturated bone boundary for a low tortuosity specimen (alpha = 1.05). Models: Biot low frequency range model (B_LF) [1], Biot high frequency range model (B_HF) [2] and modified by Johnson et al. [20] Biot model. Calculations was performed at 1 MHz

model with the Johnson, Koplik and Dashen corrections have been used to predict wave attenuation in cancellous bones, respectively in Hosokawa and Otani [35, 36] and in Fellah et al. [42–45]. In these studies the tortuosity was almost equal to 1, and the viscous characteristic length was very small (5 µm [43–45]). It has been seen in Fig. 5.8b that the impact of the viscodynamic correction functions will be large for such values of tortuosity and viscous characteristic length. Such low values of viscous characteristic lengths, which is linked to the radius of the narrow pores, seems unlikely when compared to pore size distribution measured by microtomography (a typical value of 230 µm was reported for the minimum size of the pores in human femoral cancellous bones specimens [51, 112]). Therefore accordingly to Williams [54] and Haire [33] who assumed values of pore size parameter Λ to be half of the mean trabecular plate separation, the expected values of Λ should be about 100 µm. Nevertheless, a direct comparison between studies is hardly possible due to the differences in specimens anatomical origins and micro-architecture (range of porosity, degree of anisotropy etc.).

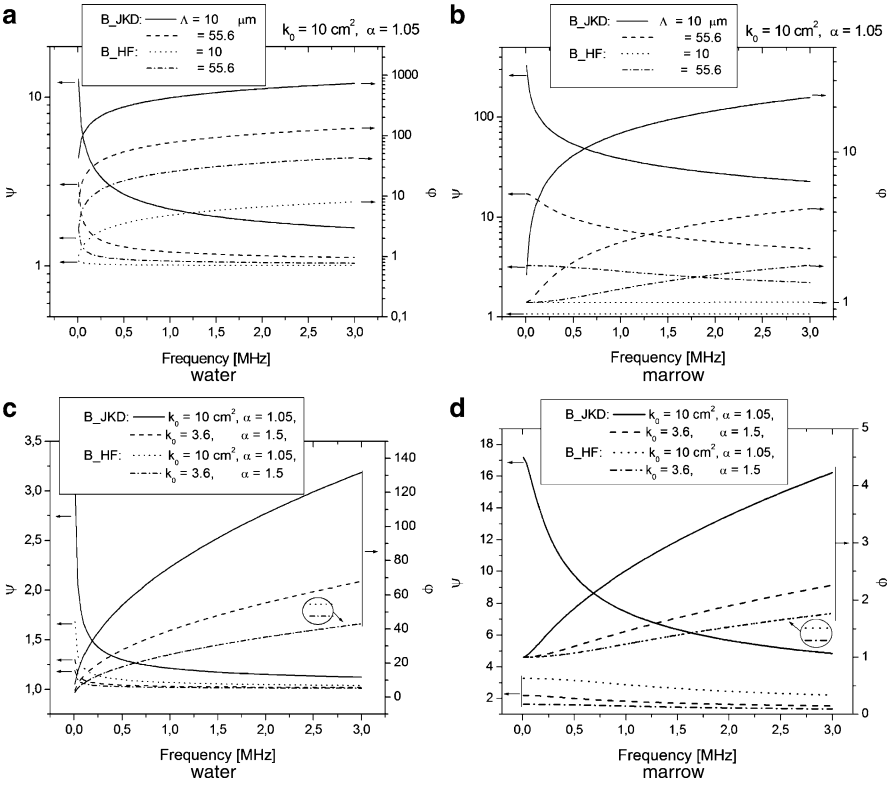

Fig. 5.8 Dependence of the viscodynamic correction functions on frequency for B_HF and B_JKD models and for two permeabilities (k_o), two tortuosities (α), two viscous characteristic lengths (Λ), and two saturating fluids (water and marrow)

Whether these values of tortuosity and viscous characteristic length are relevant, and therefore whether the impact of the corrections functions on the predicted attenuation may be so important, remains therefore an open question.

What can be learned from the parametric study is that the measurements on large sets of specimens (representative of parameters variability) will be necessary to be able to conclude quantitatively on the validity of the models.

5.5 Conclusions

The Biot's theory of poromechanics is an attractive candidate to model ultrasonic wave propagation in cancellous bones because of the two-phase nature of the medium. One advantage of this model is that it can take into account the intrinsic properties of the solid skeleton and of the fluid filling pores, as well as the macroscopic characteristics of the structure of the bone.

The existence of the two longitudinal waves predicted by the theory has been confirmed experimentally *in vitro* for cancellous bones saturated with marrow, water and alcohol [21, 22, 27, 37, 39, 41–45, 47, 53, 54, 77–82]. Until now, only one study reported the measurement of two waves *in vivo* [59], but no direct evidence exists that these two waves are linked to the Biot longitudinal waves.

The difficulty in the experimental observation of two waves may be caused by small amplitude of one of them and/or their overlapping in the time domain. Anderson et al. [97] have shown that such an overlap was highly probable in cancellous bones, particularly in the case, when the speeds of both waves are very close. In addition, they reported that a consequence of the use of traditional signal processing techniques on a signal that includes two pulses (e.g. a fast and a slow wave) having positive dispersion, even when the amplitude of one of them is very small, is negative dispersion of the phase velocity of transmitted waveform. Many authors have reported such negative dispersion [107], and it is therefore likely that overlapped pulses may commonly propagate in the material (see Chap. 12). Whether the overlapping pulses are due to poro-elastic propagation or they are caused by the other mechanisms such as phase cancellation [94, 97, 113] remain open question.

Despite the success in predicting the existence of two waves and potentially explaining negative dispersion, the ability of the theory to predict ultrasound propagation parameters in cancellous bone has been limited. With the proper adjustment of some of the input parameters, the predictions of the fast wave velocity have been found to be pretty accurate, but the Biot's model has not yet been able to predict accurately the measured attenuation, except in studies performed on limited groups of specimens [21, 42–45]. Because the theoretical predictions are very sensitive to the input parameters, which demonstrate large variability between specimens, it is difficult yet to conclude on the relevance of the model. A more definitive conclusion might be reached after measurements on enlarged sets of bone specimens will have been performed.

The model predictions presented in the light of the experimental results obtained in the literature have given insight into theoretical areas which need to be more exploited. One of the most important finding of the parametric studies performed here was the important contribution of the bone boundaries on the loss of wave energy. Moreover, the crucial role of tortuosity (the parameter describing alignment of the trabecular pattern) and of the viscodynamic parameters along with the characteristic size of pores was shown both on the intrinsic wave attenuation in the material and on the division of incident wave energy on the fast and slow wave at the bone boundaries. Future studies on the separation of the transmitted wave energy, due to transmission at the boundaries, and inside the bone material may give insight into the real physics associated with wave propagation in the cancellous bones.

One of the disadvantages of the Biot's model as a source of information about the bone status is the number of input parameters required to calculate its predictions. Moreover, the parametric studies presented here have proven that the model predictions are sensitive to number of parameters, particularly tortuosity, permeability, viscous characteristic length, some of them being difficult to measure experimentally.

Another, essential drawback of the Biot's theory to model wave propagation in cancellous bone is that the medium lies at the limits of the theory's domain of validity, when the ratio of wavelengths to the size of the bone micro-heterogeneities (trabecular thickness and trabecular spacing) is considered [78]. When this ratio is too small, scattering effects may appear and the theory is not valid anymore. Indeed, scattering is present in cancellous bones (see Chap. 6), and its relative contribution to total attenuation cannot be neglected. The presence of scattering may explain some of the observed discrepancies between experimental results and predictions of attenuation from the models. When scattering is considered, one source of additional attenuation not included in Biot model come from longitudinal-to-shear mode conversion by the trabeculae, associated with high absorption of the shear waves in the solid matrix [82, 114]. The Biot model can be complemented to include such effects through assumption of viscoelastic properties of the intrinsic trabecular bone material. Nevertheless, more research is certainly needed in this area before the models can be used for explaining *in vitro* or *in vivo* data.

Despite severe limitations in the current use of Biot's model, due to imprecise input parameters and incomplete description of all physical interactions occurring between ultrasound and bone in the models, the poroelastic nature of cancellous bone might be exploited in the future as a new way to probe bone micro-architectural properties. A first approach has been proposed for measurement at the distal radius [46] and is expected to be successful in providing information on the structure and elasticity of trabecular bone complementary to the bone density measured by current X-rays absorptiometry techniques. However, Biot modeling has yet to be established as a valid theoretical framework to interpret the data obtained with this approach.

References

1. M. A. Biot, "Theory of propagation of elastic waves in a fluid-saturated porous solid. I. Low-frequency range," The Journal of the Acoustical Society of America **28**(2), 168–178 (1956).
2. M. A. Biot, "Theory of propagation of elastic waves in a fluid-saturated porous solid. II. Higher frequency range," The Journal of the Acoustical Society of America **28**(2), 179–191 (1956).
3. M. A. Biot, "Generalized theory of acoustic propagation in porous dissipative media," The Journal of the Acoustical Society of America **34**(9A), 1254–1264 (1962).
4. A. Bedford and D. S. Drumheller, "Theories of immiscible and structured mixtures," International Journal of Engineering Science **21**(8), 863–960 (1983).
5. C. Truesdell, ed., *Rational thermodynamics* (Springer, New York, 1986).
6. J. L. Auriault, "Dynamic behavior of a porous medium saturated by a Newtonian fluid," International Journal of Engineering Science **18**, 775–785 (1980).
7. S. R. Pride, A. F. Gangi, and F. D. Morgan, "Deriving the equations of motion for porous isotropic media," Journal of the Acoustical Society of America **92**, 3278–3290 (1992).
8. T. J. T. Spanos, *The thermophysics of porous media*, Monographs and surveys in pure and applied mathematics (Chapman & Hall, CRC, Boca Raton, 2002), Vol. 126, p. 220.
9. T. Bourbie, O. Coussy, and B. Zinszner, "Acoustics of porous media" (Gulf Publ. Comp., Houston, 1987).

10. M. Bruneau and C. Potel, eds., *Materials and acoustics handbook* (ISTE, John Wiley & Sons London, 2009), p. 919.
11. J. M. Carcione, *Handbook of geophysical exploration. Section I, Seismic exploration*, *Wave fields in real media: wave propagation in anisotropic, anelastic, porous and electromagnetic media*, 2nd ed., (Elsevier, Amsterdam; Boston, 2007).
12. H. Deresiewicz and R. Skalak, "On uniqueness in dynamic poroelasticity," Bulletin of the Seismological Society of America **53**(4), 783–788 (1963).
13. K. Wu, Q. Xue, and L. Adler, "Reflection and transmission of elastic waves from a fluid-saturated porous solid boundary," The Journal of the Acoustical Society of America **87**(6), 2349–2358 (1990).
14. M. Cieszko and J. Kubik, "Derivation of matching conditions at the contact surface between fluid-saturated porous solid and bulk fluid," Transport in Porous Media **34**, 319–336 (1999).
15. B. Gurevich and M. Schoenberg, "Interface conditions for Biot's equations of poroelasticity," Journal of the Acoustical Society of America **105**, 2585–2589 (1999).
16. M. D. Sharma and M. L. Gogna, "Wave propagation in anisotropic liquid-saturated porous solids," The Journal of the Acoustical Society of America **90**(2), 1068–1073 (1991).
17. G. Yang, J. Kabel, B. van Rietbergen, A. Odgaard, R. Huiskes, and S. C. Cowin, "The anisotropic Hooke's law for cancellous bone and wood," Journal of Elasticity **53**(2), 125–146 (1998).
18. M. S. Diallo and E. Appel, "Acoustic wave propagation in saturated porous media: reformulation of the Biot/Squirt flow theory," Journal of Applied Geophysics **44**(4), 313–325 (2000).
19. J. Dvorkin and A. Nur, "Dynamic poroelasticity: a unified model with the squirt and Biot mechanisms," Geophysics **58**(4), 524–533 (1993).
20. D. L. Johnson, J. Koplik, and R. Dashen, "Theory of dynamic permeability and tortuosity in fluid-saturated porous media," Journal of Fluid Mechanics **176**, 379–402 (1987).
21. K. I. Lee, H.-S. Roh, and S. W. Yoon, "Acoustic wave propagation in bovine cancellous bone: application of the modified Biot–Attenborough model," The Journal of the Acoustical Society of America **114**(4), 2284–2293 (2003).
22. K. I. Lee and S. W. Yoon, "Comparison of acoustic characteristics predicted by Biot's theory and the modified Biot-Attenborough model in cancellous bone," Journal of Biomechanics **39**(2), 364–368 (2006).
23. S. Picotti, J. M. Carcione, J. G. Rubino, J. E. Santos, and F. Cavallini, "A viscoelastic representation of wave attenuation in porous media," Computers and Geosciences **36**, 44–53 (2010).
24. D. Tsiklauri, "Phenomenological model of propagation of the elastic waves in a fluid-saturated porous solid with nonzero boundary slip velocity," Journal of the Acoustical Society of America **112**(3 Pt 1), 843–849 (2002).
25. J. R. Banavar and D. L. Johnson, "Characteristic pore sizes and transport in porous media," Physical Review B Condensed Matter **35**(13), 7283–7286 (1987).
26. D. L. Johnson, J. Koplik, and L. M. Schwartz, "New pore-size parameter characterizing transport in porous media," Physical Review Letters **57**(20), 2564–2567 (1986).
27. N. Sebaa, Z. E. A. Fellah, W. Lauriks, and C. Depollier, "Application of fractional calculus to ultrasonic wave propagation in human cancellous bone," Signal Processing **86**(10), 2668–2677 (2006).
28. M. Schoenberg, "Wave propagation in alternating solid and fluid layers" Wave Motion **6**(3), 303–320 (1984).
29. S. M. Rytov, "Acoustical properties of a thinly laminated medium," Soviet Physics Acoustics **2** (1956).
30. L. M. Brekhovskikh, *Waves in layered media* (Academic Press, New York, 1960), p. 561.
31. T. J. Plona and D. L. Johnson, "Experimental study of the two bulk compressional modes in water-saturated porous structures," presented at the IEEE Ultrasonics Symposium, New York, 1980.
32. T. J. Plona, K. W. Winkler, and M. Schoenberg, "Acoustic waves in alternating fluid/solid layers," The Journal of the Acoustical Society of America **81**(5), 1227–1234 (1987).

33. T. J. Haire and C. M. Langton, "Biot theory: a review of its application to ultrasound propagation through cancellous bone," Bone **24**(4), 291–295 (1999).
34. R. Lakes, H. S. Yoon, and J. L. Katz, "Slow compressional wave propagation in wet human and bovine cortical bone," Science **220**(4596), 513–515 (1983).
35. A. Hosokawa and T. Otani, "Ultrasonic wave propagation in bovine cancellous bone," The Journal of the Acoustical Society of America **101**(1), 558–562 (1997).
36. A. Hosokawa and T. Otani, "Acoustic anisotropy in bovine cancellous bone," The Journal of the Acoustical Society of America **103**(5), 2718–2722 (1998).
37. E. R. Hughes, T. G. Leighton, G. W. Petley, and P. R. White, "Ultrasonic propagation in cancellous bone: a new stratified model," Ultrasound in Medicine and Biology **25**(5), 811–821 (1999).
38. M. Kaczmarek, J. Kubik, and M. Pakula, "Wave propagation in saturated high porosity materials," in *Poromechanics III - Biot Centennial (1905–2005)*, Y. N. Abousleiman, A. H.-D. Cheng, and F.-J. Ulm, eds. (Taylor and Francis Group, London, 2005), pp. 223–229.
39. M. Kaczmarek, J. Kubik, and M. Pakula, "Short ultrasonic waves in cancellous bone," Ultrasonics **40**(1–8), 95–100 (2002).
40. K. I. Lee, V. F. Humphrey, T. G. Leighton, and S. W. Yoon, "Predictions of the modified Biot-Attenborough model for the dependence of phase velocity on porosity in cancellous bone," Ultrasonics **46**(4), 323–330 (2007).
41. L. Cardoso, F. Teboul, L. Sedel, C. Oddou, and A. Meunier, "*In vitro* acoustic waves propagation in human and bovine cancellous bone," Journal of Bone and Mineral Research **18**(10), 1803–1812 (2003).
42. Z. A. Fellah, N. Sebaa, M. Fellah, F. G. Mitri, E. Ogam, W. Lauriks, and C. Depollier, "Application of the biot model to ultrasound in bone: direct problem," IEEE Transactions on Ultrasonics Ferroelectrics and Frequency Control **55**(7), 1508–1515 (2008).
43. Z. E. Fellah, J. Y. Chapelon, S. Berger, W. Lauriks, and C. Depollier, "Ultrasonic wave propagation in human cancellous bone: application of Biot theory," The Journal of the Acoustical Society of America **116**(1), 61–73 (2004).
44. N. Sebaa, Z. A. Fellah, M. Fellah, E. Ogam, F. G. Mitri, C. Depollier, and W. Lauriks, "Application of the Biot model to ultrasound in bone: inverse problem," IEEE Transactions on Ultrasonics Ferroelectrics and Frequency Control **55**(7), 1516–1523 (2008).
45. N. Sebaa, Z. E. Fellah, M. Fellah, E. Ogam, A. Wirgin, F. G. Mitri, C. Depollier, and W. Lauriks, "Ultrasonic characterization of human cancellous bone using the Biot theory: inverse problem," The Journal of the Acoustical Society of America **120**(4), 1816–1824 (2006).
46. I. Mano, K. Horii, S. Takai, T. Suzaki, H. Nagaoka, and T. Otani, "Development of Novel Ultrasonic Bone Densitometry Using Acoustic Parameters of Cancellous Bone for Fast and Slow Waves," Japan Journal of Applied Physics **45**(5B), 4700 (2006).
47. K. Mizuno, M. Matsukawa, T. Otani, P. Laugier, and F. Padilla, "Propagation of two longitudinal waves in human cancellous bone: an *in vitro* study," The Journal of the Acoustical Society of America **125**(5), 3460–3466 (2009).
48. F. Padilla and P. Laugier, "Phase and group velocities of fast and slow compressional waves in trabecular bone," The Journal of the Acoustical Society of America **108**(4), 1949–1952 (2000).
49. A. Hosokawa, "Simulation of ultrasound propagation through bovine cancellous bone using elastic and Biot's finite-difference time-domain methods," The Journal of the Acoustical Society of America **118**(3), 1782–1789 (2005).
50. A. Hosokawa, "Ultrasonic pulse waves in cancellous bone analyzed by finite-difference time-domain methods," Ultrasonics **44**(Supplement 1), e227–e231 (2006).
51. G. Haiat, F. Padilla, F. Peyrin, and P. Laugier, "Fast wave ultrasonic propagation in trabecular bone: numerical study of the influence of porosity and structural anisotropy," The Journal of the Acoustical Society of America **123**(3), 1694–1705 (2008).
52. K. A. Wear, A. Laib, A. P. Stuber, and J. C. Reynolds, "Comparison of measurements of phase velocity in human calcaneus to Biot theory," The Journal of the Acoustical Society of America **117**(5), 3319–3324 (2005).

53. J. L. Williams, "Ultrasonic wave propagation in cancellous and cortical bone: prediction of some experimental results by Biot's theory," The Journal of the Acoustical Society of America **91**(2), 1106–1112 (1992).
54. J. L. Williams, Grimm, M. J., Wehrli, F. W., Foster, K. R., and Chung, H.-W., "Prediction of frequency and pore size dependent attenuation of ultrasound in trabecular bone using Biot's theory," in *Mechanics of Poroelastic Media*, A. P. S. Selvadurai, ed. (Kluwer, Dordrecht, 1996), pp. 263–274.
55. K. A. Wear, "Group velocity, phase velocity, and dispersion in human calcaneus *in vivo*," The Journal of the Acoustical Society of America **121**(4), 2431–2437 (2007).
56. P. N. J. Rasolofosaon, "Importance of interface hydraulic condition on the generation of second bulk compressional wave in porous media," Applied Physics Letters **52**(10), 780–782 (1988).
57. D. L. Johnson, D. L. Hemmick, and H. Kojima, "Probing porous media with first and second sound. I. Dynamic permeability," Journal of Applied Physics **76**(1), 104–114 (1994).
58. D. L. Johnson, T. J. Plona, and H. Kojima, "Probing porous media with first and second sound. II. Acoustic properties of water-saturated porous media," Journal of Applied Physics **76**(1), 115–125 (1994).
59. T. Yamamoto, T. Otani, H. Hagino, H. Katagiri, T. Okano, I. Mano, and R. Teshima, "Measurement of human trabecular bone by novel ultrasonic bone densitometry based on fast and slow waves," Osteoporosis International **20**(7), 1215–1224 (2009).
60. R. Barkmann, S. Lusse, B. Stampa, S. Sakata, M. Heller, and C. C. Gluer, "Assessment of the geometry of human finger phalanges using quantitative ultrasound *in vivo*," Osteoporosis International **11**(9), 745–755 (2000).
61. J. Grondin, Q. Grimal, K. Engelke, and P. Laugier, "Potential of first arriving signal to assess cortical bone geometry at the Hip with QUS: a model based study," Ultrasound in Medicine and Biology **36**(4), 656–666 (2010).
62. M. Pakula, F. Padilla, P. Laugier, and M. Kaczmarek, "Application of Biot's theory to ultrasonic characterization of human cancellous bones: determination of structural, material, and mechanical properties," The Journal of the Acoustical Society of America **123**(4), 2415–2423 (2008).
63. M. Salome, F. Peyrin, P. Cloetens, C. Odet, A. M. Laval-Jeantet, J. Baruchel, and P. Spanne, "A synchrotron radiation microtomography system for the analysis of trabecular bone samples," Medical Physics **26**(10), 2194–2204 (1999).
64. Y. P. Arramon and E. A. Naumann, "Intrinsic permeability of Cancellous bone," in *Bone Mechanics Handbook*, S. C. Cowin, ed. (CRC Press, Boca Raton, 2000), pp. 25.1–25.17.
65. M. J. Grimm and J. L. Williams, "Measurements of permeability in human calcaneal trabecular bone," Journal of Biomechanics **30**(7), 743–745 (1997).
66. E. A. Nauman, K. E. Fong, and T. M. Keaveny, "Dependence of intertrabecular permeability on flow direction and anatomic site," Annals of Biomedical Engineering **27**(4), 517–524 (1999).
67. S. Hengsberger, J. Enstroem, F. Peyrin, and P. Zysset, "How is the indentation modulus of bone tissue related to its macroscopic elastic response? A validation study," Journal of Biomechanics **36**(10), 1503–1509 (2003).
68. P. K. Zysset, X. E. Guo, C. E. Hoffler, K. E. Moore, and S. A. Goldstein, "Elastic modulus and hardness of cortical and trabecular bone lamellae measured by nanoindentation in the human femur," Journal of Biomechanics **32**(10), 1005–1012 (1999).
69. J. Litniewski, "Determination of the elasticity coefficient for a single trabecula of a cancellous bone: scanning acoustic microscopy approach," Ultrasound in Medicine and Biology **31**(10), 1361–1366 (2005).
70. C. H. Turner, J. Rho, Y. Takano, T. Y. Tsui, and G. M. Pharr, "The elastic properties of trabecular and cortical bone tissues are similar: results from two microscopic measurement techniques," Journal of Biomechanics **32**(4), 437–441 (1999).
71. A. P. Roberts and E. J. Garboczi (personal communication, Jan, 2002).
72. A. P. Roberts and E. J. Garboczi (personal communication, May 8, 2002).

73. L. J. Gibson, "The mechanical behaviour of cancellous bone," Journal of Biomechanics **18**(5), 317–328 (1985).
74. M. Biot and D. Willis, "The elastic coefficients of the theory of consolidation," Journal of Applied Mechanics **24**, 179–191 (1957).
75. G. P. Liney, C. P. Bernard, D. J. Manton, L. W. Turnbull, and C. M. Langton, "Age, gender, and skeletal variation in bone marrow composition: a preliminary study at 3.0 Tesla," Journal of Magnetic Resonance Imaging **26**(3), 787–793 (2007).
76. C. P. Bernard, G. P. Liney, D. J. Manton, L. W. Turnbull, and C. M. Langton, "Comparison of fat quantification methods: a phantom study at 3.0T," Journal of Magnetic Resonance Imaging **27**(1), 192–197 (2008).
77. R. B. Ashman, J. D. Corin, and C. H. Turner, "Elastic properties of cancellous bone: measurement by an ultrasonic technique," Journal of Biomechanics **20**(10), 979–986 (1987).
78. E. R. Hughes, T. G. Leighton, G. W. Petley, P. R. White, and R. C. Chivers, "Estimation of critical and viscous frequencies for Biot theory in cancellous bone," Ultrasonics **41**(5), 365–368 (2003).
79. C. M. Langton, C. F. Njeh, R. Hodgskinson, and J. D. Currey, "Prediction of mechanical properties of the human calcaneus by broadband ultrasonic attenuation," Bone **18**(6), 495–503 (1996).
80. M. L. McKelvie, *Ultrasonic propagation in cancellous bone* (University of Hull, Hull, 1988).
81. M. M. Mohamed, L. T. Shaat, and A. N. Mahmoud, "Propagation of ultrasonic waves through demineralized cancellous bone," IEEE Transactions on Ultrasonics Ferroelectrics and Frequency Control **50**(3), 279–288 (2003).
82. M. Pakula, F. Padilla, and P. Laugier, "Influence of the filling fluid on frequency-dependent velocity and attenuation in cancellous bones between 0.35 and 2.5 MHz," The Journal of the Acoustical Society of America **126**(6), 3301–3310 (2009).
83. J. J. Kaufman, G. Luo, and R. S. Siffert, "On the relative contributions of absorption and scattering to ultrasound attenuation in trabecular bone: a simulation study," presented at the 2003 Proceedings of the IEEE Ultrasonics Symposium, Honolulu (2003).
84. P. H. Nicholson and M. L. Bouxsein, "Bone marrow influences quantitative ultrasound measurements in human cancellous bone," Ultrasound in Medicine and Biology **28**(3), 369–375 (2002).
85. J. M. Alves, J. T. Ryaby, J. J. Kaufman, F. P. Magee, and R. S. Siffert, "Influence of marrow on ultrasonic velocity and attenuation in bovine trabecular bone," Calcified Tissue International **58**(5), 362–367 (1996).
86. J. D. Bryant, "On the mechanical function of marrow in long bones," Engineering in Medicine **17**(2), 55–58 (1988).
87. W. Lin, Y. X. Qin, and C. Rubin, "Ultrasonic wave propagation in trabecular bone predicted by the stratified model," Annals of Biomedical Engineering **29**(9), 781–790 (2001).
88. M. L. McKelvie and S. B. Palmer, "The interaction of ultrasound with cancellous bone," Physics in Medicine and Biology **36**(10), 1331–1340 (1991).
89. L. Cardoso, Meunier, A., Oddou, C., "*In vitro* acoustic wave propagation n human and bovine cancellous bone as predicted by Biot's theory," Journal of Mechanics in Medicine and Biology **8**(2), 183–201 (2008).
90. E. R. Hughes, T. G. Leighton, P. R. White, and G. W. Petley, "Investigation of an anisotropic tortuosity in a Biot model of ultrasonic propagation in cancellous bone," The Journal of the Acoustical Society of America **121**(1), 568–574 (2007).
91. S. Chaffai, F. Padilla, G. Berger, and P. Laugier, "*In vitro* measurement of the frequency-dependent attenuation in cancellous bone between 0.2 and 2 MHz," The Journal of the Acoustical Society of America **108**(3 Pt 1), 1281–1289 (2000).
92. K. A. Wear, A. P. Stuber, and J. C. Reynolds, "Relationships of ultrasonic backscatter with ultrasonic attenuation, sound speed and bone mineral density in human calcaneus," Ultrasound in Medicine and Biology **26**(8), 1311–1316 (2000).
93. P. Droin, G. Berger, and P. Laugier, "Velocity dispersion of acoustic waves in cancellous bone," IEEE Transactions on Ultrasonics Ferroelectrics and Frequency Control **45**(3), 581–592 (1998).

94. K. R. Waters and B. K. Hoffmeister, "Kramers-Kronig analysis of attenuation and dispersion in trabecular bone," The Journal of the Acoustical Society of America **118**(6), 3912–3920 (2005).
95. P. H. Nicholson, G. Lowet, C. M. Langton, J. Dequeker, and G. Van der Perre, "A comparison of time-domain and frequency-domain approaches to ultrasonic velocity measurement in trabecular bone," Physics in Medicine and Biology **41**(11), 2421–2435 (1996).
96. K. A. Wear, "Measurements of phase velocity and group velocity in human calcaneus," Ultrasound in Medicine and Biology **26**(4), 641–646 (2000).
97. C. C. Anderson, K. R. Marutyan, M. R. Holland, K. A. Wear, and J. G. Miller, "Interference between wave modes may contribute to the apparent negative dispersion observed in cancellous bone," The Journal of the Acoustical Society of America **124**(3), 1781–1789 (2008).
98. H. Aygun, K. Attenborough, M. Postema, W. Lauriks, and C. M. Langton, "Predictions of angle dependent tortuosity and elasticity effects on sound propagation in cancellous bone," The Journal of the Acoustical Society of America **126**(6), 3286–3290 (2009).
99. K. I. Lee, E. R. Hughes, V. F. Humphrey, T. G. Leighton, and M. J. Choi, "Empirical angle-dependent Biot and MBA models for acoustic anisotropy in cancellous bone," Physics in Medicine and Biology **52**(1), 59–73 (2007).
100. J. L. Williams and J. L. Lewis, "Properties and an anisotropic model of cancellous bone from the proximal tibial epiphysis," Journal of Biomechanical Engineering **104**(1), 50–56 (1982).
101. K. Attenborough, "Acoustical characteristics of rigid fibrous absorbents and granular materials," The Journal of the Acoustical Society of America **73**(3), 785–799 (1983).
102. P. H. Nicholson, R. Strelitzki, R. O. Cleveland, and M. L. Bouxsein, "Scattering of ultrasound in cancellous bone: Predictions from a theoretical model," Journal of Biomechanics **33**(4), 503–506 (2000).
103. J. L. Buchanan and R. P. Gilbert, "Determination of the parameters of cancellous bone using high frequency acoustic measurements," Mathematical and Computer Modelling **45**(3–4), 281–308 (2007).
104. J. L. Buchanan, R. P. Gilbert, and K. Khashanah, "Determination of the parameters of cancellous bone using low frequency acoustic measurements," Journal of Computational Acoustics **12**(2), 99–126 (2004).
105. W. Lauriks, J. Thoen, I. Van Asbroeck, G. Lowet, and G. Van Der Perre, "Propagation of ultrasonic pulses through trabecular bone," Journal of Physics IV France **04**(C5), C5-1255-C1255-1258 (1994).
106. J. F. Allard, *Propagation of sound in porous media* (Elsevier Applied Science, London New York, 1993), pp. XIII–284.
107. G. Haiat, A. Lhemery, F. Renaud, F. Padilla, P. Laugier, and S. Naili, "Velocity dispersion in trabecular bone: influence of multiple scattering and of absorption," The Journal of the Acoustical Society of America **124**(6), 4047–4058 (2008).
108. K. A. Wear, "A stratified model to predict dispersion in trabecular bone," IEEE Transactions on Ultrasonics Ferroelectrics and Frequency Control **48**(4), 1079–1083 (2001).
109. A. S. Aula, J. Toyras, M. A. Hakulinen, and J. S. Jurvelin, "Effect of bone marrow on acoustic properties of trabecular bone – 3D finite difference modeling study," Ultrasound in Medicine and Biology **35**(2), 308–318 (2009).
110. C. F. Njeh and C. M. Langton, "The effect of cortical endplates on ultrasound velocity through the calcaneus: an *in vitro* study," The British Journal of Radiology **70**(833), 504–510 (1997).
111. M. A. Biot, "Theory of deformation of a porous viscoelastic anisotropic solid," Journal of Applied Physics **27**(5), 459–467 (1956).
112. D. Ulrich, B. van Rietbergen, A. Laib, and P. Ruegsegger, "The ability of three-dimensional structural indices to reflect mechanical aspects of trabecular bone," Bone **25**(1), 55–60 (1999).
113. A. Q. Bauer, K. R. Marutyan, M. R. Holland, and J. G. Miller, "Is the Kramers-Kronig relationship between ultrasonic attenuation and dispersion maintained in the presence of apparent losses due to phase cancellation?," The Journal of the Acoustical Society of America **122**(1), 222–228 (2007).
114. K. A. Wear, "Mechanisms for attenuation in cancellous-bone-mimicking phantoms," IEEE Transactions on Ultrasonics Ferroelectrics and Frequency Control **55**(11), 2418–2425 (2008).

Chapter 6
Scattering by Trabecular Bone

Frédéric Padilla and Keith Wear

Abstract This chapter reviews models for scattering of ultrasound by cancellous bone, methods for measuring scattering, and empirical results. Theory and measurements are presented for the dependence of backscatter on frequency and mean trabecular thickness. Additional topics discussed include the inverse problem (that is, estimating cancellous bone properties based on scattering measurements), the extent of multiple scattering in cancellous bone, and the role of scattering in determining attenuation. The potential advantages and intrinsic difficulties of backscatter as a clinical measurement are discussed. Results of clinical trials are presented.

Keywords Anisotropy · Apparent backscatter coefficient · Attenuation · Role of scattering · Autocorrelation · Backcatter · Backscatter coefficient measurement · Binary mixture model · Born approximation · Broadband Ultrasound Backscatter · Faran cylinder model · Multiple scattering · Shear waves · Thin cylinder model · Trabecular thickness · Velocity dispersion · Weak scattering model

6.1 Introduction

6.1.1 General Considerations

Trabecular bone is a scattering medium, as reported by numerous scattering measurements in vitro [1–28] and in vivo [27, 29–31].

F. Padilla (✉)
Université Pierre et Marie Curie, CNRS, Laboratoire d'Imagerie Parametrique, UMR 7623, F-75006, Paris, France
and
University of Michigan Medical Center, Department of Radiology, Ann Arbor, MI, USA
e-mail: fpadilla@umich.edu

K. Wear
Center for Devices and Radiological Health, U.S. Food and Drug Administration, Silver Spring, MD, USA
e-mail: keith.wear@fda.hhs.gov

P. Laugier and G. Haïat (eds.), *Bone Quantitative Ultrasound*,
DOI 10.1007/978-94-007-0017-8_6,

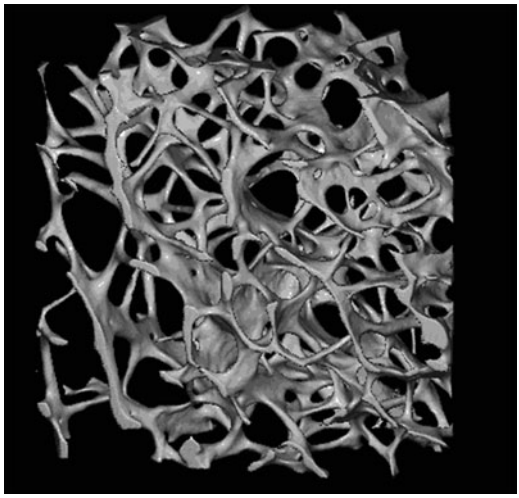

Fig. 6.1 3-D reconstruction of trabeculae structure of a human femur after synchrotron micro-tomography experiments. The spatial resolution is 10 µm (With courtesy of Françoise Peyrin (ESRF – CNRS Creatis UMR 5515))

Scattering has been reported in trabecular bone even at low frequencies (0.5 MHz), and multiple scattering has been reported to potentially occur at higher frequencies [2, 6].

Human trabecular micro-structure (Fig. 6.1) is composed of a heterogeneous and anisotropic porous network (porosity between 75% and 95% [3,32]) of interconnected solid trabeculae (approximate size 50–150 µm, mean interdistance 50–1500 µm [3,32]) embedded in bone marrow. The impedance mismatch between the trabeculae (∼7.5 MRayl [33]) and the saturating viscous fluid-like marrow (1.5 MRayl) is high, and therefore the trabeculae are likely candidates to act as scatterers.

6.1.2 What to Expect from Scattering?

Backscatter is an important parameter as it conveys information about bone microstructure, which is one of the determinants of bone fragility [34–37]. The question is how to extract this information from the measurements?

This can be done by using regression models from experimental data, for example by studying the relationships between micro-architectural parameters and ultrasound backscatter. This approach is however very limited because of the difficulty of obtaining large sets of specimens and because of the co-variance of the micro-achitectural parameters among themselves and with bone density [3, 12]. The variability of such estimators is too large to be clinically useful [12].

Direct modeling of scattering, followed by the resolution of an inverse problem, is an alternative [1, 5, 17, 38]. Modeling scattering in trabecular bone will also provide an answer to the question of the relative roles of scattering and absorption in the attenuation measured in transmission [5, 39], and could also potentially give some insight into some unexplained experimental observations such as negative frequency-dispersion of velocity [40].

The ability to demonstrate that backscatter measurement can provide information complementary to bone mass is an important issue with respect to the clinical usefulness of the technique. The success of this approach depends also on the development of accurate scattering models.

Finally, the main advantage of a characterization technique based on scattering measurement, and especially on backscattering measurements, is that it requires access to only one side of the bone inspected. As with classical echography, access to central skeletal sites would be facilitated compared to transmission measurement techniques. However, only moderate success have been reported so far.

6.1.3 Intrinsic Difficulties of Scattering Measurements in Cancellous Bones

Scattering measurements in cancellous bone can be quite challenging. One reason for this is that, at diagnostic frequencies, echoes from cancellous bone are the result of summation of scattered waves from many unresolvable trabeculae throughout a resolution volume. Therefore, the magnitude of the echo can exhibit considerable variability due to the extent to which the individual scattered waves interfere constructively or destructively [24]. The variability of scattered signals is exacerbated by the fact that cancellous bone samples tend to be quite small and do not provide much opportunity to perform spatial averaging. A second factor that complicates scattering measurements from cancellous bone is the high attenuation coefficient, which limits depth of penetration into the bone. Compensation of measurements for the effects of attenuation is mathematically complex and requires careful attention to windowing functions [41]. Furthermore, attenuation coefficient is often measured in transmission experiments and tends to be overestimated due to phase cancellation at the receiving transducer. The use of this overestimated attenuation coefficient for the compensation of backscatter measurements in human calcaneus in vitro has been shown to result in overestimation of (1) backscatter coefficient at 500 kHz by an amount on the order of 60%, and (2) average exponent of frequency dependence (n where backscatter coefficient is assumed to be proportional to f^n) by an amount on the order of 0.3 [42].

6.2 Scattering Models for Cancellous Bones

6.2.1 Preliminary Considerations

Cancellous bone is a two-component medium. One component is the solid mineralized trabecular network. The other component is marrow (in vivo) or water (in vitro). The interfaces between the solid and fluid components may scatter incident ultrasound waves. Cancellous bone has extremely complicated structure, as

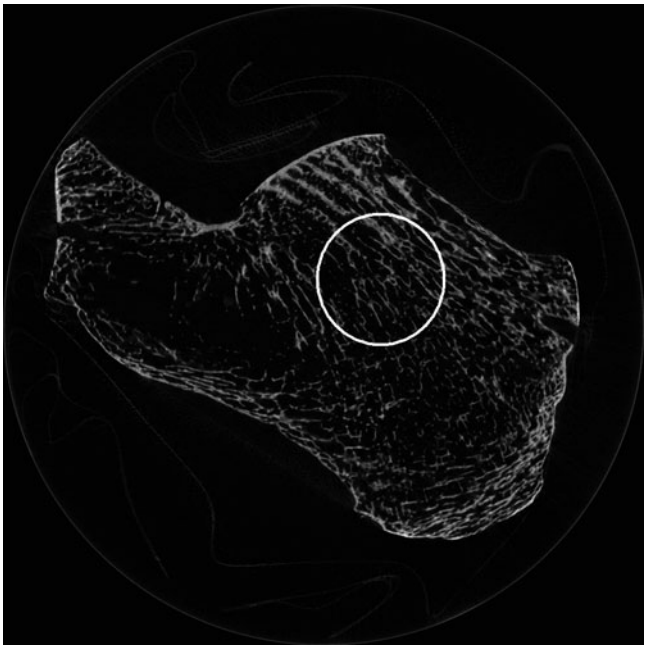

Fig. 6.2 Micro computed tomographic image of human calcaneus slice. Thread-like trabeculae may be seen. Some trabeculae appear to terminate as they move into and out of the imaging plane. A typical beam cross section at 500 kHz (about 13 mm in diameter) is shown (Image acquired by Andres Laib, Scanco Medical AG, Brüttisellen, Switzerland)

shown in Figs. 6.1 and 6.2. The theoretical models described below make many simplifying assumptions in order to obtain analytic solutions. Nevertheless, some of these models predict dependences of backscatter coefficients on frequency and cancellous bone micro-architectural properties that are consistent with experimental measurements in vitro. The reader may refer to Chap. 10 for more information on the linear acoustics in trabecular bone.

The Faran Cylinder Model, Thin Cylinder Model, and Weak Scattering Model are presented in the section. A few other approaches assuming multiple scattering have been also proposed to predict scattering by trabecular bone and will be described in Sect. 6.4.

6.2.2 Faran Cylinder Model

The Faran Cylinder Model represents trabeculae as solid cylinders embedded in fluid (marrow in vivo or water in vitro), as shown in Fig. 6.2. The scattered field from a single trabecula may be predicted using Faran's theory [43]. This model is particularly appropriate for predicting the dependence of backscatter coefficient on

frequency and trabecular thickness, as opposed to predicting the absolute level of backscatter. Two different formulations of the Faran Cylinder Model were developed independently.

One formulation assumed a lattice structure of regularly-spaced parallel trabeculae [14,15]. The scattered waves by such a structure were analyzed with a multilayer grating model. Using Born approximation and Fraunhoffer diffraction formulas, the scattered wave was expressed in terms of two parameters characteristic of the medium: the cylinder diameter and the spatial period of the network. The authors proposed to use the position of the grating lobes as a function of the scattering angles and the frequency to estimate the two parameters. Measurements in a bandwidth 1–3 MHz on one slab of human heel and one slab of bovine thigh trabecular bones did provide correct order of magnitude for both estimated parameters. A prototype was realized and tested on a formalinized human heel bone. Again, correct orders of magnitude were obtained. Because only two bone samples were interrogated (one human and one bovine) and no precise comparison was provided between estimated parameters and actual values of mean trabecular thickness and spacing, it is difficult to assess the robustness of the method.

The other formulation assumed that trabeculae were positioned sufficiently randomly that the incoherent contribution to scattering dominates the coherent contribution (i.e., the phase difference between scattered signals from pairs of cylinders was assumed to be uniformly distributed between 0 and 2π) [22]. A more recent variation assumed that trabeculae were positioned quasi-periodically [21]. The Incoherent Faran Cylinder Model predicts that if (1) the cylinder diameter is much smaller than a wavelength and (2) multiple scattering is negligible, then the backscatter coefficient at low frequencies (below 1 MHz) from human cancellous calcaneus should vary approximately as frequency cubed [22, 25] and trabecular thickness cubed [28]; both predictions are consistent with experimental measurements [22, 28]. The mean trabecular thickness in human calcaneus, about 127 µm [44], is much smaller than the wavelength at the typical diagnostic frequency of 500 kHz, about 3 mm, in the surrounding fluid. The Faran Cylinder Model has been shown to accurately predict attenuation due to scattering in cancellous-bone-mimicking phantoms [45]. The Incoherent Faran Cylinder Model has been extended to include cylinders with randomly varying diameters [46]. A cylinder scattering model has also been shown to be useful for predicting phase velocity and dispersion in cancellous bone [40]. The model accurately predicts the dependence of phase velocity and dispersion on trabecular thickness and trabecular spacing in cancellous-bone-mimicking phantoms [47].

6.2.3 Thin Cylinder Model

The Thin Cylinder Model predicts scattered signals by integrating the two-way transducer directivity pattern along a cylindrical scatterer [48]. While the Faran Cylinder Model allows for arbitrary cylinder diameter, the Thin Cylinder Model

requires that cylinder diameter be much less than a wavelength. This is not a serious limitation for human cancellous bone. For example, the mean trabecular thickness in human calcaneus is about 127 µm [44] whereas a typical measurement wavelength can be on the order of 3 mm (at 500 kHz). The Thin Cylinder Model is somewhat more flexible than the Faran Cylinder Model because it allows for arbitrary length and orientation of cylinder scatterers. Although for typical experiments and for clinical bone sonometry (in which the calcaneus is interrogated in the medio-lateral orientation), trabeculae are typically longer than the beam width and oriented approximately perpendicular to the beam, the added flexibility of the Thin Cylinder Model allows for slight irregularities in trabecular orientation and length. The Thin Cylinder Model predicts the relationship between the cylinder length and the exponent of a power law fit to backscatter coefficient versus frequency, which is four for very short (compared to a wavelength) cylinders and asymptotically approaches three for very long cylinders. The Thin Cylinder Model offers an explanation for why experimental measurements of this exponent vary between approximately 3.2 [22] and 3.4 [4] rather than being equal to 3 (the value predicted by the incoherent Faran Cylinder Model). The difference may be attributed to finite effective length of cylinders. The Thin Cylinder Model has been verified with measurements on nylon wires in water [39].

6.2.4 Weak Scattering Model

By "Weak Scattering Model" we mean an adaptation to bone of the Weak Scattering Model that was widely used to predict scattering by soft tissues [49–58]. In this approach, trabecular bone is considered as a random medium: a collection of random scatterers (trabeculae) in an ambient fluid. The fundamental difference with the Faran Cylinder Model is that the scatterers are not considered discrete anymore, but the medium is now described like a continuously varying medium. So far, the approach has been used only to model bone as a *fluid* random medium, i.e. neglecting the propagation of shear waves in the scatterers, and describing the trabeculae as fluid heterogeneities, whose acoustic properties differ from those of the ambient fluid [1, 4, 5, 16, 17, 38, 59, 60]. The first use of such a model was made neglecting the density fluctuations in the trabeculae [16, 60], using the so-called Binary Mixture Model, which has been shown to be useful in soft tissues [58]. Then density fluctuations were taken into account [1, 4, 5, 17, 38, 59].

Several assumptions are necessary to derive this model based on the Born approximation [61]. (1) The field on a scatterer is assumed to be not affected by the other scatterers. This condition imposes restrictions on the values of density and compressibility fluctuations, coupled to restrictions on the scatterers dimensions compared to the wavelength. This last one is easily fulfilled since the wavelength in water or marrow at 0.5 MHz is about 3 mm and the typical trabecular diameter (e.g. human calcaneus) is about 120 µm [3]. Given the high density and compressibility fluctuations encountered, the condition ensuring the convergence of the

perturbation expansion used to calculate the pressure is barely satisfied at 0.5 MHz (see Sobczyk [62] for a medium characterized by an exponential autocorrelation function Chap. 3, Eqs. 3–32). Strictly speaking, at 1 MHz, the condition is not satisfied. However, we will see that the Weak Scattering Model nevertheless gives results that are very consistent with measurements in cancellous bone. (2) In the current derivation of the model applied to bone, absorption is neglected: this is a strong approximation which has to be taken into account in the experimental procedure by compensating for attenuation losses during propagation. (3) The scattering volume is far from the transducer. (4) Finally, the medium is supposed to be isotropic. The Weak Scattering Model based on these assumptions has been shown to result in predictions consistent with measurements in cancellous bone (see Sect. 6.3.2).

Following these assumptions, the differential scattering cross section can be expressed in terms of the three-dimensional spatial Fourier transform of the density and compressibility fluctuations.

If the microstructure is known, which can be the case when the specimens are imaged with high-resolution micro-tomography, the numerical 3-D volumes can be used to compute the spatial Fourier transform of the medium. This has been done with success to validate the model [4, 59]: Results have shown that the model can predict both the magnitude and the frequency dependence of the backscatter coefficient with a root mean square error of 1 dB.

More generally, the microstructure is unknown and can then be described in terms of its auto-correlation function [52, 61]. Different analytical forms of autocorrelation functions have been used so far [1, 4, 5, 17, 38], like Gaussian, exponential, etc… and have given accurate prediction of the backscatter coefficient. The advantage of this formulation is to make possible the resolution of an inverse problem, by adjusting the correlation length used in the model to fit experimental data. This point will be discussed in Sect. 6.3.2.

Using an analytical autocorrelation function to describe the micro-structure, some authors tried to estimate the attenuation due to scattering by computing the total scattering cross section. When only the mean fluctuations in velocity are taken into account, the Binary Mixture Model predicts nonlinear dependence of BUA on porosity as observed in cancellous bone [63] and a quasi-linear dependence of attenuation due to scattering with frequency over a limited bandwidth for sufficiently small scatterers [16]. When both velocity and density fluctuations were considered, the model also predicted a nonlinear dependence of BUA on porosity [1]. These results should however be considered with caution, because the derivation of the total scattering cross section assumes low level of attenuation, which seems incompatible with the results of the computations [1, 16, 60].

6.2.5 Comparison of Models

The Incoherent Faran Cylinder Model and the Weak Scattering Model, which have received far more experimental validation than the other models, have relative

strengths and weaknesses. Both models ignore multiple and coherent scattering. One relative disadvantage of the Incoherent Faran Cylinder Model is that trabeculae can deviate from a true cylindrical shape because of long-range curvature. As can be seen in Fig. 6.2, the curvature is often not dramatic on the scale of an ultrasonic beam width (typically about 13 mm at 500 kHz). Another disadvantage of the Incoherent Faran Cylinder Model is that cancellous bone can contain small non-cylindrical plate-like structures. Scattering from small plates may help explain measurements of backscatter coefficient that vary with frequency slightly more rapidly than the cubic dependence predicted by the Incoherent Faran Cylinder Model (since scattering from structures small compared with the wavelength is proportional to frequency to the fourth power) (see Sect. 6.3.2.). The Incoherent Faran Cylinder Model may be more appropriate for low density bone, in which rod-like structures dominate. The Weak Scattering model, with its statistical characterization of cancellous bone, is more flexible than the Incoherent Faran Cylinder Model in its ability to accommodate complex microstructure and its potential to provide a solution to the inverse problem.

One relative disadvantage of the Weak Scattering Model is that it requires that the acoustic properties (density and sound speed) within the two-component trabecular bone medium deviate only slightly from their mean values (spatial mean throughout the entire scattering volume). Density and sound speed of trabeculae may deviate substantially from density (approximately $1\mathrm{g/cm^3}$) and sound speed (approximately 1500 m/s) of the fluid filler. In addition, the Weak Scattering Model does not allow yet for shear wave propagation within trabeculae. Shear wave propagation has been measured in cortical bone [64] (see Chap. 13) and is therefore plausible within trabeculae. Simulations suggest, however, that shear waves within the trabecular network may play a negligible role in backscattering properties of cancellous bone [65]. The Incoherent Faran Cylinder Model allows for arbitrary contrast in acoustic properties, anisotropy, and the propagation of shear waves in the trabecular material.

Despite (1) the simplicity of these models relative to the true structure of cancellous bone and (2) the differences in their underlying assumptions, the Incoherent Faran Cylinder Model and the Weak Scattering Model predict similar frequency-dependent backscatter coefficients that agree well with measurements in human calcaneus in vitro [4, 22] and human femur in vitro [66], as shown in Fig. 6.3.

6.3 Estimation of Cancellous Bone Properties Using Scattering

6.3.1 Experimental Methods

Quantitative measurements of backscatter coefficient are performed using substitution measurement: the backscattered signals are compared to signals measured after reflection on a perfect reflector placed at a distance from the transducer equal to that

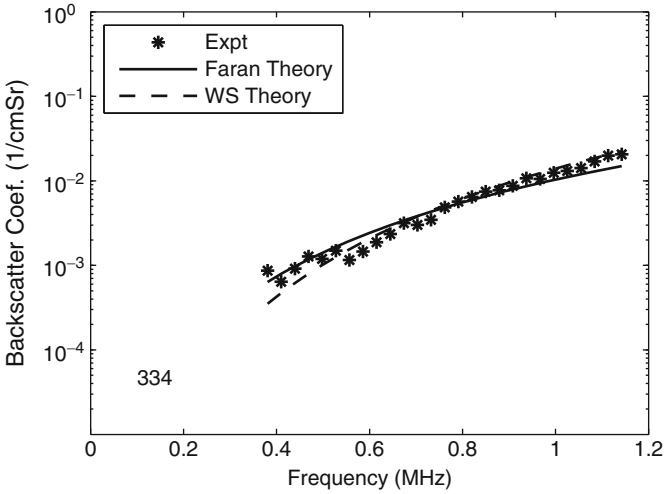

Fig. 6.3 Backscatter coefficient from human calcaneus sample in vitro. Incoherent Faran Cylinder Model predictions (*solid line*) and Weak Scattering Model predictions (*dashed line*) are also shown

of the scattering volume of the specimen under study, or compared to signals measured in a calibrated phantom. In order to perform measurements that isolate small volumes that include only cancellous bone and exclude cortical bone, these measurements are usually performed using focused transducers. Signals from a region of interest (ROI) of typically approximately 1 cm in diameter are selected, the size of the ROI being chosen to minimize variance due to spatial heterogeneity while allowing statistical averaging over a certain number of independent lines to reduce speckle noise.

Typically, the backscatter coefficient is calculated by computing the ratio of the frequency power spectrum of the time-weighted echo signal to the power spectrum of the reference signal. The echo-signal is time-weighted to select a desired physical location in the bone specimen. Care must be given to compensate backscatter measurements for attenuation, time-gate function and frequency-dependent scattering volume (diffraction). Details for several approaches can be found in several papers (e.g. [4, 20, 22, 67]). Provided the phase velocities of the sample and water are reasonably well matched, a requirement comfortably met for measurements on trabecular bone [68, 69] the effect of diffraction is small and can be neglected [70, 71]. The compensation for attenuation is a particularly sensitive issue and it has been demonstrated that compensation functions used for low attenuating soft tissues should be modified to take into account the large attenuation values encountered in bones [17]. With this method, the intrinsic backscatter coefficient of the scattering volume is obtained, which is independent of the characteristics of the measuring device and of experimental conditions. When no compensation for attenuation is made, one often refers to the "apparent" backscatter coefficient.

6.3.2 Experimental Results

Although the expansive literature on experimental measurements on cancellous bone is briefly summarized here, a more detailed discussion may be found in reference [72].

The measured backscatter coefficient has been found to be an increasing function of bone volume fraction, as measured by bone mineral density (BMD). Moderate correlations (typical R^2 of 0.7) were reported by several authors between integrated backscatter coefficient (or IBC i.e. backscatter coefficient averaged over the frequency bandwidth, also named BUB for broadband ultrasound backscatter coefficient) in vitro in human calcaneum [12, 20] and femur [32] in the clinical frequency range, but also at higher frequencies (0.5–5 MHz) in human trabecular specimens of femur and tibia [8, 13, 18]. The backscatter coefficient at 500 kHz has been found to exhibit moderate correlation to BMD in vitro in human cancellous calcaneal bone [26]. A non-linear trend was reported in bovine femurs, going to a maximum of the backscatter coefficient at 800 kHz for an apparent density of 0.6 g/cm^3 [1]. Apparent (not compensated for attenuation) integrated backscatter has been reported to decrease gradually with BMD in bovine cancellous tibia [10, 11], illustrating the confounding effect that attenuation (increasing with bone density) can have on the estimation of backscatter coefficient when it is not compensated for.

Over a limited band of frequencies (e.g. the transducer bandwidth), the frequency dependence of backscatter coefficient may be approximated by the exponent of a power law fit to backscatter coefficient versus frequency (i.e. backscatter coefficient is proportional to f^n). The value of the exponent n has been measured in human calcaneus to be in the range of 3.26–3.38 [4, 22]. A similar value of 3.1 has been measured in human femur [41]. The Incoherent Faran Cylinder Model predicts a value of $n = 3$ when the trabecular diameter is much smaller than a wavelength [22], i.e. in agreement with Rayleigh scattering by cylinders in the low ka regime where $k = 2\pi/\lambda$, λ = wavelength and a = trabecular radius. Typical values for ka are about 0.1–0.2 in the frequency band 0.5–1 MHz. Multiple scattering, scattering from finite-length cylinders, and scattering from small plates and cross-struts may partly explain why measured exponents tend to be greater than 3. The Weak Scattering Model predicts a value near 3.48 for human calcaneus [4]. Therefore, experimental measurements are in reasonable agreement to within experimental error with both the Incoherent Faran Cylinder Model and the Weak Scattering Model. A two-component Weak Scattering Model has also shown good agreement with measurements of frequency-dependent backscatter in bovine cancellous bone [5]. The frequency dependence however cannot be used on an individual basis to distinguish specimens (i.e. normal versus osteoporosis) because the variation in frequency dependence of measurements of the backscatter coefficient can entirely be attributed to random interference noise (speckle noise), arising from insufficient statistical averaging [17, 24].

Backscatter coefficient from human calcaneus in vitro has been shown to be approximately proportional to trabecular thickness (Tb.Th) to the 2.8 power, which is close to 2.9 power predicted by the Incoherent Faran Cylinder [28].

Moderate relationships between broadband backscatter coefficient and micro architectural parameters have been reported in human specimens [3, 13, 32, 73]. At the femur, correlation between BUB and micro-architectural parameters were reported to be slightly lower than at the calcaneum (best correlation coefficient obtained between BUB and bone surface/bone volume, with R values -0.86 at the calcaneum [3] and -0.65 at the femur [32]). Interestingly, it has been reported that the best linear multivariate model to predict BUB from micro-architectural parameters included trabecular thickness and trabecular spacing, predicting that an increase of trabecular number (number of scatterers) and an increase of trabecular thickness (size of scattering particle, i.e. trabeculae) will be associated with an increase of BUB, which is consistent with scattering theories [32]. However, it is interesting to note that after adjustment for density, the variance of BUB attributable uniquely to individual architectural parameters was at best 4% [3, 32, 73]. These results suggest that even if information about micro-architecture is conveyed by the backscattered waves, the causal relationships between e.g. BUB and micro-architecture deduced from such empirical studies cannot be used to predict micro-architectural features.

Backscatter coefficient in human calcaneus in vitro has been measured to be 50% higher in the mediolateral (ML) direction than in the anteroposterior (AP) direction [23]. In the ML orientation, the ultrasound propagation direction is approximately perpendicular to the trabecular axes. In the AP orientation, a wide range of angles between the ultrasound propagation direction and trabecular axes is encountered. The higher backscatter in the ML direction may be due to the fact that the trabeculae are oriented in such a way to present the maximum cross sectional area available to intercept (and therefore, scatter) the incident ultrasound beam [23]. Increased backscatter in the ML direction (compared with the AP direction) has also been reported in bovine tibia [11].

Most in vitro studies of the ultrasonic properties of cancellous bone involve defatted bone specimens immersed in water tanks. In these experiments, water in vitro substitutes for marrow in vivo as the fluid filler within the porous trabecular matrix. Studies have shown that bone samples filled with marrow exhibit similar backscatter to bone samples filled with water [74, 75].

Mechanical properties are important because they are related to fracture risk, the primary clinical endpoint. BUB has been found to correlate weakly but significantly with Young's modulus and ultimate strength in bovine cancellous femur [9] and human cancellous femur and tibia [8, 13]. The standard deviation of apparent integrated backscatter within a region of interest (ROI) has been found to show a strong correlation ($R^2 = 0.67$) with bone ultimate strength in human cancellous femur and tibia [19].

6.3.3 Estimation of Trabecular Thickness Using the Weak Scattering Model

The Weak Scattering Model can be used to estimate the trabecular thickness from experimental backscatter coefficient measurements [5, 17, 38]. To do so, an analytical expression of the backscatter coefficient in terms of the spatial

auto-correlation function of the medium is used, and the theoretical correlation length is adjusted by least square regression so that the root mean square error between the predicted and the experimental backscatter coefficient is minimized over the frequency bandwidth (0.4–1.2 MHz).

In this approach, one presupposes known a certain number of variables of the model, leaving the correlation length the only unknown. These variables are: the density and compressibility of the saturating fluid and the trabeculae material, as well as the bone volume fraction. Typical values characteristics in bone tissues are used ($\rho_{bone} = 1800\,kg/m^3$, $\rho_{fluid} = 1000\,kg/m^3$, $c_{bone} = 3300\,m/s$ and $c_{fluid} = 1500\,m/s$ in [5, 17, 38]). These values have been assumed to be constant throughout the specimens, i.e. neglecting intra and inter specimen variability. The bone volume fraction can be assessed from 3-D images micro architecture obtained from micro-tomography experiments [17, 38] or using Archimedes' principle [5] (although Archimedes' principle may be inaccurate for media such as cancellous bone that can absorb water [76]).

Because scatterer size is the usual interpretation for the correlation length [77, 78], to validate the model, the estimated correlation length was compared to the mean trabecular thickness values derived from 3-D microarchitecture [17, 38] or estimated on 2D optical images of slices of the bone volume [5].

Different forms of autocorrelation functions have been studied. In human trabecular bones, in which the expected range of variation of trabecular thickness (Tb.Th) is small, Gaussian, exponential, densely populated medium autocorrelation functions have given good predictions of Tb.Th [17, 38]. Using Gaussian autocorrelation function in human calcaneum, predicted mean Tb.Th was $130 \pm 6.5\,\mu m$ and estimated Tb.Th was $140 \pm 10\,\mu m$ [38], while in human femur predicted Tb.Th was $132 \pm 12\,\mu m$ and estimated Tb.Th was $134 \pm 15\,\mu m$ [17]. These good values obtained on average over a group of specimens are counterbalanced by moderate prediction at the individual level. The correlation coefficient between predicted correlation length and measured Tb.Th was found to be $R^2 = 0.44$ at the femur [17] and 0.51 at the calcaneum [38]. In bovine tibiae, the correlation between predicted values obtained using a densely populated model and measured ones was superior ($R^2 = 0.81$) [5]. This might be due to the larger range of values of Tb.Th in the group of bovine specimens (100–600 μm) [5] compared to a much narrow range in human bones (typically 100–150 μm [17, 38]).

The moderate correlations observed at the individual level are the results of some limitations associated with the approach. Some are related to the model itself. The correct choice of values of the characteristics of the media used in the computation is an issue. Variations in material properties of cancellous bone have been shown to have a significant effect on backscatter [46, 79] as well as a minor impact on speed of sound and BUA in transmission [80]. Therefore, further refinements of the model might be achieved by a fine-tuning of material properties and by taking into account their inter-specimens variability. The choice of the autocorrelation function has also to be validated: this could be achieved by estimating true 3D correlation function from 3D microstructures images. Such a preliminary study on a set of three specimens has indicated that Gaussian autocorrelation function is suitable for human femoral trabecular bones [81], but a more extensive analytical description

of acoustical properties fluctuations is required. Interestingly, one study [5] used a combination of two functions to closely approximate the backscatter coefficient in bovine bones, and to estimate the two mean Tb.Th observed in their specimens, where supposedly rod-like and plate-like structures are found. Another study [7] demonstrated that amplitude and frequency dependence was modified when taking into account a distribution of size for Tb.Th. Whether or not such an approach could improve size estimation in human bone where the size distribution is much narrower would be interesting to test. The model also assumes weak scattering and isotropy. These assumptions have been shown to result in predictions consistent with measurements in cancellous bone (see Sects. 6.2.4 and 6.3.2). There is to date no evidence that multiple scattering plays a role in the clinical frequency range (see Sect. 6.4). Finally, an additional limitation of the model is that it neglects shear wave propagation in the scatterers. How this might influence the estimator is to date unknown.

Other sources of errors comprise experimental uncertainties: measurement errors and compensation for attenuation. This last point is critical since it has been shown that accurate attenuation compensation is difficult to reach in highly attenuating medium like trabecular bones [17]. From simulations of backscattered signals [17], it was reported that even an imperfect attenuation compensation function did not result in a significant bias in Tb.Th estimates. However, the exact influence of attenuation still remains to be determined.

A major limitation arises from the limited number of independent backscatter signals available for averaging, due to the small size and heterogeneity of the specimens. This results in speckle noise, which will determine most of the variability of the measurements of frequency dependence of the backscatter coefficient, and a fraction of the variability of its amplitude [17, 24, 82]. Taking into account measurement errors (reported precision of the frequency averaged backscatter coefficient is 2.8–4% [3, 5, 17, 24, 38]), it was estimated that the total uncertainty on Tb.Th estimates is of the order of 7 μm [17].

So in the current state of the art, what is the meaningful clinical value of this approach? A comparison between the precision of such an estimator and the biological variability of Tb.Th has shown that only extreme values of Tb.Th (i.e. very thin or very thick) could be distinguished [17]. Moreover, after adjustment for bone density, it was shown that the precision of the estimator was too low to be able to catch small differences in Tb.Th values expected, meaning that no complementary information to a measure of bone density would be provided. Therefore, potential clinical usefulness of the approach will require a significant reduction in speckle noise and measurement errors and/or the development of other and more precise microstructural estimators.

6.4 Is Cancellous Bone a Multiple Scattering Medium?

Models described in the previous section rely on an assumption of single scattering. This assumption, which gave promising results for the modeling of backscatter coefficient, has never been directly confirmed. Only a few publications addressed

the question of multiple scattering in trabecular bone and are reviewed in this section.

Multiple scattering, if present, is usually assumed to have a minor effect in the low frequency regime used in clinical devices. This is supported by the observation that the contribution of the coherent wavefront is predominant on the transmitted signal. However, because the size of the beam at 500 kHz is large compared to the micro-structure characteristic dimensions, a self-averaging process is taking place, leading to a relative decrease of the incoherent part of the field.

The only published evidence that multiple scattering can occur in trabecular bone is found in references [2,6]. In these studies, it was experimentally demonstrated that the coherent backscattering effect could be observed in trabecular bone insonified at 3 MHz. The coherent backscattering manifests itself as an enhancement of the mean energy reflected in the direction of backscattering. Because its origin lies in the constructive interference of waves propagating through reciprocal paths that have been scattered at least twice, its manifestation is a signature of the presence of multiple scattering.

One study [6] used an ultrasonic array of 96-elements of 0.39 mm in size to measure the angular dependence of the average backscattered intensity as a function of time: in presence of multiple scattering, the angular distribution of the backscatter intensity narrows with time. The time dependence of this narrowing can be used to estimate the scattering mean-free path in bone (l_s). Combined with measurements of the coherent wave in transmission, it can also lead to an estimation of the absorption mean-free path (l_a). In the measured specimen the following estimates were obtained: $2.3\,mm < l_s < 8\,mm$, and $l_a^{'} > 3.2\,mm$. These results suggest that at high frequencies (in this study at 3 MHz), multiple scattering will take place in trabecular bones as soon as the propagation distance is longer than a few millimeters.

The same group of authors addressed the question of the inverse problem in a subsequent publication [2]. They were able to achieve local measurement of the diffusion constant D by using Gaussian beamforming to produce virtual sources and receivers with a beam waist of 1 mm. The diffusion constant, which characterizes the rate of growth of the diffusive halo due to multiple scattering, was compared to local measurement of BMD. As expected, the highest values for the diffusion constant were obtained for the areas where the bone was less dense, hence, the weaker scattering. The interesting result came from the fact that the contrast in D was of a factor 10, whereas the contrast in BMD was only 3.

Another possible manifestation of multiple scattering is negative velocity frequency dispersion. Negative velocity dispersion was observed experimentally in trabecular bones (see Chap. 12). One study [40] proposed a model of multiple scattering to estimate velocity dispersion in trabecular bones, taking into account the coupling of multiple scattering and absorption phenomena. The trabecular microstructure was modeled as a collection of cylinders with axes oriented perpendicular to the propagation direction (trabeculae) and embedded in a visco-elastic surrounding medium (marrow). In the frequency range 0.4–0.8 MHz, positive and negative velocity dispersions were estimated that spanned the range of values in trabecular bone reported in the literature. This approach was interesting, but a direct comparison to experimental data in cancellous bone was not performed. However,

the model accurately predicted dispersion in cancellous-bone-mimicking phantoms consisting of parallel nylon wires in water [47].

Another approach [83, 84] proposed also to model trabecular bone as a multiple scattering medium. But instead of assuming that scattering had its origin in the trabeculae, this approach, assuming only fluid media, described trabecular bone as a homogenized nondissipative poroelastic medium using Biot's theory (the reader is referred to Chap. 5 for a review of the Biot theory and its application to model ultrasound propagation in trabecular bones), in which large cylindrical pores filled with marrow would act as scatterers. These cylindrical pores were assumed to be 1–2 mm in diameter with an axis oriented perpendicular to the incident direction. This approach used two multiple scattering theories: Foldy-Twersky and Waterman-Truel theories.

The results of the computations, when compared to typical values measured on bones with equivalent porosity, predicted BUA levels of approximately one-fifth of those measured and an over-estimation of SOS of approximately 140 m/s. A major limitation of this approach, besides drastic approximation on the geometry of the scatterers, came from the fact that mode conversions were neglected. However, even including mode conversions, due to the very high discrepancies observed between predicted and measured BUA and SOS, it is in the current state not possible to determine the relevance of the model.

To conclude this section, experimental evidence of multiple scattering at frequencies close to the clinical range has still to be demonstrated. Indirect demonstration, using models to predict experimental features, did not yet prove to be efficient. The only direct evidence was obtained at higher frequency. A potential application of higher frequency multiple scattering effects could be to provide information on micro-architectural features, assuming direct relationships can be derived between micro-architectural characteristics and multiple scattering metrics like the diffusion constant. To date, the current results available do not suggest that multiple scattering plays a dominant role in the attenuation measured in transmission in the clinical frequency range.

6.5 Clinical Applications of Scattering

The conventional QUS measurements, BUA and SOS, are through-transmission measurements that require two transducers. Backscatter only requires one transducer and therefore is applicable to skeletal sites such as the hip and spine where through-transmission measurements are difficult. Unfortunately, only modest clinical success has been reported so far for backscatter, however. This may be due to high variability of backscatter measurements due to speckle noise [24] and the distorting effects of rough cortical bone surfaces.

In a feasibility study involving ten normal human volunteers, backscatter from calcaneus at 2.25 MHz was found to exhibit a moderate correlation ($R^2 = 0.76$) with BMD measured using x-ray computed tomography [29].

While BMD is an important clinical indicator, fracture risk is the most important clinical endpoint. The ability for backscatter from calcaneus to measure fracture risk (either vertebral, wrist, and/or hip fracture) was investigated retrospectively in 210 postmenopausal women (including 60 with osteoporotic fractures) and 30 healthy premenopausal controls [30]. Backscatter measured over the range from 200–600 kHz was found to be moderately predictive of fracture risk (age adjusted odds ratio: 1.58; 95% CI: 1.14–2.19).

The effect of age on calcaneal backscatter at 1 MHz was investigated in 47 women (average age: 58 years, standard deviation: 13 years) [27]. The average backscatter coefficient (measured in 1/cmSr) was found to decline by approximately 1 dB per decade (for ages between 30 and 90).

Since frequency-dependent attenuation in bone has the effect of a low-pass filter, it causes a downshift in the center frequency of the backscattered spectrum. Therefore, the centroid downshift of the backscattered spectrum is an index of attenuation, which is known to have a high correlation with BMD. It was found in a feasibility study involving nine women that the backscattered spectral centroid shift from vertebral bodies (L3 and L4) exhibits a modest correlation ($R^2 = 0.37$) with BMD [31].

6.6 Discussion and Conclusion

6.6.1 Evidence of Scattering in Cancellous Bones

Many measurements of the scattering by trabecular bone have been reported. Both single and multiple scattering can take place, although in different frequency regimes. There is to date no direct evidence that multiple scattering plays a role at clinically relevant frequencies (below 1 MHz). Scattering is assumed to originate from the trabeculae. The frequency dependence observed is in agreement with Rayleigh scattering by cylinders in a low range of *ka*.

Backscatter coefficient is sensitive to variations in bone volume fraction, although the correlation between the two quantities has been found to be modest. Backscatter coefficient can also be predicted using micro-architectural parameters, and is anisotropic. Its correlation to mechanical properties is moderate.

6.6.2 Role of Scattering in Attenuation

Attenuation is the combined result of absorption and scattering. Incident longitudinal waves may be scattered into longitudinal waves (longitudinal-longitudinal or LL scattering) and/or shear waves (longitudinal-shear or LS scattering) [39]. Since most direct measurements of backscattering in bone only reveal LL scattering, many papers simply describe their measurements as “backscatter”, leaving it implicit that

"backscatter" includes only LL backscatter [4, 22]. While attenuation in cancellous bone is approximately proportional to frequency to the first power, LL backscatter coefficient is approximately proportional to frequency to the third power (in the diagnostic frequency range, 300–700 kHz) [22]. This suggests that total scatter, not just backscatter, is likely to also vary nonlinearly with frequency. For example, the Incoherent Faran Cylinder Model predicts that total scatter, not just backscatter, should be approximately proportional to frequency to the third power [22]. The inconsistency of frequency dependencies for attenuation and scattering led several authors to suggest that LL scattering may be only a minor contribution to attenuation at diagnostic frequencies [4, 22]. Further, some authors suggested that absorption may be the primary source of attenuation [4, 22, 85]. However, the importance of LS scattering was not fully appreciated at that time. Recent simulations have suggested that LS scattering may be significant [65, 86–88] but would only exceed absorption at high frequencies (above approximately 600 kHz) [86], which are at the high end of the diagnostic range (300–700 kHz).

The idea that LS scattering can result in quasi-linear attenuation is supported by (1) attenuation measurements in soft-tissue-mimicking phantoms consisting of graphite particles suspended in gelatin [89], (2) attenuation and scattering measurements in cancellous-bone mimicking phantoms consisting of nylon wire filaments embedded in a soft-tissue mimicking fluid [39], and (3) attenuation measurements in human cancellous bones in vitro with different filling fluids (alcohol versus water) [90].

Because of high shear attenuation coefficients, shear waves scattered by trabeculae may be transient. Shear attenuation coefficients in bovine cancellous bone have been estimated to be approximately 17 dB/mm (at 1 MHz) [95], implying that shear wave power is reduced by approximately 98% for each mm of propagation. Moreover, shear waves generated from graphite particles suspended in gelatin have been described as "evanescent" [89]. The mode-converted shear wave may have transient significance in the immediate proximity of the scatterer, but due to high attenuation it is likely rapidly extinguished. If LS scattering is significant, then the relative roles of absorption and scattering in cancellous bone (even at high frequencies, above 600 kHz) will depend somewhat on the relative roles of absorption and scattering of mode-converted shear waves. If the rapid attenuation of mode-converted shear waves is primarily due to absorption, then absorption would be the dominant loss mechanism even at high frequencies, albeit with the caveat that the ultrasonic energy briefly takes the form of a transient shear wave prior to absorption.

6.6.3 Perspectives

The current methods have shown so far only a limited clinical usefulness to predict fracture risk in vivo [30] as well as to predict trabecular thickness in vitro [1, 5, 17, 38]. How to improve the technique?

For the current strategy of trabecular thickness estimation, one major limitation comes from the speckle noise. Different options can be envisaged such as varying the angle of insonification, varying the frequencies of the incident waves, and improving the statistical averaging. Complementary signal processing can also be applied to extract complementary architectural features such as trabecular spacing [91]. Alternative scattering models may be considered such as the first order multiple scattering model [92] or the Bourret [93] approximation to estimate the transmitted energy in random media, both of them being a priori compatible with experimental data.

An alternative strategy would be to change the point of view for the description of the micro-structure. The current methods have been focused on trying to extract a single parameter (Tb.Th, defined from image analysis on real micro-structure) from information that is by essence of statistical nature (i.e. the auto-correlation function). Because of the co-variance of the micro-architectural parameters is very high, an analytical description of the micro-structure might simply not be the most adequate, and evaluation of parameters like Tb.Th might not be the most relevant approach to follow. Preliminary study on the subject was proposed [81], and more work is needed to quantify the relevance of statistical description of the micro-architecture to predict ultrasonic as well as mechanical properties of trabecular bone.

Finally, scattering being sensitive to the anisotropy of the trabecular network, backscattering measurement at different angles could be used to estimate an anisotropy index. Because anisotropy of the trabecular network is a relevant adjunct to bone density for the estimation of bone strength [94], adding an estimation of anisotropy to standard backscatter coefficient measurement in vivo might be a way to improve bone fragility prediction.

Acknowledgments We acknowledge funding support from the US Food and Drug Administration Office of Women's Health.

References

1. K. N. Apostolopoulos and D. D. Deligianni, "Influence of microarchitecture alterations on ultrasonic backscattering in an experimental simulation of bovine cancellous bone aging," Journal of the Acoustical Society of America **123**(2), 1179–1187 (2008).
2. A. Aubry, A. Derode, and F. Padilla, "Local measurements of the diffusion constant in multiple scattering media: application to human trabecular bone imaging," Applied Physics Letters **92**, 124101–124101/124103 (2008).
3. S. Chaffai, F. Peyrin, S. Nuzzo, R. Porcher, G. Berger, and P. Laugier, "Ultrasonic characterization of human cancellous bone using transmission and backscatter measurements: relationships to density and microstructure," Bone **30**(1), 229–237 (2002).
4. S. Chaffaï, V. Roberjot, F. Peyrin, G. Berger, and P. Laugier, "Frequency dependence of ultrasonic backscattering in cancellous bone: autocorrelation model and experimental results," Journal of the Acoustical Society of America **108**(5), 2403–2411 (2000).
5. D. D. Deligianni and K. N. Apostolopoulos, "Characterization of dense bovine cancellous bone tissue microstructure by ultrasonic backscattering using weak scattering models," Journal of the Acoustical Society of America **122**(2), 1180–1190 (2007).

6. A. Derode, V. Mamou, F. Padilla, F. Jenson, and P. Laugier, "Dynamic coherent backscattering in a heterogeneous absorbing medium: application to human trabecular bone characterization," Applied Physics Letters **87**, 114101–114101-3 (2005).
7. X. Guo, D. Zhang, and X. Gong, "Evaluation of ultrasonic scattering in human cancellous bone by using a binary mixture model," Physics in Medicine and Biology **52**(1), 29–40 (2007).
8. M. A. Hakulinen, J. S. Day, J. Toyras, M. Timonen, H. Kroger, H. Weinans, I. Kiviranta, and J. S. Jurvelin, "Prediction of density and mechanical properties of human trabecular bone in vitro by using ultrasound transmission and backscattering measurements at 0.2–6.7 MHz frequency range," Physics in Medicine and Biology **50**(8), 1629–1642 (2005).
9. M. A. Hakulinen, J. Toyras, S. Saarakkala, J. Hirvonen, H. Kroger, and J. S. Jurvelin, "Ability of ultrasound backscattering to predict mechanical properties of bovine trabecular bone," Ultrasound in Medicine and Biology **30**(7), 919–927 (2004).
10. B. K. Hoffmeister, C. I. Jones, 3rd, G. J. Caldwell, and S. C. Kaste, "Ultrasonic characterization of cancellous bone using apparent integrated backscatter," Physics in Medicine and Biology **51**(11), 2715–2727 (2006).
11. B. K. Hoffmeister, S. A. Whitten, and J. Y. Rho, "Low-megahertz ultrasonic properties of bovine cancellous bone," Bone **26**(6), 635–642 (2000).
12. F. Jenson, F. Padilla, V. Bousson, C. Bergot, J. D. Laredo, and P. Laugier, "In vitro ultrasonic characterization of human cancellous femoral bone using transmission and backscatter measurements: relationships to bone mineral density," Journal of the Acoustical Society of America **119**(1), 654–663 (2006).
13. J. P. Karjalainen, J. Toyras, O. Riekkinen, M. Hakulinen, and J. S. Jurvelin, "Ultrasound backscatter imaging provides frequency-dependent information on structure, composition and mechanical properties of human trabecular bone," Ultrasound in Medicine and Biology **35**(8), 1376–1384 (2009).
14. K. Kitamura, H. Nishikouri, S. Ueha, S. Kimura, and N. Ohtomo, "Estimation of trabecular bone axis for characterization of cancellous bone using scattered ultrasonic wave," Japan Journal of Applied Physics **37**, 3082–3087 (1998).
15. K. Kitamura, H. Pan, S. Ueha, S. Kimura, and N. Ohtomo, "Ultrasonic scattering study of cancellous bone for osteoporosis diagnosis," Japan Journal of Applied Physics **35**, 3156–3162 (1996).
16. P. H. F. Nicholson, R. Strelitzki, R. O. Cleveland, and M. L. Bouxsein, "Scattering of ultrasound in cancellous bone:predictions from a theoretical model," Journal of Biomechanics **33**, 503–506 (2000).
17. F. Padilla, F. Jenson, and P. Laugier, "Estimation of trabecular thickness using ultrasonic backcatter," Ultrason Imaging **28**(1), 3–22 (2006).
18. O. Riekkinen, M. A. Hakulinen, M. J. Lammi, J. S. Jurvelin, A. Kallioniemi, and J. Toyras, "Acoustic properties of trabecular bone – relationships to tissue composition," Ultrasound in Medicine and Biology **33**(9), 1438–1444 (2007).
19. O. Riekkinen, M. A. Hakulinen, J. Toyras, and J. S. Jurvelin, "Spatial variation of acoustic properties is related with mechanical properties of trabecular bone," Physics in Medicine and Biology **52**(23), 6961–6968 (2007).
20. V. Roberjot, P. Laugier, P. Droin, P. Giat, and G. Berger, "Measurement of integrated backscatter coefficient of trabecular bone," presented at the IEEE Ultrasonics Symposium, San Antonio, TX, 1996.
21. D. Ta, W. Wang, K. Huang, Y. Wang, and L. H. Le, "Analysis of frequency dependence of ultrasonic backscatter coefficient in cancellous bone," Journal of the Acoustical Society of America **124**(6), 4083–4090 (2008).
22. K. A. Wear, "Frequency dependence of ultrasonic backscatter from human trabecular bone: theory and experiment," Journal of the Acoustical Society of America **106**(6), 3659–3664 (1999).
23. K. A. Wear, "Anisotropy of ultrasonic backscatter and attenuation from human calcaneus: implications for relative roles of absorption and scattering in determining attenuation," Journal of the Acoustical Society of America **107**(6), 3474–3479 (2000).

24. K. A. Wear, "Fundamental precision limitations for measurements of frequency dependence of backscatter: applications in tissue-mimicking phantoms and trabecular bone," Journal of the Acoustical Society of America **110**(6), 3275–3282 (2001).
25. K. A. Wear, "Measurement of dependence of backscatter coefficient from cylinders on frequency and diameter using focused transducers – with applications in trabecular bone," Journal of the Acoustical Society of America **115**(1), 66–72 (2004).
26. K. A. Wear and D. W. Armstrong, "The relationship between ultrasonic backscatter and bone mineral density in human calcaneus," IEEE Transactions on Ultrasonics Ferroelectrics and Frequency Control **47**(4), 777–780 (2000).
27. K. A. Wear and D. W. Armstrong, "Relationship among calcaneal backscatter, attenuation, sound speed, hip bone mineral density, and age in normal adult women," Journal of the Acoustical Society of America **110**(1), 573–578 (2001).
28. K. A. Wear and A. Laib, "The dependence of ultrasonic backscatter on trabecular thickness in human calcaneus: theoretical and experimental results," IEEE Transactions on Ultrasonics Ferroelectrics and Frequency Control **50**(8), 979–986 (2003).
29. K. A. Wear and B. S. Garra, "Assessment of bone density using ultrasonic backscatter," Ultrasound in Medicine and Biology **24**(5), 689–695 (1998).
30. C. Roux, V. Roberjot, R. Porcher, S. Kolta, M. Dougados, and P. Laugier, "Ultrasonic backscatter and transmission parameters at the os calcis in postmenopausal osteoporosis," Journal of Bone and Mineral Research **16**(7), 1353–1362 (2001).
31. B. S. Garra, M. Locher, S. Felker, and K. A. Wear, "Measurements of ultrasonic backscattered spectral centroid shift from spine in vivo: methodology and preliminary results," Ultrasound in Medicine and Biology **35**(1), 165–168 (2009).
32. F. Padilla, F. Jenson, V. Bousson, F. Peyrin, and P. Laugier, "Relationships of trabecular bone structure with quantitative ultrasound parameters: in vitro study on human proximal femur using transmission and backscatter measurements," Bone **42**(6), 1193–1202 (2008).
33. J. Litniewski, "Determination of the elasticity coefficient for a single trabecula of a cancellous bone: scanning acoustic microscopy approach," Ultrasound in Medicine and Biology **31**(10), 1361–1366 (2005).
34. "Consensus development conference: diagnosis, prophylaxis, and treatment of osteoporosis," American Journal of Medicine **94**(6), 646–650 (1993).
35. M. Hudelmaier, A. Kollstedt, E. M. Lochmuller, V. Kuhn, F. Eckstein, and T. M. Link, "Gender differences in trabecular bone architecture of the distal radius assessed with magnetic resonance imaging and implications for mechanical competence," Osteoporosis International **16**(9), 1124–1133 (2005).
36. A. M. Parfitt, C. H. E. Mathews, A. R. Villanueva, M. Kleerekoper, B. Frame, and D. S. Rao, "Relationships between surface, volume and thickness of iliac trabecular bone in aging and in osteoporosis," Journal of Clinical Investigation **72**, 1396–1409 (1983).
37. T. Steiniche, P. Christiansen, A. Vesterby, C. Hasling, R. Ullerup, L. Mosekilde, and F. Melsen, "Marked changes in iliac crest bone structure in postmenopausal osteoporotic patients without any signs of disturbed bone remodeling or balance," Bone **15**(1), 73–79 (1994).
38. F. Jenson, F. Padilla, and P. Laugier, "Prediction of frequency-dependent ultrasonic backscatter in cancellous bone using statistical weak scattering model," Ultrasound in Medicine and Biology **29**(3), 455–464 (2003).
39. K. A. Wear, "Mechanisms for attenuation in cancellous-bone-mimicking phantoms," IEEE Transactions on Ultrasonics Ferroelectrics and Frequency Control **55**(11), 2418–2425 (2008).
40. G. Haiat, A. Lhemery, F. Renaud, F. Padilla, P. Laugier, and S. Naili, "Velocity dispersion in trabecular bone: influence of multiple scattering and of absorption," Journal of the Acoustical Society of America **124**(6), 4047–4058 (2008).
41. F. Padilla, F. Jenson, and P. Laugier, "Influence of the precision of spectral backscatter measurements on the estimation of scatterers size in cancellous bone," Ultrasonics **44** (Suppl 1), e57–60 (2006).
42. K. A. Wear, "The effect of phase cancellation on estimates of broadband ultrasound attenuation and backscatter coefficient in human calcaneus in vitro," IEEE Transactions on Ultrasonics Ferroelectrics and Frequency Control **55**, 384–390 (2008).

43. J. J. Faran, "Sound scattering by solid cylinders and spheres," Journal of the Acoustical Society of America **23**(4), 405–418 (1951).
44. D. Ulrich, B. van Rietbergen, A. Laib, and P. Ruegsegger, "The ability of three-dimensional structural indices to reflect mechanical aspects of trabecular bone," Bone **25**(1), 55–60 (1999).
45. K. A. Wear, "Ultrasonic attenuation in parallel-nylon-wire cancellous-bone-mimicking phantoms," Journal of the Acoustical Society of America **124**(6), 4042–4046 (2008).
46. J. Litniewski, A. Nowicki, and P. A. Lewin, "Semi-empirical bone model for determination of trabecular structure properties from backscattered ultrasound," Ultrasonics **49**(6–7), 505–513 (2009).
47. K. A. Wear, "The dependencies of phase velocity and dispersion on trabecular thickness and spacing in trabecular bone-mimicking phantoms," Journal of the Acoustical Society of America **118**(2), 1186–1192 (2005).
48. K. A. Wear and G. R. Harris, "Frequency dependence of backscatter from thin, oblique, finite-length cylinders measured with a focused transducer-with applications in cancellous bone," Journal of the Acoustical Society of America **124**(5), 3309–3314 (2008).
49. D. J. Coleman, M. J. Rondeau, R. H. Silverman, R. Folberg, V. Rummelt, S. M. Woods, and F. L. Lizzi, "Correlation of microcirculation architecture with ultrasound backscatter parameters of uveal melanoma," European Journal of Ophthalmology **5**(2), 96–106 (1995).
50. E. J. Feleppa, A. Kalisz, J. B. Sokil-Melgar, F. L. Lizzi, Tian-Liu, A. L. Rosado, M. C. Shao, W. R. Fair, Yu-Wang, M. S. Cookson, and V. E. Reuter, "Typing of prostate tissue by ultrasonic spectrum analysis," IEEE Transactions on Ultrasonics Ferroelectrics and Frequency Control **43**(4), 609–619 (1996).
51. T. J. Hall, M. F. Insana, L. A. Harrison, and G. G. Cox, "Ultrasonic measurement of glomerular diameters in normal adult humans," Ultrasound in Medicine and Biology **22**(8), 987–997 (1996).
52. M. F. Insana and D. G. Brown, "Acoustic scattering theory applied to soft biological tissues," in *Ultrasonic Scattering in Biological Tissues*, K. K. Shung and G. A. Thieme, eds. (CRC Press, Boca Raton, FL, 1993).
53. F. L. O. Lizzi, M.; Feleppa, E. J.; Rorke, M. C.; Yaremko, M. M., "Relationship of ultrasonic spectral parameters to features of tissue microstructure," IEEE-Transactions-on-Ultrasonics,-Ferroelectrics-and-Frequency-Control **34**(3), 319–329 (1986).
54. F. L. Lizzi, M. Greenebaum, E. J. Feleppa, M. Elbaum, and D. J. Coleman, "Theoretical framework for spectrum analysis in ultrasonic tissue characterization," Journal of the Acoustical Society of America **73**(4), 1366–1373 (1983).
55. F. L. Lizzi, D. L. King, M. C. Rorke, J. Hui, M. Ostromogilsky, M. M. Yaremko, E. J. Feleppa, and P. Wai, "Comparison of theoretical scattering results and ultrasonic data from clinical liver examinations," Ultrasound in Medicine and Biology **14**(5), 377–385 (1988).
56. M. L. Oelze, W. D. O'Brien, Jr., J. P. Blue, and J. F. Zachary, "Differentiation and characterization of rat mammary fibroadenomas and 4T1 mouse carcinomas using quantitative ultrasound imaging," IEEE Transactions on Medical Imaging **23**(6), 764–771 (2004).
57. F. Ossant, M. Lebertre, L. Pourcelot, and F. Patat, "Ultrasonic characterization of maturation of fetal lung microstructure: an animal study," Ultrasound in Medicine and Biology **27**(2), 157–169 (2001).
58. C. M. Sehgal, "Quantitative relationship between tissue composition and scattering of ultrasound," Journal of the Acoustical Society of America **94**(4), 1944–1952 (1993).
59. F. Padilla, F. Peyrin, and P. Laugier, "Prediction of backscatter coefficient in trabecular bones using a numerical model of three-dimensional microstructure," Journal of the Acoustical Society of America **113**(2), 1122–1129 (2003).
60. R. Strelitzki, P. H. Nicholson, and V. Paech, "A model for ultrasonic scattering in cancellous bone based on velocity fluctuations in a binary mixture," Physiological Measurement **19**(2), 189–196 (1998).
61. P. M. Morse and K. U. Ingard, *Theoretical acoustics* (Princeton University Press, Princeton, NJ, 1968).
62. K. Sobczyk, *Stochastic wave propagation* (Elsevier, New York, 1985).

63. L. Serpe and J. Y. Rho, "The nonlinear transition period of broadband ultrasonic attenuation as bone density varies," Journal of Biomechanics **29**, 963–966 (1996).
64. D. E. Grenoble, J. L. Katz, K. L. Dunn, K. L. Murty, and R. S. Gilmore, "The elastic properties of hard tissues and apatites," Journal of Biomedical Materials Research **6**(3), 221–233 (1972).
65. E. Bossy, F. Padilla, F. Peyrin, and P. Laugier, "Three-dimensional simulation of ultrasound propagation through trabecular bone structures measured by synchrotron microtomography," Physics in Medicine and Biology **50**(23), 5545–5556 (2005).
66. K. A. Wear, F. Padilla, and P. Laugier, "Comparison of the Faran cylinder model and the weak scattering model for predicting the frequency dependence of backscatter from human cancellous femur in vitro," Journal of the Acoustical Society of America **124**(3), 1408–1410 (2008).
67. K. A. Wear, T. A. Stiles, G. R. Frank, E. L. Madsen, F. Cheng, E. J. Feleppa, C. S. Hall, B. S. Kim, P. Lee, W. D. O'Brien, Jr., M. L. Oelze, B. I. Raju, K. K. Shung, T. A. Wilson, and J. R. Yuan, "Interlaboratory comparison of ultrasonic backscatter coefficient measurements from 2 to 9 MHz," Journal of Ultrasound in Medicine **24**(9), 1235–1250 (2005).
68. P. Laugier, P. Droin, A. M. Laval-Jeantet, and G. Berger, "In vitro assessment of the relationship between acoustic properties and bone mass density of the calcaneus by comparison of ultrasound parametric imaging and QCT," Bone **20**, 157–165 (1997).
69. D. Hans, P. Dargent-Molina, A. M. Schott, J. L. Sebert, C. Cormier, P. O. Kotzki, P. D. Delmas, J. M. Pouilles, G. Breart, and P. J. Meunier, "Ultrasonographic heel measurements to predict hip fracture in elderly women: the EPIDOS prospective study," Lancet **348**(9026), 511–514 (1996).
70. P. Droin, G. Berger, and P. Laugier, "Velocity dispersion of acoustic waves in cancellous bone," IEEE Transactions on Ultrasonics Ferroelectrics and Frequency Control **45**, 581–592 (1998).
71. J. J. Kaufman, W. Xu, A. E. Chiabrera, and R. S. Siffert, "Diffraction effects in insertion mode estimation of ultrasonic group-velocity," IEEE Transactions on Ultrasonics Ferroelectrics and Frequency Control **42**(2), 232–242 (1995).
72. K. A. Wear, "Ultrasonic scattering from cancellous bone: a review," IEEE Transactions on Ultrasonics Ferroelectrics and Frequency Control **44**, 1432–1441 (2008).
73. P. H. F. Nicholson, R. Müller, X. G. Cheng, P. Rüegsegger, G. Van der Perre, J. Dequeker, and S. Boonen, "Quantitative ultrasound and trabecular architecture in the human calcaneus," Journal of Bone and Mineral Research **16**(10), 1886–1892 (2001).
74. B. K. Hoffmeister, J. A. Auwarter, and J. Y. Rho, "Effect of marrow on the high frequency ultrasonic properties of cancellous bone," Physics in Medicine and Biology **47**(18), 3419–3427 (2002).
75. P. H. F. Nicholson and M. L. Bouxsein, "Bone marrow influences quantitative ultrasound measurements in human cancellous bone" (2002).
76. K. A. Wear, A. Laib, A. P. Stuber, and J. C. Reynolds, "Comparison of measurements of phase velocity in human calcaneus to Biot theory," Journal of the Acoustical Society of America **117**(5), 3319–3324 (2005).
77. M. F. Insana, "Modeling acoustic backscatter from kidney microstructure using an anisotropic correlation function," Journal of the Acoustical Society of America **97**(1), 649–655 (1995).
78. M. F. Insana, T. J. Hall, and J. L. Fishback, "Identifying acoustic scattering sources in normal renal parenchyma from the anisotropy in acoustic properties," Ultrasound in Medicine and Biology **17**(6), 613–626 (1991).
79. K. A. Wear, "The effect of trabecular material properties on the frequency dependence of backscatter from cancellous bone," Journal of the Acoustical Society of America **114**(1), 62–65 (2003).
80. G. Haiat, F. Padilla, F. Peyrin, and P. Laugier, "Variation of ultrasonic parameters with microstructure and material properties of trabecular bone: a 3D model simulation," Journal of Bone and Mineral Research **22**(5), 665–674 (2007).
81. F. Padilla, Q. Grimal, and P. Laugier, "Ultrasonic propagation through trabecular bone modeled as a random medium," Japanese Journal of Applied Physics **47**(5), 4220–4222 (2008).
82. F. L. Lizzi, E. J. Feleppa, M. Astor, and A. Kalisz, "Statistics of ultrasonic spectral parameters for prostate and liver examinations," IEEE Transactions on Ultrasonics Ferroelectrics and Frequency Control **44**(4), 935–942 (1997).

83. F. Luppe, J. M. Conoir, and H. Franklin, "Scattering by a fluid cylinder in a porous medium: application to trabecular bone," Journal of the Acoustical Society of America **111**(6), 2573–2582 (2002).
84. F. Luppe, J. M. Conoir, and H. Franklin, "Multiple scattering in a trabecular bone: influence of the marrow viscosity on the effective properties," Journal of the Acoustical Society of America **113**(5), 2889–2892 (2003).
85. F. Padilla and P. Laugier, "Prediction of ultrasound attenuation in cancellous bones using poroelasticity and scattering theories," presented at the 2001 IEEE Ultrasonics Symposium Proceedings, Vols. 1 and 2, New York, 2001.
86. E. Bossy, P. Laugier, F. Peyrin, and F. Padilla, "Attenuation in trabecular bone: a comparison between numerical simulation and experimental results in human femur," Journal of the Acoustical Society of America **122**(4), 2469–2475 (2007).
87. G. Haiat, F. Padilla, R. Barkmann, C. C. Gluer, and P. Laugier, "Numerical simulation of the dependence of quantitative ultrasonic parameters on trabecular bone microarchitecture and elastic constants," Ultrasonics **44** (Suppl 1), e289–294 (2006).
88. F. Padilla, E. Bossy, G. Haiat, F. Jenson, and P. Laugier, "Numerical simulation of wave propagation in cancellous bone," Ultrasonics **44** (Suppl 1), e239–243 (2006).
89. J. G. Mottley and J. G. Miller, "Anisotropy of the ultrasonic attenuation in soft tissues: measurements in vitro," Journal of the Acoustical Society of America **88**, 1203–1210 (1990).
90. M. Pakula, F. Padilla, and P. Laugier, "Influence of the filling fluid on frequency-dependent velocity and attenuation in cancellous bones between 0.35 and 2.5 MHz," Journal of the Acoustical Society of America **126**(6), 3301–3310 (2009).
91. W. C. Pereira, L. S. Bridal, A. Coron, and P. Laugier, "Singular spectrum analysis applied to backscattered ultrasound signals from in vitro human cancellous bone specimens," IEEE Transactions on Ultrasonics Ferroelectrics and Frequency Control **51**(3), 302–312 (2004).
92. A. Ishimaru, *Wave propagation and scattering in random media* (Academic Press, New York, 1978).
93. S. M. Rytov, Y. A. Kravtsov, and V. I. Tatarskii, *Principle of statistical radiophysics IV: wave propagation through random media* (Springer, Berlin, Germany, 1989).
94. G. Haiat, F. Padilla, M. Svrcekova, Y. Chevalier, D. Pahr, F. Peyrin, P. Laugier, and P. Zysset, "Relationship between ultrasonic parameters and apparent trabecular bone elastic modulus: a numerical approach," Journal of Biomechanics **42**(13), 2033–2039 (2009).
95. A. Hosokawa, "Simulation of ultrasound propagation through bovine cancellous bone using elastic and Biot's finite-difference time-domain methods," Journal of the Acoustical Society of America **118**(3), 1782–1789 (2005).

Chapter 7
Guided Waves in Cortical Bone

Maryline Talmant, Josquin Foiret, and Jean-Gabriel Minonzio

Abstract In the last decade, several experimental studies have shown that long cortical bones act as a natural waveguide at ultrasonic frequencies despite attenuation in bone material and heterogeneity in elastic and geometrical properties. Propagation in waveguides consists in a variety of dispersive waves, each one with its own frequency-dependent field distribution across the section of the waveguide. Guided waves are extensively used particularly in non destructive evaluation. Technologically adapted devices have been developed for instance for structure health monitoring. In the bone assessment field, guided waves analysis might answer to the attempt of multiple bone property determination, as cortical thickness and elasticity. These properties are in turn relevant indicators of biomechanical competence. One of the most promising recent developments in this field is the so called "axial transmission" technique.

Keywords Arrays · Axial transmission · Bone characterization · Bone strength · Clinical devices · Cylindrical waveguide · Elastic anisotropy · Elastic waveguide · Instrumentation · Lamb waves · Long cortical bone · Material characterization · Multi component signal · Partial waves · Signal processing · Singular value decomposition

7.1 Introduction

A waveguide can be seen as a slender body, with a cross section of finite dimensions. A system of incident-reflected wave forms a standing wave across the finite section such that propagation and energy flow are guided along the boundaries of the waveguide. In contrast with bulk waves in unbounded medium, guided waves

M. Talmant (✉), J. Foiret, and J.-G. Minonzio
Université Pierre et Marie Curie, CNRS UMR 7623, Laboratoire d'Imagerie Parametrique,
15 rue de l'école de médecine, F-75006, Paris, France
e-mail: maryline.talmant@upmc.fr; josquin.foiret@upmc.fr; jean-gabriel.minonzio@upmc.fr

P. Laugier and G. Haïat (eds.), *Bone Quantitative Ultrasound*,
DOI 10.1007/978-94-007-0017-8_7,

adapt their wavelength to the finite dimensions of the waveguide at each frequency. This results in a variety of dispersive guided waves, each one with a varying phase velocity with frequency and its own frequency-dependent wavefield across the section. Guided waves in homogeneous stress free plates known as Lamb waves and guided waves in tubes are analyzed in standard textbooks [1–4].

Evidence of guided wave propagation in long cortical bones is reported in several experimental studies [5–9] carried out in the axial transmission configuration introduced in Chap. 3. Measured guided waves in bones in vitro are identified as fundamental flexural or higher order guided waves by comparison with dispersion curves calculated in homogeneous waveguides, such as plates and tubes. On the clinical side, despite these promising results, measurements of higher order guided waves are not currently performed on bone sites. Such measurements would increase the number of ultrasound indicators of biomechanical bone competence and have the potential to feed inversion schemes used to determine a combination of bone properties, i.e. cortical thickness and elastic properties.

Guided waves are widely used in different fields such as transducers design, geophysics and non-destructive testing. For instance, they are attractive, due to their ability to provide means of quick, long range inspection of large structures and/or defect localization [10, 11]. Guided waves are often presented [12] as an advantageous alternative to the pulse-echo technique based on bulk waves which locally test the structure below the transducer. Guided waves are also used for non-destructive material characterization [13, 14], for instance due to the demand of measuring elastic constant of fiber reinforced composite materials. However, guided mode signal analysis is challenging because the signal typically contains multiple dispersive modes implying that the pulse shape changes as it propagates along the waveguide. In practice, it can be preferred to select a particular mode and suppress or minimize the other undesired modes using a specific transducer design. Alternatively, dedicated signal processing techniques, for instance Fourier or time frequency transforms [15, 16], are used in order to provide phase velocity dispersion curves of all excited waves from multi component overlapping signals. On the theoretical side, models are developed to take into account heterogeneity in elasticity and/or change of the cross section which may be encountered in structures of engineering importance [17–20].

In the more recent bone assessment field, guided wave analysis is not yet as mature as in non destructive testing. For instance, it has been observed that signal processing techniques used in multi component signals is less efficient applied on in vivo measured signals. Consequently, all possible observable modes are not identified in clinical measurements. Moreover, in in vitro measurements, the whole set of individual properties of bone samples under testing i.e. the thickness, elastic coefficients and mass density is usually not completely known. Thus, a rigorous identification of dispersion curves measured on bones and the assessment of velocity measurement accuracy are not currently accessible. Nevertheless, according to in vitro sample experiments, a simple model of homogeneous waveguide captures already a major part of the bone response.

The chapter is organized as follows. In the first section, basic notions on guided wave propagation in reference or idealized waveguides such as plates and tubes, is reported. The next section is devoted to signal processing used for analysis of signals measured in axial transmission. The state of the art of axial transmission results obtained on bone is then reported. In the final section, the most recent developments in the field and the remaining challenges are discussed.

7.2 Idealized Waveguides

Many characteristic features, namely the spectrum, the fields, the excitability of guided waves and the response to a transient load, are captured by the simple case of an infinite isotropic plate of uniform thickness with stress free surfaces [21]. A detailed analysis of physical phenomenon in infinite layer is available in several textbooks [1–4]. This section intends to facilitate the introduction to guided waves in an anisotropic medium, reducing the discussion to graphical considerations and avoiding report on mathematical derivations.

7.2.1 Infinite Isotropic Plate

In Fig. 7.1, the plate is infinite in the direction (Ox_1) and (Ox_2) and has a uniform thickness e. The plate material consists of a linearly elastic isotropic non dissipative material with constant density and elastic coefficients. Time harmonic fields in the plate must satisfy both the linear equation of motion in the elastic material which constitutes the plate and the stress free boundary conditions.

In unbounded isotropic medium, for any propagation direction, plane waves are either pure shear or pure longitudinal. On the one hand, the P wave is longitudinally polarized with respect to the propagation direction. Its wave number k_{L} verifies $k_{\mathrm{L}} = \omega/c_{\mathrm{L}}$, where ω is the angular frequency and c_{L} is the bulk wave velocity of

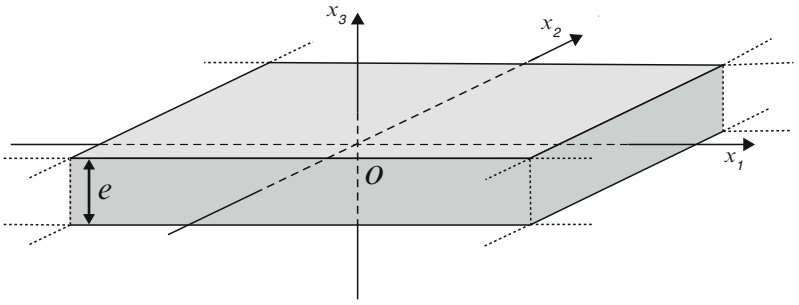

Fig. 7.1 Geometry of the infinite free plate waveguide

the P wave. On the other hand, the shear wave is normally polarized with respect to the propagation direction. Similarly, its wave number k_T satisfies $k_T = \omega/c_T$. Two orthogonally polarized shear waves are distinguished: for instance considering a propagation in the (Ox_1) direction, the *SV*, or shear vertical, wave particle displacement is in the (Ox_3) direction while the *SH*, or shear horizontal, wave induces displacements in the (Ox_2) direction.

Snell's law at free stress boundaries indicates that an incident *SH* wave do not couple to either *P* or *SV* waves. In contrast, an incident *SV* wave or an incident *P* wave reflects into both *P* and *SV* wave. As a consequence, two uncoupled classes of guided waves arise in an isotropic infinite layer with stress free boundaries. One class results from the reflection of *SH* waves, with the particle displacement in the plane (Ox_1x_2). The second class is plane strain guided waves resulting from the coupling of *P* and *SV* waves. This second class of guided waves corresponds to the Rayleigh-Lamb waves. Particle motions of Rayleigh-Lamb waves occur in the plane (Ox_1x_3). Rayleigh-Lamb waves and *SH* guided waves thus propagate independently. Attention is focused in the following to Rayleigh-Lamb waves because of the loading conditions imposed by the usual sources under interest. Piezoelectric emitting transducers acting normally to the surface as piston do not transmit *SH* waves.

The harmonic field of the guided waves in the plate is a superposition of incident and reflected *P* and *SV* fields illustrated in Fig. 7.2. These elementary components of the guided wave field are usually called partial waves.

According to Snell's law, incident and reflected partial *P* and *SV* waves must have the same component k in the x_1 direction. The transverse and the axial wave numbers of partial waves are related by

$$p^2 = \left(\frac{\omega}{c_L}\right)^2 - k^2, \text{ and } \quad q^2 = \left(\frac{\omega}{c_T}\right)^2 - k^2, \tag{7.1}$$

with p and q the *P* and *SV* wave numbers in the x_3 direction respectively. A variation in k is induced by a change in the direction of propagation of the partial waves accordingly.

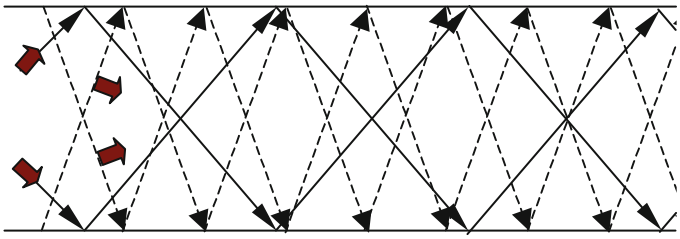

Fig. 7.2 Partial wave pattern of Lamb wave propagation in an isotropic plate with free boundaries. *Continuous lines* represent incident and reflected longitudinal partial waves and *dashed lines* represent incident and reflected vertically polarized shear waves. *Very thick arrows* show the polarization (After Auld [1])

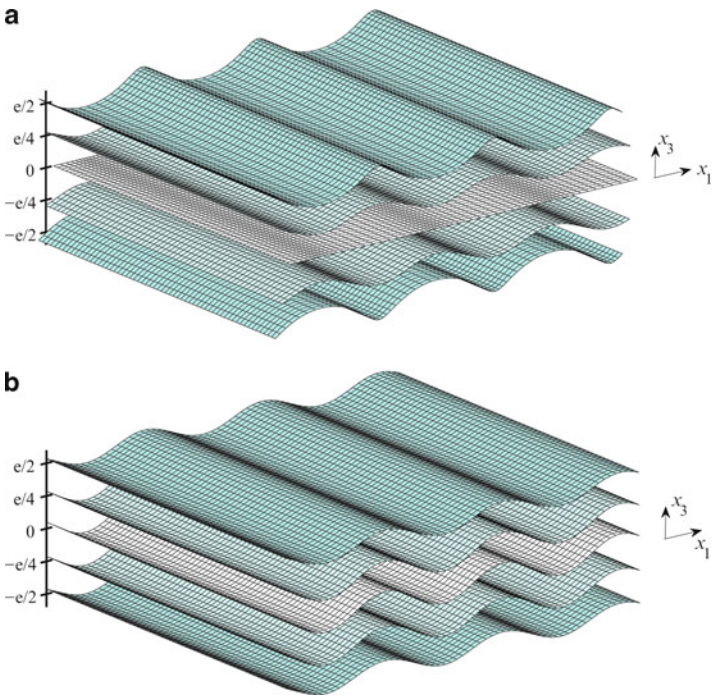

Fig. 7.3 Displacement for symmetric S (**a**) and anti-symmetric A (**b**) Rayleigh-Lamb waves in an isotropic plate. The symmetry is defined with respect to the (Ox_1x_2) plane

In addition, because of the plate symmetry with respect to the median (Ox_1x_2) plane, guided waves in the elastic layer may be split up into two independent systems: one with symmetric motion, denoted S, and the other with anti-symmetric motion, denoted A. Figure 7.3 illustrates symmetric and anti-symmetric motions, respectively. For symmetric motion, the displacement component u_1 in the longitudinal x_1 direction has the same sign in the upper and lower halves of the plate and the displacement u_3 has opposite signs. For anti-symmetric motion, the displacement u_1 has the opposite sign in the upper and lower halves of the plate while the displacement u_3 has the same sign.

From these considerations, the guided wave resulting from the combination of partial waves with the same component k along the direction parallel to the boundaries can be expressed as a standing wave in the x_3 direction and a propagating wave in x_1 direction. The fields can be written in a general form as

$$\left[A_{\mathrm{L}}(e^{ipx_3} \pm e^{-ipx_3}) + A_{\mathrm{T}}(e^{iqx_3} \pm e^{-iqx_3})\right] e^{i(kx_1 - \omega t)} \tag{7.2}$$

The phase velocity c_{ph} of the guided wave, defined as the common trace velocity (velocity along the x_1 direction) of all partial waves, satisfies:

$$c_{ph} = \frac{\omega}{k} \tag{7.3}$$

Non-trivial combination of partial waves (i.e. A_L and A_T not identically equal to zero) satisfying stress free conditions at the boundaries of the plate of thickness e must verify the so called dispersion relation which can be written, for symmetric waves, as [1,4]

$$(k^2+q^2)^2\cos(pd)\sin(qd)-4k^2pq\sin(pd)\cos(qd)=0, \tag{7.4}$$

where $d=e/2$ is half the plate thickness, p and q are the transverse wave numbers of the partial waves, as defined by Eq. 7.1. For anti-symmetric, similar equation is obtained by commuting sine and cosine functions.

Equation 7.4 relates the product frequency×thickness fe and the dimensionless wave number ke. It defines the permissible frequencies of guided waves. For a given ke, there are an infinite number of discrete frequencies allowed. In contrast with propagation in unbounded medium, a variety of guided waves can propagate in a plate.

Given the bulk wave velocities c_L and c_T, the pairs (fe,ke) solutions of the dispersion equation are calculated and the fields in the plate (particle displacements, stresses) are known within a constant. The Lamb frequency spectrum (i.e. the whole set of solutions of the dispersion equation) is highly structured.

In the next paragraph, few characteristics of the Lamb frequency spectrum and related quantities are illustrated from calculations with material parameters $c_L = 4000\,\mathrm{m}\cdot\mathrm{s}^{-1}$ and $c_T = 1800\,\mathrm{m}\cdot\mathrm{s}^{-1}$ which are used in several numerical studies as plausible velocities on cortical bone according to reference by E. Bossy et al. [22] (see Chap. 13 for details). This results in a Poisson's ratio $\nu = 0.37$ or equivalently a ratio $\kappa = c_L/c_T$ equal to 2.22.

Figure 7.4a shows the Lamb frequency spectrum for real valued wave numbers ke in the (fe,ke) plane. The solutions of the dispersion equation are calculated point by point and a given branch of the spectrum is constituted according to the apparent continuity of the solutions as fe and ke increases. For a given plate thickness e, the plane (fe,ke) is basically the plane of temporal frequency and spatial frequency in which each plane wave, i.e. a term defined by $\exp[i(kx_1-\omega t)]$ is represented by a point of coordinates (f,k) with $f=\omega/2\pi$. In experimental works, raw data are obtained in this last plane after decomposition of time-distance series into plane waves, using spatio-temporal Fourier transforms, as illustrated in Fig. 7.13b.

In the plane (fe,ke), the locations of constant phase velocity c_{ph} are along straight lines passing through the origin. In Fig. 7.4a, such lines corresponding to c_L and c_T are indicated by P and SV respectively. Alternatively, according to Eq. 7.3, the solutions of the dispersion equation can be shown as phase velocity curves as function of frequencies, as shown by Fig. 7.4b.

Waves associated to anti-symmetric motion in the plate are indicated by the letter A_i, the ones associated to symmetric motion by the letter S_i. They are numerated in Fig. 7.4 following their apparition order at $ke=0$. Because anti-symmetric and symmetric motions are uncoupled, A and S branches can intersect, as for instance S_2 and A_2 do.

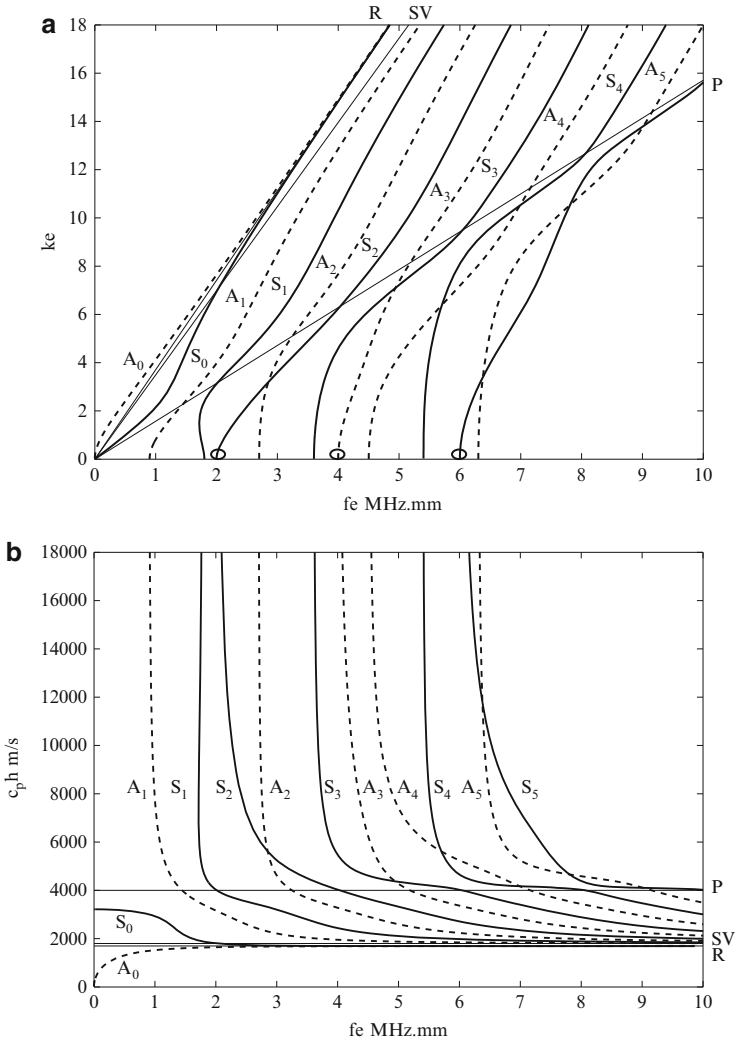

Fig. 7.4 Dispersion curves for the twelve first Rayleigh-Lamb waves for infinite isotropic free plate for $\kappa = c_L/c_T = 2.22$. Upper plot (**a**) is in the (fe, ke) plane, lower plot (**b**) shows phase velocities curves as function of the product frequency $\times$ thickness fe. The ellipses indicate the simple thickness-stretch frequencies in the plate. *Continuous lines and dashed lines* represent respectively the symmetric S_i and anti-symmetric A_i modes. Lines denoted respectively P, SV and R represent the bulk wave and Rayleigh wave velocities respectively. The modes are numerated following their apparition order

The lowest branches called A_0 and S_0 on Fig. 7.4 form a particular set of branches. The branches A_i and S_i with $i > 0$ are called the higher order modes. At $ke = 0$, each of them starts, with infinite phase velocity, at a distinct frequency called cut-off frequency fe^c which fall into two classes:

$$fe^{c,SV} = 0.5nc_T, \text{ or } fe^{c,P} = 0.5nc_L \quad \text{with } n = 1,2,3.... \tag{7.5}$$

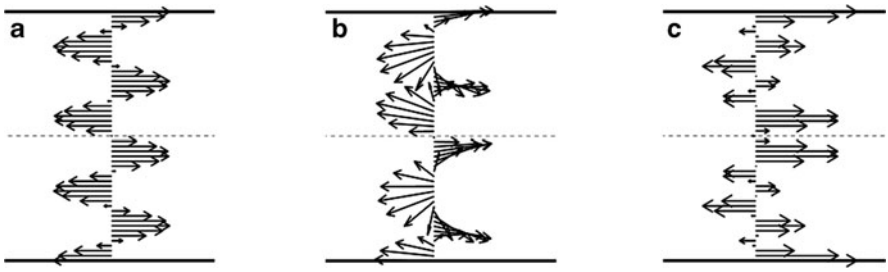

Fig. 7.5 Rayleigh-Lamb wave displacements field distribution for the anti-symmetric A_5 wave (**a**) at cut off frequency $fe^{c,SV} = 3.5c_T$ (**b**) at a frequency slightly higher than $fe^{c,SV}$ and (**c**) associated Poynting vector distribution. One anti-symmetric (A_5) mode is shown as an example

When $k = 0$, all partial waves are oriented along the Ox_3 direction and in such case of normal incidence, partial P and SV waves are uncoupled in the plate. Motion in the plate is purely either longitudinally or transversely polarized. For instance, Fig. 7.5a shows the displacement field in the plate for the A_5 wave at its cut-off frequencies $fe^{c,SV} = 3.5c_T$. It can be observed that the displacement is horizontal. It is due only to the shear partial wave and $3.5\lambda_T$ stands across the thickness where λ_T is wavelength of the shear partial wave for the specific frequency. This is an example of simple thickness shear waves which occurs at $fe^{c,SV}$ while simple thickness-stretch occurs at $fe^{c,P}$.

The field distribution across the plate thickness changes when fe and ke increases along a dispersion curve accordingly to the specific wave considered. For a frequency slightly higher than the cut-off frequency (Fig. 7.5b), the particle displacement is now elliptically polarized as partial waves acquire a new orientation. Along a dispersion curve the displacement is alternatively predominantly of dilatational type and of shear type. In Fig. 7.5c, the energy flow also shows variations across the thickness. For k values such that $k/\omega < 1/c_L$, both p and q are real and both P and SV partial wavefield vary as sine or cosine functions with x_3. For $k/\omega > 1/c_L$, the transverse wavenumber p of the partial P wave becomes imaginary, the partial P wave becomes inhomogeneous with an amplitude exponentially decreasing in the x_3 direction. As a consequence the P wavefield starts to become confined near the boundaries. The limiting field pattern is then predominantly a shear motion plus a longitudinal motion localized at the boundaries.

In contrast with upper branches, the two first modes A_0 and S_0 do not present cut-off frequencies. At the low frequency limit and large wavelength, consistently with thin plate theories, the A_0 branch reaches the limit of a flexural wave with purely normal displacement while the S_0 branch evolves as the extensional plate wave. Its phase velocity is constant and equal to $[E(1-\nu^2)/\rho]^{1/2}$ here E is the Young modulus of the material, and ρ is the mass density. The S_0 branch displays less dispersion below $fe = 1\,\mathrm{MHz\,mm}$.

For short wavelengths and high frequencies, A_0 and S_0 branches independently evolve as the Rayleigh wave branch, the well known surface wave on a free half space which has a velocity slightly lower than the shear wave velocity. A detailed

discussion of the whole spectrum is beyond the scope of this paper and we refer to Mindlin [23] and reports on his work [1, 3] for a complete and comprehensive analysis.

In summary, Rayleigh-Lamb waves adapt their wavelength to the finite dimensions of the plate at each frequency, which results in a variety of dispersive waves, each associated with specific field distribution across the section of the waveguide. All results reported above concern free vibrations of the plate. No source was considered. When a force is applied on the plate, waves are not equally well excited. When a source excites the plate and a receiver captures the axially transmitted signal, the excitability of a mode with a given transducer arrangement is dependent on the similarity between the mode shape and the field induced by the transducer. They are several ways of calculating the strength of the plate response among them the modal decomposition based on the orthogonality between Lamb modes [1, 24–28], and the integral transform [2, 3]. A comprehensive view of the variation of the transfer function is contained in the specific impedance of each wave. The specific impedance is defined by the ratio of the normal stress to the normal displacement, calculated in the free regime [1].

Figure 7.6 shows a plot of the magnitude of the transfer function, as derived from integral transform [2], for a surface traction force applied normally to the upper surface along a line infinite in the (Ox_2) direction and the normal displacement is supposed to be measured. A plate of thickness $e = 2\,\text{mm}$ is considered which is consistent with a mean value of a human radius bone sample. For frequency lower than 400 kHz, the response of an A_0 wave appears predominant compared to the S_0 wave response. Around cut-off frequencies, higher order modes, which appear as simple thickness stretch modes as S_2 for instance, present a remarkably higher transfer functions than branches as A_1 and A_2 which appear as thickness shear waves around cut-off frequencies.

Efficiency of excitation of Lamb waves depends on both the transfer function of each branch and the properties of the source in spatial-temporal domain. Some transducers, as for example laser interferometer, can transmit a short time signal with a large spatial and temporal frequency bandwidth. In this case, the guided waves are

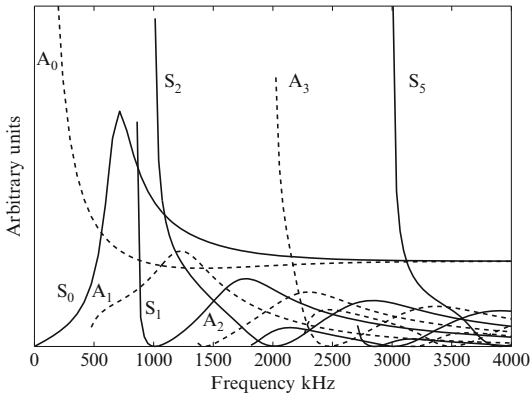

Fig. 7.6 Magnitude of the transfer function as function of frequency of an isotropic plate of thickness $e = 2\,\text{mm}$ when the applied stress is a traction normal to the upper surface of the isotropic plate and the normal displacement is supposed to be measured. The waves are numerated following their apparition order

excited in a large (f,k) domain. In the contrary, an angled wedge transducer piezoelectric element [11] generates mode in a more restrained (f,k) domain fixed by the angle of the wedge according to Snell's law. As a general rule, an emitting transducer must be adapted to fit the wavelength and frequency of the excited mode. In the area of non destructive testing, selective excitation and detection are often performed. For instance, the interdigital (comb) transducers select guided waves by matching the spatial distribution of applied surface traction to the wavelength of the propagating mode.

When transient sources are considered, a simple sketch of the different arrivals can be drawn from approximate theories [3]. At a given distance of propagation, the dominant contribution to the signal at a time t comes from frequency components (fe,ke) such that

$$t = \frac{x_1}{c_g(fe,ke)}, \quad \text{and} \quad c_g = \left(\frac{\partial fe}{\partial ke}\right), \tag{7.6}$$

where c_g is the group velocity of a given Lamb wave. The group velocity shown on Fig. 7.7 is the local slope of the dispersion curves in the (fe,ke) plane.

The low frequency components of the S_0 wave arrive first and present small amplitude (Fig. 7.6). Frequency components associated to maximum of group velocities arrive later with a higher amplitude than S_0. Next, the A_0 wave arrives with a high amplitude. Higher modes around cutoff frequencies yield the latest time components.

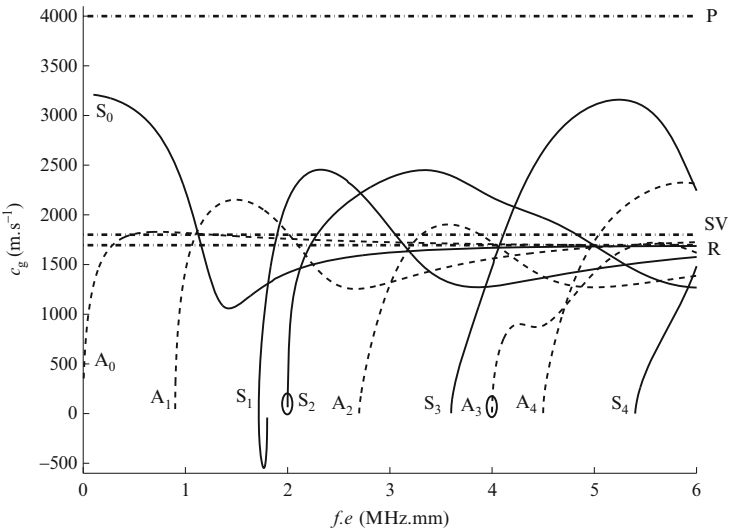

Fig. 7.7 Group velocity curves for infinite isotropic free plate for $\kappa = 2.22$. The ellipses indicate the simple thickness-stretch frequencies. *Continuous lines* and *dashed lines* represent respectively the symmetric S_i and anti-symmetric A_i modes. Lines denoted respectively P, SV and R represent the bulk and Rayleigh velocities respectively. The modes are numerated following their apparition order

The shape of cortical bone is obviously closer to cylindrical geometry than to the plane geometry and so we report briefly in the next paragraph on guided waves in stress free tubes.

7.2.2 *Infinite Free Isotropic Tube*

On planar infinite waveguide, the effect of finite cross section is limited to one dimension. A cylindrical stress-free tube is an example of guidance in two dimensions. Pioneering investigation of free harmonic waves on isotropic hollow tubes are due to Gazis [29] but detailed report can be found in textbooks for instance by Auld [1] and Rose [30].

Free time-harmonic guided wave are searched now as $\Theta(\theta)R(r)e^{i(kz-\omega t)}$, where r, θ and z are cylindrical coordinates illustrated on Fig. 7.8.

As for plates, guided waves are due to the interaction of shear and longitudinal waves at the boundaries of the waveguide and the relation between the component k and p or k and q of the partial waves still holds (Eq. 7.1), where k is the component along z direction and p and q are the radial component of the wavevector of the partial waves.

Condition of free stress are now expressed at the boundaries of the tube, i.e. the inner radius a and the outer radius b. As a consequence, the characteristic equation is $f(fb, kb; a/b) = 0$, where k is now the component of the wavevector in the z axial direction of the tube. The solution of the characteristic equation are obtained as the pairs (fb, kb) when the value of the ratio a/b is fixed. Similarly to the plate case, standing waves occur in the radial direction but the wavefield is now expressed as cylindrical functions. Standing waves occur now also in the θ direction associated to sinusoidal functions.

As for plates, an infinite number of branches are found as solution of the characteristic equation. Consistently with the axial symmetry of the waveguide, the guided

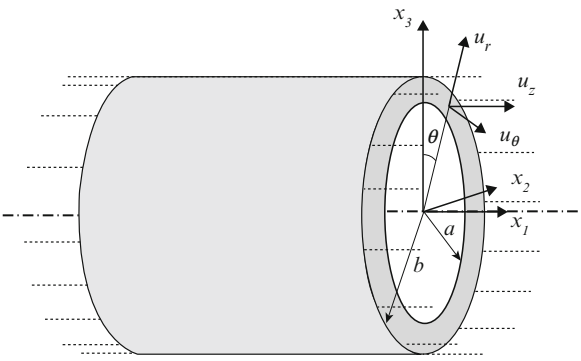

Fig. 7.8 Free tube waveguide geometry

waves fall into different classes according to the symmetry of the displacement, as plate modes fall into *A* and *S* modes. The so-called longitudinal waves, denoted $L(0,i), i = 1,2\ldots$ are such that particle displacement has only radial and axial components and is independent of circumferential position In contrast, flexural waves, denoted $F(n,m), n = 1,2\ldots$ and $m = 1,2\ldots$ have displacement in all directions. The third class is torsional waves which have only circumferential displacement. They are equivalent to *SH* waves on plates and are not considered here.

Figure 7.9 shows dispersion curves of longitudinal and flexural waves for the specific case of a ratio of inner to outer radius equal to 0.6 which is a plausible value for actual bone sites such as the radius. The six first Rayleigh-Lamb waves are shown as continuous lines. It is observed that longitudinal $L(0,i)$ branches fall into the Lamb branches [29, 31, 32] and some flexural branches $F(n,m)$ $m = 1,3,5$ fall into the longitudinal branches. Flexural branches $F(n,m)$ group with respect of the second index *m*, which corresponds to the characteristic of the standing function in the radial direction. In contrast, the group $F(n,2)$, as well as the group $F(n,4)$ fall into torsional branches not shown on the figure [29, 32].

In the area of non destructive testing of tubes, selective excitation and detection are often performed, for instance with a transducer array for axisymmetric generation which excites only longitudinal type of guided waves. Non axisymmetric

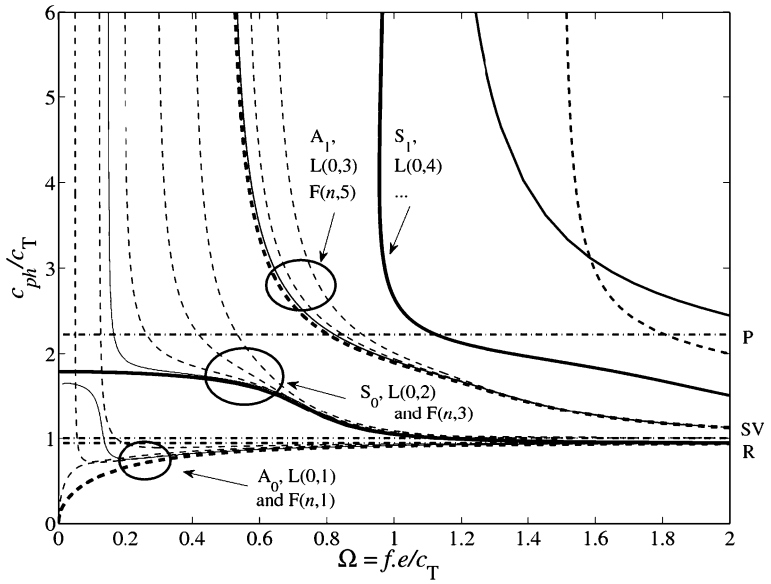

Fig. 7.9 Phase velocities for tube with inner to outer diameter equal to 0.6 and for plate of the same thickness. The ratio κ is equal to 2.22. The six first Lamb waves on plate are shown as thick dashed (antisymetric A) and continuous (symmetric S) lines, Longitudinal waves on tube $L(0,i), I =$ 1–5 are shown as thin *continuous lines*. L(0, 4) and L(0, 5) are masked by superposed Lamb waves. Flexural waves on tube $F(n,m)$ *are shown as thin dashed lines*. For $n = 1,2,3$, it is observed that $F(n,1)$ branches are grouped around the L(0, 1) branch,. $F(n,3)$ branches around the L(0, 2) branch and $F(n,5)$ branches around the L(0, 3) branch

sources can be also used when only a portion of the tube is accessible [33, 34]. In that case, flexural as well as longitudinal waves are excited. Torsional waves can be generated by contact shear wave transducer.

In axial transmission on bones, non axisymmetric sources are used and are supposed to generate flexural waves as well as longitudinal components. However, in experimental reports, mainly L type of wave are observed, According to Moilanen, the flexural component F(1, 1) can be observed. It might be assumed that the contact area of the transducer on the sample is likely a simple line, due to fact that the radius of curvature of the sample is small compared to the lateral dimension of the probe.

Despite the evidence that the geometry of cortical bone is closer to cylindrical shape than to flat plate, there is no clear evidence that tube dispersion curves bring insight in experimentally measured dispersion curves additionally to the plate model.

Up to that point, guided waves in isotropic medium was considered. However, the macroscopic anisotropic elastic behaviour of cortical bone material has long been recognized [35–38]. In the diaphyseal regions of long bones, cortical bone material is considered as transverse isotropic or orthorhombic material, consistently with the predominantly longitudinal orientation of the Haversian systems. Here, propagation of guided waves is analyzed assuming an hexagonal symmetry for bone.

7.2.3 *Infinite Free Transversely Isotropic Plate*

In this model of transversely isotropic medium five elastic stiffnesses are needed to satisfy the Hooke's law which relates stress and strain:

$$\begin{bmatrix} \sigma_1 \\ \sigma_2 \\ \sigma_3 \\ \sigma_4 \\ \sigma_5 \\ \sigma_6 \end{bmatrix} = \begin{bmatrix} C_{11} & C_{12} & C_{13} & 0 & 0 & 0 \\ C_{12} & C_{22} & C_{13} & 0 & 0 & 0 \\ C_{13} & C_{23} & C_{33} & 0 & 0 & 0 \\ 0 & 0 & 0 & C_{44} & 0 & 0 \\ 0 & 0 & 0 & 0 & C_{55} & 0 \\ 0 & 0 & 0 & 0 & 0 & C_{66} \end{bmatrix} \begin{bmatrix} \varepsilon_1 \\ \varepsilon_2 \\ \varepsilon_3 \\ 2\varepsilon_4 \\ 2\varepsilon_5 \\ 2\varepsilon_6 \end{bmatrix}, \tag{7.7}$$

where σ_i and ε_i are elements of the stress and strain tensors respectively expressed with the contracting subscript notation, i.e. $1 \rightarrow 11, 2 \rightarrow 22, 3 \rightarrow 33, 4 \rightarrow 23$, $5 \rightarrow 13, 6 \rightarrow 12$.

For numerical applications, the following values of the stiffnesses (in GPa) were taken, following [39] $C_{11} = 29.6$, $C_{22} = C_{33} = 21.5$, $C_{12} = C_{13} = C_{23} = 11.5$, $C_{44} = (C_{22} - C_{23})/2 = 5$, $C_{55} = C_{66} = 6$ and a mass density equal to $1.85\,\mathrm{kg \cdot m^{-3}}$.

In an anisotropic unbounded medium, the bulk wave velocities depends on the direction of propagation; in addition, *P* wave, *SV* waves and *SH* waves are not purely longitudinally or transversely polarized, except in specific directions. They are labelled *QP*, *QSV* and *QSH* for quasi purely polarized. Snell's law indicates that the

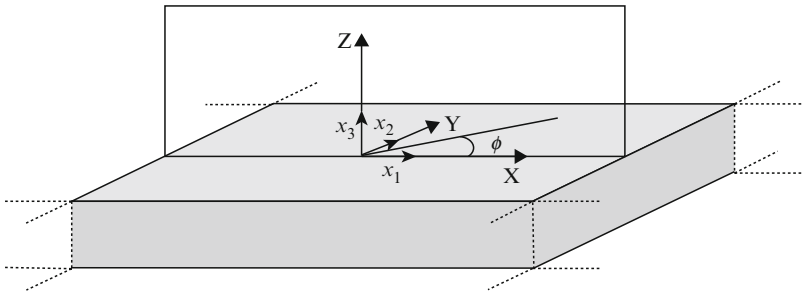

Fig. 7.10 The six fold axis of symmetry in transversely isotropic medium is denoted Z. Propagation of guided waves is analyzed for $\phi = 0°$ in a meridian plane (X, Z) which coincide with (x_1, x_3)

three polarizations may couple to each other at the boundaries. Then, the propagation of guided waves might be strongly affected by the symmetry of the material, the degree of anisotropy and the relative directions of propagation vector and principal axis of the material [40–43].

The following short discussion is reduced to the particular case of plane strain condition in transversely isotropic medium with the six fold axis of symmetry denoted X aligned parallel to the free surfaces of the plate (Fig. 7.10). In the numerical application considered here, the QP wave propagates in the longitudinal x_1 direction with a phase velocity equal to $4000\,\mathrm{m}\cdot\mathrm{s}^{-1}$ and in the transverse direction x_3 direction with a velocity equal to $3400\,\mathrm{m}\cdot\mathrm{s}^{-1}$. Its velocity continuously varies within these two values as the orientation of the partial QP wave varies in the plate. The components k and p of the wavevector of the partial P wave (Eq. 7.1) do not lie on a circle of radius ω/c_L as in the isotropic case but now on an ellipse with its major axis in the (Ox_3) direction. The anisotropy ratio C_{11}/C_{33} is equal to 1.38, which is a plausible value for cortical bone is moderate compared to what is encountered in material such as fibrous composite material.

For propagation of guided waves in the (Ox_1) direction, in the direction of the six-fold axis, the dispersion curves are shown in Fig. 7.11. Superposed as thin lines are the dispersion curves for the isotropic case considered in the previous paragraphs. In the isotropic material $c_\mathrm{L} = 4000\,\mathrm{m}\cdot\mathrm{s}^{-1}$ equal to the QP wave velocity in the longitudinal (Ox_1) direction. Anisotropy-related modifications of phase velocity curves appear. For instance, simple thickness stretch frequencies (not visible on Fig. 7.11), occur for integer number of wavelength of QP waves in the transverse direction (Ox_3) which are different from the axial direction (Ox_1).

However, branches retain their identity. Indeed, branches group as anti-symmetric and symmetric waves, higher order modes appear with cut off frequencies at simple thickness stretch or shear modes and so on. Thus, the general features of the Rayleigh-Lamb waves on isotropic plates still hold.

If the sagittal plane is not aligned with a meridian plane, but is oriented with an angle ϕ as defined on Fig. 7.10, the matrix of elastic stiffness coefficients is modified. Indeed, the stiffness coefficients are defined relatively to the principal

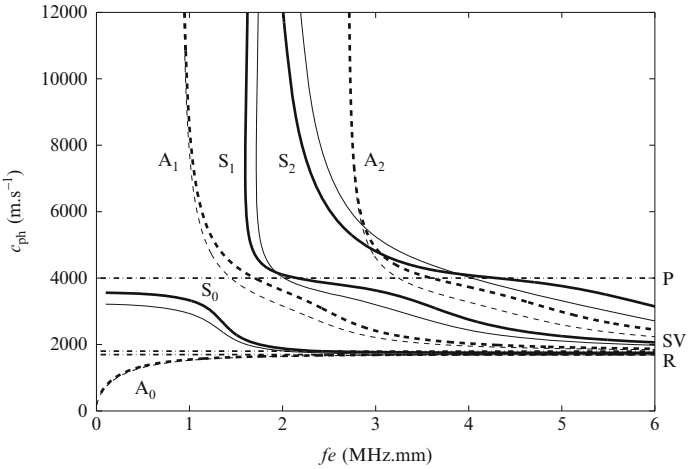

Fig. 7.11 Comparison of Rayleigh-Lamb waves for isotropic and anisotropic medium. Phase velocities vs *fe* for a transverse isotropic plate (*bold lines*). Propagation is along the (Ox_1) axis ($\phi = 0°$). For comparison, the isotropic case is plotted in thin lines. The modes are numerated following their apparition order

axis of the material and their values change with angle ϕ. As the stiffness coefficients intrinsically govern the dispersion curve, their changes automatically induce changes in dispersion curves.

The picture of guided waves in homogeneous plate provides a general framework for understanding the propagation in more sophisticated waveguides.

While it is a rough model for propagation in bones, the physical insight of Lamb guided wave are retained when considering tube or anisotropic material, as for more sophisticated models [44]. Appreciation of the changes in phase velocity induced by different models of gradually increasing sophistication depends then on the accuracy of the technique of phase velocity measurements. In addition, measurement uncertainties must be minimized for instance by a measurement protocol able to provide the best alignment of the probe with the bone axis, which is also the direction of the principal axis of symmetry of the material. Such kind of measurement protocol is already in use in clinical measurements.

7.3 Guided Wave Measurements in Axial Transmission Configuration

Guided waves are widely used in non destructive testing. Several review papers have been published as those proposed by Chimenti in 1997 [10] or Su et al. in 2006 [45] for instance. In this section, we briefly review the different experimental setups and the associated signal processing used in the axial transmission configuration. Some

methods are based on the detection and exploitation of one dominant mode and are usually frequency narrow band. Broadband signals containing multiple modes are more difficult to interpret but contain more information and are easier to generate experimentally. The techniques already employed in the bone field are mentioned.

7.3.1 Generation and Detection

Different ultrasonic transducers are used to excite and detect guided waves. A first category corresponds to transducers in contact with the inspected object: piezoelectric element [11], or interdigital (comb) transducers are widely used. The comb transducers select guided waves by matching the spatial distribution of applied surface traction to the wavelength of the propagating mode. The second category corresponds to non contact transducers: air-coupled ultrasonic transducers [46], electro-magnetic acoustic transducers [47] (EMAT, used with metallic object), or laser interferometer. Angle-adjustable transducers can be used to preferentially generate and collect one mode in accordance with Snell's law. Finally, arrays of piezoelectric elements are also used in contact with the inspected object [48] or distant from the object immersed in water [49].

7.3.2 Axial Transmission Signal Processing

Different signal processing techniques can be applied to extract guided wave velocities in axial transmission depending on the measurement configuration, i.e. the number and positions of transmitters and receivers as shown in Fig. 7.12.

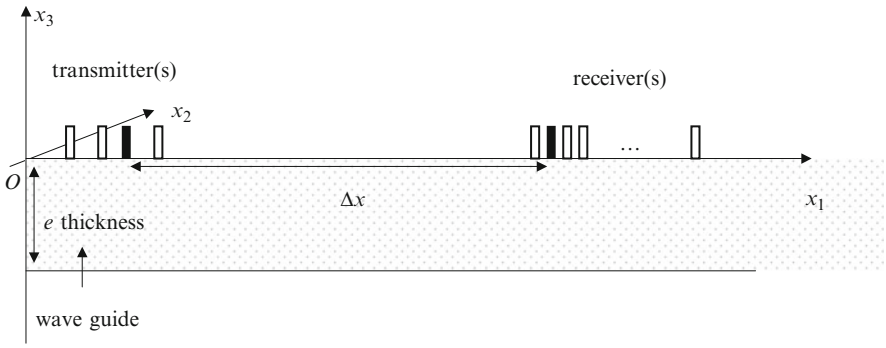

Fig. 7.12 Geometry of the axial transmission measurements: different types and configurations of transmitter(s) and receiver(s) are used to generate and detect guided waves

7.3.2.1 One Transmitter-One Receiver Configuration

Considering the one transmitter – one receiver configuration (Fig. 7.12), wave velocity can be simply computed from the measurement of the separation distance and the time-of-flight (TOF) between the two transducers. Heuristic criteria, such as TOF of the first maximum are usually used. This signal processing technique is limited by the velocity dispersion character of guided modes, i.e. by gradual change of the shape in the time domain of the wave during the propagation. On the one hand, the dispersion effects are relatively low when small propagation distances are considered. On the other hand, the identification of different modes is more difficult for short propagation distances when several modes are present. The TOF technique has been successfully used for the bone characterization in vitro and in vivo to evaluate the velocity of the first arrival signal (FAS) [50–53].

The recorded signal can be analyzed in the frequency domain using the phase spectrum method [54]. The spectrum phase slope is linked with the phase velocity. Nevertheless, the point of view is valid if a single mode is present in the whole bandwidth or at least if one mode is energetically preponderant compared to other modes. To this end, the mode can be preferentially selected at the emission using for example angle adjustable transducers. Alternatively, when the selected mode is predominant among other modes, long propagation distances can be considered in order to separate in the time domain the contributions of modes that propagates at different velocities. Such methods have been applied on in vitro bovine specimens, with long propagation distances of about 160 mm [8]. Such distances, being much larger than the usual in vivo accessible testing distance, such as for instance on the forearm, and the method is therefore restricted for in vitro experimental conditions.

Short time Fourier transform (STFT) [55] has been proposed to analyze the signal. The Fourier transform of the time-domain signal is computed while the signal is sampled by a sliding short time window resulting in a time-frequency (t, f) representation of the signal. Then group velocities can be evaluated by searching the maxima in the (t, f) domain. The time-frequency resolution can be improved using a Wigner-Ville flexible time window [16] or the wrapped frequency transform [56]. Other techniques, such as wavelet or chirplet analysis [57], have also been proposed. The choice of the waveform database is a key point of the analysis. This signal processing have been applied on in vitro samples [58]. However, the discrimination of signal from noise is still challenging with this technique.

7.3.2.2 One Transmitter and Several Receivers Configuration

Signal processing techniques can be applied to the multiple-receiver configuration, achieved by moving a single receiver or using a multi-receiver array (Fig. 7.12). Time signals, recorded at different spatial positions x_1 along the wave guide are denoted $r(x_1, t)$. For instance, the evaluation of the first arrival signal velocity can be improved using several receiver positions. In that case, the velocity is evaluated from the TOF measurement at each receiver position [22]. Sophisticated signal

processing approaches have been applied to this measurement configuration, such as the singular value decomposition (SVD). SVD is a general tool which can be applied to any data matrix, such as the matrix **r** containing the space-time domain signals $r_{ij} = r(x_i, t_j)$ [59]. This point of view has been proposed in particular in underwater acoustics, and is adapted to the case of signals from far distance sources. This signal processing has been applied in vitro on bone specimens to extract the most energetic part of the received signals [80].

Moreover, the complete set of space–time signals can be analyzed without any *a priori* using the two-dimensional spatio-temporal Fourier transform [15, 26] . Results are represented in the wave number-frequency $(k-f)$ domain. The expression of the spatio-temporal Fourier transform $R(k,f)$ is, in the general case:

$$R(k,f) = \iint_{x_1,t} r(x_1,t) e^{-i\omega t} e^{+ikx_1} dx_1 dt \tag{7.8}$$

The number and distribution of space positions is a key point for such analysis: the resolution, i.e. the possibility to discriminate two close wavenumbers k, increases with the inspected length. The experimental phase velocities are given by the maxima of the spatio-temporal Fourier transform in the (k,f) plane. The spatio-temporal Fourier transform approach has been completed by other techniques, such as the matrix pencil method [60], the linear prediction method [61], or the complex spectrum estimation method [62].

An example of a spatio-temporal Fourier transform is illustrated in Fig. 7.13. The spatio-temporal signals, shown in Fig. 7.13a, have been acquired on a 2 mm-thick copper plate with an axial transmission probe used for long bone testing. The receiving part of the probe consists of an array of 32 transducers regularly spaced in steps of around 1mm. The spatio-temporal Fourier transform is depicted in Fig. 7.13b in the (k,f) plane. The darkest zones correspond to the zone of high energy contained in the received signals. The maxima are then extracted and compared (see Fig. 7.13c) to the theoretical Rayleigh-Lamb dispersion curves, similar to those shown in Fig. 7.4a. In the case of a material without absorption, the spatio-temporal Fourier transform is adapted to evaluate most part of the dispersion curves. The spatio-temporal Fourier transform has been proposed in the bone domain in order to extract the low frequency A_0 type mode [63]. Long inspected distances and low absorption are known limitations of the spatio-temporal Fourier transform that reduce precision estimates.

7.3.2.3 Several Transmitters and Several Receivers Configuration

Other measurement configurations involve multi-emitter and multi-receiver arrays. The DORT method (decomposition of the time-reversal operator) has been applied to the distant single array configuration in pulse-echo mode to measure circumferential wave phase velocities of a hollow cylinder surrounded by water [49]. In this case, the singular value decomposition (SVD) is applied to the array response matrix

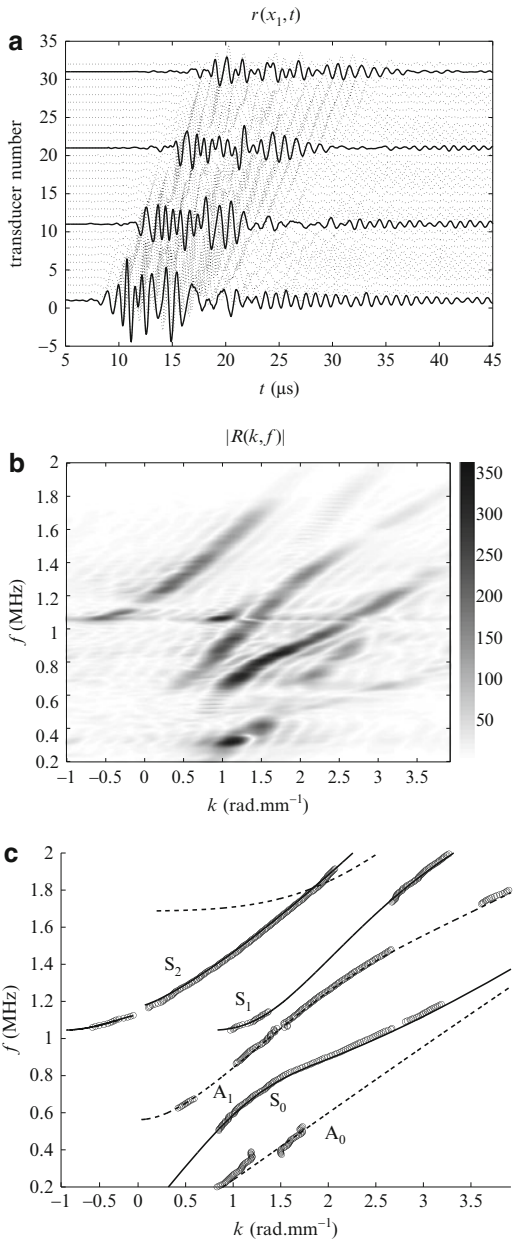

Fig. 7.13 32 time signals recorded with a axial transmission array (**a**) on a 2mm-thick copper plate, and the corresponding spatio-temporal Fourier transform (**b**). Experimental dispersion curves, given by the maxima of (**b**), are then compared with theoretical Rayleigh-Lamb modes dispersion curves (**c**)

containing the temporal Fourier transform $R_{ij}(f)$ of the received signals $r_{ij}(t)$, with i and j the emitter and receiver indices. A similar point of view has recently been adapted to the axial transmission measurement configuration between two collinear transmitter and receiver arrays [48]. The guided mode phase velocities are obtained

using a projection in the singular vectors basis. The singular vectors are determined by the SVD of the response matrix between the emitter and receiver arrays in the frequency domain. The SVD-based approach was designed to overcome the limitations of the spatio-temporal Fourier transform for receiver arrays of limited spatial extent.

The SVD of the response matrix $\mathbf{R}$ containing the time Fourier transforms $R_{ij}(f)$ of received signals at one frequency, writes:

$$\mathbf{R} = \sum_{n=1}^{N^{\mathrm{E}}} \mathbf{U}_n \sigma_n {}^t\mathbf{V}_n^*, \tag{7.9}$$

where the notations ^{t} and * denote the transpose and conjugation operations. The notation $\mathbf{V}_n$ refers to an emission singular vector, and $\mathbf{U}_n$ to a reception singular vector. The singular vectors $\mathbf{U}_n$ are normalized and define an orthogonal basis of the received signals. These two vectors are associated with the singular value σ_n. The five singular values, obtained with an axial transmission probe consisting of 5 emitters and 32 receivers for a 2 mm thick bone mimicking plate, are shown in Fig. 7.14a. This plate is made of short-fiber-filled and epoxy resin (Sawbones, Pacific Research Laboratory Inc, Vashon WA).

One of the advantages of the SVD approach lies in its ability to separate noise and signal subspaces [64]. An intermediate order m, corresponding to the limit between the two subspaces, is defined at each frequency using a threshold t_1 applied to the singular values σ_n. In the following, the signal singular vectors are retained (for $\sigma_n \geq t_1$) whereas the noise singular vectors (for $\sigma_n < t_1$) are eliminated. The threshold is illustrated in Fig. 7.14a. The retained singular vectors $\mathbf{U}_{n\leq m}$ form the basis of the signal subspace. Any spatial plane wave $\mathbf{e}^{pw}(k)$, defined on the jth receiver as

$$e_j^{pw} = \frac{1}{\sqrt{N^{\mathrm{R}}}} \exp(\mathrm{i}kx_{1j}^{\mathrm{R}}), \tag{7.10}$$

can be expressed on the signal subspace basis. The norm of the spatial plane wave writes:

$$\|\mathbf{e}^{pw}\|_{\{\mathbf{U}_{n\leq m}\}} = \sqrt{\sum_{n=1}^{m} |\langle \mathbf{e}^{pw} | \mathbf{U}_n \rangle|^2}. \tag{7.11}$$

The notation $<\mathbf{e}^{\mathrm{pw}}|\mathbf{U}_n>$ corresponds to the Hermitian scalar product, equal to ${}^t\mathbf{e}^{pw*}.\mathbf{U}_n$ and the notation $||$ designates the modulus of complex numbers. The norm of the plane wave is represented in the (k, f) plane. By construction, the value of the norm at each pixel (k, f), denoted $Norm(k, f)$ ranges from 0 to 1. The value of the pixel reflects how the spatial plane wave is represented in the basis of the signal subspace. On the one hand, if the value is small compared to 1, the spatial plane wave is absent of the received signals. On the other hand, if the value is close to 1, the spatial plane wave corresponds to a guided wave, present in the received signals. The maxima of the norm provide the phase velocities of the guided mode present in the signal

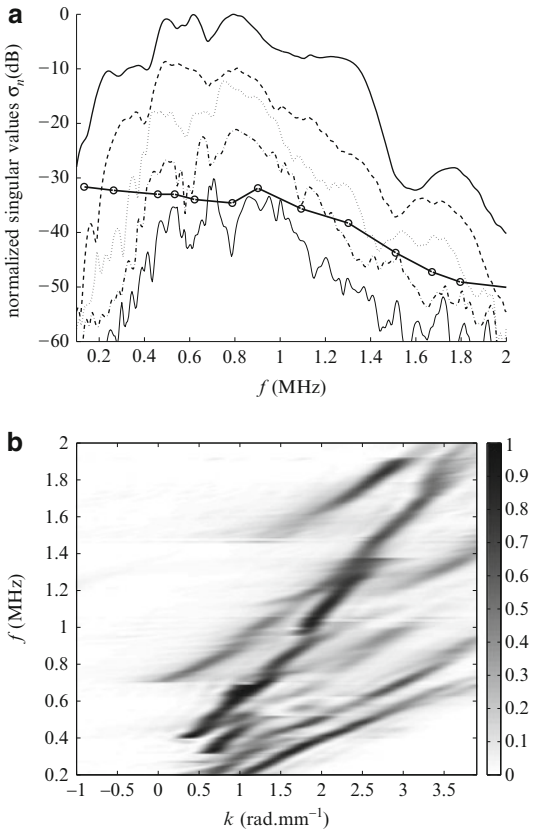

Fig. 7.14 Singular values versus frequency (MHz) for a 2 mm thick bone mimicking plate (**a**) and Norm(k, f) (**b**). The signal to noise threshold t_1 is shown with a *thick line* with *circles*

subspace as in the case of the spatio-temporal Fourier transform. An example of the *Norm* function is shown on Fig. 7.14b for the bone mimicking plate.

The SVD-based technique has been compared to the spatio-temporal Fourier transform in the case of a 2 mm thick copper plate. Figure 7.15, illustrating the distribution of the *Norm* function for a fixed frequency (1.13 MHz), demonstrates better signal-to-noise ratio of SVD compared to 2-D Fourier transform, which suggests a better ability to evaluate phase velocities in case of absorbing and noisy propagation media.

7.3.3 Determination of Thickness and/or Elastic Constants

Based on the guided wave theoretical framework, many inversion schemes have been proposed to evaluate the waveguide elastic and geometrical properties from the experimental phase or group velocities of guided waves. Because, these developments in other scientific fields may inspire future research directions in the context of bone research, some examples are listed in the following for isotropic or anisotropic medium.

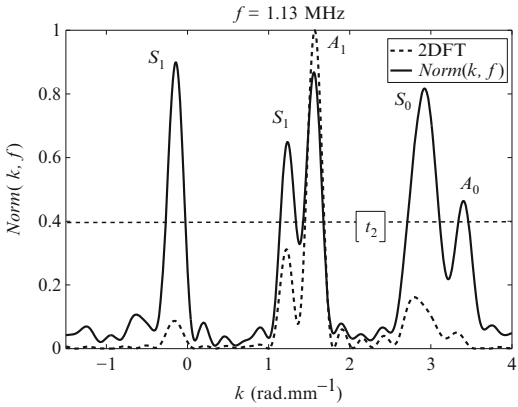

Fig. 7.15 Comparison of the two methods: $Norm(k, f)$ and 2D Fourier transform, for $f = 1.13$ MHz for a 2 mm thick copper plate. The ability to extract phase velocity is improved using the *Norm* function. The second threshold t_2 is shown with a *horizontal dashed line*

Wu and Liu [65] proposed an inverse determination of thickness and elastic properties for an isotropic bounding layer from surface wave measurements. Gao et al. [66] proposed the determination of the thickness and bulk velocities (c_L and c_T) of a thin plate comparing the experimental phase velocities of the two first Lamb modes A_0 and S_0 and the approximate expression of these modes velocities for low frequency thickness product given by Hutchins et al. [67]. More recently, Dean et al. [14] used their interferometer system to determine the thickness and elastic constant of a small aluminum plate. They used all the measured Lamb modes in their inversion. Clorennec et al. [68] proposed to evaluate the bulk velocities from the measurements of two particular resonance frequencies, associated with zero group velocity mode.

Other authors have proposed inversion methods adapted to the case of anisotropic media. Vishnuvardhan et al. [69] proposed a blind inversion method using S_0 and A_0 velocities for the complete determination of elastic moduli, material symmetries, as well as principal plane orientations of anisotropic plates. Veres et al. [70] determined the material properties of a wooden bar, modeled as an orthotropic material with nine independent constants. The material properties are found by parametric model fitting. The dispersion curves were obtained in the three-dimensional case using a semi-analytical finite element method.

Recently, in the field of bone assessment by axial transmission, such inversion schemes have been developed aiming at the determination of bone properties [6,71].

7.4 Current Measurement Techniques on Long Cortical Bone

Most of the current axial transmission devices designed for clinical use provide velocities of one or two temporal events: the first arriving signal (FAS), and the energetic late arrival (ELA). These signal components are easily identified in Fig. 7.16 which shows time series recorded at several receivers (14) with a probe operating at 1MHz obtained in vivo on a human forearm.

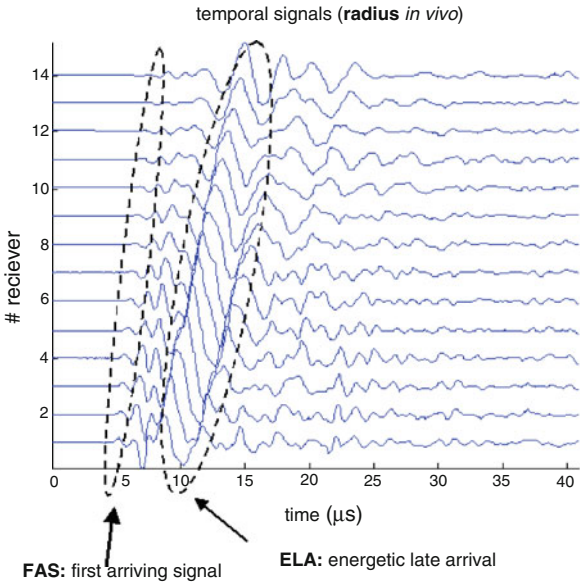

Fig. 7.16 Time series recorded at 14 receivers measured in vivo on a forearm with a probe operating at 1 MHz

7.4.1 First Arriving Signal (FAS)

The FAS is defined as the first component of the signal which emerges from noise. The velocity of the FAS is measured in the time domain. FAS velocity cannot be easily predicted by analytical or semi-analytical methods but rather conveniently by means of numerical simulations of transient ultrasound propagation, such as finite difference time domain (FDTD) simulations [22, 39, 72]. According to such FDTD simulation studies based on lossless homogeneous bone models with uniform geometries, the nature of FAS, and subsequently the FAS velocity, changes with the thickness (e) to wavelength (λ_L) ratio. The wavelength λ_L refers to the compression bulk wave inside bone, in the direction of bone axis when the model is anisotropic.

For thickness larger than λ_L, FAS is the so called lateral wave which is the trace on the surface of the compression bulk wave in the material [73]; FAS velocity does not depend on thickness and is close to c_L. For thickness around $\lambda_L/2 - \lambda_L$, the reflection of compression bulk waves on the inner surface impacts the FAS velocity. For lower thickness, FAS velocity decreases with thickness and approaches the low frequency limit of the phase velocity of the guided wave S_0 on plates. In this thickness range, thickness related variations of FAS velocity qualitatively agree with dispersion of S_0 wave [74].

The FAS velocity is expected from the model to increase nonlinearly with thickness and to reach a plateau for the thickest samples. If cortical thickness

is much larger than the wavelength (3–4 mm at frequencies close to 1 MHz) no impact on FAS of thickness variability can be expected [75] according to numerical predictions [39].

In agreement with guided waves analysis, the precursor of the signal is related to the wave component which has the highest group velocity in the probe working bandwidth. For instance, when the frequency bandwidth of the excitation signal contains low enough frequency components, the FAS is expected to originate in the S_0 wave. In this frequency domain, the S_0 wave is slightly dispersive, i.e. its waveform is expected to be only slightly distorted with propagation distance. However its amplitude is small due to the fact that it induces a quasi longitudinal displacement field across the whole thickness.

In agreement with numerical predictions, several studies on plastic samples (acrylic, PVC, perspex) with varying thickness showed that FAS velocity varies with thickness when it is smaller than the wavelength λ_L [72,76,77] or the same thickness range, the largest variations of FAS velocity were obtained for the smallest nominal frequency (200 kHz).

7.4.2 Energetic Late Arrival (ELA)

Dedicated studies were performed on the energetic late arrival (ELA). As ELA is embedded in the whole time response obtained on bone samples, specific signal processing techniques were developed. Most techniques attempted to isolate or to extract this signal component before applying a method of velocity measurement, either in the time or in the frequency domain.

In some studies, ELA is isolated from the FAS by using a source operating at two different frequencies 100 and 500 kHz [78]. Alternatively, angled beam sources can be used at two different angles [79] to isolate either FAS and ELA. In another approach, extraction of ELA from the whole signal was performed using singular value decomposition in time-space domain [59, 80]. ELA velocity is then measured in time domain.

Alternatively, Moilanen et al. [63] proposed to extract ELA from the whole signal by using a method of group velocity filtering prior to spatio-temporal Fourier transform. Variation of phase velocity of the wave associated to ELA is then provided for each sample in the whole frequency bandwidth of the source.

Based on comparison of experimental and predicted phase velocity curves this contribution for in vitro measurements is identified as the A_0 plate guided mode, or its counterpart for the tube model, the $F(1,1)$ mode.

Figure 7.17 shows FAS and ELA velocities measured on a collection of human radius samples. Phase velocity of ELA (250 kHz) is in the range 1000–2000 $m \cdot s^{-1}$ for radius samples. Typical values of FAS velocity on human bone samples are around 3000–4000 $m \cdot s^{-1}$ and the reproducibility is $\pm 25\, m \cdot s^{-1}$, i.e. 0.5% [81].

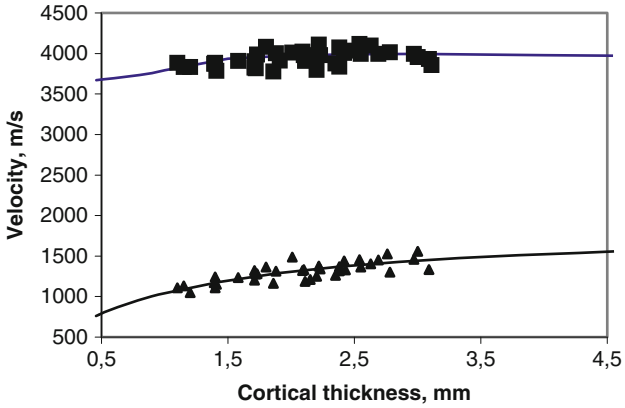

Fig. 7.17 Experimentally measured velocities as a function of thickness for human radius samples [53,80]. Experimental measurements of the FAS velocity are shown as *solid squares* while the ELA velocity are shown by solid triangles. The FAS velocities predicted by numerical simulations are shown as well as A_0 Lamb wave dispersion curve

7.4.3 Ultrasound Velocities Versus Strength Related Bone Properties

Ultrasound velocities are deterministically related to the mechanical stiffness (elastic modulus) of the material, and to its mass density (see Chap. 2). Moreover, in the case of a finite dimension bodies compared to the wavelength such as bone, ultrasound velocities are also deterministically related to geometric features such thickness or diameter.

The relationship between strength and ultrasound velocities can be established in an indirect way, by statistically relating specific aspects of strength such as porosity, mineralization or thickness to ultrasound velocities.

Experimental studies on excised human radii showed the sensitivity of FAS velocity (1 MHz operating frequency) to site-matched porosity and degree of mineralization [53] and also to intrinsic elastic properties [82]. Up to 84% of the variability of FAS was explained with a combination of cortical thickness, porosity and acoustic impedance reflecting intrinsic stiffness [82]. The sensitivity to cortical porosity was found to be $-24\,\mathrm{m}\cdot\mathrm{s}^{-1}$ per 1% increase of porosity [53] in good agreement with numerical predictions [39].

In summary of different studies on excised cadavers samples [80, 83], the FAS velocity can be considered to primarily reflect volumetric bone mineral density (vBMD) while the velocity of A_0 type of wave captures primarily information on cortical thickness and apparent vBMD, with the strongest relationship with cortical thickness (CTh).

Independent effects of CTh and BMD on FAS velocity measured at the tibia or the radius have also been documented from in vivo measurements using 250 kHz

operating frequency [75, 84]. One study found that tibial FAS velocity (250 kHz) is more strongly influenced by the BMD of the cortex near the surface than by its interior parts [75].

The direct relation of cortical FAS velocity to structural bone mechanical properties has also been investigated.

In situ measurements have been performed on cadavers at the tibia [85] with a low frequency (250 kHz) axial transmission device. Site-matched measurements of FAS and mechanical properties in tension (Young's modulus and ultimate strength) were highly correlated. However, the FAS and BMD also were correlated, and a combination of FAS and BMD did not give a better prediction of the bone mechanical properties than either variable alone. FAS velocity at the radius [86] with a high frequency (1.25 MHz) device was modestly correlated to failure load of the whole organ.

In summary, axial transmission ultrasound velocities reflect both structural and intrinsic material properties of cortical bone. Measurements in situ (radius or tibia) with current clinical devices correlate with mineral density. They also correlate with the mechanical properties of cortical bone. However, current axial transmission techniques providing a single wave velocity (either FAS or ELA) do not seem to provide additional information to that provided by DXA-based BMD in predicting structural strength of the distal radius or the tibia.

Several clinical studies devoted to fracture discrimination seem to lead to analogous conclusion [87–90] (see Chap. 14 for details). The FAS velocity allows to discriminate fractured patients from healthy subjects, while the added value brought by ultrasound axial transmission to the conventional osteoporosis screening technique (X ray absorptiometry) is not clear. To increase clinical relevance and render more attractive ultrasound technique, axial transmission faces several challenges.

7.5 Challenges

In vitro experimental studies or in vivo fracture discrimination studies were based on a unique value of velocity i.e. the FAS velocity, to date. Experimental results showing a different sensitivity of different signal components (e.g., FAS or ELA) suggest that a multi parametric approach would substantially increase the clinical potential of axial transmission. However, according to Moilanen [63,91], adding the velocity of the A_0 type of wave on in vivo measurements of the radius is unlikely to bring more differentiated information on bone, due to coupling with soft tissue. Other approaches are currently explored in which multiple propagation modes are identified and their propagation velocities are determined. The FAS velocity measured at different frequencies would warrant a collection of ultrasound parameters with an increased sensitivity to thickness. Moreover, measuring guided modes of higher order seems very attractive. The feasibility study of the measurement of their velocity has been developed by several groups, essentially on animal bone samples. Different signal processing techniques are used to extract guided mode phase or group velocities of higher order modes.

On a sheep tibia, guided waves were experimentally observed by Protopappas et al. [58] and analyzed using time-frequency transform as Rayleigh-Lamb guided modes. A_n and $S_n (0 \leq n \leq 2)$. The $L(0,n)$ longitudinal tube wave phase velocities ($1 \leq n \leq 3$) were also measured on a bovine tibia by Ta et al. [7,8]. Ta et al. used angled beam transducers in order to generate preferentially one specific mode and analyzed the received signals with the Short time Fourier transform (STFT) [7] or the phase spectrum method [8]. The method required a minimal distance between the emitter and receiver (of about 70 mm and a scanning length of about 80 mm) in order to have sufficient time separation between the different guided modes.

Hapsara and Iliescu [92] generated guided waves in a bovine bone using a planar transducer which was coupled with a cone-shaped resonant vibrator. Out-of-plane vibrations of the surface of the bone are recorded with a scanning laser vibrometer and analyzed using wavelet analysis.

The current challenge is to develop signal processing tools which provide highly reproducible velocities and are consistent with the rather small testing length used in devices designed for clinical use (around 1–2 cm). The SVD based method is one of the most promising method and is currently under testing [48]. The in vivo measurement protocol remains to be established in order to obtain accurate phase velocities. For instance, the FAS in vivo protocol requires angular scanning to prevent from misalignment between the probe and the bone axes.

Measuring several modes of propagation would provide several ultrasound based indicators of bone status. These parameters could be used in a statistical determination of fracture risks assuming that each ultrasound parameter reflects differently bone properties. In addition, several ultrasound bone parameters would help in determining bone properties such as cortical thickness, porosity from ultrasound measurements.

An inversion scheme has been implemented by Moilanen et al. to estimate cortical thickness from the phase velocity of the A_0 mode [6]. The scheme has been tested on Perspex phantoms [63] and on excised human bone specimens [6]. Ultrasonically determined thickness has been found to be strongly correlated with local cortical thickness assessed by peripheral quantitative computed tomography ($r^2 = 0.81$). In addition, the same inversion scheme has been tested in numerical simulations [91, 93] using realistic 3-D bone models with homogeneous non individualized elastic bone properties. In the simulations, the agreement between local cortical thickness and ultrasonically determined thickness was excellent $r^2 = 0.91$.

Another illustrative example of reconstruction of the distribution of the elastic stiffness coefficients from an in vivo measurements database exploits the FAS velocity [71]. In this study, the bone model is simply a thick anisotropic plate. Future developments should address the issue of identification of elastic properties at the individual level and not at a population scale. This requires unavoidably to provide more than one unique parameter (the FAS velocity) per patient.

To further develop inversion schemes, there is a clear call for models of stiffness coefficients and mass density of bone evaluated at the scale of the ultrasonic wave, i.e. at the millimeter scale, which could be tested in in vitro measurements. Once the elasticity is described at this scale, guided modes properties can be

calculated in different models, from the simplest homogeneous ideal waveguide to more realistic waveguides. Each mode of propagation has its own relationship to each material (stiffnesses, mass density) and body geometrical properties, as shown for instance for guided waves in different publications [14,69,94] or to some extent for FAS velocity [95].

In summary, since the early studies of axial transmission on peripheral bone, a variety of development has been produced. In the context of osteoporosis diagnosis, a first generation of devices has shown the ability of axially transmitted waves to discriminate osteoporotic patients from healthy subjects. However, the added value brought by current axial transmission techniques compared to X-ray absorption is not clearly established yet. The first generation of axial transmission devices was based on the analysis of a unique ultrasound parameter, which was the First Arriving Signal. The second generation exploits other components of the ultrasound signal. Based on comprehensive understanding of the phenomenon of propagation involved in the whole signal, the second generation of devices has the objective to provide several ultrasound parameters, assuming that a multiparametric approach would improve the ability of predicting fracture risk. Moreover, a multiparametric approach would feed inverse schemes to determine relevant bone properties from ultrasound measurements. These approaches could also be extended to the study of circumferential guided waves to open perspectives for fracture risk prediction at central skeletal sites such as the hip. Some studies has already been conducted by Barkmann et al. [96] for the phalange, Le Floch et al. [97] for the radius and the femur neck by Grondin et al. [98].

References

1. B. A. Auld, *Acoustic fields and waves in solids*, 2nd ed. (Krieger, Malabar, FL, 1990), Vol. **II**.
2. I. A. Viktorov, *Rayleigh and Lamb waves* (Plenum, New York, NY, 1967).
3. J. D. Achenbach, *Wave propagation in elastic solids* (Elsevier, New York, NY, 1975).
4. D. Royer and E. Dieulesaint, *Elastic waves in solids I: Free and guided propagation* (Springer, New York, 2000).
5. F. Lefebvre, Y. Deblock, P. Campistron, D. Ahite, and J. J. Fabre, "Development of a new ultrasonic technique for bone and biomaterials in vitro characterization," Journal of Biomedical Materials Research **63**(4), 441–446 (2002).
6. P. Moilanen, P. H. F. Nicholson, V. Kilappa, S. L. Cheng, and J. Timonen, "Assessment of the cortical bone thickness using ultrasonic guided waves: Modelling and in vitro study," Ultrasound in Medicine and Biology **33**(2), 254–262 (2007).
7. D. A. Ta, K. Huang, W. Q. Wang, Y. Y. Wang, and L. H. Le, "Identification and analysis of multimode guided waves in tibia cortical bone," Ultrasonics **44**, E279–E284 (2006).
8. D. Ta, W. Q. Wang, Y. Y. Wang, L. H. Le, and Y. Q. Zhou, "Measurement of the dispersion and attenuation of cylindrical ultrasonic guided waves in long bone," Ultrasound in Medicine and Biology **35**(4), 641–652 (2009).
9. A. M. Tatarinov, V. P. Egorov, and A. P. Sarvazyan, "The dual-frequency method for ultrasonic assessment of skeletal system," Acoustical Physics **55**(4–5), 665–673 (2009).
10. D. E. Chimenti, "Guided waves in plates and their use in materials characterization," Applied Mechanics Reviews **50**(5), 247–284 (1997).

11. D. N. Alleyne and P. Cawley, "The interaction of Lamb waves with defects," IEEE Transactions on Ultrasonics Ferroelectrics and Frequency Control **39**(3), 381–397 (1992).
12. P. Cawley and D. Alleyne, "The use of Lamb waves for the long range inspection of large structures," Ultrasonics **34**(2–5), 287–290 (1996).
13. S. Dahmen, H. Ketata, M. H. Ben Ghozlen, and B. Hosten, "Elastic constants measurement of anisotropic Olivier wood plates using air-coupled transducers generated Lamb wave and ultrasonic bulk wave," Ultrasonics **50**(4–5), 502–507 (2010).
14. J. L. Dean, C. Trillo, A. F. Doval, and J. L. Fernandez, "Determination of thickness and elastic constants of aluminum plates from full-field wavelength measurements of single-mode narrowband Lamb waves," The Journal of the Acoustical Society of America **124**(3), 1477–1489 (2008).
15. D. Alleyne and P. Cawley, "A 2-dimensional Fourier-transform method for the measurement of propagating multimode signals," The Journal of the Acoustical Society of America **89**(3), 1159–1168 (1991).
16. M. Niethammer, L. J. Jacobs, J. M. Qu, and J. Jarzynski, "Time-frequency representations of Lamb waves," The Journal of the Acoustical Society of America **109**(5), 1841–1847 (2001).
17. R. A. Abram, "Coupled-mode formalism for elastic waveguides," Journal of Physics D-Applied Physics **7**(10), 1329–1335 (1974).
18. V. B. Galanenko, "On coupled modes theory of two-dimensional wave motion in elastic waveguides with slowly varying parameters in curvilinear orthogonal coordinates," The Journal of the Acoustical Society of America **103**(4), 1752–1762 (1998).
19. V. Pagneux and A. Maurel, "Lamb wave propagation in elastic waveguides with variable thickness," Proceedings of the Royal Society a-Mathematical Physical and Engineering Sciences **462**(2068), 1315–1339 (2006).
20. D. E. Chimenti and B. A. Auld, "Micro and macrostructural dispersion of guided waves in solids," Wave Motion **21**, 101–114 (1995).
21. H. Lamb, "On waves in an elastic plate," Proceedings of the Royal Society of London Series a-Containing Papers of a Mathematical and Physical Character **93**(648), 114–128 (1917).
22. E. Bossy, M. Talmant, and P. Laugier, "Effect of bone cortical thickness on velocity measurements using ultrasonic axial transmission: A 2D simulation study," The Journal of the Acoustical Society of America **112**(1), 297–307 (2002).
23. R. D. Mindlin, "Waves and vibrations in isotropic elastic plates," in *Structural Mechanics*, J.N. Goodier and N. J. Hoff, eds. (Pergamon, New York, NY, 1960), pp. 199–232.
24. B. A. Auld and G. S. Kino, "Normal mode theory for acoustic waves and its application to interdigital transducer," IEEE Transactions on Electron Devices **ED18**(10), 898–908 (1971).
25. R. L. Weaver and Y. H. Pao, "Spectra of transient waves in elastic plates," The Journal of the Acoustical Society of America **72**(6), 1933–1941 (1982).
26. I. Nunez, R. K. Ing, C. Negreira, and M. Fink, "Transfer and Green functions based on modal analysis for Lamb waves generation," The Journal of the Acoustical Society of America **107**(5), 2370–2378 (2000).
27. H. Bai, J. Zhu, A. H. Shah, and N. Popplewell, "Three-dimensional steady state Green function for a layered isotropic plate," Journal of Sound and Vibration **269**(1–2), 251–271 (2004).
28. L. Moreau and M. Castaings, "The use of an orthogonality relation for reducing the size of finite element models for 3D guided waves scattering problems," Ultrasonics **48**(5), 357–366 (2008).
29. D. C. Gazis, "3-Dimensional investigation of the propagation of waves in hollow circular cylinder.1. Analytical foundation," The Journal of the Acoustical Society of America **31**(5), 568–573 (1959).
30. J. L. Rose, *Acoustic waves in solid media* (Cambridge University Press, Cambridge, UK, 1999).
31. M. G. Silk and K. F. Bainton, "Propagation in metal tubing of ultrasonic wave modes equivalent to Lamb waves," Ultrasonics **17**(1), 11–19 (1979).
32. J. Davies and P. Cawley, "The application of synthetic focusing for imaging crack-like defects in pipelines using guided waves," IEEE Transactions on Ultrasonics Ferroelectrics and Frequency Control **56**(4), 759–771 (2009).

33. J. Li and J. L. Rose, "Excitation and propagation of non-axisymmetric guided waves in a hollow cylinder," Journal of the Acoustical Society of America **109**(2), 457–464 (2001).
34. J. J. Ditri and J. L. Rose, "Excitation of guided elastic wave modes in hollow cylinders by applied surface tractions," Journal of Applied Physics **72**(7), 2589–2597 (1992).
35. R. B. Martin, D. B. Burr, and N. A. Sharkey, *Skeletal tissue mechanics* (Springer-Verlag, New York, 1998).
36. R. B. Ashman, S. C. Cowin, W. C. Van Buskirk, and J. C. Rice, "A continuous wave technique for the mesurement of the elastic properties of cortical bone," Journal of Biomechanics **17**, 349–361 (1984).
37. V. Ricos, D. R. Pedersen, T. D. Brown, R. B. Ashman, C. T. Rubin, and R. A. Brand, "Effects of anisotropy and material axis registration on computed stress and strain distributions in the turkey ulna," Journal of Biomechanics **29**(2), 261–267 (1996)
38. S.C. Cowin and R.T. Hart, "Errors in the orientation of the principal stress axes if bone tissue is modeled as isotropic," Journal of Biomechanics **23**(4), 349–352 (1990)
39. E. Bossy, M. Talmant, and P. Laugier, "Three-dimensional simulations of ultrasonic axial transmission velocity measurement on cortical bone models," The Journal of the Acoustical Society of America **115**(5), 2314–2324 (2004).
40. Y. Li and R. B. Thompson, "Influence of anisotropy on the dispersion characteristics of guided ultrasonic plate modes," The Journal of the Acoustical Society of America **87**(5), 1911–1931 (1990).
41. W. Lin and L. M. Keer, "A study of Lamb waves in anisotropic plates," The Journal of the Acoustical Society of America **92**(2), 888–894 (1992).
42. S. P. Pelts and J. L. Rose, "Source influence parameters on elastic guided waves in an orthotropic plate," The Journal of the Acoustical Society of America **99**(4), 2124–2129 (1996).
43. L. P. Solie and B. A. Auld, "Elastic waves in free anisotropic plates," The Journal of the Acoustical Society of America **54**(1), 50–65 (1973).
44. M. G. Vavva, V. C. Protopappas, L. N. Gergidis, A. Charalambopoulos, D. I. Fotiadis, and D. Polyzos, "Velocity dispersion of guided waves propagating in a free gradient elastic plate: Application to cortical bone," The Journal of the Acoustical Society of America **125**(5), 3414–3427 (2009).
45. Z. Q. Su, L. Ye, and Y. Lu, "Guided Lamb waves for identification of damage in composite structures: A review," Journal of Sound and Vibration **295**(3–5), 753–780 (2006).
46. M. Castaings and B. Hosten, "Lamb and SH waves generated and detected by air-coupled ultrasonic transducers in composite material plates," Ndt & E International **34**(4), 249–258 (2001).
47. Z. Q. Guo, J. D. Achenbach, and S. Krishnaswamy, "EMAT generation and laser detection of single lamb wave modes," Ultrasonics **35**(6), 423–429 (1997).
48. J. G. Minonzio, M. Talmant, and P. Laugier, "Guided wave phase velocity measurement using multi-emitter and multi-receiver arrays in the axial transmission configuration," The Journal of the Acoustical Society of America **127**(5) (2010).
49. C. Prada and M. Fink, "Separation of interfering acoustic scattered signals using the invariants of the time-reversal operator. Application to Lamb waves characterization," The Journal of the Acoustical Society of America **104**(2), 801–807 (1998).
50. D. Hans, S. K. Srivastav, C. Singal, R. Barkmann, C. F. Njeh, E. Kantorovich, C. C. Gluer, and H. K. Genant, "Does combining the results from multiple bone sites measured by a new quantitative ultrasound device improve discrimination of hip fracture?," Journal of Bone and Mineral Research **14**(4), 644–651 (1999).
51. P. Moilanen, P. H. F. Nicholson, T. Karkkainen, Q. Wang, J. Timonen, and S. Cheng, "Assessment of the tibia using ultrasonic guided waves in pubertal girls," Osteoporosis International **14**(12), 1020–1027 (2003).
52. M. Maata, P. Moilanen, P. Nicholson, S. L. Cheng, J. Timonen, and T. Jamsa, "Correlation of tibial low-frequency ultrasound velocity with femoral radiographic measurements and Bmd in elderly women," Ultrasound in Medicine and Biology **35**(6), 903–911 (2009).

53. E. Bossy, M. Talmant, F. Peyrin, L. Akrout, P. Cloetens, and P. Laugier, "An in vitro study of the ultrasonic axial transmission technique at the radius: 1-MHz velocity measurements are sensitive to both mineralization and intracortical porosity," Journal of Bone and Mineral Research **19**(9), 1548–1556 (2004).
54. W. Sachse and Y. H. Pao, "Determination of phase and group velocities of dispersive waves in solids," Journal of Applied Physics **49**(8), 4320–4327 (1978).
55. W. H. Prosser, M. D. Seale, and B. T. Smith, "Time-frequency analysis of the dispersion of Lamb modes," Journal of the Acoustic Society of America **105**(5), 2669–2676 (1999).
56. L. De Marchi, A. Marzani, S. Caporale, and N. Speciale, "Ultrasonic guided-waves characterization with warped frequency transforms," IEEE Transactions on Ultrasonics Ferroelectrics and Frequency Control **56**(10), 2232–2240 (2009).
57. H. Kuttig, M. Niethammer, S. Hurlebaus, and L. J. Jacobs, "Model-based analysis of dispersion curves using chirplets," The Journal of the Acoustical Society of America **119**(4), 2122–2130 (2006).
58. V. C. Protopappas, D. I. Fotiadis, and K. N. Malizos, "Guided ultrasound wave propagation in intact and healing long bones," Ultrasound in Medicine and Biology **32**(5), 693–708 (2006).
59. V. D. Vrabie, J. I. Mars, and J. L. Lacoume, "Modified singular value decomposition by means of independent component analysis," Signal Processing **84**(3), 645–652 (2004).
60. Y. Hua and T. K. Sarkar, "Matrix pencil method for estimating parameters of exponentially damped undamped sinusoids in noise," IEEE Transactions on Acoustics Speech and Signal Processing **38**(5), 814–824 (1990).
61. D. W. Tufts and R. Kumaresan, "Estimation of frequencies of multiple sinusoids – Making linear prediction perform like maximum-likelihood," Proceedings of the IEEE **70**(9), 975–989 (1982).
62. J. Vollmann, R. Breu, and J. Dual, "High-resolution analysis of the complex wave spectrum in a cylindrical shell containing a viscoelastic medium.2. Experimental results versus theory," The Journal of the Acoustical Society of America **102**(2), 909–920 (1997).
63. P. Moilanen, P. H. F. Nicholson, V. Kilappa, S. Cheng, and J. Timonen, "Measuring guided waves in long bones: Modeling and experiments in free and immersed plates," Ultrasound in Medicine and Biology **32**(5), 709–719 (2006).
64. M. Cheney, "The linear sampling method and the MUSIC algorithm," Inverse Problems **17**(4), 591–595 (2001).
65. T. T. Wu and Y. H. Liu, "Inverse determinations of thickness and elastic properties of a bonding layer using laser-generated surface waves," Ultrasonics **37**(1), 23–30 (1999).
66. W. M. Gao, C. Glorieux, and J. Thoen, "Laser ultrasonic study of Lamb waves: Determination of the thickness and velocities of a thin plate," International Journal of Engineering Science **41**(2), 219–228 (2003).
67. D. A. Hutchins, K. Lundgren, and S. B. Palmer, "A laser study of transient Lamb waves in thin materials," The Journal of the Acoustical Society of America **85**(4), 1441–1448 (1989).
68. D. Clorennec, C. Prada, and D. Royer, "Local and noncontact measurements of bulk acoustic wave velocities in thin isotropic plates and shells using zero group velocity Lamb modes," Journal of Applied Physics **101**(3) (2007).
69. J. Vishnuvardhan, C. V. Krishnamurthy, and K. Balasubramaniam, "Blind inversion method using Lamb waves for the complete elastic property characterization of anisotropic plates," The Journal of the Acoustical Society of America **125**(2), 761–771 (2009).
70. I. A. Veres and M. B. Sayir, "Wave propagation in a wooden bar," Ultrasonics **42**(1–9), 495–499 (2004).
71. C. Desceliers, C. Soize, Q. Grimal, M. Talmant, and S. Naili, "Determination of the random anisotropic elasticity layer using transient wave propagation in a fluid-solid multilayer: Model and experiments," Journal of the Acoustical Society of America **125**(4), 2027–2034 (2009).
72. P. H. F. Nicholson, P. Moilanen, T. Karkkainen, J. Timonen, and S. L. Cheng, "Guided ultrasonic waves in long bones: Modelling, experiment and in vivo application," Physiological Measurement **23**(4), 755–768 (2002).

73. E. Camus, M. Talmant, G. Berger, and P. Laugier, "Analysis of the axial transmission technique for the assessment of skeletal status," The Journal of the Acoustical Society of America **108**(6), 3058–3065 (2000).
74. P. Nicholson, S. Cheng, and J. Timonen, "Thickness effects on axial ultrasound velocity in bone," Osteoporosis International **12**(11), 987–987 (2001).
75. S. Prevrhal, T. Fuerst, B. Fan, C. Njeh, D. Hans, M. Uffmann, S. Srivastav, and H. K. Genant, "Quantitative ultrasound of the tibia depends on both cortical density and thickness," Osteoporosis International **12**(1), 28–34 (2001).
76. C. F. Njeh, D. Hans, C. Wu, E. Kantorovich, M. Sister, T. Fuerst, and H. K. Genant, "An in vitro investigation of the dependence on sample thickness of the speed of sound along the specimen," Medical Engineering & Physics **21**(9), 651–659 (1999).
77. P. Moilanen, V. Kilappa, P. H. F. Nicholson, J. Timonen, and S. Cheng, "Thickness sensitivity of ultrasound velocity in long bone phantoms," Ultrasound in Medicine & Biology **30**(11), 1517–1521 (2004).
78. A. Tatarinov, N. Sarvazyan, and A. Sarvazyan, "Use of multiple acoustic wave modes for assessment of long bones: Model study," Ultrasonics **43**(8), 672–680 (2005).
79. K. I. Lee and S. W. Yoon, "Feasibility of bone assessment with leaky Lamb waves, in bone phantoms and a bovine tibia," The Journal of the Acoustical Society of America **115**(6), 3210–3217 (2004).
80. M. Sasso, M. Talmant, G. Haiat, S. Naili, and P. Laugier, "Analysis of the Most Energetic Late Arrival in Axially Transmitted Signals in Cortical Bone," IEEE Transactions on Ultrasonics Ferroelectrics and Frequency Control **56**(11), 2463–2470 (2009).
81. E. Bossy, M. Talmant, M. Defontaine, F. Patat, and P. Laugier, "Bidirectional axial transmission can improve accuracy and precision of ultrasonic velocity measurement in cortical bone: A validation on test materials," IEEE Transactions on Ultrasonics Ferroelectrics and Frequency Control **51**(1), 71–79 (2004).
82. K. Raum, I. Leguerney, F. Chandelier, E. Bossy, M. Talmant, A. Saied, F. Peyrin, and P. Laugier, "Bone microstructure and elastic tissue properties are reflected in QUS axial transmission measurements," Ultrasound in Medicine and Biology **31**(9), 1225–1235 (2005).
83. M. Muller, P. Moilanen, E. Bossy, P. Nicholson, V. Kilappa, T. Timonen, M. Talmant, S. Cheng, and P. Laugier, "Comparison of three ultrasonic axial transmission methods for bone assessment," Ultrasound in Medicine and Biology **31**(5), 633–642 (2005).
84. H. Sievanen, S. Cheng, S. Ollikainen, and K. Uusi-Rasi, "Ultrasound velocity and cortical bone characteristics in vivo," Osteoporosis International **12**(5), 399–405 (2001).
85. S. C. Lee, B. S. Coan, and M. L. Bouxsein, "Tibial ultrasound velocity measured in situ predicts the material properties of tibial cortical bone," Bone **21**(1), 119–125 (1997).
86. M. Hudelmaier, V. Kuhn, E. M. Lochmuller, H. Well, M. Priemel, T. M. Link, and F. Eckstein, "Can geometry-based parameters from pQCT and material parameters from quantitative ultrasound (QUS) improve the prediction of radial bone strength over that by bone mass (DXA)?," Osteoporosis International **15**(5), 375–381 (2004).
87. M. Weiss, A. Ben-Shlomo, H. P., and S. Ish-Shalom, "Discrimination of proximal hip fracture by quantitative ultrasound measurement at the radius," Osteoporosis International **11**, 411–416 (2000).
88. K. M. Knapp, G. M. Blake, T. D. Spector, and I. Fogelman, "Multisite quantitative ultrasound: Precision, age- and menopause-related changes, fracture discrimination, and T-score equivalence with dual-energy X-ray absorptiometry," Osteoporosis International **12**(6), 456–464 (2001).
89. D. Hans, L. Genton, S. Allaoua, C. Pichard, and D. O. Slosman, "Hip fracture discrimination study - QUS of the radius and the calcaneum," Journal of Clinical Densitometry **6**(2), 163–172 (2003).
90. M. Talmant, S. Kolta, C. Roux, D. Haguenauer, I. Vedel, B. Cassou, E. Bossy, and P. Laugier, "In Vivo Performance Evaluation of Bi-Directional Ultrasonic Axial Transmission for Cortical Bone Assessment," Ultrasound in Medicine and Biology **35**(6), 912–919 (2009).

91. P. Moilanen, M. Talmant, P. H. F. Nicholson, S. L. Cheng, J. Timonen, and P. Laugier, "Ultrasonically determined thickness of long cortical bones: Three-dimensional simulations of in vitro experiments," The Journal of the Acoustical Society of America **122**(4), 2439–2445 (2007).
92. M. Hapsara and D. D. Iliescu, "Lamb waves detection in a bovine cortical tibia using scanning laser vibrometry - art. no. 69200N," in *Medical Imaging 2008: Ultrasonic Imaging and Signal Processing,* S. A. McAleavey and J. Dhooge, eds. (Spie-Int Soc Optical Engineering, Bellingham, WA, 2008), pp. N9200–N9200.
93. P. Moilanen, M. Talmant, V. Bousson, P. H. F. Nicholson, S. Cheng, J. Timonen, and P. Laugier, "Ultrasonically determined thickness of long cortical bones: Two-dimensional simulations of in vitro experiments," The Journal of the Acoustical Society of America **122**(3), 1818–1826 (2007).
94. D. Royer, D. Clorennec, and C. Prada, "Lamb mode spectra versus the Poisson ratio in a free isotropic elastic plate," The Journal of the Acoustical Society of America **125**(6), 3683–3687 (2009).
95. K. Macocco, Q. Grimal, S. Naili, and C. Soize, "Elastoacoustic model with uncertain mechanical properties for ultrasonic wave velocity prediction: Application to cortical bone evaluation," The Journal of the Acoustical Society of America **119**(2), 729–740 (2006).
96. R. Barkmann, S. Lusse, B. Stampa, S. Sakata, M. Heller, and C. C. Gluer, "Assessment of the geometry of human finger phalanges using quantitative ultrasound in vivo," Osteoporosis International **11**(9), 745–755 (2000).
97. V. Le Floch, G. M. Luo, J. J. Kaufman, and R. S. Siffert, "Ultrasonic Assessment of the Radius in Vitro," Ultrasound in Medicine and Biology **34**(12), 1972–1979 (2008).
98. J. Grondin, Q. Grimal, K. Engelke, and P. Laugier, "Potential of First Arriving Signal to Assess Cortical Bone Geometry at the Hip with QUS: A Model Based Study," Ultrasound in Medicine & Biology **36**(4), 656–666 (2010).

Chapter 8
Numerical Methods for Ultrasonic Bone Characterization

Emmanuel Bossy and Quentin Grimal

Abstract During the last decade the possibility of investigating the details of wave phenomena with numerical simulation has caused an evolution of the research methodology in ultrasonic bone characterization. Use of numerical simulation as a surrogate of an *in vitro* or *in vivo* experiment has been validated in some cases in which the major propagation characteristics observed experimentally could be accurately simulated in trabecular bone as well as in cortical bone. This chapter can be thought of as a guide to numerical modeling for ultrasonic bone characterization, from the definition of the model configuration (geometry, material properties, etc.) to the computation of the solutions with popular finite difference or finite element algorithms. A comprehensive review of the published works in which numerical simulation served to investigate wave phenomena in bone and surrounding structures is provided.

Keywords Finite difference · Finite element · Time integration · Boundary conditions · PML · Heterogeneous medium · Nominal model · Individualized model

8.1 Introduction

Research studies related to the ultrasonic evaluation of bone quality had until the 1990s mainly consisted of *in vivo* tests and *in vitro* experiments on phantoms and intact or machined bone samples. These led to the design of successful

E. Bossy
Institut Langevin, ESPCI ParisTech, CNRS UMR 7587, INSERM ERL U979, 10 rue Vauquelin, 75231 Paris Cedex 05, France
e-mail: Emmanuel.Bossy@espci.fr

Q. Grimal (✉)
Université Pierre et Marie Curie, CNRS, Laboratoire d'Imagerie Parametrique, F-75006, Paris, France
e-mail: Quentin.Grimal@upmc.fr

P. Laugier and G. Haïat (eds.), *Bone Quantitative Ultrasound*,
DOI 10.1007/978-94-007-0017-8_8,

quantitative ultrasound (QUS) devices for distal (heel, radius, phalanx) and central sites (proximal femur). The new possibility of investigating the details of wave phenomena with numerical simulation has caused an evolution of the research methodology in QUS during the last decade. It is now possible to start investigating a new QUS configuration by conducting a series of simulations before doing any bench-top experiment. Indeed, numerical simulation can be used as a surrogate of an experiment (virtual, or *in-silico* experiment) and the signal processing can be performed on synthetic signals as on real-life signals. The approach has been validated in some cases in which the major propagation characteristics observed experimentally could be accurately predicted by numerical simulations in trabecular bone [1, 2] as well as in cortical bone [3–5]. Numerical simulation is potentially of a great help to optimize the characteristics of an emitter–receiver system, including signal characteristics (frequency, bandwidth, and signal shape), size and number of emitter and receiver elements. Besides taking an extremely long time, the equivalent experiments would be excessively expensive. Simulation is also a versatile tool to investigate the physical mechanisms at work in a QUS configuration and allows one to perform 'experiments' that may be extremely difficult or impossible to conduct in real life. For instance, by changing the simulation parameters the evolution of the ultrasonic response to different scenario of bone evolution can be inferred: degradation of material properties and modification of the geometry to simulate osteoporosis, development of callus in fracture healing, etc. The sensitivity of ultrasound indicators (*e.g.* signal velocity and attenuation) to some bone or soft tissue characteristics (shape, material properties, etc.) can also be studied conveniently with numerical simulation: computations can be automated such that a huge number of combinations of characteristics can be tested.

The purpose of this chapter is to provide the reader with an overview of the use of numerical methods to simulate wave propagation in bones and surrounding structures. It is not intended to give a full account of the numerical algorithms but the few elements required to understand their specificities. This chapter can be thought of as a guide to QUS numerical modeling, from the definition of the configuration (geometry, material properties, etc.) to the computation of the solutions with popular algorithms.

The simplified representation of a real system (bone and soft tissue) that is used as a basis for simulation is called a *model* and includes certain key characteristics of the real system in order to account for its behavior, or at least certain behaviors which are of particular interest. Wave propagation can be simulated in a given geometrical configuration for prescribed boundary and initial conditions, equations of motion and constitutive laws (*e.g.* solid or fluid), and material properties (density, elastic properties, intrinsic attenuation, etc.) in the different media (*e.g.* bone and soft tissue). The basic model equations used to describe wave propagation in bone and soft tissue are collected in Sect. 8.2.1.1. The bounded 'domain' (area or volume) considered for the numerical simulation, called the *simulation box*, is taken around the region of interest where the wave phenomena are observed. On the boundaries of the box, special mathematical conditions are sometimes required such that the interactions of the waves with the box limits do not alter the phenomena to be observed

in the region of interest. The various boundary conditions which are relevant in QUS numerical simulations are presented in Sect. 8.2.1.2. Some characteristics of the modeled system are usually considered as *parameters* of the model. In a narrow sense, the parameters are the coefficients appearing in the partial differential equations for which numbers must be provided to run a simulation (typically material properties). However it is useful to broaden the notion of model parameters to include some geometrical features (such as the thickness of bone), emitter–receiver and signal characteristics which may be fixed for one simulation (the output of a simulation are then obtained relative to the input parameters) but may vary from one simulation to another, for instance to run a sensitivity analysis. The parameter definition strategy is dependent on the type of model: for a nominal model, an average configuration must be set while for an individualized model values associated to one specific sample should be provided. Section 8.2.2 is devoted to the geometrical configuration and model parameters.

When simple closed-form analytical or semi-analytical solutions can be derived for the model at hand, they may be extremely useful to guide the interpretation of the wave phenomena and the complex ultrasonic signals. Indeed some time-domain or frequency-domain analytical methods yield explicit relationships between a component of the synthetic signal and model parameters which provide valuable insight into the nature of the waves. When the model is so complicated that an analytical solution is not readily available one needs to resort to a numerical approach. This is in particular the case for irregular geometry and non-homogeneous media. The advent of powerful desktop computers and the availability of softwares has encouraged a quick expansion of the numerical simulation of ultrasound propagation in bone. Compared to analytical methods, numerical methods are more versatile and are very convenient to test several configurations.

The focus of the present chapter is on *time-domain* numerical methods, as opposed to frequency-domain methods. To the author's knowledge only the former have been used for the simulation of bone QUS involving the propagation of ultrasonic pulses. Indeed time-domain methods directly compute the propagation of the signal for consecutive time steps, mimicking the actual propagation of the emitted pulses; in contrast the computation of an accurate wide-band waveform with a frequency-domain approach is awkward since it requires to sum a very large number of frequency components. The simulation of vibrational techniques, which are in principle simpler from a computational viewpoint, is out of the scope of this chapter.

The various available numerical methods differ in: accuracy – is the computation result close to the exact solution? – flexibility – can the method be used for various geometrical configurations and for different constitutive laws? – efficiency – does computation requires lot of CPU time and memory space – and ease of implementation? Finite difference time domain (FDTD) methods for acoustic and elastodynamics wave propagation have been extensively developed in the beginning of the 1970s for seismic wave simulation. The basic FDTD space grid and time-stepping algorithm traces back to 1966 [6]. Although quite old, FDTD methods remain very popular for the simulation of wave phenomena. They consist in obtaining discrete equations whose unknowns are generally field values at the points of a

regular mesh. The success of FDTD schemes is largely explained by their ease of implementation and efficiency. These are a consequence of the type of space discretization (a uniform regular grid) and the explicit recurrence relationship between consecutive discrete time steps, which leads to a solution without the need to solve a large linear system of equations at each time step. An introduction to the FDTD method and its application to QUS is given in Sect. 8.2.3. The counterpart of the nice properties of the FDTD is their lack of 'geometrical flexibility', which makes the method computationally expensive in the case of complicated geometries and heterogeneous media. Nevertheless, FDTD methods have been used successfully for a very wide range of geometrical and material configurations corresponding to bone QUS applications. The finite-element methods (FEM) originated from the need for solving complex elasticity and structural analysis problems in civil and aeronautical engineering. Its development can be traced back to the early 1940s when the concept of discretization of a continuous domain into a set of discrete sub-domains, usually called elements, emerged [7, 8]. By the late 1950s, the key concepts of FEM existed essentially in the form used today. The FEM is highly flexible and is usually considered as a good choice for solving partial differential equations over domains having complicated shapes. As opposed to FDTD, its implementation requires more efforts. Its efficiency and precision depends on the choices of the numerical solvers at different steps of the solution computation. An introduction to the time-domain FEM and its application to QUS is given in Sect. 8.2.4. Other numerical methods such as boundary element methods are also popular to solve wave propagation problems. However this chapter will only deal with FDTD and FEM which are, as far as we know, the only numerical methods that have been applied to bone QUS. A case study presented in Sect. 8.2.5 is used to illustrate the application of the time-domain finite difference method and finite element method.

The last part of the chapter (Sect. 8.3) is dedicated to a comprehensive review of the literature. It intends to illustrate the broad range of problems that have been addressed with ultrasound simulation softwares, and the achievements in bone QUS which have benefited from numerical simulation.

8.2 Methodology

This section describes the general principles involved in the numerical simulation of ultrasound propagation in bone. After recalling the main model equations, we first describe the general framework for modeling ultrasound propagation in bone. This framework is independent of the numerical methods described thereafter. The basic principles of the finite difference method in time domain (FDTD) and the finite element method (FEM) are then described and illustrated on a case study.

8.2.1 Physical Modeling

8.2.1.1 Model Equations

Solving wave propagation problems, whether analytically or numerically, requires the specification of a model, mathematically described by a set of equations. Throughout this book, ultrasound propagation is always considered within the framework of continuum mechanics, *i.e.* the modeling is based on local laws of physics applied to continuous media. The quantities for which the equations are solved are referred to as the *variables* of the model. To describe the same physics, different variables may be used depending on how the laws are mathematically formulated. For instance the wave field may be described by the acoustic pressure field in fluids, whereas the displacement field is usually better suited for solid media. The particle velocity field may also be used instead of the displacement field. For a given problem, the choice of the set of variables leads to one *formulation* of the problem. Some formulations involve the pressure field alone, while others use both the displacement field and the stress tensor field. It is out of the scope of this chapter to provide a comprehensive list of the various laws and formulations used to mathematically describe ultrasonic wave propagation. We will rather provide the reader with some sets of equations that have been widely used in the field of ultrasonic propagation in bone. Although at the basis of the numerical simulation methods described in the next sections, this section discusses physical modeling rather independently of the method used to solve the problem. The reader may also refer to Chap. 2 for additional details on ultrasonic wave propagation.

In this section, the vector components of vector $\mathbf{x}$ are noted x_i where subscripts $i = \{1, \ldots, d\}$ refer to the direction of space, with d the space dimension ($d = 2$ or $d = 3$ in practice). The most fundamental law used in modeling wave propagation is derived from Newton's law of motion, applied locally to a material point of a continuous medium:

$$\rho(\mathbf{x}) \frac{\partial v_i}{\partial t}(\mathbf{x}, t) = \sum_{j=1}^{d} \frac{\partial \sigma_{ij}}{\partial x_j}(\mathbf{x}, t), \tag{8.1}$$

where ρ is the mass density, $v_i(\mathbf{x}, t)$ is the ith vector component of the particle velocity field $\mathbf{v}(\mathbf{x}, t) = \frac{\partial \mathbf{u}}{\partial t}(\mathbf{x}, t)$, $\mathbf{u}$ is the displacement field, and $\{\sigma_{ij}\}$ are the components of the stress tensor σ. Let us recall that on an elementary surface dS which normal is $\mathbf{n}$, $\sigma \cdot \mathbf{n}$dS represents the force vector applied to dS. In non-dissipative fluids, the stress tensor has diagonal terms only, all equal to the opposite of the pressure field: $\sigma_{ii} = -p(\mathbf{x}, t)$; $\sigma_{ij} = 0$ $(i \neq j)$. Equation (8.1) is a linearized approximation of Newton's law describing dynamic motion, in which static terms involving gravitation have been discarded. Newton's law is independent of the nature of the material, which has to be mathematically characterized by an additional constitutive equation, or material model, to complete the set of model equations. Note that as for any multi-scale material, the choice of the material model for bone depends on the length scale considered. Material models are further discussed in Sect. 8.2.2.3.

Due to space restrictions only one example of the generalized Hooke's law for an anisotropic viscous elastic material undergoing small deformations is given here. This writes [9]

$$\sigma_{ij}(\mathbf{x},t) = \sum_{k=1}^{d}\sum_{l=1}^{d} c_{ijkl}(\mathbf{x})\ \varepsilon_{kl}(\mathbf{x},t) + \eta_{ijkl}(\mathbf{x})\frac{\partial \varepsilon_{kl}}{\partial t}(\mathbf{x},t), \tag{8.2}$$

where ε is the strain tensor defined by $\varepsilon_{ij} = \frac{1}{2}\left(\frac{\partial u_i}{\partial x_j} + \frac{\partial u_j}{\partial x_i}\right)$, $\mathbf{c}$ is the fourth-order rigidity tensor, and η is the fourth-order viscous tensor. Equation (8.2) holds for the large class of non-homogeneous anisotropic lossy elastic media for which properties may be spatially dependent. In particular, it includes fluids, and non-dissipative media. In (8.2), viscosity is taken into account by adding a first-order time-derivative term of the strain tensor. However, other models can be considered to account for viscosity, *e.g.* introducing time-derivative term of the stress tensor.

An often-used equivalent formulation of Hooke's law is obtained by taking the time derivative of (8.2), and using symmetry properties of $\mathbf{c}$ and η:

$$\frac{\partial \sigma_{ij}}{\partial t}(\mathbf{x},t) = \sum_{k=1}^{d}\sum_{l=1}^{d} c_{ijkl}(\mathbf{x})\ \frac{\partial v_k}{\partial x_l}(\mathbf{x},t) + \eta_{ijkl}(\mathbf{x})\frac{\partial^2 v_k}{\partial t \partial x_l}(\mathbf{x},t). \tag{8.3}$$

When the space dimension is $d = 3$, $\mathbf{c}$ and η have a maximum of 21 independent coefficients for the most anisotropic class of media (six independent coefficients for $d = 2$) [10]. However, it can be shown that $\mathbf{c}$ has only two independent components for isotropic solids, and can be written as [10]

$$c_{ijkl}(\mathbf{x}) = \lambda(\mathbf{x})\delta_{ij}\delta_{kl} + \mu(\mathbf{x})(\delta_{ik}\delta_{jl} + \delta_{il}\delta_{jk}), \tag{8.4}$$

where δ_{ij} is the Kronecker symbol, and λ and μ are Lame's coefficients. Using this formulation of Hooke's law, fluid-like media (soft tissue for instance) can be simply described by setting $\mu = 0$. Lame's coefficients are of fundamental importance in wave propagation in isotropic media, as the compressional (longitudinal) wave velocity and the shear (transverse) wave velocity are given respectively by $c_L = \sqrt{\frac{\lambda+2\mu}{\rho}}$ and $c_T = \sqrt{\frac{\mu}{\rho}}$ for lossless media.

So far, the term non-homogeneous has been used to qualify a medium which properties may vary in space. Nevertheless, the term *medium* itself may carry some ambiguity, in particular in the context of the numerical simulation of wave propagation, as will be discussed further below. To avoid such ambiguity, let us precise here that by a non-homogeneous medium, we refer in this text to a medium which properties may *continuously* vary in space. By definition, spatial discontinuities may thus only occur at the boundary between two *different* media. The various equations given in this section are valid only within each medium, in the sense defined above. Additional equations defined at the boundaries between different media must be stated and verified by the field variables.

For non-homogeneous fluid-like media, (8.1) and the lossless isotropic version of (8.2) with $\mu = 0$ yield

$$\frac{\partial^2 p}{\partial t^2}(\mathbf{x},t) = \rho(\mathbf{x}) c_L^2(\mathbf{x}) \nabla . \left(\frac{1}{\rho(\mathbf{x})} \nabla p(\mathbf{x},t) \right). \tag{8.5}$$

For homogeneous media (8.5) becomes

$$\frac{\partial^2 p}{\partial t^2}(\mathbf{x},t) - c_L^2 \triangle p(\mathbf{x},t) = 0, \tag{8.6}$$

where $\triangle$ is the Laplacian operator. For isotropic solids, the natural field variable turns out to be the displacement $\mathbf{u}(\mathbf{x},t)$, and Eq. 8.1 and the lossless isotropic version of (8.2) lead to the following wave equation, which takes into account both compressional and shear waves

$$\frac{\partial^2 \mathbf{u}}{\partial t^2}(\mathbf{x},t) = (\lambda + \mu) \nabla (\nabla . \mathbf{u}(\mathbf{x},t)) + \mu \triangle \mathbf{u}(\mathbf{x},t). \tag{8.7}$$

The various equations above illustrate that several formulations can be used for a given model (here Newton's law and Hooke's law). For instance, (8.1) and (8.3) is one possible formulation, suitable for any type of elastic material, (8.5) is another formulation restricted to fluid media, (8.7) is another formulation restricted to homogeneous isotropic solids, or fluid if $\mu = 0$. For a given problem, several formulations may be used simultaneously depending on the materials involved. For instance, finite element modeling of wave propagation often use several formulations, depending on the nature of the region of space being solved: a formulation based on (8.6) can be used for fluid media, and a formulation based on (8.7) can be used for solid media. The coupling between the different regions is discussed further below.

Models based on Newton's law combined to Hooke's law encompass most models that have been used to run numerical simulations in the field of ultrasonic bone characterization. Describing alternative models that have been used to model propagation in bone, such as the Biot's model (see Chap. 5) or models involving non-local definition of stress [11], is out of the scope of this chapter. However, the basic methods and principles of numerical simulations discussed in this chapter are not restricted to the models above and can be applied to any models described by a set of partial differential equations.

8.2.1.2 Boundary Conditions

Numerical methods such as FDTD or FEM discretize space on a mesh. Handling the mesh in a computer means that meshes necessarily have a finite number of points, and therefore numerical methods based on meshes only solve the model equations in *bounded* regions of space. Two situations may be considered: (1) if the problem

involves waves that are indeed physically confined within a bounded region of space, as would be the case for a finite-size object in vacuum (into which no mechanical waves can propagate), the mesh can be designed over the entire region of interest. In this case, the field variables on the mesh boundaries must simply obey conditions that express the physics at the boundary. This has to be done whether the problem is solved numerically on a mesh or analytically on the space continuum; (2) on the other hand, one may want to numerically solve wave propagation phenomena in unbounded space, or modeled as such. This is the case for instance in the study of wave scattering by a solid object immersed in an unbounded fluid. The modeling of such unbounded domain requires specific boundary conditions, which role is to make the mesh boundaries transparent to waves incoming from within the simulation region.

In situation (1), typical boundary conditions include the Dirichlet's boundary conditions or the Neumann's boundary conditions. Dirichlet's boundary conditions correspond to forcing values of the field variable on the boundary of the domain, while Neumann's boundary conditions correspond to forcing values of the normal derivative of the field variable. The type and number of boundary conditions to be specified depend not only on the physical model, but also on the formulation used to solve the model, as illustrated on the following examples:

- The surface of a liquid in contact with vacuum can be described by forcing the pressure field to zero on the surface (homogeneous Dirichlet's condition) for a formulation based on (8.5) or (8.6).
- A liquid in contact with a rigid boundary can be described either by forcing the normal derivative of the pressure field to zero (homogeneous Neumann's condition) when using (8.5) or (8.6), or by forcing the particle displacement field or the particle velocity field to zero (homogeneous Dirichlet's condition) when using formulation based on (8.1) or (8.7).
- The boundary of a solid in vacuum can be described by forcing the stress across the boundary to zero in a formulation based on (8.3). This type of boundary conditions is often used in FEM as a good approximation for solid objects in air.

The examples above all correspond to perfectly reflecting boundaries, across which no energy is transmitted. Boundary conditions combining the Dirichlet's and Neumann's conditions (sometimes called impedance conditions) may also be used to model partially reflective interfaces.

Solving the problem posed by situation (2) have led to the development of several methods to *simulate unbounded media*. In the time-domain modeling, for a finite simulation duration T, the crudest approach for modeling unbounded space consists in using a bounded space of dimensions large enough so that reflections from the boundaries cannot reach the regions of interest within the duration T. However, in terms of computational cost, while such approach may sometimes be used for space dimensions $d = 1$ or $d = 2$, it is often impracticable for $d = 3$. Two main approaches have been developed to simulate transparent boundaries. One first approach uses a set of specific differential equations defined on the boundary, called *absorbing boundary conditions* (ABC) or transparent conditions, introduced in the late seventies [12]. A second approach consists in adding *absorbing* or *damping layers*

around the domain, in which the wave equations are solved with a damping term. The thickness of the layer and the damping term should be able to reduce the amplitude of waves during the propagation in the layer so that reflections on the outer boundaries of the layer lead to almost no reflections in the main physical domain. While more physical than ABC, this approach has a major drawback: at the entrance of the layer, waves feel an impedance mismatch which generates non-negligible artificial reflected waves, which amplitude grows with the angle of incidence. ABC remained the most efficient and preferred approach until the development in the mid-nineties of perfectly matched layers (PML). This approach is similar to that of the damping layers, but uses equations which although not describing physical propagation in any real material lead to *no reflection* for any angle of incidence. The spatial discretization involved in numerical implementation of PML causes some artificial reflections, but these can be made as small as desired by controlling the parameters of the layer such as its thickness (at some computational cost). Maintaining reasonable computational cost, PML are much more efficient than ABC for the elastodynamics equations, and are currently the most convenient way to model unbounded domains [13].

In addition to the need to handle the mesh frontiers, boundary conditions may also be required between subdomains within the simulation box. As discussed earlier in Sect. 8.2.1.1, additional equations are required at the interface between different media, to complement partial differential equations describing the physics within each media. This is in particular the case when the field variables are different in two adjacent media. These additional equations usually mathematically state physical continuity conditions. For instance, the normal velocity (or normal displacement) must usually be continuous across boundaries (this may not be true for the modeling of materials with cracks, but this case is out of the scope of this chapter). Depending on the type of media (solid or fluid in particular), tangential velocities or stress components at the boundaries may or may not be continuous. A type of boundary very often encountered within the context of bone is that between a non-viscous fluid (or fluid-like) medium and a solid medium, such as soft-tissue and cortical bone. In this case, because of the absence of tangential stress in lossless fluid, only the normal velocity and the normal component of the stress across the interface are required to be continuous across the boundary. Such explicit continuity conditions are necessary to handle interfaces between different media, based on the continuous equations given in Sect. 8.2.1.1. However, in the context of numerical methods based on a material parameter map defined on a mesh, interfaces between media can be handled in two different ways, depending on the numerical scheme. One way consists in treating different media *explicitly*, meaning that continuity conditions must be stated and computed at the coordinates of the boundaries between each media, as would be done for an analytical method of solution. The other way, specific to numerical methods based on a discrete material parameter map, consists in considering the whole simulation domain as a single medium with material properties varying in space, either smoothly or abruptly. Indeed, the notion of spatial continuity is lost in the case of discrete meshes. Accordingly, the difference between the case of space filled with a single media with strong material heterogeneity and

the case of space filled with different media becomes rather subjective. The choice of the formulation and the numerical method conditions how discontinuities between different media must be handled. Whatever the method, it is fundamental that boundaries between different media be correctly treated, as numerous wave propagation phenomena arise from such boundaries: reflection, refraction, mode conversion, etc.

8.2.1.3 Wave Generation

The model equations above have been written for the sake of clarity with no source terms. However, mechanical waves are physically generated within a material either via sources of motion or sources of stress, usually applied to some localized region of space. For modeling in the time domain, two different approaches may be used to generate ultrasound waves in the simulation domain: one may either define sources that are active at some points of the mesh during the simulation, or provide initial field values at all the grid points that will evolve in time during the calculation according to the model equations with no source terms.

Defining sources in the domain may be done either by forcing field values at some points in space (at such points, the field is *given*, not *calculated* by model equations), or by adding source terms at some points in the model equation (at such points, the field is different from the source term, and is *calculated* using the modified equation with the source term). These two ways of including sources in the model are very different: on the one hand, forcing field values provides an easy way to generate a wave of known geometry and temporal waveform, but points in space where field values are forced will act as scatterers for waves generated elsewhere. Using this approach thus usually requires that the sources be turned off (the field values are not forced anymore and obey the model equations) before any other wave (such as reflected waves) reach the source region. Forced boundary conditions on part of the mesh boundary are often used to simulate a transducer in contact with an object. On the other hand, a source term added to a field equation allows the linear superposition at the source point of the generated wave with other waves, *i.e.* active regions are transparent to waves generated elsewhere. One drawback of using source terms, except for some simple geometry (such as generation of plane-like wave), is that the field values are usually not related in a simple manner to the values of the source terms. When initial value conditions are used rather than source term, the various formulations presented in Sect. 8.2.1.1 indicate that initial conditions must be given for two field variables. For formulations based on second order time-derivative, such as equations (8.6) or (8.7), initial values must be given for both the pressure field and its time-derivative. For the velocity-stress formulation based on (8.1) and (8.3), initial values must be given for both the pressure field and the velocity field. The approach based on initial value conditions is well-suited for instance to start a simulation just before an incoming wave propagating in a homogeneous medium (and of analytically known geometrical shape) is about to be scattered in a complex manner by an object. In the context of ultrasound characterization of bone,

this situation is encountered in transverse transmission, when a focused ultrasound wave propagating in water (or homogeneous soft-tissue) is about to hit the bone sample and undergo various complex wave phenomena.

Although less frequent, both approaches, active sources and initial value conditions, can be implemented simultaneously. To conclude this section on wave generation, let us note that the model equations presented in Sect. 8.2.1.1 do not model wave propagation within ultrasound transducers. Unless additional equations are provided to explicitly model wave equations in active material (such as piezoelectric materials), transducers are not taken into account as physically active materials in the simulation domain, but are modeled by regions of space or boundary where field values are forced or source terms are provided.

8.2.2 QUS Model Configurations and Parameters

Simulation applied to biomedical applications distinguishes between *individualized* and *nominal* configurations. The former is representative of one given (or specific) biological system (subject or bone specimen) while the latter could represent almost any system; in practice, it is an average configuration (*e.g.* average bone thickness, average material properties). Nominal configurations usually serve as a basis to investigate the physical phenomena at work and the effect of coarse modifications of the system. For instance several papers have considered a nominal configuration to investigate the determinants of the first arriving signal in an axial transmission experiment: the influence of bone thickness [14], anisotropy [4], 3D geometry [4], gradients of material properties [15], and bone healing [16] have been studied based on a configuration modeling wave interaction with a bone plate. Individualized configurations can be used to investigate the variability of the ultrasound response with different systems (individuals or bone specimen) and are necessary to validate the models by comparison with site-matched measurements on the modeled system. Numerical simulations of individualized configurations are usually much more demanding since several important characteristics must be accounted for to match the physical response. In other words, such simulations are intended to give more or less quantitative results while simulations based on nominal configurations often aim at qualitative or comparative results. It is important to have in mind that a model will be constructed and used for a designed purpose. The parameters definition strategy should follow. This section discusses the main possible characteristics to include in models for the study of the interaction of ultrasound with bones.

8.2.2.1 Two-Dimensional (2D) or Three-Dimensional (3D) Problems

In 2D, all the variables and parameters are assumed to depend only on two spatial coordinates. The 2D configuration can use Cartesian or cylindrical coordinates.

In the popular 'plate' model for the study of the axial transmission of a pulse in a long bone [3, 14–17], the radius of curvature is considered to be infinite; for the study of through transmission at the radius [18] or the femoral neck [19], the length of the bone is assumed infinite and the variation of the geometry along the length is neglected. Wave propagation in the axial direction of tubular structures like long bones can be modeled using cylindrical coordinates (r, z) so that only one plane of the 3D object is represented but the equations solved are those for the 3D-cylindrical object [20]. In that case it is assumed that the variables and the geometry do not vary along the object circumference. Note that the ultrasound source and receiver configuration should also be considered when choosing the dimension: if the simulation is 2D, the transducers are modeled as infinitely long in one dimension (Cartesian coordinates) or circular (cylindrical coordinates). It is impossible to model a finite-size beam in 2D in Cartesian coordinates.

The computational requirements (memory space and computation time) are much less for 2D models than for 3D models. Furthermore, the analysis of the data is simpler because it can be visualized in a plane. While a 2D simulation can often be performed as a first step when addressing a new propagation problem, the results should be confirmed with 3D simulations: only the analysis of the 3D case can make it clear whether the phenomena of interest are actually captured with the 2D configuration. The confrontation of 2D and 3D simulations for the same object can reveal that 3D effects have different magnitudes depending on the types of waves observed (different guided waves modes, bulk waves) and the assumed material symmetry (isotropic, anisotropic) [4, 14, 21]. Some cortical bone studies have found that a 2D model may be satisfactory [4], but the best choice for the dimension depends on the phenomena of interest. In contrast, it is unlikely that a 2D simulation of US propagation in trabecular bone can yield realistic results due to the highly 3D trabecular structure.

8.2.2.2 Geometry

In a model of US propagation in cortical bone, the endosteal and periosteal surfaces have to be described with precision because the cortical shell thickness is often a key characteristic. This can be smaller than one millimeter in some areas of interest for QUS (for some radius specimen and at the proximal femur). For trabecular bone the model must include a description of the trabeculae which characteristic size is a few hundreds of microns.

The geometry of the model can be constructed explicitly upon prescribing the coordinates of the boundaries (lines or surfaces) of the different media, for instance using a Computer-aided design (CAD) software. This procedure may be convenient for nominal models for which the geometry is simple. Otherwise the geometry of the bone structures should be obtained from digitized images. In a basic model where only two or three media are represented, it is convenient to use images in integer format where each number stands for one medium. Then each number can be used as an index for the allocation of each medium properties. To obtain such images starting

from the raw data obtained from the imaging system, a more or less involved image processing is necessary. Let us consider the case of a three-media model: cortical bone, trabecular bone and soft tissue, to be constructed from a gray level raw image. The processing of the raw image consists in segmentation of the three media, *i.e.* defining the volumes corresponding to each medium. In some cases the segmentation can be done automatically simply by setting a threshold to separate the media. However in many cases segmentation is a problem, in particular when the image resolution is low. For instance when the cortical thickness is small and the resolution of the order of 100 µm, it may be difficult to separate cortical and trabecular bone at the endosteal surface due to partial volume effects and the smooth transition between cortical and trabecular bone. The segmentation of trabecular bone images has been the subject of several investigations in the context of quasi-static micro-finite element modeling; it was established that the processing may have a significant effect on the simulation results [22–24]. Fortunately, the QUS community can benefit from the advanced tools developed for the radiologists (*e.g.* MIAF: Medical Image Analysis Framework, Institute of Medical Physics, University of Erlangen, Germany [19]).

It is relatively easy to obtain a 2D description of bone geometry with high resolution digitized photographs or radiographies. These are however of very limited interest in trabecular bone studies because the trabecular network is highly 3D. To some extent 2D images may be sufficient for the cortical bone problems which can be investigated in 2D although it would be difficult to image exactly the plane which is wanted for the simulation. For 2D simulation studies on individualized cortical bone samples, it is convenient to obtain the simulation plane from 3D images.

Because of the high absorption of X-rays by bone, X-ray quantitative computed tomography (XR-QCT) is a very efficient technique to retrieve bone geometry and is it used almost exclusively. The advent of high resolution QCT system in the 1990s coincides with the development of numerical simulation for QUS [25]. With the increasing availability of standard research XR-CT systems with a resolution down to 5 microns, it has become very convenient to obtain the 3D image of the bone structure. The gold standard for high resolution bone imaging is the synchrotron radiation QCT (SR-QCT). The monochromatic beam of synchrotron radiation minimizes artifacts and the energy can be increased to obtain 3D images with a resolution better than the micrometer, together with a measurement of the local mineral content. Based on the authors' experience, for the modeling of QUS applications, modeling trabecular structures with less than ten micron resolution should not affect the results while for cortical bone applications, an image resolution in the range 50–150 µm should be sufficient to represent the cortical thickness. Note that these values are only indicative and may be hard to achieve in practice. In fact several authors have obtained reasonable results using lower resolution. Finally, note that the adequate image resolution (pixel size) is largely problem-dependent and may be influenced by the numerical scheme.

8.2.2.3 Material Properties (Mass Density and Mechanical Properties)

It is one of the major advantages of QUS over X-ray based techniques to be sensitive to the material properties of bones, in particular elastic properties. Accordingly, bone models should include a realistic representation of material properties, which may itself be referred to as a *model* of material properties. The definition of a material property assumes a length scale over which this property is defined. To a large extent, the numerical modeling of bone QUS does not need to consider the full complexity of bone organization down to the nanometer scale. Basically, it is enough to describe bone as a two-phase composite material: a relatively hard tissue and a soft phase. The soft phase corresponds to marrow in trabecular bone (inter-trabecular space) and to large pores (resorption cavities and Haversian channels) in cortical bone. In trabecular bone the hard tissue is the constitutive material of the trabeculae; in cortical bone it is the mineralized matrix in which pores are embedded. Nevertheless, one has to bear in mind that the properties of the cortical bone matrix and the trabeculae depend on the lower levels of bone organization.

The propagation model can include an *explicit description* of the material phases. This is the case for most cancellous bone simulation studies where the individual trabeculae are represented, *e.g.* based on a digital XR-CT image. Another option is to use *homogenized* material properties, that is properties which represent the average behavior of the phases (hard tissue and pores) of a material volume of the order of the wavelength, that is of the order of one millimeter. Biot's theory for poroelastic media provides such homogenized material properties which can be implemented in numerical models to account for the sub-wavelength interaction of the waves with the trabecular network [26–28]. In contrast, a purely elastic (or viscoelastic) homogenized model is considered a good choice to model cortical bone properties at a scale above one millimeter [29].

If the material model is anisotropic, the principal orientations (planes of symmetry) of the material must be defined. For long bones this is not a major difficulty since the cylindrical coordinates frame attached to the tubular bone shape is a good approximation to the material axes. In contrast the later can be complicated to define for trabecular bone or bones which cross-sectional shape significantly diverts from circular shape. The relevance of modeling anisotropy for QUS depends on the type of problem as illustrated in the literature review in Sect. 8.3.

Some studies have suggested that the overall quasi-static mechanical [30] properties of cancellous bone can be explained with an isotropic material model of the trabecular material. Consequently the material properties of the trabeculae may only have a minor impact on the (overall) ultrasonic response which may be essentially determined by the amount of bone and structure of the network. If the isotropy hypothesis is retained for the constitutive material of the trabeculae, then only two elastic coefficients need to be provided. The homogenized properties of cortical bone are transversely isotropic (TI), at least in the mid-diaphysis of long bones [34,35] (properties tend to be orthotropic closer to the diaphysis [36]). Values of typical elastic properties which can be used for a nominal model are collected in Table 8.1.

Table 8.1 Typical bone material properties (elasticity framework) which can be used as inputs for nominal bone models. The values reported in the table are as found in the literature; note that the density for the homogenized material and the tissue level properties is the same, which is somewhat inconsistent since homogenized material density should be lower to account for the pores

	Cortical bone (homogenized)	Cortical bone (matrix)	Trabecular bone (trabeculae)	Pores
Reference	[31, 32]	[31]	[1]	[33]
symmetry	*TI*	*TI*	*I*	*I*
mass density (g.cm^{-3})	1.85	1.85	1.85	1
C_{11} (GPa)	19.1	29.5	29.6	2.25
C_{22} (GPa)	19.1	29.5	29.6	2.25
C_{33} (GPa)	27.6	38.1	29.6	2.25
C_{12} (GPa)	10	11	17.6	2.25
C_{13} (GPa)	10.4	11.9	17.6	2.25
C_{23} (GPa)	10.4	11.9	17.6	2.25
C_{44} (GPa)	5.9	10.1	6	0
C_{55} (GPa)	5.9	10.1	6	0
$C_{66} = (C_{11} - C_{12})/2$ (GPa)	4.5	9.3	6	0

TI – transverse isotropic; *I* – isotropic

Mathematical homogenization techniques have enhanced our knowledge of the relationships between the homogenized properties, the matrix properties and the porous network. In cortical bone, the anisotropy at the millimeter scale is dependent on the mineralized matrix anisotropy and to a lesser extent on the oriented porosity [31, 37]. Note that due to the low porosity, the homogenized properties of cortical bone are largely dependent on the intrinsic properties of the mineralized matrix. The dependence of the homogenized elastic coefficients on the porosity has been investigated in the framework of ultrasound studies in [33] (see also Chap. 13). The authors found that all the stiffness coefficients decrease with increasing porosity, and that the decrease is more pronounced in the direction perpendicular to the pores main direction. In the latter work, the homogenized coefficients are obtained based on the simulated propagation of a 1 MHz central frequency-pulse across a millimetric volume of cortical bone with an explicit description of the porous network. Note that this 'dynamical' homogenization of elastic properties obtained through wave propagation is in global agreement with quasi-static homogenization using the Mori–Tanaka method [38] (considering the cylindrical pores are aligned and randomly distributed) or the asymtotic homogenization method [39] (considering the pores are regularly distributed on a hexagonal lattice).

Individualized models for QUS should consider sample-specific material properties in addition to the specific geometry (organ shape). At present, there seems to be no satisfactory model of homogenized trabecular bone properties for wave propagation. Biot's model is popular but fails to explain all observed wave phenomena (see Chaps. 5 and 11). A conservative option to build an individualized model of trabecular bone is to represent explicitly the trabecular network; this ensures that the essential wave phenomena are accounted for in the model. As explained above, a sample-specific choice of material properties of the trabeculae should not

considerably improve the model. An individualized model of cortical bone for QUS can use an homogenized model of bone properties with a sample-specific choice of elastic coefficients. Because of anisotropy, at least five coefficients must be set. At present there is no convenient technique to obtain these coefficients from different locations in a bone sample (elasticity may be heterogeneous). As a consequence, individualized bone models almost systematically assume nominal values of material properties (and individualized geometry). One possibility to adapt a bone model to a specific sample is to retrieve, in addition to the porosity, one or several elastic properties of the mineralized matrix with nanoindentation or acoustic microscopy and to coupled this data with a bone homogenization model [31] to obtained a set of homogenized anisotropic properties.

8.2.3 Finite Difference Time Domain Method (FDTD)

The finite difference method is a numerical method that approximates a differential equation defined over a continuous domain by a finite number of equations defined only at the points of some mesh. It is named after the fact that it replaces derivatives by finite differences. The acronym FDTD refers to the finite difference method applied in the time domain, as opposed to the frequency domain. For wave propagation solved in the time domain, it provides solutions as field values given at discrete locations in space and discrete instants in time. Although rather old, the FDTD method is very popular due to its combined simplicity and efficiency. It has been widely applied to wave propagation problems for more than 30 years in various fields, including electromagnetic, geophysics, ultrasonics. It is out of the scope of this book to provide a full account of the FDTD method, which can be found elsewhere (see [40] or [13] for instance), but rather to provide the reader with the main principles at the basis of the FDTD method, illustrated on equations relevant to ultrasound propagation in bone. As introduced in Sect. 8.1, both FDTD and FEM methods rely on space discretization defined over some mesh. In contrast to the finite element method, presented in the following section, spatial meshes used in finite difference methods consist of regular grids based on field coordinates. In this section, the FDTD method will be illustrated for a cartesian coordinate system only, but all basic principles are valid for any coordinates such as spherical or cylindrical coordinates. We will first define and give examples of some FDTD schemes commonly used to simulate ultrasound propagation.

8.2.3.1 Principles

Basically, the finite difference method is based on the Taylor expansion of differentiable functions. For a single-variable function f, the Taylor expansion is given by

$$f(a+\Delta a) = f(a) + f'(a)\Delta a + \cdots + f^{(n)}(a)(\Delta a)^n + O[(\Delta a)^{n+1}]. \tag{8.8}$$

In (8.8), a is a generic variable that may stand for the time coordinate t or spatial coordinates x, y, etc., and $O[(\Delta a)^{n+1}]$ is the residual error. Using the first-order expansion of (8.8), several expressions of the first-order derivative can be found [41]:

$$f'(a) = \frac{f(a+\Delta a) - f(a)}{\Delta a} + O(\Delta a) \tag{8.9a}$$

$$f'(a) = \frac{f(a) - f(a-\Delta a)}{\Delta a} + O(\Delta a) \tag{8.9b}$$

$$f'(a) = \frac{f(a+\frac{\Delta a}{2}) - f(a-\frac{\Delta a}{2})}{\Delta a} + O[(\Delta a)^2] \tag{8.9c}$$

Approximations in the finite difference method arise from the use of truncated Taylor expansions. The approximation is said to be of order k when the truncation corresponds to errors which are $O[(\Delta a)^k]$. In other words, a kth-order finite difference approximation means that for sufficiently small Δa, the approximation error is divided by α^k when Δa is divided by α. Accordingly, finite difference computations based on (8.9a) and (8.9b) provide first-order approximations of first-order derivatives, whereas finite difference computations based on (8.9c) provide second-order approximations of first-order derivatives. For the simulation of ultrasonic wave propagation obeying the elastodynamics equations presented in Sect. 8.2.1.1, (8.9c) is at the base of second-order FDTD schemes. Higher-order approximations may be found by using more than two field values. It is out of the scope of this chapter to provide details on such higher-order methods, which can be found elsewhere [13]. Our introduction to the FDTD method will be based on second-order FDTD schemes only, which are sufficient to understand the main principles of the method. Moreover, most applications of the FDTD method in the field of ultrasound propagation in bone actually are restricted to second-order approximations. For multivariate functions, such as spatio-temporal fields $f(x,t)$ encountered in wave propagation problems, the expression of the Taylor's expansion involves the partial derivatives of f [41]. Up to the first order term, the Taylor expansion for multivariate functions is analog to that of single-variable functions but uses the first-order partial derivatives. All following examples will assume the following second-order approximation to first-order derivative:

$$\frac{\partial f}{\partial a}(a) \approx \frac{f(a+\frac{\Delta a}{2}) - f(a-\frac{\Delta a}{2})}{\Delta a}. \tag{8.10}$$

It can be shown [13, 41] that (8.10) leads to

$$\frac{\partial^2 f}{\partial a^2}(a) \approx \frac{f(a+\Delta a) - 2f(a) + f(a-\Delta a)}{\Delta a^2}, \tag{8.11}$$

which is a second-order approximation of a second-order derivative. Equations (8.10) and (8.11) are also called centered difference approximations. The type of equation used to solve a problem depends on how the problem is formulated: as discussed in Sect. 8.2.1.1, the problem may be formulated by use of a single

second-order differential equations involving only one field variable (see (8.6) or (8.7) for instance) or a set of coupled first-order differential equations involving two types of field variables (see the velocity-stress formulation using (8.1) and (8.3) for instance), as illustrated in the following section.

8.2.3.2 FDTD Schemes: Two Examples

We now illustrate the principles introduced above on two examples. Let us start with the 1D wave equation for pressure in a lossless homogeneous fluid medium. Approximating (8.6) based on (8.11) applied to both spatial and time derivatives, one obtains the following finite difference equation:

$$\frac{p(x,t+\Delta t)-2p(x,t)+p(x,t-\Delta t)}{\Delta t^2} = c^2 \frac{p(x+\Delta x,t)-2p(x,t)+p(x-\Delta x,t)}{\Delta x^2}, \tag{8.12}$$

where Δt and Δx are respectively the time and spatial steps, and c is the speed of sound. Equation (8.12) yields in turn

$$\begin{aligned} p(x,t+\Delta t) = {} & 2p(x,t)-p(x,t-\Delta t) \\ & + \left(c\frac{\Delta t}{\Delta x}\right)^2 [p(x+\Delta x,t)-2p(x,t)+p(x-\Delta x,t)] \end{aligned} \tag{8.13}$$

Equation (8.13) is an explicit evolution equation for the pressure field: it provides the value at time $t+\Delta t$ at position x from the values at position x at two anterior time points t and $t-\Delta t$, and from spatially neighboring values at time t. In practice, initial values of the pressure field have to be provided for $t=0$ and $t=\Delta t$ at all positions in space. The evolution of the pressure field can then be calculated step by step in time over the whole spatial domain. It is apparent from (8.12) that the calculated pressure field is defined on a regular grid in space, with consecutive points Δx apart from each other. It is also clear that the two points at the boundary of the domain cannot be calculated by use of (8.12) as each has only one neighboring point, in agreement with boundary issues discussed in Sect. 8.2.1.2. The extension of this scheme to the 2D and 3D cases is straightforward.

Let us now consider the 1D velocity-stress FDTD formulation derived from (8.1) and (8.3) in the case of a lossless fluid. This formulation leads to the following expressions

$$\frac{p(x,t+\Delta t)-p(x,t)}{\Delta t} = -\lambda(x)\left[\frac{v_x(x+\frac{\Delta x}{2},t+\frac{\Delta t}{2})-v_x(x-\frac{\Delta x}{2},t+\frac{\Delta t}{2})}{\Delta x}\right] \tag{8.14a}$$

$$\frac{v_x(x,t+\Delta t)-v_x(x,t)}{\Delta t} = -\frac{1}{\rho(x,y)}\left[\frac{p(x+\frac{\Delta x}{2},t+\frac{\Delta t}{2})-p(x-\frac{\Delta x}{2},t+\frac{\Delta t}{2})}{\Delta x}\right] \tag{8.14b}$$

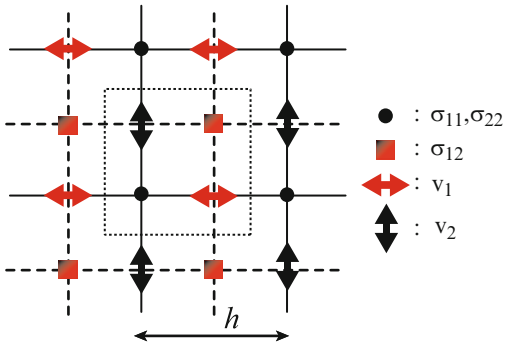

Fig. 8.1 Staggered grids used for the 2D elastodynamics leapfrog scheme. The grids for stress and velocity fields are staggered in both space and time [43]. The figure only shows staggering in space

which as (8.12) also provides explicit expressions of $p(x,t+\Delta t)$ and $v(x,t+\Delta t)$. However, in this case, as opposed to the previous example, centered difference requires that $p(x,t)$ and $v(x,t)$ be defined on staggered grids, both in space and time. Similarly, the 2D and 3D formulations also lead to staggered grids both in space and time. For solids, the principle is exactly the same, by taking into account the equations for all the stress components. This FDTD scheme was first introduced By Yee for electromagnetic in 1966 [6], and extended for the elastodynamics wave problem by Madariaga [42] and Virieux [43] for geophysics applications. It is particularly well suited to solve evolution equations given by first-order time derivatives as a function of first-order spatial derivatives, such as the Maxwell's equations in electromagnetism or the velocity-stress formulation in elastodynamics (see (8.1) and (8.3) with no viscous term). It is often referred to as the Virieux scheme, or the leapfrog method because of the structure of (8.14). Figure 8.1 illustrates for the 2D case how the grids for the stress and particle velocity fields are staggered in space.

For homogeneous fluid media, the Virieux Scheme can be shown to be equivalent to the previous scheme (see (8.12)) based on the pressure wave equation. For homogeneous isotropic solids, it can be shown to be equivalent to FDTD schemes based on (8.7). However, the staggered-grid Virieux scheme has several major advantages over formulations based on second-order differential equations for pressure or displacement fields. Not only does it work properly for both fluids and solids, but it also implicitly handles both solid/solid and fluid/solid coupling between two different materials. Both changes of materials and heterogeneities in a given material are handled in the same way by use of parameters maps defined for each grid point, with no need to explicitly state boundary conditions. Moreover, its expansion to anisotropic materials is straightforward, as it directly uses the rigidity tensor ((8.3) with no viscous term). Finally, perfectly matched layers (PML) can readily be implemented with the Virieux scheme [44]. For all these reasons, the Virieux scheme has remained extremely popular in particular in the geophysics community, where it was first introduced for elastodynamics. In the field of ultrasound propagation in bone, several groups have developed their own code based on the Virieux Scheme [2, 4, 26].[1] Other groups have also used a commercially available software, based on the second-order wave equation for the displacement

[1] http://www.simsonic.fr

field in isotropic media [3, 14, 17, 25, 45].[2] SimSonic, a FDTD code based in the Virieux scheme developed at the Laboratoire d'Imagerie Paramétrique (Université Pierre et Marie Curie-UPMC and CNRS, Paris, France) and used in several publications [1, 4, 33, 46], can be freely downloaded online.[3]

8.2.3.3 Discretization and Related Issues

As discussed above, the FDTD method discretizes spatial and temporal domains over regular grids, defined by a temporal-step Δt and a space-step h. The space-step is assumed here to be independent of the direction, *i.e.* $\Delta x = \Delta y = ... = h$. The choice of Δt and h is of crucial importance in FDTD methods. Qualitatively, both Δt and h must be chosen small enough to provide sufficiently smooth representation of the computed field. The smallness of Δt and h conditions the accuracy of the results, that is the degree of approximation introduced by the numerical method. On the other hand, Δt and h cannot be chosen independently, and must obey a so-called stability condition. The stability condition (commonly called CFL condition, from the initials of Courant, Friedrichs and Levy) depends on the numerical scheme, and insures that computed fields are stable, *i.e.* the computed fields do not blow up (or equivalently computed values remain bounded). For wave propagation problems, the CFL condition most often has the following form:

$$c\frac{\Delta t}{h} \leq \alpha_d, \tag{8.15}$$

where α_d is some dimensionless constant, which depends on the space dimension d, and c is the wave velocity. When several wave velocity values are involved, as is the case for a heterogeneous medium or different media, the largest velocity has to be used in the CFL condition. For the two schemes presented above as examples, the CFL condition is given by

$$c\frac{\Delta t}{h} \leq \frac{1}{\sqrt{d}}. \tag{8.16}$$

In practice, one usually first chooses the step-size h, based on accuracy criteria, and then uses the CFL to derive Δt and ensure stability. Note that accuracy and stability are completely independent concepts: a simulation may be stable while providing poor accuracy for coarse meshes. On the other hand, even very fine grids will yield instability if the CFL condition is not fulfilled.

The accuracy of a FDTD simulation depends on a number of factors, in addition to the step-size h: sources of error not only involve the approximation of derivative by finite difference, but also cumulative errors due to the iterative nature of the method. Therefore, the longer the simulation duration, the larger the errors. Equivalently, the larger the propagation distance, the larger the errors. One major effect generated by most FDTD schemes, including all schemes that have

[2] http://www.cyberlogic.org/software.html

[3] http://www.simsonic.fr

been used in the field of ultrasonic bone characterization, is numerical dispersion, *i.e.* the dependence of phase velocity on frequency due to the numerical method. As an important consequence, simulated ultrasound pulses are increasingly distorted during propagation. Accuracy criteria in FDTD therefore include tolerance on waveform distortion, as well as on wave amplitude. The obtained accuracy depends both on propagation distances and simulation duration. Note that numerical dispersion is not specific of finite difference schemes but is an artifact to control with most of the numerical methods, in particular those based on a discretization of the propagation domain.

For second-order FDTD schemes, a minimum spatial-step size of typically $\lambda/10$ (*i.e.* ten points per wavelength) is required. For propagation distances over several tens of wavelengths, step size as small as $\lambda/20$ may be required, depending on the desired accuracy. Moreover, for pulsed ultrasound, the accuracy strongly depends on the bandwidth: for a given central frequency, short (*i.e.* broadband) pulses will be more distorted than quasi-harmonic waves, as a value of h of one tenth of the central wavelength will correspond to less points per wavelength for the higher frequency content. For pulsed ultrasound, the number of points per wavelength should be determined based on the desired accuracy for the highest significant frequency content, which equivalently corresponds to a waveform distortion criterion. The choice of h is therefore highly subjective, and no general rules exist to determine h. Ten grid points per wavelength should be considered a minimal requirement, that moreover remains rather subjective for pulsed ultrasound. Note that for a homogeneous medium, the CFL condition turns the number of spatial grid points per wavelength into number of temporal grid points per period, with some dimensionless factor close to one. For simulations involving several media with different propagation velocities, one has to consider the *smallest* wavelength (*i.e.* the *smallest* velocity) to choose h. On the other hand, the temporal step will be derived by use of the *largest* velocity. For a large range of velocities, such as encountered for simulation in both soft tissue and bone, a consequence is that the number of spatial grid points per smallest wavelength is significantly different from the number of temporal points per period, which increases numerical dispersion. To compensate for this additional dispersion, simulation involving significantly different velocities requires grid steps finer than that for homogeneous media.

Although h has to be small enough to fulfill accuracy requirement, it also has to be small enough in order to correctly describe the geometry of propagation media, as discussed in Sect. 8.2.2. For FDTD simulation in trabecular bone structures in the MHz range, h is determined by the trabeculae dimensions: it must be small enough (at maximum on the order of a few tens of microns) to describe the bulk of individual trabeculae. Whereas the discussion above is rather general, applicable to both FEM and FDTD methods, one additional consideration conditions the choice of h in the case of FDTD methods: the use of regular grids leads to "staircases" artifacts when originally smooth interfaces are discretized on such grids. Therefore, a plane interface that is not parallel to the coordinates axes, for instance, will have some artificial roughness. In turn, this artificial roughness will create scattering, which amplitude depends on the size of the "staircases" relatively to the wavelength. As

for accuracy considerations in homogeneous media, although for a different reason, h has to be made small to decrease artificial scattering.

In summary, the spatial-step size h of a simulation has to be small enough to both correctly describe the geometry of the medium and minimize numerical dispersion. Practically, it is the computational cost that bounds the value of h to some minimal value. For a space dimension d, memory requirements scales as h^d: for fixed spatial physical dimensions, the number of points in the spatial mesh in three dimensions for instance is multiplied by $2^3 = 8$ when h is divided by 2. Moreover, because of the CFL conditions, the computational time scales as h^{d+1}: dividing h by a factor of 2 multiplies the total number of calculations by $2^{3+1} = 16$ for 3D simulations. From the point of view of computational efficiency, h must therefore be kept as large as possible, while being small enough to fulfill accuracy requirements. This point is illustrated further in the two dimensional case study presented in Sect. 8.2.5.

8.2.3.4 Concluding Remarks on the FDTD Method

As a time-domain numerical method, the results provided by a FDTD simulation include "snapshots" of field variables at chosen instants in time and temporal signals recorded at chosen points in space. Section 8.2.5 will illustrate the implementation of a FDTD computation on a case study. Let us conclude this introduction on the principles of the FDTD approach by summarizing its main advantages and disadvantages. FDTD is undoubtedly one of the most easily accessible numerical method to solve wave propagation problems: its fundamentals can be grasped easily by the non specialist, and simple though efficient algorithms may be written rapidly using standard programming languages such as C or Fortran. Yet FDTD is capable of computing numerical solutions to complex elastodynamics problems. Complex geometries may be taken into account simply by providing digitized parameters maps. It is this combination of simplicity and power that makes FDTD such a popular method. On the other hand, most of its main drawbacks come down to a problem of computational cost: the use of regular grids to describe originally smooth geometry, numerical dispersion, and cumulative errors for large duration and large propagation distance can be overcome by setting small enough grid steps. The applicability of the FDTD to a wave propagation problem is therefore essentially limited by practical computational limitations.

8.2.4 Finite Element Method (FEM)

This section intends to give the reader an account of the main concepts associated with the finite element method (FEM). The presentation is limited to linear problems. Throughout the section, space coordinates are denoted x, y, and z and time is denoted by t. Matrices and vectors will be denoted in bold face. Capital letter T in exponent denotes transposed vectors and matrices.

Let the exact solution of a set of partial differential equations in the local form such as (8.1) and (8.2) be the vector $\mathbf{u}(\mathbf{x},t)$, whose components are, for instance, the displacement in the directions x, y and z. The finite difference method uses a discretization of the problem equations in their local form and seeks the solution $\mathbf{u}(x_i,y_j,z_k;t_l)$ at prescribed points: nodes (x_i,y_j,z_k) of a spatial mesh and discrete time points t_l. In contrast, the FEM seeks an approximate solution $\hat{\mathbf{u}}(\mathbf{x},t)$ defined at any coordinate (x,y,z) and time t. This approximate solution must be found as the solution to a modified form of the original equations. This is why the starting point of the FEM formulation is not the original set of partial differential equations and boundary conditions (BC) in the local form but a weighted integral form of the latter, of which $\hat{\mathbf{u}}(\mathbf{x},t)$ appears to be a solution. The discretization in the FEM consists in splitting the computation domain in a number of parts (*e.g.* triangles or rectangles in 2D problems) referred to as *finite elements*. The FEM approximated solution $\hat{\mathbf{u}}(\mathbf{x},t)$ in the space domain is usually taken in the form

$$\mathbf{u}(\mathbf{x},t) \approx \hat{\mathbf{u}}(\mathbf{x},t) = \sum_{i=1}^{n} \mathbf{N}_i(\mathbf{x})\tilde{\mathbf{u}}_i(t), \tag{8.17}$$

which is a sum over all the finite elements. Functions $\tilde{\mathbf{u}}_i(t)$ are unknowns (typically the displacement at nodes of the mesh) and the terms $\mathbf{N}_i(\mathbf{x})$ are space *shape functions* (or basis functions) that are usually defined *locally*, on one or a few finite elements.

For stationary problems, the time-dependence can often be assumed, *e.g.* a vibrating body oscillating at a given frequency ω (which may be unknown) has a $\cos(\omega t+\phi)$ time-dependence (harmonic motion). Although linear *transient* problems can theoretically be envisaged as a superposition of harmonic problems (Fourier series decomposition), this is cumbersome from the numerical point of view. Solving the problem in time is often referred to as time integration. This can be done with a number of techniques based on finite difference approximations in time or methods derived by applying the FE concepts to the time dependance of the solution behavior.

In the sequel, we start with the presentation of the derivation of the FEM equations with a discretization in space only. In a second step we introduce the discretization in time. The derivations below follow the derivation in [47], which is one of the major references where the details of the FEM can be found.

8.2.4.1 Formulation of the FEM with Space Discretization

For the sake of the notation simplicity the variable t is omitted in this section. The problem to solve is: determining a set of unknown functions collected in the vector $\mathbf{u}$ such that it satisfies a certain set of differential equations

$$\mathscr{A}(\mathbf{u}) = \mathbf{0} \ \text{ in } \ \Omega \tag{8.18}$$

$$\mathscr{B}(\mathbf{u}) = \mathbf{0} \ \text{ on } \Gamma, \tag{8.19}$$

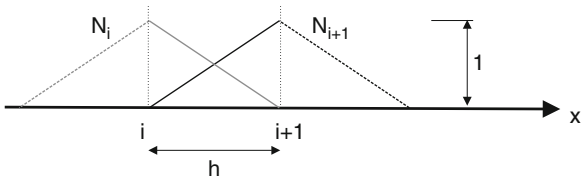

Fig. 8.2 An Example of 1D linear shape functions $N_i(x)$ defined on two consecutive elements

where the domain Ω is a volume (or surface in 2D), and Γ denotes the boundaries of Ω. Equation (8.18) are the local form of the field equations (*e.g.* Newton's law of motion (8.1)) and (8.19) are the boundary conditions. The operator $\mathscr{A}(\mathbf{u}) = [A_1(\mathbf{u})\ A_2(\mathbf{u})\ \cdots]^T$ represents the different lines of the system of partial differential equations. Similarly for $\mathscr{B}(\mathbf{u})$.

The finite element process consists in seeking the solution $\mathbf{u}$ of (8.18) and (8.19) in the approximate form (8.17). An example of a simple 1D shape function $N_i(x)$ that is linear and locally defined on two consecutive finite elements is drawn in Fig. 8.2. Denoting by $\tilde{u}_i$ the (unknown) value of the 1D displacement at node i, the shape function is defined as $N_i(x) = \frac{x-x_{i-1}}{x_i-x_{i-1}}\tilde{u}_i$ on element $[x_{i-1},x_i]$ and $N_i(x) = \frac{x_{i+1}-x}{x_{i+1}-x_i}\tilde{u}_i$ on element $[x_i,x_{i+1}]$, and is zero in the rest of the domain. As a result, the solution $u(x,t)$ is approximated on element $[x_i,x_{i+1}]$ as

$$\hat{u}(x,t) = N_i(x)\tilde{u}_i + N_{i+1}(x)\tilde{u}_{i+1},\ x \in [x_i,x_{i+1}]. \tag{8.20}$$

As the differential equation (8.18) has to be zero at each point of the domain, the following is true

$$\int_\Omega \mathbf{v}^T \mathscr{A}(\mathbf{u})\mathrm{d}\Omega \equiv 0, \tag{8.21}$$

where $\mathbf{v}$ is a set of *arbitrary* functions equal in number to the components of $\mathbf{u}$. One powerful statement follows from (8.21): if it is satisfied for *all* $\mathbf{v}$, then the differential equation (8.18) must be satisfied at all points in the domain. Similarly, we can require that the boundary conditions (8.19) verify

$$\int_\Gamma \bar{\mathbf{v}}^T \mathscr{B}(\mathbf{u})\mathrm{d}\Gamma \equiv 0, \tag{8.22}$$

for any function $\bar{\mathbf{v}}$. Finally, it is found that the integral statement that

$$\int_\Omega \mathbf{v}^T \mathscr{A}(\mathbf{u})\mathrm{d}\Omega + \int_\Gamma \bar{\mathbf{v}}^T \mathscr{B}(\mathbf{u})\mathrm{d}\Gamma = 0, \tag{8.23}$$

is satisfied for any $\mathbf{v}$ and $\bar{\mathbf{v}}$ implies that (8.18) and (8.19) are satisfied. The choice of $\mathbf{v}$ and $\bar{\mathbf{v}}$ is usually limited to bounded functions in order to avoid any infinite term in the integral. The restrictions to place on $\mathbf{u}$ depend on the order of differentiation

involved in the operators $\mathscr{A}$ and $\mathscr{B}$. For several systems of differential equations, it is possible to perform integration by part of (8.23). This leads to a more 'permissive' statement than the original problem since then a lower order of continuity is required for $\mathbf{u}$ – this statement is referred to as the *weak form* of the problem equations and is often associated with the FEM.

In the general case it is impossible to find a solution of the problem (8.18) and (8.19) in the approximate form (8.17). Fortunately an integral statement such as (8.23) allows an approximation to be made if, in place of *any functions* $\mathbf{v}$ and $\bar{\mathbf{v}}$, we use their approximations by

$$\mathbf{v}(\mathbf{x}) \approx \sum_{i=1}^{n} \mathbf{w}_i(\mathbf{x})\delta\tilde{\mathbf{u}}_i \text{ and } \bar{\mathbf{v}}(\mathbf{x}) \approx \sum_{i=1}^{n} \bar{\mathbf{w}}_i(\mathbf{x})\delta\tilde{\mathbf{u}}_i, \tag{8.24}$$

where $\delta\tilde{\mathbf{u}}_i$ are arbitrary parameters. Inserting the approximations (8.17), (8.24) into (8.23) yields

$$\delta\tilde{\mathbf{u}}_i^T \left[\int_\Omega \mathbf{w}_i^T(\mathbf{x}) \mathscr{A} \left(\sum_{i=1}^{n} \mathbf{N}_i(\mathbf{x})\tilde{\mathbf{u}}_i \right) \mathrm{d}\Omega + \int_\Gamma \bar{\mathbf{w}}_i{}^T(\mathbf{x}) \mathscr{B} \left(\sum_{i=1}^{n} \mathbf{N}_i(\mathbf{x})\tilde{\mathbf{u}}_i \right) \mathrm{d}\Gamma \right] = 0. \tag{8.25}$$

Since $\delta\tilde{\mathbf{u}}_i$ are arbitrary, (8.25) is equivalent to the set of equations

$$\int_\Omega \mathbf{w}_i^T \mathscr{A} \left(\sum_{i=1}^{n} \mathbf{N}_i(\mathbf{x})\tilde{\mathbf{u}}_i \right) \mathrm{d}\Omega + \int_\Gamma \bar{\mathbf{w}}_i{}^T \mathscr{B} \left(\sum_{i=1}^{n} \mathbf{N}_i(\mathbf{x})\tilde{\mathbf{u}}_i \right) \mathrm{d}\Gamma = 0, \text{ for } i = 1,2,\ldots,n \tag{8.26}$$

which is sufficient to determine all the unknowns $\tilde{\mathbf{u}}_i$. This equation can be interpreted as follows: if we note that $\mathscr{A}(\hat{\mathbf{u}}(\mathbf{x}))$ is the "error" due to the substitution of $\mathbf{u}(\mathbf{x})$ by $\hat{\mathbf{u}}(\mathbf{x})$, then the first integral in (8.26) is the weighted integral of the error. A similar interpretation holds for the boundary condition term. Thus the finite element process will consist in searching the coefficients $\tilde{\mathbf{u}}_i$ which make the weighted integral zero for a certain choice of functions $\mathbf{w}_i$.

Note that choosing a Dirac function for $\mathbf{w}_i(\mathbf{x})$, which value is identity at the points (x_i, y_i) of the mesh and zero elsewhere is a particular case which corresponds to a finite difference approximation. The classical choice $\mathbf{w}_i(\mathbf{x}) = \mathbf{N}_i(\mathbf{x})$, that is the same shape functions as used for the approximation of $\mathbf{u}(\mathbf{x})$ leads to the *Galerkin method* which is frequently used in practice.

For a linear system of partial differential equations where the searched function $\mathbf{u}(\mathbf{x},t)$ appears with its first and second order time derivatives (*e.g.* elastodynamics equation, wave equation), the approximated form of the equations (8.26) is after several algebraic manipulations

$$\mathbf{M}\frac{\partial^2\tilde{\mathbf{u}}(t)}{\partial t^2} + \mathbf{C}\frac{\partial\tilde{\mathbf{u}}(t)}{\partial t} + \mathbf{K}\tilde{\mathbf{u}}(t) + \mathbf{f} = \mathbf{0}, \tag{8.27}$$

where **M**, **C**, and **K** are known as the mass, damping, and stiffness matrices, **f** is the volume force vector, and $\tilde{\mathbf{u}}(t)$ is a vector that contains all the unknown functions of time (*e.g.* displacements in the three directions at all nodes of the mesh in the case of an original set of equations written for the 3D displacement). The matrices are constructed during the *assembly process* which consists in collecting the contributions of each elements to the integral equations (8.26) corresponding to the different components of **u**. In practice, the integrals are calculated over each element. Furthermore, since the shape functions are defined locally (on a few elements), usually the matrices mostly contain zeros and the non-zero terms are concentrated close to the diagonal of the matrices. This is an important aspect of the FEM: very large linear systems must be solved but due to sparsity this can be achieved at a reasonable cost with dedicated methods.

8.2.4.2 Discretization in Time

In the sequel we have substituted the notation $\mathbf{u}(t)$ to $\tilde{\mathbf{u}}$ to simplify the notations and partial derivation with respect to time are denoted with dots.

Analytical solutions of (8.27) can be obtained with respect to the time domain for a harmonic loading or if the interest is in determining the vibration modes of the system. In the general case for transient problems discretization in time is required. Several discrete time-integration algorithms are based on more or less sophisticated finite difference approximations. The so-called Newark method is a very popular one used for instance in [48]. A brief review of the numerical time-integration techniques applied to the FEM can be found in [49]. In this section we have chosen to give an account of one technique based on the FE concepts according to [47] in order to stress the specificities of the FE methods.

In a prescribed interval $[t_0, t_n]$, time is divided in time increments Δt such that

$$t_1 = \Delta t \ \cdots \ t_n = n\Delta t, \ t_{n+1} = (n+1)\Delta t \ \cdots \ t_m = m\Delta t.$$

In order to illustrate the concept of finite element time discretization, we assume that $\mathbf{u}(t_n) = \mathbf{u}_n$ and its time-derivatives are known and we present one typical single-step algorithm to calculate $\mathbf{u}(t_{n+1}) = \mathbf{u}_{n+1}$. A single-step algorithm implies a recurrence relationship involving only two consecutive time points while a multi-step algorithm can use several time points. Details and other types of algorithms can be found in [47]. Like for the finite element process applied to approximate the solution in space (see (8.23)), the starting point is the weighted integral form of (8.27)

$$\int_0^{\Delta t} \mathbf{w}(\tau)^T \left[\mathbf{M}\ddot{\mathbf{u}} + \mathbf{C}\dot{\mathbf{u}} + \mathbf{K}\mathbf{u} + \mathbf{f}\right] \mathrm{d}\tau = \mathbf{0}, \tag{8.28}$$

in which **w** is an arbitrary function. Now the time-dependence of **u** can be approximated by a certain function with unknown parameters, which will be determined by

solving (8.28). Taking the approximate form $\mathbf{w}(\tau) = W(\tau)\delta\mathbf{u}_{n+1}$, where $\delta\mathbf{u}_{n+1}$ are arbitrary parameters, leads to

$$\int_0^{\Delta t} W(\tau)\left[\mathbf{M}\ddot{\mathbf{u}} + \mathbf{C}\dot{\mathbf{u}} + \mathbf{K}\mathbf{u} + \mathbf{f}\right] = \mathbf{0}. \tag{8.29}$$

If we choose for $\mathbf{u}(t)$ a quadratic approximation in time, we have

$$\mathbf{u}(\tau) = \mathbf{u}_n + \tau\dot{\mathbf{u}}_n + \frac{1}{2}\tau^2\alpha, \tag{8.30}$$

where α is a vector of unknown parameters. Upon replacing $\mathbf{u}$ and its time derivatives in (8.29) by the form (8.30) and its derivatives with respect to τ yields after a few elementary algebraic manipulations

$$\mathbf{M}\alpha + \mathbf{C}[\dot{\mathbf{u}}_n + \theta_1\alpha\Delta t] + \mathbf{K}\left[\mathbf{u}_n + \theta_1\Delta t\dot{\mathbf{u}}_n + \frac{1}{2}\theta_2\Delta t^2\alpha\right] + \bar{\mathbf{f}} = \mathbf{0}, \tag{8.31}$$

where

$$\theta_1 = \frac{\int_0^{\Delta t} W(\tau)\tau\mathrm{d}\tau}{\Delta t\int_0^{\Delta t} W(\tau)\mathrm{d}\tau}\ ;\ \theta_2 = \frac{\int_0^{\Delta t} W(\tau)\tau^2\mathrm{d}\tau}{\Delta t^2\int_0^{\Delta t} W(\tau)\mathrm{d}\tau}\ ;\ \bar{\mathbf{f}} = \frac{\int_0^{\Delta t} W(\tau)\mathbf{f}\mathrm{d}\tau}{\int_0^{\Delta t} W(\tau)\mathrm{d}\tau}. \tag{8.32}$$

Equation (8.31) is (usually) a large system of linear equations which has to be solved to determine α at each time step. Finally the approximated displacement at $t_n + \Delta t$ is given by

$$\mathbf{u}_{n+1} = \mathbf{u}_n + \Delta t\dot{\mathbf{u}}_n + \frac{1}{2}\Delta t^2\alpha\ ;\ \dot{\mathbf{u}}_{n+1} = \dot{\mathbf{u}}_n + \Delta t\alpha\ ;\ \ddot{\mathbf{u}}_{n+1} = \alpha. \tag{8.33}$$

The choice of the weighting function $W(\tau)$ leads to a variety of different algorithms. In the frequent case where $\mathbf{M}$ and $\mathbf{C}$ are diagonal, the choice $\theta_2 = 0$ yields an explicit scheme (α can be found without the need to solve a system of equations) and can be made conditionally stable. Other choices of θ_2 lead to an implicit scheme for which stability properties depend on the choice of $W(t)$.

8.2.4.3 Concluding Remarks on the FEM

The FEM solution process can be summarized as follows:

1. Starting from the problem defined in terms of partial differential equations in the local form, the weighted integral form is constructed. These are implemented in the core of the FE programs for most common equations.
2. The type (triangles, rectangles, etc.) and order of finite elements shape functions to be used are prescribed. The user of FEM software must define these parameters. The shape functions, which are often polynomials (see (8.17)), determine

the accuracy of the calculated variable fields on each element. In a 2D problem, linear shape functions (polynomial of order one) are typically constructed from triangular elements with one node at each of the three apexes. Triangular elements with three additional nodes on the edges can be used to construct second-order shape functions. Triangular elements are more popular than rectangular elements since they are more advantageous to approximate an arbitrary boundary shape. In a triangular element of a given size, the spatial variations of the wave field can be more accurately described with second-order shape functions than with linear ones. As a consequence, the optimal size of the finite elements normally decreases with the increasing order of the shape functions. However, increasing the shape function order has a computational cost since it increases the number of nodes (not necessarily the number of elements), hence the size of the linear system to solve. The mesh of the domain Ω is constructed with prescribed constraints such as the average size of the elements. In general the mesh is not a regular grid like for the finite difference method. By default, a quite homogeneous mesh is used, *e.g.* a mesh of triangular elements with similar size and random orientation. But the mesh can also be heterogeneous: in some areas where a high precision is required, a finer mesh than in the rest of the domain can be used. Meshing of domains with complex shape may be tricky and the mesh should be optimized to prevent numerical problems during the solution process. Several commercial programs are devoted to meshing.

3. From the form (8.26), the integral on each element are computed and the terms of the mass, damping and stiffness matrix are collected.
4. For the chosen time shape functions $\mathbf{w}(\tau)$, coefficients such as θ_1 and θ_2 (8.32a,b) in the scheme presented above are calculated.
5. With the scheme presented above, at each time step: (i) the forcing term $\bar{\mathbf{f}}$ (8.32c) must be updated; (ii) α is calculated by solving the linear system (8.31), and (iii) the solution and its time derivatives (8.33) are updated.

The numerical parameters (mesh size, parameters of numerical algorithm) must be chosen such that the results be free of any numerical bias. As for the FDTD computation, the optimal mesh size (compromise between accuracy and computational cost) can be determined after a convergence study that consists in refining the mesh until the results converge to a stable solution. Contrarily to the user of most FDTD codes, the user of a FEM code will be asked to choose the order of the spatial shape functions. When possible, the implementation should be validated by comparison of computation outputs with available reference solutions (from validated codes or analytical solutions).

In practice, applying the FEM involves using a pre-processor, a solver, and a post-processor. These may be three independent softwares or a single software with three modules. After the geometry has been defined, the pre-processor builds the system of equations to be solved. Here the main operation which requires user interaction is meshing. The solver applies the chosen algorithm which essentially consists in solving the system of linear equations. Elaborated methods for linear system solving are implemented in the finite element software packages. The user may choose the solver best adapted to the type of system at hand (symmetric matrix or not, more or

less sparse matrix, etc.). With a given mesh, the efficiency (memory requirement, computation time), the convergence, the stability and the precision depends on the algorithm for time-domain solving, the choice of the basis functions (space and time), and the method used to solve the linear system. The post-processor is used to visualize the results and in some cases compute complementary quantities from the FEM solution (energy, von Mises stresses, etc.).

8.2.5 Case Study

In this section, we illustrate the implementation of a numerical model on a simple case representing the interaction of a wave generated by a point source in a medium representing soft tissue with a medium representing cortical bone (Fig. 8.3). Both FDTD and FEM methods are suitable to simulate this problem. The implementation is presented in details for the FDTD approach. Then the specificities of a FEM implementation are pointed out.

8.2.5.1 Geometrical and Material Configuration

The geometry of the problem is shown in Fig. 8.3. It consists of two linear elastic homogeneous half-space media separated by a plane interface. The upper medium Ω_1 represents soft tissue and the lower one Ω_2 represents bone. Medium Ω_1 has a fluid-like behavior in which only longitudinal waves can propagate. Medium Ω_2 has a solid-like behavior in which both longitudinal and shear waves can propagate. Both media are isotropic. At the interface $\partial\Omega$, the normal displacement (and velocity) and normal stresses are continuous. The position is specified through the Cartesian

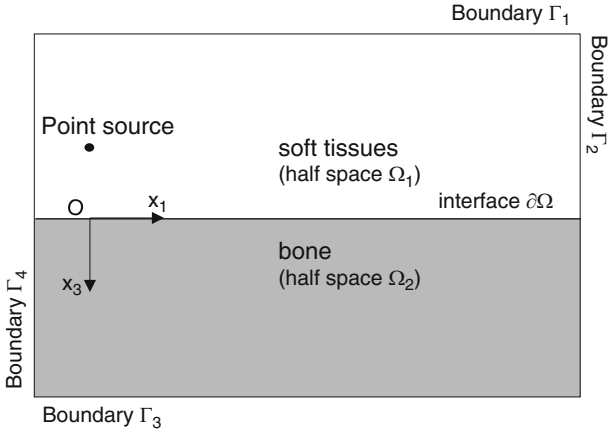

Fig. 8.3 Geometrical configuration to investigate wave reflection at the soft tissue-bone interface

Table 8.2 Specific parameters used for the implementation of the case study

Parameter	Value
Mass density in Ω_1	$1.0\,\mathrm{g/cm^3}$
Acoustic velocity in Ω_1	$1.5\,\mathrm{mm/\mu s}$
Mass density in Ω_1	$1.85\,\mathrm{g/cm^3}$
Compressional velocity in Ω_2	$4\,\mathrm{mm/\mu s}$
Shear velocity in Ω_2	$1.8\,\mathrm{mm/\mu s}$
Pulse center frequency	1.5 MHz
Pulse -6 dB bandwidth	92%
Source-interface distance d	4 mm
Source-receiver distance	16 mm

coordinates (x_1, x_2, x_3) with respect to a Cartesian reference frame $\mathbf{R}(O; \mathbf{x}_1, \mathbf{x}_2, \mathbf{x}_3)$ where O is the origin of the space and $(\mathbf{x}_1, \mathbf{x}_2, \mathbf{x}_3)$ is an orthonormal basis of this space. The x_3-axis is chosen downwards and normal to the fluid-solid interface. Domains Ω_1 and Ω_2 are defined as the half-spaces $x_3 < 0$ and $x_3 > 0$, respectively. The plane interface $\partial\Omega$ has the equation $x_3 = 0$.

Time coordinate is denoted by t. The fluid and the solid are at rest for $t < 0$. At $t = 0$, a line source parallel to $(O; \mathbf{x}_2)$, placed in the fluid at a distance d from the interface, generates a pulsed cylindrical wave. In the plane $(O; \mathbf{x}_1, \mathbf{x}_3)$ of interest for this study, the source appears as a point source S. Due to the nature of the source and to the geometrical configuration, the transverse waves polarized in the $(\mathbf{x}_1, \mathbf{x}_2)$ plane are not excited. The acoustic response in Ω_1 is sought in terms of pressure amplitudes $p(t)$ at the point receiver $R(x_R, -d)$. This source and receiver configuration is typical of the device used in the ultrasonic axial transmission technique for the evaluation of the cortical shell.

An exact analytical solution in the time-domain exists for this configuration [50, 51]; the expression of this solution can also be found in [52, 53] where it has been used to simulate wave reflection on a bone surface. The solution is available in a semi-analytic form, namely a closed-form analytic Green's function convolved with a function describing the source history. This solution can be found on-line as additional material. The synthetic signals obtained with the latter can serve as a reference to which computed signals can be compared, and allow an analysis of the convergence of the numerical solution to the exact solution. For the numerical implementation described below, the parameters are gathered in Table 8.2.

8.2.5.2 Implementation

The first step in implementing a FDTD computation is to determine the spatial (h) and temporal (Δt) discretization steps. This crucial step is however rather subjective, as it depends on the acceptable error on some arbitrary criteria. The spatial step is usually chosen first, to corresponds to some number of points per shorter wavelength involved in the various media, typically ranging from at least ten to several tens. As can be seen from the results presented further below in Fig. 8.4, spatial step sizes

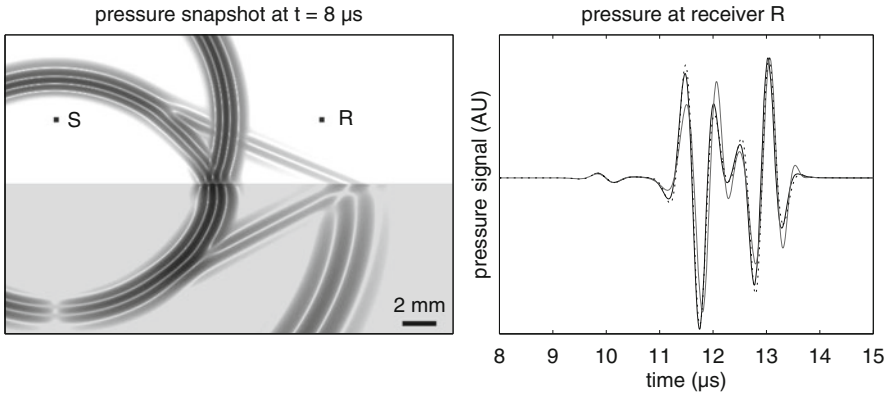

Fig. 8.4 *Left*: Snapshot of the wave field computed with the FDTD method showing the incident, reflected and transmitted waves (shear and longitudinal). The straight wave fronts are the lateral waves. Letters S and R denote the positions of the emitter and the receiver, respectively. *Right*: synthetic radio frequency signal corresponding to the pressure measured at R. The discontinous line is the exact solution (analytical formula), the gray and dark lines are the pressure history calculated with the FDTD method using $h = 0.05$ mm and $h = 0.025$ mm, respectively. The first arriving signal corresponds to the lateral wave front propagating in the fluid medium

$h = 0.05$ mm and $h = 0.025$ mm, corresponding respectively to 20 and 40 points per wavelength at 1.5 MHz in the fluid (that has the smallest velocity), give different results. A discussion on the different types of wave observed on Fig. 8.4 can be found in various references [14,52–54]. A practical way to check whether the spatial step is chosen small enough is to compared the results obtained with this step to the results obtained with a smaller step (for instance twice smaller): the step size may be considered correct if both sets of results may be considered within the acceptable error. Once the spatial step is chosen, the temporal one is derived from the CFL condition (see Sect. 8.2.3). When an exact analytical solution is available, a direct comparison can be made to estimate the errors caused by the numerical scheme. Here, the comparison with the analytical solution to the case study (see Fig. 8.4) indicates that $h = 0.05$ mm and $h = 0.025$ mm are both satisfactory as far as predicting times of flight is concerned, but indicates that a step size $h = 0.05$ mm yields errors on the order of 25% for the amplitude of the direct and reflected waves, whereas those errors decrease to less than 5% with $h = 0.025$ mm. On the other hand, $h = 0.05$ mm is sufficient to predict the amplitude of the first arriving signal within a few percent. This example illustrates that the errors are strongly dependent on the phenomena of interest, and that care must be taken when analyzing results accuracy.

In the present case, for which we used a 2D algorithm based on the Virieux scheme (see for instance [43]),[4] (8.16) holds and indicates that a maximum time step of about 8.8 ns (resp. 4.4 ns) with $c_{max} = 4$ mm/µs is necessary to ensure stability for $h = 0.05$ mm (resp. $h = 0.025$ mm). This corresponds to a sampling frequency of about 115 MHz (resp. 230 MHz), *i.e.* about 75 (resp. 150) temporal steps per

[4] http://www.simsonic.fr

period at 1.5 MHz. Note that a large difference between the smallest and the largest velocity values in the simulation box leads to a large difference between the number of temporal steps per period and the number of spatial steps per shorter wavelength. Such a situation always occurs when both soft tissue and bone are present simultaneously in a simulation. The 'imbalance' between temporal and spatial discretization that occurs in the case of large contrasts between velocities usually requires a finer discretization compared to the case of a small velocity fluctuations (such as for soft tissue alone for instance). It explains why the amplitude of the first arriving signal (propagating with the velocity $c_{max} = 4$ mm/μs) is better predicted than the amplitude of the direct and reflected wave (propagating at $c_{fluid} = 1.5$ mm/μs). This combined with the very large signal bandwidth also explains why a spatial discretization of 40 steps per shorter wavelength is necessary to predict wave amplitudes within a few percent. Let us mention the possibility to avoid such imbalance by locally adapting the spatial discretization to each media, but this leads to quite complex numerical schemes [55].

Once both the spatial and temporal steps are defined, one can describe the simulation box and the source, which are the key input data to be provided by a user to perform the FDTD calculation. A 15 mm $\times$ 20 mm simulation box, was described by a 300×400 points (resp. 600×800) map at $h = 0.05$ mm (resp. $h = 0.025$ mm) with only two values representing the fluid and the solid media. Material properties (elasticity constants, mass density) must be associated with each value of the map, to be used in the computation. Note that one could also provide as many maps as there are parameters, but this approach is not optimal in term of memory requirement for the case of two homogeneous media. As the Virieux scheme involves staggered grids, averaged properties values are usually computed when material properties are needed at staggered location relatively to the map points on which the map is defined. Such averaging is required to obtain a correct treatment of the interfaces between different media in the Virieux scheme [56]. One key advantage of the FDTD method with the Virieux scheme is that the various media in presence are simply accounted for by giving a bitmap image of the media, without explicitly stating boundaries location or type of media in presence (fluid or solid). On the other hand, complex shapes are defined on a regular grid with the resolution of the grid ('staircase' effect). The plane interface in the current case is optimum as no 'staircase' artifacts are produced. Perfectly matched layers were used on the four boundaries around the simulation box [44]. The source was defined as a point source by adding a *source term* to the discretized lossless version of (8.3) at one point located 4 mm away from the interface. Such a source term is given as a function of time, *sampled* with the temporal time step chosen above.

Once specified the total number of time steps to compute, the simulation may be started. Two types of results, snapshots or signals, may be recorded during the computation for later analysis, as discussed in Sect. 8.2.3: Fig. 8.4 shows both the magnitude of the velocity field computed at time $t = 8\,\mu s$ (derived from the fields v_x and v_y) and the pressure as a function of time recorded at location R. Multimedia movies of this case study can be downloaded on-line as additional material.

While the precise computational cost depends on both the numerical scheme and its practical implementation, the FDTD computation corresponding to our

implementation discussed above required approximately 10 MB of RAM and took on the order of 5 min on a laptop computer for $h = 0.05$ mm, and 40 MB of RAM and took on the order of 40 min on a laptop computer for $h = 0.025$ mm. To further give orders of magnitude, the equivalent 3D simulation with a $15 \times 15 \times 20\,\text{mm}^3$ simulation would take approximately 2 GB of RAM and about one day for $h = 0.05$ mm, and 16 GB of RAM and about a couple of weeks for $h = 0.025$ mm.

A typical FDTD implementation can be summarized as follows:

1. Chose the appropriate spatial and temporal steps. This may be adapted depending on initial results.
2. Provide maps of the material properties involved in the simulation box.
3. Define sources (or initial conditions).
4. Define results to be recorded: snapshots of field variables at some chosen instants and/or signals recorded at chosen location.

A complete FDTD implementation of this case study using Simsonic, including multimedia results and tools to prepare and analyze the input and output files, can be freely downloaded on-line.[5]

A FEM implementation of a configuration similar to that sketched in Fig. 8.4 was used in [15]. As opposed to the FDTD Virieux scheme, the latter uses different formulations of the basic equations for the fluid and solid parts: the acoustic wave equation (8.6) must be satisfied in medium Ω_1 and the elastodynamics wave equation (8.7) must be satisfied in medium Ω_2. As a consequence, the field variables are the pressure $p(\mathbf{x},t)$ in Ω_1 and the displacement $\mathbf{u}(\mathbf{x},t)$ in Ω_2. At the interface $\partial\Omega$, the continuity between the two media is enforced by requiring that the particle displacement in Ω_2 and the pressure in Ω_1 satisfy Euler equation of motion

$$\rho \frac{\partial^2 u_3}{\partial t^2} = -\frac{\partial p}{\partial x_3}, \tag{8.34}$$

where ρ is the fluid mass density. This implementation of the case study has the advantage to use an exact representation of the interaction of the acoustic fluid and the solid at the interface. The situation is slightly different than the FDTD implementation in which the interface in not defined explicitly: the FDTD numerical scheme performs an averaging of the fluid and solid properties at the interface. This however has no consequence on the validity of the computations if the grid is fine enough as mentioned above (see comparison with exact analytical solution). With the FEM, the average element size of the meshes in the fluid and solid parts can be different to account for the different wavelengths. This may be an advantage to optimize computation costs. The problem was implemented in Comsol Multiphysics and a time-domain solver adapted to the formulation was chosen. The FEM implementation yields the same wave field and synthetic radio-frequency pressure signal at the receiver than the FDTD implementation.

[5] http://www.simsonic.fr

Another implementation of the FEM method presented in [48] is also relevant to solve the case study. The formulation uses the same equations as the FEM implementation in [15] but takes advantage of the invariance of the configuration in direction $\mathbf{x}_1$: a 1D spatial Fourier transform is performed for the direction $\mathbf{x}_1$ which introduces the Fourier parameter k_1. Then the weak form of the problem equations are constructed and the spatial discretization is only performed in direction $\mathbf{x}_3$, which is very efficient from a computational viewpoint. A time-domain solver yields the solution in the k_1-x_3-time space. Finally an inverse Fourier transform yields the result in the space-time domain. The two FEM implantations briefly described here are only two possibilities among several options available in commercial FEM codes. An introduction to advanced methods to solve wave propagation in elastic media can be found in [13, 57].

8.3 Literature Review

In this section, we illustrate how numerical approaches have been applied to the ultrasonic characterization of bone. While the references list has been made as exhaustive as possible, our objective here is to illustrate the power of numerical modeling rather than providing a detailed discussion of all studies. In particular, we focus on the rationale for numerical modeling in various situations, rather than on results, most of which are discussed in other chapters of this book (see for example Chaps. 6, 8, 11, and 14). Beside bone characterization, numerical simulations of ultrasound propagation in bone have also been performed to study various propagation effects such as focusing through bone. The discussion of related publications ([58, 59] for instance) is out of the scope of this chapter.

8.3.1 Numerical Methods to Interpret QUS Experiments

A first key benefit of numerical modeling based on the FDTD or FEM methods is the better understanding of complex propagation phenomena that such methods can involve. In many experimental situations, the very origin of the measured signals has often remained poorly understood until numerical modeling provided new insights.

8.3.1.1 Cortical Bone

Numerical modeling was first applied to transverse transmission to elucidate propagation paths through human phalanges [60], as part of an experimental study: 2D FDTD was used to analyze ultrasound pathways through an idealized ring geometry and identify in the measured signal two contributions from waves traveling through the medullary canal and the cortical shell. FDTD was also applied to model the axial

transmission technique on the diaphysis of long bones such as the radius. The first simulation studies were limited to 2D models in which the bone was simply modeled by an elastic isotropic plate [3,14]. It was demonstrated that the nature of the first arriving signal (FAS) depends on the cortical thickness to wavelength ratio: for some range of transmitter–receiver distances, the FAS corresponds to a lateral wave for thickness larger than the wavelength and to a S_0 Lamb wave for thickness less than a quarter of a wavelength. Three-dimensional (3D) FDTD simulations then supplemented these findings by demonstrating that no significant differences exist between plate models (2D) and tube models (3D) as far as the FAS is concerned [4]. Even for simple 2D model geometries such as plates, analytical approaches such as Lamb waves theory cannot always be used to predict experimentally observed phenomena: for intermediate thicknesses, the FAS results from complex interferences between different modal contributions, and direct predictions from Lamb wave theory do not correspond to measured or simulated velocity and attenuation results [17].

The simulations discussed above have been performed on nominal model geometries, such as plates or tubes. However an important asset of FEM and FDTD based simulations is the possibility to use individualized geometries, derived from the measurement of a bone specimen with X-ray computed tomography (CT) technique or magnetic resonance imaging (MRI). Figure 8.5 shows a 3D cortical bone volume obtained from an X-ray CT reconstruction and a snapshot taken from a 3D FDTD simulation performed with this volume as input geometry. Such simulations on realistic bone structures confirmed earlier results obtained on idealized geometries, but in addition provided direct comparisons of experimental and simulated measurements performed on a same set of samples. Such comparisons are necessary to validate simulation approaches when the simulations are expected to provide realistic simulated signals. Another cortical bone site of major interest for QUS measurements is the femur neck. A 2D simulation study using individualized femur neck cross-sections geometries and nominal material properties established that the early arriving signal observed in experiments is associated to the propagation of a guided wave in the cortical shell [19].

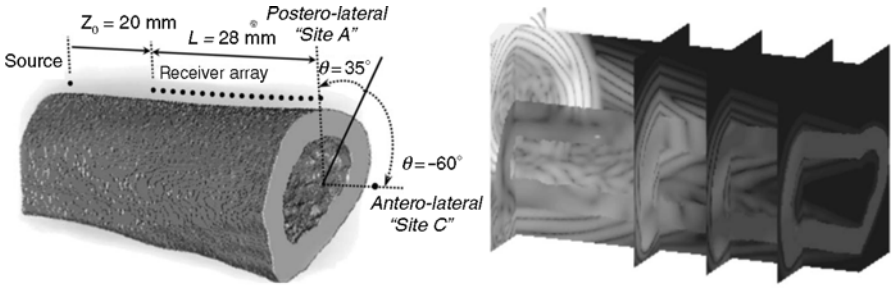

Fig. 8.5 *Left*: digitized cortical bone geometry derived from X-ray computed tomography. *Right*: 3D snapshot obtained from FDTD calculations, illustrating guided wave propagation along the cortical shell. Reprinted with permission from [21]. Copyright 2007, Acoustical Society of America

Besides providing information on the nature of the measured signals in the case of complex cortical bone geometries, numerical simulations can also be used to understand the effects of heterogeneities such as gradients of mechanical properties on the measurements. For instance, both FDTD [4] and FEM [15] simulations have been performed to derive an equivalent contributing depth to the lateral wave, observed in the case of thick cortical shells investigated by axial transmission. Numerical simulations have also been used to interpret signals measured when ultrasound propagates across simple model fractures in cortical bone [16, 61]. Resorting to numerical simulation is necessary even for fractures modeled as simple gaps between intact cortical parts. More details on the guided wave theory can be found in Chap. 7 and on propagation in cortical bone in Chap. 13.

8.3.1.2 Trabecular Bone

In trabecular bone, the complexity arises rather from the media than from the type of wave measured. Most often, measured signals indeed correspond to the contribution of quasi-plane wave either transmitted through or backscattered by the trabecular structure. Numerical modeling is the sole approach that allows taking into account the exact geometry of trabecular bone, untractable by analytical approaches. Figure 8.6 illustrates the propagation of a quasi-plane wave into trabecular bone. The first study of ultrasound propagation in bone with numerical simulation were actually 2D FDTD calculations performed on slices of trabecular bone obtained by X-ray computed micro-tomography [25]. Although these simulations were 2D, and could therefore not describe the full complexity of three dimensional propagation in trabecular bone, this first work paved the way for 3D studies to come a few years later. Using 3D maps of trabecular structures, various phenomena observed experimentally have been reproduced by FDTD calculations [1], further confirming the relevance of numerical approaches: in the MHz range, simulated attenuation was

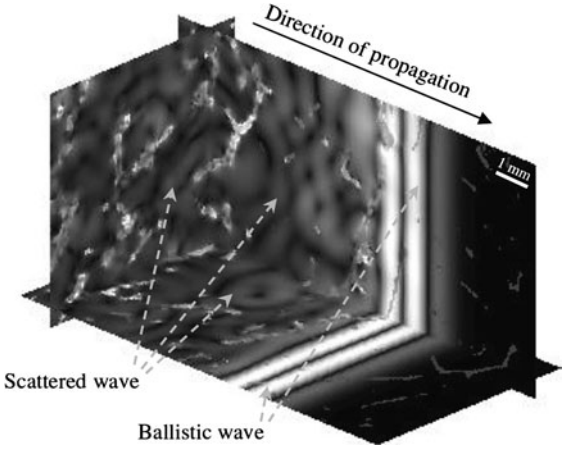

Fig. 8.6 3D snapshot obtained from FDTD calculations, illustrating the propagation of a quasi-plane wave through trabecular bone. The trabecular bone geometry was derived from high-resolution synchrotron computed micro-tomography. Reprinted with permission from [1]. Copyright 2005, IOP Publishing Limited

found to vary linearly with frequency and negative velocity dispersion was observed in some cases. The observation of two compressional waves, commonly referred to as the fast and slow waves, was also simulated for appropriate alignments [1, 2]. Numerous FDTD simulations have then been performed to investigate and better understand various parameters that influence the measured signals. In [1], the importance of mode conversion from compressional to shear waves has been emphasized by comparing simulations results obtained in solid and fluid bone models. Such a study cannot be undertaken experimentally, and illustrates a situation where numerical modeling is the only possible approach. Several numerical studies have been conducted to better understand the origin and propagation of the fast and slow waves observed in some situations. Not only are some types of results reachable only through simulations, such as snapshots of the two waves propagating inside trabecular bone, but simulations also allow changing and controlling parameters with a unique flexibility: some bone properties may be changed on a given numerical sample while maintaining other constants, while in experiments with real bone samples, several samples have to be used to vary the properties, most often all varying simultaneously. In [62], a condition to observe two non overlapping fast and slow waves, given by a relationship between the bone volume fraction and the degree of anisotropy, was proposed based on a large number of simulation results obtained by controlling the bone volume fraction through numerical erosion procedures. In [63], the authors used FDTD numerical simulations in conjunction with experimental results to show that the attenuation of the fast wave is higher in the early state of propagation in trabecular bone. A direct comparison of simulated and experimental measurements has also been performed in trabecular samples [64, 65]. The fact that absorption was not taken into account in the numerical model was assumed to be responsible for the differences in simulated and experimental values, and used to discuss the relative contributions of absorption and scattering to the total attenuation.

8.3.2 Parametric Studies

As discussed in the previous section, numerical modeling is a valuable tool to better understand the nature of the waves propagating in bone. But it is also a fundamental tool to determine and understand the bone properties involved in QUS measurements.

On the one hand, numerical simulations can be used to model and understand the experimentally observed dependence of QUS measurements on bone properties. For instance, several simulation studies in cortical bone demonstrated the dependence of axial transmission measurements on cortical thickness [3–5, 14, 21]. In this case, simulation approaches have the advantage over experimental approaches that both nominal geometries and individualized geometries can be studied, and that cortical thickness can be varied while keeping all other parameters constant. Several numerical studies of the axial transmission technique have also been conducted in

the context of fracture healing. The first study consisted of 2D FDTD simulations of wave propagation through models of fracture [16, 61], to help understanding the interaction of the lateral wave or guided Lamb waves with the fracture site. Based on an idealized healing process, it was shown that the velocity of the first arriving signal increased during the various healing stages, but could not reflect changes in callus geometry [16]. In [61], the effect of a model fracture on the peak amplitude of the measured signal was studied, and results interpreted with the aids of 2D snapshots from the simulations. Modeling the different healing stages in further 2D simulations, it was then suggested that the change in signal amplitude with the callus geometry and elastic properties could potentially be used to monitor the healing process [66]. With the objective to study the sensitivity of the lateral wave or guided waves to fracture healing, more realistic models have then been conducted using 3D FEM [20, 67]. Guided waves were shown to be sensitive to material and geometrical changes that take place during healing [20, 67], and it was suggested that different combinations of guided waves could be used to evaluate the healing process at different stages [20]. It was also shown that the dispersion of guided waves was significantly influenced by the irregularity and anisotropy of the bone. This conclusion was similar to that drawn in [21], where it was shown using 3D FDTD simulations that modeling the natural variability in bone geometry played a major role in modeling physical experiments. These conclusions further illustrate the necessity to resort to numerical simulations conducted on realistic geometries in order to model real experiments. Figure 8.7 shows the model geometry used in [67] and gives a typical example of a FEM mesh. FEM was also used to infer the possible changes in guided waves behavior due to modification in human mandibles [68]: a single sample was used, and osteoporotic bones were simulated by reducing the thickness of the cortical bone and changing the density and elastic constants of the trabecular bone.

On the other hand, numerical modeling is also a powerful tool to investigate the influence of some bone properties *independently*, whereas experimental approaches

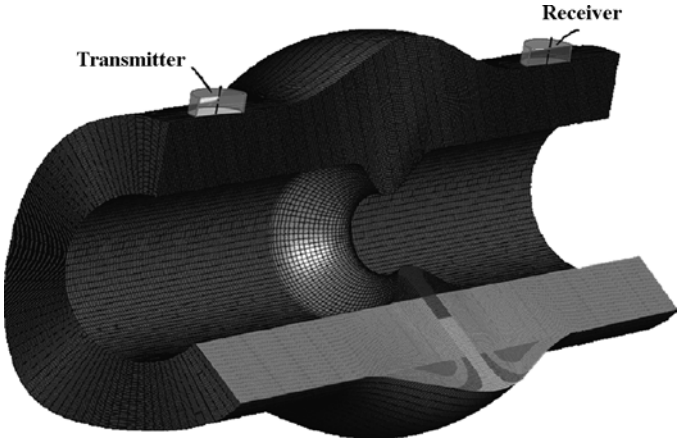

Fig. 8.7 3D FEM mesh used to describe a model of cortical bone with a healing fracture. Reprinted with permission from [69]. Copyright 2008 IEEE

usually have to deal with interdependent bone properties. On trabecular bone, realistic 3D bone structures obtained from X-ray computed micro-tomography have been used in numerical simulations to elucidate bone properties that influence QUS measurements. In contrast to experimental approaches, bone properties can be varied independently from one another. In [1], simulated broadband ultrasonic attenuation values were shown to correlate strongly with bone volume fraction, for *fixed* bone material properties. The sensitivity of broadband attenuation and speed of sound in response to differences in bone strength was investigated by varying independently the bone volume fraction and the material elastic properties [70]. In [71], it was concluded based on simulation results that the amount and quality of bone marrow significantly influence the acoustic properties of trabecular bone, and consequently suggested that inter-individual variability in the composition of bone marrow may increase uncertainty in clinical applications. Although these last results are in contradiction with recent experimental results [72] for yet unexplained reasons, numerical simulations remain a powerful modeling tool to help understanding experimental results.

8.3.2.1 Sensitivity of Ultrasound to Bone Properties

In addition to help elucidating the bone properties that influence ultrasound measurements, numerical modeling has also been used to quantitatively study the sensitivity to such properties. As discussed above, numerical modeling is particularly appropriate for such studies, as several parameters may be controlled independently from one another. Moreover, processing of the numerical bone structure can be performed to simulate physiological changes such as decrease in bone mass. Numerical modeling in this case is not only a surrogate to experimental approaches but also a unique tool allowing virtual experiments that fundamentally are not possible in the real world. Using a set of 3D bone structures derived from X-ray synchrotron micro-tomography, FDTD simulations have been used to study the sensitivity of ultrasound parameters to several bone properties [46, 73]: various numerical scenarios of virtual osteoporosis were implemented by data processing algorithms (such as erosion procedures) that modify the bone structure or/and by changing the bone density and the bone elastic constants. It was shown that bone alterations caused by variation in the bone volume fraction were predominant on broadband ultrasonic attenuation and speed of sound, although material and structural properties also play a role [46]. Numerical modeling is the only way to independently assess the effects of bone properties on QUS parameters in this case, as the bone properties in real samples are strongly intercorrelated. In addition, numerical processing allows the investigation of a much larger region in the parameters space, unaccessible with usually small sets of samples. Similar approaches were used to study the influence of bone volume fraction and structural anisotropy on the fast [62, 74] and slow [74] wave propagation.

In cortical bone, the sensitivity of axial transmission QUS measurements to cortical thickness was quantitatively assessed by use of FDTD simulations on both model geometries and realistic geometries obtained from X-ray computed tomography. Not

only were the simulations used to assess the sensitivity of QUS measurements to cortical thickness, but also to better understand cortical thickness estimates derived from both experimental and simulated measurements [5, 21]. FDTD simulations have also been used to validate stochastic approaches aimed at identifying the random anisotropic elasticity tensor from measurements [75]. In the context of bone healing, the effect of various stages of fracture healing on the amplitude of 200 KHz ultrasonic waves propagating in a bone plate across an idealized fracture has been modeled numerically using 2D FDTD simulations [66].

8.3.3 Models Assessment

While numerical modeling is particularly appropriate, if not the only method, to solve wave propagation in realistic bone models, it is also a relevant tool to assess propagation models themselves. Such models may assume simplified bone geometries or new model equations for effective homogenized media. In this context, numerical simulations can be used either to assess and validate alternative models better suited to analytical description, often associated to deeper physical insights, or to solve wave propagation in simplified models which remain untractable analytically.

In cortical bone, plate or tube models were extensively studied by use of numerical modeling, as discussed in Sect. 8.3.1.1, and validated as valuable models for specific situations. The importance of taking into account soft tissue loading in the modeling of axial transmission has also been demonstrated using numerical simulations [76, 77]. Propagation in trabecular bone has been modeled numerically with various bone models based on a simplified description of the propagation medium. In [78], the trabecular structure was analyzed using 3D X-ray microcomputed tomography, and simplified by regularly arranging spherical pores in a solid bone matrix. Trabecular bone structures have also been numerically generated with Gaussian random fields having first and second order statistical properties identical to those experimentally measured, and used to compute attenuation coefficient from FDTD simulations of through transmission measurements [79].

Numerical modeling was also used to solve wave propagation in effective bone media, such as described by the Biot's theory for instance. 2D FDTD computations based on the Biot's equation were used to analyze the propagation of the fast and slow waves in trabecular bone [26, 27]. Two-dimensional FEM was used to solve wave propagation in trabecular bone described by the anisotropic Biot's theory immersed in a standard acoustic fluid [28].

8.3.4 Multi-Scale Approaches

Numerical modeling can be performed at several scales, as illustrated in the previous paragraphs. Moreover, it can also couple results obtained at different scales.

Many effective properties can be defined at the macroscopic scale, which depend on microscopic properties. For instance, modeling ultrasound propagation in cortical bone in the MHz range over whole bone samples requires such effective elastic constants as input parameters. Numerical simulations can actually be used both to determine some effective constants and/or to compute solutions in models requiring such effective parameters, by performing simulations at different scales.

FDTD has been used to derive effective anisotropic elastic constants in cortical bone by simulating through-transmission velocity measurements based on cortical bone samples described at the microstructural scale, using either modeled [4] or real [33] geometry to describe the cortical microporosity. Such effective constants can then be used as input parameters in simulations performed on samples described macroscopically. FEM simulations performed at different time scales can both provide macroscopic effective constants and simulate ultrasonic propagation: using FEM in the static regime with an X-ray based microscopic description of trabecular bone structure and FEM in the MHz range, several studies compared computed effective Young's modulus and computed quantitative ultrasound parameters [80, 81]. The two sets of values computed at different scales were then analyzed as for experimental results. Such numerical studies mimic the corresponding experimental approaches, but provide a complete control of all the numerous parameters, and help determining the most relevant properties. In [70], the authors compared simulated QUS parameters obtained using FDTD with macroscopic effective constants derived from a cellular model.

8.4 Conclusion

Numerical models of quantitative ultrasound experiments are a fantastic source of knowledge. The calculated model response in various configurations (geometry, material properties, emitter–receiver configuration) shed light on the behavior of the real system. The basic physical processes at work and the sensitivity of ultrasound to bone properties can be analyzed in details. The introduction of numerical methods in the field of QUS in the 1990s has increased the possibilities of modeling. Versatile computer codes are available which enable to investigate several configurations with a moderate effort. The purpose of this chapter was to review the use of numerical modeling in QUS until today and provide the reader with a basic understanding of the methodology and theory for numerical modeling.

Given the potential of numerical codes and the availability of high-resolution 3D images of bone structure, there may be a temptation to build very detailed models using all the available information. In fact the action of modeling does not precisely consist in building the most faithful image of the real system; modeling rather consists in intelligently choosing the relevant features of the physical experiment to model, in order to account for and mimic a given phenomenon or set a of phenomena. The first thing to decide may be the level of details to include in the model: a nominal model must retain only little details otherwise it may not be representative of most systems; in contrast an individualized model must account for the details

which make the specificity of the sample at hand. If one specific question is to be addressed by the model, the best model will probably be one specifically designed for the aimed purpose, which only accounts for the features that should be relevant; spurious details can considerably increase the complexity of the model response and blur the useful information. While choosing the details to include in a model, one may question the consistency of the modeling: is it meaningful to use a highly precise geometrical model of one specimen if its mechanical properties are not known and must be set to nominal values? The features to include in a model should be carefully selected by the physicist based on *a priori* knowledge on the problem. Hopefully the literature review and the list of references in this chapter will help the reader in this task.

The response of a model may be flawed due to: (i) model assumptions and (ii) numerical errors. In order for the results to be interpreted on a physical basis, the numerical errors should be minimized; in practice the main numerical parameters (mesh size, time step, order of the finite element or finite difference approximations, etc.) are chosen such that the numerical error estimated in a simple configuration is below a reasonable threshold. If an analytical solution is available for a problem simpler but similar to the problem of interest, this can help optimize the choice of the numerical parameters. Most often, error estimates are not directly available. However, they can be estimated by comparing results obtained with significantly different discretization steps: if the difference between results is smaller than the acceptable error, one may consider the larger discretization steps to be acceptable. In other words, it is crucial that simulation results be independent of parameters related to the numerical method, within the acceptable error. While this may not be necessary when a comparison with either analytical or experimental results is available, it is fundamental that pure simulation results can be assessed in terms of sensitivity to numerical parameters. So far, such assessments have usually not been performed in the published works in bone QUS (see [71] as an exception), and should be taken into account in future works. The QUS problems tackled with numerical techniques have used exclusively FDTD or FEM methods. In the large majority of the paper cited, the use of FDTD rather than FEM appears to be essentially explained by the availability of a software in a laboratory or cultural preference of the authors. As a matter of facts, for the precision required in QUS applications, both methods can be used indifferently in most cases. The main issue for the choice between one or the other method is probably the discretization of the domain: FEM discretization is intrinsically adapted to complex domain shapes while standard FDTD requires regular grids. This however has not appeared to be a limitation of FDTD in practical applications to bone.

Model assumptions are intrinsic to the idealization process and can be estimated through comparison with experiments. Note that one danger of numerical simulation is to focus on some phenomena which are observable in the simulations but for various reasons cannot be observed on real bones due to the intrinsic limitations of the model. Models should be validated as early as possible in the modeling process. Typically, one may start comparing the model response with experiments for simple geometries (*e.g.* plates or tubes) and known material properties before undertaking validation on bone.

The essence of QUS is to obtain indicators of bone status, typically bone strength for the diagnosis of osteoporosis, or fracture gap properties for the monitoring of healing. About ten years after the introduction of numerical simulation in QUS, and the publication of more than fifty papers in the field, one may wonder to which extent numerical methods have contributed to establish existing QUS methods or develop new ones. Obviously, there has been a forward leap in our understanding of the physics of wave propagation in cortical as well as trabecular bone. The dependence on cortical thickness of the type of wave corresponding to the first arriving signal in the axial transmission configuration is a good example for cortical bone. The importance of the orientation of the trabecular network on the possibility to observe both the Biot's slow and fast waves is a good example in trabecular bone. One of the reasons why understanding the physics is highly important is because it helps to formulate a clear, although often complicated, physical explanation to our measurements. This is required for the penetration of QUS in the clinics since QUS researchers must be able to provide such explanation. A QUS technique needs to be sensitive to one or several indicators of bone status. Several authors have used numerical simulations to try quantifying the sensitivity of ultrasound to some bone properties. Simulation is especially useful toward this goal since it allows to test various emitter–receiver configurations and signal processing, parameters on which the sensitivity is critically dependent. Once the sensitivity to a bone property is established based on a model, it is likely that this property may actually be measured *in vivo*, provided the model is realistic enough.

QUS indicators of bone status are in most cases numbers which cannot be related in a simpler manner to physical bone properties. For instance the time of flight and attenuation measured in a through transmission configuration at the heel or the proximal femur do not give a specific information on the properties of trabecular and cortical bone (inter-trabecular spacing, thickness, elastic properties, material density, etc.), although strongly correlated to some of these properties. It is likely that the *in vivo* measurement of some properties of trabecular and cortical bone would yield better indicators of bone status. Because ultrasound propagation in bone is so complex, it is usually impossible to derive a straightforward one-to-one relationship between ultrasound signals and bone properties. In a few cases models have been used to derive such relationships with simplifying assumptions [5, 21]. In cases where several properties have a coupled effect on the signal (bone thickness and elasticity for instance) it is unlikely that one-to-one relationships can be derived. Instead a model can be incorporated in an inverse problem algorithm [75]. In the inverse problem approach, the bone parameters to measure may be assimilated to the model parameters. Then bone properties can be found after the optimization of model parameters so that the model response matches the experimental response. For the inverse problem approach, numerical simulation can be useful at two stages: (i) to design the best 'forward model' to be incorporated in the inverse problem algorithm, *i.e.* with the minimum number of parameters; (ii) if the forward model is so complex that the synthetic response cannot be calculated with an analytical method, a numerical method of solution will be used to solve the forward problem in the optimization process. The sensitivity analyses already conducted by various authors

pave the way for the design of 'good' forward models. With the increasing power of desktop computers, solving inverse problems based on numerical models will be a realistic option in a near future.

Acknowledgements The authors are grateful to Lucie Fréret for providing helpful comments and suggestions.

References

1. E. Bossy, F. Padilla, F. Peyrin, and P. Laugier, "Three-dimensional simulation of ultrasound propagation through trabecular bone structures measured by synchrotron microtomography", Physics in Medicine and Biology **50**, 5545–5556 (2005).
2. Y. Nagatani, H. Imaizumi, T. Fukuda, M. Matsukawa, Y. Watanabe, and T. Otani, "Applicability of finite-difference time-domain method to simulation of wave propagation in cancellous bone", Japanese Journal of Applied Physics Part 1-Regular Papers Brief Communications and Review Papers **45**, 7186–7190 (2006).
3. P. Nicholson, P. Moilanen, T. Kärkkäinen, J. Timonen, and S. Cheng, "Guided ultrasonic waves in long bones: modelling, experiment and application", Physiological Measurements **23**, 755–768 (2002).
4. E. Bossy, M. Talmant, and P. Laugier, "Three-dimensional simulations of ultrasonic axial transmission velocity measurement on cortical bone models", Journal of the Acoustical Society of America **115**, 2314–2324 (2004).
5. P. Moilanen, M. Talmant, V. Bousson, P. H. F. Nicholson, S. Cheng, J. Timonen, and P. Laugier, "Ultrasonically determined thickness of long cortical bones: two-dimensional simulations of in vitro experiments", Journal of the Acoustical Society of America **122**, 1818–1826 (2007).
6. K. Yee, "Numerical solutions of initial boundary value problems involving maxwell's equations in isotropic media", IEEE Transactions on Antennas and Propagation **AP-14**(3), 302–307 (1966).
7. A. Hrenikoff, "Solution of problems of elasticity by the framework method", Journal of Applied Mechanics **A8**, 169–175 (1941).
8. R. Courant, "Variational methods for the solution of problems of equilibrium and vibrations", Bulletin of the American Mathematical Society **49**, 1–61 (1943).
9. B. A. Auld, *Acoustic Fields and waves in solids*, 2nd edition (Krieger Publishing Company, Malabar) (1990).
10. D. Royer and E. Dieulesaint, *Elastic waves in solids I*, 2nd edition (Springer-Verlag, Berlin) (1999).
11. M. G. Vavva, V. C. Protopappas, L. N. Gergidis, A. Charalambopoulos, D. I. Fotiadis, and D. Polyzos, "Velocity dispersion of guided waves propagating in a free gradient elastic plate: application to cortical bone", Journal of the Acoustical Society of America **125** (2009).
12. B. Engquist and A. Majda, "Absorbing boundary conditions for the numerical simulation of waves", Mathematics of Computation **31**, 629–651 (1977).
13. G. C. Cohen, *Higher-order numerical methods* (Springer, Berlin) (2002).
14. E. Bossy, M. Talmant, and P. Laugier, "Effect of bone cortical thickness on velocity measurements using ultrasonic axial transmission: a 2d simulation study", Journal of the Acoustical Society of America **112**, 297–307 (2002).
15. G. Haiat, S. Naili, Q. Grimal, M. Talmant, C. Desceliers, and C. Soize, "Influence of a gradient of material properties on ultrasonic wave propagation in cortical bone: application to axial transmission", Journal of the Acoustical Society of America **125**, 4043–4052 (2009).
16. V. C. Protopappas, D. I. Fotiadis, and K. N. Malizos, "Guided ultrasound wave propagation in intact and healing long bones", Ultrasound in Medicine and Biology **32**, 693–708 (2006).

17. S. P. Dodd, J. L. Cunningham, A. W. Miles, S. Gheduzzi, and V. F. Humphrey, "Ultrasonic propagation in cortical bone mimics", Physics in Medicine and Biology **51**, 4635–4647 (2006).
18. V. Le Floch, D. J. McMahon, G. Luo, A. Cohen, J. J. Kaufman, E. Shane, and R. S. Siffert, "Ultrasound simulation in the distal radius using clinical high-resolution peripheral-ct images", Ultrasound in Medicine and Biology **34**, 1317–1326 (2008).
19. J. Grondin, Q. Grimal, K. Engelke, and P. Laugier, "Potential of first arriving signal to assess cortical bone geometry at the hip with qus: a model based study", Ultrasound in Medicine and Biology **4**, 656–666 (2010).
20. X. Guo, D. Yang, D. Zhang, W. Li, Y. Qiu, and J. Wu, "Quantitative evaluation of fracture healing process of long bones using guided ultrasound waves: a computational feasibility study", Journal of the Acoustical Society of America **125**, 2834–2837 (2009).
21. P. Moilanen, M. Talmant, P. H. F. Nicholson, S. Cheng, J. Timonen, and P. Laugier, "Ultrasonically determined thickness of long cortical bones: three-dimensional simulations of in vitro experiments", Journal of the Acoustical Society of America **122**, 2439–2245 (2007).
22. W. Pistoia, B. van Rietbergen, A. Laib, and P. Rüegsegger, "High-resolution three-dimensional-pqct images can be an adequate basis for in-vivo micro-fe analysis of bone", Journal of Biomechanical Engineering **123**, 176–183 (2001).
23. Y. N. Yeni, G. T. Christopherson, X. N. Dong, D. G. Kim, and D. P. Fyhrie, "Effect of micro-computed tomography voxel size on the finite element model accuracy for human cancellous bone", Journal of Biomechanical Engineering **127**, 18 (2005).
24. C. S. Rajapakse, J. Magland, X. H. Zhang, X. S. Liu, S. L. Wehrli, X. E. Guo, and F. W. Wehrli, "Implications of noise and resolution on mechanical properties of trabecular bone estimated by image-based finite-element analysis", Journal of Orthopaedic Research **27**, 1263–1271 (2009).
25. G. M. Luo, J. J. Kaufman, A. Chiabrera, B. Bianco, J. H. Kinney, D. Haupt, J. T. Ryaby, and R. S. Siffert, "Computational methods for ultrasonic bone assessment", Ultrasound in Medicine and Biology **25**, 823–830 (1999).
26. A. Hosokawa, "Simulation of ultrasound propagation through bovine cancellous bone using elastic and biot's finite-difference time-domain methods", Journal of the Acoustical Society of America **118**, 1782–1789 (2005).
27. A. Hosokawa, "Ultrasonic pulse waves in cancellous bone analyzed by finite-difference time-domain methods", Ultrasonics **44** (Suppl 1), E227–E231 (2006).
28. V. Nguyen, S. Naili, and S. Sansalone, "Simulation of ultrasonic wave propagation in anisotropic cancellous bone immersed in fluid", Wave Motion **47**, 117–129 (2009).
29. Q. Grimal, K. Raum, A. Gerisch, and P. Laugier, "About the determination of the representative volume element size in compact bone", in *Proceedings of the 19 ème Congrès Français de Mécanique* (2009), 6 pages.
30. J. Kabel, B. van Rietbergen, M. Dalstra, A. Odgaard, and R. Huiskes, "The role of an effective isotropic tissue modulus in the elastic properties of cancellous bone", Journal of Biomechanics **32**, 673–680 (1999).
31. Q. Grimal, K. Raum, A. Gerisch, and P. Laugier, "Derivation of the mesoscopic elasticity tensor of cortical bone from quantitative impedance images at the micron scale", Computer Methods in Biomechanics and Biomedical Engineering **11**, 147–157 (2008).
32. W. R. Taylor, E. Roland, H. Ploeg, D. Hertig, R. Klabunde, M. D. Warner, M. C. Hobatho, L. Rakotomanana, and S. E. Clift, "Determination of orthotropic bone elastic constants using fea and modal analysis", Journal of Biomechanics **35**, 767–773 (2002).
33. C. Baron, M. Talmant, and P. Laugier, "Effect of porosity on effective diagonal stiffness coefficients (c(ii)) and elastic anisotropy of cortical bone at 1 MHz: a finite-difference time domain study", Journal of the Acoustical Society of America **122**, 1810–1817 (2007).
34. H. S. Yoon and J. L. Katz, "Ultrasonic wave propagation in human cortical bone–ii. measurements of elastic properties and microhardness", Journal of Biomechanics **9**, 459–464 (1976).
35. H. Yoon and J. Katz, "Ultrasonic wave propagation in human cortical bone-i. theoretical considerations for hexagonal symmetry", Journal of Biomechanics **9**, 407–412 (1976).
36. A. A. Espinoza Orias, J. M. Deuerling, M. D. Landrigan, J. E. Renaud, and R. K. Roeder, "Anatomic variation in the elastic anisotropy of cortical bone tissue in the human femur", Journal of Biomedical Materials Research **2**, 255–263 (2009).

37. J. M. Crolet, M. Racila, R. Mahraoui, and A. Meunier, “A new numerical concept for modeling hydroxyapatite in human cortical bone”, Computer Methods in Biomechanics and Biomedical Engineering **8**, 139–143 (2005).
38. C. Baron, Q. Grimal, M. Talmant, and P. Laugier, “Investigation of the porous network as a determinant of the overall stiffness of cortical bone: Mori-tanaka model vs. ultrasound propagation”, Journal of the Acoustical Society of America **123**, 3514 (2008).
39. W. J. Parnell and Q. Grimal, “The influence of mesoscale porosity on cortical bone anisotropy. investigations via asymptotic homogenization”, Journal of the Royal Society Interface **6**, 97–109 (2009).
40. K. Kunz, *The finite difference time domain method for electromagnetics* (CRC Press, Boca Raton) (1993).
41. K. F. Riley, M. P. Hobson, and S. J. Bence, *Mathematical methods for physics and engineering*, 3 edition (Cambridge University Press, Cambridge, UK) (2006).
42. R. Madariaga, “Dynamics of an expanded circular fault”, Bulletin of the Seismological Society of America **66**, 639–666 (1976).
43. J. Virieux, “P-sv wave propagation in heterogeneous media: velocity-stress finite-difference method.”, Geophysics **51**, 889–901 (1986).
44. F. Collino and C. Tsogka, “Application of the pml absorbing layer model to the linear elastodynamic problem in anisotropic heterogeneous media”, Geophysics **66**, 294–307 (2001).
45. M. A. Hakulinen, J. S. Day, J. Toyras, H. Weinans, and J. S. Jurvelin, “Ultrasonic characterization of human trabecular bone microstructure”, Physics in Medicine and Biology **51**, 1633–1648 (2006).
46. G. Haiat, F. Padilla, F. Peyrin, and P. Laugier, “Variation of ultrasonic parameters with microstructure and material properties of trabecular bone: a 3D model simulation”, Journal of Bone and Mineral Research **22**, 665–674 (2007).
47. O. C. Zienkiewicz, R. L. Taylor, and J. Z. Zhu, *The finite element method: its basis and fundamentals*, 6 edition (Elsevier, Burlington) (2005).
48. C. Desceliers, C. Soize, Q. Grimal, G. Haiat, and S. Naili, “A time-domain method to solve transient elastic wave propagation in a multilayer medium with a hybrid spectral-finite element space approximation”, Wave Motion **45**, 383–399 (2008).
49. S. Modak and E. Sotelino, “The generalized method for structural dynamics applications”, Advances in Engineering Software **33**, 565–575 (2002).
50. L. Cagniard, *Reflection and Refraction of Progressive Seismic Waves* (Gauthier-Villars, Paris) (1962), translation and revision by Flinn, E.A., and Dix, C.H., of Cagniard, L., 1939. Réflexion et Réfraction des Ondes Séismiques Progressives.
51. A. de Hoop, “A modification of cagniard’s method for solving seismic pulse problems”, Applied Scientific Research **8**, 349–356 (1960).
52. Q. Grimal and S. Naili, “A theoretical analysis in the time-domain of wave reflection on a bone plate”, Journal of Sound and Vibration **298**, 12–29 (2006).
53. K. Macocco, Q. Grimal, S. Naili, and C. Soize, “Elastoacoustic model with uncertain mechanical properties for ultrasonic wave velocity prediction; application to cortical bone evaluation”, Journal of Acoustical Society of America **119**, 729–740 (2006).
54. E. Camus, M. Talmant, G. Berger, and P. Laugier, “Analysis of the axial transmission technique for the assessment of skeletal status”, Journal of Acoustical Society of America **108**, 3058–3065 (2000).
55. J. Diaz and P. Joly, “Robust high order non-conforming finite element formulation for time domain fluid-structure interaction”, Journal of Computational Acoustics **13**, 403–431 (2005).
56. R. W. Graves, “Simulating seismic wave propagation in 3d elastic media using staggered-grid finite differences”, Bulletin of the Seismological Society of America **86**, 1091–1106 (1996).
57. N. A. Kampanis, V. Dougalis, and V. Ekaterinaris, *Effective computational methods for wave propagation* (Chapman & Hall/CRC, Boca Raton) (2008).
58. J. F. Aubry, M. Tanter, M. Pernot, J. L. Thomas, and M. Fink, “Experimental demonstration of noninvasive transskull adaptive focusing based on prior computed tomography scans”, The Journal of the Acoustical Society of America **113**, 84–93 (2003).

59. F. Marquet, M. Pernot, J. F. Aubry, G. Montaldo, L. Marsac, M. Tanter, and M. Fink, "Non-invasive transcranial ultrasound therapy based on a 3d CT scan: protocol validation and in vitro results", Physics in Medicine and Biology **54**, 2597–2613 (2009).
60. R. Barkmann, S. Lüsse, B. Stampa, S. Sakata, M. Heller, and C.-C. Glüer, "Assessment of the geometry of human finger phalanges using quantitative ultrasound in vivo", Osteoporosis International **11**, 745–755 (2000).
61. S. P. Dodd, J. L. Cunningham, A. W. Miies, S. Gheduzzi, and V. F. Humphrey, "An in vitro study of ultrasound signal loss across simple fractures in cortical bone mimics and bovine cortical bone samples", Bone **40**, 656–661 (2007).
62. G. Haiat, F. Padilla, F. Peyrin, and P. Laugier, "Fast wave ultrasonic propagation in trabecular bone: numerical study of the influence of porosity and structural anisotropy", Journal of the Acoustical Society of America **123**, 1694–1705 (2008).
63. Y. Nagatani, K. Mizuno, T. Saeki, M. Matsukawa, T. Sakaguchi, and H. Hosoi, "Numerical and experimental study on the wave attenuation in bone - fdtd simulation of ultrasound propagation in cancellous bone", Ultrasonics **48**, 607–612 (2008).
64. F. Padilla, E. Bossy, and P. Laugier, "Simulation of ultrasound propagation through three-dimensional trabecular bone structures: comparison with experimental data", Japanese Journal of Applied Physics Part 1-Regular Papers Brief Communications and Review Papers **45**, 6496–6500 (2006).
65. E. Bossy, P. Laugier, F. Peyrin, and F. Padilla, "Attenuation in trabecular bone: a comparison between numerical simulation and experimental results in human femur", Journal of the Acoustical Society of America **122**, 2469–2475 (2007).
66. S. Gheduzzi, S. P. Dodd, A. W. Miles, V. F. Humphrey, and J. L. Cunningham, "Numerical and experimental simulation of the effect of long bone fracture healing stages on ultrasound transmission across an idealized fracture", Journal of the Acoustical Society of America **126**, 887–894 (2009).
67. V. C. Protopappas, I. C. Kourtis, L. C. Kourtis, K. N. Malizos, C. V. Massalas, and D. I. Fotiadis, "Three-dimensional finite element modeling of guided ultrasound wave propagation in intact and healing long bones", Journal of the Acoustical Society of America **121**, 3907–3921 (2007).
68. A. Mahmoud, D. Cortes, A. Abaza, H. Ammar, M. Hazey, P. Ngan, R. Crout, and O. Mukdadi, "Noninvasive assessment of human jawbone using ultrasonic guided waves", IEEE Transactions on Ultrasonics Ferroelectrics and Frequency Control **55**, 1316–1327 (2008).
69. V. C. Protopappas, M. G. Vavva, D. I. Fotiadis, and K. N. Malizos, "Ultrasonic monitoring of bone fracture healing", IEEE Transactions on Ultrasonics Ferroelectrics and Frequency Control **55**, 1243–1255 (2008).
70. G. Haiat, F. Padilla, and P. Laugier, "Sensitivity of qus parameters to controlled variations of bone strength assessed with a cellular model", IEEE Transactions on Ultrasonics Ferroelectrics and Frequency Control **55**, 1488–1496 (2008).
71. A. S. Aula, J. Toyras, M. A. Hakulinen, and J. S. Jurvelin, "Effect of bone marrow on acoustic properties of trabecular bone-3d finite difference modeling study", Ultrasound in Medicine and Biology **35**, 308–318 (2009).
72. M. Pakula, F. Padilla, and P. Laugier, "Influence of the filling fluid on frequency-dependent velocity and attenuation in cancellous bones between 0.35 and 2.5 MHz", Journal of the Acoustical Society of America **126**, 3301–3310 (2009).
73. G. Haiat, F. Padilla, R. Barkmann, C. C. Gluer, and P. Laugier, "Numerical simulation of the dependence of quantitative ultrasonic parameters on trabecular bone microarchitecture and elastic constants", Ultrasonics **44**, E289–E294 (2006).
74. A. Hosokawa, "Effect of minor trabecular elements on fast and slow wave propagations through a stratified cancellous bone phantom at oblique incidence", Japanese Journal of Applied Physics **48** (2009).
75. C. Desceliers, C. Soize, Q. Grimal, M. Talmant, and S. Naili, "Determination of the random anisotropic elasticity layer using transient wave propagation in a fluid-solid multilayer: model and experiments", Journal of the Acoustical Society of America **125**, 2027–2034 (2009).

76. P. Moilanen, M. Talmant, V. Kilappa, P. Nicholson, S. L. Cheng, J. Timonen, and P. Laugier, "Modeling the impact of soft tissue on axial transmission measurements of ultrasonic guided waves in human radius", Journal of the Acoustical Society of America **124**, 2364–2373 (2008).
77. M. G. Vavva, V. C. Protopappas, L. N. Gergidis, A. Charalambopoulos, D. I. Fotiadis, and D. Polyzos, "The effect of boundary conditions on guided wave propagation in two-dimensional models of healing bone", Ultrasonics **48**, 598–606 (2008).
78. A. Hosokawa, "Development of a numerical cancellous bone model for finite-difference time-domain simulations of ultrasound propagation", IEEE Transactions on Ultrasonics Ferroelectrics and Frequency Control **55**, 1219–1233 (2008).
79. F. Padilla, Q. Grimal, and P. Laugier, "Ultrasonic propagation through trabecular bone modeled as a random medium", Japanese Journal of Applied Physics **47**, 4220–4222 (2008).
80. L. Goossens, J. Vanderoost, S. Jaecques, S. Boonen, J. D'Hooge, W. Lauriks, and G. Van der Perre, "The correlation between the sos in trabecular bone and stiffness and density studied by finite-element analysis", IEEE Transactions on Ultrasonics Ferroelectrics and Frequency Control **55**, 1234–1242 (2008).
81. G. Haiat, F. Padilla, M. Svrcekova, Y. Chevalier, D. Pahr, F. Peyrin, P. Laugier, and P. Zysset, "Relationship between ultrasonic parameters and apparent trabecular bone elastic modulus: a numerical approach", Journal of Biomechanics **42**, 2033–2039 (2009).

Chapter 9
Homogenization Theories and Inverse Problems

Robert P. Gilbert, Ana Vasilic, and Sandra Ilic

Abstract Various approaches are presented for modelling the acoustic response of cancellous bone to ultrasound interrogation. As the characteristic pore size in cancellous bone is much smaller than a typical bone sample, there is a clear scale separation (micro versus macro). Thus, our modelling methods are mainly based on homogenization techniques and numerical upscaling. First, we consider the so-called direct problems and present models for both periodically perforated domain and a domain with random distribution of pores, as well as nonlinear model with a shear-thinning viscoelastic material emulating the blood-marrow mixture. A numerical procedure is given for the upscaling of a diphasic mixture using different trabeculae thicknesses and various frequencies for the ultrasound excitation. Finally, the results of a quite accurate two-dimensional inversion for the Biot parameters are presented. Further details for these different problems are amply described in the literature cited in the bibliography.

Keywords Homogenization · Cancellous bone · Inverse problems

9.1 Introduction

Osteoporosis is characterized by a decrease in strength of the bone matrix. Currently, bone mineral density (**BMD**) is the gold standard for *in vivo* assessment of fracture risk of bones and is measured using X-ray absorptiometric techniques [18].

R.P. Gilbert (✉)
Department of Mathematical Sciences, University of Delaware, Newark, DE 19716, USA
e-mail: gilbert@math.udel.edu

A. Vasilic
Department of Mathematical Sciences, UAE University, P.O. Box 17551, Al Ain, Abu Dhabi, UAE
e-mail: vasilic@uaeu.ac.ae

S. Ilic
Lehrstuhl für Allgemeine Mechanik, Ruhr Universität Bochum IA 3/129, Universitätsstrasse 150, D-44780 Bochum, Deutschland
e-mail: Sandra.Ilic@ruhr-uni-bochum.de

P. Laugier and G. Haïat (eds.), *Bone Quantitative Ultrasound*,
DOI 10.1007/978-94-007-0017-8_9,

However, only 70–80% of the variance of bone strength is accounted for by bone density. As the brittleness of bone depends on more factors than bone density, biologists believe that quantitative ultrasound techniques (QUS) could provide an important new diagnostic tool [28, 30, 60]. Moreover, in contrast to X-ray densitometry, ultrasound does not ionize the tissue, and its implementation is relatively inexpensive. Since the loss of bone density and the destruction of the bone microstructure are most evident in osteoporotic cancellous bone, it is natural to consider the possibility of developing accurate ultrasound models for the insonification of cancellous bone. It would be of enormous clinical advantage if an accurate method could be developed using ultrasound interrogation to determine whether one had osteoporosis. We have derived various cancellous bone models in other papers [13–16]. In this chapter we construct the acoustic response equations by considering a random distribution of pores. In the following sections we construct various models for the acoustic response of bone to QUS.

9.2 Diphasic Macroscopic Model for Cancellous Bone

Cancellous bone is a poroelastic matrix made up of trabeculae (the elastic matrix) and blood-marrow (the fluid filled pores). Most of the models of acoustic properties of cancellous bone are based on different adaptations of Biot's theory [4–6]. This theory predicts two compressional waves: a fast wave, where the fluid and solid move in phase, and a slow wave where fluid and solid move out of phase. In our previous work [25, 26] using homogenization methods we derived the effective equations in the monophasic time-harmonic case and computed the material properties coefficients. Gilbert et al. [21, 34] also considered a similar problem of interaction between an elastic matrix and an incompressible fluid or slightly compressible fluid, filling the pore space. In this section we consider the case when solid matrix and the fluid filling the pores move out of phase. Original equations of Biot concentrate on this particular situation and his heuristic modeling assures a kind of Darcy law for the difference between effective velocities of the solid and fluid part. Asymptotic modeling of this case was undertaken by Auriault [3], Burridge and Keller [17], Levy [51], Mikelić [56], Nguetseng [62], Sanchez-Palencia [67] and it is customary to set *dimensionless viscosity* for the diphasic problem to be $\mu\varepsilon^2$ and then to study the two-scale asymptotic expansion.

We define dimensionless coordinates in terms of characteristic lengths and reference values of the physical parameters. Let ℓ be the characteristic length of a microscopic cell; whereas, L is the characteristic length at the macroscopic scale. When monochromatic insonification of the bone is used, the wave frequency ω is sufficiently low so that resonance effects are avoided, i.e. the wave length is an order of magnitude larger that the pore size [21]. Thus, we assume that the wave length of the acoustic signal, λ, is related to the macroscopic length L by $2\pi L = \lambda$. The relation between ℓ and L is given by the small parameter ε, $\varepsilon L = \ell$. In terms of the

characteristic lengths ℓ and L we introduce the dimension-less coordinates $y = X/\ell$, and $x = X/L$, where X is taken to be a physical space variable. Then $x = \varepsilon y$, and y is referred to as the fast variable.

9.2.1 Two-Scale Convergence

Let us first introduce the notation we use for periodically perforated medium.

$$\begin{aligned}
\Omega &=]0,L[^n, n = 2,3 \text{ is an } L \text{ cell},\\
\Omega_s^\varepsilon &= \text{ the solid part of } \Omega,\\
\Omega_f^\varepsilon &= \text{the fluid part of } \Omega,\\
\mathscr{Y} &=]0,1[^n, n = 2,3 \text{ is a unit periodicity cell},\\
\mathscr{Y}_s &= \text{ the solid part of } \mathscr{Y}, \text{ and}\\
\mathscr{Y}_f &= \mathscr{Y}\setminus\mathscr{Y}_s = \text{the fluid part of } \mathscr{Y},
\end{aligned}$$

and the fluid-solid interface is indicated by $\Gamma_\varepsilon := \partial\Omega_s^\varepsilon \cap \partial\Omega_f^\varepsilon$. For a detailed description of the construction of Ω_s and Ω_f, please refer to [26].

We consider in the solid part

$$-\omega^2\rho_s\mathbf{u}^\varepsilon - \operatorname{div}(\sigma^{s,\varepsilon}) = \mathbf{F}\rho_s \text{ in } \Omega_s^\varepsilon, \tag{9.1}$$

where the constitutive relations can be written as

$$\sigma_{ij}^{s,\varepsilon} = a_{ijkl}e(\mathbf{u}^\varepsilon)_{kl}, \quad e(\mathbf{u}^\varepsilon)_{ij} := \frac{1}{2}\left(\frac{\partial u_i^\varepsilon}{\partial x_j} + \frac{\partial u_j^\varepsilon}{\partial x_i}\right),$$

whereas, in the fluid part we consider the Stokes system

$$-\omega^2\rho_f\,\mathbf{u}^\varepsilon - \operatorname{div}(\sigma^{f,\varepsilon}) = \mathbf{F}\rho_f \qquad \text{in } \Omega_f^\varepsilon, \tag{9.2}$$

where

$$\sigma^{f,\varepsilon} := -p^\varepsilon I + 2i\omega\eta\varepsilon^r e(\mathbf{u}^\varepsilon) + i\omega\xi\varepsilon^r \operatorname{div}\mathbf{u}^\varepsilon I. \tag{9.3}$$

Here η and ξ are viscosity coefficients of the fluid subject to the following conditions:

$$\eta > 0, \qquad \frac{\xi}{\eta} > -\frac{2}{3}. \tag{9.4}$$

The positive numbers ρ_s, ρ_f are the densities of the mass of the solid and the fluid, respectively, in the reference state at rest; and c is the velocity of sound. For more information, we refer to [62].

In (9.3) ε^r in the viscosity term describes three different regimes: $r = 0$ is the monophasic-elastic regime, $r = 1$ is monophasic-viscoelastic [25, 26], and $r = 2$ corresponds to diphasic motion of fluid and solid [3, 34]. In this section, we focus our attention on the diphasic case ($r = 2$).

At the interface between fluid and solid parts we have

$$[\mathbf{u}^\varepsilon] = 0 \text{ on } \Gamma_\varepsilon \tag{9.5}$$

as the statement of continuity of displacements. The normal stresses are balanced by

$$\sigma^{s,\varepsilon} \cdot \nu = \sigma^{f,\varepsilon} \cdot \nu \text{ on } \Gamma_\varepsilon \tag{9.6}$$

At the outer boundary we suppose periodicity, i.e.

$$\{\mathbf{u}^\varepsilon, p^\varepsilon\} \text{ are } L-\text{periodic.} \tag{9.7}$$

Under the assumption that the fluid is slightly compressible, the variation of pressure from the rest state is small and is proportional to $-c^2\rho_f \operatorname{div}\mathbf{u}^\varepsilon$, thus the expression (9.3) reads

$$\sigma^{f,\varepsilon} := c^2\rho_f \operatorname{div}\mathbf{u}^\varepsilon I + 2i\omega\eta\varepsilon^2 e(\mathbf{u}^\varepsilon) + i\omega\xi\varepsilon^2 \operatorname{div}\mathbf{u}^\varepsilon I. \tag{9.8}$$

The weak formulation which corresponds to (9.1)–(9.7) is given by:
Find $\mathbf{u}^\varepsilon \in H^1_{\text{per}}(\Omega)^n$ such that

$$\begin{aligned} -\omega^2 \int_\Omega \rho_\varepsilon \mathbf{u}^\varepsilon(x)\bar{\phi}(x) + 2i\omega\eta\varepsilon^2 \int_{\Omega_f^\varepsilon} e(\mathbf{u}^\varepsilon) : e(\bar{\phi}) + i\omega\xi\varepsilon^2 \int_{\Omega_f^\varepsilon} \operatorname{div}\mathbf{u}^\varepsilon \operatorname{div}\bar{\phi} \\ + c^2\rho_f \int_{\Omega_f^\varepsilon} \operatorname{div}\mathbf{u}^\varepsilon \operatorname{div}\bar{\phi} + \int_{\Omega_s^\varepsilon} \mathbf{A}\,(e(\mathbf{u}^\varepsilon)) : e(\bar{\phi}) = \int_\Omega \mathbf{F}\rho_\varepsilon\bar{\phi}, \qquad \forall\phi \in H^1_{per}(\Omega)^n, \end{aligned} \tag{9.9}$$

where $\bar{\cdot}$ denotes the complex conjugate and

$$\rho_\varepsilon = \rho_f \chi_{\Omega_f^\varepsilon} + \rho_s \chi_{\Omega_s^\varepsilon}. \tag{9.10}$$

Here $H^1_{per}(\Omega)^n$ is taken to be the space of $H^1(\Omega \times Y)$ functions which are periodic on Y.

Theorem 1. *For some suitably small $\omega > 0$ and any $\mathbf{F} \in L^2(\Omega)^n$, there is a unique $\mathbf{u}^\varepsilon \in H^1_{per}(\Omega)$ that solves the variational Equation (9.9). Moreover, there exists a constant C, independent of ε, such that*

$$||\mathbf{u}^\varepsilon||_{L^2(\Omega)^n} \le C,\ ||\nabla\mathbf{u}^\varepsilon||_{L^2(\Omega_s^\varepsilon)^{n^2}} \le C,\ ||\nabla\mathbf{u}^\varepsilon||_{L^2(\Omega_f^\varepsilon)^{n^2}} \le \frac{C}{\varepsilon}$$

Note that the real and imaginary parts of (9.9) are not coercive on $H_0^1(\Omega)$. Nevertheless, the sum of the two parts is coercive (see, e.g. [67, Chap. 8], [62]). Therefore, existence and uniqueness of the solution $\mathbf{u}^\varepsilon$ to (9.9) for the above defined ω follows as a direct consequence of the complex variant of the Lax–Milgram theorem [24, 26].

In order to prove the main convergence results of we need the notion of *two-scale convergence* which was introduced in [61] and developed further in [2].

Definition 1. A sequence $\{w^\varepsilon\} \subset L^2(\Omega)$ is said to *two-scale converge* to a limit $w \in L^2(\Omega \times \mathscr{Y})$ iff for any $\sigma \in C^\infty(\Omega; C^\infty_{\text{per}}(\mathscr{Y}))$ ("per" denotes one-periodicity) one has

$$\lim_{\varepsilon \to 0} \int_\Omega w^\varepsilon(x)\sigma\left(x, \frac{x}{\varepsilon}\right)\, dx = \int_\Omega \int_{\mathscr{Y}} w(x,y)\sigma(x,y)\, dy\, dx.$$

Lemma 1. *From each bounded sequence in $L^2(\Omega)$ one can extract a subsequence which two-scale converges to a limit $w \in L^2(\Omega \times \mathscr{Y})$ [61].*

Lemma 2. *(i) Let w^ε and $\varepsilon\nabla_x w^\varepsilon$ be bounded sequences in $L^2(\Omega)$. Then there exists a function $w \in L^2(\Omega; H^1_{\text{per}}(\mathscr{Y}))$ and a subsequence such that both w^ε and $\varepsilon\nabla_x w^\varepsilon$ two-scale converge to w and $\nabla_y w$, respectively.*

(ii) Let w^ε and $\nabla_x w^\varepsilon$ be bounded sequences in $L^2(\Omega)$. Then there exists functions $w \in L^2(\Omega)$, $\mathbf{v} \in L^2(\Omega; H^1_{\text{per}}(\mathscr{Y}))$ and a subsequence such that both w^ε and $\nabla_x w^\varepsilon$ two-scale converge to w and $\nabla_x w(x) + \nabla_y v(x,y)$, respectively [2, 61].

If we have two different estimates for gradients in the solid and in the fluid part, then the classical way to proceed is by extending the deformation from Ω_f^ε to Ω and then passing to the limit $\varepsilon \to 0$. It is sufficient to suppose the Lipschitz regularity for the pore boundaries.

To pass to the two-scale limits, it is convenient to rewrite our equations in terms of pressure. To this end, we need to extend the pressure field p^ε (originally defined only in the fluid part) to the whole Ω^ε.

$$\tilde{p}^\varepsilon = \begin{cases} -c^2\rho_f \operatorname{div}\mathbf{u}^\varepsilon(x) + \frac{c^2\rho_f}{|\Omega|}\displaystyle\int_{\Omega_f^\varepsilon} \operatorname{div}\mathbf{u}^\varepsilon(x)dx\ , x \in \Omega_f^\varepsilon, \\ \frac{c^2\rho_f}{|\Omega|}\displaystyle\int_{\Omega_f^\varepsilon} \operatorname{div}\mathbf{u}^\varepsilon(x)dx \qquad\qquad , x \in \Omega_s^\varepsilon. \end{cases} \tag{9.11}$$

A priori estimates and sequential compactness properties of two-scale convergence [2] imply that there exist subsequences (not relabeled) such that [21]

$$\mathbf{u}^\varepsilon \to \mathbf{u}^0(x) + \chi_{\mathscr{Y}_f}(y)\mathbf{v}(x,y) \text{ in the two-scale sense,} \tag{9.12}$$

$$\chi_{\Omega_s^\varepsilon}\nabla\mathbf{u}^\varepsilon \to \chi_{\mathscr{Y}_s}(y)[\nabla_x\mathbf{u}^0(x) + \nabla_y\mathbf{u}^1(x,y)] \text{ in the two-scale sense,} \tag{9.13}$$

$$\varepsilon\chi_{\Omega_f^\varepsilon}\nabla\mathbf{u}^\varepsilon \to \chi_{\mathscr{Y}_f}(y)\nabla_y\mathbf{v}(x,y) \text{ in the two-scale sense,} \tag{9.14}$$

$$\tilde{p}^\varepsilon \to \tilde{p}^0 \text{ in the two-scale sense.} \tag{9.15}$$

In terms of $\tilde{p}^{\varepsilon}$, the weak formulation (9.9) becomes: Find $\mathbf{u}^{\varepsilon} \in H^1_{\text{per}}(\Omega)^n$ such that

$$-\omega^2 \int_{\Omega} \rho_{\varepsilon}\, \mathbf{u}^{\varepsilon}(x)\bar{\phi}(x) + 2i\omega\eta\varepsilon^2 \int_{\Omega_f^{\varepsilon}} e(\mathbf{u}^{\varepsilon}) : e(\bar{\phi}) + i\omega\xi\varepsilon^2 \int_{\Omega_f^{\varepsilon}} \operatorname{div}\mathbf{u}^{\varepsilon}\, \operatorname{div}\bar{\phi}$$

$$+ \int_{\Omega_f^{\varepsilon}} \tilde{p}^{\varepsilon}\, \operatorname{div}\bar{\phi} + \int_{\Omega_s^{\varepsilon}} \mathbf{A}\,(e(\mathbf{u}^{\varepsilon})) : e(\bar{\phi}) = \int_{\Omega} \mathbf{F}\rho_{\varepsilon}\bar{\phi}, \qquad \forall \phi \in H^1_{per}(\Omega)^n, \tag{9.16}$$

By passing to the limit as $\varepsilon \to 0$, and choosing appropriate test functions, $\varphi(x)$, $\varepsilon\psi\left(x, \frac{x}{\varepsilon}\right)$ or $\zeta\left(x, \frac{x}{\varepsilon}\right)$, it may be shown [21,27] that the variational formulation (9.16) yields the system:

$$-\omega^2\rho \int_{\Omega} \mathbf{u}^0\bar{\varphi} - \omega^2 \int_{\Omega} \left(\int_{y_f} \rho_f \mathbf{v} \right) \bar{\varphi} + \int_{\Omega} \int_{\mathscr{Y}_s} A(e_x(\mathbf{u}^0) + e_y(\mathbf{u}^1)) : e_x(\bar{\varphi})$$

$$+ \int_{\Omega} \int_{y_f} \tilde{p}^{\varepsilon}\, \operatorname{div}_x\bar{\varphi} = \int_{\Omega} \rho\mathbf{F}\bar{\varphi}, \tag{9.17}$$

$$\int_{\Omega} \int_{\mathscr{Y}_s} A(e_x(\mathbf{u}^0) + e_y(\mathbf{u}^1)) : e_y(\bar{\psi}) + \int_{\Omega} \int_{y_f} \tilde{p}^{\varepsilon}\, \operatorname{div}_y\bar{\psi} = 0, \tag{9.18}$$

$$-\omega^2 \int_{\Omega} \int_{y_f} \rho_f(\mathbf{u}^0 + \mathbf{v})\bar{\zeta} + 2i\mu\omega \int_{\Omega} \int_{y_f} e_y(\mathbf{v}) : e_y(\bar{\zeta}) + \int_{\Omega} \int_{y_f} \tilde{p}^{\varepsilon}\, \operatorname{div}_x\bar{\zeta} = \int_{\Omega} \int_{y_f} \rho_f \mathbf{F}\bar{\zeta}, \tag{9.19}$$

for all test functions $\varphi \in H^1_{\text{per}}(\Omega)^n, \psi \in L^2(\Omega, H^1_{\text{per}}(\mathscr{Y}))^n, \zeta \in L^2(\Omega, H^1_{\text{per}}(\mathscr{Y}))^n$, such that $\zeta = 0$ on $\bar{\mathscr{Y}}_s$, $\operatorname{div}_y\zeta = 0$ on $\mathscr{Y}_f$, and

$$\{\mathbf{u}^0, \mathbf{u}^1, \mathbf{v}, \tilde{p}^0\} \text{ are } L\text{-periodic in } x.$$

Therefore, we have the following:

Lemma 3. *The limit functions* $\mathbf{u}^0 \in H^1_{\text{per}}(\Omega)^n$, $\mathbf{u}^1 \in L^2(\Omega; H^1(\mathscr{Y}_s)/\mathbb{C})^n$, $\mathbf{v} \in L^2(\Omega; H^1_{\text{per}}(\mathscr{Y}))^n$, $\tilde{p}^0 \in L^2(\Omega; L^2(\mathscr{Y}))$ *satisfy the system (9.17)–(9.19) with* $\mathbf{v} = 0$ *on* $\bar{\mathscr{Y}}_s$.

Using the strong equivalence of (9.17), after eliminating the expressions for $\mathbf{u}^1$ and $\mathbf{v}$ [21, 27], we obtain a pair of equations relating the effective pressure p^0 and displacement $\mathbf{u}^0$:

$$-\omega^2\rho\mathbf{u}^0-\omega^2\sum_{i,j}\mathbf{e}_i\mathscr{A}_{ij}(\omega)\left[\frac{\partial p^0}{\partial x_j}(x)-\rho_f\omega^2u_j^0(x)\right]$$
$$-\operatorname{div}_x\left\{A^He_x(\mathbf{u}^0)\right\}-\operatorname{div}_x\left\{p^0\mathscr{B}^H\right\}+|\mathscr{Y}_f|\nabla_xp^0=\rho\mathbf{F}-\rho_f\omega^2\sum_{i,j}\mathbf{e}_i\mathscr{A}_{ij}(\omega)F_j(x), \tag{9.20}$$

$$-\frac{|\mathscr{Y}_f|}{c^2}p^0=\operatorname{div}_x\left\{\left(|\mathscr{Y}_f|-\omega^2\mathscr{A}(\omega)\right)\rho_f\mathbf{u}^0+\mathscr{A}(\omega)\left[-\rho_f\mathbf{F}(x)+\nabla p^0(x)\right]\right\}$$
$$-\rho_f\mathscr{C}^H:e(\mathbf{u}^0)-\rho_fp^0\int_{\mathscr{Y}_s}\operatorname{div}_y\mathbf{w}^0\,dy. \tag{9.21}$$

where

$$A^H_{klij}:=\left(\int_{\mathscr{Y}_s}A\left(\frac{e_i\otimes e_j+e_j\otimes e_i}{2}+e_y(\mathbf{w}^{ij})\right)\right)_{kl},\quad \mathscr{B}^H:=\int_{\mathscr{Y}_s}Ae_y(\mathbf{w}^0), \tag{9.22}$$

$$\mathscr{A}_{ij}(\omega):=\int_{y_f}w_i^j(y,\omega)dy,\quad \mathscr{C}^H_{ij}:=\int_{\mathscr{Y}_s}\operatorname{div}_y\mathbf{w}^{ij}(y)\,dy. \tag{9.23}$$

Equations (9.20) and (9.21) determine p^0 and $\mathbf{u}^0$. Note that the coefficients A^H_{klij}, $\mathscr{B}^H$, $\mathscr{A}_{ij}$, and $\mathscr{C}^H_{ij}$ may be exactly computed using known bone properties. In the monophasic case we have done this and recovered a system of equations having more coefficients than the Biot model; however, the non-Biot coefficients are 10^{-3} times smaller than the Biot coefficients. This leads one to believe that a Biot-type model is reasonable; however, homogenization provides a precise way to compute these coefficients otherwise known, at least partially, in a heuristic manner [25, 26].

9.3 Random Distribution of Pores

Stochastic Two-Scale Homogenization permits us to treat the case of random pore size distributions. It was developed in [12] and used in modeling a randomly fractured media [11]. Stochastic two-scale convergence was also used for two phase flows in porous media [9, 10]. Here we assume the media as randomly fissured with the fissures being statistically homogeneous. Although the underlying stochastic process does not necessarily have to be ergodic we assume it is in this case. This allows us to obtain an explicit and easier computational auxiliary problem in a Representative Elementary Volume.

Following Jikov, Kozlov and Oleinik [49], and Bourgeat, Mikelić and Piatnitski [11] we introduce the ε-problem as follows:

Let (Ω, Ξ, μ) be a probability space, and assume that an n-dimensional, dynamical system $\mathscr{T}$ is given on Ω, such that:

1. $\mathscr{T}(0) = \mathbf{I}d$ on Ω and $\mathscr{T}(x_1 + x_2) = \mathscr{T}(x_1)\mathscr{T}(x_2)$ for all $x_1, x_2 \in \mathbb{R}^n$.
2. $\forall x \in \mathbb{R}^n$ and $\forall E \in \Xi$, $\mu(\mathscr{T}(x)(E)) = \mu(E)$, i.e. μ is an invariant measure for $\mathscr{T}$.
3. $\forall E \in \Xi$ the set $\{(x, \omega) \in \mathbb{R}^n \times \Omega : \mathscr{T}(x)\omega \in E\}$ is an element of the σ-algebra $\mathscr{L} \times \Xi$ on $\mathbb{R}^n \times \Omega$, where $\mathscr{L}$ is the usual Lebesgue σ-algebra on $\mathbb{R}^n$, i.e. $\mathscr{T}$ is a semi flow.

We suppose that $L^2(\Omega) := L^2(\Omega, \Xi, \mu)$ is separable and the dynamical system $\{\mathscr{T}(x)\}$ is ergodic. Next, in order to define the fluid part (blood-marrow) and the solid part (trabeculae), we fix a set $\mathscr{F} \in \Xi$ such that $\mu(\mathscr{F}) > 0$ and $\mu(\Omega \setminus \mathscr{F}) > 0$. We define a random pore structure $F(\omega) \subset \mathbb{R}^n, \omega \in \Omega$ obtained from $\mathscr{F}$ by setting

$$F(\omega) = \{x \in \mathbb{R}^n : \mathscr{T}(x)\omega \in \mathscr{F}\} \tag{9.24}$$

and assuming that $F(\omega)$ is open and connected for almost all $\omega \in \Omega$. The random skeleton (trabeculae) is then constructed by setting

$$\mathscr{M} := \Omega \setminus \mathscr{F}, \quad M(\omega) = \mathbb{R}^n \setminus F(\omega) \text{ and } M_\varepsilon(\omega) = \left\{x \in \mathbb{R}^n : \varepsilon^{-1}x \in M(\omega)\right\}. \tag{9.25}$$

Now let G be a smooth bounded domain in $\mathbb{R}^n$ and after having chosen our random structure in $\mathbb{R}^n$, we set

$$G_1^\varepsilon := \{x \in G : \operatorname{dist}(x, \partial G) \geq \varepsilon\},$$

and introduce the random pore system by $G_f^\varepsilon(\omega) = G \setminus \overline{M_\varepsilon(\omega) \cap G_1^\varepsilon}$, and $G_s^\varepsilon(\omega) = G \setminus \overline{G_f^\varepsilon(\omega)}$ is then the random skeletal system in the domain $G \subset \mathbf{R}^n$.

The equations of motion may now be written as

$$\rho_s \partial_t^2 u^\varepsilon - \operatorname{div}(\mathbf{A}e(\mathbf{u}^\varepsilon)) = f\rho_s \text{ in } G_s^\varepsilon(\omega) \times (0, T) \tag{9.26}$$

$$\rho_f \partial_t^2 u^\varepsilon - \operatorname{div}(-p^\varepsilon \mathbf{I} + 2\mu\varepsilon^r e(\partial_t \mathbf{u})) = f\rho_f \text{ in } G_f^\varepsilon(\omega) \times (0, T) \tag{9.27}$$

$$[u^\varepsilon] = 0 \text{ on } \partial G_s^\varepsilon \cap G_f^\varepsilon, \quad \sigma^s\left(\mathscr{T}\left(\tfrac{x}{\varepsilon}\right)\omega\right) \cdot \nu = \sigma^f\left(\mathscr{T}\left(\tfrac{x}{\varepsilon}\right)\omega\right) \cdot \nu \tag{9.28}$$

where ν is the outer normal vector, $e(\cdot) = 1/2(\nabla \cdot + \nabla^T \cdot)$ and $[\cdot]$ represents the jump of the function across the boundary. In (9.27), ε^r in the viscosity term describes three different regimes, $r = 0$ is the monophasic-elastic regime, $r = 1$ is monophasic-viscoelastic and $r = 2$ corresponds to diphasic motion of fluid and solid [3, 34].

The variational formulation, for almost any realization, which corresponds to (9.26)–(9.28) is given by:

Find $\mathbf{u}^\varepsilon \in H^1(0, T; H^1(G)^n)$ with $\dfrac{d^2\mathbf{u}^\varepsilon}{dt^2} \in L^2(0, T; L^2(G)^n)$ such that

$$\frac{d^2}{dt^2}\int\limits_{G\times\Omega}\rho^{\varepsilon}\mathbf{u}^{\varepsilon}(t)\varphi\,dx\,d\mu+\frac{d}{dt}\int\limits_{G_f^{\varepsilon}\times\Omega}2\mu e(\mathbf{u}^{\varepsilon}(t)):e(\varphi)\,dx\,d\mu$$

$$+\int\limits_{G_s^{\varepsilon}\times\Omega}Ae(\mathbf{u}^{\varepsilon}(t)):e(\varphi)\,dx\,d\mu+\int\limits_{G_f^{\varepsilon}\times\Omega}c^2\rho_f\mathrm{div}\,\mathbf{u}^{\varepsilon}\,\mathrm{div}\varphi\,dx\,d\mu$$

$$=\int\limits_{G\times\Omega}\rho^{\varepsilon}\mathbf{F}\cdot\varphi\,dx\,d\mu,\qquad\forall\varphi\in H^1(G\times\Omega)^n,\qquad(a.e.)\text{ in }]0,T[,\tag{9.29}$$

where

$$\rho^{\varepsilon}=\rho_f\chi_{G_f^{\varepsilon}}+\rho_s\chi_{G_s^{\varepsilon}}.\tag{9.30}$$

Using argumentation similar to that in [34] it is easy to show that by setting $\varphi=\partial_t\mathbf{u}$ in the variational formulation we get the estimates

$$\left\|\partial_t\mathbf{u}^{\varepsilon}\right\|_{L^{\infty}\left(0,T;L^2(G)^n\right)}\le C\left\|\mathbf{F}\right\|_{L^2(]0,T[\times G)^n}=C(\mathbf{F}),\tag{9.31}$$

$$\left\|e(\mathbf{u}^{\varepsilon})\right\|_{L^{\infty}\left(0,T;L^2(G_s^{\varepsilon})^{n^2}\right)}\le C(\mathbf{F}),\tag{9.32}$$

$$\left\|e\left(\partial_t\mathbf{u}^{\varepsilon}\right)\right\|_{L^2\left(0,T;L^2(G_f^{\varepsilon})^{n^2}\right)}\le C(\mathbf{F}).\tag{9.33}$$

9.3.1 Stochastic Two-Scale Convergence

In order to discuss the homogenization of the elliptic operator portion of our system, we first must introduce some preliminary concepts. We recall that a vector field $\mathbf{f}=<f_1,f_2,\ldots,f_n>$, $f_i\in L^2_{\mathrm{loc}}(\mathbb{R}^n)$ is called *vortex free* in $\mathbb{R}^n$ if

$$\int\limits_{\mathbb{R}^n}\left(f_i\frac{\partial\phi}{\partial x_j}-f_j\frac{\partial\phi}{\partial x_i}\right)dx=0,\quad\forall\phi\in C_0^{\infty}(\mathbb{R}^n).$$

It is well-known that any vortex-free field may be expressed as a potential. A vector field is said to be *solenoidal* in $\mathbb{R}^n$ if

$$\int\limits_{\mathbb{R}^n}f_i\frac{\partial\phi}{\partial x_i}dx=0,\quad\forall\phi\in C_0^{\infty}(\mathbb{R}^n).$$

In a random setting we shall refer to a vector field $\mathbf{f}\in\mathbf{L}^2(\Omega):=(L^2(\Omega))^n$ as *potential* (*solenoidal*) if almost all of its realizations $\mathbf{f}(\mathscr{T}(x)\omega)$ are potential (solenoidal)

in $\mathbb{R}^n$. It is known that the convergence in $\mathbf{L}^2(\Omega)$ implies the convergence of almost all realizations in $\mathbf{L}^2_{\text{loc}}(\mathbb{R}^n)$ [49]. In the random setting we use the following spaces:

$$\mathscr{V}^2_{\text{pot}}(\Omega) = \left\{\mathbf{f} \in \mathbf{L}^2_{\text{pot}}(\Omega), \mathbb{E}\{\mathbf{f}\} = 0\right\}, \tag{9.34}$$

$$\mathscr{V}^2_{\text{sol}}(\Omega) = \left\{\mathbf{f} \in \mathbf{L}^2_{\text{sol}}(\Omega), \mathbb{E}\{\mathbf{f}\} = 0\right\}, \tag{9.35}$$

where $\mathbf{L}^2_{\text{pot}}(\Omega)$, respectively $\mathbf{L}^2_{\text{sol}}(\Omega)$, is the set of all $\mathbf{f} \in (L^2(\Omega))^n$ such that a.a. realizations $\mathbf{f}(\mathscr{T}(x)\omega)$ are potential, respectively solenoidal, in $\mathbb{R}^n$. The spaces of potential and solenoidal vector fields $\mathbf{L}^2_{\text{pot}}(\Omega)$ and $\mathbf{L}^2_{\text{sol}}(\Omega)$ respectively, form closed sets in $\mathbf{L}^2(\Omega)$. Here $\mathbb{E}\{\mathbf{f}\}$ means the integral of $\mathbf{f}$ with respect to the probability distribution of the random variable x. Moreover, we have

Lemma 4 (Weyl's Decomposition [49]). *The following orthogonal decompositions are valid:*

$$L^2(\Omega) = \mathscr{V}^2_{\text{pot}}(\Omega) \oplus \mathscr{V}^2_{\text{sol}}(\Omega) \oplus \mathbb{R}$$

$$L^2(\Omega) = \mathscr{V}^2_{\text{pot}}(\Omega) \oplus L^2_{\text{sol}}(\Omega).$$

We consider a random-coefficient matrix $\mathscr{A}(\omega) := [a_{ij}(\omega)]$ defined in Ω, where $a_{ij} \in l^\infty(\Omega)$ and satisfy the ellipticity condition

$$a_{ij}(\omega)\xi_i\xi_j \geq c_1|\xi|^2, \quad c_1 > 0, \quad \text{for} \quad a.a. \quad \omega \in \Omega.$$

In this work we are concerned with homogenization of elliptic operators having the realizations $\mathscr{A}(x) := \mathscr{A}(\mathscr{T}(x)\omega)$. After [49] we define the homogenized matrix $\mathscr{A}^0$ as follows: for each $\xi \in \mathbb{R}^n$ consider the problem

$$\left\langle \phi \cdot \mathscr{A}(\xi + \mathbf{v}) \right\rangle = 0, \quad \forall \phi \in \mathscr{V}^2_{\text{pot}}; \quad \mathbf{v} \in \mathscr{V}^2_{\text{pot}}, \tag{9.36}$$

which is equivalent to

$$\mathbf{v} \in \mathscr{V}^2_{\text{pot}}, \quad \mathscr{A}(\xi + \mathbf{v}) \in \mathbf{L}^2_{\text{sol}}. \tag{9.37}$$

It is obvious that for a typical realization (9.37) is an elliptic equation in $\mathbb{R}^n$, i.e.

$$\text{div}\,(\mathscr{A}(x)(\xi + \nabla u)) = 0,$$

where $u(x)$ is the potential function for the vector field $\mathbf{v} = \mathbf{v}(\mathscr{T}(x)\omega)$ and $\mathscr{A}(x) = \mathbf{A}(\mathscr{T}(x)\omega)$. It is natural then to define the homogenized matrix $\mathscr{A}$ as

$$\mathscr{A}^0\xi := \left\langle \mathscr{A}(\xi + \mathbf{v}) \right\rangle, \tag{9.38}$$

where $\mathbf{v}$ is a solution of (9.36). It is easy to show that if $\mathscr{A}$ is elliptic then $\mathscr{A}^0$ is elliptic as well. See Chap. 7 in [49] for further details.

In order to prove the main convergence results of this paper we use the notion of *stochastic two-scale convergence in the mean* which was introduced in [12] and developed further in [11, 49]. We say that an element $\psi \in L^2(G \times \Omega)$ is admissible if the function

$$\psi_{\mathscr{T}} : (x, \omega) \to \psi(x, \mathscr{T}(x)\omega), \quad (x, \omega) \in G \times \Omega, \tag{9.39}$$

defines an element of $L^2(G \times \Omega)$.

Definition 2. The sequence $\{w^\varepsilon\} \subset L^2(G \times \Omega)$ is said to converge stochastically two-scale in the mean (s.2-s.m.) to a limit $w \in L^2(G \times \Omega)$ iff for any admissible $\psi \in L^2(G \times \Omega)$ we have

$$\lim_{\varepsilon \to 0} \int\limits_{G \times \Omega} w^\varepsilon(x, \omega) \psi\left(x, \mathscr{T}\left(\frac{x}{\varepsilon}\right)\right) dx d\mu = \int\limits_{G \times \Omega} w(x, \omega) \psi(x, \omega)\, dx d\mu.$$

The following Lemma is a variant of one found in Bourgeat–Mikelić–Wright [12]

Lemma 5. *Let $\{\mathbf{u}^\varepsilon\} \in H^1(G)$ be such a sequence that*

$$\begin{cases} \|\mathbf{u}^\varepsilon\|_{L^2(G)} & \leq C, \\ \|\nabla \mathbf{u}^\varepsilon\|_{L^2(G(\omega))} & \leq C, \end{cases} \tag{9.40}$$

Then there exists functions $\mathbf{u}^0 \in H^1(G)$, $\mathbf{u}^1 \in L^2(G, H^1(\Omega)^n)$, such that up to a subsequence,

$$\mathbf{u}^\varepsilon \overset{\text{s.2-s.m}}{\longrightarrow} \mathbf{u}^0(x,t), \tag{9.41}$$

$$\nabla \mathbf{u}^\varepsilon \overset{\text{s.2-s.m}}{\longrightarrow} \nabla_x \mathbf{u}^0(x,t) + \nabla_\omega \mathbf{u}^1(x, \omega, t). \tag{9.42}$$

We first notice that our estimates satisfy the conditions of the above lemma, so we may pass to the limit as $\varepsilon \to 0$ in the variational formulation (9.29). Now, if we assume that $\varphi \in C^\infty(G)^n$, $\psi(x, \mathscr{T}(\frac{x}{\varepsilon})\omega) \in C^\infty(G \times \Omega)$, and let $\bar{\rho} = |G_f|\rho_f + |G_m|\rho_s$, we have the following limits:

$$\int_{G \times \Omega} \rho^\varepsilon \frac{d^2}{dt^2} \mathbf{u}^\varepsilon \left(\varphi(x) + \varepsilon \psi(x, \mathscr{T}\left(\frac{x}{\varepsilon}\right)\omega)\right) dx d\mu \to \int_{G \times \Omega} \bar{\rho} \frac{\partial^2}{\partial t^2} \mathbf{u}^0(x,t) \varphi(x)\, dx d\mu,$$

$$\begin{aligned} &2\mu \int_{G \times \Omega} \chi_{G_f^\varepsilon} e(\partial_t \mathbf{u}^\varepsilon) : e\left(\varphi(x) + \varepsilon \psi(x, \mathscr{T}\left(\frac{x}{\varepsilon}\right)(\omega)\right) dx d\mu \\ &\quad \to 2\mu \int\limits_{G \times \Omega} \chi_{\mathscr{F}}(\omega) \left[e_x(\partial_t \mathbf{u}^0) + e_\omega\left(\partial_t \mathbf{u}^1\right)\right] : \left[e_x(\varphi) + e_\omega\left(\psi(x, \omega)\right)\right] dx d\mu, \end{aligned}$$

$$\int\limits_{G\times\Omega} \chi_{G_s^\varepsilon} Ae(\mathbf{u}^\varepsilon(t)) : e\left(\varphi(x)+\varepsilon\psi\left(x,\mathscr{T}\left(\frac{x}{\varepsilon}\right)(\omega)\right)\right)$$
$$\to \int\limits_{G\times\Omega} \chi_{\mathscr{M}}(\omega) A\left(e_x(\mathbf{u}^0)+e_\omega(\mathbf{u}^1)\right) : \left(e_x(\varphi)+e_\omega(\psi(x,\omega))\right),$$

$$c^2\rho_f \int\limits_{G\times\Omega} \chi_{G_f^\varepsilon} \operatorname{div}\mathbf{u}^\varepsilon \left(\operatorname{div}\left(\varphi(x)+\varepsilon\psi\left(x,\mathscr{T}\left(\frac{x}{\varepsilon}\right)(\omega)\right)\right)\right)$$
$$\to c^2\rho_f \int\limits_{G\times\Omega} \chi_{\mathscr{F}}(\omega)\left(\operatorname{div}\mathbf{u}^0+\operatorname{div}\mathbf{u}^1\right)\left(\operatorname{div}_x\varphi+\operatorname{div}_\omega\psi\right),$$
$$\int\limits_{G\times\Omega} \rho^\varepsilon \mathbf{F}\left(\varphi+\varepsilon\psi\left(x,\mathscr{T}\left(\frac{x}{\varepsilon}\right)(\omega)\right)\right) \to \int\limits_G \bar{\rho}\mathbf{F}\varphi(x)\,dx.$$

The stochastic two-scale convergence then leads to the following problem: Find $\mathbf{u}^0 \in H^3\left(0,T;L^2(G\times\Omega)^n\cap H^2(0,T;H^1(G\times\Omega)^n)\right.$ and $\left.\mathbf{u}^1 \in H^2(0,T;L^2(G\times\Omega;H^1(G\times\Omega)/\mathbb{R})^n\right)$, such that

$$\frac{d^2}{dt^2}\int\limits_{G\times\Omega}\bar{\rho}\mathbf{u}^0(t)\varphi\,dx\,d\mu + c^2\rho_f|\mathscr{F}|\int\limits_G \operatorname{div}_x\mathbf{u}^0(t)\operatorname{div}_x\varphi\,dx\,d\mu$$
$$+c^2\rho_f\int\limits_{G\times\Omega}\chi_{\mathscr{F}}\operatorname{div}_\omega\mathbf{u}^1(t)\operatorname{div}_x\varphi\,dx\,d\mu$$
$$+2\mu\int\limits_{G\times\Omega}\chi_{\mathscr{F}}\left(e_x\left(\frac{\partial\mathbf{u}^0}{\partial t}(t)\right)+e_\omega\left(\frac{\partial\mathbf{u}^1}{\partial t}(t)\right)\right) : e_x(\varphi)\,dx\,d\mu$$
$$+\int\limits_{G\times\Omega}\chi_{\mathscr{M}}A\left(e_x(\mathbf{u}^0(t))+e_\omega(\mathbf{u}^1(t))\right) : e_x(\varphi)\,dx\,d\mu$$
$$=\int\limits_{G\times\Omega}\bar{\rho}\mathbf{F}(t)\varphi\,dx\,d\mu, \qquad \forall\varphi\in H^1(G)^n,\ t>0, \tag{9.43}$$

$$2\mu\int\limits_{G\times\Omega}\chi_{\mathscr{F}}\left(e_x\left(\frac{\partial\mathbf{u}^0}{\partial t}(t)\right)+e_\omega\left(\frac{\partial\mathbf{u}^0}{\partial t}(t)\right)\right) : e_\omega(\psi)\,dx\,d\mu$$
$$+\int\limits_{G\times\Omega}\chi_{\mathscr{M}}A\left(e_x(\mathbf{u}^0(t))+e_\omega(\mathbf{u}^1(t))\right) : e_\omega(\psi)\,dx\,d\mu$$
$$+c^2\rho_f\int\limits_G \operatorname{div}_x\mathbf{u}^0\left(\int\limits_{\mathscr{F}}\operatorname{div}_\omega\psi\right)dx\,d\mu$$
$$+c^2\rho_f\int\limits_{G\times\Omega}\chi_{\mathscr{F}}\operatorname{div}_\omega\mathbf{u}^1\operatorname{div}_\omega\psi\,d\mu\,dx=0,\ \forall\psi\in L^2(0,T;H^1(\Omega)^n). \tag{9.44}$$

$$\mathbf{u}^0(0) = \partial_t \mathbf{u}^0(0) = 0, \qquad \mathbf{u}^1(0) = 0. \tag{9.45}$$

To show uniqueness it is sufficient to prove that for $\mathbf{F} = 0$ we have only the trivial solution $\mathbf{u}^0 = 0, \mathbf{u}^1 = 0$. This is obtained by taking $\varphi = \partial_t \mathbf{u}^0$, and $\psi = \partial_t \mathbf{u}^1$ as test functions in (9.43), (9.44) and adding the two equations together [37].

To eliminate $\mathbf{u}^1$ from the effective equations, we construct a special form ansatz, namely

$$\mathbf{u}^1(x,\omega,t) = \sum_{i,j} \left\{ A^{ij}(\omega) \left(e_x(\mathbf{u}^0)\right)_{ij}(x,t) + \int_0^t B^{ij}(\omega, t-\tau) \left(e_x(\mathbf{u}^0)\right)_{ij}(x,\tau) d\tau \right\} \tag{9.46}$$

Then

$$\partial_t \mathbf{u}^1 = \sum_{i,j} \left\{ A^{ij}(y) \left(e_x(\partial_t \mathbf{u}^0)\right)_{ij}(x,t) + B^{ij}(\omega,0) \left(e_x(\mathbf{u}^0)\right)_{ij}(x,t) - \int_0^t \partial_\tau B^{ij}(\omega, t-\tau) \left(e_x(\mathbf{u}^0)\right)_{ij}(x,\tau) d\tau \right\}.$$

Now we substitute the above $\mathbf{u}^1(x,\omega,t)$ and $\partial_t \mathbf{u}^1$ into (9.44) and obtain the following auxiliary problems [37]:

$$\begin{cases} \int\limits_G \chi_{\mathscr{F}} \left(\dfrac{e_i \otimes e_j + e_j \otimes e_i}{2} + e_\omega\left(A^{ij}\right) \right) : e_\omega(\psi) = 0, \forall \psi \in H^1(\Omega)^n, \\ A^{ij} \in H^1(\mathscr{F})^n. \end{cases} \tag{9.47}$$

In $\mathscr{M}$, A^{ij} is described by

$$\begin{cases} \operatorname{div}_\omega \left(A \left(\dfrac{e_i \otimes e_j + e_j \otimes e_i}{2} + e_\omega(A^{ij}) \right) \right) = 0 \ \text{ in } \ \mathscr{M}, \\ A^{ij}\big|_{\partial\mathscr{M}\setminus\partial\Omega} = A^{ij}\big|_{\partial\mathscr{F}\setminus\partial\Omega}, \ A^{ij} \in H^1(\mathscr{M})^n. \end{cases}$$

While the initial values for the kernel B^{ij} are computed from

$$\begin{cases} 2\mu \int\limits_{\mathscr{F}} e_\omega(B^{ij}(0)) : e_\omega(\psi) \\ +c^2 \rho_f \int\limits_{\mathscr{F}} \left(\operatorname{div}_\omega A^{ij} + \delta_{ij} \right) \operatorname{div}_\omega \psi = 0, \ \forall \psi \in H^1(\Omega), \\ B^{ij}(0) \in H^1(\Omega). \end{cases} \tag{9.48}$$

We rewrite (9.48) in the strong equivalent form;

$$\begin{cases} -2\mu\Delta_\omega B^{ij}(0) = c^2\rho_f \nabla_\omega \operatorname{div}_\omega A^{ij}, \\ \left(2\mu e_\omega(B^{ij}(0)) + c^2\rho_f(\operatorname{div}_\omega A^{ij} + \delta_{ij})I\right)\cdot \nu = 0 \ \text{ on } \partial\mathscr{F}\setminus\partial\mathscr{M}. \end{cases} \tag{9.49}$$

We now can construct the kernel function for B^{ij} from

$$\begin{cases} 2\mu \int\limits_{\mathscr{F}} e_\omega\left(\dfrac{\partial B^{ij}}{\partial t}\right) : e_\omega(\psi) + \int\limits_{\mathscr{M}} A e_\omega\left(B^{ij}\right) : e_\omega(\psi) \\ +c^2\rho_f \int\limits_{\mathscr{F}} \operatorname{div}_\omega B^{ij} \operatorname{div}_\omega \psi = 0, \quad \forall \psi \in H^1(\Omega), \end{cases} \tag{9.50}$$

where $B^{ij}(0)$ is given in $\mathscr{F}$ by (9.49). Now, (9.43) becomes

$$\bar\rho \frac{\partial^2 \mathbf{u}^0}{\partial t^2} - \operatorname{div}_x \left\{ \mathscr{A}^{slco} e_x\left(\partial_t \mathbf{u}^0(x,t)\right) + \mathscr{B}^{slco} e_x\left(\mathbf{u}^0(x,t)\right) + \int_0^t \mathscr{C}^{slco}(t-\tau) e_x\left(\mathbf{u}^0(x,\tau)\right) d\tau \right\} = \bar\rho \mathbf{F}(x,t) \tag{9.51}$$

$$\mathbf{u}^0(0) = 0, \qquad \partial_t \mathbf{u}^0(0) = 0. \tag{9.52}$$

where the effective coefficients tensors are given by

$$\mathscr{A}^{slco}_{ijkl} := 2\mu \int_\Omega \chi_{\mathscr{F}} \left(\frac{e_i\otimes e_j + e_j\otimes e_i}{2} + e_\omega\left(A^{ij}\right)_{kl} \right) d\mu,$$

$$\mathscr{B}^{slco}_{ijkl} := \int_\Omega \chi_{\mathscr{M}} \left(A\left(\frac{e_i\otimes e_j + e_j\otimes e_i}{2} + e_\omega\left(A^{ij}\right) \right) \right)_{kl} d\mu + \int_\Omega \chi_{\mathscr{F}} \left(2\mu \left(e_\omega(B^{ij}(\Omega,0))\right)_{kl} + c^2\rho \left(\operatorname{div}_\omega A^{ij} + \delta_{ij}\right)\delta_{kl} \right) d\mu,$$

$$\mathscr{C}^{slco}_{ijkl}(t) := \int_{\mathscr{F}} \left(2\mu \left(e_\omega\left(\frac{\partial B^{ij}}{\partial t}\right)\right)_{kl} + c^2\rho_f \operatorname{div}_\omega B^{ij}\delta_{ij}\delta_{kl} \right)(\omega,t)\, d\mu + \int_{\mathscr{M}} \left(A e_\omega\left(B^{ij}\right)\right)_{kl}(\omega,t)\, d\mu.$$

Proving uniqueness of the solution for (9.51)–(9.52) is reduced to proving that the effective tensor composed of the Laplace transforms $\gamma\mathscr{A}^{slco} + \mathscr{B}^{slco} + \hat{\mathscr{C}}^{slco}$ is

positive definite. Establishing the required positive definiteness is along the same lines as in the proof of Lemma 11 in [34].

In summary, we derived an effective model for acoustic wave propagation in solid-fluid composite with microstructure. The microstructural geometry was modeled as a realization of a stationary random field with built-in scale separation. Application of the stochastic two-scale convergence in the mean yields a two-velocity effective system coupling the leading term in the asymptotics $\mathbf{u}^0$ with a corrector $\mathbf{u}^1$. We introduced an ansatz for the corrector that enables its elimination from the system and reduces the two-velocity system to a smaller system of effective equations for the leading term alone. The effective equations model a single phase, uniform viscoelastic medium with long time history dependence.

9.4 Blood-Marrow Mixture as a Non-Newtonian Fluid

In the Biot model the pore space is filled by a single-viscosity fluid, whereas the fluid filling the pores in actual bone consists of a blood-marrow mixture, which is better modeled as a complex polymer. This suggests that, for the **low frequency case** ($\omega < 100\,\mathrm{KHz}$) a shear thinning non-Newtonian fluid modeling the blood-marrow mixture should lead to a more accurate results [65, 68, 71]. As the Biot model really comes from mixture theory, it might be expected that a simple two-scale homogenization, including the complex nature of the blood-marrow mixture, should give more physically accurate coefficients. For low frequency ultrasound ($\omega < 100\,\mathrm{KHz}$) marrow significantly decreases ultrasound velocity but increases attenuation, attenuation slope and backscatter when compared with defatted bone [59]. Moreover, the impact of marrow on **QUS** measurements is greater at lower bone mineral density (**BMD**). A quantitative acoustic model must take into account that cancellous bone is mostly blood and marrow. In this section cancellous bone is modeled as a periodic two-phase material consisting of a porous viscoelastic matrix (trabeculae) filled with a non-Newtonian fluid (marrow).

We assume that the solid phase (trabeculae) is a Kelvin-Voight viscoelastic material with the constitutive equation

$$\sigma^{s,\varepsilon} = Ae(\mathbf{u}^\varepsilon) + Be(\mathbf{v}^\varepsilon), \quad e(\mathbf{u}^\varepsilon)_{ij} := \frac{1}{2}\left(\frac{\partial u_i^\varepsilon}{\partial x_j} + \frac{\partial u_j^\varepsilon}{\partial x_i}\right), \tag{9.53}$$

where $\mathbf{v}^\varepsilon$ denotes velocity, $\mathbf{u}^\varepsilon = \int_0^t \mathbf{v}^\varepsilon(\cdot,\tau)d\tau$ is the displacement, and $\sigma^{s,\varepsilon}$ is the stress tensor. The equations of motion in the solid part are then given by

$$\rho_s \partial_t \mathbf{v}^\varepsilon - \mathrm{div}(Ae(\mathbf{u}^\varepsilon) + Be(\mathbf{v}^\varepsilon)) = \rho_s \mathbf{F} \tag{9.54}$$

in $\Omega_s^\varepsilon \times]0,T[$. Here $\mathbf{F}$ is the mass density of the external fore (e.g. gravity) and we assume that $\mathbf{F}$ is a constant vector.

In the fluid part, we model the blood marrow mixture as a non-Newtonian shear thinning fluid [65,68,71]. To this end, we use Carreau law, which takes into account that polymers show a finite nonzero constant Newtonian viscosity at very low shear rates [1],

$$\eta_r\left(e(\dot{\mathbf{u}})\right) = \eta_r\left(e(\dot{\mathbf{u}})\right) := (\eta_0 - \eta_\infty)\left(1 + \lambda |e(\dot{\mathbf{u}})|^2\right)^{\frac{r}{2}-1} + \eta_\infty \tag{9.55}$$

$$1 < r < 2, \quad \eta_0 > \eta_\infty \geq 0, \quad \lambda > 0. \tag{9.56}$$

The parameter η_∞ is usually very small. Therefore, we set $\eta_\infty = 0$ and use the so-called Bird–Carreau law. It should be noted that for $\eta_\infty > 0$, the term containing η_∞ yields a standard linear Navier–Stokes type constitutive equation. Because the first term in (9.55) is sub-linear, the second term would dominate with the resulting case being very similar to the linear theory. In particular, available a priori estimates would be L^2-based, rather than L^r-based. The case $\eta_\infty = 0$ is thus more difficult and mathematically more interesting.

By taking $\mathbf{v} = \dot{\mathbf{u}}$ and making the standard small compressibility approximation we remove the pressure from the system [21]. Now the equations in the fluid part become

$$\rho_f \partial_t \mathbf{v}^\varepsilon - \operatorname{div}(\sigma^{f,\varepsilon}) = \rho_f \mathbf{F} \tag{9.57}$$

in $\Omega_f^\varepsilon \times]0,T[$, where

$$\sigma^{f,\varepsilon} := c^2 \rho_f \operatorname{div}\mathbf{u}^\varepsilon I + 2\mu\, \eta_r\left(e(\mathbf{v}^\varepsilon)\right) e(\mathbf{v}^\varepsilon). \tag{9.58}$$

The transition conditions between fluid and solid parts are given by the continuity of displacement

$$[\mathbf{u}^\varepsilon] = 0 \text{ on } \Gamma_\varepsilon \times]0,T[, \tag{9.59}$$

where $[\cdot]$ indicates the jump across the boundary, and the continuity of the contact force

$$\sigma^{s,\varepsilon} \cdot \nu = \sigma^{f,\varepsilon} \cdot \nu \text{ on } \Gamma_\varepsilon \times]0,T[, \tag{9.60}$$

where Γ_ε denotes the boundary between fluid and solid. At the exterior boundary we impose zero boundary conditions for $\mathbf{u}^\varepsilon$ and $\mathbf{v}^\varepsilon$.

The initial conditions are

$$\begin{aligned} \mathbf{u}^\varepsilon(0,x) &= 0, \quad \text{in } \Omega \\ \mathbf{v}^\varepsilon(0,x) &= \mathbf{v}_0, \quad \text{in } \Omega. \end{aligned} \tag{9.61}$$

To write the weak formulation of the system (9.53)–(9.61), it is convenient to introduce θ^ε – the characteristic function of Ω_s^ε. Note that $\theta^\varepsilon(x) = \theta(\frac{x}{\varepsilon})$ and $\theta(y)$ is the characteristic function of the solid part of the unit cell (periodically extended to the whole space). Now, we can define the composite density ρ^ε and composite stress as

$$\rho^\varepsilon = \rho_s \theta^\varepsilon + \rho_f (1 - \theta^\varepsilon) \tag{9.62}$$

$$\sigma^{\varepsilon} = \sigma^{s,\varepsilon}\theta^{\varepsilon} + \sigma^{f,\varepsilon}(1-\theta^{\varepsilon}) \tag{9.63}$$

In the following we shall also use the notation

$$\sigma^{\varepsilon} = T^{\varepsilon}(e(\mathbf{v}^{\varepsilon})),$$

where

$$T^{\varepsilon}(\phi)\left(x,\frac{x}{\varepsilon},t\right) = \theta^{\varepsilon}A\left(\int_0^t \phi\right) + \theta^{\varepsilon}B\phi + (1-\theta^{\varepsilon})c^2\rho_f \mathrm{tr}\left(\int_0^t \phi\right) I + (1-\theta^{\varepsilon})2\mu\,\eta_r(\phi)\phi \tag{9.64}$$

Also, define

$$T^{0}(\phi)(x,y,t) = \theta(y)A\left(\int_0^t \phi\right) + \theta(y)B\phi + (1-\theta(y))c^2\rho_f \mathrm{tr}\left(\int_0^t \phi\right) I + (1-\theta(y))2\mu\,\eta_r(\phi)\phi \tag{9.65}$$

for each smooth, symmetric matrix function $\phi(x,y,t)$. Here, tr ϕ denotes trace of the matrix ϕ. Multiplying (9.54), (9.57) by a smooth test function ϕ, equal to zero on $\partial\Omega$ and equal to zero for $t = T$, formally integrating by parts and using boundary and interface conditions we can write the weak formulation of the problem (9.53)–(9.61):

$$-\int_{\Omega} \rho^{\varepsilon}\mathbf{v}_0\cdot\phi(x,0)dx - \int_0^T\int_{\Omega} \rho^{\varepsilon}\mathbf{v}^{\varepsilon}\cdot\partial_t\phi\,dxdt + \int_0^T\int_{\Omega} \sigma^{\varepsilon} : e(\phi)dxdt = \int_0^T\int_{\Omega} \rho^{\varepsilon}\mathbf{F}\cdot\phi, \tag{9.66}$$

for each $\phi \in C^{\infty}(]0,T[, C_0^{\infty}(\Omega)^n)$ such that $\phi(T,x) = 0$.

We assume that for each $\varepsilon > 0$, the problem (9.66) has a finite energy weak solution satisfying $\mathbf{v}^{\varepsilon} \in L^{\infty}(0,T;L^2(\Omega)^n)$, $\mathbf{u}^{\varepsilon} \in L^{\infty}(0,T;L^2(\Omega)^n)$, $e(\mathbf{v}^{\varepsilon}) \in L^r(0,T;L^r(\Omega)^n)$, $e(\mathbf{u}^{\varepsilon}) \in L^{\infty}(0,T;L^r(\Omega)^n)$, where r is the constant in the power or Carreau law. Moreover, in Ω_s we have $e(\mathbf{v}^{\varepsilon}) \in L^2(0,T;L^2(\Omega_s)^n)$, $e(\mathbf{u}^{\varepsilon}) \in L^{\infty}(0,T;L^2(\Omega_s)^n)$. These assumptions are reasonable and the following theorem shows that the above inclusions follow naturally from energy estimates. Hence, the existence of the solution can be established using an approximation procedure, the energy estimates and monotonicity of the principal part of the operator of the problem.

Theorem 2. *The finite energy weak solutions are bounded uniformly in ε, i.e.*

$$\| \mathbf{u}^{\varepsilon} \|_{L^{\infty}([0,T],L^2(\Omega)^n)} \le C, \quad \| \mathbf{v}^{\varepsilon} \|_{L^{\infty}([0,T),L^2(\Omega)^n)} \le C,$$

$$\| e(\mathbf{u}^{\varepsilon}) \|_{L^{\infty}(0,T;L^r(\Omega)^n)} \le C, \quad \| e(\mathbf{v}^{\varepsilon}) \|_{L^r(0,T;L^r(\Omega)^n)} \le C,$$

$$\| e(\mathbf{u}^\varepsilon) \|_{L^\infty(0,T;L^2(\Omega_s^\varepsilon)^n)} \le C, \quad \| e(\mathbf{v}^\varepsilon) \|_{L^2(0,T;L^2(\Omega_s)^n)} \le C,$$

$$\| \operatorname{div}\mathbf{u}^\varepsilon \|_{L^\infty(0,T;L^2(\Omega)^n)} \le C, \quad \| \rho^\varepsilon \partial_t \mathbf{v}^\varepsilon \|_{L^r(0,T;W^{-1,r}(\Omega)^n))} \le C,$$

$$\| \sigma^\varepsilon \|_{L^r(0,T;L^r(\Omega)^{n\times n}))} \le C,$$

where C denotes a generic constant independent of ε (but possibly dependent on T, Ω, ellipticity constants for the tensors A, B, viscosity of the fluid, parameters η_0, λ in the Carreau law, and also on ρ_s and ρ_f). The number r is a power in Carreau law.

A priori estimates in Theorem 2 and sequential compactness properties of two-scale convergence imply that for almost all $t \in [0,T]$ there exist subsequences $\mathbf{v}^\varepsilon$, σ^ε (not relabeled), and functions $\overline{\mathbf{v}} \in L^r([0,T];W^{1,r}(\Omega)^n)$, $\mathbf{w} \in L^r([0,T];L^r(\Omega, W^{1,r}_{\mathrm{per}}(\mathscr{Y})/\mathbb{R})^n)$, and $\sigma^0 \in L^r([0,T];L^r(\Omega\times Y/\mathbb{R})^{n\times n})$, such that

$$\mathbf{v}^\varepsilon \to \overline{\mathbf{v}}(t,x) \text{ in the two-scale sense,} \tag{9.67}$$

$$e(\mathbf{v}^\varepsilon) \to e_x(\overline{\mathbf{v}})(t,x) + e_y(\mathbf{w})(t,x,y) \text{ in the two-scale sense,} \tag{9.68}$$

$$\sigma^\varepsilon \to \sigma^0 \text{ in the two-scale sense.} \tag{9.69}$$

Next, we pass to the limit as $\varepsilon \to 0$ in (9.66) using a generic test function $\phi(x,t)$. Let

$$\overline{\rho} = \int_{\mathscr{Y}} (\rho_s \theta(y) + \rho_f(1-\theta(y)))dy. \tag{9.70}$$

Noting the well known fact that $\rho^\varepsilon \to \overline{\rho}$ weak-$\star$ in $L^\infty(\Omega)$ allows us to pass to the limit in the first term in the left hand side of (9.66), and also in the right hand side. To pass to the limit in the second term in the left hand side, we use Lemma due to Lions [52], which yields $\rho^\varepsilon \mathbf{v}^\varepsilon \to \overline{\rho}\overline{\mathbf{v}}$ in the sense of distributions on $(0,T)\times\Omega$. In the term containing σ^ε we use the fact that two-scale convergence $\sigma^\varepsilon \to \sigma^0$ implies weak convergence of σ^ε to $\int_{\mathscr{Y}} \sigma^0(x,y,t)dy$ [2, 61, 79]. Combining the above results we obtain

$$-\int_\Omega \overline{\rho}\mathbf{v}_0\cdot\phi(x,0)dx - \int_0^T\int_\Omega \overline{\rho}\overline{\mathbf{v}}\cdot\partial_t\phi dxdt + \int_0^T\int_\Omega \left(\int_{\mathscr{Y}} \sigma^0(x,y,t)dy\right) : e(\phi)dxdt$$
$$= \int_0^T\int_\Omega \overline{\rho}\mathbf{F}\cdot\phi, \tag{9.71}$$

which is a weak formulation of

$$\bar{\rho}\partial_t\overline{\mathbf{v}} - \operatorname{div}_x \int_Y \sigma^0(x,y,t)dy = \bar{\rho}\mathbf{F}, \tag{9.72}$$

together with the initial condition $\overline{\mathbf{v}}(x,0) = \mathbf{v}_0$.

Next we take $\phi^\varepsilon(x,t) = \varepsilon\phi(x, \frac{x}{\varepsilon}, t)$ as a test function in the (9.66). Passing to the limit as $\varepsilon \to 0$ yields

$$0 = \int_Y \sigma^0 : e(\phi(y,t))dy = -\int_Y \mathrm{div}_y \sigma^0 \cdot \phi(y,t)dy,\ \forall \phi(y,t), \tag{9.73}$$

which is a weak formulation of the equation

$$\mathrm{div}_y \sigma^0(x,y,t) = 0. \tag{9.74}$$

To obtain a closed-form effective system from equations (9.72), (9.74) we should specify an effective constitutive equation, that is, describe the dependence of the limiting stress tensor σ^0 on the gradients of $\overline{\mathbf{v}}$ and $\mathbf{w}$. First, we prove a lemma that essentially provides monotonicity of the operators associated with σ^ε.

Lemma 6. *For each fixed $\tau \in (0,T)$, let $\xi_\tau \in C^\infty([0,T])$ be such that*

(i) $d_t \xi_\tau \le 0$,
(ii) $\xi_\tau(t) = 1$ for $t \in [0,\tau]$, and $\xi_\tau(T) = 0$.

Then, for each pair of symmetric matrices $\phi, \psi \in C^\infty(\Omega \times Y \times [0,T])^{n\times n}$, we have

$$\int_0^T \int_\Omega (T^\varepsilon(\phi) - T^\varepsilon(\psi)) : (\phi - \psi)\,\xi_\tau dxdt \ge 0 \tag{9.75}$$

where T^ε is defined by (9.64).

One of the key ingredients in proving the above lemma is the fact that the nonlinear terms in the stress can be expressed in terms of convex potential. We have

$$\eta_r(|\phi|)\phi = \nabla_\phi F(|\phi|),$$

for each smooth symmetric matrix function ϕ, where

$$F(s) = \frac{1}{r\lambda}(\eta_0 - \eta_\infty)(1+\lambda s^2)^{r/2} + \frac{1}{2}\eta_\infty s^2.$$

Then $F(|\phi|)$ is a convex function of ϕ [36].

Lemma 6 enables us to use classical Minty-Browder monotonicity argument to obtain the closed form of the effective constitutive equations. Namely, we prove that

Theorem 3. *The effective stress satisfies*

$$\sigma^0 = T^0(e_x(\overline{\mathbf{v}}) + e_y(\mathbf{w})),$$

where T^0 is given by (9.65).

It should be noted that the proof of Theorem 3 is not straight-forward, due to the presence of inertial terms in constitutive equations. For the details, please refer to [36, 73].

Now we can specify the effective equations. Combining Theorem 3 with (9.72), (9.74) we obtain

$$\overline{\rho}\partial_t \overline{\mathbf{v}} - \operatorname{div} \int_{\mathscr{Y}} T^0(e_x(\overline{\mathbf{v}}) + e_y(\mathbf{w}))dy = \overline{\rho}\mathbf{F}, \tag{9.76}$$

$$\operatorname{div}_y \left(T^0(e_x(\overline{\mathbf{v}}) + e_y(\mathbf{w}))\right) = 0, \tag{9.77}$$

where T^0 is given by (9.65).

The effective constitutive equations provide an explicit dependence of the effective stress on the sum $e(\overline{\mathbf{v}}) + e_y(\mathbf{w})$. The equations are of the two-velocity type, that is the equation for the effective velocity $\overline{\mathbf{v}}$ is coupled to the equation for the corrector velocity $\mathbf{w}$. The first equation governs the evolution of $\overline{\mathbf{v}}$, while the second is the corrector equation for $\mathbf{w}$ (also an evolution equation, but of a different type [36]). Elimination of the corrector term in two-scale non-linear systems is an open problem of significant interest. This problem arises not only for acoustic equations, but also for other types of homogenization problems (e.g. in plasticity and for non-Newtonian flows). The initial conditions for (9.76) are $\overline{\mathbf{v}}(x,0) = \mathbf{v}_0$ and the natural condition $\overline{\mathbf{u}}(x,0) = 0$, where $\overline{\mathbf{u}} = \int_0^t \overline{\mathbf{v}}(\tau,\cdot)d\tau$ is the effective displacement. It seems that the effective equations describe a single phase non-linear viscoelastic material, but this fact is a bit concealed by the implicit structure of these equations.

9.5 Numerical Upscaling

Multiscale FEM belongs to the group of homogenization methods applicable only in the case of statistically uniform materials [28, 57, 58, 72, 75–77]. For this kind of materials, it is typical that they possess a representative volume element (**RVE**) whose analysis yields the effective material parameters. However, there is a limiting condition; namely, the ratio of the characteristic lengths of RVE and the simulated body has to tend to zero. This is from where the usual terminology macro- and micro- scale is derived. As both scales are analyzed simultaneously, the standard notation distinguishes between quantities related to the different scales by introducing an overbar symbol. Thus position vector, displacements vector, strain tensor, stress tensor, and potential respectively are denoted by

$$\bar{\mathbf{x}}, \bar{\mathbf{u}}, \bar{e}, \bar{\sigma}, \bar{\psi} = \bar{\psi}(\bar{e}, \bar{\mathbf{x}}) \qquad \text{at the macrocontinuum level} \tag{9.78}$$

$$\mathbf{x}, \mathbf{u}, e, \sigma, \psi = \psi(e, \mathbf{x}) \qquad \text{at the microcontinuum level} \tag{9.79}$$

In the recent works of Ilic, Hackl, Gilbert [45, 46] a multiscale FEM is used to model acoustic properties of cancellous bone. While in multiscale FEM it is usual that the RVE contains a sufficiently large number of cells in order to obtain an effective average, in this work we use instead a single element in which we may vary the thickness and nature of the trabeculae. It is assumed that the solid frame

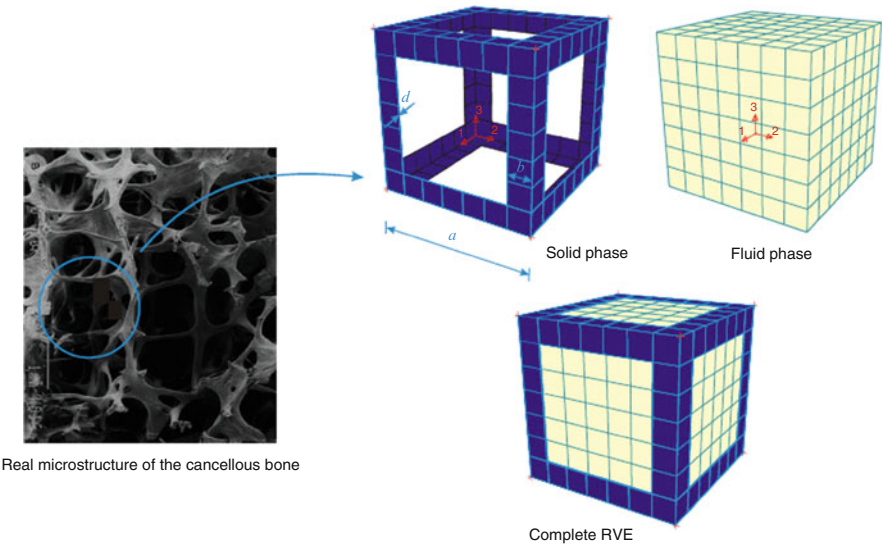

Fig. 9.1 Real bone microstructure and corresponding RVE

of the cancellous bone consisted of shell elements, see Fig. 9.1. Moreover, to obtain a measure of non-periodicity we arbitrarily rotate the RVE at each point, as this destroys the periodic matching of boundary conditions.

The method is based on the principle of volume averaging, leading to the definition of the macrostress tensor in the form

$$\bar{\sigma} = \frac{1}{V}\int_{\mathscr{B}} \sigma \, dV \tag{9.80}$$

where the integration is carried out over a suitable RVE, denoted by $\mathscr{B}$, with the volume V. The well-posedness of the problem on the microscale still requires the equality of macrowork with the volume average of microwork

$$\bar{\sigma} : \bar{e} = \frac{1}{V}\int_{\mathscr{B}} \sigma : e \, dV \tag{9.81}$$

which is known as Hill–Mandel macrohomogeneity condition [40–42,45,54,55,70]. Expression (9.81) is satisfied by three types of boundary conditions at the microlevel: i.e. static, kinematic and periodic boundary conditions. The microdeformation is assumed to be dependent on the macrostrain tensor $\bar{e}$ and on the microfluctuations $\tilde{\mathbf{u}}$ such that $\mathbf{u} = \bar{e}\mathbf{x} + \tilde{\mathbf{u}}$. This separation of scales leads to the decomposition of the strain tensor into the mean part and the micro-fluctuation part:

$$e = \bar{e} + \tilde{e}, \qquad \tilde{e} = \frac{1}{2}\left(\nabla\tilde{\mathbf{u}} + \nabla^T\tilde{\mathbf{u}}\right).$$

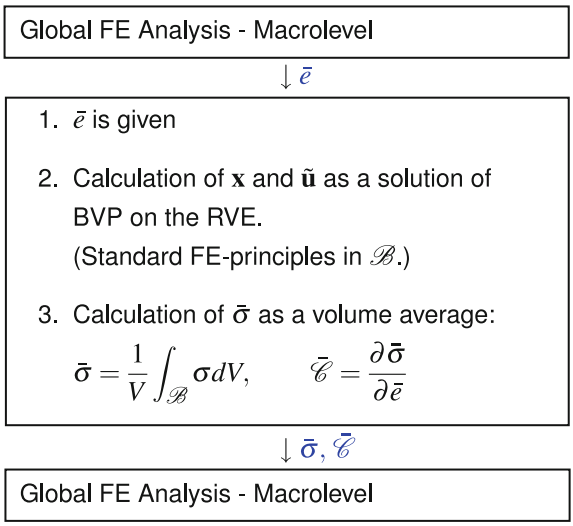

Fig. 9.2 Connection of scales in the program code

Such a decomposition permits splitting the problem of simulation of a heterogeneous body into two parts, each consisting of one boundary value problem (**BVP**). The first BVP relates to the simulation of the homogenized macroscopic body and the second one to the analysis of the RVE. We used FEM to solve both BVPs. The interaction of micro- and macro- level computation is schematically represented by Fig. 9.2. Moreover, using the described theory and standard program FEAP, a new multiscale FE program was written [45].

The right choice of the RVE is an important requirement for the multiscale **FEM** to work well. In the case of the cancellous bone, a cube-shaped RVE consisting of solid frame and fluid core is chosen within this work. The solid part consists of thin walls so that the complete geometry of RVE can be described by three parameters: side length a, wall thickness d and wall width b. Figure 9.1 shows an example of the real microstructure of cancellous bone affected by osteoporosis, and a proposal for the corresponding RVE. To calculate the effective material parameters, a dynamic analysis of the proposed RVE is necessary, and periodic excitation is preferable because of its simplicity. In such a case, the load and induced deformations are harmonic functions in time with frequency ω. To describe the problem completely, the constitutive laws of the fluid and solid phase still need to be stated precisely. Regarding the bone material, a linear analysis is typical so that for the solid part a linear relation between stresses and strains $(9.82)_2$ and for the marrow the constitutive law of barotropic fluids are assumed (9.83). The state of deformations in the solid part can now be described by the system

$$-\omega^2 \rho_s \mathbf{u} - \nabla \cdot \sigma_s = \rho_s \mathbf{b}(\mathbf{x}), \quad \sigma_s = \mathscr{C} : e \tag{9.82}$$

and in the fluid part by:

$$-\omega^2\rho_f\mathbf{u}-\nabla\cdot\sigma_f=\rho_f\mathbf{b}(\mathbf{x}),$$
$$\sigma_f=c^2\rho_f\nabla\cdot\mathbf{u}\mathbb{I}+2i\omega\eta e+i\omega\xi\nabla\cdot\mathbf{u}\mathbb{I}. \tag{9.83}$$

Here $\mathscr{C}$ is the elasticity tensor of the solid phase, c the sound velocity of the marrow so that $c=\sqrt{K/\rho_f}$, K is the bulk modulus, and η and ξ are the viscosity coefficients. The indices s and f are used to distinguish the phases. Furthermore, the coupling condition between the phases requires that there is no deformation jump on the interface of phases. Recall that all the expressions (9.82), (9.83) are defined in the complex domain. The material parameters of the solid phase, bulk modulus K_s and shear modulus μ_s are also complex-valued and they can be written in the form $K_s=K_s^R+iK_s^I$, $\mu_s=\mu_s^R+i\mu_s^I$, where the imaginary parts are related to the real ones according to

$$K_s^I=\frac{\delta}{\pi}K_s^R \quad \text{and} \quad \mu_s^I=\frac{\delta}{\pi}\mu_s^R,$$

where δ denotes the logarithmic decrement [13, 15]. Due to the geometric properties, we are going to model the solid phase by using the shell elements (see for example [47]). But as the shell elements already implemented in the program FEAP [78] are not applicable for simulations in the complex domain, further adaption has been necessary. In particular we focused on the extension of an element convenient for simulation of flat and shallow shells. The formulation of this element is based on the superposition of the linear theory for a plate loaded in its plane and a plate loaded by bending, whose potentials are

$$\Pi_p^e=\Pi_p^{e,int}+\Pi_p^{e,ext}=\frac{1}{2}\int_{\mathscr{A}^e}\mathbf{u}^T\cdot\mathbf{L}_p^T\cdot\mathscr{C}_p\cdot\mathbf{L}_p\cdot\mathbf{u}\,d\alpha+\Pi_p^{e,ext}, \tag{9.84}$$

$$\Pi_b^e=\Pi_b^{e,int}+\Pi_b^{e,ext}=\frac{1}{2}\int_{\mathscr{A}^e}\theta^T\cdot\mathbf{u}^T\cdot\mathbf{L}_b^T\cdot\mathscr{C}_b\cdot\mathbf{L}_b\cdot\theta\,d\alpha+\Pi_b^{e,ext}. \tag{9.85}$$

Hereafter subscript p is taken to denote the plate loaded in its plane and subscript b for the bending of plate. $\mathbf{L}_p$ and $\mathbf{L}_b$ are linear operators and $\mathscr{C}_p$ and $\mathscr{C}_b$ material tensors whose precise definition can be found in the literature [5, 19, 28, 30, 35]. The integration is carried out over the middle area of the element $\mathscr{A}^e$. As expression (9.84) depends on the displacements $\mathbf{u}_p=\{u,v\}^T$ and (9.85) on the rotations $\theta=\{\theta_x,\theta_y\}^T$, a **FE** approximation

$$\mathbf{u}^m=\mathbf{N}^m\cdot\hat{\mathbf{a}}^{me},$$

$$\mathbf{u}^m=\{u,v,\theta_x,\theta_y\}^T,$$
$$\hat{\mathbf{a}}_i^m=\{\hat{u}_i,\hat{v}_i,\hat{\theta}_{zi},\hat{w}_i,\hat{\theta}_{xi},\hat{\theta}_{yi}\}^T,$$

leads after substitution into the first variation of (9.84) and (9.85) to the weak form of the problem

$$\delta\Pi^e = (\delta\hat{\mathbf{a}}^{me})^T \cdot \left(\int_{\mathscr{A}^e} (\mathbf{N}^m)^T \cdot \mathbf{L}^T \cdot \mathscr{C} \cdot \mathbf{L} \cdot \mathbf{N}^m \, d\alpha \right) \cdot \hat{\mathbf{a}}^{me} + \delta\Pi^{e,ext},$$

$$= (\delta\hat{\mathbf{a}}^{me})^T \cdot \left(\int_{\mathscr{A}^e} (\mathbf{B}^m)^T \cdot \mathscr{C} \cdot \mathbf{B}^M \, d\alpha \right) \cdot \hat{\mathbf{a}}^{me} + \delta\Pi^{e,ext}. \tag{9.86}$$

In the above expressions, $\mathbf{N}^m$ represents the matrix of the shape functions, and superscript m indicates that a modified approximation is used ($\hat{\theta}_{zi}$ and $\hat{w}_i$ are used in the approximation of the vector $\mathbf{u}$). The symbol $\hat{a}^{me}$ relates to the vector of the element **DOF**s and $\hat{a}_i^m$ to the vector of the nodal **DOF**s. The matrices appearing in (9.86) are composed as follows

$$\mathbf{L} = \begin{bmatrix} \mathbf{L}_p & 0 \\ 0 & \mathbf{L}_b \end{bmatrix}, \quad \mathbf{B}^m = \mathbf{L} \cdot \mathbf{N}^m, \quad \mathscr{C} = \begin{bmatrix} \mathscr{C}_p & 0 \\ 0 & \mathscr{C}_b \end{bmatrix}. \tag{9.87}$$

The application of the element in the dynamic case also requires inclusion of the kinetic energy E_k,

$$E_k = \frac{1}{2} \int_{\Omega} \rho \dot{\mathbf{u}}^T \cdot \dot{\mathbf{u}} \, dv \tag{9.88}$$

and its variation

$$\delta \int_0^t E_k(\dot{\mathbf{u}}) \, dt = -\int_0^t \int_{\Omega} \rho \delta \mathbf{u}^T \cdot \ddot{\mathbf{u}} \, dv \, dt = \omega^2 \int_0^t \int_{\Omega} \rho \delta \mathbf{u}^T \cdot \mathbf{u} \, dv \, dt. \tag{9.89}$$

As this expression only depends on the acceleration and indirectly on the displacements, a simplified FE approximation may be introduced. See the thesis by Sandra Ilic [42] and also the papers [43–46] for more complete details of the above discussion.

In order to model the fluid phase an extension to the complex domain was necessary for the eight-node cubic element chosen to simulate the marrow part. As in this case the derivation procedure is much simpler, it can be stated directly using the complex form of the potential characteristic for this element [45]

$$L = \frac{1}{2} \int_{\Omega} \rho \dot{\mathbf{u}}_c^T \cdot \dot{\mathbf{u}}_c \, \mathrm{div} - \frac{1}{2} \int_{\Omega} \varepsilon_c \cdot \mathscr{C}_c \cdot \varepsilon_c \, dv - \Pi^{ext}. \tag{9.90}$$

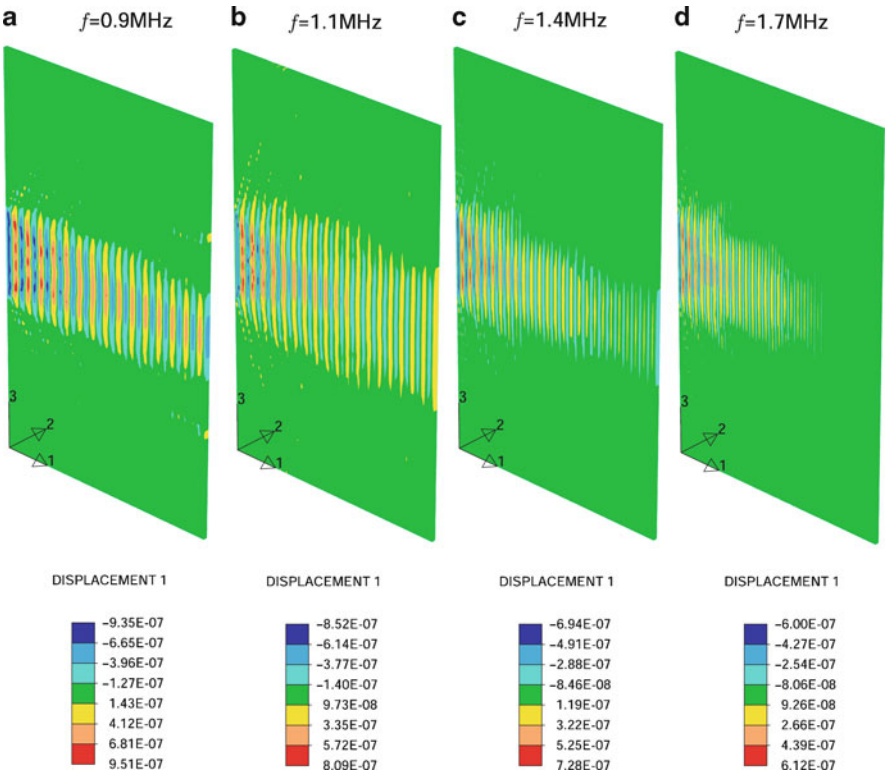

Fig. 9.3 Dependency of attenuation on frequency of excitation

In [44] some results were presented concerning the propagation of waves of different frequencies through samples with different material parameters. These are computer simulations to check the experimentally obtained result that increasing excitation frequency and material density cause increasing attenuation. In Fig. 9.3 the influence of increasing excitation frequency on the attenuation of the signal is demonstrated. For this simulation the type of material microstructure in the simulations is fixed, and sound excitation at different frequencies is applied. As the influence of attenuation is more noticeable in the case of higher frequencies, excitation is simulated in the domain 0.9–1.7 MHz. The study of the relationship between attenuation and density is more complicated than of the influence of excitation frequency. This can be expected, because the RVE geometry presented earlier is determined by three parameters (wall thickness d, wall width b and side length a). Correspondingly, three different types of tests can be carried out. In each group of tests, two of the geometrical parameters have to be kept constant and the remaining one is varied. Results are shown in Fig. 9.4.

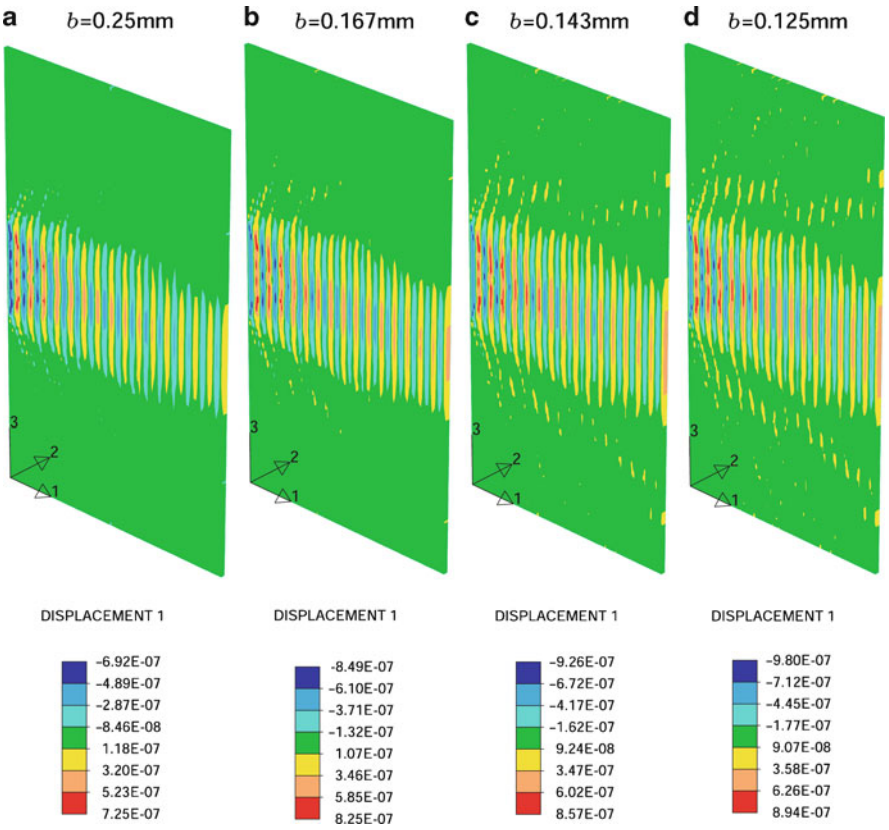

Fig. 9.4 Dependency of attenuation on microstructure

9.6 Inverse Problems

In our models of bone, the matrix (solid part) was considered to be linear and elastic and the interstitial region saturated by a viscous fluid described by the compressible Navier–Stokes equations. Utilizing the techniques of homogenization, we were able to derive a set of effective visco-elastic equations for the acoustic modeling of poro-elastic materials. The reason we use homogenized (effective) equations, rather than direct simulation of ultrasound propagation in bone, is due to the fact that ultrasound assessment of bone qualities is posed as an inverse problem of evaluating effective properties of bones and statistical data on microstructure (such as porosity) from ultrasound measurement. Typical scale of trabecular bone spacing is 0.5–2 mm with thickness 50–150 μm. In the low frequency range (<100 KHz), the wavelength is longer than 15 mm; hence homogenized theory can be applied. Biomechanicians [28, 29, 48, 53] have frequently used Biot's equations to model bone as a poroelastic medium, consisting of an elastic frame with interstitial pore

fluid. In the present discussion we follow this approach. However, we have used models that have been obtained by homogenization methods which produce a more complicated model. These models are not in contradiction to the Biot model as the non-Biot coefficients are orders of magnitude smaller that the others [25, 26]. To emulate the experiments of Hosokawa and Otani [48] and Williams et al. [74], for the case of a femur we considered a two dimensional cross-section to be a reasonable physical approximation for the problem. In this case, we sought to consider the **inverse problem** for a two-dimensional sample of cancellous bone by using acoustic pressure data at different locations in the water tank (See also the paper by Laugier et al. [66]). It was done by minimizing the difference with respect to an appropriate norm between the given acoustic pressure data (considered as a data vector) and the acoustic pressure predicted by the homogenized equations over a set of effective parameters. This required solving the effective equations (direct problem) and a nonlinear inverse problem. We should mention that, contrary to what one might think, no three-dimensional inversions have to date been made despite the scientifically important work done in the papers [7, 19, 20, 22, 23, 63, 64, 66, 69]. They consider either one-dimensional inversion approaches or three-dimensional direct problems, i.e. observing wave propagation through the matrix of one of the micro computed tomography (μCT) scans. The inverse problem we considered should not be confused with the reconstruction of microstructure from (μCT) obtained using a synchrotron or with the correlation analysis performed on macroscopic parameters. Our inverse problems for cancellous bone bring significant improvements to the existing models, as they are truly two-dimensional. We intend to extend this method to the fully three-dimensional bone sample.

In what follows, we explain what we have done in the **low frequency range**, by first recalling to the reader what the Biot equations are. In the Biot model the motion of the frame and fluid within the bone pores are tracked by the vectors $\mathbf{u} = [u_1, u_2, u_3]$ and $\mathbf{U} = [U_1, U_2, U_3]$ respectively. The constitutive equations used by Biot are those of an isotropic linear elastic material with terms added to account for the interaction of the frame and interstitial fluid. These equations described in Cartesian coordinates.

$$\begin{aligned} &\textbf{Solid part:} \quad \sigma_{ii} = 2\mu e_{ii} + \lambda e + Q\varepsilon,\ \sigma_{ij} = \mu e_{ij} \text{ for } i \neq j, \\ &\textbf{Fluid part:} \quad \sigma = Qe + R\varepsilon, \end{aligned}$$

where e_{ij} is the ij component of the stress tensor and the solid and fluid dilatations are given by

$$e = \nabla \cdot \mathbf{u} = \sum_{i=1}^{3} \frac{\partial u_i}{\partial x_i}, \quad \varepsilon = \nabla \cdot \mathbf{U} = \sum_{i=1}^{3} \frac{\partial U_i}{\partial x_i}.$$

The complex frame shear modulus μ can be measured. The other parameters λ, R, and Q occurring in the constitutive equations are calculated from the measured or estimated values of the parameters given in Table 9.1 using the formulas

Table 9.1 Parameters in the Biot model

Symbol	Description
ρ_f	Density of the pore fluid
ρ_r	Density of frame material
μ	Complex frame shear modulus
K_b	Complex frame bulk modulus
K_f	Fluid bulk modulus
K_r	Frame material bulk modulus
β	Porosity
η	Viscosity of pore fluid
k	Permeability
α	Structure constant
a	Pore size parameter

$$\lambda = K_b - \frac{2}{3}\mu + \frac{(K_r - K_b)^2 - 2\beta K_r(K_r - K_b) + \beta^2 K_r^2}{D - K_b},$$
$$R = \frac{\beta^2 K_r^2}{D - K_b}, \qquad Q = \frac{\beta K_r\left((1-\beta)K_r - K_b\right)}{D - K_b}, \qquad D = K_r(1 + \beta(K_r/K_f - 1)).$$

The bulk and shear moduli K_b and μ are often given an imaginary part to account for frame viscoelasticity. The equations of motion are

$$\mu\nabla^2\mathbf{u} + \nabla[(\lambda+\mu)e + Q\varepsilon] = \frac{\partial^2}{\partial t^2}(\rho_{11}\mathbf{u} + \rho_{12}\mathbf{U}) + b\frac{\partial}{\partial t}(\mathbf{u} - \mathbf{U}),$$
$$\nabla[Qe + R\varepsilon] = \frac{\partial^2}{\partial t^2}(\rho_{12}\mathbf{u} + \rho_{22}\mathbf{U}) - b\frac{\partial}{\partial t}(\mathbf{u} - \mathbf{U}),$$

where ρ_{11} and ρ_{22} are density parameters for the solid and fluid, respectively, ρ_{12} is a density coupling parameter, and b is a dissipation parameter. These are calculated from the inputs of Table 9.1 using the formulas

$$\rho_{11} = (1-\beta)\rho_r - \beta(\rho_f - m\beta)\rho_{12} = \beta(\rho_f - m\beta),$$
$$\rho_{22} = m\beta^2 \quad b = \frac{F\left(a\sqrt{\omega\rho_f/\eta}\right)\beta^2\eta}{k},$$

where $m = \frac{\alpha\rho_f}{\beta}$ and the multiplicative factor $F(\zeta)$, which was introduced in [4] to correct for the invalidity of the assumption of Poiseuille flow at high frequencies.

The Biot model predicts that a poroelastic medium will have two dilatational (compressional) waves, sometimes referred to as the fast and slow waves, as well as a shear wave. The presence of two dilatational waves is usually attributed to the in-phase and out-of-phase motions of the frame and fluid. Our studies of determining the Biot coefficients of cancellous bone [13, 14, 16, 39] by inverting the acoustic pressure have been promising. See also [32, 33]. The estimates of the parameter values were taken from the literature, obtained by *in vitro* experimental measurement, or in the case of permeability characterized as estimates without elaboration.

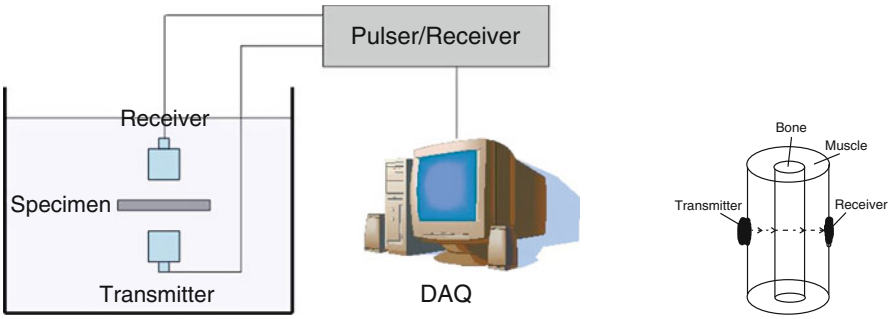

Fig. 9.5 Schematic for the *in vitro* (*left*) and *in vivo* (*right*) experiments

In Fig. 9.5 the classical experimental setup for the osteoporosis experiment is shown. A segment of cancellous bone is submerged in a water bath. An ultrasonic transmitter is placed on one side of the segment and a receiving hydrophone on the other side. In [31] we considered an *in vivo* interrogation of bone surrounded by muscle. The muscle was modeled as an isotropic elastic material. In this problem we only tried to recover the bone porosity, which was done quite accurately. In [16] and [14] Buchanan, Gilbert and Khashanah investigated the extent to which the most important parameters of the Biot model could be recovered by acoustic interrogation in a numerical experiment which simulated in two dimensions the physical experiment of Hosokawa and Otani [48]. The finite element method was used to simulate both the target pressure data and the trial data used in the parameter recovery algorithm. In more recent work we have used analytical methods to simplify the problem of reflections from the tank walls. This has the virtue of permitting use of higher frequencies in the low 100 KHz range, which is closer to the frequencies used in clinical ultrasound experiments. Using frequencies in the range mentioned above we were able to determine, for the *in vitro* case, the parameters β, k, a, α and the real part of K_b and μ in the table above [13–15]. An attempt on the *in vivo* simulation of the bone density problem was given in [39]; see also [38]. The inversion procedure uses a fairly precise grid to construct the pressure field in the water tank containing the bone specimen and a less accurate method for doing the inversion. See the papers [13, 15, 16] for further details.

In Table 9.2 we list the accuracy of the three-phase Nelder-Mead annealing process we developed for inverting the two dimensional inversion of the Biot–Stoll model. For purposes of comparison we computed the mean and standard deviation of all Phase 3 answers whose objective function value was within a factor of 2 of the lowest value and used these to find a 95% confidence interval for the mean. Instances of underestimation, indicated by "*" were more common, however only the underestimation of the error for the structure factor in Problem 83w was severe. On the other hand the overestimations of the error are less severe than with minimum/maximum/midpoint approach and on the whole better characterize the actual errors.

Table 9.2 Phase 3 percentage errors when using mean values for Problems 71–91w. Estimated errors are calculated from 95% confidence intervals. The numbers 71, 75, 79, etc. refer to the porosity of the cancellous bone

Problem		β	k	a	α	$\mathrm{Re}\,K_b$	$\mathrm{Re}\,\mu$
71w	Error (%)	0.12	1.83	5.41	0.55	0.71	3.44
	Estimated error (%)	0.22	8.34	9.49	1.10	11.27	3.61
75w	Error (%)	0.00	21.20	22.86	0.34	9.19	6.34
	Estimated error (%)	0.19	30.41	38.40	1.19	12.24	15.15
79w	Error (%)	0.14	1.17	4.10	0.32	7.67	1.64
	Estimated error (%)	0.12*	36.14	44.77	0.99	9.00	1.44*
83w	Error (%)	0.94	23.30	25.94	2.78	0.02	0.02
	Estimated error (%)	1.27	17.71*	17.87*	0.87*	0.99	0.66
87w	Error (%)	0.03	2.57	4.15	0.33	6.86	7.10
	Estimated error (%)	0.30	32.76	27.61	0.90	39.87	13.19
91w	Error (%)	0.56	23.52	17.41	1.24	21.12	34.73
	Estimated error	0.99	17.14*	16.44*	0.86*	26.49	22.22*

In the Biot model [4–6] the motion of the skeletal frame and the interstitial fluid within are tracked by position vectors u^s and U^s respectively. The coupling between the fluid part (marrow) and elastic matrix (trabecular bone) is described by the Johnson–Koplik–Dashen model [50]. In this model, the dynamic tortuosity $\alpha(\omega)$ is expressed as a function of tortuosity α_∞, pore fluid viscosity η, pore fluid density ρ_f, permeability k, porosity β, the angular frequency ω and the viscous characteristic length Λ

$$\alpha(\omega) = \alpha_\infty \left(1 + \frac{\eta\beta}{i\omega\alpha_\infty\rho_f k} \sqrt{1 + i\frac{4\alpha_\infty^2 k^2 \rho_f \omega}{\eta\Lambda^2\beta^2}} \right), \quad i = \sqrt{-1}. \tag{9.91}$$

The effective elastic constants P, Q, and R are related to β, bulk modulus of the pore fluid K_f, bulk modulus of the trabecular bone K_s, bulk modulus of the porous skeletal frame K_b and the shear modulus of the composite as well as the skeletal frame N:

$$P := \frac{(1-\beta)\left(1-\beta-\dfrac{K_b}{K_s}\right) + \beta\dfrac{K_s}{K_f}K_b}{1-\beta-\dfrac{K_b}{K_s}+\beta\dfrac{K_s}{K_f}} + \frac{4}{3}N,$$

$$Q := \frac{\left(1-\beta-\dfrac{K_b}{K_s}\right)\beta K_s}{1-\beta-\dfrac{K_b}{K_s}+\beta\dfrac{K_s}{K_f}},$$

$$R := \frac{\beta^2 K_s}{1-\beta-\dfrac{K_b}{K_s}+\beta\dfrac{K_s}{K_f}}. \tag{9.92}$$

It is convenient to write the Biot–Johnson–Koplik–Dashen model in matrix form

$$\begin{pmatrix} P & Q \\ Q & R \end{pmatrix} \begin{pmatrix} \dfrac{d^2\hat{u}^s}{dx^2} \\ \dfrac{d^2\hat{U}^s}{dx^2} \end{pmatrix} = -\omega^2 \begin{pmatrix} \tilde{\rho}_{11} & \tilde{\rho}_{12} \\ \tilde{\rho}_{12} & \tilde{\rho}_{22} \end{pmatrix} \begin{pmatrix} \hat{u}^s \\ \hat{U}^s \end{pmatrix}.$$

This implies

$$\begin{pmatrix} \dfrac{d^2\hat{u}^s}{dx^2} \\ \dfrac{d^2\hat{U}^s}{dx^2} \end{pmatrix} = \frac{-\omega^2}{PR-Q^2} \begin{pmatrix} R\tilde{\rho}_{11}-Q\tilde{\rho}_{12} & R\tilde{\rho}_{12}-Q\tilde{\rho}_{22} \\ -Q\tilde{\rho}_{11}+P\tilde{\rho}_{12} & -Q\tilde{\rho}_{12}+P\tilde{\rho}_{22} \end{pmatrix} \begin{pmatrix} \hat{u}^s \\ \hat{U}^s \end{pmatrix}.$$

Current research has been directed towards using the Biot–Johnson–Koplik–Dashen model to do the one dimensional model *in vivo*, i.e. a muscle-cortical bone-cancellous bone system and to repeat the previous work on the two dimensional model.

9.7 Concluding Remarks

In Sect. 9.3 we derived an effective model for acoustic wave propagation in solid-fluid composites with microstructure. The microstructural geometry was modeled as a realization of a stationary random field with built in scale separation. The main technical tool used is stochastic two-scale convergence in the mean introduced by Bourgeat, Mikelić and Wright [12]. This technique produces a two-velocity effective system coupling the leading term in the asymptotics with a corrector. Following the ideas of [8] it is possible to find an ansatz to eliminate the corrector and reduce the two-velocity system to a smaller system of effective equations for the leading term alone. These equations model a single phase, uniform viscoelastic medium with long time history dependence.

We plan in a future paper to do some numerical experiments based on the methodology we have developed.

Acknowledgements This work was partially supported by the NSF under Grant DMS-0920850.

References

1. Agassant, J. F., Avenas, P., Sergent, J., and Carreau, P.: Polymer Processing, Principles and Modeling, Hasser, Munich (1993)
2. Allaire, G.: Homogenization and two-scale convergence, SIAM J. Math. Anal. **23**(6), 1482–1518 (1992)
3. Auriault, J.-L.: Poroelastic Media, Homogenization and Porous Media, Interdisciplinary Applied Mathematics, Springer, Berlin, 163–182 (1997)
4. Biot, M. A.: Theory of propagation of elastic waves in a fluid-saturated porous solid. I. Lower frequency range, and II. Higher frequency range, J. Acoust. Soc. Am. **28**(2), 168–191 (1956)
5. Biot, M. A.: Generalized theory of acoustic propagation in porous dissipative media, J. Acoust. Soc. Am. **34**, 1254–1264 (1962)
6. Biot, M. A.: Mechanics of deformation and acoustic propagation in porous media, J. Appl. Phys. **33**, 1482–1498 (1962)
7. Bossy, E., Padilla, F., Peyrin, F., and Laugier, P.: Three-dimensional simulation of ultrasound propagation through trabecular bone structures measured by synchrotron microtomography, Phys. Med. Biol. **59**, 5545–5556 (2005)
8. Bourgeat, A. and Badea, A.: Homogenization of two phase flow through a randomly heterogeneous porous media, in Mathematical Modelling of Flow through Porous Media, Eds. A. Bourgeat, C. Carasso, S. Luckhaus, A. Mikelic, World Scientific, Singapore (1996)
9. Bourgeat, A., Kozlov, S. M., and Mikelić, A.: Effective equations of two-phase in random media, Calc. Var. Partial Diff. **3**, 385–406 (1995)
10. Bourgeat, A., Luckhaus, S., and Mikelić, A.: Convergence for the homogenization process for a double porosity model of immiscible two-phase flow, SIAM J. Math. Anal. **27**, 1520–1543 (1996)
11. Bourgeat, A., Mikelić, A., and Piatnitski, A.: On the double porosity model of single phase flow in random media, Asymptotic Anal. **34**, 311–332 (2003)
12. Bourgeat, A., Mikelić, A., and Wright, S.: On the stochastic two-scale convergence in the mean and applications, J. Reine Angew. Math. **456**, 19–51 (1994)
13. Buchanan, J. L. and Gilbert, R. P.: Determination of the parameters of cancellous bone using high frequency acoustic measurements, Math. Comput. Model. **45**(3-4), 281–308 (2007)
14. Buchanan, J. L. and Gilbert, R. P.: Measuring Osteoporosis Using Ultrasound, in Advances in Scattering and Biomedical Engineering, Eds. D. I. Fotiadis, C. V. Massalas, World Scientific, Singapore, 484–494 (2004)
15. Buchanan, J. L. and Gilbert, R. P.: Determination of the parameters of cancellous bone using high frequency acoustic measurements II: Inverse problems, J. Comput. Acoust. **15**(2), 199–220 (2007)
16. Buchanan, J. L., Gilbert, R. P., and Khashanah K.: Determination of the parameters of cancellous bone using low frequency acoustic measurements, J. Comput. Acoust. **12**(2), 99–126 (2004)
17. Burridge, R. and Keller, J. B.: Poroelasticity equations derived from microstructure, J. Acoust. Soc. Am. **70**, 1140–1146 (1981)
18. Chaffai, S., Padilla, F., Berger, G., and Lauguier, P.: In vitro measurement of the frequency dependent attenuation in cancellous bone between 0.2 and 2 MHz, J. Acoust. Soc. Am. **108**, 1281–1289 (2000)
19. Chaffai, S., Peyrin, F., Nuzzo, S., Porcher, R., Berger, R., and Laugier, P.: Ultrasonic characterization of human cancellous bone using transmission and backscatter measurements: Relationships to density and microstructure, Bone **30**(1), 229–237 (2002)
20. Chaffai, S., Roberjot, V., Peyrin, F., Berger, R., and Laugier, P.: Frequency dependence of ultrasonic backscattering in cancellous bone: autocorrelation model and experimental results, J. Acoust. Soc. Am. **108**, 2403–2411 (2000)
21. Clopeau, Th., Ferrín, J. L., Gilbert, R. P., and Mikelić, A.: Homogenizing the acoustic properties of the seabed II, Math. Comput. Modelling **33**, 821–841 (2001)

22. Droin, P., Laugier, P., and Berger, G.: Ultrasonic attenuation and dispersion of cancellous bone in the frequency range 200–600 KHz, preprint Acoustical Imaging (1997)
23. Droin, P., Berger, G., and Laugier, P.: Velocity dispersion of acoustic waves in cancellous bone, IEEE Trans. Ultrason. Ferroelectr. Freq. Control. **45**, 581–592 (1998)
24. Evans, L. C.: Partial Differential Equations, Graduate Studies in Mathematics **19**, AMS (2000)
25. Fang, M., Gilbert, R. P., Guyenne, P., and Vasilic, A.: Numerical homogenization of the time harmonic acoustics of bone: the monophasic case, Int. J. Multiscale Com. **5**, 461–471 (2007)
26. Fang, M., Gilbert, R. P., Panchenko, A., and Vasilic, A.: Homogenizing the Time Harmonic Acoustics of Bone: The Monophasic case, Math. Comput. Model. **46**, 331–340 (2007)
27. Fang, M., Gilbert, R. P., and Vasilic, A.: Upscaling of the time harmonic acoustics of bone: Diphasic Case, work in progress (2011)
28. Fellah, Z. E. A., Chapelon, Y., Berger, S., Lauriks, W., and Depollier, C.: Ultrasonic wave propagation in human cancellous bone: Application of Biot theory, J. Acoust. Soc. Am. **116**, 61–73 (2004)
29. Fellah, Z. E. A., Mitri, F. G., Fellah M., Ogam, E., and Depollier C.: Ultrasonic characterization of porous absorbing materials: Inverse problem, J. Sound Vib. **302**, 746–759 (2007)
30. Fry, F. J. and Barger, J. E.: Acoustical properties of the human skull, J. Acoust. Soc. Am. **63**(5), 1576–1590 (1978)
31. Gilbert, R. P., Groby, J. P., Liu, Y., Ogam, E., Wirgin, A., and Xu, Y.: Computing porosity of cancellous bone using ultrasonic waves II: the muscle, cortical, cancellous bone system, Math. Comput. Model. **50**(3-4), 421–429 (2009)
32. Gilbert, R. P., Guyenne, P., and Hsiao, G. C.: Determination of cancellous bone density using low frequency acoustic measurements, Appl. Anal. **87**, 1213–1225 (2008)
33. Gilbert, R. P., Hsiao, G. C., and Xu, L.: On the Variational Formulation of a Transmission Problem for the Biot Equations, Appl. Anal. **89**(5), 745–755 (2010)
34. Gilbert, R. P. and Mikelić, A.: Homogenizing the acoustic properties of the seabed I, Lakshmikantham's legacy: a tribute on his 75th birthday, Nonlinear Anal. Ser. A: Theory Methods **40**(1-8), 185–212 (2000)
35. Gilbert, R. P. and Panchenko, A.: Acoustics of a stratified poroelastic composite, Zeit. fuer Analysis u. i. Anwendungen **18**, 977–1001 (1999)
36. Gilbert, R. P., Panchenko, A., and Vasilic, A.: Homogenizing the acoustics of cancellous bone with an interstitial non-newtonian fluid, nonlinear analysis, available online June 2010, doi:10.1016/j.physletb.2003.10.071
37. Gilbert, R. P., Panchenko, A., and Vasilic, A.: Acoustic Propagation in Random Saturated Medium: The Monophasic Case, Math. Method Appl. Sci., available online September 2010, doi: 10.1002/mma.1360
38. Gilbert, R. P., Xu, Y., and Zhang, S.: Computing porosity of cancellous bone using ultrasonic waves, J. Appl. Funct. Anal. **2**, 185–196 (2007)
39. Gilbert, R. P., Xu, Y., and Zhang, S.: Mathematical model for evaluation of osteoporosis, Adv. Appl. Anal. 57–67 (2007)
40. Hill, R.: Elastic properties of reinforced solids: some theoretical principles, J. Mech. Phys. Solids **11**(5), 357–372 (1963)
41. Hill, R.: On constitutive macro-variables for heterogeneous solids at finite strain, Proc. R. Soc. Lond. A **326**, 131–147 (1972)
42. Ilic, S.: Application of the multiscale FEM to the modeling of composite materials, Ph.D. Thesis, Ruhr University Bochum (2008)
43. Ilic, S. and Hackl, K.: Homogenisation of random composites via the multiscale finite-element method, PAMM **4**, 326–327 (2004)
44. Ilic, S. and Hackl, K.: Application of the multiscale FEM to the modeling of heterogeneous materials, Proceedings of the First Seminar on The Mechanics of Multifunctional Materials, Bad Honnef, Germany, 47–51 (2007)
45. Ilic, S., Hackl, K., and Gilbert, R. P.: Application of the multiscale FEM to the modeling of the cancellous bone, Biomech. Model. Mechanobiol. **9**(1), 87–102 (2009)

46. Ilic, S., Hackl, K., and Gilbert, R. P.: Application of a biphasic representative volume element to the simulation of wave propagation through cancellous bone I, Theoretical and Computation Acoustics, World Scientific (to appear) (2011)
47. Hackl, K.: A framework for nonlinear shells based on generalized stress and strain measures, Int. J. Solids Struct. **34**(13), 1609–1632 (1997)
48. Hosokawa, A. and Otani, T.: Ultrasonic wave propagation in bovine cancellous bone, J. Acoust. Soc. Am. **101**, 558–562 (1997)
49. Jikov, V. V., Kozlov, S. M., and Oleinik, O. A.: Homogenization of Differential Operators and Integral Functionals, Springer, Berlin (1994)
50. Johnson, D. L., Koplik, J., and Dashen, R.: Theory of dynamic permeability and tortuosity in fluid-saturated porous media, J. Fluid Mech. **176**, 379–402 (1987)
51. Levy, T.: Propagation waves in a fluid-saturated porous elastic solid, Int. J. Eng. Sci. **17**, 1005–1014 (1979)
52. Lions, P.- L.: Mathematical Topics in Fluid Mechanics, v.2, Clarendon Press, Oxford (1998)
53. McKelvie, M. L. and Palmer, S. B.: The interaction of ultrasound with cancellous bone, Phys. Med. Biol. **36**, 1331–1340 (1991)
54. Miehe, C., Schotte, J., and Schroder, J.: Computational micro-macro transition and overall moduli in the analysis of polycrystals at large strains, Comp. Mat. Sci. **16**, 372–382 (1998)
55. Miehe, C., Schotte, J., and Lambrecht, M.: Homogenisation of inelastic solid materials at finite strains based on incremental minimization principles, J. Mech. Phys. Solids **50**, 2123–2167 (2002)
56. Mikelić, A.: Mathematical derivation of the Darcy-type law with memory effects governing transient flow through porous medium, Glasnik Matematički **29**(49), 57–77 (1994)
57. Mura, T.: Micromechanics: Overall Properties of Heterogeneous Solids, Kluwer Academic Publishers, Groningen (1993)
58. Nemat-Nasser, S. and Hori, M.: Micromechanics: overall properties of heterogeneous materials, North-Holland series in applied mathematics and mechanics, **37** (1993)
59. Nicholson, P. H. F. and Bouxsein, M. L.: Bone marrow influences quantitative ultrasound measurements in human cancellous bone, Ultrasound Med. Biol. **28**(3), 369–375 (2002)
60. Njeh, C. F., Hans, D., Fuerst, T., Glüer, C. C., and Genant, H. K.: Quantitative Ultrasound; Assessment of Osteoporosis and Bone Status, London, Martin Duniz, 391–399 (1999)
61. Nguetseng, G.: A general convergence result for a functional related to the theory of homogenization, SIAM J. Math. Anal. **20**, 608–623 (1989)
62. Nguetseng, G.: Asymptotic analysis for a stiff variational problem arising in mechanics, SIAM J. Math. Anal. **20**(3), 608–623 (1990)
63. Padilla, F., Jenson, F., Bousson, V., Peyrin, F., and Laugier, P.: Relationships of trabecular bone structure with quantitative ultrasound parameters: in vitro study on human proximal femur using transmission and backscatter measurements, Bone **42**, 1193–1202 (2008)
64. Padila, F., Peyrin, F., and Laugier, P.: Prediction of backscatter coefficient in trabecular bones using a numerical model of three-dimensional microstructure, J. Acoust. Soc. Am. **113**, 1122–1129 (2003)
65. Picart, C., Piau, J-M., Galliard, H., and Carpentier, P.: Human blood shear yield stress and its hematocrit dependence, J. Rheol. **42**(1), 1–12 (1998)
66. Saied, A., Raum, K., Leguerney, L., and Laugier, P.: Spatial distribution of anisotropic acoustic impedance as assessed by time-resolved 50-mHz scanning acoustic microscopy and its relation porosity in human cortical bone, Bone **43**, 187–194 (2008)
67. Sanchez-Palencia E.: Non-Homogeneous Media and Vibration Theory, Springer Lecture Notes in Physics **129**, 158–190 (1980)
68. Sankara, D. S. and Hemalathab, K.: Non-Newtonian fluid flow model for blood flow through a catheterized artery – Steady flow, Appl. Math. Model. **31**(9), 1847–1864 (2007)
69. Sasso, M., Haïat, G., Talmant, Laugier, P. and Naili, S.: Singular value decomposition-based wave extraction in axial transmission; Application to cortical bone ultrasonic characterization, IEEE Trans. Ultrason. Ferroelectr. Freq. Control. **55**(6), 1328–1332 (2008)
70. Schröder, J.: Homogenisierungsmethoden der nichtlinearen Kontinuumsmechanik unter Beachtung von Stabilitats Problemen, Habilitationsshrift, Universität Stuttgart (2000)

71. Thurston, G. B.: Viscoelasticity of Human Blood, Biophysical J. **12**, 1205–1217 (1972)
72. Torquato, S.: Random Heterogeneous Materials: Microstructure and Macroscopic Properties, Springer Verlag, New York (2002)
73. Vasilic, A.: Homogenizing Acoustic Properties of Cancellous Bone, Ph.D. diss., University of Delaware (2009)
74. Williams, K. L., Jackson, D. R., Thorsos, E. I., Tang, D., and Schock, S. G.: Comparison of sound speed and attenuation measured in a sandy sediment to predictions based on the Biot theory of porous media, IEEE J. Oceanic Eng. **27**(3), 413–428 (2002)
75. Willis, J. R.: Variational and related methods for the overall properties of composites, Adv. Appl. Mech. **21**, 1–78 (1981)
76. Willis, J. R.: Elasticity theory of composites, Mechanics of solids, THE RODNEY HILL 60TH ANNIVERSARY VOLUME, Pergamon, Oxford, 653–686 (1982)
77. Willis, J. R.: The overall elastic response of composite materials, J. Appl. Mech. **50**, 1202–1209 (1983)
78. Zienkiewicz, O. C. and Taylor, R. L.: The Finite Element Method, Butterworth-Heinemann, Atlanta, GA (2000)
79. Zhikov, V. V.: On two-scale convergence, J. Math. Sci. **120**(3), 1328–1352 (2004)

Chapter 10
Linear Acoustics of Trabecular Bone

Janne P. Karjalainen, Ossi Riekkinen, Juha Töyräs, and Jukka S. Jurvelin

Abstract During the two recent decades, quantitative ultrasound (QUS) methods have been developed for in vivo diagnostics of trabecular bone. Mostly, trabecular bone QUS measurements are conducted in through-transmission and pulse-echo geometry. Since the first in vivo QUS measurements at the heel, the research efforts have also been focused on enabling QUS measurements at important fracture sites, such as proximal femur or lumbar vertebra. This chapter introduces the experimental QUS methods and reviews the recent developments in in vitro and in vivo measurement methods and results on linear acoustic properties of trabecular bone. Specifically, ultrasound parameters determined in through-transmission and pulse-echo measurements are introduced and their frequency dependency as well as feasibility for characterization of bone density, structure, composition and mechanical properties is reviewed. Finally, potential of QUS for clinical diagnostics of osteoporosis and prediction of bone fracture risk are discussed, with some suggestions of future lines for development of ultrasound diagnostics of bone disorders.

Keywords AA · AIB · Apparent integrated backscatter · Attenuation · Attenuation compensation · Average attenuation · Backscatter · Bone composition · Bone marrow · Bone mechanics · Bone structure · Broadband ultrasound attenuation · Broadband ultrasound backscatter · BUA · BUB · Cancellous bone · Dual frequency ultrasound · Frequency slope of apparent backscatter · FSAB · Integrated reflection coefficient · IRC · Linear acoustics · nBUA · Normalized broadband ultrasound attenuation · Pulse-echo · Reflection · SOS · Spectrum centroid shift · Speed of sound · Through-transmission · Time slope of apparent backscatter · Trabecular bone · TSAB · Ultrasound velocity

J.P. Karjalainen, O. Riekkinen, J. Töyräs, and J.S. Jurvelin (✉)
Department of Physics and Mathematics, University of Eastern Finland, POB 1627, FI-70211 Kuopio, Finland
e-mail: janne.karjalainen@uef.fi; ossi riekkinen@uef.fi; Juha.Toyras@kuh.fi; jukka.jurvelin@uef.fi

P. Laugier and G. Haïat (eds.), *Bone Quantitative Ultrasound*,
DOI 10.1007/978-94-007-0017-8_10,

10.1 Introduction

Human bones are under a continuous renewal process. The renewal occurs at the surface of trabecular bone tissue and is controlled by the tissue metabolism. As osteoporosis affects the bone metabolism, the osteoporotic changes are considered to be first detected in the trabecular bone matrix with a large surface to volume ratio. Therefore, diagnosis of osteoporosis (see Chap. 4) is made at skeletal sites composed mainly of trabecular bone (e.g. calcaneus, proximal femur, vertebra). As most easily accessed, the calcaneus has been the first location for in vivo ultrasonic measurements of bone properties using a through-transmission (TT) technique [1]. Since then, several clinical devices have been developed for calcaneal measurements. With these devices the broadband ultrasound attenuation (BUA) and speed of sound (SOS) are classically determined. Currently, the calcaneus provides the only clinically validated ultrasound measurement location with a substantial prove of hip fracture prediction [2, 3].

The heel ultrasound has not been able to supersede the X-ray methods. Currently, osteoporosis is diagnosed as reduced areal bone mineral density at the proximal femur (neck or total proximal femur) and lumbar vertebra (L2–L4 or L1–L4) using the dual-energy X-ray absorptiometry (DXA). Some criticism has been laid upon the calcaneal measurements because the properties of the trabecular bone at heel may reflect poorly the bone properties at the central skeleton [4]. Similarly as with the X-ray devices, the best fracture risk prediction in specific bones may be obtained only by making the QUS measurements at the same anatomical location. The most severe location for osteoporotic fractures in terms of morbidity and mortality is the hip [5].

The use of QUS techniques has also been limited due to obvious error sources in the measurement. First, the soft tissue overlying the bone, even though thin, can produce significant errors on the measurements [6–10]. Further, variations in the size of the calcaneus [11–13] and the anatomical location of actual measurement in each individual [14–17] have presented additional challenges for the clinical measurements. For improved localization of the measurements, imaging QUS devices have been introduced and indeed the precision of the measurements has improved [14, 18–22].

The acoustic properties of trabecular bone have been widely investigated in vitro in both through-transmission and pulse-echo (PE) geometry [23–28]. Using PE methods, typical parameters include the integrated reflection coefficient (IRC), broadband ultrasound backscatter (BUB) and apparent integrated backscatter (AIB). Recently, other parameters, such as the time slope of apparent backscatter (TSAB) and the frequency slope of apparent backscatter (FSAB), were also applied for characterization of trabecular bone [29]. Previous studies indicate a significant potential of these parameters to reflect structure, density, composition and mechanical properties of trabecular bone [26, 29–34].

During the recent decade, the research on novel techniques in QUS has been strongly guided by certain lines of development: (1) application of in vivo TT measurements for the proximal femur and (2) development of PE measurements for in vivo use. In principle, PE ultrasound measurements could be conducted at

most skeletal locations, e.g. at the hip. Further, PE ultrasound possesses intriguing versatility as only one transducer is needed for measurement of the ultrasonic backscatter from the trabecular matrix or for the determination of the thickness of cortical layer [35,36]. Thereby, PE – geometry may enable separate analyses of both bone compartments (i.e. trabecular and cortical bone).

Measurement of the speed of sound at the diaphysis of long bones (axial transmission) is also widely applied for assessment of cortical bone density, thickness and even fracture susceptibility [37–40]. Different sound wave propagation modes can be detected in human cortex (longitudinal, shear and guided waves), which are related to different bone properties. These techniques are under active development and research towards improved precision and accuracy. The axial transmission techniques are covered by Chaps. 3 and 8 of the present book and will not be discussed further in this chapter.

In this chapter, experimental in vitro and in vivo methods in through-transmission and pulse-echo geometries for determination of trabecular bone acoustic properties are described. Further, some results from the numerical simulations of ultrasound propagation, attenuation and backscatter in bone are presented to substantiate the experimental findings. Then, the most recent developments and research results are reviewed. Finally, the future prospects and foundations for clinical applicability are discussed.

10.2 Experimental Methods and Parameters for Quantitative Bone Ultrasound

According to linear acoustics (see Chap. 2), the travelling ultrasound wave induces variations in pressure, density and temperature that are small compared to their baseline values in the medium. This is the normal assumption for ultrasound propagation in trabecular bone. However, the non-linear acoustic properties are also under an active present research (see the Chap. 15 on non-linear ultrasound in the present book).

Ultrasound interacts with bone tissue via reflection, refraction, scattering and absorption. The physical interactions and their magnitude depend on the mechanical properties of the tissue, which are controlled by tissue composition and microstructure. Absorption losses, e.g. mode conversion and transformation of acoustic energy to heat by viscous relaxation processes, are determined by material properties (i.e. composition of the tissue). The tissue composition also contributes to the acoustic impedance and therefore directly affects the strength of reflection (or scattering) occurring at the individual trabeculae-marrow interfaces. The degree of scatter is determined largely by the size, shape, distribution and elasticity of the scatterers [41, 42]. Therefore, thickness and shape of the trabeculae are critical for physical interactions as well. When the thickness of individual trabeculae (Tb.Th.) is greater or alternatively equal to/smaller than the ultrasound wavelength the dominant phenomenon is reflection or scattering, respectively. As the trabecular

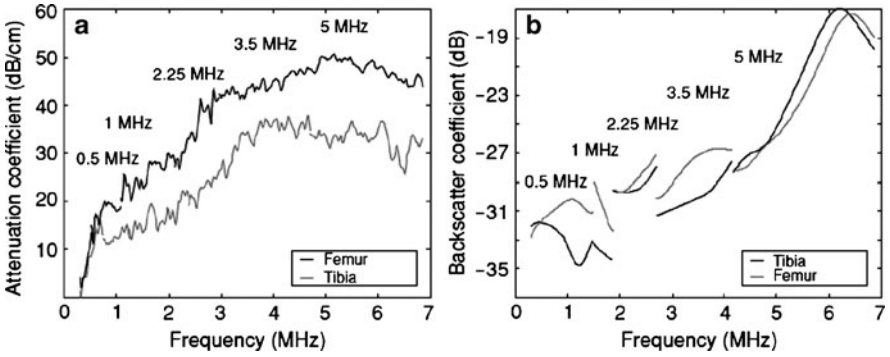

Fig. 10.1 Attenuation (**a**) and backscatter (**b**) coefficients as a function of ultrasound frequency for human trabecular bone samples with different ultimate strengths (Femur: 10.0 MPa; Tibia: 4.2 MPa) (Reprinted from Hakulinen et al. [45], IOP Publishing Ltd.)

orientation in human skeleton varies along the Wolff's law, the acoustic properties are anisotropic and depend on the direction of the ultrasound propagation in respect to the primary direction of the mechanical loading of the bone.

The relative contribution of scattering to energy loss of ultrasound beam in trabecular bone, in comparison to that of absorption, has been an issue for model analyses [43]. The relative involvement of both physical mechanisms has not been clearly explained, however, at diagnostic frequencies (0.2–0.6 MHz) the absorption may have a larger contribution to the total attenuation than the scattering [41, 44]. In general, experimental results have confirmed the theoretical predictions of the increase in the attenuation coefficient and backscatter coefficient along frequency [6, 45] (Fig. 10.1). Jenson et al. reported that the backscatter coefficient increases at a lower frequency range (0.4–1.2 MHz) from approximately −35 to −20 dB [46]. These physical issues are addressed in detail in Chap. 6 of this book.

Most quantitative parameters calculated from the measured ultrasound signals rely on the use of a substitution technique. In the substitution technique, the ultrasound signal obtained from the sample, determined either in time domain or in frequency domain, is normalized by the reference signal obtained from the measurement through a water bath (TT-geometry) [1] or from a perfect (or known) reflector (e.g. polished steel plate or water-air interface) at a focal distance (end of the near field) (PE-geometry) [47]. Thereby, the effects of the measurement setup and hardware originated errors are minimized.

The first quantitative ultrasound measurements in vivo at human heel were done by Langton et al. in 1984 in through-transmission geometry [1]. In TT geometry, two transducers are placed on the opposing sides of the sample at a controlled distance. One transducer emits and the second one receives the pulse transmitted through the bone. Motorized scanning devices (Fig. 10.2) are often used for acquisition of parametric images of the bones. Using these image maps the mean values and standard deviations of the acoustic parameters can be calculated, desirable for trabecular

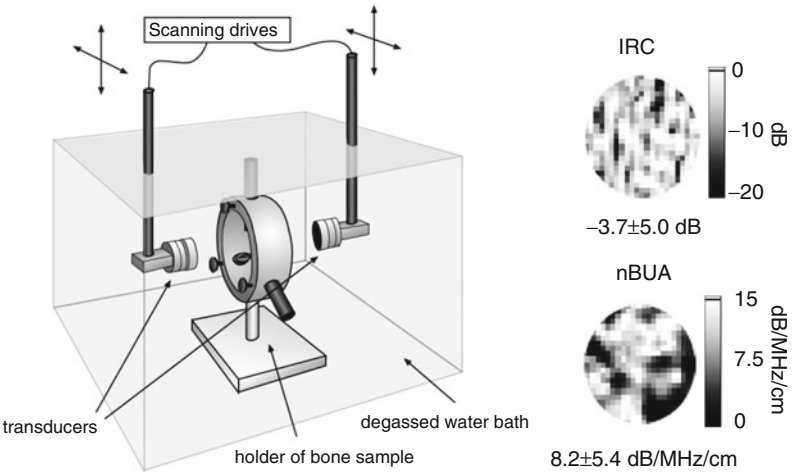

Fig. 10.2 An example of experimental setup for in vitro ultrasound measurements. Parametric images (both PE (IRC) and TT (nBUA) parameters) of the sample can be acquired as the transducers on the opposite sides are attached to the scanning drives (Adapted from Riekkinen O, Kuopio University Publications C. Natural and Environmental Sciences 244 (2008) and Hakulinen et al. [45], IOP Publishing Ltd.)

bone specimens with spatially varying properties. In the pulse-echo geometry a single transducer is used for transmitting and receiving the pulse, potentially enabling the measurements at arbitrary skeletal locations in vivo.

10.2.1 Ultrasound Reflection and Backscatter Parameters

For calculation of different parameters from an ultrasound signal, measured from a trabecular bone sample using the PE-technique, specific time windows are used to gate regions of interest from the time domain signal (Fig. 10.3). The length of the time window for reflection (e.g. used for determination of IRC) can be determined as the width of the reference signal reflected from a perfect reflector (polished steel plate or water-air interface). When an attenuating material is placed between the transducer and bone, the reflected ultrasound pulse gets wider due to the low-pass filtering by the interfering material. This should be considered especially for in vivo applications.

The centre of the reflected pulse can be determined as the maximum of the envelope of the signal. In case of pure trabecular bone samples, the time window for backscatter parameters (e.g. for determination of parameters AIB, BUB) can be located right after the IRC window. To verify that no energy from the surface reflection is included in the backscatter window, the backscatter window may also be delayed leaving a gap between the two time windows. The duration of the pulse varies as

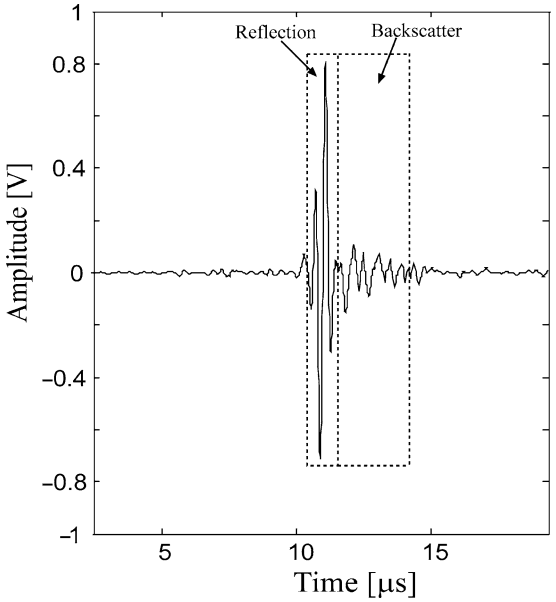

Fig. 10.3 A typical ultrasound signal with the regions of interest (ROI) for analyses of the reflection and backscatter parameters

Table 10.1 Mathematical definitions of common ultrasound reflection and backscatter parameters

Parameter	Equation	
IRC	$\frac{1}{\Delta f}\int_{\Delta f} 20\log_{10}\left(\frac{A_n(f)}{A_r(f)}\right)$	(10.1)
AIB	$\frac{1}{\Delta f}\int_{\Delta f} 20\log_{10}\left(\frac{A_b(f)}{A_r(f)}\right)$	(10.2)
BUB	$\frac{1}{\Delta f}\int_{\Delta f}\left(20\log_{10}\left(\frac{A_b(f)}{A_r(f)}\right)+\beta\right)$	(10.3)

The Δf is the frequency band for analysis (determined as the part of the spectrum above the −6dB). The $A(f)$ denotes the amplitude spectrum of a signal. The subscripts n and r refer to signal gated at surface reflection of sample and perfect reflector, respectively. The subscript b refers to backscatter window inside the bone. The β is the attenuation compensation term (see Eqs. 10.6 and 10.7)

a function of the frequency and therefore the length of the time window should be matched with the frequency in use. The mathematical definitions for typical PE parameters are presented in the Table 10.1.

For calculation of BUB, different functions have been applied for compensating the attenuation inside trabecular bone. Each of those requires prior knowledge of the

frequency dependent attenuation coefficient α and sound speed c in the trabecular bone. These can be determined with the through-transmission measurements. For compensation of the attenuation in scattering medium O'Donnel and Miller [48] proposed the following equation

$$\beta_{OM} = e^{4\cdot\alpha\cdot x_0}\left(\frac{2\cdot\alpha\cdot c\cdot t_w}{e^{\alpha\cdot c\cdot t_w} - e^{-\alpha\cdot c\cdot t_w}}\right), \tag{10.4}$$

where t_w is the length of the backscatter time window. If the backscatter time window is placed directly after the reflection, the propagation distance of sound wave within the sample x_0 can be written as follows

$$x_0 = \frac{ct_w}{4}. \tag{10.5}$$

Equation 10.4 is determined for the power spectra of the attenuation. For use of the amplitude spectra, a square root is placed over the Eq. 10.4. By taking the logarithm, multiplying by 20 (decibel transformation) and inserting Eq. 10.5 yields

$$\beta_{OM} = 20\log_{10}\left(e^{\frac{1}{2}\alpha\cdot c\cdot t_w}\left(\frac{2\cdot\alpha\cdot c\cdot t_w}{e^{\alpha\cdot c\cdot t_w} - e^{-\alpha\cdot c\, t_w}}\right)^{\frac{1}{2}}\right). \tag{10.6}$$

The O'Donnel and Miller compensation has been formulated for an average backscatter function measured from a volume containing randomly distributed cylindrical scatterers. Therefore, it may be suitable for compensating backscattering from the trabecular bone samples that have been measured by averaging backscatter signals over the sample (e.g. laterally scanned trabecular samples, if the trabeculae are considered to be randomly distributed).

Nicholson and Bouxsein [49] applied a straightforward attenuation compensation function simply by combining the measured attenuation, speed of sound and time window length in use as follows

$$\beta_{NB} = \frac{\alpha c t_w}{2}. \tag{10.7}$$

No perfect mathematical expression exists for compensation of the attenuation in the tissue. However, both of the presented functions have been used in measurements of trabecular bone. Enhancements are constantly made and comparisons between different techniques have been presented [50,51]. Nonetheless, the attenuation compensation would require prior knowledge of attenuation coefficient and speed of sound in tissue, which makes the application of BUB clinically difficult. Instead, the AIB requires no attenuation compensation, making it more suitable for in vivo measurements.

Other parameters in addition to AIB, with no need for attenuation compensation, have also been introduced. The parameters, such as time slope of apparent backscatter (TSAB) and frequency slope of apparent backscatter (FSAB) have

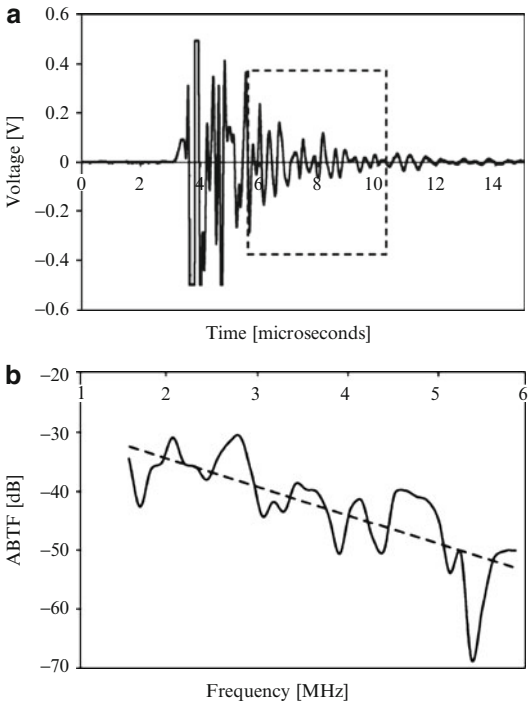

Fig. 10.4 (**a**) Example of a backscatter signal at 5 MHz and (**b**) the associated apparent backscatter transfer function (ABTF). The dashed rectangle indicates the portion of the signal that is analyzed to obtain the ABTF. The slope of the dashed line shown in the lower panel is used to determine FSAB for this specific signal (Reproduced from Hoffmeister et al. [29] © 2008 IEEE)

been originally developed for characterization of soft tissues by Miller et al. [52]. and Lizzi et al. [53], respectively. These parameters, and especially AIB, have been applied also for measurements of bone properties by many research groups [29–31, 34, 54, 55]. In measurements of TSAB from human bones, Hoffmeister et al. [29] used six overlapping windows for determination of AIB at different time points. The length of each window was selected as the duration of five cycles of the transducer centre frequency (five/transducer centre frequency [MHz]). Each subsequent window was adjusted by a delay to fit all windows within 4 μs. The TSAB was finally obtained as a slope of the linear regression to six AIB values plotted against time. For analyses of FSAB, Hoffmeister et al. selected one time window equal to ten cycles of the transducer centre frequency (Fig. 10.4). FSAB was obtained as the slope of the linear regression over the −6 dB bandwidth of the apparent backscatter transfer function $(\mathrm{ABTF} = 10^{*}\log(\mathrm{A_b}/\mathrm{A_r}))$.

Another approach for estimation properties of trabecular bone from the backscatter measurements is the determination of the spectral centroid shift [56, 57]. In linearly attenuating medium the spectral centroid is shifted downward by amount determined as a product of the attenuation coefficient of the medium, sound wave propagation distance and the square of the bandwidth of the pulse. Experimentally, the centroid shift can be determined simply by finding the frequency difference between the maxima of the reference pulse spectrum and the spectrum of the pulse measured from the sample.

10.2.2 Ultrasound Through-Transmission Parameters

For calculation of through-transmission parameters, the ultrasound pulse is transmitted through the bone and recorded at the opposite side. In in vivo measurements, due to the contributions of the surrounding soft tissues, cortical bone and trabecular matrix the transmitted pulse interacts through several phenomena, including absorption, scattering, reflection, diffraction and mode conversion. The pulse is attenuated and the time-of-flight is altered when compared to the reference in the substitution technique. In TT geometry, the parameters most often determined are the BUA and SOS at the frequency range 0.2–0.6 MHz (Table 10.2). Since their introduction, these parameters have been applied in many clinical devices. However, among manufacturers the determination of especially SOS varies from device to another. Several different algorithms for determination of SOS have been developed [58], (e.g. leading edge, thresholding, zero crossing, cross-correlation and maximum envelope) and a method for standardization of the SOS (determined with different time of flight algorithms) has been proposed [59].

The average attenuation (AA) is determined as the absolute attenuation (in dB) over the effective frequency band (above −6 dB) rather than as a slope of the linear part of the attenuation spectrum (BUA). As an index for bone density, (linear) mathematical combinations of BUA and SOS are in use in some commercial instruments for calcaneal measurements.

The values of the most TT parameters, as well as those of PE parameters, depend on the frequency in use (Table 10.3). In general, the ultrasound parameters show significant linear correlations with the bone mineral density of trabecular bone. However, BUA has been found both numerically and experimentally to exhibit significant non-linearity in trabecular bone with high BMD (Fig. 10.5).

Table 10.2 Mathematical definitions of through-transmission parameters, SOS, BUA and average attenuation (AA)

Parameter	Equation	
SOS	$\frac{c_w x_b}{x_b - (\Delta t c_w)}$	(10.8)
Attenuation[a]	$\frac{20}{x_b}\left(\log_{10}\left(\frac{A_w(f)}{A_s(f)}\right) + \log_{10}(T_{ws}T_{sw})\right)$	(10.9)
AA	$\frac{20}{\Delta f \cdot x_b}\int_{\Delta f}\left(\log_{10}\left(\frac{A_w(f)}{A_s(f)}\right) + \log_{10}(T_{ws}T_{sw})\right)$	(10.10)

c_w – sound speed in water, x_b – thickness of the sample, Δt – time of flight difference through the water bath with and without the sample, A_w and A_s, ultrasound pressure amplitude spectra measured through the water bath without and with the sample, respectively

[a]Normalized Broadband Ultrasound Attenuation (nBUA) is determined as a slope of the linear part of attenuation spectrum normalized with the sample thickness x_b

Table 10.3 The mean values (±SD) of human trabecular bone (distal femur/proximal tibia, n = 25) acoustic properties as a function of the transducer centre frequency

	Frequency				
Parameter	0.5 MHz	1.0 MHz	2.25 MHz	3.5 MHz	5.0 MHz
SOS (m/s)	2177 ± 701	1709 ± 500	1690 ± 321	1601 ± 273	1639 ± 385
AA (dB/cm)	17.6 ± 4.1	25.7 ± 8.5	29.3 ± 11.1	36.4 ± 10.5	42.8 ± 13.0
nBUA (dB/cm/MHz)	15.4 ± 25.0	16.6 ± 12.2	13.8 ± 6.2	12.4 ± 6.5	9.1 ± 2.9
IRC (dB)	−22.5 ± 3.3	−17.8 ± 2.8	−10.1 ± 2.8	−10.8 ± 3.1	−10.1 ± 3.2
BUB (dB)	−26.3 ± 4.7	−20.8 ± 5.9	−15.5 ± 4.3	−16.5 ± 3.0	−16.5 ± 3.8

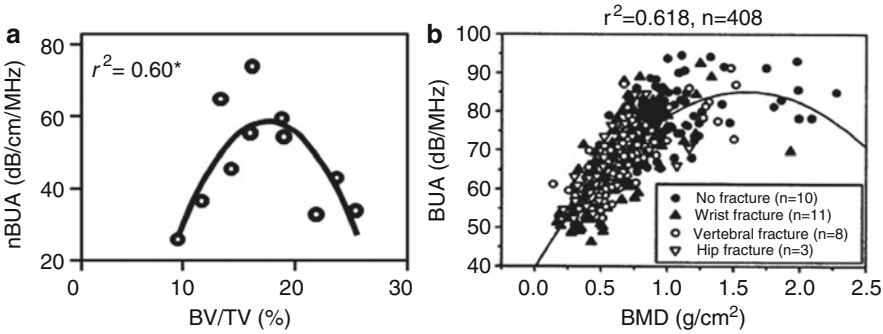

Fig. 10.5 Broadband ultrasound attenuation (BUA/nBUA) as a function of bone volume fraction or bone mineral density (BMD). (**a**) 3-D finite difference model simulations (*left*) suggest that nBUA depends non-linearly on the bone volume fraction (BV/TV). (**b**) Qualitatively similar non-linearity for BUA versus BMD has been revealed in in vivo heel measurements (Data adapted from A. S. Aula et al. [60] Copyright (2009), with permission from Elsevier and reprinted from Toyras et al. [61] Copyright (2002), with permission from Elsevier)

10.3 Dual Frequency Ultrasound Technique

The soft tissue overlying the bone can produce significant errors on the ultrasound measurements [6–8]. The dual frequency ultrasound (DFUS) technique has been introduced for determination of soft tissue composition and correction of measured ultrasound reflection parameters [62, 63]. In DFUS, the soft tissue layer is considered to be composed of lean and fat tissue. Further, known frequency dependent values of ultrasound attenuation coefficient and speed of sound in lean and fat tissue are required (Fig. 10.6). Finally, the reflections at the soft tissue interfaces (i.e. lean and fat tissue interface) and at soft tissue – bone interface are considered to be independent of the frequency. Then, the measured ultrasound reflection amplitude (A_n) at two different frequencies can be written out as

$$A_{n,l} = H_l e^{-2\alpha_{a,l}x_a} \cdot e^{-2\alpha_{m,l}x_m} A_{r,l}, \tag{10.11}$$

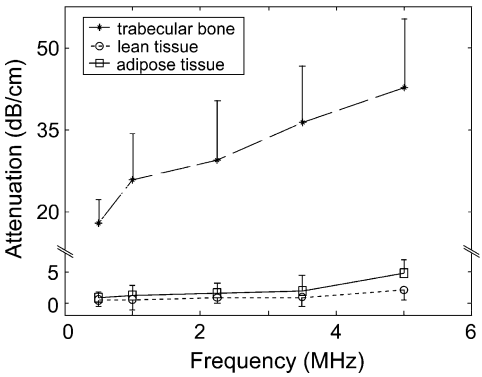

Fig. 10.6 The average ultrasound attenuation (mean + SD) in trabecular bone, lean and adipose tissues. The values for attenuation coefficient and sound speed in lean and adipose tissues at two specific frequencies (e.g. 2.25 and 5.0 MHz) are used in DFUS analysis (Reprinted from Riekkinen et al. [6] Copyright (2006) with permission from Elsevier)

and

$$A_{n,h} = H_h e^{-2\alpha_{a,h}x_a} \cdot e^{-2\alpha_{m,h}x_m} A_{r,h}, \tag{10.12}$$

where the l and h refer to low and high frequencies and the a and m to fat (adipose) and lean (muscle) tissues, respectively. The reflection term H includes the reflections at the surfaces of the soft tissue layers and the bone.

The time of flight (TOF) of the reflection from the bone surface can be written as follows

$$TOF = 2\left(\frac{x_a}{c_a} + \frac{x_m}{c_m}\right). \tag{10.13}$$

Now the thickness of the lean tissue can be calculated as

$$x_m = \left(\frac{TOF}{2} - \frac{x_a}{c_a}\right) c_m. \tag{10.14}$$

The thickness of adipose tissue x_a can be derived from (10.11) and (10.12) and inserting Eq. 10.14 yields

$$x_a = \frac{\ln\left(\frac{A_{n,l}}{A_{r,l}}\right) - \ln\left(\frac{A_{n,h}}{A_{r,h}}\right) - (TOF \cdot c_m(\alpha_{m,h} - \alpha_{m,l}))}{(2\alpha_{a,h} - 2\alpha_{a,l}) - \frac{c_m}{c_a}(2\alpha_{m,h} - 2\alpha_{m,l})} \tag{10.15}$$

Finally, the $IRC_{uncorrected}$ determined from the bone can be corrected as

$$IRC_{corrected} = IRC_{uncorrected} + 2x_a\alpha_a + 2x_m\alpha_m. \tag{10.16}$$

The $IRC_{uncorrected}$ is the integrated reflection coefficient determined over the frequency range of the spectrum above −6 dB. Same correction for soft tissue effects applies also for backscatter parameters (Fig. 10.7). In case of intact bone samples or in vivo application, the attenuation occurring within the cortical bone must also be taken into account to analyse pure backscatter from the trabecular bone.

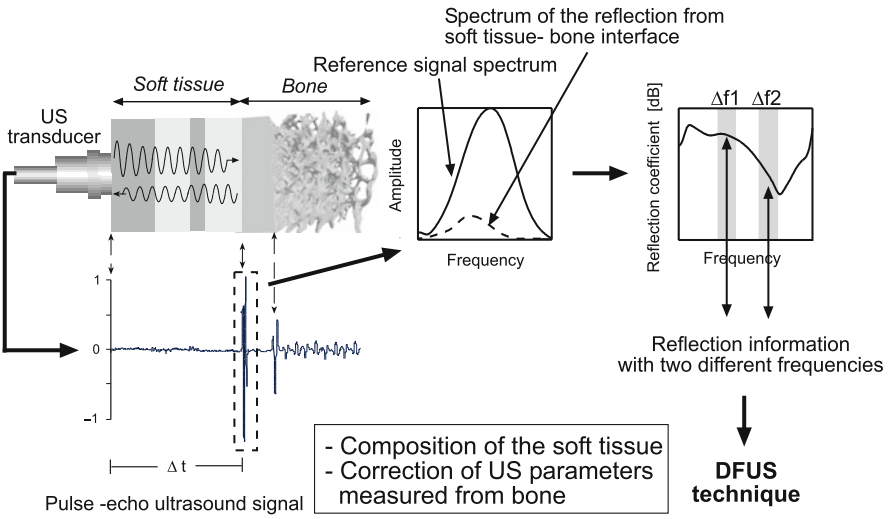

Fig. 10.7 The dual frequency ultrasound (DFUS) technique. The ultrasound echo from the bone surface is used to analyse the composition of soft tissue overlying the bone. With this information, the backscattering parameters of bone can be corrected to be independent of soft tissue thickness or composition. The two frequencies used for the DFUS analyses can be selected from a single broadband reflection spectrum

The DFUS technique has been validated in in vitro [62] and in vivo [63] PE-measurements. In in vitro study at 2.25 and 5.0 MHz, using human trabecular bone samples with and without overlying soft tissue, the DFUS technique decreased the error induced by soft tissues in reflection and backscatter parameters from 127% to 24% and from 59% to −5%, respectively [62]. In an in vivo case study conducted on a bodybuilder at the distal femur during a 21-week training and dieting period, the DFUS technique enabled the determination of local soft-tissue composition, as verified by comparison with the DXA determined local soft tissue composition ($r = 0.91, n = 8, p < 0.01$). Further, the technique eliminated the soft tissue-induced error from IRC measured for the bone [63].

The DFUS solution can also be derived for the bone TT ultrasound measurement by determining the reflection either from the bone surfaces at both sides of the sample or by conducting a measurement through the soft tissues adjacent to the bone, similarly as in the DXA. The transmitted pulse through bone is attenuated by the fat and muscle tissues overlying the bone, interactions in the bone and reflections at the bone-muscle interfaces. The attenuation caused by the reflection at the interface of different soft tissues is considered negligible. Then, the frequency spectrum of the attenuation coefficient in the bone corrected with soft tissue induced attenuation can be written out as

$$\alpha_b(f) = \frac{8.686}{x_b}\left[\ln\left(\frac{A_w(f)}{A_s(f)}\right) - \alpha_m(f)x_m - \alpha_f(f)x_f - \ln\left(T_{mb}T_{bm}\right)\right], \qquad (10.17)$$

where the α is the attenuation coefficient and f is the frequency. Subscripts b, m and f refer to bone, muscle and fat tissue, respectively. The subscripts mb and bm of the transmission coefficients T refer to the direction ultrasound propagates at the interface of the tissues, muscle to bone and bone to muscle, respectively. The A_s is the amplitude of the measured pulse through the soft tissues and the bone. In this equation the attenuation coefficient is normalized with the thickness of the bone x_b. Now the normalized BUA (nBUA) ($\mathrm{dB\,MHz^{-1}cm^{-1}}$) can be calculated as the fitted slope to the linear part of the attenuation coefficient spectrum. To assess nBUA independently of overlying soft tissue the measured attenuation spectrum $\ln(A_w/A_s)$ needs to be compensated for the attenuation in muscle and fat tissue. The tissue specific attenuation spectra $\alpha_m(f)$ and $\alpha_f(f)$ (Np/cm), multiplied with the DFUS resolved thicknesses, are subtracted from the logarithmic attenuation spectrum before the acquisition of the spectral slope for determination of BUA.

In the TT geometry, the applicability of DFUS for correction of BUA with three (1–3) soft tissue and bone mimicking elastomer phantoms (nBUA1.4–10 $\mathrm{dB\,MHz^{-1}cm^{-1}}$; SOS 1553–1586 m/s) was analyzed. At frequency range 1–2 MHz (transducer centre frequency 5 MHz) the attenuation was linear ($r > 0.99$) in phantom materials. Two soft tissue phantoms (1 and 2) were used as interfering layers on top of the bone mimicking phantom (thickness 10.2 mm). Three interfering layers were constructed by varying thickness of phantoms 1 and 2, i.e. 1.19 and 3.22 mm (composition 1), 2.00 and 1.85 mm (composition 2) and 3.01 and 0.97 mm (composition 3), respectively. Then, using the DFUS technique, the thicknesses of the interfering layers (phantoms 1 and 2) were obtained by measurement of IRC from the surface of the bone phantom 3. The transmission spectra with interfering layers were compensated for the attenuation with the spectra measured on phantoms 1 and 2 adjusted with the DFUS resolved thicknesses (Table 10.4). By applying the DFUS correction, the error in the IRC was reduced from 103.6% to 5.6% and the error in nBUA was reduced from 61.6% to 10.1% on the average. At present, the DFUS has not used in in vivo TT-measurements. The in vivo feasibility should be investigated in future studies.

Table 10.4 Application of the DFUS technique for through-transmission measurements of bone-soft tissue mimicking phantoms

Parameter	Interfering Composition 1	Interfering Composition 2	Interfering Composition 3
nBUA ($\mathrm{dBMHz^{-1}cm^{-1}}$)	5.2	5.0	5.8
$\mathrm{nBUA^{corr}}$ ($\mathrm{dBMHz^{-1}cm^{-1}}$)[a]	3.4	3.5	4.0
IRC (dB)	−62.9	−62.9	−67.5
$\mathrm{IRC^{corr}}$ (dB)[b]	−33.9	−30.4	−35.9

Three different compositions to simulate variable soft tissue layers were measured. After DFUS correction improved agreement with the true parameter values (nBUA = 3.3 $\mathrm{dBMHz^{-1}cm^{-1}}$; IRC = −31.7 dB) of the bone mimicking phantom was revealed

[a]The nBUA measured without interfering layers was 3.3 $\mathrm{dBMHz^{-1}cm^{-1}}$

[b]The IRC measured without interfering layers was −31.7 dB

10.4 Relationships of Ultrasound Parameters with Bone Structure, Composition and Mechanical Properties

There is a growing body of evidence on the relationships between different ultrasound parameters and structure, composition and mechanical properties of trabecular bone. Mostly, these relationships have been revealed by investigating statistically significant associations between the QUS and reference data obtained experimentally from the same in vitro bone samples. Further, several studies have applied theoretical model analyses to improve understanding on the characteristic relationships between the structure, composition and acoustic properties of trabecular bone. To gain in depth information, the reader is referred to the review articles by Wear (2008) [43], Langton and Njeh (2008) [64] and Laugier (2008) [65].

Based on physical acoustics, ultrasound backscattering is related to the structure and composition of the bone. Thus, the backscattering parameters may provide comprehensive information about the properties of trabecular bone. This information may associate more closely with the bone strength than the BMD does. Further, the acoustic parameters may be influenced by alterations in organic phase of the bone – which is not the case in DXA derived parameters. However, a solid evidence for demonstrating these benefits of ultrasound is still mostly lacking. Absolutely, more theoretical research is needed to fully understand the sound wave interactions within the complex trabecular structure.

10.4.1 Pulse-Echo Measurements

In the literature, pulse-echo parameters measured from bone have been determined using ultrasound frequencies from 0.5 to 10 MHz. Linear correlations with variable strength have been demonstrated between the pulse-echo parameters (IRC, BUB, AIB) and structural parameters of trabecular bone, such as trabeculae thickness and separation obtained from the micro CT-analyses (Table 10.5). The strength of correlation between BUB and trabecular thickness seems to relate to ultrasound frequency in use, being stronger at lower frequencies (0.5–1.0 MHz) than at higher frequencies (2.25 MHz). However, BUB is sensitive for bone volume fraction and structure within wide range of ultrasound frequencies (0.5–2.25 MHz, Table 10.5). On the other hand, AIB associates with the trabeculae separation and bone volume fraction, but not with the trabeculae thickness, at the centre frequencies of 1.0 and 5.0 MHz. Obviously, as the AIB and BUB differ only by the attenuation compensation (described in Sect. 10.2), the attenuation depends on Tb.Th and produces the significant association also between the BUB and Tb.Th. This issue is difficult to investigate experimentally but should be addressed by numerical model analyses which can be used to improve the understanding on the contribution of different properties of trabecular bone to the ultrasound backscatter.

Table 10.5 Linear correlation coefficients (r) between the pulse-echo ultrasound parameters (IRC, AIB and BUB) in vitro and human (except citation 24, bovine bone) trabecular bone ultimate strength, collagen content of bone matrix (CC/BV), bone volume fraction (BV/TV), trabeculae thickness (TrTh) and separation (TrSp). Center frequency of ultrasound transducers used is also presented

Study	Frequency (MHz)	Parameter	Ultimate strength	CC/BV	BV/TV	TrTh	TrSp
Karjalainen et al. [31]	1.0	IRC	0.86^{**}	-0.32	0.85^{**}	0.48^{*}	-0.66^{**}
Hakulinen et al. [45]	2.25	IRC	0.85	–	–	–	–
Hakulinen et al. [26]	3.5	IRC	–	–	0.77^{**}	0.37	-0.57^{**}
Karjalainen et al. [31]	5.0	IRC	0.77^{**}	-0.55^{*}	0.80^{**}	0.35	-0.58^{**}
Karjalainen et al. [31]	1.0	AIB	0.62^{**}	-0.23	0.66^{**}	0.28	-0.57^{**}
Hoffmeister et al. [30]	1.0	AIB	–	–	$0.08^{\dagger}$	–	–
Hoffmeister et al. [29]	1.0	AIB	0.62^{**}	–	–	–	–
Karjalainen et al. [31]	5.0	AIB	0.28	-0.74^{**}	0.46^{*}	0.11	-0.53^{*}
Hoffmeister et al. [30]	5.0	AIB	–	–	$0.90^{**\dagger}$	–	–
Hoffmeister et al. [29]	7.5	AIB	0.77^{**}	–	–	–	–
Chaffai et al. [66]	0.5	BUB	–	–	0.91^{**}	0.86^{**}	-0.79^{**}
Padilla et al. [32]††	1.0	BUB	–	–	0.69^{**}	0.59^{**}	-0.62^{**}
Padilla et al. [32]††	2.25	BUB	0.74	–	–	–	–
Hakulinen et al. [26]	2.25	BUB	–	–	0.87^{**}	0.46^{*}	-0.69^{**}
Riekkinen et al. [33]	2.25	BUB	–	-0.5^{*}	0.87^{**}	–	–

$^{*}p < 0.05$; $^{**}p < 0.01$; †Volumetric BMD; ††Spearman correlation coefficient

Hoffmeister et al. [55]. found, using an ultrasound transducer with a center frequency of 2.25 MHz, that AIB increased significantly (13.9–14.9%) after decollagenization of trabecular bone samples. Further, AIB at 5 MHz frequency associated significantly with the collagen content of human trabecular bone matrix (Table 10.5). In addition, when the effect of trabeculae thickness (Tb.Th), separation (Tb.Sp) and the mineral content of trabecular bone matrix were minimized (partial correlation) the correlation between the collagen content and AIB was significant ($r = -0.65$, $n = 20$, $p < 0.01$) [31]. AIB values measured with 5.0 MHz seem to be more sensitive for collagen content of bone matrix than for bone volume fraction (Table 10.5).

The properties of bone marrow also contribute to interactions of sound wave within trabecular bone. This can be expected because of the different acoustic properties of yellow (adipose) and red (hematopoietic) marrow. The effect of variations in marrow composition on ultrasound parameters has been simulated and experimentally measured by replacing the marrow with either alcohol or water [49,67,68]. Experimentally, substitution of bone marrow with water decreased the attenuation, BUA and BUB, and increased the phase velocity [49, 68]. Similar observations for the BUB and attenuation were reported in numerical simulations, and the SOS was found to increase after the substitution of marrow with water [67]. However, this is not fully consistent as previous studies have also reported that the replacement of bone marrow with water has negligible effects on the nBUA or SOS [69, 70]. In simulations, the change in ultrasound parameters depended on bone volume

fraction [67]. Therefore, discrepancies in previous results may relate to variations in bone densities of trabecular samples in use and further investigations on bone samples with highly variable mineral density or volume fraction are warranted.

All pulse-echo parameters (IRC, BUB and AIB) have been shown to correlate significantly with the ultimate strength of human trabecular bone (Table 10.5). Consistently at both low and high ultrasound frequencies, AIB served as a significant predictor of ultimate strength (Table 10.5). Interestingly, by combining the reflection and backscattering parameters, e.g. IRC and spatial standard deviation of AIB, the prediction value for ultimate strength of human trabecular bone was found to increase up to $r = 0.92$ in an in vitro study ($n = 19$, $p = 0.01$, Fig. 10.8) [34].

In in vivo studies imaging devices help to improve localization of the measurements. Imaging, realized by either phased array [27, 57] or scanning systems [71], has been applied for measurements of backscatter parameters. The backscatter parameters measured at the calcaneus have been related with the calcaneal BMD [27] and occurrence of fractures [71] at the frequency range of 0.2–2.25 MHz. At the higher frequency (2.25 MHz), the linear correlation between BUB and BMD, was 0.87 ($n = 10$) (Table 10.6). At the lower frequency (0.5 MHz), the linear correlation

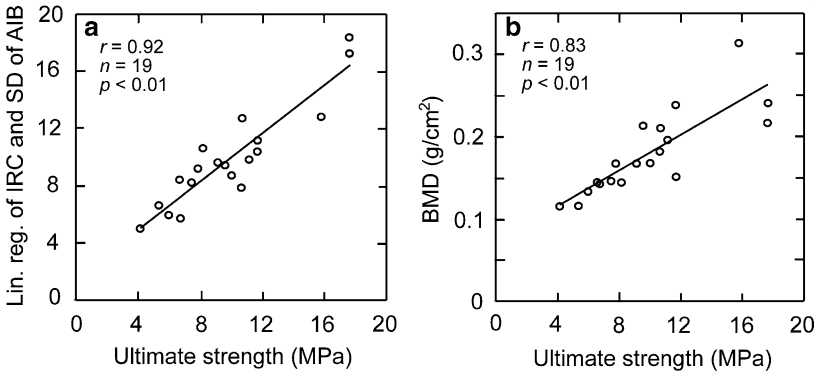

Fig. 10.8 (**a**) The linear combination of the mean value of the IRC and standard deviation (SD) of the AIB within the ROI served as a strong predictor ($r = 0.92$) of the human trabecular bone ultimate strength. Both pulse-echo ultrasound and (**b**) BMD measured with DXA predicted trabecular bone strength similarly (Reprinted from Riekkinen et al. [34], IOP Publishing Ltd.)

Table 10.6 Prediction of bone mineral density (BMD) in vivo by using the pulse-echo ultrasound parameters (BUB and centroid shift). BUB is measured from the calcaneus and compared to BMD at calcaneus and proximal femur. Centroid shift is measured at the lumbar spine (L3–L4) through the abdomen and compared to the BMD at the same site

Study	Frequency (MHz)	Parameter	Site	BMD_{calc}	BMD_{hip}	BMD_{spine}
Roux et al. [71]	0.5	BUB	Calc.		0.34*	
Wear and Garra [27]	2.25	BUB	Calc.	0.87**		
Garra et al. [57]	2.5	Centroid shift	Spine			0.61

*$p < 0.05$; **$p < 0.01$

between BUB and BMD of total hip was much lower ($r = 0.34$, $n = 240$), however statistically significant [71]. Further, the BUB was able to discriminate the fracture and non-fracture patient groups.

Only one study has reported data on ultrasound measurements at lumbar spine in vivo [57]. The measurements were obtained through the abdomen at the centre frequency of 2.5 MHz. The authors showed a moderate linear correlation between the centroid shift of the ultrasound backscattered spectrum and the BMD of vertebrae ($r = 0.61$, $n = 9$, $p < 0.05$). However, the small number of patients is a limitation for the final conclusions of this preliminary study.

10.4.2 Through-Transmission Measurements

The through-transmission techniques have a longer history than the pulse-echo techniques for determination of acoustic properties of trabecular bone. In this section, only the newest applications and results are introduced.

The ultrasound through-transmission parameters at heel correlate more closely with the heel BMD values than those of the central skeletal sites, e.g. hip and spine. This is an obvious motivation, accompanied by the fact that the site specific measurement is needed for the best prediction for fractures and for introduction of the TT ultrasound measurements at the proximal femur. Both slices from the proximal femur and intact proximal femora have been investigated in vitro [23, 32, 58, 72–75] and in vivo [74, 76–78]. In the former case, BUA and SOS correlated highly significantly with the BMD and the microarhitectural parameters, e.g. trabeculae spacing ($r = 0.74$–0.90 and $r = -0.79$–0.81, respectively) [32, 72]. Interestingly, SOS was usually a better predictor of BMD than BUA in intact samples ($r = 0.78$–0.96 versus $r = 0.70$–0.87) [73, 74]. However, the linear combination of SOS and BUA associated even more strongly with the BMD ($r = 0.95$) [73].

In 2008, after more than 20 years history of ultrasound research for osteoporosis diagnostics, a through-transmission technique suitable for in vivo measurement of proximal femur was introduced [76–78]. A relatively good estimated precision (CV = 0.5%) of SOS measurement was reported, i.e. comparable with that of calcaneal QUS devices [77]. First clinical results for women with or without fracture reveal encouraging performance of the technique (Table 10.7).

The linear combination of SOS values measured through the soft tissue, through cortical bone (edge of bone on 2D SOS image) and through trabecular region (Fig. 10.9) correlated significantly with the total hip BMD ($r = 0.85$). In addition, the hip TT ultrasound served as similar predictor of fractures as the hip DXA [76].

In vivo ultrasound measurements of lumbar spine are challenging due to the large amount of soft tissue overlying the bone, as well as due to the complex form of the vertebrae. The spinous processes form a large error source for through-transmission measurements in antero-posterior direction whereas the pulse-echo measurements may be done through the abdomen [57]. The first in vitro TT-measurements with intact samples have been conducted in the medio-lateral direction [79]. Indeed, the

Table 10.7 Through transmission parameters, i.e. broadband ultrasound attenuation (BUA), speed and attenuation of sound (SOS and attenuation, respectively) associate significantly with the structural and mechanical properties of trabecular bone in vitro and in vivo at the proximal femur and spine

Study/Site	Frequency (MHz)	Parameter	BMD	BV/TV	TrTh	TrSp	Failure load
In vitro slices							
[72] Fem.	0.5	BUA	0.85–0.90**				
[32] Fem.	1.0	nBUA	0.79**†	0.83**	0.57**	−0.79**	
	1.0	SOS	0.74**†	0.81**	0.43**	−0.81**	
Intact							
[73] Fem.	0.5	SOS	0.78–0.95**				
	0.5	BUA	0.70–0.85**				
[74] Fem.	0.5	SOS	0.90–0.96**				
	0.5	BUA	0.78–0.87**				
[79] Spine	1.0	SOS	0.75*				0.71*
	1.0	BUA	0.63*				0.80**
	1.0	Att.	0.79**				0.93**
In vivo							
[76] Fem.	0.6	SOS	0.75–0.76**				
	0.6	BUA	0.51**				

*$p < 0.05$; **$p < 0.01$; †Volumetric BMD

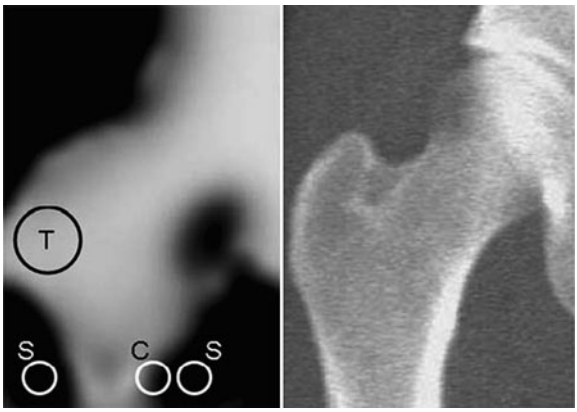

Fig. 10.9 Ultrasound attenuation through the human proximal femur may be compared to X-ray attenuation (*left and right images*, respectively). Linear combination of speed of sound in different region of interests (t – trabecular region, c – cortical region and s – soft tissue regions) may provide a significant prediction value for BMD (Adapted from Barkmann et al. [76] Copyright (2009) with kind permission from Springer Science + Business Media)

attenuation of ultrasound in the medio-lateral direction predicted more closely the failure load of vertebrae ($r = 0.93$, $n = 11$, $p < 0.01$) than the BMD ($r = 0.78$, $n = 11$, $p < 0.01$) [79]. For successful application of spinal measurements in vivo, more research is needed and e.g. uncertainties related to variable soft tissues have to be addressed.

10.5 Clinical Suitability of Quantitative Bone Ultrasound

Osteoporosis is a rapidly growing musculoskeletal health problem and, at the moment, it is estimated that 200 million people around the world suffer from it [80]. However, a majority of osteoporotic patients are not diagnosed until low-trauma fractures occur. For effective management of osteoporosis, early diagnostics should focus on screening of individuals at risk before fractures occur. This is possible only if effective diagnostics can be realized at the primary health care level. At the moment, primary healthcare practitioners typically make a referral to major hospitals and an axial DXA measurement of areal BMD (g/cm^2) is performed to diagnose osteoporosis. In addition to BMD, several qualities (including composition and structure) contribute to the total strength of the bone and only a moderate prediction of fracture risk is achieved by DXA. Actually, a majority of the low trauma fractures occurs in individuals with normal areal BMD [81]. It could be argued whether the DXA or the quantitative computed tomography (QCT) with limited information on bone quality can serve as optimal diagnostic techniques [82, 83]. The DXA devices are mostly available only in major hospitals, and due to costs and the radiation dose, these devices are not optimal for screening purposes.

The site specific areal BMD is needed for the best prediction of fractures at the lumbar spine and proximal femur using DXA [84, 85]. This information highlights the potential of local ultrasound measurements at the severe fracture sites. However, the QUS measurements of heel have also been shown to predict bone fractures [86–89], including the fractures at the hip [3, 90–93] and vertebrae [94–96] in specific populations similarly as axial BMD measurement [86–88, 94–96]. Thus, the peripheral measurements may still be suitable for screening a large number of patients. The potential of peripheral ultrasound measurements is also highlighted by the promising results with a highly portable and low-cost heel device [97].

In summary, there is a growing need for a reliable and affordable bone diagnostics, applicable at the primary health care level for fracture prediction and osteoporosis management. At the moment (2010), the through-transmission technique has successfully been applied for measuring hip, the most severe osteoporotic fracture site. When measuring central skeletal sites, the soft tissues overlying the bones and the complex shape of bone, e.g. the proximal femur or lumbar spine, produce challenges for successful quantitative ultrasound analysis of trabecular bone. The axial TT-devices may be large, similar in size to DXA instruments, and portability, important advantage of the use of ultrasound, is lost. The traditional pulse-echo ultrasound imaging technique also shows potential for bone diagnostics. However, the clinical feasibility PE-ultrasound has not been established although one in vivo study on ultrasound backscatter measurements at the central skeleton has been published [57]. When considering the in vivo feasibility, the inherent challenges of bone QUS measurements apply to PE techniques as well and more in vivo studies are needed. However, the potential of these techniques has been evidenced by high number of in vitro experimental and computational studies. As a main goal, the QUS techniques should be evaluated for most effective prediction of bone fractures. Considering the safety (non-ionizing), portability and the reasonable price of

the ultrasound devices, the novel techniques may enhance the management of osteoporosis and fracture prevention by providing the future diagnostic solution for small practices and health care centers.

References

1. C. M. Langton, S. B. Palmer, and R. W. Porter, "The measurement of broadband ultrasonic attenuation in cancellous bone," Eng Med **13**(2), 89–91 (1984).
2. D. Hans, C. Durosier, J. A. Kanis, H. Johansson, A. M. Schott-Pethelaz, and M. A. Krieg, "Assessment of the 10-year probability of osteoporotic hip fracture combining clinical risk factors and heel bone ultrasound: the EPISEM prospective cohort of 12,958 elderly women," J Bone Miner Res **23**(7), 1045–1051 (2008).
3. D. Hans, P. Dargent-Molina, A. M. Schott, J. L. Sebert, C. Cormier, P. O. Kotzki, P. D. Delmas, J. M. Pouilles, G. Breart, and P. J. Meunier, "Ultrasonographic heel measurements to predict hip fracture in elderly women: the EPIDOS prospective study," Lancet **348**(9026), 511–514 (1996).
4. F. Eckstein, M. Matsuura, V. Kuhn, M. Priemel, R. Muller, T. M. Link, and E. M. Lochmuller, "Sex differences of human trabecular bone microstructure in aging are site-dependent," J Bone Miner Res **22**(6), 817–824 (2007).
5. J. R. Center, T. V. Nguyen, D. Schneider, P. N. Sambrook, and J. A. Eisman, "Mortality after all major types of osteoporotic fracture in men and women: an observational study," Lancet **353**(9156), 878–882 (1999).
6. O. Riekkinen, M. A. Hakulinen, M. Timonen, J. Töyras, and J. S. Jurvelin, "Influence of overlying soft tissues on trabecular bone acoustic measurement at various ultrasound frequencies," Ultrasound Med Biol **32**(7), 1073–1083 (2006).
7. M. Gomez, F. Aguado, J. Manuel, J. M. Menendez, M. Revilla, L. F. Villa, J. Cortes, and H. Rico, "Influence of soft tissue (fat and fat-free mass) on ultrasound bone velocity: an in vivo study," Invest Radiol **32**(10), 609–612 (1997).
8. P. O. Kotzki, D. Buyck, D. Hans, E. Thomas, F. Bonnel, F. Favier, P. J. Meunier, and M. Rossi, "Influence of fat on ultrasound measurements of the os calcis," Calcif Tissue Int **54**(2), 91–95 (1994).
9. C. Chappard, E. Camus, F. Lefebvre, G. Guillot, J. Bittoun, G. Berger, and P. Laugier, "Evaluation of error bounds on calcaneal speed of sound caused by surrounding soft tissue," J Clin Densitom **3**(2), 121–131 (2000).
10. A. Johansen and M. D. Stone, "The effect of ankle oedema on bone ultrasound assessment at the heel," Osteoporos Int **7**(1), 44–47 (1997).
11. J. Töyras, H. Kröger, and J. S. Jurvelin, "Bone properties as estimated by mineral density, ultrasound attenuation, and velocity," Bone **25**(6), 725–731 (1999).
12. S. Cheng, C. F. Njeh, B. Fan, X. Cheng, D. Hans, L. Wang, T. Fuerst, and H. K. Genant, "Influence of region of interest and bone size on calcaneal BMD: implications for the accuracy of quantitative ultrasound assessments at the calcaneus," Br J Radiol **75**(889), 59–68 (2002).
13. C. Y. Wu, C. C. Gluer, M. Jergas, E. Bendavid, and H. K. Genant, "The impact of bone size on broadband ultrasound attenuation," Bone **16**(1), 137–141 (1995).
14. E. Diessel, T. Fuerst, C. F. Njeh, D. Hans, S. Cheng, and H. K. Genant, "Comparison of an imaging heel quantitative ultrasound device (DTU-one) with densitometric and ultrasonic measurements," Br J Radiol **73**(865), 23–30 (2000).
15. J. Damilakis, A. Papadakis, K. Perisinakis, and N. Gourtsoyiannis, "Broadband ultrasound attenuation imaging: influence of location of region of measurement," Eur Radiol **11**(7), 1117–1122 (2001).
16. J. P. van den Bergh, C. Noordam, A. Ozyilmaz, A. R. Hermus, A. G. Smals, and B. J. Otten, "Calcaneal ultrasound imaging in healthy children and adolescents: relation of the ultrasound

parameters BUA and SOS to age, body weight, height, foot dimensions and pubertal stage," Osteoporos Int **11**(11), 967–976 (2000).
17. J. P. van den Bergh, C. Noordam, J. M. Thijssen, B. J. Otten, A. G. Smals, and A. R. Hermus, "Measuring skeletal changes with calcaneal ultrasound imaging in healthy children and adults: the influence of size and location of the region of interest," Osteoporos Int **12**(11), 970–979 (2001).
18. J. Damilakis, G. Papadokostakis, K. Perisinakis, T. G. Maris, and A. H. Karantanas, "Hip fracture discrimination by the Achilles Insight QUS imaging device," Eur J Radiol **63**(1), 59–62 (2007).
19. J. Damilakis, K. Perisinakis, and N. Gourtsoyiannis, "Imaging ultrasonometry of the calcaneus: dependence on calcaneal area," Calcif Tissue Int **67**(1), 24–28 (2000).
20. C. Roux, B. Fournier, P. Laugier, C. Chappard, S. Kolta, M. Dougados, and G. Berger, "Broadband ultrasound attenuation imaging: a new imaging method in osteoporosis," J Bone Miner Res **11**(8), 1112–1118 (1996).
21. P. Laugier, G. Berger, P. Giat, P. Bonnin-Fayet, and M. Laval-Jeantet, "Ultrasound attenuation imaging in the os calcis: an improved method," Ultrason Imaging **16**(2), 65–76 (1994).
22. P. Laugier, B. Fournier, and G. Berger, "Ultrasound parametric imaging of the calcaneus: in vivo results with a new device," Calcif Tissue Int **58**(5), 326–331 (1996).
23. G. Haiat, F. Padilla, R. Barkmann, S. Kolta, C. Latremouille, C. C. Gluer, and P. Laugier, "In vitro speed of sound measurement at intact human femur specimens," Ultrasound Med Biol **31**(7), 987–996 (2005).
24. C. F. Njeh, C. W. Kuo, C. M. Langton, H. I. Atrah, and C. M. Boivin, "Prediction of human femoral bone strength using ultrasound velocity and BMD: an in vitro study," Osteoporos Int **7**(5), 471–477 (1997).
25. M. A. Hakulinen, J. Töyras, S. Saarakkala, J. Hirvonen, H. Kröger, and J. S. Jurvelin, "Ability of ultrasound backscattering to predict mechanical properties of bovine trabecular bone," Ultrasound Med Biol **30**(7), 919–927 (2004).
26. M. A. Hakulinen, J. S. Day, J. Töyras, H. Weinans, and J. S. Jurvelin, "Ultrasonic characterization of human trabecular bone microstructure," Phys Med Biol **51**(6), 1633–1648 (2006).
27. K. A. Wear and B. S. Garra, "Assessment of bone density using ultrasonic backscatter," Ultrasound Med Biol **24**(5), 689–695 (1998).
28. K. A. Wear, A. P. Stuber, and J. C. Reynolds, "Relationships of ultrasonic backscatter with ultrasonic attenuation, sound speed and bone mineral density in human calcaneus," Ultrasound Med Biol **26**(8), 1311–1316 (2000).
29. B. K. Hoffmeister, D. P. Johnson, J. A. Janeski, D. A. Keedy, B. W. Steinert, A. M. Viano, and S. C. Kaste, "Ultrasonic characterization of human cancellous bone in vitro using three different apparent backscatter parameters in the frequency range 0.6–15 MHz," IEEE Trans Ultrason Ferroelectr Freq Control **55**(7), 1442–1452 (2008).
30. B. K. Hoffmeister, C. I. Jones, III, G. J. Caldwell, and S. C. Kaste, "Ultrasonic characterization of cancellous bone using apparent integrated backscatter," Phys Med Biol **51**(11), 2715–2727 (2006).
31. J. P. Karjalainen, J. Toyras, O. Riekkinen, M. Hakulinen, and J. S. Jurvelin, "Ultrasound backscatter imaging provides frequency-dependent information on structure, composition and mechanical properties of human trabecular bone," Ultrasound Med Biol **35**(8), 1376–1384 (2009).
32. F. Padilla, F. Jenson, V. Bousson, F. Peyrin, and P. Laugier, "Relationships of trabecular bone structure with quantitative ultrasound parameters: in vitro study on human proximal femur using transmission and backscatter measurements," Bone **42**(6), 1193–1202 (2008).
33. O. Riekkinen, M. A. Hakulinen, M. J. Lammi, J. S. Jurvelin, A. Kallioniemi, and J. Töyras, "Acoustic properties of trabecular bone-relationships to tissue composition," Ultrasound Med Biol **33**(9), 1438–1444 (2007).
34. O. Riekkinen, M. A. Hakulinen, J. Töyräs, and J. S. Jurvelin, "Spatial variation of acoustic properties is related with mechanical properties of trabecular bone," Phys Med Biol **52**, 6961–6968 (2007).

35. J. Karjalainen, O. Riekkinen, J. Töyräs, H. Kröger, and J. S. Jurvelin, "Ultrasonic assessment of cortical bone thickness *in vitro* and *in vivo*," IEEE Trans Ultrason Ferroelectr Freq Control **55**(10), 2191–2197 (2008).
36. K. A. Wear, "Autocorrelation and cepstral methods for measurement of tibial cortical thickness," IEEE Trans Ultrason Ferroelectr Freq Control **50**(6), 655–660 (2003).
37. M. Muller, D. Mitton, P. Moilanen, V. Bousson, M. Talmant, and P. Laugier, "Prediction of bone mechanical properties using QUS and pQCT: study of the human distal radius," Med Eng Phys (2007).
38. M. Muller, P. Moilanen, E. Bossy, P. Nicholson, V. Kilappa, J. Timonen, M. Talmant, S. Cheng, and P. Laugier, "Comparison of three ultrasonic axial transmission methods for bone assessment," Ultrasound Med Biol **31**(5), 633–642 (2005).
39. P. Moilanen, P. H. Nicholson, T. Karkkainen, Q. Wang, J. Timonen, and S. Cheng, "Assessment of the tibia using ultrasonic guided waves in pubertal girls," Osteoporos Int **14**(12), 1020–1027 (2003).
40. M. Talmant, S. Kolta, C. Roux, D. Haguenauer, I. Vedel, B. Cassou, E. Bossy, and P. Laugier, "In vivo performance evaluation of bi-directional ultrasonic axial transmission for cortical bone assessment," Ultrasound Med Biol (2009).
41. K. A. Wear, "Frequency dependence of ultrasonic backscatter from human trabecular bone: theory and experiment," J Acoust Soc Am **106**(6), 3659–3664 (1999).
42. J.-F. Chen and J. A. Zagzebski, "Frequency dependence of backscatter coefficient versus scatterer volume fraction," IEEE Trans Ultrason Ferroelectr Freq Control **43**(3), 345–353 (1996).
43. K. A. Wear, "Ultrasonic scattering from cancellous bone: a review," IEEE Trans Ultrason Ferroelectr Freq Control **55**(7), 1432–1441 (2008).
44. E. Bossy, P. Laugier, F. Peyrin, and F. Padilla, "Attenuation in trabecular bone: a comparison between numerical simulation and experimental results in human femur," J Acoust Soc Am **122**(4), 2469–2475 (2007).
45. M. A. Hakulinen, J. S. Day, J. Töyras, M. Timonen, H. Kröger, H. Weinans, I. Kiviranta, and J. S. Jurvelin, "Prediction of density and mechanical properties of human trabecular bone in vitro by using ultrasound transmission and backscattering measurements at 0.2–6.7 MHz frequency range," Phys Med Biol **50**(8), 1629–1642 (2005).
46. F. Jenson, F. Padilla, and P. Laugier, "Prediction of frequency-dependent ultrasonic backscatter in cancellous bone using statistical weak scattering model," Ultrasound Med Biol **29**(3), 455–464 (2003).
47. R. A. Sigelmann and J. M. Reid, "Analysis and measurement of ultrasound backscattering from an ensemble of scatterers excited by sine-wave bursts," J Acoust Soc Am **53**, 1351–1355 (1973).
48. M. O'Donnell and J. G. Miller, "Quantitative broadband ultrasonic backscatter: an approach to nondestructive evaluation in acoustically inhomogenous materials," J Appl Phys **52**(2), 1056–1065 (1981).
49. P. H. Nicholson and M. L. Bouxsein, "Bone marrow influences quantitative ultrasound measurements in human cancellous bone," Ultrasound Med Biol **28**(3), 369–375 (2002).
50. T. A. Bigelow and W. D. O'Brien, Jr., "Scatterer size estimation using a generalized ultrasound attenuation compensation function to correct for focusing," IEEE Ultrasonics Symposium Honolulu, 1026–1029 (2003).
51. M. L. Oelze and W. D. O'Brien, Jr., "Frequency-dependent attenuation-compensation functions for ultrasonic signals backscattered from random media," J Acoust Soc Am **111**(5 Pt 1), 2308–2319 (2002).
52. J. G. Miller, J. E. Perez, and B. E. Sobel, "Ultrasonic characterization of myocardium," Prog Cardiovasc Dis **28**(2), 85–110 (1985).
53. F. L. Lizzi, M. Ostromogilsky, E. J. Feleppa, M. C. Rorke, and M. M. Yaremko, "Relationship of ultrasonic spectral parameters to features of tissue microstructure," IEEE Trans Ultrason Ferroelectr Freq Control **34**(3), 319–329 (1987).
54. B. K. Hoffmeister, J. A. Auwarter, and J. Y. Rho, "Effect of marrow on the high frequency ultrasonic properties of cancellous bone," Phys Med Biol **47**(18), 3419–3427 (2002).

55. B. K. Hoffmeister, S. A. Whitten, S. C. Kaste, and J. Y. Rho, "Effect of collagen and mineral content on the high-frequency ultrasonic properties of human cancellous bone," Osteoporos Int **13**(1), 26–32 (2002).
56. K. A. Wear, "Characterization of trabecular bone using the backscattered spectral centroid shift," IEEE Trans Ultrason Ferroelectr Freq Control **50**(4), 402–407 (2003).
57. B. S. Garra, M. Locher, S. Felker, and K. A. Wear, "Measurements of ultrasonic backscattered spectral centroid shift from spine in vivo: methodology and preliminary results," Ultrasound Med Biol **35**(1), 165–168 (2009).
58. G. Haiat, F. Padilla, R. O. Cleveland, and P. Laugier, "Effects of frequency-dependent attenuation and velocity dispersion on in vitro ultrasound velocity measurements in intact human femur specimens," IEEE Trans Ultrason Ferroelectr Freq Control **53**(1), 39–51 (2006).
59. K. A. Wear, "A method for improved standardization of in vivo calcaneal time-domain speed-of-sound measurements," IEEE Trans Ultrason Ferroelectr Freq Control **55**(7), 1473–1479 (2008).
60. A. S. Aula, J. Töyras, M. Hakulinen, and J. S. Jurvelin, "Effect of bone marrow on acoustic properties of trabecular bone – 3D finite difference modeling study," Ultrasound Med Biol **35**(2), 308–318 (2009).
61. J. Töyras, M. T. Nieminen, H. Kröger, and J. S. Jurvelin, "Bone mineral density, ultrasound velocity, and broadband attenuation predict mechanical properties of trabecular bone differently," Bone **31**(4), 503–507 (2002).
62. O. Riekkinen, M. A. Hakulinen, J. Töyras, and J. S. Jurvelin, "Dual-frequency ultrasound–new pulse-echo technique for bone densitometry," Ultrasound Med Biol **34**(10), 1703–1708 (2008).
63. J. Karjalainen, J. Töyras, T. Rikkonen, J. S. Jurvelin, and O. Riekkinen, "Dual-frequency ultrasound technique minimizes errors induced by soft tissue in ultrasound bone densitometry," Acta Radiol **49**, 1038–1041 (2008).
64. C. M. Langton and C. F. Njeh, "The measurement of broadband ultrasonic attenuation in cancellous bone–a review of the science and technology," IEEE Trans Ultrason Ferroelectr Freq Control **55**(7), 1546–1554 (2008).
65. P. Laugier, "Instrumentation for in vivo ultrasonic characterization of bone strength," IEEE Trans Ultrason Ferroelectr Freq Control **55**(6), 1179–1196 (2008).
66. S. Chaffai, F. Peyrin, S. Nuzzo, R. Porcher, G. Berger, and P. Laugier, "Ultrasonic characterization of human cancellous bone using transmission and backscatter measurements: relationships to density and microstructure," Bone **30**(1), 229–237 (2002).
67. A. S. Aula, J. Toyras, M. A. Hakulinen, and J. S. Jurvelin, "Effect of bone marrow on acoustic properties of trabecular bone – 3D finite difference modeling study," Ultrasound Med Biol **35**(2), 308–318 (2009).
68. M. Pakula, F. Padilla, and P. Laugier, "Influence of the filling fluid on frequency-dependent velocity and attenuation in cancellous bones between 0.35 and 2.5 MHz," J Acoust Soc Am **126**(6), 3301–3310 (2009).
69. C. M. Langton, C. F. Njeh, R. Hodgskinson, and J. D. Currey, "Prediction of mechanical properties of the human calcaneus by broadband ultrasonic attenuation," Bone **18**(6), 495–503 (1996).
70. C. F. Njeh and C. M. Langton, "The effect of cortical endplates on ultrasound velocity through the calcaneus: an in vitro study," Br J Radiol **70**(833), 504–510 (1997).
71. C. Roux, V. Roberjot, R. Porcher, S. Kolta, M. Dougados, and P. Laugier, "Ultrasonic backscatter and transmission parameters at the os calcis in postmenopausal osteoporosis," J Bone Miner Res **16**(7), 1353–1362 (2001).
72. F. Padilla, L. Akrout, S. Kolta, C. Latremouille, C. Roux, and P. Laugier, "*In vitro* ultrasound measurement at the human femur," Calcif Tissue Int **75**(5), 421–430 (2004).
73. G. Haiat, F. Padilla, R. Barkmann, S. Dencks, U. Moser, C. C. Gluer, and P. Laugier, "Optimal prediction of bone mineral density with ultrasonic measurements in excised human femur," Calcif Tissue Int **77**(3), 186–192 (2005).
74. R. Barkmann, P. Laugier, U. Moser, S. Dencks, F. Padilla, G. Haiat, M. Heller, and C. C. Gluer, "A method for the estimation of femoral bone mineral density from variables of ultrasound transmission through the human femur," Bone **40**(1), 37–44 (2007).

75. S. Dencks, R. Barkmann, F. Padilla, G. Haiat, P. Laugier, and C. C. Gluer, "Wavelet-based signal processing of in vitro ultrasonic measurements at the proximal femur," Ultrasound Med Biol **33**(6), 970–980 (2007).
76. R. Barkmann, S. Dencks, P. Laugier, F. Padilla, K. Brixen, J. Ryg, A. Seekamp, L. Mahlke, A. Bremer, M. Heller, and C. C. Gluer, "Femur ultrasound (FemUS)-first clinical results on hip fracture discrimination and estimation of femoral BMD," Osteoporos Int **21**(6), 969–976 (2010).
77. R. Barkmann, P. Laugier, U. Moser, S. Dencks, M. Klausner, F. Padilla, G. Haiat, M. Heller, and C. C. Gluer, "In vivo measurements of ultrasound transmission through the human proximal femur," Ultrasound Med Biol (2008).
78. R. Barkmann, P. Laugier, U. Moser, S. Dencks, M. Klausner, F. Padilla, G. Haiat, and C. C. Gluer, "A device for in vivo measurements of quantitative ultrasound variables at the human proximal femur," IEEE Trans Ultrason Ferroelectr Freq Control **55**(6), 1197–1204 (2008).
79. P. H. Nicholson and R. Alkalay, "Quantitative ultrasound predicts bone mineral density and failure load in human lumbar vertebrae," Clin Biomech (Bristol, Avon) **22**(6), 623–629 (2007).
80. U. Tarantino, G. Cannata, D. Lecce, M. Celi, I. Cerocchi, and R. Iundusi, "Incidence of fragility fractures," Aging Clin Exp Res **19**(4 Suppl), 7–11 (2007).
81. A. Cranney, S. A. Jamal, J. F. Tsang, R. G. Josse, and W. D. Leslie, "Low bone mineral density and fracture burden in postmenopausal women," Cmaj **177**(6), 575–580 (2007).
82. J. E. Adams, "Quantitative computed tomography," Eur J Radiol **71**(3), 415–424 (2009).
83. H. H. Bolotin, "DXA in vivo BMD methodology: an erroneous and misleading research and clinical gauge of bone mineral status, bone fragility, and bone remodelling," Bone **41**(1), 138–154 (2007).
84. D. Marshall, O. Johnell, and H. Wedel, "Meta-analysis of how well measures of bone mineral density predict occurrence of osteoporotic fractures," BMJ **312**(7041), 1254–1259 (1996).
85. M. L. Bouxsein, L. Palermo, C. Yeung, and D. M. Black, "Digital X-ray radiogrammetry predicts hip, wrist and vertebral fracture risk in elderly women: a prospective analysis from the study of osteoporotic fractures," Osteoporos Int **13**(5), 358–365 (2002).
86. J. Huopio, H. Kröger, R. Honkanen, J. Jurvelin, S. Saarikoski, and E. Alhava, "Calcaneal ultrasound predicts early postmenopausal fractures as well as axial BMD. A prospective study of 422 women," Osteoporos Int **15**(3), 190–195 (2004).
87. A. Stewart, V. Kumar, and D. M. Reid, "Long-term fracture prediction by DXA and QUS: a 10-year prospective study," J Bone Miner Res **21**(3), 413–418 (2006).
88. A. Moayyeri, S. Kaptoge, N. Dalzell, S. Bingham, R. N. Luben, N. J. Wareham, J. Reeve, and K. T. Khaw, "Is QUS or DXA better for predicting the 10-year absolute risk of fracture?," J Bone Miner Res (2009).
89. F. Marin, J. Gonzalez-Macias, A. Diez-Perez, S. Palma, and M. Delgado-Rodriguez, "Relationship between bone quantitative ultrasound and fractures: a meta-analysis," J Bone Miner Res **21**(7), 1126–1135 (2006).
90. H. Dobnig, J. C. Piswanger-Solkner, B. Obermayer-Pietsch, A. Tiran, A. Strele, E. Maier, P. Maritschnegg, G. Riedmuller, C. Brueck, and A. Fahrleitner-Pammer, "Hip and nonvertebral fracture prediction in nursing home patients: role of bone ultrasound and bone marker measurements," J Clin Endocrinol Metab **92**(5), 1678–1686 (2007).
91. I. Guessous, J. Cornuz, C. Ruffieux, P. Burckhardt, and M. A. Krieg, "Osteoporotic fracture risk in elderly women: estimation with quantitative heel US and clinical risk factors," Radiology **248**(1), 179–184 (2008).
92. K. T. Khaw, J. Reeve, R. Luben, S. Bingham, A. Welch, N. Wareham, S. Oakes, and N. Day, "Prediction of total and hip fracture risk in men and women by quantitative ultrasound of the calcaneus: EPIC-Norfolk prospective population study," Lancet **363**(9404), 197–202 (2004).
93. M. A. Krieg, J. Cornuz, C. Ruffieux, G. Van Melle, D. Buche, M. A. Dambacher, D. Hans, F. Hartl, H. J. Hauselmann, M. Kraenzlin, K. Lippuner, M. Neff, P. Pancaldi, R. Rizzoli, F. Tanzi, R. Theiler, A. Tyndall, C. Wimpfheimer, and P. Burckhardt, "Prediction of hip fracture risk by quantitative ultrasound in more than 7000 Swiss women $>$ or $=$ 70 years of age: comparison of three technologically different bone ultrasound devices in the SEMOF study," J Bone Miner Res **21**(9), 1457–1463 (2006).

94. C. C. Gluer, R. Eastell, D. M. Reid, D. Felsenberg, C. Roux, R. Barkmann, W. Timm, T. Blenk, G. Armbrecht, A. Stewart, J. Clowes, F. E. Thomasius, and S. Kolta, "Association of five quantitative ultrasound devices and bone densitometry with osteoporotic vertebral fractures in a population-based sample: the OPUS Study," J Bone Miner Res **19**(5), 782–793 (2004).
95. B. Frediani, C. Acciai, P. Falsetti, F. Baldi, G. Filippou, C. Siagkri, A. Spreafico, M. Galeazzi, and R. Marcolongo, "Calcaneus ultrasonometry and dual-energy X-ray absorptiometry for the evaluation of vertebral fracture risk," Calcif Tissue Int **79**(4), 223–229 (2006).
96. R. Hollaender, F. Hartl, M. A. Krieg, A. Tyndall, C. Geuckel, C. Buitrago-Tellez, M. Manghani, M. Kraenzlin, R. Theiler, and D. Hans, "Prospective evaluation of risk of vertebral fractures using quantitative ultrasound measurements and bone mineral density in a population-based sample of postmenopausal women: results of the Basel Osteoporosis Study," Ann Rheum Dis **68**(3), 391–396 (2009).
97. J. J. Kaufman, G. Luo, and R. S. Siffert, "A portable real-time ultrasonic bone densitometer," Ultrasound Med Biol **33**(9), 1445–1452 (2007).

Chapter 11
The Fast and Slow Wave Propagation in Cancellous Bone: Experiments and Simulations

Atsushi Hosokawa, Yoshiki Nagatani, and Mami Matsukawa

Abstract Cancellous bone consists of a complex solid trabecular network structure filled with soft bone marrow. The use of a short and broadband ultrasound incident pulse enables the experimental observation of a two longitudinal wave phenomenon, consistently with Biot's prediction for porous media. This chapter is a review of the experimental studies and discusses theoretical interpretations, including the Biot's theory and modified Biot's models. The inhomogeneous nature of cancellous bone often results in some discrepancies between theory and experimental results. However, the two-wave phenomenon may provide detailed information on the structure and characteristics of cancellous bone, beyond conventional quantitative ultrasound (QUS) parameters. In order to understand this complex wave propagation in cancellous bone, numerical simulations offer an interesting and powerful alternative to intractable analytical approaches. Recent progress in computer performances enables the visualization of wave propagation using for example finite difference numerical methods, combined with three-dimensional numerical models of actual cancellous bone structures. In addition, the numerical investigation using virtual trabecular structures brings insightful view into the two-wave phenomenon, which cannot be obtained using the experiments. Finally, this chapter also refers to a new in vivo technique based on the two-wave phenomenon.

Keywords Angle-dependent Biot's model (stratified Biot's model) · Anisotropy · Artificial model of trabecular structure · Bayesian probability theory · Biot's theory · Bone mineral density (BMD) · Bone volume fraction (BV/TV) · Cancellous

A. Hosokawa (✉)
Akashi National College of Technology, 679-3 Nishioka, Uozumi, 674-8501 Akashi, Japan
e-mail: hosokawa@akashi.ac.jp

Y. Nagatani
Kobe City College of Technology, 8-3 Gakuenhigashi, Nishiku, 651-2194 Kobe, Japan
e-mail: nagatani@ultrasonics.jp

M. Matsukawa
Doshisha University, 1-3 Tatara Miyakodani, 610-0321 Kyotanabe, Japan
e-mail: mmatsuka@mail.doshisha.ac.jp

P. Laugier and G. Haïat (eds.), *Bone Quantitative Ultrasound*,
DOI 10.1007/978-94-007-0017-8_11,

bone · Cancellous bone phantom · Clinical application · Degree of anisotropy (DA) · Erosion/dilation procedure · Fast and slow waves · Finite element method (FEM) · Finite-difference time-domain (FDTD) method · Focused (concave) transmitter · Frequency-dependent ultrasound attenuation (FDUA) · Image processing technique · Inhomogeneous · In-silico approach · LD-100 · Mode conversion · Modified Biot-Attenborough (MBA) model · Numerical simulation · Overlapping fast and slow waves · Poly(vinylidene fluoride) (PVDF) transducer · Scalogram · Scattering · Short-time Fourier transform · SimSonic · Spectrograms · Stratified model · (Schoenberg's model) · Synchrotron radiation microcomputed tomography (SR-μ CT) · Trabecular length Trabecular microstructure · Trabecular orientation · Trabecular thickness · Two-wave phenomenon · Virtual specimen · Viscous friction · Wave separation technique · Wavelet transform · X-ray μ CT

11.1 Introduction

The main consequences of osteoporosis are dynamic structural changes, such as loss of bone mass and alterations of microstructure, that manifest in cancellous bone. Many clinically available quantitative ultrasound (QUS) technologies focus on the measurements on cancellous bone sites, such as the heel. The difficulty with ultrasound measurements of cancellous bone and their interpretation comes from the complex marrow-filled solid trabecular structure interacting with ultrasound waves. Complex interaction phenomena between propagating ultrasound waves and bone arise from such an inhomogeneous and anisotropic porous medium [1]. The Biot's theory [2, 3] (see Chap. 5 for more details) describing wave propagation in porous media has been applied to cancellous bone, predicting two kinds of longitudinal waves, referred to as fast and slow waves. Following the seminal work of McKelvie and Palmer [4], several models based on the Biot's theory have been introduced and have enjoyed varying degrees of success.

However, as pointed out by Kaufman et al. [5] the analytic solutions to propagation in cancellous bone have some limitations due to the associated irregular geometry and inhomogeneous character of bone. Actually, dramatic variations of bone volume fraction and important fluctuations of trabecular orientation can be observed not only between different cancellous bone specimens, but also within a single skeletal site like for example the epiphysis of long bones [6]. This is one reason why many research studies have been mainly based on experimental data, both in vitro and in vivo. In the 1990s, another approach to solve this problem consisted in the use of computer simulations of ultrasound wave propagation. Following the successful application of numerical simulations to electromagnetic waves propagation, simulation studies have been widely spread to understand the nature of elastic wave propagation in bone. One novel idea was to solve the wave propagation equations using approaches like finite-difference time-domain (FDTD) [7] or finite element methods (FEM) in combination with the actual three-dimensional (3-D) structure

of bone obtained by high-resolution synchrotron radiation microcomputed tomography (SR-μCT) or X-ray μ CT.

This chapter introduces the interesting wave propagation phenomena in cancellous bone, from both the experimental and simulation points of view. Especially, focusing on the propagation of two longitudinal waves, results are discussed in light of theoretical predictions. The two longitudinal waves convey broader information on cancellous bone characteristics than the conventional simple QUS parameters like speed of sound (SOS) or broadband ultrasound attenuation (BUA), because wave propagation strongly depends on the structural properties of the cancellous bone.

11.2 Experimental Approach: Measurement of Fast and Slow Waves

11.2.1 Observation of Fast and Slow Waves

The experimental observation of the fast and slow longitudinal waves propagating in cancellous bone was first reported by Hosokawa and Otani [8]. In their in vitro experiments, bovine cancellous bone with bone marrow in situ was used. The cancellous bone specimens with approximately 25 mm in size and 9 mm in thickness were cut from the distal epiphysis of the femora. The specimens were immersed in water and degassed to remove air bubbles before performing the experiments. Ultrasound pulse waves propagating through the specimens were observed by a water-immersion ultrasound technique, in which a pair of broadband (0.1–10 MHz) poly(vinylidene fluoride) (PVDF) transducers with a flat surface were used. A short pulse wave with a center frequency of 1 MHz was applied to the specimen at normal incidence in the thickness direction. The direction of propagation corresponded to the superoinferior (SI) direction, which is designated as the longitudinal direction in Hosokawa and Otani [8]. In this direction, the trabecular elements were strongly oriented. The observed waveforms are shown in Fig. 11.1, and Fig. 11.1a and b show respectively the waveforms for the specimens with low and high bone volume fractions (BV/TV) of 0.17 and 0.25. In both figures, two distinct longitudinal waves, referred to as the fast and slow waves, can be clearly observed. As the volume fraction of the solid bone increases and the fraction of the pore spaces filled with bone marrow decreases, the amplitude of the fast wave becomes greater and the amplitude of the slow wave becomes smaller. Therefore, it can be deduced that the fast and slow waves are respectively associated with the trabecular elements and pore spaces in cancellous bone. The fast wave speed was slower than the speed in bovine cortical bone, which can be explained by the fact that cancellous bone is not dense but porous. On the other hand, the slow wave speed was close to the speed in bone marrow. In general, the fast and slow waves are respectively composed of the

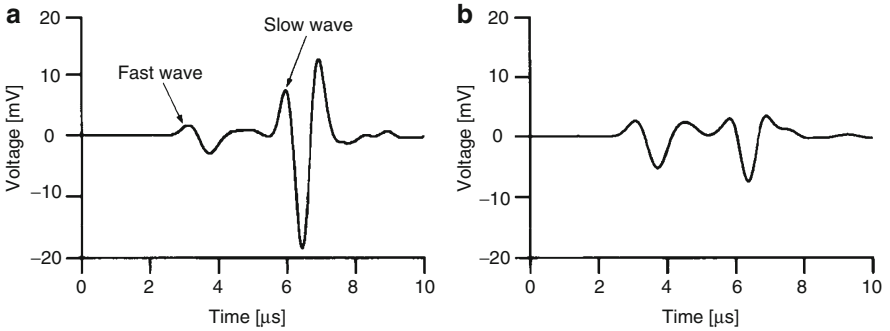

Fig. 11.1 Experimentally observed fast and slow wave modes propagating through bovine femoral cancellous bone with bone volume fractions (BV/TV) of (**a**) 0.17 and (**b**) 0.25 in the superoinferior (SI) direction (Reprinted with permission from [8] copyright (1997), Acoustical Society of America)

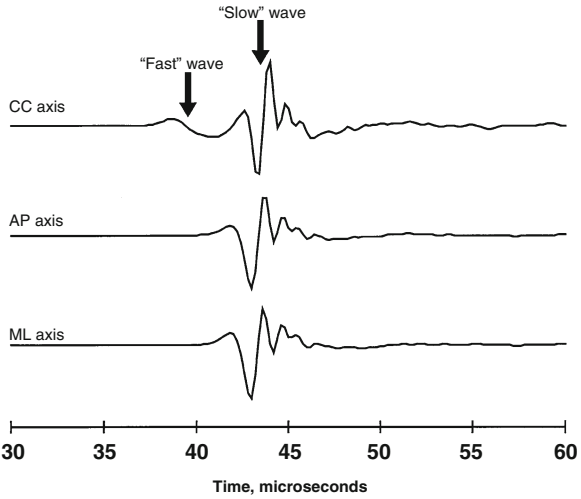

Fig. 11.2 Typical ultrasound pulse waveforms propagating through human vertebral cancellous bone in three orthogonal directions. The CC (craniocaudal) axis corresponds to the SI (superoinferior) axis (Reprinted from [14] copyright (1998) with permission from Elsevier)

low- and high-frequency components [9, 10], which can be clearly observed in the upper waveform of Fig. 11.2.

Two major factors influencing the possibility of observing the fast and slow waves must be considered. The first one corresponds to the transducers properties used for transmitting and receiving the ultrasound pulse wave. Because the propagation times of the fast and slow waves are comparable, a very short pulse wave is required for observing the two waves separately, as shown in Fig. 11.1. The observation of both waves cannot necessarily be realized by increasing the frequency because the attenuation of the fast wave is high at frequencies over 1 MHz (see

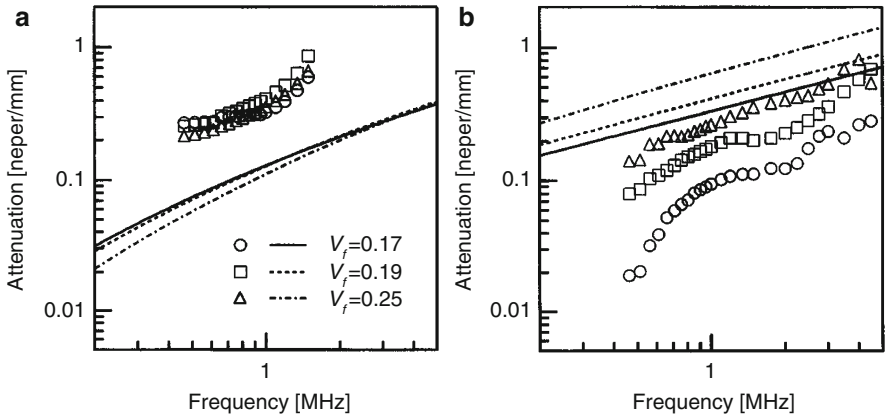

Fig. 11.3 Comparison between theoretical results calculated using the Biot's model and experimental results for attenuation coefficients of (**a**) fast and (**b**) slow waves in bovine cancellous bone. V_f represents the bone volume fraction (BV/TV) (Reprinted with permission from [8] copyright (1997), Acoustical Society of America)

Fig. 11.3a). Some broadband transducers made of piezoelectric ceramics, typically lead-zirconate-titanate (PZT), used in the nondestructive testing have a bandwidth of only a few MHz, and therefore, slight oscillations can be caused in the output signal. On the other hand, transducers made of piezoelectric polymer films [11–13], such as PVDF, have a much broader bandwidth over 10 MHz, that is a good temporal resolution, despite a limited output. When focused transducers with a concave surface are used, the output can be enlarged and the spatial resolution becomes higher.

The second factor required for the observation of two waves is the direction of wave propagation relatively to the anatomical orientation of cancellous bone. Nicholson et al. [14] experimentally observed pulse waveforms propagating through human vertebral cancellous bone in three orthogonal directions of the CC (craniocaudal), AP (anteroposterior), and ML (mediolateral) axes. The observed waveforms are shown in Fig. 11.2, where two waves can be observed in the CC direction, but only a single wave is observed in the other directions. The trabecular orientation was strong in the CC direction, which corresponds to the SI direction, but weak in the AP and ML directions. Hosokawa and Otani [15], and Mizuno et al. [6] also demonstrated that cancellous bone had a strong acoustic anisotropy and that the observed waveform propagating through bone changed with the propagation direction to the trabecular orientation. As described above, it can be considered that the fast and slow waves propagate mainly in the trabeculae and in the saturating medium (water or bone marrow), respectively. In the propagation parallel to the major trabecular orientation, two propagation paths along the major trabecular and saturating medium parts can be clearly separated, which results in the observation of the two waves. In the propagation perpendicular to the major trabecular orientation,

on the other hand, the propagation path across both major trabecular and pore parts can be scarcely separated, strictly slight separation of two paths along the minor trabecular and pore parts can be generated. This results in the large overlap of the two waves and then, it appears as if only a single wave propagates. In conclusion, the separation of the fast and slow waves becomes clearer as the trabecular orientation becomes stronger in the propagation direction, i.e., as the degree of anisotropy (DA) increases. In transverse transmission techniques, which are widely used to measure QUS parameters of speed of sound (SOS) and broadband ultrasound attenuation (BUA), the ultrasound wave propagates through the calcaneus in the ML direction perpendicular to the trabecular orientation and therefore, the two waves cannot be observed.

The observation of the fast and slow waves in cancellous bone under various conditions has been reported. Table 11.1 summarizes the specimens and experimental conditions necessary to observe the waveform separated into the two waves. For instance, two waves were also observed for specimens saturated with water instead of bone marrow.

11.2.2 Application of Theoretical Models

Several theoretical models have been used to explain the propagation of both the fast and slow waves in cancellous bone. The application of Biot's theory [2, 3] (see Chap. 5) to cancellous bone was proposed [4, 25] before the first observation of the fast and slow waves. The Biot's theory predicts that two longitudinal waves, which were denoted as "waves of the first and second kind", can propagate through a fluid-saturated porous elastic solid. Therefore, it was considered that the experimentally observed fast and slow waves in cancellous bone most probably corresponded to the two waves predicted in the Biot's theory, and subsequently the Biot's theory was applied to predict the propagation properties of both waves [8, 15, 16]. The comparison of the theoretical propagation properties calculated by the Biot's model with the experimental results is shown in Figs. 11.3 [8] and 11.4 [24]. In calculating the propagation speed of the fast wave as a function of BV/TV, the exponent parameter value (see details in Sect. 5.3.2), which depends on the trabecular structure, was adjusted to fit the experimental results. Then, the other propagation properties were calculated using the adjusted value. For both bovine and human cancellous bone specimens, as shown in Fig. 11.4, the fast wave speed increases with BV/TV while the slow wave speed slightly decreases. The theoretical results for the propagation speeds of both the fast and slow waves are in a good agreement with the experimental results for both bovine and human specimens. However, in Fig. 11.3, the theoretical results for the frequency dependences of the attenuation coefficients at three values of BV/TV (V_f) largely deviate from the experimental results. In particular, the experimental attenuation coefficient of the fast wave (Fig. 11.3a) is larger than that of the slow wave (Fig. 11.3b) throughout the frequency range, which contradicts the theoretical results. In the Biot's theory, it is specified that the slow

Table 11.1 Specimen and experimental conditions in clearly separating fast and slow waves in cancellous bone

Specimen conditions			Experimental conditions		
Bone	BV/TV	Filling fluid	Transducer type	Propagation direction	Reference
Bovine femur	0.17, 0.25	Bone marrow	PVDF (0.1–10 MHz)	Longitudinal direction	[8]
Human vertebra		Bone marrow	Broadband (1 MHz)	Craniocaudal direction	[14]
Bovine femur	0.18	Bone marrow	PVDF (0.1–10 MHz)	Longitudinal direction	[15]
Bovine femur	0.19–0.12	Water	PVDF	Longitudinal direction	[16]
Bovine femur, tibia	0.35	Bone marrow	Resonance (1 MHz)	Parallel direction to the trabeculae	[17]
Bovine tibia		Water	Panametrics V306 (2.25 MHz)	Superoinferior direction	[18]
Bovine femur, vertebra		Bone marrow, Water Alcohol	Panametrics V302SU (1 MHz), V304SU (2.25 MHz)	Trabecular-oriented direction	[9, 19]
Bovine femur		Water	Panametrics V323SU (2.25 MHz)		[10]
Human femur, tibia					
Human femur	0.12–0.23	Water	Panametrics A306S (2.25 MHz)	Trabecular-aligned direction	[20]
Human femur	0.06–0.41	Water	Panametrics A303S (1 MHz)	Trabecular-aligned direction	[1, 21–23]
Bovine femur		Water	A pair of Toray custom-made PVDF focus transmitter and self-made PVDF receiver	Parallel to the predominant trabecular orientation	[6]
Human femur	0.19, 0.30	Water	A pair of Toray custom-made PVDF focus transmitter and home-made PVDF flat receiver	Main load direction	[24]

The longitudinal and craniocaudal directions correspond to the superoinferior direction

wave is more attenuated than the fast wave [2, 3]. In addition, it is observed in the experimental results that the fast wave attenuation rapidly increases over 1 MHz, which is not predicted by theoretical results.

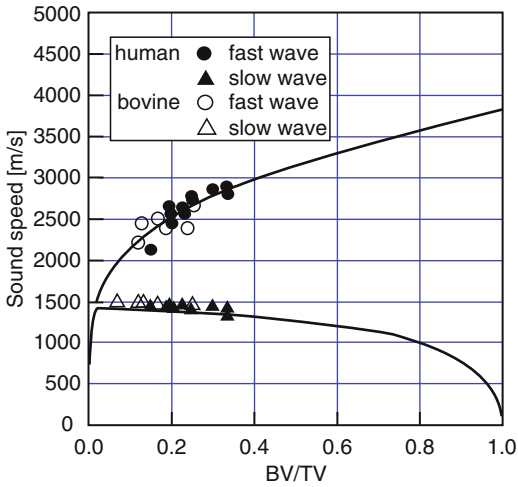

Fig. 11.4 Comparison between theoretical results calculated using the Biot's model and experimental results for propagation speeds of fast and slow waves in bovine and human cancellous bones (Reprinted with permission from [24] copyright (2009), Acoustical Society of America)

The discrepancy between the theoretical and experimental attenuation coefficients can be due to the fact that the Biot's model only considers absorption loss due to the viscous friction at interfaces between the solid and fluid, and does not account for additional sources of energy loss. In particular, scattering effects (see Chap. 6) are neglected by assuming that the ultrasound wavelength is sufficiently large in comparison with the pore size in cancellous bone. However, pore size in the approximate range of 0.5–1.5 mm for human femoral cancellous bone [27] is comparable to the wavelength of 1.5 mm at 1 MHz in water. The rapid increase in the attenuation coefficient of the fast wave observed in Fig. 11.3a could be due to the rising contribution with frequency of scattering to total loss. Haire and Langton [28] indicated in their review of the application of the Biot's model to cancellous bone that inaccurate prediction of the attenuation coefficients was partially due to incomplete understanding of the parameters in the model. Then, the modified Biot's models have been developed. Lee et al. [29–31] theoretically estimated the propagation properties using the modified Biot-Attenborough (MBA) model [32]. The comparisons between the theoretical and experimental results are shown in Fig. 11.5, where a good agreement can be observed for not only the propagation speeds (Fig. 11.5a) but also for attenuation coefficients (Fig. 11.5b). Fellah et al. [1, 20–23] analytically reproduced the fast and slow waveforms propagating through human cancellous bone slabs using the Biot's model modified by the theory of Johnson et al. [33] (Biot-Johnson model), as shown in Fig. 11.6, and they were able to give estimates of bone structural parameters by solving the inverse problem. Lee et al. [31] and Hughes et al. [34] calculated the fast and slow wave speeds as a function of the angle of the main trabecular orientation, by introducing an angle-dependent structural parameter in the Biot's model. Hughes et al. called this model the stratified Biot's model.

With the Biot's models, the stratified model, namely Schoenberg's model [35], has been applied to the propagation of both the fast and slow waves in cancellous

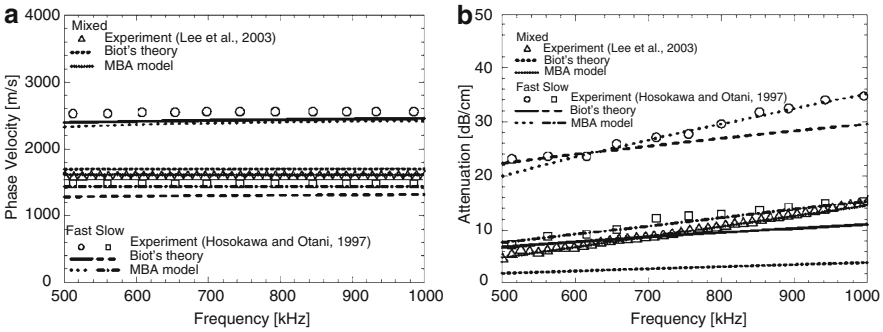

Fig. 11.5 Comparison between theoretical results calculated using the MBA model and experimental results for (**a**) propagation speeds and (**b**) attenuation coefficients of fast and slow waves in bovine cancellous bone. "Mixed" represents completely overlapped fast and slow waves (Reprinted from [30] copyright (2006) with permission from Elsevier)

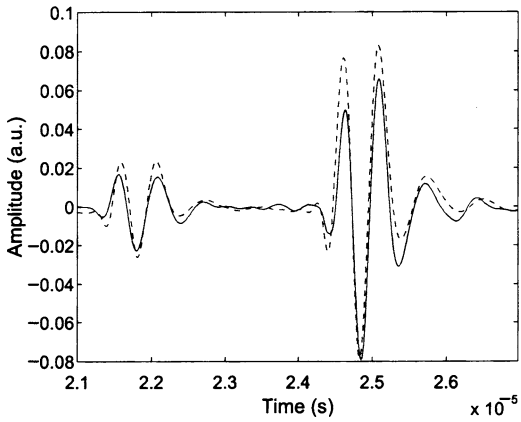

Fig. 11.6 Comparison between theoretical result (*dashed line*) calculated using the modified Biot's model and experimental result (*solid line*) for fast and slow waveforms in human cancellous bone (Reprinted with permission from [20] copyright (2004), Acoustical Society of America)

bone [17, 36]. The stratified model, which is composed of periodically alternating trabecular and fluid layers, is an idealized model of cancellous bone with a strongly oriented trabecular structure. Using this model, the propagation speeds of both waves can be easily calculated as a function of the angle of the trabecular orientation, although the attenuation coefficients cannot be calculated. Results calculated using the stratified model are compared to experimental results in Fig. 11.7. In both theoretical and experimental results, the fast wave speed decreases when the angle between the trabecular orientation and the propagation direction increases, which can cause the overlap of the fast and slow waves. Thus, the acoustic anisotropy of cancellous bone can be interpreted in the context of the stratified model. The comparison with the angle-dependent Biot's model (stratified Biot's model) was performed by Lee et al. [31] and Hughes et al. [34]. The results obtained by Hughes et al. are shown in Fig. 11.7. In spite of a much simpler model, the dependence

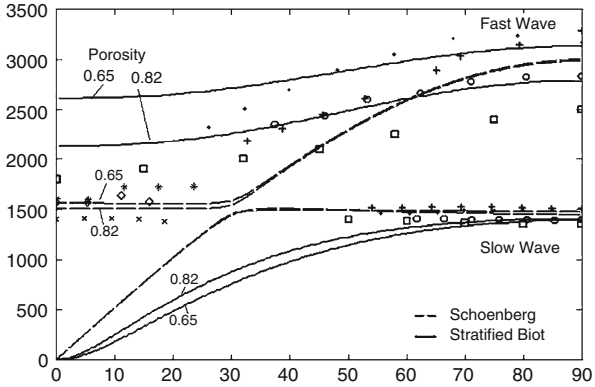

Fig. 11.7 Comparison between theoretical results calculated using the stratified and angle-dependent Biot's models and experimental results for propagation speeds of fast and slow waves in bovine cancellous bone. The vertical and horizontal axes represent the propagation speed (m/s) and the angle of the trabecular orientation (°), respectively. The values of 0 and 90 in the horizontal axis correspond to the perpendicular and parallel trabecular orientations (Reprinted with permission from [34] copyright (2007), Acoustical Society of America)

of both the fast and slow wave speeds on the angle between the trabecular orientation and the propagation direction is appropriately predicted by the stratified model. Based on the stratified model, moreover, Pakula et al. [9, 19] developed a microcontinual cellular model for a short ultrasound waves and compared it with the macrocontinual Biot's model. Hosokawa [37–39] developed cancellous bone phantoms consisting of stratified layers with trabecular rods or pore spaces in the direction perpendicular to layers, and investigated the effects of the perpendicular trabeculae and pores on the fast and slow waves. The author found that both the fast and slow wave amplitudes could be decreased owing to the scattering caused by the perpendicular trabeculae and pores.

The Biot's models require many parameters, including not only the material parameters of the solid and fluid but also the structural parameters of the porous frame. In Biot's models (and particularly in the modified Biot's models), various additional structural parameters are introduced. For cancellous bone, however, most of these structural parameters can easily be evaluated neither in vitro nor in vivo. In addition, these parameters are not directly connected to the real bone structure and their meanings are difficult to interpret. On the other hand, the stratified model is simpler as fewer parameters required. The stratified model provides some insight into the effect of the macroscopic structure in cancellous bone, that is the effect of main trabecular orientation. However, modeling idealized stratified structures cannot provide a comprehensive understanding of the interaction between ultrasound and real complex trabecular microstructures. Therefore, the actual propagation phenomena of the fast and slow waves are likely not strictly the same as the phenomena predicted by the stratified model [40]. Thus, both models have merits and limitations. Furthermore, cancellous bone is highly inhomogeneous and the

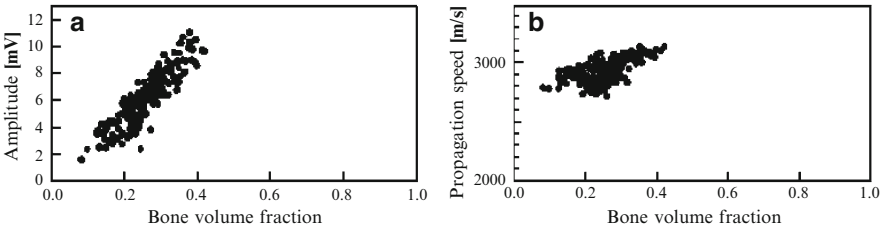

Fig. 11.8 Amplitude (**a**) and propagation speed (**b**) of fast wave in bovine cancellous bone as a function of bone volume fraction (BV/TV). The data was obtained from various positions of a specimen by using a focused PVDF transmitter (Reprinted with permission from [43] copyright (2005), The Japanese Society of Applied Physics)

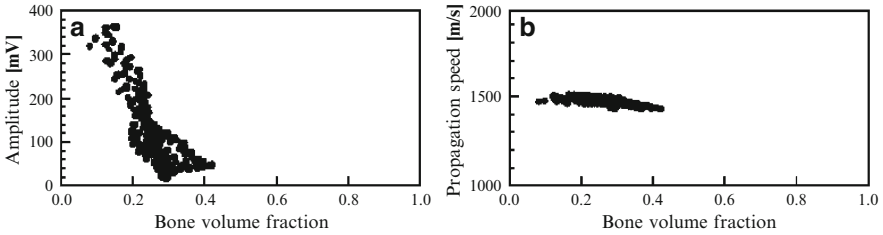

Fig. 11.9 Amplitude (**a**) and propagation speed (**b**) of slow wave in bovine cancellous bone as a function of bone volume fraction (BV/TV). The data was obtained from various positions of a specimen by using a focused PVDF transmitter (Reprinted with permission from [43] copyright (2005), The Japanese Society of Applied Physics)

propagation properties largely vary with the position in the bone (see Figs. 11.8 and 11.9). In previously performed theoretical analyses, only averaged properties over the analyzed region of cancellous bone have been taken into account.

11.2.3 Effect of Structure on the Wave Propagation

The effects of both macroscopic and microscopic trabecular structures on the ultrasound waves must be elucidated to derive better understanding of the propagation phenomena in cancellous bone. Depending on the macroscopic trabecular orientation, as described in Sect. 11.2.1, time separation (or overlap) of the fast and slow waves may occur, which can affect the estimation of the propagation properties. Nicholson et al. [14] experimentally showed that the propagation properties in the SI (CC) direction, in which the fast and slow waves could be observed, were different from those in the other orthogonal directions. The authors also showed evidence that the correlations with BV/TV of the propagation properties in the CC direction, except for the attenuation coefficient at 600 kHz, were much lower than in perpendicular directions. In addition, strong dependences on various microstructural

parameters, such as DA, were observed in the CC direction. These can be explained by the fact that the propagation properties, except for the wave speed measured from the first zero-crossing time, were derived using the entire waveform including both the fast and slow waves. Thus, the estimated parameters did not reflect the true properties of either the fast or the slow wave, but rather of a mixture of both waves. In fact, Cardoso et al. [10] showed that the fast and slow waves had lower and higher frequency spectral contents respectively (see Sect. 11.4.1 for details) and proposed to define a new parameter termed frequency-dependent ultrasound attenuation (FDUA) that can be computed separately for each wave component using time-frequency analysis. Marutyan et al. [41, 42] showed, using various theoretical and experimental models, that a mixed waveform composed of interfering (i.e., overlapping in time) fast and slow waves could result in apparent anomalous negative velocity dispersion (see Chap. 12). In conclusion, the consideration of the dependence of the two-wave propagation phenomenon on the trabecular orientation is essential for accurate estimates of the propagation properties.

Variations of experimental peak-to-peak amplitudes and propagation speeds as a function of BV/TV are shown in Fig. 11.8 for the fast wave and in Fig. 11.9 for the slow wave [43]. The data were obtained from various positions of a bovine cancellous bone specimen by using a focused PVDF transmitter. Figures 11.8 and 11.9 clearly show that both wave amplitude and speed are correlated with BV/TV, positively for the fast wave and negatively for the slow wave. The results show evidences of a high residual variability in the propagation properties of both the fast and slow waves around the regression line, which are thought to be an effect of the variability in the trabecular microstructure. Hosokawa et al. [16] compared the Biot's model to the experimental results using bovine cancellous bone specimens dissolved by sulfuric acid solution. By the dissolution, the trabecular structure changed from orthotropy to isotropy with decreasing BV/TV and the decrease of the fast wave speed with decreasing BV/TV could be explained using the exponent parameter which depends on the trabecular structure [26] in the Biot's model (see Sect. 5.3.2). Cardoso et al. [44] measured the fast and slow wave speeds for various bovine and human specimens and explained using the same parameter that the large variability in both wave speeds was due to the trabecular microstructure. As shown in Fig. 11.10, Mizuno et al. [6] experimentally demonstrated that the fast wave speed was highly correlated with the averaged trabecular length in the propagation direction. Figure 11.10 includes data not only for the fast wave separated from the slow wave in the direction parallel to the trabecular orientation (highest speed values) but also for the mixed waveform (overlapping fast and slow waves) in the perpendicular direction (lowest speed values). In both cases, the fast wave speed was measured from the early arriving wavefront. Accordingly, the correlation of the fast wave speed with the averaged trabecular length cannot depend on the separation of the two waves.

Despite these preliminary results, the effects of the trabecular microstructure have not yet been understood in detail and more investigations are thus required. However, the detailed investigations using only experimental approaches appear to be difficult because of the tremendous variability of microstructure in cancellous

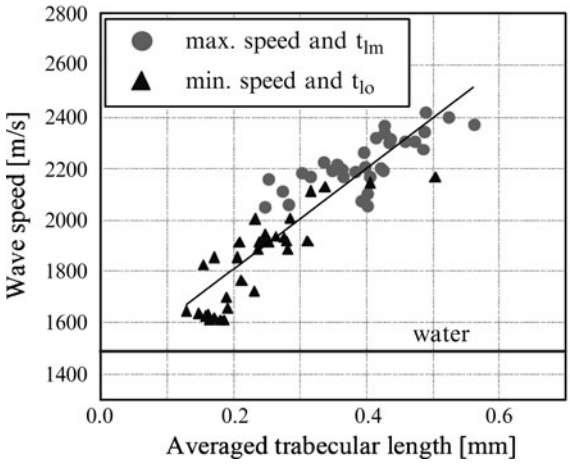

Fig. 11.10 Relation between propagation speed of fast wave in bovine cancellous bone and averaged trabecular length in the propagation direction. The *circular* and *triangle* plots respectively represent the fastest wave speeds in the direction parallel and perpendicular to the trabecular orientation. t_{lm} and t_{lo} are respectively trabecular lengths in the parallel and perpendicular directions (Reproduced with authorization from [6] © IEEE 2008)

bone. Numerical approaches using FDTD computations with realistic cancellous bone models reconstructed from 3-D μCT datasets (in which various trabecular structures can be easily manipulated by image processing techniques) are useful for investigating the impact of in cancellous bone microstructure on propagation characteristics (see Chap. 8 and next section for details).

11.3 Comparative Study of Experiments and Simulations

11.3.1 Simulation of Two-Wave Phenomenon

In the previous section, the experimentally measured behavior of the fast and slow waves was described and compared to theoretical approaches. In addition to such experimental approaches, investigations using numerical simulations were found to be also useful to gain deep understanding of the two-wave phenomenon. A proper 3-D visualization of the propagation offers a large amount of information including distinction of longitudinal and shear waves, circumferential wave or wave refraction in the specimens, scattering from trabeculae into marrow etc., which can be difficult to deduce from experimental data. Such knowledge may play a role in developing future in vivo diagnostic systems. In addition, modern capacities of computers allow rapid generations of virtual specimens by controlled numerical variations of

microstructural or material parameters of the specimens. This in silico approach is believed to provide deep insight into the two-wave phenomenon.

Many approaches for simulations in bone have been proposed and performed [5]. The main simulation technique is FDTD simulation. This method, which has been historically widely applied for simulation of electro-magnetic fields [45], was extended to treat wave propagation in elastic materials by Virieux [46]. The reader is referred to Chap. 8 for a comprehensive analysis of FDTD simulation. In this section, the investigations of ultrasound propagation in cancellous bone using FDTD simulations are mainly described. In following simulation studies, pore spaces are assumed to be filled with liquid or marrow.

The first finite difference (strictly, not FDTD) simulation of ultrasound in cancellous bone was performed by Luo et al. [47]. The authors discussed the relationship between trabecular structure and wave propagation using a 2-D model taken from X-ray CT datasets. However, the separation of two waves was not obtained and one possible reason could be the imperfect modeling of the trabecular network connectivity from 2-D models.

The first 3-D FDTD simulation by Bossy et al. [48] targeted wave propagation in cortical bone. Then, in 2005, the same group presented 3-D FDTD simulations for cancellous bone [7]. In their study, 3-D cancellous bone structures (Fig. 11.11) were reconstructed from human femur specimens measured with high resolution SR-μCT. Propagation was simulated with the "SimSonic" software, based on an FDTD algorithm, which computed a numerical solution to 3-D linear elastic wave equations. The numerical bone model was placed between two unfocused transducers. Bone tissue was assumed to be isotropic and non-absorbing. The size of the simulation models, shown in Fig. 11.11, was $5.6 \times 5.6 \times 10.86\,\mathrm{mm}^3$ and the resolution was 30 μm. Under these conditions, the separation of the incident pulse waveform into two waves was seen only when the ultrasound propagated parallel to the main trabecular orientation (see Fig. 11.12). Note that the transmitter and the

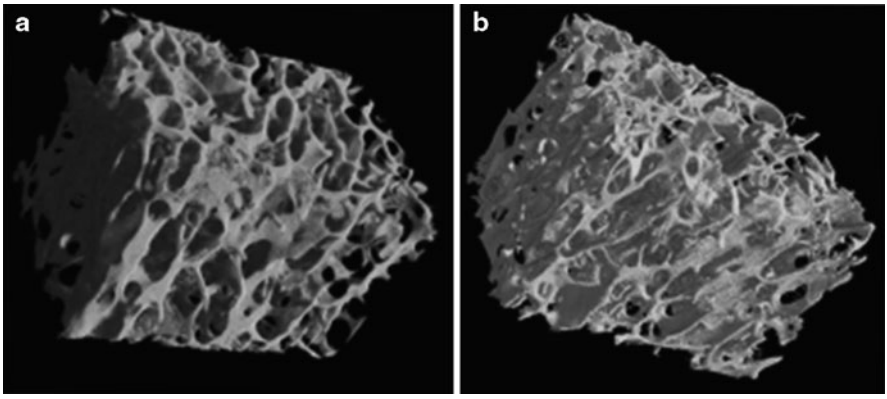

Fig. 11.11 Three-dimensional view of synchrotron microtomographic reconstruction of typical dense (**a**) and porous (**b**) trabecular samples (Reproduced from [7] copyright 2005. Permission granted from IOP Publishing limited)

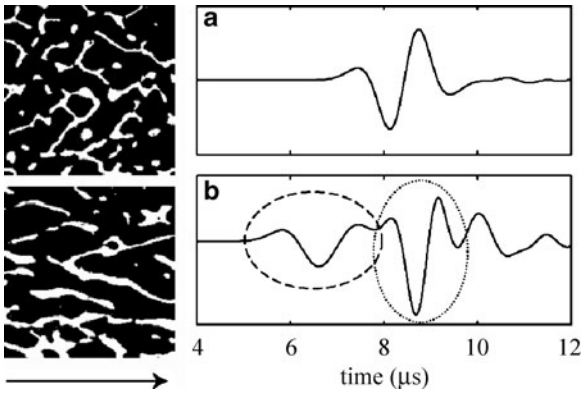

Fig. 11.12 Signal measured through an anisotropic sample. (**a**) The ultrasonic wave propagates across the main orientation of the trabeculae. (**b**) The ultrasonic wave propagates parallel to the main orientation of the trabeculae. Only in case (**b**), two waves are observed (Reproduced from [7] copyright 2005. Permission granted from IOP Publishing limited)

receivers were placed in direct contact with the solid portion so that the ultrasound wave was directly applied to the bone structure. The propagation characteristics of both waves were not investigated in detail in Bossy's study. In a subsequent study by Haïat et al. [49] where a thin water layer was positioned between the source and the trabecular network in order to avoid any direct excitation of the trabecular network, both fast and slow wave could also be observed for a propagation direction parallel to the trabecular alignment.

Nagatani et al. [50, 51] analyzed the wave propagation focusing on two-wave phenomena using 3-D bovine femur models. Figure 11.13 shows snapshots of the distribution of sound pressure in liquid and the root-mean-square value of normal stresses in solid at the central plane of the 3-D simulation field. Figure 11.13a–c show the results without any bone specimen (only water in accounted for) and Fig. 11.13d–f show the results with the specimen. The separation of fast wave and slow wave can be noticed. Ultrasound waves are reradiated from the solid into the liquid. A clear in-phase wavefront gradually forms, which is called "fast wave."

The effect of changes of BV/TV (resulting from the application of an erosion/dilation procedure) was studied by Haïat et al. [49] for fixed sample and probing direction (Fig. 11.14). Results showing the dependence of the amplitude and speed of the fast wave were in good qualitative agreement with previous experimental results [8–10]. Additionally, combined effects of BV/TV and structural anisotropy were investigated. The authors concluded that the higher the structural anisotropy, the lower the BV/TV needs to be to observe non overlapping fast and slow waves.

Fewer studies using finite element modeling (FEM) approaches [52, 53] were performed to describe wave propagation in cancellous bone. On the other hand, numerical computations of the fast and slow waveforms were also performed by solving the Biot's wave equations, in which attenuation terms due to the scattering were

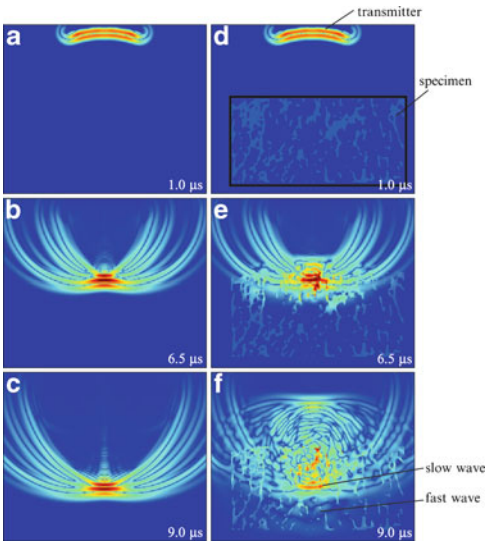

Fig. 11.13 Snapshots of the distribution of sound pressure in the x-z plane of the three-dimensional simulation field. Figures (**a**) to (**c**) show the results without specimen, (**d**) to (**f**) show the results with specimen (Reprinted with permission from [51] copyright (2009), Acoustical Society of Japan)

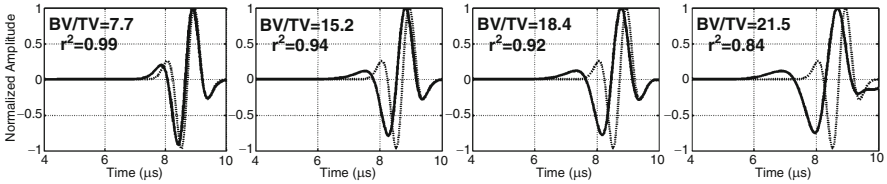

Fig. 11.14 Simulated signals obtained for four bone models BV/TV of 7.7%, 15.2%, 18.4%, and 21.5%, respectively. For each signal, the value of the determination coefficient of a linear fit of the attenuation coefficient versus frequency method is indicated (Reprinted with permission from [49] copyright (2008), Acoustical Society of America)

originally added, using FDTD computations [54, 55]. Moreover, the calculations of the Biot's equations using FEM computations were proposed [56].

11.3.2 Comparison Between Numerical and Experimental Results

For the practical use of simulations, the reliability of the results should be confirmed by comparative study to experimental observations. For example, Bossy et al. [57] used a SR-μCT model of the actual specimen to confirm the similar tendency of BUA as a function of BV/TV between simulation and experiment.

Nagatani et al. [50, 51] compared numerical FDTD predictions using 3-D models derived from X-ray μCT images of measured bovine femur specimens. Focused (concave) transmitters were used in order to measure the localized characteristics by moving the transducers with about 1 mm increments both in simulation and

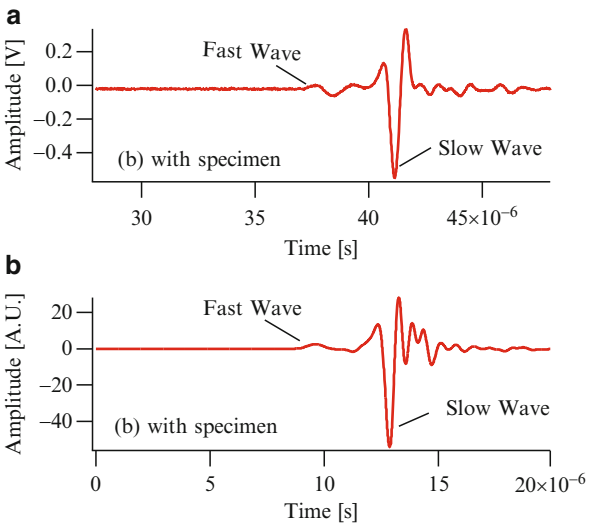

Fig. 11.15 (**a**) Experimentally observed waveform and (**b**) simulated waveform when the ultrasound transmitted to the same position (Reprinted with permission from [51] copyright (2009), Acoustical Society of Japan, The Japan Society of Applied Physics)

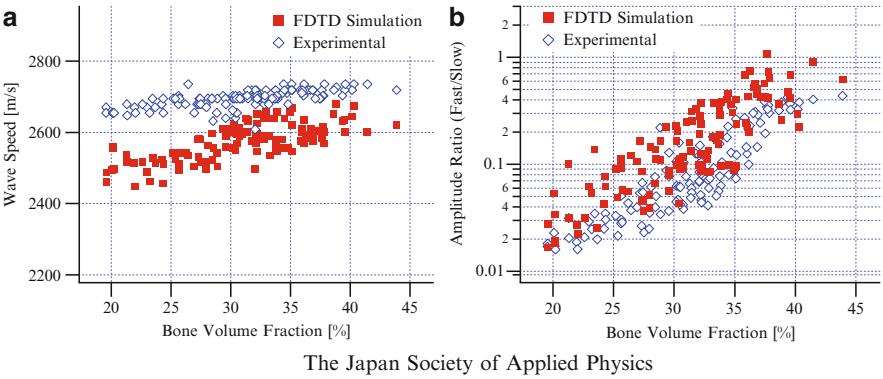

Fig. 11.16 Relationship between BV/TV (bone volume fraction) and (**a**) speed of fast wave and (**b**) peak amplitude ratio of fast and slow waves. The same unique specimen was used for both the simulation and the experiment (Reprinted with permission from [51] copyright (2009), Acoustical Society of Japan, The Japan Society of Applied Physics)

experiments. Examples of propagated waveforms when the ultrasound transmitted to the same position in experiments and simulations show good agreement between simulated and experimental waveforms (Fig. 11.15). Figure 11.16 shows the relationship between BV/TV and (a) fast wave speed and (b) amplitude ratio of two waves. A similar tendency between simulations and experiments can be seen.

We should mention that these simulation results are in good agreement with experimental data despite several limitations in the simulation conditions

such as absence of friction loss at the interface between solid and liquid, lossless propagation media, assumption of isotropic bone tissue. These assumptions imply that the effect of trabecular structure is dominant in wave propagation in cancellous bone. Of course, absorption in real cancellous bone can contribute to the total attenuation through several mechanisms [57]. More comprehensive investigations including physical effects such as absorption, elasticity, and inertia should be performed in future works. In addition, Bossy et al. [7] pointed the major role of mode conversion of the incident acoustic wave to shear waves in bone to explain the large contribution of scattering to the overall attenuation. The contribution of each attenuation mechanism should be checked precisely in future work.

Focused transducers are often used for clinical measurements. Interestingly Nagatani et al. [50, 51] reported that simulations of acoustic field using a focused transducer were in good agreement with experiments. Moreover, it is significant that the authors used numerical cancellous bone models reconstructed from commercial X-ray μCT, which indicate that accurate simulations could be realized using X-ray μCT with relatively low resolution.

As mentioned above, simulations provide visual dynamic images of complex propagation phenomena. In addition, the confirmation of the reliability of simulations results gives confidence on the accuracy of the numerical models to predict wave propagation characteristics.

11.3.3 Effect of Trabecular Structure on the Two-Wave Propagation

In addition to the visualization of wave propagation, the possibility of investigating any experimental condition (transmitter, receiver, specimen, etc.) is another advantage of numerical simulations. In order to evaluate the attenuation of propagating waves in bone, Nagatani et al. [58] virtually eliminated 1-mm-slice from left or right side surface of a parallelepiped specimen. Then, they calculated the attenuation value (dB/mm) of the fast wave within each 1-mm-slice. Figure 11.17a shows the fast wave attenuation when the wave propagates from left-side surface and Fig. 11.7b shows the results from the right-side surface. These data show that the attenuation of the fast wave is always higher in the early stage of propagation regardless of the propagating direction in the specimen. Then, the attenuation gradually decreases and becomes almost constant as the wave propagates in deeper layers of the structure. This tendency was similar in simulation and experimental measurements, although the measurement was performed only from one side. These results indicate that the fast wave requires a certain propagation distance to form an in-phase wavefront with steady attenuation. The experimental attenuation values obtained from both sides cannot be performed because we can only slice the specimen from one side. Therefore, the above investigation could be realized only by simulations, which demonstrates the powerful benefits of simulations.

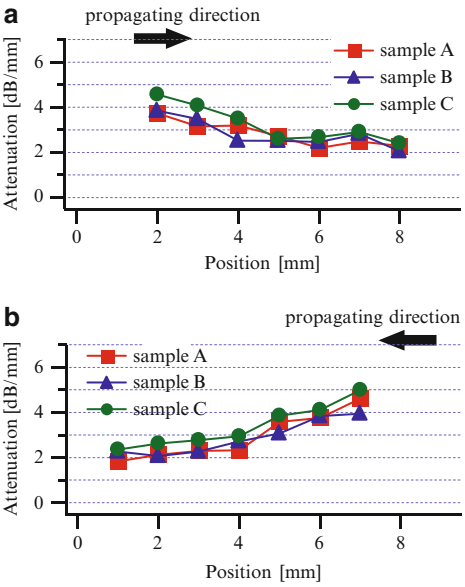

Fig. 11.17 Distributions of numerically simulated fast wave attenuation. (**a**) Attenuation when the wave propagates from *left* surface. (**b**) Attenuation when the wave propagates from *right* surface. The three samples (A to C) used in (**a**) and (**b**) are identical (Reprinted from [58] copyright (2008) with permission from Elsevier)

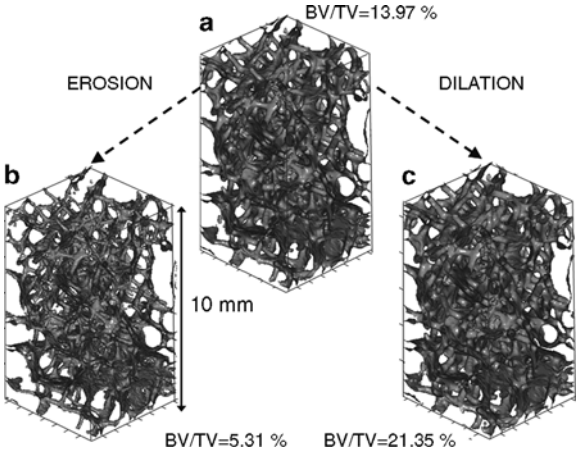

Fig. 11.18 Illustration of the microarchitecture alteration scenarios. Images represent the 3-D trabecular structures. (**a**) Original sample. (**b**) Eroded structure. (**c**) Dilated cartographies (From Haiat et al. [59] copyright (2007), American Society for Bone and Mineral Research), reprinted with permission of John Wiley & Sons, Inc.)

Luo et al. [47] virtually changed the trabecular thickness of 2-D bone models (reconstructed from X-ray CT scans) using an image processing technique. Haïat et al. [49, 59] and Hosokawa [60, 61] also processed 3-D models of real trabecular structures. Figure 11.18 shows the variations of BV/TV created virtually from a unique model by Haïat. As shown in Fig. 11.19, Hosokawa showed evidence that the relation between the eroding direction of trabecular thickness and the direction of wave propagation affects wave propagation even when BV/TV and the geometrical structure remain the same.

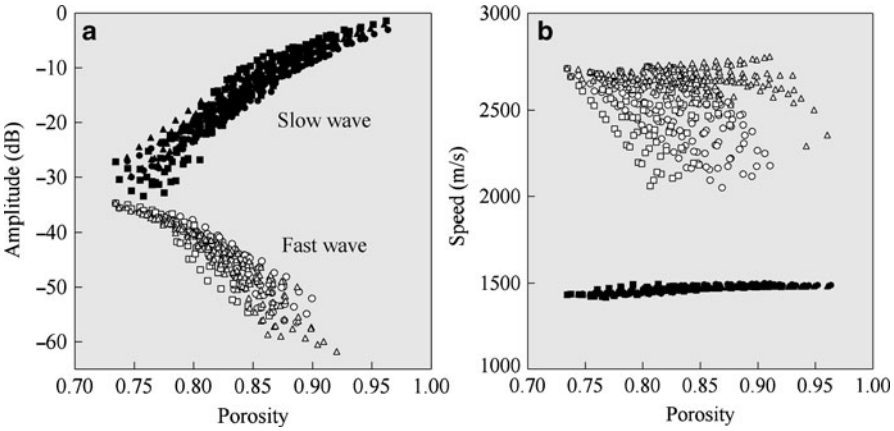

Fig. 11.19 Simulated results of (**a**) wave amplitudes and (**b**) propagation speeds of the fast and slow waves in the major trabecular direction of the cancellous bone models, as a function of porosity varied by three patterns of erosion procedures (Reproduced with authorization from [60] © IEEE 2009)

On the other hand, Hosokawa [62, 63] and Padilla et al. [64] generated artificial models of trabecular structures, by assuming aggregation of spherical pores and by assuming Gaussian random field distributions in order to investigate by FDTD the effects of BV/TV, trabecular thickness, alignment, and network structure.

11.4 Towards Clinical Application of the Two-Wave Phenomenon

11.4.1 Wave Separation Techniques

In practical situations, wave separation is often difficult because of the overlapping of the two waves. Successful wave separation may give access to new indicators, including speeds, amplitudes, and spectral characteristics separately for the fast and slow waves. Wave separation was attempted using signal processing techniques either in the time or frequency domain. In general, fast wave has faster speed, smaller amplitude, and lower frequency component. Most techniques for wave separation are based on these characteristics.

Cardoso et al. [10] successfully observed the two-wave separation in experimental spectrograms obtained by short-time Fourier transform (Fig. 11.20). The results indicated a lower frequency for the fast wave compared to the slow wave. Applying a Fourier transform to the overall recorded waveform, the authors also found that the slope of the low frequency part of spectrum (Fast FDUA) was different from the slope of the high frequency part (Slow FDUA) (see Fig. 11.21). Hasegawa et al. [65]

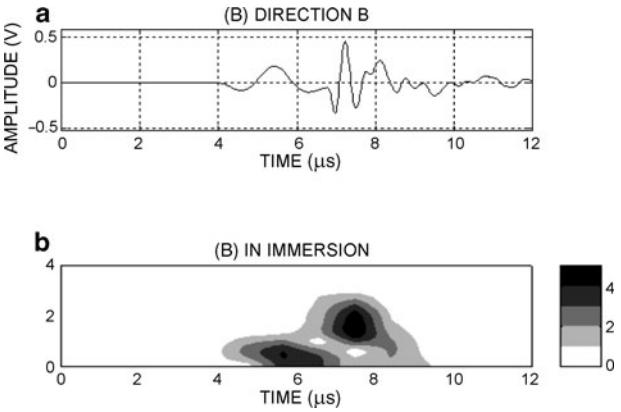

Fig. 11.20 (**a**) Signal transmitted through a human femoral head tested in immersion. Two waves components can be seen. (**b**) Spectrogram of the signal showing different frequency contents and time localizations (From Cardoso et al. [10] copyright (2003), American Society for Bone and Mineral Research), reprinted with permission of Wiley)

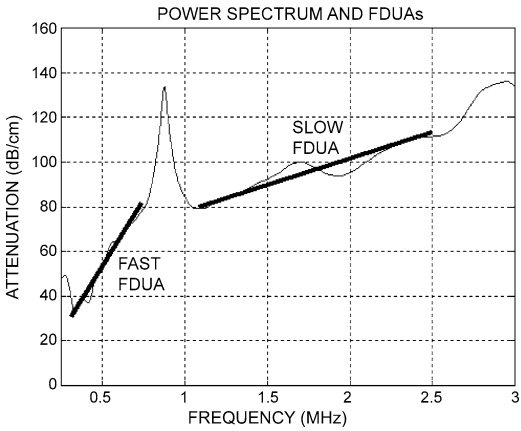

Fig. 11.21 Power spectrum of the overall recorded signal for a cancellous bone specimen and the related calculated FDUA for the fast wave (slope of the low frequency part of the signal) and slow wave (slope of the high frequency part) (From Cardoso et al. [10] copyright (2003), American Society for Bone and Mineral Research, reprinted with permission of John Wiley & Sons, Inc.)

applied a wavelet transform analysis. They fitted a 2-D function to the scalogram and were able to distinguish two wave components. As a result, the amplitudes of the higher and lower frequency components showed good correlation with BV/TV, respectively. They also discussed the characteristics of the two components focusing on the temporal distributions in scalograms.

Other approaches, such as processing the signals in the time domain are worth being mentioned [49, 66]. The most efficient method to date was proposed by Marutyan et al. [66] who applied Bayesian probability theory [67] to separate virtually created mixed waveforms and extract their individual propagation characteristics (see Chap. 12).

However, these various methods are still under development. Future improvements are still needed before these signal processing techniques can be applied in clinical applications.

11.4.2 In Vivo Application

The concept of two longitudinal wave propagation in cancellous bone has been applied in a series of in vivo studies by Otani et al. [43, 68, 69]. The authors developed and introduced a new in vivo QUS device, LD-100 (OYO Electric) shown in Fig. 11.22, which evaluates the cancellous part at the distal portion of the radius. In this technique, the bone density and bone elasticity were derived from the measured ultrasound wave parameters of the fast and slow waves.

It has been experimentally observed that the propagation speed of the fast wave increases with the mass density of cancellous bone (Fig. 11.8b) [43], consistently with Biot predictions [8]. The amplitudes of both waves also change due to the mass density, and positive and negative correlations were observed for the fast and slow waves (Figs. 11.8a and 11.9a), respectively [43]. Otani [43] assumed a simple model of wave propagation path in the radius and considered wave propagation through all intervening media (soft tissues and bone). The cancellous bone density could be derived from in vivo ultrasound data of human cancellous bone [43, 68, 69]. Subsequent estimates of cancellous bone elasticity could be obtained from the velocity and the estimated bone density.

LD-100 measurements, making use of the several echo modes in the observed signals, provide quantitative estimates of several parameters such as cancellous bone density (expressed in bone mineral density or bone volume fraction) and elasticity, cortical bone thickness, and radius of the cancellous compartment. The ultrasound

Fig. 11.22 Outside view of LD-100. The measurement system is connected to the computer where the parameters are estimated from the fast and slow wave characteristics (Reprinted with permission from [68] copyright (2006), The Japanese Society of Applied Physics)

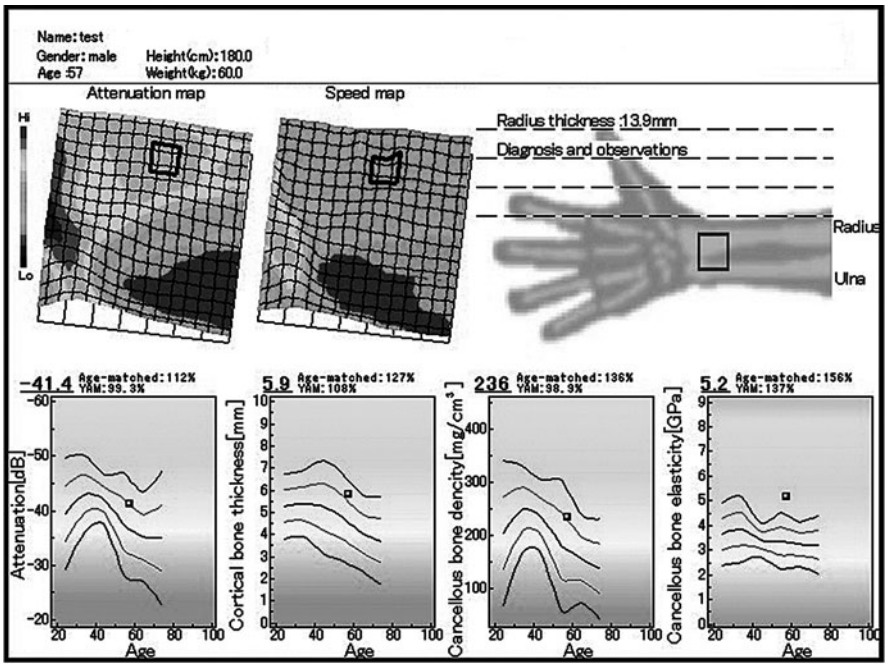

Fig. 11.23 Display of 2-D images and measured values of LD-100. The *upper left* figure are the 2-D maps of pseudo-attenuation and speed obtained from the first scan (Reprinted with permission from [68] copyright (2006), The Japanese Society of Applied Physics)

beam width at the focus is approximately 1.5–2.0 mm for a single sinusoidal pulse, which is regarded as the actual spatial resolution of the measurement. The interesting feature of the system is the first (rough) and second (precise) two-axis scanning of the measurement site. An example of 2-D images and measured values of LD-100 is shown in Fig. 11.23. Upper images show the pseudo-attenuation image and pseudo-SOS image, which were obtained from the overall transmitted signals including both the fast and slow waves at the first scanning, and the area of the first scanning at the left hand distal radius. Thick squares in 2-D images indicate the area of the second scanning. Measured values obtained by the second scanning with age-dependent reference curves are shown in the graphs below.

LD-100 provides estimates of bone mineral density (BMD, mg/cm^3) from the measured amplitude of the slow wave using the experimentally established relationship, whereas the conventional devices indirectly assess BMD using QUS parameters. Thus, the direct comparison of BMD at the same site between the ultrasound and radiological methods becomes possible. BMD data from 175 volunteers aged from 22 to 87 years old (average 59.0) shown in Fig. 11.24 evidence strong correlation between BMD measured by LD-100 and that measured by peripheral quantitative CT (pQCT) (Medizintechnik XCT-960).

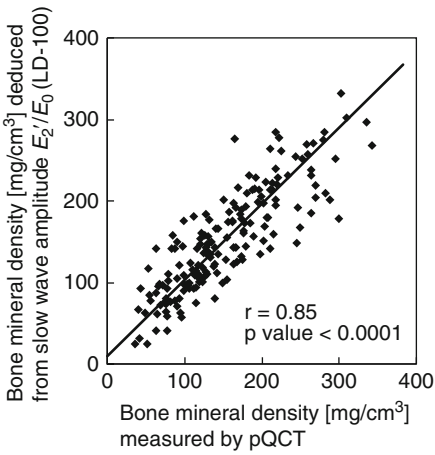

Fig. 11.24 Bone mineral density deduced from slow wave amplitude plotted against pQCT bone mineral density. The slow wave amplitudes were obtained from the measurement by LD-100 (Reproduced from [68] with permission)

11.5 Conclusions

Many studies have investigated the two-wave phenomenon in cancellous bone from both experimental and simulation points of view. Several discrepancies between original Biot's theory and experimental results (i.e. attenuation) have been partly overcome using modified Biot's models. However, as pointed out in this chapter, these models request many parameters, which are often difficult to estimate. In addition, theories cannot include the effect of the actual inhomogeneity of cancellous bone structure. Although these theoretical approaches still face some difficulties, the experimental measurements of both fast and slow waves are believed to provide information on bone structure beyond mere bone density. Actually, the fast wave speed and amplitude change dynamically, reflecting the characters of trabecular network structure in the propagation path, such as degree of anisotropy and bone volume fraction. Further detailed analysis of material and structural determinants of propagation speeds and amplitudes of both fast and slow waves are still required before these propagation characteristics can be implemented in an innovative tool to evaluate the bone structure in vivo. Such measurements have been already implemented in a new QUS system named LD-100, which can directly estimate BMD values. The estimated BMD by LD-100 is in good accordance with the BMD obtained by pQCT.

The two-wave phenomenon has also been studied using numerical simulations. Finite-difference time-domain methods coupled to realistic 3-D cancellous bone models, enabling the visualization of wave propagation in cancellous bone, were found to be very useful to understand the nature of wave propagation. The introduction of virtual cancellous bone or virtual treatment to the actual 3-D structures provides interesting results beyond experiments and induces active discussions on this phenomenon.

References

1. Z. E. A. Fellah, N. Sebaa, M. Fellah, F. G. Mitri, E. Ogam, W. Lauriks, and C. Depollier, "Application of the Biot model to ultrasound in bone: Direct problem," IEEE Transactions on Ultrasonics, Ferroelectrics, and Frequency Control **55**, 1508–1515 (2008).
2. M. A. Biot, "Theory of propagation of elastic waves in fluid-saturated porous solid. I. Low-frequency range," The Journal of the Acoustical Society of America **28**, 168–178 (1956).
3. M. A. Biot, "Theory of propagation of elastic waves in fluid-saturated porous solid. II. Higher frequency range," The Journal of the Acoustical Society of America **28**, 179–191 (1956).
4. M. L. McKelvie and S. B. Palmer, "The interaction of ultrasound with cancellous bone," Physics in Medicine and Biology **36**, 1331–1340 (1991).
5. J. J. Kaufman, G. Luo, and R. S. Siffert, "Ultrasound simulation in bone," IEEE Transactions on Ultrasonics, Ferroelectrics, and Frequency Control **55**, 1205–1218 (2008).
6. K. Mizuno, M. Matsukawa, T. Otani, M. Takada, I. Mano, and T. Tshujimoto, "Effects of structural anisotropy of cancellous bone on speed of ultrasonic fast waves in the bovine femur," IEEE Transactions on Ultrasonics, Ferroelectrics, and Frequency Control **55**, 1480–1487 (2008).
7. E. Bossy, F. Padilla, F. Peyrin, and P. Laugier, "Three-dimensional simulation of ultrasound propagation through trabecular bone structures measured by synchrotron microtomography," Physics in Medicine and Biology **50**, 5545–5556 (2005).
8. A. Hosokawa and T. Otani, "Ultrasonic wave propagation in bovine cancellous bone," The Journal of the Acoustical Society of America **101**, 558–562 (1997).
9. M. Kaczmarek, J. Kubik, and M. Pakula, "Short ultrasonic waves in cancellous bone," Ultrasonics **40**, 95–100 (2002).
10. L. Cardoso, F. Teboul, L. Sedel, C. Oddou, and A. Meunier, "In vitro acoustic waves propagation in human and bovine cancellous bone," Journal of Bone and Mineral Research **18**, 1803–1812 (2003).
11. Y. Nakamura and T. Otani, "Frequency response of a piezoelectric polymer film hydrophone and an elastic wave induced on the backing surface," Japanese Journal of Applied Physics **31** Supplement 31-1, 266–268 (1991).
12. Y. Nakamura, T. Kawabata, and T. Otani, "Anomalous directivity of a piezoelectric polymer film hydrophone," Japanese Journal of Applied Physics **32**, 2288–2290 (1993).
13. Y. Nakamura and T. Otani, "Study of surface elastic wave induced on backing material and diffracted field of a piezoelectric polymer film hydrophone," The Journal of the Acoustical Society of America **94**, 1191–1199 (1993).
14. P. H. F. Nicholson, R. Müller, G. Lowet, X. G. Cheng, T. Hildebrand, P. Rüegsegger, G. van der Perre, J. Dequeker, and S. Boonen, "Do quantitative ultrasound measurements reflect structure independently of density in human vertebral cancellous bone?," Bone **23**, 425–431 (1998).
15. A. Hosokawa and T. Otani, "Acoustic anisotropy in bovine cancellous bone," The Journal of the Acoustical Society of America **103**, 2718–2722 (1998).
16. A. Hosokawa, T. Otani, T. Suzaki, Y. Kubo, and S. Takai, "Influence of trabecular structure on ultrasonic wave propagation in bovine cancellous bone," Japanese Journal of Applied Physics **36**, 3233–3237 (1997).
17. E. R. Hughes, T. G. Leighton, G. W. Petley, and P. R. White, "Ultrasonic propagation in cancellous bone: A new stratified model," Ultrasound in Medicine and Biology **25**, 811–821 (1999).
18. B. K. Hoffmeister, S. A. Whitten, and Y. Rho, "Low-megahertz ultrasonic properties of bovine cancellous bone," Bone **26**, 635–642 (2000).
19. M. Pakula and J. Kubik, "Propagation of ultrasonic waves in cancellous bone. Micro and macrocontinual approach," *Poromechanics II*, edited by J.-L. Auriault *et al.* (Swets & Zeitlinger, Lisse, 2002), pp. 65–70.
20. Z. E. A. Fellah, J. Y. Chapelon, S. Berger, W Lauriks, and C. Depollier, "Ultrasonic wave propagation in human cancellous bone: Application of Biot theory," The Journal of the Acoustical Society of America **116**, 61–73 (2004).

21. N. Sebaa, Z. E. A. Fellah, M. Fellah, E. Ogam, A. Wirgin, F. G. Mitri, C. Depollier, and W. Lauriks, "Ultrasonic characterization of human cancellous bone using the Biot theory: Inverse problem," The Journal of the Acoustical Society of America **120**, 1816–1824 (2006).
22. N. Sebaa, Z. E. A. Fellah, W. Lauriks, and C. Depollier, "Application of fractional calculus to ultrasonic wave propagation in human cancellous bone," Signal Processing **86**, 2668–2677 (2006).
23. N. Sebaa, Z. E. A. Fellah, M. Fellah, E. Ogam, F.G. Mitri, C. Depollier, and W. Lauriks "Application of the Biot model to ultrasound in bone: Direct problem," IEEE Transactions on Ultrasonics, Ferroelectrics, and Frequency Control **55**, 1516–1523 (2008).
24. K. Mizuno, M. Matsukawa, T. Otani, P. Laugier, and F. Padilla, "Propagation of two longitudinal waves in human cancellous bone: An in vitro study," The Journal of the Acoustical Society of America **125**, 3460–3466 (2009).
25. J. L. Williams, "Ultrasonic wave propagation in cancellous and cortical bone: Prediction of some experimental results by Biot's theory," The Journal of the Acoustical Society of America **91**, 1106–1112 (1992).
26. L. J. Gibson, "The mechanical behaviour of cancellous bone," Journal of Biomechanics **18**, 317–328 (1985).
27. D. Ulrich, B. van Rietbergen, A. Laib, and P. Ruegsegger, "The ability of three-dimensional structural indices to reflect mechanical aspects of trabecular bone," Bone **25**, 55–60 (1999).
28. T. J. Haire and C. M. Langton, "Biot theory: A review of its application to ultrasound propagation through cancellous bone," Bone **24**, 291–295 (1999).
29. K. I. Lee, H. –S. Roh, and S. W. Yoon, "Acoustic wave propagation in bovine cancellous bone: Application of the modified Biot-Attenborough model," The Journal of the Acoustical Society of America **114**, 2284–2293 (2003).
30. K. I. Lee and S. W. Yoon, "Comparison of acoustic characteristics predicted by Biot's theory and the modified Biot-Attenborough model in cancellous bone," Journal of Biomechanics **39**, 364–368 (2006).
31. K. I. Lee, E. R. Hughes, V. F. Humphrey, T. G. Leighton, and M. J. Choi, "Empirical angle-dependent Biot and MBA models for acoustic anisotropy in cancellous bone," Physics in Medicine and Biology **52**, 59–73 (2007).
32. H. S. Roh, K. I. Lee, and S. W. Yoon, "Acoustic characteristics of a non-rigid porous medium with circular cylindrical pores," Journal of the Korean Physical Society **43**, 55–65 (2003).
33. D. L. Johnson, J. Koplik, and R. Dashen, "Theory of dynamic permeability and tortuosity in fluid-saturated porous media," The Journal of Fluid Mechanics **176**, 379–402 (1987).
34. E. R. Hughes, T. G. Leighton, P. R. White, and G. W. Petley, "Investigation of an anisotropic tortuosity in a Biot model of ultrasonic propagation in cancellous bone," The Journal of the Acoustical Society of America **121**, 568–574 (2007).
35. M. Schoenberg, "Wave propagation in alternating solid and fluid layers," Wave Motion **6**, 303–320 (1984).
36. F. Padilla and P. Laugier, "Phase and group velocities of fast and slow compressional waves in trabecular bone," The Journal of the Acoustical Society of America **108**, 1949–1952 (2000).
37. A. Hosokawa, "Ultrasonic pulse waves propagating through cancellous bone phantoms with aligned pore spaces," Japanese Journal of Applied Physics **45**, 4697–4699 (2006).
38. A. Hosokawa, "Influence of minor trabecular elements on fast and slow wave propagations through cancellous bone," Japanese Journal of Applied Physics **47**, 4170–4175 (2008).
39. A. Hosokawa, "Effect of minor trabecular elements on fast and slow wave propagations through a stratified cancellous bone phantoms at oblique incidence," Japanese Journal of Applied Physics **48**, 07GK07-1-07GK07-7 (2009).
40. A. Hosokawa, "Numerical investigation of ultrasound wave propagation in cancellous bone with oblique trabecular orientation," *Proceedings of 20th International Congress on Acoustics [CD-ROM]*, 2010, p367 (7 pages).
41. K. R. Marutyan, M. R. Holland, and J. G. Miller, "Anomalous negative dispersion in bone can result from the interference of fast and slow waves," The Journal of the Acoustical Society of America **120**, EL55–EL61 (2006).

42. C. C. Anderson, K. R. Marutyan, M. R. Holland, K. A. Wear, and J. G. Miller, "Interference between wave modes may contribute to the apparent negative dispersion observed in cancellous bone," The Journal of the Acoustical Society of America **124**, 1781–1789 (2008).
43. T. Otani, "Quantitative estimation of bone density and bone quality using acoustic parameters of cancellous bone for fast and slow waves," Japanese Journal of Applied Physics **44**, 4578–4582 (2005).
44. L. Cardoso, A. Meunier, and C. Oddou, "In vitro acoustic wave propagation in human and bovine cancellous bone as predicted by Biot's theory," Journal of Mechanics in Medicine and Biology **8**, 183–201 (2008).
45. K. S. Yee, "Numerical solution of initial boundary value problems involving Maxwell's equations in isotropic media," IEEE Transactions on Antennas and Propagation **14**, 302–307 (1966).
46. J. Virieux, "P-SV wave propagation in heterogeneous media: Velocity-stress finite-difference method," Geophysics **51**, 889–901 (1986).
47. G. Luo, J. J. Kaufman, A. Chiabrera, B. Blanco, J. H. Kinney, D. Haupt, J. T. Ryaby, and R. S. Siffert, "Computational methods for ultrasonic bone assessment," Ultrasound in Medicine and Biology **25**, 823–830 (1999).
48. E. Bossy, M. Talmant, and P. Laugier, "Three dimensional simulations of ultrasonic axial transmission velocity measurement on cortical bone models," The Journal of the Acoustical Society of America **115**, 2314–2324 (2004).
49. G. Haïat, F. Padilla, F. Peyrin, and P. Laugier, "Fast wave ultrasonic propagation in trabecular bone: Numerical study of the influence of porosity and structural anisotropy," The Journal of the Acoustical Society of America **123**, 1694–1705 (2008).
50. Y. Nagatani, H. Imaizumi, T. Fukuda, M. Matsukawa, Y. Watanabe, and T. Otani, "Applicability of finite-difference time-domain method to simulation of wave propagation in cancellous bone," Japanese Journal of Applied Physics **45**, 7186–7190 (2006).
51. Y. Nagatani, K. Mizuno, T. Saeki, M. Matsukawa, T. Sakaguchi, and H. Hosoi, "Propagation of fast and slow waves in cancellous bone: Comparative study of simulation and experiment," Acoustical Science and Technology **30**, 257–264 (2009).
52. L. Goossens, J. Vanderoost, S. Jaecques, S. Boonen, J. D'hooge, W. Lauriks, and G. van der Perre, "The correlation between the SOS in trabecular bone and stiffness and density studied by finite-element analysis," IEEE Transactions on Ultrasonics, Ferroelectrics, and Frequency Control **55**, 1234–1242 (2008).
53. G. Haïat, F. Padilla, M. Svrcekova, Y. Chevalier, D. Pahr, F. Peyrin, P. Laugier, and P. Zysset, "Relationship between ultrasonic parameters and apparent trabecular bone elastic modulus: A numerical approach," Journal of Biomechanics **42**, 2033–2039 (2009).
54. A. Hosokawa, "Simulation of ultrasound propagation through bovine cancellous bone using elastic and Biot's finite-difference time-domain methods," The Journal of the Acoustical Society of America **118**, 1782–1789 (2005).
55. A. Hosokawa, "Ultrasonic pulse waves in cancellous bone analyzed by finite-difference time-domain method," Ultrasonics **44**, e227–e231 (2006).
56. V. –H. Nguyen, S. Naili, and V. Sansalone, "Simulation of ultrasonic wave propagation in anisotropic cancellous bone immersed in fluid," Wave Motion **47**, 117–129 (2010).
57. E. Bossy, P. Laugier, F. Peyrin, and F. Padilla, "Attenuation in trabecular bone: A comparison between numerical simulation and experimental results in human femur," The Journal of the Acoustical Society of America **122**, 2469–2475 (2007).
58. Y. Nagatani, K. Mizuno, T. Saeki, M. Matsukawa, T. Sakaguchi, and H. Hosoi, "Numerical and experimental study on the wave attenuation in bone –FDTD simulation of ultrasound propagation in cancellous bone," Ultrasonics **48**, 607–612 (2008).
59. G. Haïat, F. Padilla, F. Peyrin, and P. Laugier, "Variation of ultrasonic parameters with microstructure and material properties of trabecular bone: A 3D model simulation," Journal of Bone and Mineral Research **22**, 665–674 (2007).
60. A. Hosokawa, "Numerical analysis of variability in ultrasound propagation properties induced by trabecular microstructure in cancellous bone," IEEE Transactions on Ultrasonics, Ferroelectrics, and Frequency Control **56**, 738–747 (2009).

61. A. Hosokawa, "Effect of porosity distribution in a propagation direction on ultrasound waves through cancellous bone," IEEE Transactions on Ultrasonics, Ferroelectrics, and Frequency Control **57**, 1320–1328 (2010).
62. A. Hosokawa, "Effect of trabecular irregularity on fast and slow wave propagations through cancellous bone," Japanese Journal of Applied Physics **46**, 4862–4867 (2007).
63. A. Hosokawa, "Development of a numerical cancellous bone model for finite-difference time-domain simulations of ultrasound propagation," IEEE Transactions on Ultrasonics, Ferroelectrics, and Frequency Control **55**, 1219–1233 (2008).
64. F. Padilla, Q. Grimal, and P. Laugier, "Ultrasonic propagation through trabecular bone modeled as a random medium," Japanese Journal of Applied Physics **47**, 4220–4222 (2008).
65. S. Hasegawa, Y. Nagatani, K. Mizuno, and M. Matsukawa, "Wavelet transform analysis of ultrasonic wave propagation in cancellous bone," Japanese Journal of Applied Physics **49**, 07HF28-1-07HF28-5 (2010).
66. K. R. Marutyan, G. L. Bretthost, and J. G. Miller, "Bayesian estimation of the underlying bone properties from mixed fast and slow mode ultrasonic signals," The Journal of the Acoustical Society of America **121**, EL8–EL15 (2007).
67. E. T. Jaynes, *Probability Theory: The Logic of Science*, edited by G. L. Bretthorst (Cambridge, University Press, Cambridge, UK, 2003).
68. I. Mano, K. Horii, S. Takai, T. Suzaki, H. Nagaoka, and T. Otani, "Development of novel ultrasonic bone densitometry using acoustic parameters of cancellous bone for fast and slow waves," Japanese Journal of Applied Physics **45**, 4700–4702 (2006).
69. T. Otani, I. Mano, T. Tsujimoto, T. Yamamoto, R. Teshima, and H. Naka, "Estimation of in vivo cancellous bone elasticity," Japanese Journal of Applied Physics **48**, 07GK05-1-07GK05-5 (2009).

Chapter 12
Phase Velocity of Cancellous Bone: Negative Dispersion Arising from Fast and Slow Waves, Interference, Diffraction, and Phase Cancellation at Piezoelectric Receiving Elements

Christian C. Anderson, Adam Q. Bauer, Karen R. Marutyan, Mark R. Holland, Michal Pakula, G. Larry Bretthorst, Pascal Laugier, and James G. Miller

Abstract Frequency-dependent phase velocity measurements may prove useful in bone quality assessment. However, the physical mechanisms of ultrasonic wave propagation in cancellous bone that govern phase velocity are not yet fully understood, particularly the phenomena that lead to the observed anomalous negative dispersion. This chapter provides an overview of phase velocity studies of cancellous bone, especially negative dispersion, and proposals for resolving the apparent conflict with the causality-imposed Kramers-Kronig relations.

Keywords Artifact · Bayesian · Negative dispersion · Phase cancellation · Phase velocity

12.1 Introduction

Clinical bone sonometry devices make use of speed of sound (SOS) and broadband ultrasonic attenuation (BUA) data acquired in investigations of the calcaneus (heel bone) to determine indices of bone quality. Accurate and reproducible methods for measuring these quantities are therefore of particular relevance in the use of quantitative ultrasound for the assessment of bone status.

C.C. Anderson, A.Q. Bauer, K.R. Marutyan, M.R. Holland, G.L. Bretthorst, and J.G. Miller (✉)
Department of Physics, Box 1105, Washington University, 1 Brooking Drive – Saint Louis, MO 63130, USA
e-mail: canderson@wustl.edu; abauer@hbar.wustl.edu; karenmarutyan@gmail.com; mrh@wuphys.wustl.edu; larry@bayes.wustl.edu; jgm@wuphys.wustl.edu

M. Pakula
Kazimierz Wielki University, Jana Karola Chodkiewicza 30, Bydgoszcz, Poland
e-mail: michalp@ukw.edu.pl

P. Laugier
Université Pierre et Marie Curie, CNRS, Laboratoire d'Imagerie Parametrique, 15, rue de L'Ecole de Medecine, 75006 Paris, France
e-mail: pascal.laugier@upmc.fr

P. Laugier and G. Haïat (eds.), *Bone Quantitative Ultrasound*,
DOI 10.1007/978-94-007-0017-8_12,

Although SOS and BUA have each been shown to be effective in evaluating bone quality, the complicated manner in which ultrasonic waves propagate through the porous architecture of cancellous bone can confound measurement efforts. Group velocity is often used to compute SOS, and the time-of-flight measurements used to compute the group velocity can be affected by frequency-dependent effects such as attenuation and dispersion [1–3]. In some cases, the signals obtained after the ultrasonic pulse has passed through cancellous bone are markedly different from the transmitted signal [2–8], making the determination of appropriate timing markers for time-of-flight measurements difficult. Moreover, information about bone quality might be suppressed when velocities for all frequencies in the experimental bandwidth are compressed to yield a single value for group velocity, the SOS for the sample. These factors provide motivation for determining the frequency-dependent phase velocity. If the dispersion information is preserved, some of the frequency-dependent sources of error in SOS measurements may be mitigated, and access to the dispersion information itself may provide additional parameters for bone assessment.

12.2 Calculation of Phase Velocity

Phase velocity can be determined using a phase spectroscopy approach in which the unwrapped phase of a signal propagated through bone is compared with the unwrapped phase of a signal propagated through a non-dispersive reference medium such as water. The phase velocity is then given by

$$v_{phase}(\omega) = v_{water}\left[1 - \frac{v_{water}}{d}\frac{\Delta\phi(\omega)}{\omega}\right]^{-1} \tag{12.1}$$

where v_{water} is the velocity in water, d is the sample thickness, $\Delta\phi(\omega)$ is the difference in unwrapped phase between the sample and reference signals, and ω is angular frequency.

Although phase velocity can be determined in this straightforward fashion, its use as a reliable indicator of bone quality is hampered because the physics of ultrasonic waves in cancellous bone that relate to dispersion remains incompletely understood. One example is the apparent conflict between the dispersion predicted by the causality-imposed Kramers-Kronig (KK) relations and that observed experimentally.

12.3 Anomalous Negative Dispersion in Cancellous Bone

The Kramers-Kronig relations are causality-imposed mathematical properties that connect the real and imaginary parts of physical response functions [9]. The transfer function corresponding to linear ultrasonic wave propagation can be written as a

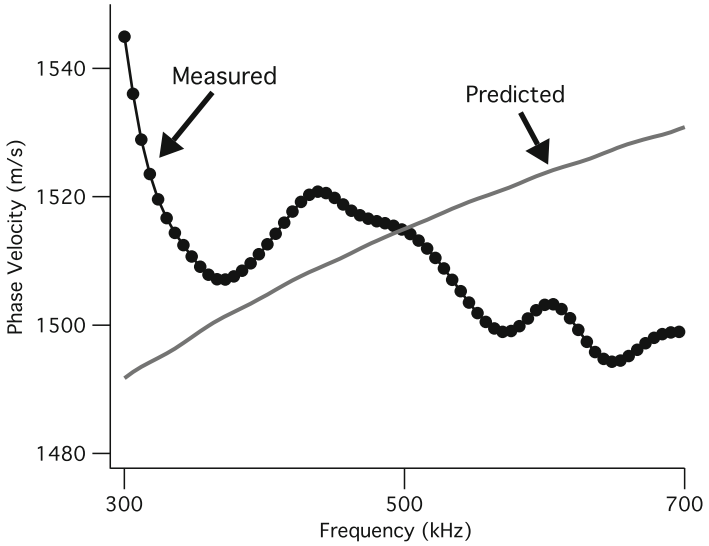

Fig. 12.1 Illustration of anomalous negative dispersion observed in cancellous bone. The dispersion curve predicted by the causality-imposed Kramers-Kronig relations is shown in *gray*, and the measured dispersion exhibited by a cancellous bone specimen is shown in *black*. The frequency dependences of the two curves differ substantially

causal response function, and therefore the real part of the transfer function (which is related to the phase velocity of waves propagating in bone) can be obtained from the imaginary part (which is related to the attenuation coefficient) [10–20]. The consensus of many laboratories is that the experimentally determined attenuation coefficient of cancellous bone rises approximately linearly with frequency. Indeed, the general agreement regarding the linear behavior of the attenuation coefficient is the reason that BUA continues to be a widely used metric in clinical assessment. When reliable but approximate forms of the Kramers-Kronig relations are used to determine the dispersion of a medium with a linearly increasing attenuation coefficient, the predicted result is a phase velocity curve that increases logarithmically with frequency – that is, the dispersion is expected to be *positive* [17, 21, 22]. However, empirical results obtained in cancellous bone often show the opposite relationship. Many laboratories report phase velocities that *decrease* with frequency, a phenomenon often referred to as *negative dispersion* [2–4, 17, 21–26]. Thus, as shown in Fig. 12.1, an apparent conflict exists between the causal KK predictions and experimental results in many (but not all) interrogated sites of cancellous bone.

12.4 Proposed Explanations of Negative Dispersion in Bone

A number of suggested explanations for the anomalous behavior of the frequency dependence of the phase velocity exist, but a consensus has yet to be reached regarding which of these is dominant. Broadly speaking, the proposals fall into

two distinct groups: those that propose novel understandings of acoustic wave propagation in bone, and those that extend or reinterpret how the KK relations should be applied to poroelastic media. One proposed approach in the latter category is the use of a higher order approximation to the exact KK relations [17]. The Kramers-Kronig relations can be extended using the method of subtractions to account for negative dispersion, but doing so requires introducing an additional adjustable parameter in the form of a "subtraction frequency." The physical role of the subtraction frequency, however, remains unclear.

Another interpretation is that the KK relations are by their nature unable to accurately depict empirically determined dispersions accurately because the relations involve integrals over an infinite bandwidth, whereas experimental bandwidths are finite. In this view, the necessary truncation of the KK integrals to predict measurable dispersions results in large errors, and the observed negative dispersion in cancellous bone simply reflects the true properties of cancellous bone. However, the KK relations have been shown to be quite reliable in predicting dispersion over a limited bandwidth even in the presence of substantial phase aberration and phase cancellation [27]. Although the truncated KK relations have known limitations [19], their robustness even under challenging experimental circumstances [18, 27] suggests that these relations are likely to remain valid in porous media.

Other proposals to explain the anomalous dispersion involve unique or improved theoretical understandings of ultrasonic wave propagation in bone. One widely-used model for cancellous bone is the stratified model, in which the bone structure is modeled as alternating fluid and solid layers [28–31]. This model can predict negative dispersion [29, 30], although the physical architecture of cancellous bone appears different from that exhibited by a periodic layered structure. A different proposal by Chakraborty involves a non-local extension of Biot theory, which can give rise to negative dispersion under some circumstances [32], Still another explanation, suggested by Haiat et al., is that the coupling of multiple scattering and absorption mechanisms may contribute to negative dispersion [33].

12.5 Interfering Wave Modes

The primary focus in this chapter will be on an alternative to these explanations based on a careful examination of the received signals and how they are processed to obtain the dispersion. Qualitative characteristics of ultrasonic data acquired on cancellous bone may provide clues for explaining the negative dispersion. As mentioned above, the ultrasonic signals that are received after they have propagated through cancellous bone can vary considerably from the transmitted signals. A contributing factor to the large qualitative differences between transmitted and received signals is that porous materials such as cancellous bone can support the propagation of more than one compressional wave mode, as described in previous chapters [5–7, 34]. Theoretical models for ultrasonic wave propagation in bone, including Biot theory [35–44] and stratified media theory [28–31], each predict the existence

of two compressional waves. These waves, commonly distinguished by their relative velocities as "fast waves" and "slow waves," have been observed in data acquired by a number of laboratories [5–7, 34]. Occasionally, the transit times of the fast and slow waves are different enough that they are separated in the time-domain data. In these cases, velocity and attenuation measurements can be performed on each wave mode independently by applying an appropriate windowing function to the data. Although this approach is straightforward in laboratory investigations, clinical sonometers might not provide this option.

Under most circumstances, the times of flight for the fast and slow waves are sufficiently similar that they arrive at the receiving transducer only a short time apart, resulting in an overlap in the acquired data. The degree of overlap can vary significantly from sample to sample or even at different spatial locations within the same sample due to the considerable heterogeneity of cancellous bone. When overlap occurs, a suitable location for a windowing function is much less clear, and measurement of separate fast and slow wave properties becomes difficult or impossible. If the experimental conditions are such that there is little overt evidence of overlap between the two waves, the acquired data are likely to be processed as if only one wave is present. Under these circumstances, a negative dispersion can be observed [21, 22, 45]. Thus, the observed anomalous dispersion might appear to be an intrinsic property of the bone, when in fact it is an artifact caused by processing a multi-modal signal under the assumption that the received signal is comprised of one wave.

Numerical simulations confirm that when two waves with ultrasonic velocity and attenuation properties similar to those in cancellous bone interfere with one another in the acquired data, negative dispersion can occur even though the attenuation coefficient retains its linear-with-frequency behavior. The signals composed of interfering waves can exhibit artifactual dispersions, including negative dispersion, even though the individual fast and slow waves that comprise them each exhibit positive, linearly increasing dispersions, in accordance with the KK relations. This phenomenon is illustrated in Fig. 12.2, where two simulated waves with unremarkable dispersions (top panel) interfere to produce a simulated received signal with an anomalous negative dispersion (bottom panel).

12.6 Analysis of Interfering Waves Using Bayesian Probability Theory

If interference between the fast and slow waves is responsible for the anomalous negative dispersion, methods for recovering the properties of the individual fast and slow waves from acquired data in which the waves strongly overlap are useful. In addition to resolving a portion or a majority of dispersion artifacts in conventionally analyzed data, such methods may enhance bone quality assessment by permitting the component waves to be analyzed in place of or in addition to the analysis of the

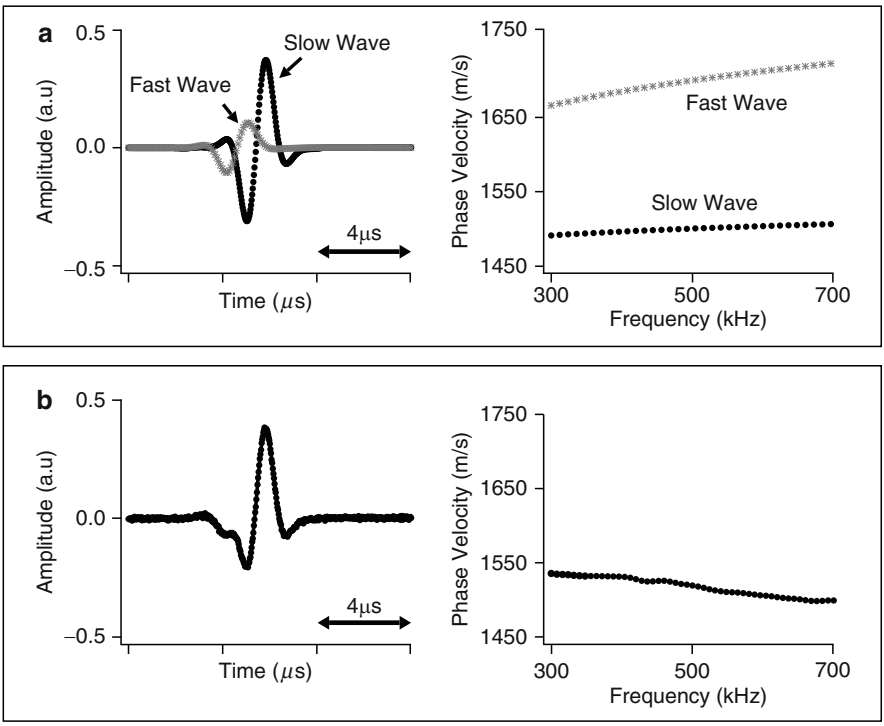

Fig. 12.2 Simulated fast and slow waves (panel **a**, *left*), each exhibiting logarithmically increasing dispersions (panel **a**, *right*) can interfere to produce a mixed mode waveform (panel **b**, *left*) with an anomalous negative dispersion (panel **b**, *right*)

entire received signal. One such method for recovering these properties makes use of Bayesian probability theory, an approach suited for addressing inverse problems [46, 47].

In the Bayesian approach, a model for the received signal is constructed by specifying velocity and attenuation parameters for each of the fast and slow waves. To ensure agreement with the KK relations, the model requires that the dispersions for each wave are dependent upon the frequency dependence of their respective attenuation coefficients. Bayes' theorem is then applied to obtain optimal estimates of the model parameters in the form of marginal posterior probability distributions. In this way, attenuation coefficient and the phase velocity values (and their corresponding frequency dependences, as described by BUA and dispersion) for both the fast and the slow waves for a given received signal can be estimated, even in the presence of substantial overlap and interference between the two wave modes in acquired data. This technique has been extensively tested using both simulated data and experimental data acquired on well-controlled two-component phantoms as well as bone [48–51].

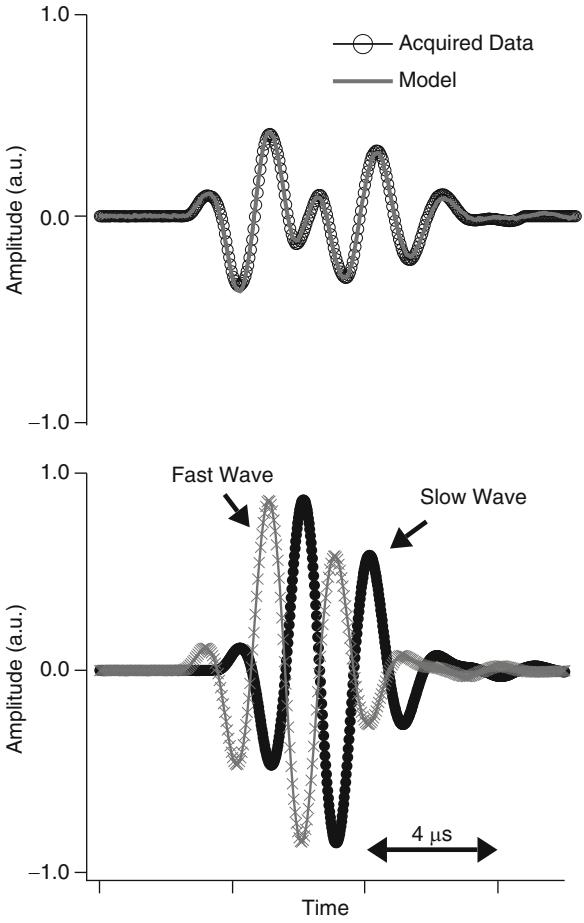

Fig. 12.3 A signal acquired on a two-component phantom composed of acrylic and polycarbonate plastics (*open circles, top*) is plotted along with the model signal obtained using Bayesian probability theory (*gray line, top*). The individual fast and slow waves that combine to form the model signal are shown in the *bottom* panel. Although the fast and slow waves are approximately 180 degrees out of phase, the model shows good agreement with the acquired data

A signal acquired on a two-component phantom constructed from acrylic and polycarbonate thermoplastics is show in the top panel of Fig. 12.3. The phantom was designed so that a portion of the transmitted signal passed through acrylic, and the remainder propagated through polycarbonate. The difference in the speeds of sound of the two media caused two waves to be present in the acquired data. The model for this signal produced by the Bayesian calculations is superimposed on the acquired signal (top panel in Fig. 12.3, gray line). The model signal is composed of a fast wave and a slow wave, which are plotted in the bottom panel of Fig. 12.3. There is good agreement between the model and the acquired data despite the approximately 180° phase difference between the fast and slow waves.

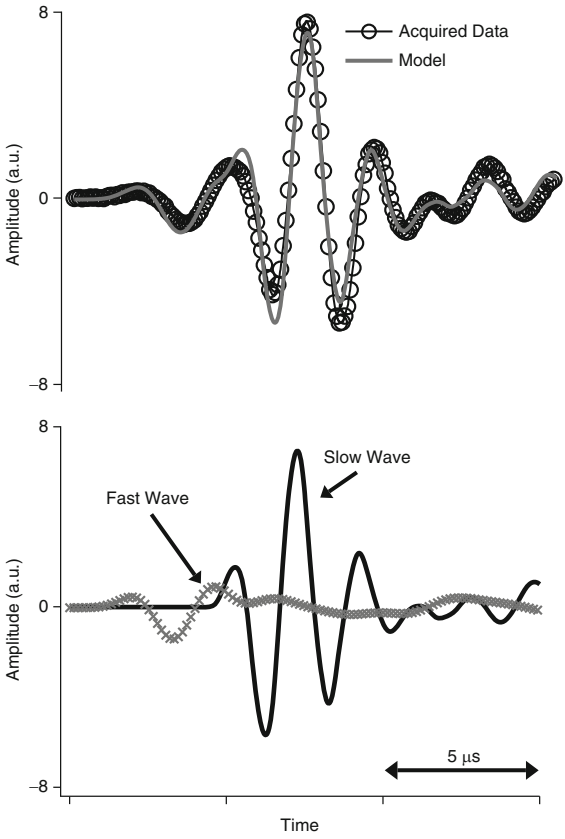

Fig. 12.4 A signal acquired on a human femur condyle specimen is displayed in the top set of axes, with the model constructed using Bayesian probability theory superimposed. Probability theory can determine the individual fast and slow waves that comprise the model, and those waves are shown on the bottom set of axes

Figure 12.4 displays data acquired on a human femur condyle in the top panel, with the model obtained using Bayesian probability theory superimposed. The individual fast and slow waves that comprise the model are shown in the bottom panel.

12.7 Phase Cancellation and Diffraction Effects

In addition to the effects discussed thus far, diffraction and interference effects arising from spatial variations in the local values of phase velocity can result in signals at the receiver plane that exhibit some of the same complicating features as those that arise from fast and slow wave propagation [52–56]. Phase cancellation across the face of a piezoelectric receiving transducer can result from detecting such an ultrasonic field over a finite aperture [52,54,56–60]. Apparent negative dispersion can arise under these circumstances [45]. The use of two-dimensional arrays of small aperture receiving transducer elements can provide approaches for mitigating some of the resulting artifacts. Still other (diffraction-related) artifacts can result if the

physical dimensions of the receiving aperture are not sufficiently large [55]. In spite of these complications, the Bayesian approach appears to be sufficiently robust as to yield the proper values for the underlying ultrasonic properties [49].

12.8 Conclusion

Measurements of phase velocity are straightforward and increasingly standard in many laboratory studies, and it seems reasonable to speculate that information contained in such measurements may be clinically relevant. However, the clinical potential of phase velocity has yet to be realized, perhaps due at least in part to the lack of a complete understanding of the mechanisms that give rise to the experimentally observed dispersion in cancellous bone. The anomalous negative dispersion observed in cancellous bone, an apparent violation of some forms of the Kramers-Kronig relations, is particularly confounding, and several research efforts have focused on resolving this contradiction. One hypothesis is that negative dispersion is an artifact that arises when data containing two overlapping waves are analyzed under the implicit assumption that only one wave is present. Bayesian probability theory has been proposed as a method for analyzing such data to recover the properties of each individual wave. However, several complicating experimental factors, including diffraction and phase cancellation at a receiving aperture, may also play a role in the measured dispersion.

Acknowledgments Work presented in this chapter was supported by NIH grants R01HL40302 and R01AR057433 and by NSF grant CBET-0717830.

References

1. K. A. Wear, "The effects of frequency-dependent attenuation and dispersion on sound speed measurements: applications in human trabecular bone," IEEE Transactions on Ultrasonics, Ferroelectrics, and Frequency Control **47**(1), 265–273 (2000).
2. R. Strelitzki and J. Evans, "On the measurement of the velocity of ultrasound in the os calcis using short pulses," European Journal of Ultrasound **4**(3), 205–213 (1996).
3. P. H. Nicholson, G. Lowet, C. M. Langton, J. Dequeker, and G. Van der Perre, "A comparison of time-domain and frequency-domain approaches to ultrasonic velocity measurement in trabecular bone," Physics in Medicine and Biology **41**(11), 2421–2435 (1996).
4. P. Droin, G. Berger, and P. Laugier, "Velocity dispersion of acoustic waves in cancellous bone," IEEE Transactions on Ultrasonics, Ferroelectrics, and Frequency Control **45**(3), 581–592 (1998).
5. A. Hosokawa and T. Otani, "Ultrasonic wave propagation in bovine cancellous bone," The Journal of the Acoustical Society of America **101**(1), 558–562 (1997).
6. A. Hosokawa and T. Otani, "Acoustic anisotropy in bovine cancellous bone," The Journal of the Acoustical Society of America **103**(5 Pt 1), 2718–2722 (1998).
7. K. Mizuno, M. Matsukawa, T. Otani, P. Laugier, and F. Padilla, "Propagation of two longitudinal waves in human cancellous bone: an in vitro study," The Journal of the Acoustical Society of America **125**(5), 3460–3466 (2009).

8. R. Strelitzki, A. J. Clarke, and J. A. Evans, "The measurement of the velocity of ultrasound in fixed trabecular bone using broadband pulses and single-frequency tone bursts," Physics in Medicine and Biology **41**(4), 743–753 (1996).
9. J. S. Toll, "Causality and the dispersion relation: logical foundations," Physical Review **104**(6), 1760–1770 (1956).
10. M. O'Donnell, E. Jaynes, and J. Miller, "General relationships between ultrasonic attenuation and dispersion," The Journal of the Acoustical Society of America **63**(6), 1935–1937 (1978).
11. M. O'Donnell, E. T. Jaynes, and J. G. Miller, "Kramers-Kronig relationship between ultrasonic attenuation and phase velocity," The Journal of the Acoustical Society of America **69**(3), 696–701 (1981).
12. K. Waters, M. Hughes, G. Brandenburger, and J. Miller, "On a time-domain representation of the Kramers-Kronig dispersion relations," The Journal of the Acoustical Society of America **108**(5 Pt 1), 2114–2119 (2000).
13. K. Waters, M. Hughes, J. Mobley, G. Brandenburger, and J. Miller, "Kramers-Kronig dispersion relations for ultrasonic attenuation obeying a frequency power law," 1999 IEEE International Ultrasonics Symposium Proceedings **99CH37027**, 537–541 (1999).
14. K. R. Waters, M. S. Hughes, J. Mobley, G. H. Brandenburger, and J. G. Miller, "On the applicability of Kramers–Krönig relations for ultrasonic attenuation obeying a frequency power law," The Journal of the Acoustical Society of America **108**(2), 556–563 (2000).
15. K. Waters, M. Hughes, J. Mobley, and J. Miller, "Differential forms of the Kramers-Kronig dispersion relations," IEEE Transactions on Ultrasonics, Ferroelectrics, and Frequency Control **50**(1), 68–76 (2003).
16. K. Waters, J. Mobley, and J. Miller, "Causality-imposed (Kramers-Kronig) relationships between attenuation and dispersion," IEEE Transactions on Ultrasonics, Ferroelectrics, and Frequency Control **52**(5), 822–823 (2005).
17. K. R. Waters and B. K. Hoffmeister, "Kramers-Kronig analysis of attenuation and dispersion in trabecular bone," The Journal of the Acoustical Society of America **118**(6), 3912–3920 (2005).
18. J. Mobley, K. Waters, C. Hall, J. Marsh, and M. Hughes, "Measurements and predictions of the phase velocity and attenuation coefficient in suspensions of elastic microspheres," The Journal of the Acoustical Society of America **106**(2), 652–659 (1999).
19. J. Mobley, K. R. Waters, and J. G. Miller, "Finite-bandwidth effects on the causal prediction of ultrasonic attenuation of the power-law form," The Journal of the Acoustical Society of America **114**(5), 2782–2790 (2003).
20. J. Mobley, K. R. Waters, and J. G. Miller, "Causal determination of acoustic group velocity and frequency derivative of attenuation with finite-bandwidth Kramers-Kronig relations," Physical Review E **72**(1 Pt 2), 016604 (2005).
21. C. C. Anderson, K. R. Marutyan, M. R. Holland, K. A. Wear, and J. G. Miller, "Interference between wave modes may contribute to the apparent negative dispersion observed in cancellous bone," The Journal of the Acoustical Society of America **124**(3), 1781–1789 (2008).
22. K. R. Marutyan, M. R. Holland, and J. G. Miller, "Anomalous negative dispersion in bone can result from the interference of fast and slow waves," The Journal of the Acoustical Society of America **120**(5 Pt 1), EL55–61 (2006).
23. K. A. Wear, "Measurements of phase velocity and group velocity in human calcaneus," Ultrasound in Medicine & Biology **26**(4), 641–646 (2000).
24. K. A. Wear, "Group velocity, phase velocity, and dispersion in human calcaneus in vivo," The Journal of the Acoustical Society of America **121**(4), 2431–2437 (2007).
25. M. Pakula, F. Padilla, and P. Laugier, "Influence of the filling fluid on frequency-dependent velocity and attenuation in cancellous bones between 0.5 and 2.5 MHz," The Journal of the Acoustical Society of America **126**(6), 3301–3310 (2009).
26. K. A. Wear, "Frequency dependence of average phase shift from human calcaneus in vitro," The Journal of the Acoustical Society of America **126**(6), 3291–3300 (2009).
27. A. Bauer, K. Marutyan, M. Holland, and J. Miller, "Is the Kramers-Kronig relationship between ultrasonic attenuation and dispersion maintained in the presence of apparent losses due to phase cancellation?" The Journal of the Acoustical Society of America **122**(1), 222–228 (2007).

28. E. R. Hughes, T. G. Leighton, G. W. Petley, and P. R. White, "Ultrasonic propagation in cancellous bone: a new stratified model," Ultrasound in Medicine & Biology **25**(5), 811–821 (1999).
29. T. J. Plona, K. W. Winkler, and M. Schoenberg, "Acoustic waves in alternating fluid/solid layers," The Journal of the Acoustical Society of America **81**(5), 1227–1234 (1987).
30. K. Wear, "A stratified model to predict dispersion in trabecular bone," IEEE Transactions on Ultrasonics, Ferroelectrics, and Frequency Control **48**(4), 1079–1083 (2001).
31. W. Lin, Y. X. Qin, and C. Rubin, "Ultrasonic wave propagation in trabecular bone predicted by the stratified model," Annals of Biomedical Engineering **29**(9), 781–790 (2001).
32. A. Chakraborty, "Prediction of negative dispersion by a nonlocal poroelastic theory," The Journal of the Acoustical Society of America **123**(1), 56–67 (2008).
33. G. Haïat, A. Lhémery, F. Renaud, F. Padilla, P. Laugier, and S. Naili, "Velocity dispersion in trabecular bone: influence of multiple scattering and of absorption," The Journal of the Acoustical Society of America **124**(6), 4047–4058 (2008).
34. G. Haïat, F. Padilla, F. Peyrin, and P. Laugier, "Fast wave ultrasonic propagation in trabecular bone: numerical study of the influence of porosity and structural anisotropy," The Journal of the Acoustical Society of America **123**(3), 1694–1705 (2008).
35. M. Biot, "Theory of propagation of elastic waves in a fluidsaturated porous solid. I. Low–frequency range," The Journal of the Acoustical Society of America **28**(2), 168–178 (1956).
36. M. Biot, "Theory of propagation of elastic waves in a fluid–saturated porous solid. II. Higher frequency range," The Journal of the Acoustical Society of America **28**(2), 179–191 (1956).
37. T. J. Haire and C. M. Langton, "Biot theory: a review of its application to ultrasound propagation through cancellous bone," Bone **24**(4), 291–295 (1999).
38. J. L. Williams, "Ultrasonic wave propagation in cancellous and cortical bone: prediction of some experimental results by Biot's theory," The Journal of the Acoustical Society of America **91**(2), 1106–1112 (1992).
39. K. I. Lee, E. R. Hughes, V. F. Humphrey, T. G. Leighton, and M. J. Choi, "Empirical angle-dependent Biot and MBA models for acoustic anisotropy in cancellous bone," Physics in Medicine and Biology **52**(1), 59–73 (2007).
40. Z. Fellah, N. Sebaa, M. Fellah, F. Mitri, E. Ogam, W. Lauriks, and C. Depollier, "Application of the biot model to ultrasound in bone: direct problem," IEEE Transactions on Ultrasonics, Ferroelectrics, and Frequency Control **55**(7), 1508–1515 (2008).
41. Z. E. A. Fellah, J. Y. Chapelon, S. Berger, W. Lauriks, and C. Depollier, "Ultrasonic wave propagation in human cancellous bone: application of Biot theory," The Journal of the Acoustical Society of America **116**(1), 61–73 (2004).
42. M. L. McKelvie and S. B. Palmer, "The interaction of ultrasound with cancellous bone," Physics in Medicine and Biology **36**(10), 1331–1340 (1991).
43. N. Sebaa, Z. Fellah, M. Fellah, E. Ogam, F. Mitri, C. Depollier, and W. Lauriks, "Application of the Biot model to ultrasound in bone: inverse problem," IEEE Transactions on Ultrasonics, Ferroelectrics, and Frequency Control **55**(7), 1516–1523 (2008).
44. M. Pakula, F. Padilla, P. Laugier, and M. Kaczmarek, "Application of Biot's theory to ultrasonic characterization of human cancellous bones: determination of structural, material, and mechanical properties," The Journal of the Acoustical Society of America **123**(4), 2415–2423 (2008).
45. A. Q. Bauer, K. R. Marutyan, M. R. Holland, and J. G. Miller, "Negative dispersion in bone: the role of interference in measurements of the apparent phase velocity of two temporally overlapping signals," The Journal of the Acoustical Society of America **123**(4), 2407–2414 (2008).
46. E. T. Jaynes and G. L. Bretthorst, *Probability theory: the logic of science* (Cambridge University Press, Cambridge, 2003).
47. D. S. Sivia and J. Skilling, *Data analysis: a Bayesian tutorial* (Oxford University Press, New York, 2006).
48. C. C. Anderson, K. R. Marutyan, K. A. Wear, M. R. Holland, J. G. Miller, and G. L. Bretthorst, "Model selection in ultrasonic measurements on trabecular bone," AIP Conference Proceedings **954**, 337–345 (2007).

49. C. C. Anderson, M. Pakula, M. R. Holland, P. Laugier, G. L. Bretthorst, and J. G. Miller, "Decomposition of interfering ultrasonic waves in bone and bone-mimicking materials," AIP Conference Proceedings **1193**, 321–328 (2009).
50. K. R. Marutyan, G. L. Bretthorst, and J. G. Miller, "Bayesian estimation of the underlying bone properties from mixed fast and slow mode ultrasonic signals," The Journal of the Acoustical Society of America **121**(1), EL8–15 (2007).
51. K. R. Marutyan, C. C. Anderson, K. A. Wear, M. R. Holland, J. G. Miller, and G. L. Bretthorst, "Parameter estimation in ultrasonic measurements on trabecular bone," AIP Conference Proceedings **954**, 329–336 (2007).
52. L. Busse and J. Miller, "Detection of spatially nonuniform ultrasonic radiation with phase sensitive (piezoelectric) and phase insensitive (acoustoelectric) receivers," The Journal of the Acoustical Society of America **70**(5), 1377–1386 (1981).
53. R. Strelitzki, S. C. Metcalfe, P. H. Nicholson, J. A. Evans, and V. Paech, "On the ultrasonic attenuation and its frequency dependence in the os calcis assessed with a multielement receiver," Ultrasound in Medicine & Biology **25**(1), 133–141 (1999).
54. K. A. Wear, "The effect of phase cancellation on estimates of calcaneal broadband ultrasound attenuation in vivo," IEEE transactions on Ultrasonics, Ferroelectrics, and Frequency Control **54**(7), 1352–1359 (2007).
55. A. Q. Bauer, C. C. Anderson, M. R. Holland, and J. G. Miller, "Bone sonometry: reducing phase aberration to improve estimates of broadband ultrasonic attenuation," The Journal of the Acoustical Society of America **125**(1), 522–529 (2009).
56. K. A. Wear, "The effect of phase cancellation on estimates of broadband ultrasound attenuation and backscatter coefficient in human calcaneus in vitro," IEEE Transactions on Ultrasonics, Ferroelectrics, and Frequency Control **55**(2), 384–390 (2008).
57. A. Bauer, C. Anderson, M. Holland, and J. Miller, "Measurement artifacts in sonometry of cancellous bone: the relative impact of phase cancellation and interference on measurements of phase-distorting phantoms," 2008 IEEE International Ultrasonics Symposium Proceedings **CFP08ULT**, 137–141 (2008).
58. J. R. Klepper, G. H. Brandenburger, J. W. Mimbs, B. E. Sobel, and J. G. Miller, "Application of phase-insensitive detection and frequency-dependent measurements to computed ultrasonic attenuation tomography," IEEE Transactions on Bio-Medical Engineering **28**(2), 186–201 (1981).
59. G. W. Petley, P. A. Robins, and J. D. Aindow, "Broadband ultrasonic attenuation: are current measurement techniques inherently inaccurate?," British Journal of Radiology **68**(815), 1212–1214 (1995).
60. J. Pohlhammer, C. Edwards, and W. D. O'Brien, "Phase insensitive ultrasonic attenuation coefficient determination of fresh bovine liver over an extended frequency range," Medical Physics **8**(5), 692–694 (1981).

Chapter 13
Linear Ultrasonic Properties of Cortical Bone: In Vitro Studies

Guillaume Haïat

Abstract An increasing interest is placed in the ultrasonic characterization of cortical bone because its quality has now become accessible. The aim of this chapter is to review the results obtained in the literature with the different experimental approaches carried out in vitro. Different quantitative ultrasonic bone parameters such as the ultrasonic velocity and the attenuation coefficient are studied. The frequency dependence of attenuation (which corresponds to broadband ultrasonic attenuation, BUA) and of phase velocity (velocity dispersion) is investigated in particular. The dependence of all ultrasonic parameters on the direction of propagation relatively to the bone axis as well as to bone properties such as the type of microstructure, volumetric bone mineral density and mass density is also reviewed. The results presented in this chapter show the potentiality of ultrasonic parameters to assess cortical bone properties.

Keywords Anisotropic medium · Attenuation · Bone mineral density · Broadband ultrasonic attenuation · Cortical bone · Dispersion · Dispersive medium · Haversian structure · Heterogeneous medium · Homogenized mechanical properties · Kramers-Kronig relationships · Microstructure · Multiscale medium · Osteons · Phase velocity · Plexiform · Quantitative ultrasound imaging · Speed of sound · Structure · Transverse transmission · Viscoelasticity

13.1 Introduction

In this chapter, a brief literature review is realized on the works studying the linear properties of cortical bone in vitro. All effects related to non linear wave propagation phenomena (in particular related to the presence of micro-cracks), which are studied in Chap. 15, will not be described in what follows. This study is restricted to

G. Haïat (✉)
CNRS, B2OA UMR 7052, 10, avenue de Verdun, 75010 Paris, France
e-mail: guillaume.haiat@univ-paris-est.fr

P. Laugier and G. Haïat (eds.), *Bone Quantitative Ultrasound*,
DOI 10.1007/978-94-007-0017-8_13,

all experiments performed on non living tissues (ex vivo). Studying cortical bone in vitro has the advantage of working in controlled experimental conditions and thus corresponds to more fundamental works compared to in vivo studies where different problems arise such as the influence of bone geometry (i.e. accessibility) and possible movements or temperature variation of the body, which might influence the bone ultrasonic response. In vitro, the samples may be cut into simple shapes or intact. The surrounding soft tissues are often removed to obtain a better understanding of the ultrasonic response of the bone structure itself.

13.1.1 Why Assessing Cortical Bone Acoustical Properties?

Initially, most applications of quantitative ultrasonic (QUS) techniques in bone were confined to cancellous bone characterization (see Chap. 10) because the most commonly site measured with QUS techniques is the calcaneus, which is mostly composed of trabecular bone. However, more and more interest is now placed in cortical bone exploration [1] since it accounts for 80% of the skeleton, supports most of the load of the body and is mainly involved in many osteoporotic fractures. Furthermore, cortical bone is affected by age-related bone resorption and osteoporosis [2]. It undergoes an increase in porosity as well as a cortical shell thinning, which has been shown to be determinant in fracture risk [3]. In addition, mineralization of cortical bone increases with age or disease [4], leading to an increased stiffness [5] and fragility.

The development of new QUS devices now enables the in vivo evaluation of cortical bone with specific devices such as the axial transmission technique. This last technique allows the in vivo assessment of the cortical layer of the mid tibia [6], distal radius [7] and of several sites including ulna, finger phalanxes, metacarpal or metatarsus [8]. The transverse transmission technique may also be used for both cortical and trabecular bone evaluation on sites such as wrist bones or phalanx [9, 10]. As this chapter only studies in vitro experimental work, axial transmission techniques will not be reviewed herein and readers are referred to Chaps. 3 and 7 for more information on this subject.

Currently, the two main parameters measured with QUS techniques are the wave velocity (Speed Of Sound, SOS) and the slope of the curve of the frequency-dependent attenuation (normalized Broadband Ultrasonic Attenuation, nBUA). The development of QUS techniques is still limited since the information potentially available in the ultrasonic wave propagating in bone tissue is not fully analyzed and parameters such as bone material properties or micro-structural parameters may still be difficult to recover. The interaction between ultrasound and bone remains poorly understood from a physical point of view due to the complex nature of the cortical bone structure.

13.1.2 Cortical Bone: A Complex Medium

Cortical bone is a complex multiscale medium spanning many length scales and described in Chap. 1. At the scale of several hundred nanometres, mineralized bone is composed of elementary components such as hydroxyapatite, cylindrically shaped collagen molecules and water. At the scale of 1–10 µm, bone is constituted by the ultrastructure composed of collagen fibers and extrafibrillar spaces. At the scale of several hundred micrometers to several millimeters, the microstructure is constituted by cylindrical units called osteons.

Besides its multiscale nature, cortical bone is highly heterogeneous at the organ scale and its mechanical properties depend on the cross-sectional and axial anatomical position [11]. Porosity in the radial direction (which is associated with the bone cross-section) is heterogeneous at all ages and for both genders [11–13]. The mean porosity in the endosteal region (inner part of the bone) is higher than in the periosteal region (outer part of the bone). This is especially evident in elderly subjects, due to the predominance of age-related bone resorption in the endosteal region [12]. The aforementioned heterogeneity of bone porosity is likely to lead to a gradient of bone material properties, which may affect bone quality and susceptibility to fracture. In addition, this gradient of material properties has been shown to have an important effect on its ultrasonic response [14, 15].

Cortical bone is an anisotropic medium because of its highly oriented, mineralized collagen fibrils structure. Different assumptions regarding the type of anisotropy of the cortical bone structure have been done in the literature. Some authors [15–21] have assumed that cortical bone can be considered as transverse isotropic (five independent elastic coefficients), which corresponds to the situation where bone elastic properties are similar in the transverse directions but are different in the axial direction. Others have made the more general assumption of orthotropy [16, 19, 22–24] (with three perpendicular planes of symmetry) where nine elastic coefficients are needed to fully characterize the medium. Wave propagation in anisotropic media is quiet different than in isotropic media [25] as quasi longitudinal (respectively transverse) wave modes propagate instead of pure longitudinal (respectively transverse) wave modes. Briefly, the direction of propagation of the energy in an anisotropic medium is not necessarily perpendicular to the wavefront. As a consequence, a wave generated at a given interface will not in general propagate in the direction normal to this interface. The direction of polarization of the wave (which corresponds to the direction of the displacement induced by the wave) is not necessarily parallel to the wave vector in the case of a longitudinal wave. However, it remains difficult to quantitatively evaluate the effect of anisotropy on wave propagation in cortical bone by studying only one direction of propagation and most authors have simply neglected the aforementioned phenomena, thus assuming longitudinal wave propagation perpendicular to the interface.

Section 13.2 describes different multimodal experimental approaches. In Sect. 13.3, ultrasonic velocity measurements are studied. Like every biological media, cortical bone is an attenuating medium. The viscoelastic and heterogeneous nature of cortical bone constitute two reasons explaining why relatively

important values of the attenuation coefficient have been measured in cortical bone (see Sect. 13.4). Diffusion of the elastic wave by bone heterogeneities as well as viscoelastic absorption within bone tissue are the two main concurring phenomena explaining the attenuation in cortical bone. Like all attenuating media, cortical bone is a dispersive medium and phase velocity has been shown to depend on frequency (see Sect. 13.5).

13.2 Material and Methods

13.2.1 Cortical Bone Samples

Both cylindrical and cubic samples have been used in ultrasonic experiments, but cubic samples have the advantage of allowing assessment of material properties in different directions, which gives access to bone anisotropy.

The cortical bone samples are often obtained from long bones such as femurs and cut as shown schematically in Fig. 13.1, which also shows the terminology used for the anatomical locations and the orientation of the axis relatively to the bone axis.

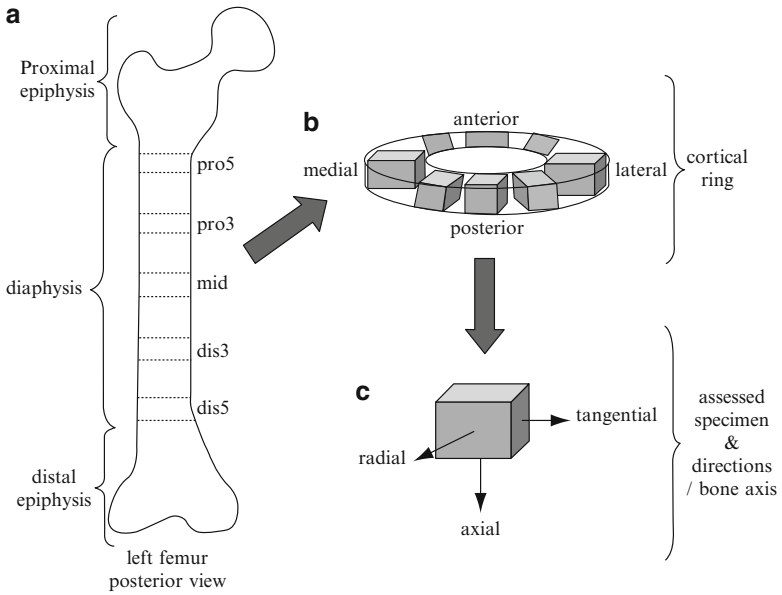

Fig. 13.1 Schematic representation of the spatial distribution of the bone samples. (**a**) Locations where the intact femur is cut to obtain the cortical rings. (**b**) Quadrant positions of the eight parallelepipedic samples around each cortical ring. (**c**) Illustration of the orientation of the three directions (Reprinted from [26] copyright 2007 with permission from Elsevier)

13.2.2 Microstructure Assessment

The different cortical bone samples may be classified as a function of their type of microstructure. In this aim, each sample can be analyzed using an optical microscope. The porotic microstructure differs from the other ones by a larger pore size comprised between 50 and 300 µm compared with pores sizes in Haversian (20 ∼ 50 µm) and plexiform structures (8 ∼ 12 µm). Porotic microstructure is mostly found near the part where muscles adhere [27–30]. The last microstructure is referred to as "mixed microstructure" and corresponds to samples where two different microstructures can be found. Representations of the four kinds of cortical bovine bone microstructure are shown in Fig. 13.2.

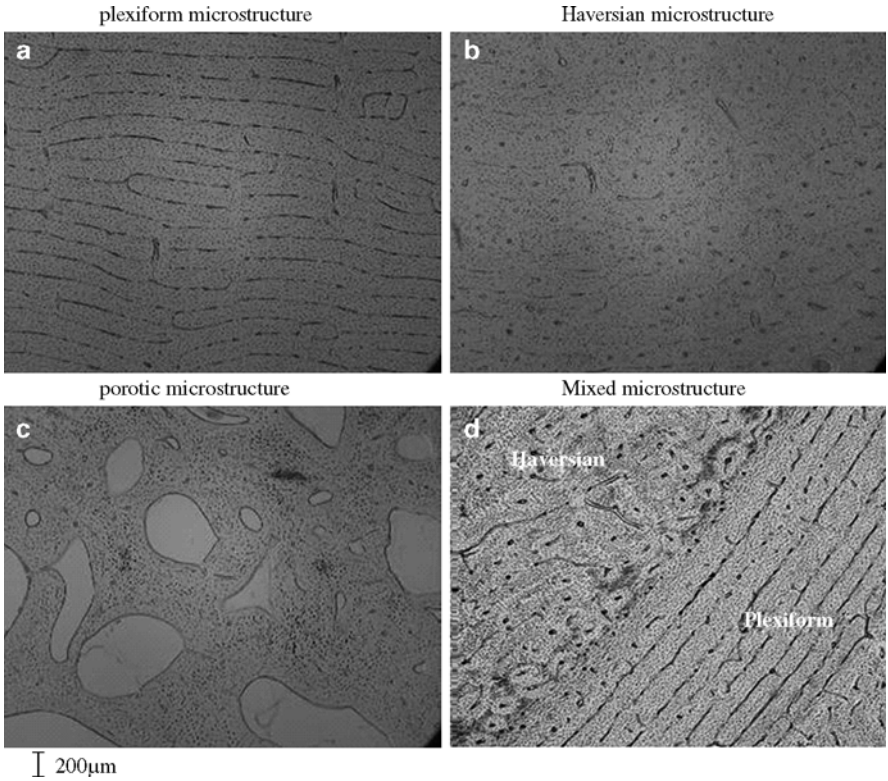

Fig. 13.2 Optical microscopy images of the four types of cortical bovine bone microstructure: (**a**) plexiform, (**b**) Haversian, (**c**) porotic and (**d**) mixed microstructure (Reprinted from [31] copyright (2008) with permission from Elsevier)

13.2.3 Density Measurements

In what follows, the ultrasonic parameters are compared with mass density and volumetric bone mineral density (vBMD). For each sample, mass density can be determined from Archimedes' principle using an accurate balance. vBMD can be determined by a dual X-Ray absorptiometry working in high resolution mode.

13.2.4 Ultrasonic Measurements

Most experimental devices used to measure ultrasonic parameters in cortical bone are through transmission devices composed of two ultrasonic transducers, an emitter and a receiver mounted co-axially, as shown in Fig. 13.3. The transducers may be either focused or planar. Both transducers may be positioned in direct contact with the bone sample using coupling ultrasonic gel or immersed in water as it is the case in Fig. 13.3. The most commonly used method is a substitution technique which consists in performing the ultrasonic measurement without the sample (only water is present between the transducers) and then in inserting the sample between the transducers. The emitter is driven by a function generator. Received signals are amplified using a wide-band amplifier and digitized PCI card or an oscilloscope. Each received signal is then transferred to a personal computer for off-line analysis. Some authors [32, 33] have performed 2-D image of wave velocity by displacing the sample using a 2-D scanning mechanical device, allowing an assessment of the anatomical dependence of wave velocity.

In all cases, it is mandatory to have a precise knowledge of the size L of the sample in the direction parallel to the ultrasonic propagation in order to retrieve accurate values of the ultrasonic parameters.

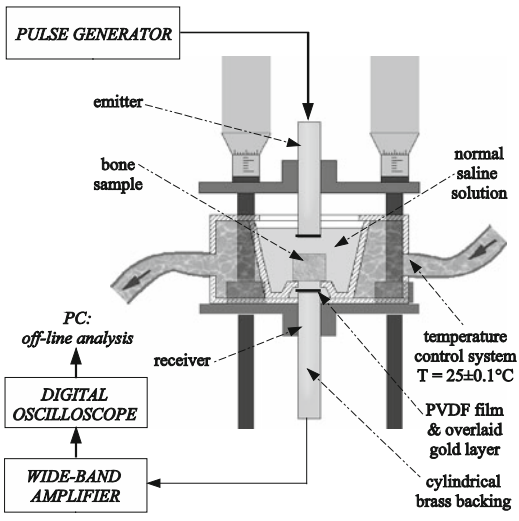

Fig. 13.3 Schematic representation of the experimental set-up used in [26, 30, 31]. (Reprinted from [26] copyright (2007) with permission from Elsevier.) Note that some authors [32–36] have used a single transducer adopting an echo-mode set up using the reflections of the ultrasonic pulse on both interfaces perpendicular to the beam axis

Cortical bone being a solid medium, shear waves may propagate in addition to longitudinal wave. Transverse wave velocity measurements have been carried out in [23, 24] using the same principle of the measurement as the one used for longitudinal wave modes except that shear wave transducers were employed. The authors found transverse wave velocity around 1800 m/s.

13.2.5 Choice of the Frequency

The choice of the centre frequency of the transducer results from a compromise between a sufficiently small wavelength so that the ultrasonic wave is sensitive to bone heterogeneities and the requirement of an acceptable signal-to-noise ratio for all samples and all directions. The choice of the frequency range consists in a compromise between a satisfactory linear variation of the apparent phase velocity and of the attenuation coefficient versus frequency for all samples in order to derive an accurate value of nBUA and dispersion and a sufficient amount of information contained within the bandwidth.

13.3 Velocity Measurements

The first ultrasonic measurements performed in cortical bone were made in the late 1940s and early 1950s in Germany [37–39]. Since then, wave velocity measurements in cortical bone have become a widely developed experimental approach and only papers from the 1970s and later are considered in the present literature review.

13.3.1 Different Velocity Estimations

The ultrasonic velocity may be estimated using the group velocity, the phase velocity or the signal velocity. The apparent phase velocity in bone $V_\varphi(f)$ is deduced from the difference $\varphi(f)$ between the phase of the reference signal transmitted in water and the phase of the signal transmitted through the bone sample. The phase of each signal is evaluated as the argument of the spectrum obtained using a Fast Fourier Transform. This phase difference is unwrapped as described in [40,41]. The apparent phase velocity is then given by:

$$V_\varphi(f) = \frac{1}{\frac{1}{V_r} - \frac{\varphi(f)}{2\pi f L}} \tag{13.1}$$

where f is the frequency and V_r is the wave velocity in water, which is assumed to be independent of the frequency. The computation of the apparent phase velocity may lead to biased estimate of the intrinsic phase velocity, due to diffraction

effects occurring between the two identical transducers [42]. A set of approximate corrections can be used in insertion techniques to relate observed experimental signals to the phase velocity [43,44]. This method has been applied by Droin et al. [40] so only the basic relations are noted here. The analysis is based on the excitation of longitudinal waves in a liquid medium by a finite circular piston source in an infinite rigid baffle radiating into a semi-infinite medium. In this method, the corrected phase difference $\varphi^c(f)$ used to compute the corrected phase velocity in bone $V_b^c(f)$ is obtained from the uncorrected phase difference $\varphi(f)$ through [40,43,44]:

$$\varphi^c(f) = \varphi(f) - \arg\left(\frac{\int_0^\infty J_1^2(Y)e^{jY^2\frac{S}{4\pi}}dY}{\int_0^\infty J_1^2(Y)e^{jY^2\frac{S_w}{4\pi}}dY}\right) \tag{13.2}$$

where, J_1 is the first order Bessel function of order zero. The quantities $S_w = \frac{HV_r}{a^2 f}$ and $S = \frac{(H-L)V_r + LV_b(4MHz)}{a^2 f}$ are respectively the Fresnel parameter for the water and water-sample-water paths, where a is the transducer radius (4 mm) and H is the distance between the emitter and the receiver. The corrected phase velocity $V_b^c(f)$ is obtained using Eq. 13.1, with $\phi^c(f)$ instead of $\phi(f)$.

To compute the signal and group velocities, the time-of-flight t_{sample} of ultrasound pulse waveforms transmitted through the bone sample is measured using an appropriate time marker such as the time of the first zero crossing (for the signal velocity) and the time of the maximum of the envelop (for the group velocity). The comparison of the resulting time delay with the system response t_{water} (reference signal transmitted through water) yields the value of the speed of sound (SOS) for the considered waveform:

$$SOS = \frac{L}{\frac{L}{V_r} + (t_{sample} - t_{water})} \tag{13.3}$$

It has been shown in trabecular bone studies that the results obtained in terms of wave velocity is highly dependent on the method used to estimate speed of sound [45,46] due to the frequency dependence of the attenuation coefficient and of the velocity dispersion of trabecular bone. Cortical bone is also a dispersive medium, but to a lesser extent compared to trabecular bone (see Sects. 13.4 and 13.5 of the present chapter). A comparison between the different wave velocity measurements in cortical bone has been made in [35]. However, the method used by the different authors is often not detailed so that it is difficult to determine what has been done. More work on the comparison between the different results of ultrasonic velocity obtained with the various methods is required to elucidate this problem.

13.3.2 Order of Magnitude

Table 13.1 shows the ranges of variation obtained in the literature with different centre frequencies and bone samples.

Table 13.1 Minimum, maximum and averaged values of the ultrasonic velocity found in the literature for different center frequencies, samples and direction of propagation

Reference	Number of samples	Direction of propagation	Specimen type	Center frequency (MHz)	Averaged velocity (m/s)	Range of variation (m/s)
[47]	4	Radial	Bovine	0.5	3000	2900–3100
[48]	11	Axial	Bovine, wet	10	3886	3881–3920
			Bovine, dry		4236	4200–4310
		Tangential	Bovine, wet		3471	3180–3490
			Bovine, dry		3605	3460–3790
		Radial	Bovine, wet		3205	3160–3270
			Bovine, dry		3402	3330–3480
[33]	4	Axial	Human femur	5	4178	3400–4600
[30]	3	Axial	Bovine femur	4	4264	SD: 120
		Radial			3453	SD: 80
		Tangential			3677	SD: 130
[36]	4	Axial	Bovine femur	5	4290	4280–4310
				10	4333	4300–4380
				20	4350	4320–4380
				30	4400	4370–4410
				50	4470	4450–4490
				100	4410	4370–4450
		Radial		5	3450	3400–3480
				10	3520	3510–3520
				20	3540	3530–3550
				30	3580	3570–3600
				50	3620	3610–3640
				100	3630	3630–3640
[49]	–	Axial	Rat femur	50	4246	SD: 17
		Radial			3782	SD: 20

SD: standard deviation

As shown in Table 13.1, the wave velocity is higher in dry samples than in wet samples. All data obtained from the various investigators indicate that wave velocity in the axial direction is the highest compared to the two other directions. However, the comparison between the radial and tangential directions remains controversial.

13.3.3 Homogenized Mechanical Properties

Ultrasound measurements allow to derive homogenized material properties at the scale of the tested sample if mass density is simultaneously measured. However, the sensitivity of the considered ultrasonic wave to bone heterogeneity is limited approximately by the wavelength λ of the pulse. According to the comparison of the wavelength λ in cortical bone and of the typical size D of the sample, two different wave modes are expected.

Table 13.2 Young's modulus found for the three perpendicular directions in different studies

Reference	Type of bone	Symmetry	E_{axial} (GPa)	$E_{tangential}$ (GPa)	E_{radial} (GPa)
[19]	Human femur	TI	27.4	18.8	18.8
[24]	Bovine femur	Orthotropic	21.9	14.6	11.6
[23]	Human femur	Orthotropic	20	13.4	12
[16]	Human tibia	Orthotropic	20.7	12.2	11.7

TI corresponds to transverse isotropic

When $\lambda \ll D$, the propagation mode is referred to as "bulk wave mode". Since the cross-sectional dimension of the sample is large compared to the wavelength, the wave does not "see" the sample boundaries. The ultrasonic velocity V_{bulk} then writes:

$$V_{bulk} = \sqrt{\frac{C_{11}}{\rho}} \tag{13.4}$$

where ρ is the homogenised mass density of the sample and $C_{11} = C_{1111}$ is the elastic constant in the direction 1 of wave propagation. Using adapted formulae obtained from linear elasticity [25], it is then possible to retrieve the value of the Young's modulus. Due to the value of the wavelength in cortical bone compared to the typical size of samples, the bulk wave mode is by far the most commonly used modality [16, 19, 23, 24]. Table 13.2 [50] shows typical order of magnitude obtained in the literature for the different Young's moduli and the corresponding assumption used for the anisotropy.

When $\lambda \gg D$, the propagation mode is referred to as "bar wave mode" and the entire sample is then insonified. In this case, the ultrasonic velocity V_{bar} writes:

$$V_{bar} = \sqrt{\frac{E_1}{\rho}} \tag{13.5}$$

where E_1 is the apparent Young's modulus in the direction *1*. The bar wave mode has been used by different authors [34,51,52] in cortical bone to quantify the anisotropic properties of cortical bone. The elastic properties derived from bulk and bar wave modes propagation are different in nature and provide complementary data [34].

13.3.4 Dependence on the Anatomical Location

There have been relatively few studies on the spatial dependence of the ultrasonic velocity in cortical bone. Mainly, a dependence of the ultrasonic velocity on the circumferential location has been reported in [16,48]. Yamato et al. [30,53] showed for the same samples that ultrasonic wave velocity was higher in the anterior positions than in the posterior positions. Similar results have been obtained by Bensamoun et al. [32, 33] in a study where a cartography of the axial ultrasonic wave velocity was realized.

13.3.5 Relation with Bone Mineral Density

Bone material properties at the macroscale depend on the components at the microscopic scale such as volume fractions of hydroxyapatite, collagen and water as well as on the microstructure [54, 55]. These results have been confirmed experimentally in a study showing that the ultrasonic velocity is influenced by changes of the organic matrix [20].

The relationship between ultrasonic velocity and mass density and bone mineral density has recently been investigated. Yamato et al. [30, 53] have evidenced a significant (positive) correlation ($r^2 = 0.5$) between the axial velocity and mass density in bovine cortical bone samples. More recently, the same team has shown a correlation between the axial ultrasonic velocity and volumetric BMD [56, 57].

However, an important dispersion of the values obtained for wave velocity was obtained, especially for plexiform microstructures where the values of mass density are the highest.

13.3.6 Relation with Hydroxyapatite Crystallite Orientation

The preferred orientation of the c-axis of hydroxyapatite (HAp) crystallites is also a factor playing a role in anisotropy and inhomogeneity of the bone elastic properties. The effect of the orientation of HAp crystallites on the ultrasonic wave velocity was investigated in bovine cortical bone samples [56–59]. The integrated intensity of the (0002) peak obtained using X-ray diffraction was estimated to evaluate the amount of preferred orientation of HAp crystallites. The ultrasonic velocity distribution pattern was similar to the distribution of integrated intensity of (0002). These results show that velocity measurement in cortical bone may also reveal information about HAp crystallite orientation.

13.4 Attenuation Measurements

13.4.1 Frequency-Dependent Attenuation

The frequency-dependent attenuation coefficient $\alpha(f)$ can be derived from the ratio of the magnitude spectrum of the pulse transmitted in bone $|A_b(f)|$ with the magnitude spectrum of the reference wave $|A_r(f)|$ [40]. Magnitude spectra are obtained using a fast Fourier transform algorithm. The quantity $\alpha(f)$, expressed in decibel, is given by:

$$\alpha(f) = \frac{1}{L}(20\log_{10}(e))\left(\ln\frac{|A_r(f)|}{|A_b(f)|} + \ln(T(f))\right) \tag{13.6}$$

The term $T(f)$ is introduced to correct from losses due to transmission effects at the two bone/water interfaces and corresponds to the transmission coefficient of the pulse through the sample:

$$T(f) = \frac{4Z_r(f)Z_b(f)}{|Z_r(f) + Z_b(f)|^2} \tag{13.7}$$

where $Z_r(f) = \rho_r V_r(f)$ and $Z_b(f) = \rho_b V_b(f)$ are respectively the acoustic impedance of the reference medium and bone sample. ρ_r and $V_r(f)$ designate respectively the density and the velocity in the reference medium; ρ_b and $V_b(f)$ are respectively the density and the velocity in the bone sample. The values of the velocity $V_b(f)$ should be determined for each sample and each direction [30, 60]. Broadband ultrasonic attenuation (BUA) is defined as the slope of the frequency dependent attenuation and is evaluated using a least-square linear regression within the bandwidth of interest. The value of BUA, when normalized by sample thickness, is referred to as normalized BUA (nBUA) and is equivalent to the frequency slope of the attenuation coefficient.

13.4.2 Order of Magnitude

Table 13.3 shows the different values of the attenuation coefficient obtained in different samples at various frequencies.

Table 13.3 Values of the attenuation coefficient for different frequencies, bone samples and directions of propagation

Reference	Specimen type	Direction of propagation	Centre frequency (MHz)	Mean value of α (dB/cm)
[36]	Bovine	Axial	5	40
			10	60
		Radial	5	55
			10	90
[61]	Bovine	Axial	0.4	12
[35]	Bovine	Axial	5	10.4
			10	20
		Tangential	5	21.7
			10	35
		Radial	5	26
			10	52
	Human	Axial	5	26
			10	61
		Radial	5	39
			10	130

Table 13.4 Results obtained from attenuation measurements in various cortical bone specimens at different frequencies

References	Precision (%)	Type of bone	Samples number	Frequency range (MHz)	Direction	nBUA ($dB\,cm^{-1}$) (MHz^{-1})
[35]	10–15 (CV)	Human femur	4	2–7	Axial	∼3
				8–16	Axial	∼9
		Bovine femur	1	1–7	Axial	∼2
					Radial	∼3
					Tangential	∼3
				8–16	Axial	∼3
					Radial	∼7
					Tangential	∼7
[49]	6.3 (CV)	Horse Metacarpal	– (in vivo)	0.2–0.6	–	6.1
[36]	–	Bovine femur	4	0–25	Axial	∼3
			4	0–30	Radial	∼4
[47]	4.8 (CV)	Bovine femur	5	0.3–0.7	Radial	5–12
[61]	4 (CV)	Bovine femur	120	0.2–0.6	–	10–18
[61]	4 (CV)	Bovine femur	120	0.2–0.6	–	10–18
[26,31]	12 (CV)	Bovine femur	120	3.5–4.5	Axial	3.2 ± 2
	10 (CV)				Radial	4.2 ± 2.4
	12 (CV)				Tangential	4.4 ± 2.9

CV = coefficient of variation

As shown in Table 13.3, the attenuation coefficient has an anisotropic behaviour for the same reasons as the one explained in Sects. 13.1 and 13.3.

The frequency dependence of the attenuation coefficient is of interest since nBUA is used in the clinic in the context of trabecular bone studies. Table 13.4 shows the different values obtained in the literature for nBUA. Han et al. [47] and Serpe and Rho [61] have reported nBUA values around 0.5 MHz in bovine cortical bone. Langton et al. [49] have reported in vivo nBUA values in the same frequency range on horses. Lakes et al. [35] have investigated attenuation in wet cortical bone over a large bandwidth (1–16 MHz). Lees and Klopholz [36] have also evaluated ultrasonic attenuation in wet cortical bone but on a larger frequency range (5–100 MHz). Saulgozis et al. [62, 63] have shown on human tibiae in vivo that attenuation can be related to fracture healing. In a systematic study [26,31] performed with samples obtained from three bovine femoral bone specimen (see Fig. 13.1), the frequency dependence of the attenuation coefficient was investigated in cortical bone around 4 MHz. At these frequencies, the wave length in cortical bone is around 1 mm, which is higher but of the same order of magnitude than the typical size of the main structures (osteons) in bovine cortical bone. For all bone samples, the measured attenuation coefficient showed a quasi-linear variation with frequency in a 1 MHz-wide frequency bandwidth comprised between 3.5 and 4.5 MHz. nBUA could therefore be evaluated in this frequency range with an acceptable accuracy.

In what follows, we focus on a multimodality study including ultrasonic measurements, bone mineral density measurements using DXA and optical microscopy [26, 31], which constitutes a powerful approach in order to investigate the dependence of nBUA on bone properties.

13.4.3 Effect of the Direction of Propagation

As shown in Fig. 13.4, nBUA values obtained in the axial direction are significantly smaller than nBUA values obtained in the radial and tangential directions [26]. ANOVA revealed a significant directional effect ($p < 0.002$). Tuckey-Kramer multiple comparisons revealed a significant difference between axial and radial direction and between axial and tangential directions. However no significant difference was found between radial and tangential directions.

For all anatomical positions, nBUA values obtained in the axial direction were the smallest. Scattering effects can be a reason that might explain the dependence of nBUA on the direction of propagation. In bovine cortical bone, lamellae and osteons are aligned in the axial direction. Therefore, the wave crosses more pores when it propagates perpendicular to the axial direction (i.e. in the radial or tangential directions), and is therefore more strongly attenuated. The lamellae structure also seems to induce scattering effects at the interfaces due to the small difference in the acoustic impedance.

The dependence of nBUA on the direction of propagation can be compared with that found in the study of Yamato et al. [30, 53] where SOS measurements were performed with the same samples in the three directions of propagation. The results obtained with SOS and nBUA can be explained qualitatively by the relative orientation of the direction of propagation and of the main direction of the pores. In the

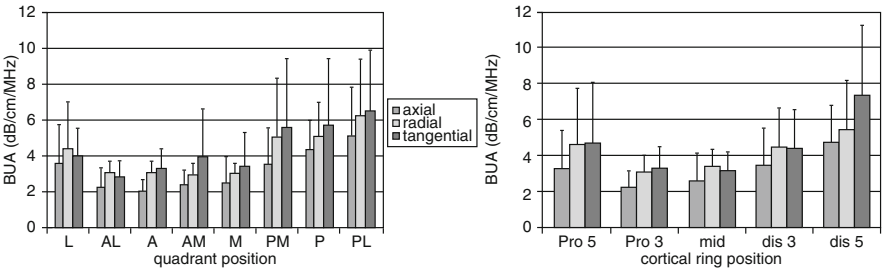

Fig. 13.4 Mean nBUA values and standard deviation (*solid line* on the bar diagram) as a function of (**a**) the quadrant position and (**b**) the position along the bone axis. L is lateral quadrant, AL is antero-lateral quadrant, A is anterior quadrant, AM is antero-medial quadrant, M is medial quadrant, PM is postero-medial quadrant, P is posterior quadrant, and PL is postero-lateral quadrant. Pro5 and pro3 correspond to the cortical rings in the proximal part at 5 and 3 cm from the central part of the shaft. Mid corresponds to the cortical ring at the center part of the shaft. Dis5 and dis3 corresponds to the cortical rings in the distal part at 5 and 3 cm, respectively from the central part of the shaft (Reprinted from [26] copyright (2007) with permission from Elsevier)

axial direction, ultrasonic waves always propagate parallel to the lamellae and osteonal structures. They are then less affected by the pores and interfaces than in the radial or tangential directions

13.4.4 Effect of the Anatomical Location

To assess the influence of the anatomical position on nBUA values, results were first averaged according to the quadrant position and then to the position along the bone axis [26]. The variation of nBUA values as a function of the position along the bone axis (proximal, medial or distal position) is summarized in Fig. 13.4 for the three directions of propagation. The highest nBUA values are obtained in the distal part of the bone whereas the smallest nBUA values can be found in the centero-proximal part of the bone. The variation of nBUA values (averaged according to the position along the bone axis) as a function of the quadrant position are summarized in Fig. 13.4. nBUA values are the highest in the postero-lateral position and the smallest in the antero-medial part. ANOVA test revealed a significant anatomical position effect ($p < 0.005$) for the quadrant and cortical ring position for each of the three directions. The dependence of nBUA on the anatomical location presents the opposite behavior than the one obtained for SOS [30], since nBUA increases with porosity, due to scattering phenomena. This dependence may be explained by the distribution of pore size for the different microstructures. Moreover, this opposite behavior of nBUA compared to SOS might also be due to bone viscoelastic properties. In order to explain in more details our results, the bone matrix viscoelastic behavior should be investigated at a lower scale in the future.

13.4.5 Effect of the Microstructure

The 120 bovine cortical bone samples were manually classified into 4 different histological groups [31]: 47% had a plexiform (Pl) microstructure, 19% a Haversian (H) microstructure, 8% a porotic microstructure (Po) and 26% a mixed microstructure (M) made of samples displaying a combined microstructure.

The average and standard deviation of nBUA values are summarized in Table 13.5 together with density and volumetric Bone Mineral Density (vBMD) for each type of microstructure. In the three directions, plexiform microstructures gave the lowest nBUA values; Haversian nBUA values were greater than plexiform nBUA values but smaller than porotic nBUA. Consistently, mixed microstructure exhibits nBUA values ranging between plexiform and Haversian nBUA values and similar to the overall average nBUA value. vBMD and density value variations are similar but evolve in the opposite way compared to nBUA values for each histological group.

ANOVA analysis revealed a significant effect of microstructure ($p < 10^{-5}$) and of the direction of propagation ($p < 0.002$) on nBUA values. For the axial direction, the Tuckey-Kramer analysis revealed that nBUA values of the plexiform and

Table 13.5 Averaged and standard deviation values of the broadband ultrasonic attenuation in the axial, radial and tangential directions together with sample thickness, density and bone mineral density measured with DXA for the 4 histological groups: Pl, H, Po and M corresponding respectively to the plexiform, Haversian, porotic and mixed microstructures. Table reprinted from [31] copyright (2008), with permission from Elsevier

	Pl	H	Po	M	All structures pooled
nBUA ($dB.MHz^{-1}.\ cm^{-1}$)					
Axial	$2.1 \pm 0.8^{\dagger,\#}$	$4.2 \pm 1.5^{*,\#}$	$7.5 \pm 1.8^{*,\dagger}$	$3.3 \pm 1.8^{*,\#}$	3.2 ± 2.0
Radial	$3.1 \pm 0.8^{\dagger,\#}$	$5.4 \pm 2.2^{*,\#}$	$9.9 \pm 2.8^{*,\dagger}$	$3.5 \pm 0.8^{\dagger,\#}$	4.2 ± 2.4
Tangential	$3.0 \pm 1.1^{\dagger,\#}$	$6.3 \pm 3.1^{*,\#}$	$10.3 \pm 3.6^{*,\dagger}$	$4.1 \pm 1.9^{\dagger,\#}$	4.5 ± 2.9
Density (g/cm^3)	$2.09 \pm 0.02^{\dagger,\#}$	$2.03 \pm 0.04^{*,\#}$	$1.95 \pm 0.05^{*,\dagger}$	$2.06 \pm 0.02^{*,\dagger,\#}$	2.06 ± 0.05
vBMD (g/cm^3)	$1.47 \pm 0.04^{\dagger,\#}$	$1.42 \pm 0.06^{*,\#}$	$1.29 \pm 0.06^{*,\dagger}$	$1.47 \pm 0.06^{\dagger,\#}$	1.45 ± 0.07

The last column shows each quantity averaged for all samples
* significantly different from Pl group
† significantly different from H group
# significantly different from Po group

porotic microstructure were significantly different from those obtained in mixed and Haversian microstructure ($p < 0.005$). However no significant difference was found between the nBUA values obtained in Haversian and mixed microstructures. Similar results were found for density and vBMD values as a function of each histological group. Moreover, in the radial and tangential directions, no significant difference was found between nBUA values in plexiform and mixed microstructures.

The relation between bone microstructure and nBUA may help to understand the dependence of nBUA on the anatomical location described in the last subsections. Lipson and Katz [64] have related bone structure to the remodeling rate, which is regulated by the mechanical stress locally applied to bone. They have shown that Haversian (respectively plexiform) microstructure is predominant in regions of important (respectively low) mechanical stress. In consequence, they mentioned that Haversian microstructure is mainly found in postero-lateral regions and plexiform microstructure in antero-medial regions of the femur. Here, it was found that plexiform microstructure is predominant in the anterior, medial and lateral parts and in posterior part of the mid-diaphysis. Haversian microstructure was mostly found at the diaphysis extremity, in the posterior part. Eventually, porotic microstructure was found in regions where muscles adhere, that is proximal postero-medial part and distal postero-lateral part. nBUA being higher in Haversian than in plexiform microstructure, the anatomical repartition of bone structure may explain the variation of nBUA along the bone axis and circumference.

13.4.6 Correlation with Bone Mineral Density

Data for the correlation between nBUA and density/vBMD in the three directions are summarized in Table 13.6 including equation of the linear regression analysis,

Table 13.6 Determination coefficient (R^2), p-value and root mean square error (RMSE) and equation of the linear regression analysis for the linear regression analysis between nBUA and mass density and nBUA and vBMD for the three directions

	Mass density (ρ)	vBMD
Axial nBUA		
Equation	$nBUA = -34.6\rho + 74.6$	$nBUA = -18.6\,vBMD + 30.1$
R^2	0.65	0.44
p	$<10^{-5}$	$<10^{-5}$
RMSE	1.2	1.5
Radial nBUA		
Equation	$nBUA = -41.9\rho + 90.2$	$nBUA = -25.2\,vBMD + 40.6$
R^2	0.67	0.57
p	$<10^{-5}$	$<10^{-5}$
RMSE	1.4	1.6
Tangential nBUA		
Equation	$nBUA = -47.9\rho + 103.2$	$nBUA = -26.8\,vBMD + 43.2$
R^2	0.55	0.39
p	$<10^{-5}$	$<10^{-5}$
RMSE	2.3	2.0

determination coefficient (R^2), p-value and RMSE. Table 13.6 shows that nBUA values are correlated with vBMD and mass density for all directions of propagation.

As shown in Table 13.6, nBUA decreases with increasing vBMD and density values in cortical bone whereas the opposite behavior has been observed in cancellous bone [65–67]. Results are consistent with previous studies on nBUA measured over a wide range of vBMD [68] and density [61]. These results show that for low density samples (cancellous bone), nBUA increases when density increases and that for high density samples (cortical bone), nBUA decreases when density increases. Moreover, the correlation coefficient between nBUA and density values found for cortical bone is comparable with the values obtained for human trabecular bone sample in vitro ($R^2 = 0.69 - 0.98$) [69] and much higher than what was found by Evans et Tavakoli [70] ($R^2 = 0.11$) in bovine trabecular bone. The correlation coefficient between nBUA and density found in the present study ($R^2 = 0.65$) is slightly higher than the correlation coefficient between axial SOS and density ($R^2 = 0.5$) obtained with the same samples in Yamato et al. [30] which suggests that nBUA exhibit a better correlation with density than SOS.

Interestingly, no correlation was found between nBUA and density when considering plexiform samples only. Moreover, the correlation between nBUA and vBMD ($R^2 = 0.13, p < 0.05$) found for plexiform samples is lower than the one obtained for all structures pooled without plexiform samples (nBUA versus vBMD: $R^2 = 0.49, p < 10^{-5}$, nBUA versus density: $R^2 = 0.59, p < 10^{-5}$). The absence of correlation obtained for the plexiform microstructure may be explained by the smaller effects of scattering due to the lower pore size. In plexiform samples, the influence of density (or vBMD) is reduced and the contribution of bone viscoelastic properties (which depend weakly on vBMD or density) to nBUA values may be more important.

13.4.7 Effect of Viscoelastic and of Scattering Phenomena

Ultrasonic attenuation in bone may result from two different but coupled phenomena: scattering and viscoelasticity. Scattering may occur in cortical bone primarily because of the presence of fluid-filled pores (strong impedance mismatch) but also when the wave goes through interfaces between lamellaes and osteons in interstitial bone tissue. Scattering effects are shown to impact significantly nBUA values in the three directions. Scattering phenomena may also explain the effect of microstructure on attenuation. Because the mean nBUA values obtained for each type of microstructure are similar to the repartition of pore sizes (8–12 μm) for plexiform microstructure, 20–50 μm for Harversian microstructure and 50–300 μm for porotic microstructure, the data seem to reflect the scattering regime.

However, viscoelasticity may also contribute to ultrasonic attenuation in bone. Briefly, absorption can be caused by the viscoelasticity [2] of the bone matrix, which has been modeled in different studies [71–73]. Interstitial tissue between osteons in Haversian microstructure and interfaces between lamellae in plexiform microstructure are known to exhibit a viscoelastic behavior [74, 75]. Moreover, Haversian microstructure contains more interstitial bone than plexiform microstructure. Therefore, bone viscoelastic behavior may also contribute to explain the higher nBUA values obtained for Haversian microstructure than for plexiform microstructure.

13.5 Dispersion Measurements

Velocity dispersion is defined as the slope of the curve of the phase velocity as a function of frequency. Dispersion is an important parameter since it affects SOS measurements. As recalled in Sect. 13.3, there are many different ways of measuring SOS in the laboratory and in the clinics. Wear [76,77] has reported on differences in methods for measuring ultrasonic velocity in bone, including phase and group velocities as well as transit-time-based SOS estimates. Time-of-flight measurements are subject to bias due to the modification of the pulse shape during propagation through bone by frequency-dependent attenuation [76,77] and dispersion [46,78] producing artefacts in SOS measurements. In addition, the ultrasonic velocity obtained using axial transmission devices may also be measured using different signal processing techniques such as time markers (First Arriving Signal, FAS) [79], 2-D fast Fourier transform (FFT) analysis (phase velocity) [80, 81], time frequency analysis (group velocity) [10, 82] or wave extraction techniques [26]. In axial transmission, velocity dispersion measured is influenced by the geometry (e.g. guided wave effects, see Chap. 7 for more details) as well as by phenomena occurring in the bulk of the material. For all these reasons, dispersion is an important acoustical property, influencing significantly any velocity measurements.

13.5.1 Order of Magnitude

Many research groups focused on dispersion studies in trabecular bone [40, 46, 83–87], but considerably less attention has been given to cortical bone. A pioneering work was carried out by Yoon and Katz [88] where the authors were able to measure the ultrasonic velocity as a function of frequency between 2 and 10 MHz in three samples of cortical bone. They found values of dispersion around 13 $m \cdot s^{-1} \cdot MHz^{-1}$. Another work was carried out by Lakes et al. [35] where the authors measured ultrasonic velocity in cortical bone between 1–12 MHz for about ten different frequencies. However, it is not easy to discuss these data in terms of dispersion due to the scale of the graph. In a more recent study, the "sonic" velocity [36] was measured using different transducers in 4 samples of bovine cortical bone, between 5–10 MHz. Dispersion was found to be around 8 ± 4.9 $m \cdot s^{-1} \cdot MHz^{-1}$ in the axial direction, and 13 ± 6.2 $m \cdot s^{-1} \cdot MHz^{-1}$ in the radial direction.

In a recent study [89], samples obtained from three bovine femoral bone specimens (see Fig. 13.1) were used to investigate the dependence of velocity dispersion on bone parameters [89] in the same frequency bandwidth as the one described in Sect. 13.4. In spite of a non-linear variation of the apparent phase velocity over a wide frequency range, the frequency dependence of the apparent phase velocity is quasi-linear over the 1 MHz restricted frequency range around 4 MHz, for all samples in the three directions. The precision of dispersion measurements in the axial (radial and tangential, respectively) direction is equal to 1.3 $m \cdot s^{-1} \cdot MHz^{-1}$ (respectively 0.8 and 1.3 $m \cdot s^{-1} \cdot MHz^{-1}$).

13.5.2 Effect of the Direction of Propagation

Average and standard deviation values of dispersion obtained for the three directions of propagation are summarized in Table 13.7. In average, dispersion values obtained

Table 13.7 Average and standard deviation of the dispersion values in the axial, radial and tangential directions together with density and apparent volumetric bone mineral density measured by DXA for the 4 histological groups.

	Plexiform	Haversian	Porotic	Mixed	All structures pooled
Dispersion ($ms^{-1}\,MHz^{-1}$)					
Axial	$6.1 \pm 3.9^{\#,\in}$	10.6 ± 8.3	$14.7 \pm 6.1^{*}$	$8.5 \pm 5.8^{*}$	8 ± 6.3
Radial	$5.6 \pm 4.6^{\dagger,\#}$	$9.6 \pm 6.0^{*}$	$14.3 \pm 5.5^{*,\in}$	$5.8 \pm 2.4^{\#}$	$6.9 \pm 5.3^{\#}$
Tangential	$5.8 \pm 6.3^{\#}$	5.6 ± 8.0	$20.7 \pm 13.9^{*,\in}$	$4 \pm 9.9^{\#}$	$6.3 \pm 9.2^{\#}$
Density ($g.cm^3$)	$2.09 \pm 0.02^{\dagger,\#}$	$2.03 \pm 0.04^{*,\#}$	$1.95 \pm 0.05^{*,\dagger}$	$2.06 \pm 0.02^{*,\dagger,\#}$	2.06 ± 0.05
BMD ($g.cm^3$)	$1.47 \pm 0.04^{\dagger,\#}$	$1.42 \pm 0.06^{*,\#}$	$1.29 \pm 0.06^{*,\dagger}$	$1.47 \pm 0.06^{\dagger,\#}$	1.45 ± 0.07

The last column shows each quantity averaged for all samples
* significantly different from Pl group
† significantly different from H group
$^{\#}$ significantly different from Po group
$^{\in}$: significantly different from M group

in the axial direction are higher than the ones obtained in the radial and tangential directions. However, the ANOVA test does not reveal a significant directional effect ($p = 0.2$, $F = 1.6$).

13.5.3 Effect of the Anatomical Location

To assess the influence of the anatomical position on dispersion values, results are first averaged according to the quadrant position and then to the position along the bone axis for the three specimens [89]. A diagram of the dispersion values as a function of the anatomical position is shown in Fig. 13.5, which displays the results obtained in the axial direction (this direction is of importance in the context of axial transmission). The highest dispersion values are obtained in the distal part of the bone whereas the smallest dispersion values can be found in the centero-proximal part of the bone. Similar results are obtained for the two other directions of propagation (data not shown). Dispersion values are the highest in the postero-lateral position and the smallest in the anterior part. Again, similar results are obtained for the two other directions of propagation (data not shown). The ANOVA test reveals a significant anatomical position effect of the position around the bone circumference ($p < 2.10^{-6}, F = 25; p < 10^{-10}, F = 45; p < 3.10^{-4}, F = 13$ for the axial, radial and tangential directions, respectively) and for the position along the bone axis ($p < 2.10^{-2}, F = 2.7; p < 8.10^{-3}, F = 3.6; p < 3.10^{-2}, F = 2.6$ for the axial, radial and tangential directions, respectively).

13.5.4 Effect of the Microstructure

The influence of bone microstructure on dispersion measurements is evaluated by averaging dispersion values for each type of microstructure [89]. The average and

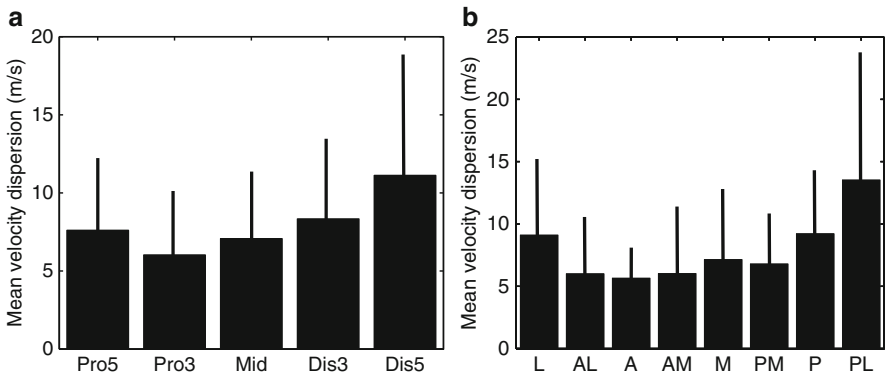

Fig. 13.5 Mean dispersion values and standard deviation (*solid line* on the bar diagram) as a function of (**a**) the position along the bone axis for the axial direction and (**b**) the quadrant position for the axial direction. Same notations as in Fig. 13.4 are used

standard deviation of dispersion values for each histological group are summarized in Table 13.7, together with density and vBMD measurements. For the axial and radial directions of propagation, plexiform microstructures give the lowest mean dispersion values; Haversian dispersion values are greater than plexiform dispersion values but smaller than porotic dispersion. However, results in the tangential direction are slightly different as plexiform and Haversian dispersion values are similar and mixed microstructures give the lowest values of dispersion. vBMD and density variations are similar but evolve in the opposite way compared to dispersion values obtained for each histological group in the axial and radial directions. ANOVA analysis reveals a significant effect of microstructure on dispersion values ($p < 3.10^{-2}$, $F = 2.9$; $p < 10^{-6}$, $F = 9.3$ and $p < 2.10^{-3}$, $F = 5.7$ for the axial, radial and tangential directions respectively). For the axial direction, the Tuckey-Kramer analysis reveals that dispersion values are significantly different ($p < 0.001$) for plexiform and porotic microstructures, and for plexiform and mixed microstructures. No significant difference is found for the other microstructures. For the radial direction, dispersion values are significantly different ($p < 10^{-5}$) for plexiform and porotic microstructures, for plexiform and Haversian microstructures, and for mixed and porotic microstructures. For the tangential direction, dispersion values are significantly different ($p < 0.003$) for plexiform and porotic microstructures, and for mixed and porotic microstructures.

13.5.5 Correlation with Bone Mineral Density

Dispersion values are positively correlated with vBMD and with mass density in the radial direction [89]; the determination coefficient (R^2) between dispersion and vBMD in the radial direction is equal to 0.4 (Root Mean Square error: RMSE $= 3.3\,\mathrm{m \cdot s^{-1}}$, $p < 10^{-5}$). However, dispersion is not correlated with vBMD in the axial and tangential directions. The determination coefficient (R^2) between dispersion and mass density is equal to 0.33 (Root Mean Square error: RMSE $= 3.5\,\mathrm{m \cdot s^{-1} \cdot MHz^{-1}}$, $p < 10^{-5}$) in the radial directions.

13.5.6 Negative Values of Velocity Dispersion

In this study [89], negative values of dispersion were obtained in nine samples. Table 13.8 shows the characteristics of the samples where negative dispersion is measured, together with the mean value and standard deviation (corresponding to the reproducibility of the measurements) of the dispersion and the direction of propagation. The reproducibility of the measurement obtained for the samples where negative dispersion is measured is slightly higher than the average reproducibility. However, this relatively poor precision does not affect the main conclusion obtained on negative dispersion because in all cases, the standard deviation is lower

Table 13.8 Characteristics of the samples where negative values of dispersion are measured with our ultrasonic device. The dispersion value and standard deviation and the direction of propagation are also indicated

Bovine number	Axial position	Quadrant position	Type of Structure	Direction of propagation	Dispersion value ($m \cdot s^{-1} \cdot MHz^{-1}$)
1	Pro5	P	M	Tan	-13 ± 3.5
1	Dis5	A	M	Tan	-12.4 ± 5.9
1	Dis5	AM	M	Tan	-5.2 ± 2.7
1	Dis5	AL	M	Tan	-10.9 ± 3.2
2	Dis5	A	M	Tan	-7 ± 4
2	Dis5	AM	M	Ax	-3.3 ± 1.1
2	Dis5	AM	M	Tan	-5.5 ± 1.9
3	Dis5	AM	Ha	Tan	-21.1 ± 4.8
3	Dis5	PM	M	Tan	-16.2 ± 6.1

in absolute value than the mean dispersion value. Negative values of dispersion are measured mostly in the tangential direction of propagation (eight samples out of nine). Moreover, about 89% of the samples for which negative values of dispersion are measured are of mixed microstructure, which is higher than the total proportion of mixed microstructure (26%).

A possible explanation of the negative values of dispersion has been given in a recent study, in the context of trabecular bone [90] (see Chap. 12 of the present book) where the authors nicely showed that negative values of dispersion may result from the interference of two broadband ultrasonic pulses arriving on the receiver with a time delay. A similar interpretation could be applied to the case of cortical bone, which is a heterogeneous medium where wave splitting may occur, when different parts of the wavefront propagate at different sound speed [30, 53]. This effect is likely to be more pronounced for the mixed structures which are inherently more heterogeneous. In the tangential direction, the mean apparent phase velocity is equal to $3617 \pm 113\,m \cdot s^{-1} \cdot MHz^{-1}$, $3513 \pm 162\,m \cdot s^{-1} \cdot MHz^{-1}$ and $3283 \pm 147\,m \cdot s^{-1} \cdot MHz^{-1}$ in plexiform, Haversian and porotic microstructures, respectively [30]. Two ultrasonic pulses may interfere with a time delay depending on the respective velocity in both media and on the sample length, leading to a comparable situation as the one obtained by Marutyan et al.

The structural organization of bovine cortical bone has been shown to be approximately axially symmetric [91]. The model of Marutyan et al., in combination with the description of the microstructural organization of cortical bone, may explain (i) why most samples with negative dispersion are of mixed microstructure and (ii) why all bone samples with negative dispersion are measured in the axial or tangential direction. In addition, the relatively poor reproducibility obtained for samples with negative dispersion may also be roughly explained by the model of Marutyan et al., who showed that dispersion was strongly sensitive to the relative amplitude of both interfering components. The amplitude of the two wavefronts may be affected by a slightly different positioning of the sample relatively to the transducer locations.

Here, negative values of dispersion were never measured in porous microstructure, which might seem surprising because porous microstructures are known to lead to the propagation of two longitudinal wave modes (as described by the Biot theory [92, 93]), which may lead to negative dispersion [90]. However, the possibility of measuring two separated longitudinal wave modes propagating in trabecular bone depends on a complex combination of several factors, such as bone volume fraction, direction of propagation and structural anisotropy [94] (see Chaps. 5 and 11). There is no evidence to suggest that these conditions are fulfilled in the case of cortical bone in the framework of our experimental setup.

Another possible physical explanation for negative values of dispersion may be multiple scattering phenomena, which are known to be responsible for negative values of dispersion in trabecular bone [95]. However, further investigation is needed to evidence such effect as no reports could be found in the literature on multiple scattering in cortical bone. Note that negative values of velocity dispersion have also been obtained in Swine cortical bone samples in a recent study [96].

13.5.7 Relationship with Broadband Ultrasonic Attenuation

13.5.7.1 Correlation nBUA/Dispersion

Broadband ultrasonic attenuation (nBUA) measurements (given by the slope of the frequency dependent attenuation coefficient versus frequency) have been performed on the same samples [26, 31] (see Sect. 13.3) and are compared with the dispersion results. Figure 13.6 shows the relationship between dispersion and nBUA values for all bone samples and in the three directions of propagation.

The dashed black and gray lines of Fig. 13.6 show the linear regression between dispersion and nBUA values obtained respectively in the radial ($R^2 = 0.73, p < 10^{-5}$) and axial ($R^2 = 0.28, p < 10^{-5}$) directions. The linear regression obtained for the tangential direction is not indicated because no correlation was found for this direction.

In Sect. 13.4, we have shown that nBUA is significantly correlated with vBMD for the three directions (R^2 comprised between 0.55 and 0.67). The correlation between nBUA and vBMD, together with the correlation between dispersion and nBUA in the radial direction may explain our results showing that the dispersion and vBMD values are also correlated in the radial direction.

13.5.7.2 Using Kramers-Kronig Relationship?

In order to better understand the results shown in Fig. 13.6, we used the formulae obtained in [97, 98], describing the local Kramers-Kronig (KK) relationships to derive an expression between the frequency dependence of the attenuation coefficient and that of phase velocity, assuming that (i) the attenuation coefficient is known over

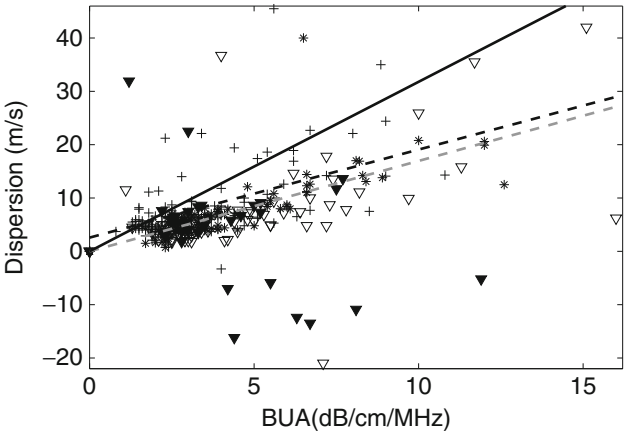

Fig. 13.6 Dependence of dispersion values as a function of nBUA values for each direction of propagation. Crosses correspond to the axial direction of propagation and stars to the radial one. *Filled triangles* correspond to samples of mixed microstructure measured in the tangential direction and *open triangles* correspond to samples of other microstructure measured in the tangential direction. The *solid black line* shows the results obtained by using the Kramers-Kronig relationships. The *dashed black* and *gray lines* show the linear regression between dispersion and nBUA values obtained respectively in the radial ($R^2 = 0.73, p < 10^{-5}$) and axial ($R^2 = 0.28, p < 10^{-5}$) directions (no correlation was obtained in the tangential direction)

the entire frequency bandwidth, (ii) the system is linear, (iii) causality is respected, (iv) the attenuation and dispersion do not vary rapidly as a function of frequency and (v) the material is homogenous. Assuming a linear variation of the attenuation coefficient versus frequency over the entire bandwidth, the KK relationships lead to a logarithmic variation of phase velocity as a function of frequency. The slope D of the phase velocity at 4 MHz as a function of frequency is an estimate of dispersion and is then given by [97, 98]:

$$D = \frac{100 \cdot BUA \cdot \mathrm{V_b^2(f)}}{8.68 \cdot \pi^2 \cdot \mathrm{f}} \tag{13.8}$$

provided that $nBUA$ and f are respectively given in $\mathrm{dB.MHz^{-1}.cm^{-1}}$ and in MHz. The solid black line in Fig. 13.6 corresponds to the representation of the relation given by Eq. (13.8). Here, $\mathrm{V_b^{(f)}} = \mathrm{V_b^{(4\,MHz)}}$ is chosen equal to $3305\,\mathrm{m \cdot s^{-1}}$, because this value corresponds approximately to the mean phase velocity for the radial direction, which exhibits the best correlation between nBUA and dispersion.

The KK relationships predict an increase of dispersion values when nBUA increases, which is consistent with the results shown in Fig. 13.6 for the radial and axial directions. However, the slope of the linear fit obtained between the dispersion and nBUA values is overestimated by the KK relationships compared to the experimental results in the axial and radial directions.

Several reasons may explain this discrepancy. First, KK relationships cannot be applied when two waves overlap, resulting in phase cancellation effects. Bone is an heterogeneous structure in which the Kramers-Kronig argument must be applied with caution. Second, the non linear variation of the attenuation coefficient [26] as a function of frequency over the entire frequency bandwidth, which is an assumption used to derive Eq. 13.8, may also cause this same discrepancy. More generally, it seems that some difficulties may come from the interpretation of the general Kramers-Kronig relationships using a linear frequency-dependence for attenuation and dispersion. The linear fit of phase velocity in the considered frequency range is actually an approximation of the real dispersion. In addition, the signal spectra used here are inherently bandwidth limited by the transducers and therefore it was necessary to extend the attenuation law from the measured bandwidth over all frequencies [99].

13.6 Conclusion

In this chapter, we have reviewed the different results obtained in the literature dealing with in vitro quantitative ultrasonic parameters applied to cortical bone samples. Mainly, three parameters have been investigated: the ultrasonic velocity, broadband ultrasonic attenuation and velocity dispersion. The results presented in the present review might help understanding the interaction between an ultrasonic wave and this complex (heterogeneous, viscoelastic) medium, which may lead to new developments in the domain of ultrasonic devices applied to bone characterization. Interestingly, different multimodality analyses have shown that these three parameters are related to the direction of propagation as well as to different bone properties such as volumetric bone mineral density, mass density and the type of microstructure. These results show the potentiality of ultrasonic techniques to investigate cortical bone quality.

References

1. H. Rico, “The therapy of osteoporosis and the importance of cortical bone,” Calcif Tissue Int **61**, 431–432 (1997).
2. S. C. Cowin, *Bone Mechanics Handbook*, 2nd ed. (CRC Press, Boca Raton, 2001).
3. P. M. Mayhew, C. D. Thomas, J. G. Clement, N. Loveridge, T. J. Beck, W. Bonfield, C. J. Burgoyne, and J. Reeve, “Relation between age, femoral neck cortical stability, and hip fracture risk,” Lancet **366**(9480), 129–135 (2005).
4. M. Grynpas, “Age and disease-related changes in the mineral of bone,” Calcif Tissue Int **53**, S57–64 (1993).
5. J. D. Currey, “The relationship between the stiffness and the mineral content of bone,” J Biomech **2**(4), 477–480 (1969).
6. J. Foldes, A. M. Parfitt, M. S. Shih, D. S. Rao, and M. Kleerekoper, “Structural and geometric changes in iliac bone: relationship to normal aging and osteoporosis,” J Bone Miner Res **6**(7), 759–766 (1991).

7. E. Bossy, M. Talmant, M. Defontaine, F. Patat, and P. Laugier, "Bidirectional axial transmission can improve accuracy and precision of ultrasonic velocity measurement in cortical bone: a validation on test materials," IEEE Trans Ultrason Ferroelectr Freq Control **51**(1), 71–79 (2004).
8. R. Barkmann, E. Kantorovich, C. Singal, D. Hans, H. K. Genant, M. Heller, and C. C. Gluer, "A new method for quantitative ultrasound measurements at multiple skeletal sites: first results of precision and fracture discrimination," J Clin Densitom **3**(1), 1–7 (2000).
9. R. Barkmann, S. Lusse, B. Stampa, S. Sakata, M. Heller, and C. C. Gluer, "Assessment of the geometry of human finger phalanges using quantitative ultrasound in vivo," Osteoporos Int **11**(9), 745–755 (2000).
10. I. Mano, K. Horii, S. Takai, T. Suzaki, H. Nagaoka, and T. Otani, "Development of novel ultrasonic bone densitometry using acoustic parameters of cancellous bone for fast and slow waves," Jpn J Appl Phys **45**(5B), 4700–4702 (2006).
11. V. Sansalone, S. Naili, V. Bousson, C. Bergot, F. Peyrin, J. D. Laredo, and G. Haïat, "Determination of the heterogeneous anisotropic elastic properties of human femoral bone: from nanoscopic to organ scale," J Biomech **43**(10), 1857–1863 (2010).
12. V. Bousson, A. Meunier, C. Bergot, E. Vicaut, M. A. Rocha, M. H. Morais, A. M. Laval-Jeantet, and J. D. Laredo, "Distribution of intracortical porosity in human midfemoral cortex by age and gender," J Bone Miner Res **16**(7), 1308–1317 (2001).
13. C. D. Thomas, S. A. Feik, and J. G. Clement, "Regional variation of intracortical porosity in the midshaft of the human femur: age and sex differences," J Anat **206**(2), 115–125 (2005).
14. S. Naili, M.-B. Vu, Q. Grimal, M. Talmant, C. Desceliers, C. Soize, and G. Haïat, "Influence of viscoelastic and viscous absorption on ultrasonic wave propagation in cortical bone: application to axial transmission," J Acoust Soc Am **127**(4), 2622–2634 (2010).
15. G. Haïat, S. Naili, Q. Grimal, M. Talmant, C. Desceliers, and C. Soize, "Influence of a gradient of material properties on ultrasonic wave propagation in cortical bone: application to axial transmission," J Acoust Soc Am **125**(6), 4043–5052 (2009).
16. J. Y. Rho, "An ultrasonic method for measuring the elastic properties of human tibial cortical and cancellous bone," Ultrasonics **34**(8), 777–783 (1996).
17. H. S. Yoon and J. L. Katz, "Ultrasonic wave propagation in human cortical bone-II. Measurements of elastic properties and microhardness," J Biomech **9**(7), 459–464 (1976).
18. X. N. Dong and X. E. Guo, "The dependence of transversely isotropic elasticity of human femoral cortical bone on porosity," J Biomech **37**(8), 1281–1287 (2004).
19. H. S. Yoon and J. L. Katz, "Ultrasonic wave propagation in human cortical bone-I. Theoretical considerations for hexagonal symmetry," J Biomech **9**(7), 407–412 (1976).
20. S. S. Mehta, O. K. Oz, and P. P. Antich, "Bone elasticity and ultrasound velocity are affected by subtle changes in the organic matrix," J Bone Miner Res **13**(1), 114–121 (1998).
21. J. L. Katz and A. Meunier, "The elastic anisotropy of bone," J Biomech **20**, 1063–1070 (1987).
22. B. K. Hoffmeister, S. R. Smith, S. M. Handley, and J. Y. Rho, "Anisotropy of Young's modulus of human tibial cortical bone," Med Biol Eng Comput **38**(3), 333–338 (2000).
23. R. B. Ashman, S. C. Cowin, W. C. Van Buskirk, and J. C. Rice, "A continuous wave technique for the mesurement of the elastic properties of cortical bone," J Biomech **17**, 349–361 (1984).
24. W. Van Buskirk, S. Cowin, and R. Ward, "Ultrasonic measurement of orthotropic elastic constants of bovine femoral bone," J Biomech Eng **2**, 67–72 (1981).
25. D. Royer and E. Dieulesaint, *Elastic Waves in Solids I: Free and Guided Propagation* (New York, 2000).
26. M. Sasso, G. Haïat, Y. Yamato, S. Naili, and M. Matsukawa, "Frequency dependence of ultrasonic attenuation in bovine cortical bone: an in vitro study," Ultrasound Med Biol **33**(12), 1933–1942 (2007).
27. Y. Yamato, H. Kataoka, M. Matsukawa, K. Yamazaki, T. Otani, and A. Nagano, "Distribution of longitudinal wave velocities in bovine cortical bone in vitro.," Jpn J Appl Phys **44**(6B), 4622–4624 (2005).
28. M. Locke, "Structure of long bones in mammals," J Morphol **262**(2), 546–565 (2004).
29. J. Currey, "Comparative mechanical properties and histology of bone," Am Zool **24**(5), 5–12 (1984).

30. Y. Yamato, M. Matsukawa, T. Otani, K. Yamazaki, and A. Nagano, "Distribution of longitudinal wave properties in bovine cortical bone in vitro," Ultrasonics **44**(Suppl 1), e233–237 (2006).
31. M. Sasso, G. Haïat, Y. Yamato, S. Naili, and M. Matsukawa, "Dependence of ultrasonic attenuation on bone mass and microstructure in bovine cortical bone," J Biomech **41**(2), 347–355 (2008).
32. S. Bensamoun, J.-M. Gherbezza, J.-F. de Belleval, and M.-C. Ho Ba Tho, "Transmission scanning acoustic imaging of human cortical bone and relation with the microstructure," Clin Biomech **19**, 639–647 (2004).
33. S. Bensamoun, M.-C. Ho Ba Tho, S. Luu, J.-M. Gherbezza, and J.-F. de Belleval, "Spatial distribution of acoustic and elastic properties of human femoral cortical bone," J Biomech **37**, 503–510 (2004).
34. Q. Grimal, S. Haupert, D. Mitton, L. Vastel, and P. Laugier, "Assessment of cortical bone elasticity and strength: mechanical testing and ultrasound provide complementary data," Med Eng Phys **31**(9), 1140–1147 (2009).
35. R. S. Lakes, H. S. Yoon, and J. L. Katz, "Ultrasonic wave propagation and attenuation in wet bone," J Biomed Eng **8**, 143–148 (1986).
36. S. Lees and D. Z. Klopholz, "Sonic velocity and attenuation in wet compact cow femur for the frequency range 5 to 100 MHz," Ultrasound Med Biol **18**(3), 303–308 (1992).
37. H. Theismann and F. Pfander, "Über die Durchlässigkeit des Knochens für Ultraschall," Strahlentherapie **80**, 607–610 (1949).
38. W. Güttner, "Die Energieverteilung im menschlichen Körper bei Ultraschall-Einstrahlung," Acustica **4**, 547–554 (1954).
39. D. Goldman and T. Hueter, "Tabular data of the velocity and absorption of high frequency sound in mammalian tissues," J Acoust Soc Am **28**, 35–37 (1956).
40. P. Droin, G. Berger, and P. Laugier, "Velocity dispersion of acoustic waves in cancellous bone," IEEE Trans Ultrason Ferroelec Freq Contr **45**(3), 581–592 (1998).
41. W. A. Verhoef, J. T. M. Cloosterman, and J. M. Thijssen, "Diffraction and velocity dispersion effectson the estimation of ultrasound attenuation and velocity in biological tissues," IEEE Trans Biomed Eng **32**, 521–529 (1985).
42. G. S. Kino, *Acoustic Waves: Devised Imaging and Analog Signal* (Prentice Hall, New Jersey, 1987).
43. J. J. Kaufman, W. Xu, A. E. Chiabrera, and R. S. Siffert, "Diffraction effects on insertion mode estimation of ultrasonic group velocity," IEEE Trans Ultrason Ferroelect Freq Contr **42**, 232–242 (1995).
44. W. Xu and K. J, "Diffraction methods for insertion ultrasound attenuation estimation," IEEE trans Biomed Eng **40**(6), 563 (1993).
45. G. Haiat, F. Padilla, R. Barkmann, S. Dencks, U. Moser, C. C. Gluer, and P. Laugier, "Optimal prediction of bone mineral density with ultrasonic measurements in excised human femur," Calcif Tissue Int **77**(3), 186–192. Epub 2005 Sep 2015 (2005).
46. G. Haïat, F. Padilla, R. Cleveland, and P. Laugier, "Effect of frequency dependent attenuation and dispersion on different speed of sound measurements on human intact femur," IEEE Trans Ultrason Ferroelectr Freq Control **53**(1), 39–51 (2006).
47. S. Han, J. Rho, J. Medige, and I. Ziv, "Ultrasound velocity and broadband attenuation over a wide range of bone mineral density," Osteoporos Int **6**(4), 291–296 (1996).
48. S. Lees, P. F. Cleary, J. D. Heeley, and E. L. Gariepy, "Distribution of sonic plesio-velocity in a compact bone sample," J Acoust Soc Am **66**(3), 641–646 (1979).
49. C. M. Langton, A. V. Ali, C. M. Riggs, G. P. Evans, and W. Bonfield, "A contact method for the assessment of ultrasonic velocity and broadband attenuation in cortical and cancellous bone," Clin Phys Physiol Meas **11**, 243–249 (1990).
50. C. F. Njeh, D. Hans, T. Fuerst, C.-C. Glüer, and H. K. Genant, "Ultrasonic studies of cortical bone in vitro," in *Quantitative Ultrasound Assessment of Osteoporosis and Bone Status* (Martin Dunitz, London, 1999), p. 177.
51. W. Abendschein and G. W. hyatt, "Ultrasonic and selected physical properties of bone," Clin Orthop Relat Res **69**, 294–301 (1970).

52. W. Bonfield and A. Tulley, "Ultrasonic analysis of the Young's modulus of cortical bone," J Biomed Eng **4**, 23–27 (1982).
53. Y. Yamato, H. Kataoka, M. Matsukawa, K. Yamazaki, T. Otani, and A. Nagano, "Distribution of longitudinal wave velocities in bovine cortical bone in vitro.," Jpn J Appl Phys **44**(6B), 4622–4624 (2005).
54. C. Hellmich, J. Barthelemy, and L. Dormieux, "Mineral–collagen interactions in elasticity of bone ultrastructure – a continuum micromechanics approach," Eur J Mech A Solids **23**, 783–810 (2004).
55. C. Hellmich and F. J. Ulm, "Micromechanical model for ultrastructural stiffness of mineralized tissues," J Eng Mech **128**(8), 898–908 (2002).
56. Y. Yamato, M. Matsukawa, H. Mizukawa, T. Yanagitani, K. Yamazaki, and A. Nagano, "Distribution of hydroxyapatite crystallite orientation and ultrasonic wave velocity in ring-shaped cortical bone of bovine femur," IEEE Trans Ultrason Ferroelectr Freq Control **55**(6), 1298–1303 (2008).
57. Y. Yaoi, K. Yamamoto, Y. Yamato, T. Yanagiteani, M. Matsukawa, K. Yamazaki, and A. Nagano, "Distribution of longitudinal wave velocity and hydroxyapatite crystallite orientation in bovine cortical bone," Acoust Sci Tech **30**(4), 306–309 (2009).
58. Y. Yamato, M. Matsukawa, T. Yanagitani, K. Yamazaki, H. Mizukawa, and A. Nagano, "Correlation between hydroxyapatite crystallite orientation and ultrasonic wave velocities in bovine cortical bone," Calcif Tissue Int **82**(2), 162–169 (2008).
59. Y. Yaoi, K. Yamamoto, T. Nakatsuji, T. Yanagitani, M. Matsukawa, K. Yamazaki, and A. Nagano, "Anisotropy of longitudinal wave velocity an hydroxyapatite orientation in bovine cortical bone," Jpn J Appl Phys **48**(4), 07GK06 (2009).
60. Y. Yamato, H. Kataoka, M. Matsukawa, K. Yamazaki, T. Otani, and A. Nagano, "Distribution of longitudinal wave velocities in bovine cortical bone in vitro," Jpn J Appl Phys **44**(6B), 4622–4624 (2005).
61. L. Serpe and J. Y. Rho, "The nonlinear transition period of broadband ultrasonic attenuation as bone density varies," J Biomech **29**, 963–966 (1996).
62. J. Vilks, G. O. Pfafrod, K. A. Yanson, and Y. Z. Saulgozis, "An experimental study of the effect of fracture and operative intervention on acoustical properties of human tibial bone," Mech Compos Mater **10**, 771–778 (1977).
63. J. Saulgozis, I. Pontaga, G. Lowet, and G. Van der Perre, "The effect of fracture and fracture fixation on ultrasonic velocity and attenuation," Physiol Meas **17**, 201–211 (1996).
64. S. F. Lipson and J. L. Katz, "The relationship between elastic properties and microstructure of bovine cortical bone," J Biomech **17**(4), 231–240 (1984).
65. G. Haïat, F. Padilla, R. Barkmann, C. C. Gluer, and P. Laugier, "Numerical simulation of the dependence of quantitative ultrasonic parameters on trabecular bone microarchitecture and elastic constants," Ultrasonics **44**(1), e289–294 (2006).
66. F. Jenson, F. Padilla, V. Bousson, C. Bergot, J. D. Laredo, and P. Laugier, "In vitro ultrasonic characterization of human cancellous femoral bone using transmission and backscatter measurements: relationships to bone mineral density," J Acoust Soc Am **119**(1), 654–663 (2006).
67. G. Haiat, F. Padilla, F. Peyrin, and P. Laugier, "Variation of ultrasonic parameters with microstructure and material properties of trabecular bone: a 3D model simulation," J Bone Miner Res **22**(5), 665–674 (2007).
68. S. Han, J. Rho, J. Medige, and I. Ziv, "Ultrasound velocity and broadband attenuation over a wide range of bone mineral density," Osteoporosis Int **6**(4), 291–296 (1996).
69. C. F. Njeh, C. M. Boivin, and C. M. Langton, "The role of ultrasound in the assessment of osteoporosis: a review," Osteoporosis Int **7**, 7–22 (1997).
70. J. A. Evans and M. B. Tavakoli, "Ultrasonic attenuation and velocity in bone," Phys Med Biol **35**(10), 1387–1396 (1990).
71. N. Sasaki, Y. Nakayama, M. Yoshikawa, and A. Enyo, "Stress relaxation function of bone and bone collagen," J Biomech **26**(12), 1369–1376 (1993).
72. T. Iyo, Y. Maki, N. Sasaki, and M. Nakata, "Anisotropic viscoelastic properties of cortical bone," J Biomech **37**(9), 1433–1437 (2004).

73. T. Iyo, N. Sasaki, Y. Maki, and M. Nakata, "Mathematical description of stress relaxation of bovine femoral cortical bone," Biorheology **43**(2), 117–132 (2006).
74. R. S. Lakes and J. L. Katz, "Viscoelastic properties of wet cortical bone – II. Relaxation mechanisms," J Biomech **12**, 679–687 (1979).
75. R. S. Lakes and S. Saha, "Cement line motion in bone," Science **204**, 501–505 (1979).
76. K. A. Wear, "The effects of frequency-dependant attenuation and dispersion on sound speed measurements: applications in human trabecular bone," IEEE Trans Ultrason Ferroelect Freq Contr **47**(1), 265–273 (2000).
77. K. A. Wear, "A numerical method to predict the effects of frequency-dependent attenuation and dispersion on speed of sound estimates in cancellous bone," J Acoust Soc Am **109**(3), 1213–1218 (2001).
78. K. A. Wear, "The dependence of time-domain speed-of-sound measurements on center frequency, bandwidth, and transit-time marker in human calcaneus in vitro," J Acoust Soc Am **122**(1), 636–644 (2007).
79. E. Bossy, M. Talmant, F. Peyrin, L. Akrout, P. Cloetens, and P. Laugier, "An in vitro study of the ultrasonic axial transmission technique at the radius: 1-MHz velocity measurements are sensitive to both mineralization and intracortical porosity.," J Bone Miner Res **19**(9), 1548–1556 (2004).
80. P. Moilanen, "Ultrasonic guided waves in bone," IEEE Trans Ultrason Ferroelectr Freq Control **55**(6), 1277–1286 (2008).
81. F. Lefebvre, Y. Deblock, P. Campistron, D. Ahite, and J. J. Fabre, "Development of a new ultrasonic technique for bone and biomaterials in vitro characterization," J Biomed Mater Res **63**(4), 441–446 (2002).
82. V. C. Protopappas, D. I. Fotiadis, and K. N. Malizos, "Guided ultrasound wave propagation in intact and healing long bones," Ultrasound Med Biol **32**(5), 693–708 (2006).
83. P. H. F. Nicholson, G. Lowet, C. M. Langton, J. Dequeker, and G. Van der Perre, "A comparison of time-domain and frequency domain approaches to ultrasonic velocity measurement in trabecular bone," Phys Med Biol **41**, 2421–2435 (1996).
84. R. Strelitzki and J. A. Evans, "On the measurement of the velocity of ultrasound in the os calcis using short pulses," Eur J Ultrasound **4**, 205–213 (1996).
85. K. Wear, "Measurements of phase velocity and group velocity in human calcaneus," Ultrasound Med Biol **26**(4), 641–646 (2000).
86. K. A. Wear, "A stratified model to predict dispersion in trabecular bone," IEEE Trans Ultrason Ferroelect Freq Control **48**(4), 1079–1083 (2001).
87. K. A. Wear, "Group velocity, phase velocity, and dispersion in human calcaneus in vivo," J Acoust Soc Am **121**(4), 2431–2437 (2007).
88. H. S. Yoon and J. L. Katz, "Ultrasonic wave propagation inhuman cortical bone-II. Measurements of elastic properties and microhardness," J Biomech **9**, 459–464 (1976).
89. G. Haiat, M. Sasso, S. Naili, and M. Matsukawa, "Ultrasonic velocity dispersion in bovine cortical bone: an experimental study," J Acoust Soc Am **124**(3), 1811–1821 (2008).
90. K. R. Marutyan, G. L. Bretthorst, and J. G. Miller, "Bayesian estimation of the underlying bone properties from mixed fast and slow mode ultrasonic signals," J Acoust Soc Am **121**(1), EL8–15 (2007).
91. M. Locke, "Structure of long bones in mammals," J Morphol **262**(2), 546–565 (2004).
92. M. A. Biot, "Theory of propagation of elastic waves in a fluid-saturated porous solid. I. Low-frequency range," J Acoust Soc Am **28**(2), 168–178 (1956).
93. M. A. Biot, "Theory of propagation of elastic waves in a fluid-saturated porous solid. II. Higher frequency range," J Acoust Soc Am **28**(2), 179–191 (1956).
94. G. Haiat, A. Lhemery, F. Renaud, F. Padilla, P. Laugier, and S. Naili, "Velocity dispersion in trabecular bone: influence of multiple scattering and of absorption," J Acoust Soc Am **124**(6), 4047–4058 (2008).
95. G. Haïat, F. Padilla, P. Laugier, S. Lonné, and S. Naili, "Modeling the frequency dependence of phase velocity in phantoms of trabecular bone," presented at the International congress on ultrasonics, Vienna, Austria, 2007.

96. T. Koizumi, K. Yamamoto, T. Nakatsuji, and M. Matsukawa, "Dispersion of Longitudinal Wave Velocity in Swine Cortical Bone," presented at the 2009 IEEE International Ultrasonics Symposium, Roma, Italy, 2009.
97. M. O'Donnell, E. T. Jaynes, and J. G. Miller, "General relationships between ultrasonic attenuation and dispersion," J Acoust Soc Am **63**(6) (1978).
98. M. O'Donnell, E. T. Jaynes, and J. G. Miller, "Kramers-Kronig relationship between ultrasonic attenuation and phase velocity," J Acoust Soc Am **69**(3), 696–701 (1981).
99. K. R. Waters, M. S. Hughes, G. H. Brandeburger, and J. G. Miller, "On the applicability of Kramers-Krönig relations for ultrasonic attenuation obeying a frequency power law," J Acoust Soc Am **108**(2), 556–563 (2000).

Chapter 14
Ultrasonic Monitoring of Fracture Healing

Vasilios C. Protopappas, Maria G. Vavva, Konstantinos N. Malizos, Demos Polyzos, and Dimitrios I. Fotiadis

Abstract Quantitative ultrasound has been used to evaluate bone fracture healing for over five decades. Animal and clinical studies have showed that the propagation velocity and attenuation are significantly different between fresh fractures, bone unions, and delayed unions or non-unions. Follow-up measurements have also indicated that the velocity typically increases during healing which makes feasible to monitor the healing progress and early distinguish between normal healing and delayed unions. Researchers have recently used computer simulations aiming to gain insight into the underlying mechanisms of wave propagation in healing bones and interpret real measurements. In this chapter we present the state of the art in the field and provide an extensive review of the relevant literature.

Keywords Bone phantoms · Callus tissue · First-arriving signals (FAS) · Fracture healing · Guided waves · Monitoring · Non-union · Numerical simulations · Propagation velocity · Time-frequency analysis

V.C. Protopappas (✉) and D. Polyzos
Department of Mechanical Engineering and Aeronautics, University of Patras, GR 26 500 Patras, Greece
e-mail: vprotop@mech.upatras.gr; polyzos@mech.upatras.gr

M.G. Vavva
Research Academic Computer Technology Institute, University Campus of Patras, GR 26 500 Patras, Greece
e-mail: mvavva@cc.uoi.gr

K.N. Malizos
Department of Orthopaedic Surgery & Musculoskeletal Trauma, University Hospital of Larissa, School of Health Sciences, University of Thessaly, GR 412 22 Larissa, Greece
e-mail: malizos@med.uth.gr

D.I. Fotiadis
Unit of Medical Technology and Intelligent Information Systems, Department of Material Sciences and Engineering, University of Ioannina, GR 45 110 Ioannina, Greece
e-mail: fotiadis@cs.uoi.gr

P. Laugier and G. Haïat (eds.), *Bone Quantitative Ultrasound*,
DOI 10.1007/978-94-007-0017-8_14,

14.1 Introduction

Millions of fractures occur annually as a result of traumatic injuries or pathological conditions. Bone fracture healing is a self-regulated regenerative process which involves the spatial and temporal coordinated action of many different cell types and proteins and the expression of hundreds of genes. Fundamental processes in the healing course are the formation, progressive differentiation and ossification of the fracture callus tissue which occur until the repairing bone regains its initial mechanical properties, structural integrity and geometry.

The time to healing is an important parameter related to fracture characteristics, magnitude of tissue damage, patient's general health and mode of treatment. Although most fractures will successfully heal within a few months, 5–10% of cases experience complications, such as delayed union or pseudarthrosis (non-union), which require further conventional or surgical secondary procedures. In both types of complication, the already prolonged treatment period further extends and becomes responsible for substantial morbidity and interference with personal and vocational productivity which in turn result in major direct and indirect personal, societal and monetary costs.

In clinical practice, bone healing is evaluated by means of serial clinical and radiographic examinations; however, both of them are largely dependent on orthopaedic surgeons' expertise and clinical judgment [1]. From a biomechanical point of view, the healing bone exhibits a gradual increase in its strength and stiffness until these properties are sufficient for weight bearing which is an indication for bone union. In this respect, significant research has been carried out for the development of biomechanical methods for directly or indirectly assessing the rate of increase of the mechanical properties and thus providing quantitative monitoring means. Biomechanical monitoring of fracture healing can assist the treating physicians in early detecting healing complications, determining the progress of the healing process and defining an objective and measurable endpoint of the healing course. Among the various biomechanical methods that have been proposed for the monitoring of fracture healing in long bones [2], the most popular ones include the attachment of strain gauges to external fixation devices for measuring the axial or bending deformation [2–4], the use of vibrational testing [3, 5, 6] and the acoustic emission technique [7]. All these methods are successful in determining the extrinsic mechanical properties of the healing bone, such as the stiffness, and have managed to provide useful indications on the healing progress. However, they are generally influenced by gross properties, such as the type and size of bone, the type and geometry of fracture, etc. Furthermore, most of the above methods may only be performed in clinical settings where an expert is needed to configure the measuring set-up and a number of them can be applied only to fracture cases treated with external fixators several of which further require the temporary removal of the frame of the fixation device [2–6].

Quantitative ultrasound has been used to evaluate and monitor fracture healing for over five decades [8]. The most suitable technique for examining long bones is the axial transmission (see Chaps. 3 and 7 for more details on this technique) in

which the transmitter and the receiver(s) are placed on each side of the fracture site. The velocity of the ultrasonic waves propagating along the longitudinal axis of the bone is typically used as a parameter for monitoring bone healing. As opposed to the above-mentioned biomechanical methods which measure the properties of the whole bone as a system, the ultrasonic testing evaluates the changes of the callus tissue itself during the healing process from the early inflammation stage, the endochondral and intramembranous ossification stages up to the bone remodeling stage. The marked differences in the callus properties compared to those of the cortical bone bring about a change (reduction) in the ultrasound velocity as the waves propagate across the fracture region. As healing progresses, the callus properties are gradually evolving which is reflected in the ultrasound propagation velocity. Results from animal [9–15] and clinical [3, 9, 12, 16–18] studies have shown that the ultrasound velocity is significantly different between fresh fractures, bone unions, and delayed unions or non-unions. Serial follow-up measurements [3, 14, 15, 18] have demonstrated that ultrasound velocity changes (typically increases) during healing which makes feasible to monitor the healing progress and early distinguish between cases of normal healing and delayed unions. The propagation velocity is also sufficiently correlated with the mechanical properties of the healing bone and with the density of the callus tissue [8]. Similar observations have been made with regard to other propagation characteristics, such as attenuation, velocity dispersion of guided waves, etc., and will be presented in the following sections. In some research works, ultrasonography [19] and power Doppler ultrasonography [20] have been used to assess the appearance and neo-vascularization of the callus tissue during healing; however, ultrasonography is not covered by this chapter.

This chapter presents the state of the art and provides an extensive review of most of the studies in the literature dealing with bone healing monitoring by ultrasonic means. The chapter is organized as follows: First, the ultrasonic methods that have been proposed in the literature for examining long bones are described. Thereafter, we present the experimental studies by classifying them into two broad categories; (a) those that do not involve serial ultrasound measurements over the healing period but rather involve patients measured at different healing stages or bone specimens from animal subjects that were sacrificed at various post-operative time-points, and (b) in vivo studies with serial follow-up measurements. A separate subsection is devoted to studies that make use of phantoms of fractured bones for investigating the effect of various fracture characteristics (gap width, depth, etc.) on the measured quantities. Finally, an overview of the computational studies for simulation of ultrasound propagation in models of healing bones is presented.

14.2 Ultrasonic Configurations and Measured Quantities

Axial-transmission is the most common technique for evaluating the status of long bones and this is also the case for fracture healing. The transducers are placed on each side of the fracture at a fixed distance as shown in Fig. 14.1, but also configurations in which the receiver is progressively shifted to scan also the region above the

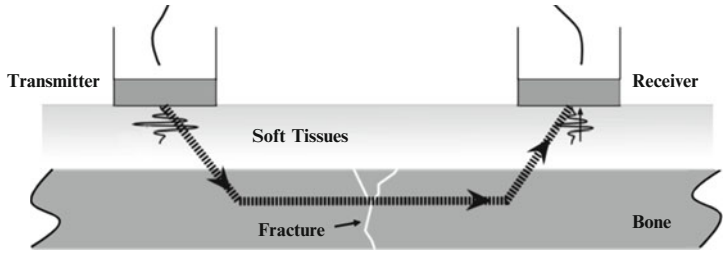

Fig. 14.1 Ultrasonic evaluation of fractured long bones using the axial transmission technique

fracture area have also been proposed [17, 21]. In vivo, the transducers are typically positioned externally on the skin but in a recent study their attachment onto the bone surface through implantation has been tested and evaluated in vivo [14, 15]. Either configurations, i.e. percutaneous or directly on the bone surface after removing the overlying soft tissues, have been used ex vivo on bone specimens.

The most widely-measured ultrasonic quantity in fracture healing assessment is the ultrasound propagation velocity. Due to the different properties between the callus and cortical bone, the measured ultrasound velocity is an "average" value over the whole propagation path, i.e. the segments of the intact cortical bone and the healing area. In this sense, the value of the velocity is a function of the distance between the transducers for a given fracture, as opposed to osteoporosis studies where the velocity is practically independent of the distance. An extension to this is that the scanning method does not provide any longer with arrival times which are linearly related to the transducer separation but their relation depends on the position of the receiver, i.e. over the fracture zone or above the intact segment.

Besides ultrasound velocity, the attenuation of the propagated waves has also been used for monitoring purposes [17, 21–24]. In most studies, the attenuation is simply derived from the amplitude of the first half cycle of the first arriving signal (FAS). In addition, recent studies have made use of the guided wave theory to investigate whether the dispersion of the velocity and attenuation of individual guided modes can be used for fracture healing monitoring [21, 25, 26].

14.3 Experimental Studies

14.3.1 Ultrasonic Evaluation of Fracture Healing

The propagation velocity in fractured human bones was measured in vivo for the first time by Anast et al. in [16]. Velocity measurements were performed on different patients with fractured bones corresponding to various healing stages and were also compared to the control values from the contralateral healthy bones. It was found that upon full weight-bearing, the velocity was 80% of the control value. In a femoral fracture model on 40 guinea pigs [9] which were sacrificed

at the sixth month post-operatively, the velocity across both the fractured and the control bones were measured using 100 kHz ultrasonic pulses. The bones were clinically and radiographically classified as: (a) completely healed, (b) partially-healed, and (c) non-unions. It was found that for completely healed bones, partially-healed bones, and non-unions, the velocities were on average 94%, 81% and 67% of the control value, respectively, which indicated that the propagation velocity was in agreement with clinical and radiographic assessments.

In another animal study [10] on a mid-femoral graft model of 96 guinea pigs, the authors investigated whether ultrasound velocity is related to the modulus of elasticity of the healing bone. The soft tissues were removed from the excised bones and the ultrasound velocity was measured at 100 kHz. The modulus of elasticity was first calculated by multiplying the square of the measured velocity by the mass density of the specimen and thereafter by three-point bending. It was demonstrated that the modulus of elasticity determined biomechanically was linearly related with that determined by ultrasound. Another study on 36 rabbit tibiae [11] investigated the relationships of ultrasound velocity (using 500 kHz and 1 MHz excitations) with the load at failure, stiffness and modulus of elasticity determined by three-point bending. It was found that the correlation coefficient of the velocity with the load at failure was $R = 0.46$ at 500 kHz and $R = 0.57$ at 1 MHz, with the stiffness $R = 0.57$ at 500 kHz and $R = 0.51$ at 1 MHz, and with the elastic modulus $R = 0.35$ at 500 kHz and $R = 0.63$ at 1 MHz. The correlation coefficients were higher for the 1 MHz measurements but the authors provided no justification of their findings. A possible explanation could be that at 1 MHz, the FAS wave propagated as a subsurface wave, known also as lateral (or head) wave [27], which travels at the bulk longitudinal velocity of the medium, whereas at 500 kHz the FAS wave due to a longer wavelength corresponded to a different type of wave whose velocity is influenced by the physical (vertical) dimensions of the healing bone. In a more recent study [28], 15 sheep with a tibial diaphyseal transverse osteotomy treated by external fixation were divided into three groups and sacrificed at 30, 45 and 60 days. The tibiae were removed and their diameters were measured in both the sagittal and frontal planes. The velocity across the bones was measured in a water tank using the through-transmission technique at the level of the former osteotomy in both the sagittal and frontal planes. It was found that the diameters of the fractured tibiae decreased with time in both planes as a result of bone remodeling which is typical in the secondary type of healing.[1] Ultrasound velocity increased with time from 2290 to 2399 and to 2382 m/s in the sagittal plane, and from 2376 to 2472 and to 2466 m/s in the frontal plane. It was also found that there was a significant negative correlation between the diameter and the velocity ($R = -0.90$ for the sagittal and -0.92 for the frontal planes).

A different configuration has been proposed in [17] for the determination of the ultrasound velocity and attenuation in fractured bones. Four 200-kHz transducers were arranged in a row along the bone axis with the two central transducers being the transmitters and placed on each side of the fracture line.

[1] Secondary healing is the most frequent healing type when an external fixation device is used.

The propagation velocity was simply measured by using the two remaining transducers as receivers. For calculating the attenuation, the transmitters were excited one after the other with pulses such that the corresponding amplitudes of the first half cycle at a receiver to be equal and thereafter the same procedure was followed with respect to the other receiver. From the excitations applied to the transmitters in these four measurements, the ultrasound attenuation coefficient in bone could be calculated without being influenced from the surrounding soft tissues and any other coupling at the bone-transducer interface. This measuring technique was used in vivo on 53 healthy men, on seven patients with a 1-week old tibial fracture and on six patients with a 3-week old tibial fracture. The velocity and attenuation in normal tibiae were (mean value $\pm$ standard error) $3614 \pm 32\,\mathrm{m/s}$ and $5.5 \pm 0.4\,\mathrm{dB \cdot MHz^{-1}\,cm^{-1}}$, respectively. The velocity in the fractured tibiae one week after fracture was significantly decreased to $2375 \pm 82\,\mathrm{m/s}$, whereas the attenuation increased to $17.8 \pm 3.9\,\mathrm{dB \cdot MHz^{-1}\,cm^{-1}}$. Even three weeks after fracture, the velocity ($2882 \pm 90\,\mathrm{m/s}$) and attenuation ($10.4 \pm 3.6\,\mathrm{dB \cdot MHz^{-1}\,cm^{-1}}$) values were still significantly different from the control values. In situ experiments on tibiae with artificially-induced fractures verified the in vivo observations. Ex vivo measurements on bones before and after the removal of the soft tissues and of the periosteum revealed that almost no differences existed, whereas the application of internal fixation to the bones slightly affected the velocity, but significantly increased the attenuation.

Two recent ex vivo studies [21,22] also investigated the attenuation of ultrasound during healing. Two bovine femora, stripped of the soft tissues, were used before and after the production of a transverse and an oblique fracture. The fracture gaps were widened in three steps of 2 mm. The scanning method (200 KHz) was used in which the arrival time and the amplitude of the first peak of the FAS wave were recorded for each transducer separation step. It was found that the transverse fracture was accompanied by typical changes in the arrival time, i.e. an extra time delay compared with the baseline measurement and the delay increased as the fracture gap widened. A similar effect was seen with the oblique fracture experiments but a much lower time delay was observed for the smallest gap width compared with the transverse case. Regarding the signal amplitude measurements, the transverse case resulted in characteristic curves involving peaks due to wave interference and a significant loss in signal amplitude relative to the baseline data. As the gap width increased, the signal loss was also increased. Similar curves were recorded for the oblique case but with higher signal loss for a given gap width compared to the transverse case. When removing the marrow, they found no significant effect on the change in arrival time and signal amplitude. The ex vivo observations were compared with computational experiments which are presented in Sect. 14.4.

14.3.2 Ultrasonic Monitoring of Fracture Healing

In this subsection, we only present studies which involved serial follow-up ultrasound measurements on the same subjects since such study design allows

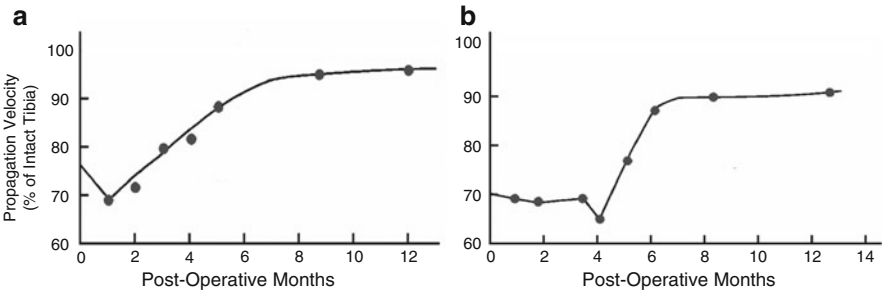

Fig. 14.2 Change of ultrasound velocity throughout the healing period in (**a**) normally healing tibia, and (**b**) delayed union (Modified from [18])

the investigation of the monitoring capabilities of ultrasound and as it was proved to reveal many interesting findings. Gerlanc et al. [18] conducted a clinical study on 21 patients with closed diaphyseal tibial fracture and 12 patients who had sustained a tibial fracture 1–40 years ago. All subjects had been followed from the time of fracture for a minimum of 3 months. Velocity measurements were performed on both the fractured and the contralateral tibiae, initially within a few days from fracture and afterwards every time a radiograph was taken. Ultrasound measurements (100 kHz) were performed by placing the transducers at specific bony landmarks (the tibial tubercle and the medial malleolus). Velocity was expressed as a percentage of the values in control tibia. The variation of velocity over healing time in the case of a normal healing course is shown in Fig. 14.2a. The initial measurement indicated a 24% reduction in velocity followed by a further 7% decrease by the end of the first month. This further decrease was attributed by the authors to the resorption of the fracture margins and the structural and metabolic bone changes that occur during the initial healing stages. As healing progressed, the velocity started increasing and by the time of clinical and radiographic bony union, the velocity had reached or slightly exceeded that of the initial post-fracture value. When the patients were able of comfortable ambulation, the velocity had returned to 80–88% of that in the intact tibia. The authors observed that in general, the rate of velocity increase was higher for non-comminuted, non-displaced fractures than for severe fractures. Further measurements on patients with old fractures demonstrated that the velocity was on average 96% of the intact value, with none of them reaching that of the control bone. In one case of delayed union (see Fig. 14.2b), it was noticed that the velocity remained almost constant at 70% for the first five months, next increased rapidly to 90% by the eighth month, and then reached a plateau until the end of the follow-up period. Therefore, serial velocity measurements are able to monitor a dynamic healing process and are in parallel with the clinical and radiographic patterns.

A study on rabbit ulnar fractures [13] involved serial ultrasound measurements performed at various post-operative weeks. An “ultrasonic healing index” was defined as the ratio of the amplitude of the FAS wave received from the healing limb

to that from the contralateral. The results showed that the ultrasonic healing index increased linearly with healing time. Additional ex vivo experiments demonstrated that the healing index was also positively correlated with the bending strength of bone. Although the authors concluded that the healing index, which in essence expresses attenuation, could be used as a quantitative measure of fracture healing, no comparisons were made with clinical and radiographic assessments.

Cunningham et al. [3] conducted a clinical study on 20 patients treated by cast for closed diaphyseal tibial fracture. The propagation velocity was determined from 1 MHz ultrasound measurements carried out during the normal appointment of the patient in the clinic. The ultrasound transducers were placed on the medial side of the tibia at the upper and lower thirds of its length. The authors presented velocity graphs only for two patients. For the first patient whose fracture was assessed to be clinically united at 20 weeks, the velocity was gradually increasing increased over the healing period approaching that of the control bone. At the time of bone union, the velocity was lower than the control by 350 m/s (19% difference). The authors also performed vibration measurements on healing tibia and noticed a similar increase in the frequency of the bending modes during healing. For the second patient whose fracture was clinically and radiographically evaluated as delayed union, the velocity was decreasing for the first 17 weeks and afterwards it started to increase with a slow rate reaching at 81% of the control bone at the 47^{th} post-fracture week. A similar pattern of variation was also seen for the vibration measurements. An interesting finding observed in both healing cases was that the measured velocity across the control bone was also varying (generally increasing) over the post-fracture period. Although the authors did not provide any explanation for this unexpected observation, one possible reason could be that the increased loading that the uninjured bone takes during the healing period has a temporal effect on its density and mechanical properties. The authors pointed out that measurements should be performed on both bones and the velocity should be expressed as percentage values. In addition, they concluded that their preliminary results from all the patients suggested that a velocity threshold greater than 80% could be clinically used as criterion of bony union.

In an in vivo study on a sheep tibial osteotomy model [14, 15], a system for the ultrasonic monitoring and stimulation of bone healing was introduced that proposed the attachment of two miniature transducers directly onto the bone's surface through a semi-invasive surgical technique. The transducers were placed anterolateraly on each side of the fracture line with a 25 mm separation. Ultrasound measurements were obtained from the intact bones before the performance of the osteotomy and afterwards from the healing bones on a 4-day basis until the 100th post-operative day. Three typical velocity evolution patterns were observed among all test subjects. The first was similar to that reported in [18] (see Fig. 14.2a) and was observed for 19 animals in which secondary healing took place as assessed by radiographs. More specifically, the velocity was initially reduced on average by 17% just after the realization of the osteotomy and continued to decrease by a further 13% until the 38^{th} day. Such decrease was also observed in [18] and can be largely explained by the inflammatory response and the increased osteoclastic activity that occur at the early

stages of secondary healing which cause further broadening of the fracture gap. From that point onwards, the velocity started to gradually increase as a result of the formation and consolidation of the callus. The second pattern, which was observed for three animals, was described by a steady increase in velocity after the osteotomy, revealing thus a different type of healing. For this animal group, radiographs showed that primary (direct) healing occurred which is characterized by direct bony union across the fracture gap, rather than callus formation. The third pattern corresponded to two non-union cases and was not described by any systematic change in the velocity. Therefore, it was shown that the variation of the velocity not only monitors a dynamic healing process but also reflects the pathway of healing. The results were further analyzed to investigate whether the variation of velocity could early distinguish between healing and non-healing bones. For this purpose, the animals were divided into two healing groups; the first included animals that reached radiographic healing and the second those with non-healing. It was shown that on average the velocity across bones that eventually reached bone union was higher than those with non-healing even from the 50^{th} post-operative day; however, statistically significant differences were only observed from the 80^{th} post-operative day onwards. Also, the velocity exceeded 80% of the intact bone value on the 70^{th} post-operative day. Bone densitometry and three-point bending showed that the velocity on the 100th day was highly correlated with the square root of the Young modulus ($R = 0.81$) and the ultimate strength ($R = 0.75$) as well as with the density of the callus ($R = 0.81$).

14.3.3 Studies Using Phantoms of Healing Bones

In an experimental study [29], acrylic plates were used to simulate the cortex of a long bone. The plates were immersed in a water tank and two 200 kHz transducers were positioned perpendicularly to the water surface, 2 mm above the plate. Ultrasound measurements were performed initially on an intact plate using the scanning technique. The slope of the line that describes the transducer separation as a function of the FAS arrival time yields the bulk longitudinal velocity. With this technique the influence of the overlying soft tissues is eliminated provided that their thickness remains constant over the scanning region. In order to investigate the type of the FAS wave, the authors made the hypothesis that the wave propagates from the transmitter to the receiver along a path corresponding to the minimum propagation time. According to this hypothesis, the FAS wave is first introduced to the plate at the first critical angle [27], then propagates along the plate as a longitudinal wave, and finally leaves the plate at the first critical angle to reach the receiver. The minimum propagation time was computed analytically and found to be in excellent agreement with the experimental measurements. This hypothesis on the propagation path is simply based on ray theory and is practically valid when the transducers operate at low frequencies and have small contact area. Under such conditions, the transducers transmit over a wide angular range and thus can emit and receive significant

energy in the direction of the first critical angle. Although not discussed by the authors, the FAS wave does not propagate along the medium as a pure bulk wave, but rather along its subsurface as a lateral wave. Another issue to consider is that the ray theory is no longer a valid assumption when the plate thickness is smaller than the wavelength in bone. In such cases, a modal approach is necessary to describe wave propagation and the FAS wave corresponds to a low-order guided wave mode [30]. In a second series of experiments in the same study [29], the plate was transversely cut throughout its thickness and the two fragments were repositioned such that the intra-fragmentary distance was 0, 10 and 20 mm. The fracture gap was first filled with water and next with a PVC block (bulk velocity 2995 m/s). The recorded FAS arrival time was plotted against the distance between the transducers for each fracture case. It was found that when the two fragments were in direct contact, the measurement curve was identical to that obtained from the intact plate indicating that the presence of a perfectly-reduced fracture does not affect the propagation time. For the cases where a gap existed between the two fragments, as long as the receiver was over the second fragment, the propagation times had a constant offset, depending on the gap width and the difference in velocity between the material in the gap (water or PVC) and the plate. However, the slopes of the curves that describe the FAS arrival time versus the transducers' distance for each material (water or PVC) were the same and equal to the bulk velocity of the plate. When the receiver moved over the fracture gap, it was shown that the slope of the curve yields the velocity of the material in the gap; however, the authors claimed that this could be feasible when the fracture gap is large enough, typically over 20 mm.

Similar experiments were performed in another study [31] on two sliding acrylic blocks of 15 mm thickness which simulated a fractured long bone. A 1 mm thick layer of natural rubber (bulk velocity 1600 m/s) was used as tissue equivalent material and was placed on the top of the blocks. The phantom was placed in a water tank and the width of the fracture gap was gradually set from 0.1–2.0 mm using 0.1 mm increments. For each setting, ultrasound velocity measurements were performed using the commercial system SoundScan 2000 (Myriad Ultrasound Systems Ltd, Israel) which incorporates two sets of transducers into a single probe. The first set operates at 250 kHz and is mounted at an angle to the skin with the transducers separated by 50 mm and was used to carry out axial transmission measurements. The second set operates at 1 MHz with its transducers mounted perpendicular to the skin to perform echo signal measurements for determining the thickness of the overlying soft tissues which would correct the propagation distance for different soft tissue thicknesses. It was demonstrated that the measured velocity was decreasing as the gap increased and was also in perfect agreement with that predicted theoretically.

Experiments on immersed Sawbones plates [24] were carried out to supplement the ex vivo studies [21, 22] regarding the attenuation of ultrasound during healing. The fracture was simulated by a 4 mm transverse gap, while the early inflammatory stage was simulated by water. Hard callus formation was simulated by bone cement which was initially inserted only within the gap and later was also placed at the top surface of the plate having a dome shape. Ultrasound measurements at 200 KHz

showed that a large drop in FAS amplitude was observed for the inflammatory stage and when bone cement substituted for the water in the gap, the signal loss was reduced significantly. Adding a callus to the top surface resulted in increased signal loss which indicated that the callus itself can give rise to strong scattering/re-radiation.

14.4 Computational Studies

Although the literature of the use of computational models for the study of cortical and cancellous bone is quite rich [32] (see Chap. 8), their use in the context of fracture healing is relative new. The first computational study of ultrasound propagation in a healing long bone was published in 2006 [26]. A 2-D model of an elastic isotropic plate (4 mm thick, bulk longitudinal and shear velocities 4063 and 1846 m/s, respectively) was developed similar to those used in osteoporosis studies [32]. The fracture gap was modeled as a 2 mm wide transverse discontinuity at the middle of the plate's length, while the consolidation of callus was simulated by a simple 7-stage process. The callus tissue was assumed to be homogeneous and isotropic with properties evolving throughout the stages. At each stage, the material properties of the callus were given by a linear combination of the properties of blood and cortical bone. At the first healing stage, the callus was assigned the properties of blood which corresponds to the haematoma that follows a fracture, whereas at later stages the callus was modeled as a solid with properties gradually approximating those of cortical bone as a result of callus mineralization and ossification. The callus geometrical model included two cases. In the first, the geometry was not taken into account and the callus simply filled the fracture gap, whereas in the second, the callus was described by two regions outside the plate borders in order to simulate the periosteal and endosteal formation of callus. Axial transmission was simulated by a transmitter and a receiver placed in direct contact with the plate's upper surface. Two broadband excitations were examined with central frequencies of 500 kHz and 1 MHz resulting in 8 mm and 4 mm wavelengths in bone, respectively. The bone plate was assumed to be in vacuum neglecting thus the presence of soft tissues. Solution to the elastic wave propagation problem was achieved using the finite-difference method [32]. Analyzing initially the simulated signals from the intact plate, it was proved that the FAS wave propagated as a non-dispersive lateral wave. When the callus was incorporated into the model, the FAS remained a lateral wave and its velocity was gradually increasing during the healing stages. The FAS velocity at each stage was independent of the excitation frequency or the callus geometry.

In a subsequent study by the same group [33], the model of the healing bone was enhanced by assuming the callus tissue to be an inhomogeneous material consisting of six different ossification regions (Fig. 14.3). The healing course was simulated by a three-stage process in which the properties of each region evolved corresponding to various types of soft tissues that participate in the healing process. In addition,

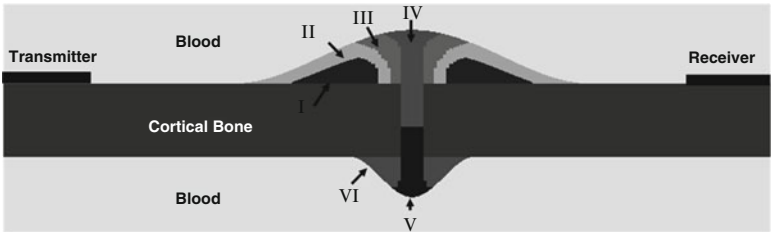

Fig. 14.3 2-D model of a healing bone immersed in blood occupying the semi-infinite spaces together with the transmitter–receiver arrangement. The Latin numbers indicate the six ossification regions of the callus tissue [33]

three different boundary conditions were investigated. In the first, the healing bone was assumed immersed in blood which occupied the semi-infinite spaces over the surfaces of the plate (Fig. 14.3), the second involved a 2 mm-thick layer of blood on the upper side and a semi-infinite space consisted of bone marrow on the lower side of the plate, and a the third case involved three finite layers (blood, cortical bone and bone marrow). It was found that at the first stage the FAS velocity decreased from the intact bone value, then remained the same between the first and the second stages, and increased at the third stage. No significant differences were observed in the FAS velocity between the various boundary conditions cases (free or fluid-loading) suggesting that the lateral wave is not influenced by loading conditions. The fact that the velocity remained constant between the first and the second stage indicates that the propagation of the FAS wave was only affected by the material that filled the fracture gap (which was the same for those two stages) and that the FAS is insensitive to changes that occur in the whole structure of the callus tissue.

Dodd et al. [21–23] complemented their ex vivo findings by investigating the effect of different fracture gap sizes and geometries on the FAS amplitude and attenuation using 2-D computational models. Bone was modeled as an isotropic plate immersed in water and two different types of oblique fractures were modeled. Simulation of axial transmission at 200 kHz was performed using the finite-difference method. Comparisons between the computational and experimental results showed similar arrival time variations and signal amplitude patterns. Furthermore, it was made clear that an oblique fracture causes a reduction in the extra time delay of the propagating wave compared with the transverse case, and also an additional decrease in the corresponding signal amplitude. Furthermore, the angle of the fracture line was found to affect the FAS amplitude and more specifically the greater the angle, the higher the signal loss. However, the effect of the various healing stages on the FAS amplitude was not investigated, but rather only the initial inflammatory healing stage was examined. This limitation was addressed in a subsequent computational study [24] in which the healing was simulated by seven stages with the callus size being reduced during the last stages as a result of bone remodeling (Fig 14.4). The results from the simulations demonstrated that, in addition to a reduction in FAS amplitude due to the presence of fracture, the alterations in cal-

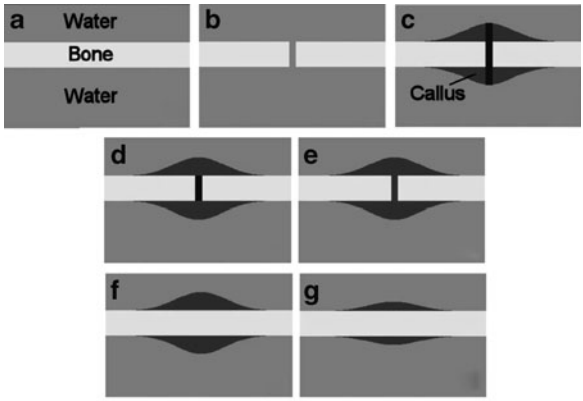

Fig. 14.4 Modeling of six stages of secondary healing in which callus properties and geometry gradually evolve [24]

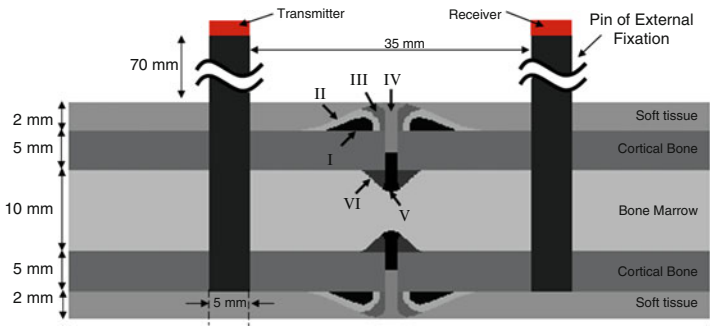

Fig. 14.5 2-D model of a healing bone in which the transmitter and receiver are attached at the pins of an external fixation device [34]

lus geometry and properties caused considerable changes in the signal amplitude, especially at the inflammatory and remodeling stages. By analyzing snapshots of the simulations for each healing stage, the authors concluded that the callus acts both as a waveguide aiding the transmission of the acoustic pulse beyond the fracture site and as an additional load on the bone plate giving rise to an increased re-radiation which appears to dominate the signal loss.

In another 2-D computational study [34], an alternative measurement set-up was modeled in which of the transducers are placed at the extracorporeal tips of the pins of an already applied external fixation device (Fig. 14.5). The model of healing bone was similar to that in [33], while the pins were modeled as 5-mm thick stainless steel rods. In order to address realistic conditions in which the orthopeadic surgeons do not insert the pins perpendicular to the bone axis but rather at small inclinations, different cases of pin inclination angles were also investigated. The velocity values calculated from the simulations generally increased throughout the healing stages;

however, the longer FAS propagation path (due to the presence of the pins) decreases the sensitivity of the proposed method compared to the traditional ones. It was also made clear that pin inclination had generally no significant impact on the velocity measurements. This was an *in silico* validation of an innovative configuration which can offer several advantages in vivo since the measurements are affected neither by the overlying soft tissue, especially for examining deep bones, nor by any variations in transducers' re-positioning during follow-up examinations.

A current trend in ultrasonic evaluation of bone healing is the use of guided waves as a means to supplement the traditional velocity and attenuation measurements. This was firstly addressed in [26,33] where a time-frequency (t-f) methodology was followed for the representation of the propagating guided modes. Mode identification was performed by using the group velocity dispersion curves predicted by the Lamb wave theory [27,35]. Among the multiple modes that were detected, the S2 and the A3 Lamb modes were found to dominate (Fig. 14.6a). When applying different boundary conditions, the analysis was performed with the use of the modified dispersion curves that include the loading effect of the surrounding medium [27]. As opposed to the lateral wave, the effect of the boundary conditions on the modes was significant and thus cannot be ignored when analyzing real measurements. T-f analysis of the signals from the simulated stages showed that both the properties and geometry of the callus affected the dispersion of the theoretically-anticipated Lamb modes (Fig. 14.6b–d). The modes were gradually reconstructed towards the theoretical ones during callus consolidation.

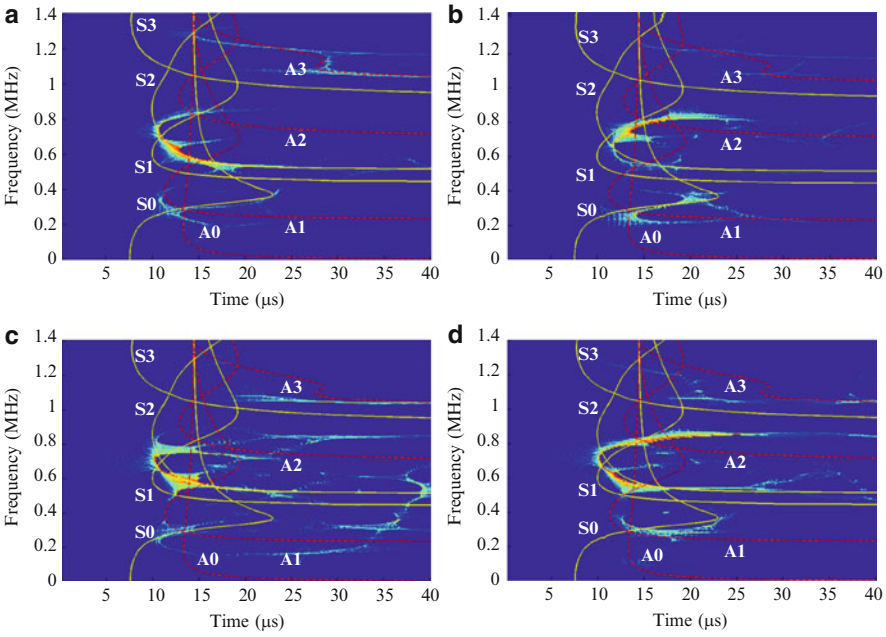

Fig. 14.6 T-f representations of signals obtained from: (**a**) intact plate, and from the (**b**) first, (**c**) third, and (**d**) fifth healing stages of the model in [26] after 1 MHz broadband excitations. Theoretical group velocity dispersion curves of the Lamb modes are superimposed on the t-f images

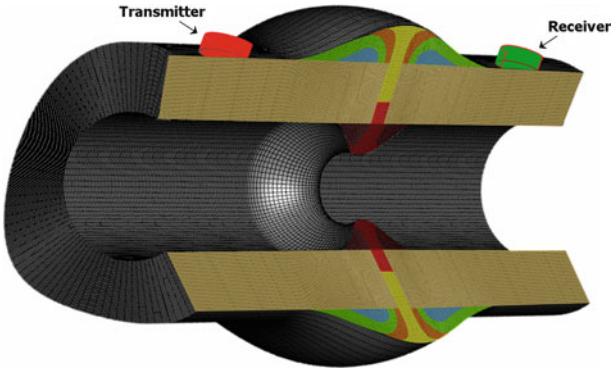

Fig. 14.7 Finite element model of a sheep tibia incorporating the fracture callus (sagittal section) together with the transmitter-receiver configuration [26]

The above simulation studies were further extended to more realistic conditions by considering the 3-D geometry and anisotropy of the bone and of the fracture callus tissue [25]. First, a structure with idealized geometry (hollow circular cylinder) was examined for two cases of material symmetry: isotropy and transverse isotropy. Next, the real geometry of the diaphysis of an intact sheep tibia was modeled while the callus was inserted at the middle of the bone's length (Fig. 14.7). The callus consisted of six ossification regions and healing proceeded in three simulated stages as in [33]. Axial transmission measurements were performed using a broadband 1 MHz excitation. Two sites of transmitter-receiver positioning were examined corresponding to regions where the cortical shell has different physical characteristics (i.e. local thickness and curvature). Bone was considered free of tractions on the inner and outer surfaces. Solution to the 3-D elastic wave propagation problem was performed using the explicit elastodynamics finite element analysis. Concerning the intact models, it was observed that the FAS wave corresponded to a lateral wave, as in the 2-D models [26, 33], and its velocity was not affected by the curvature of the cortex and remained almost the same between the two different material symmetry assumptions. On the other hand, the anatomical characteristics of the measurement site as well as bone anisotropy had a major effect on the propagation of high-order modes. For both material symmetry cases, the high-order modes in bone were significantly different from those observed in the cylindrical model and from those predicted by the tube theory [36]. The effect was less pronounced on the dispersion of the fundamental tube modes, i.e. the longitudinal $L(0,1)$ and the flexural $F(1,1)$ modes, indicating that 2-D and 3-D simulations on idealized geometries have limited efficiency in predicting wave-guidance phenomena in real bones. For the fractured tibia, it was demonstrated that the FAS velocity measurements cannot reflect the material and mechanical changes taking place in the whole structure of callus, which is in accordance with previous findings from the 2-D studies [26, 33]. Conversely, guided waves were sensitive to both the geometry and the properties of callus.

Guo et al. in a subsequent study [37] performed numerical simulations using a 3-D finite element model of healing bone similar to that in [25] in order to quantify the characteristics of longitudinal tube modes during the simulated healing process. Excitation was performed by a broadband impulse and the displacements were recorded at a series of discrete positions. The recorded signals were analyzed with the mode extraction technique that gives the waveforms of the individual modes. The energy and the effective velocity of the first energy peak of each extracted mode were calculated for every simulated healing stage. From the analysis, the authors proposed which tube modes are more sensitive to each healing stage.

14.5 Conclusion

Quantitative ultrasound has attracted significant interest in the monitoring of bone fracture healing. The results from animal and clinical studies demonstrated that the ultrasound velocity is significantly different between healed bones and delayed unions or non-unions and is also sufficiently correlated with the breaking load, stiffness, strength, Young's modulus of the healing bone and with the density of callus. Studies involving follow-up measurements have shown that the pattern of velocity variation is also consistent with the biology of the secondary and the primary type of healing. An empirical velocity threshold of 80% of the control bone value can be used as a criterion of bony union. A smaller number of studies have additionally shown that the attenuation of the FAS wave can characterize the status of the healing bone and monitor the healing process. However, it is difficult to provide reference velocity and attenuation values for each stage of healing. This is due to many reasons, the most significant of which are: (a) the transducer separation in each study was different, (b) the characteristics of the fractures (fracture gap, the type of fracture, etc.) were not the same nor systematically classified into groups, and (c) a wide range of frequencies have been employed (from 100 to 1 MHz).

Wave propagation in healing long bones has recently been studied with the use of computer simulations in order to elucidate the influence of various parameters (e.g. callus properties, frequency of ultrasound, transducers' arrangement, etc.) on the characteristics of wave propagation, analyze the various propagating wave types and also overcome the inherent difficulties in obtaining specimens of healing bone with known properties. A series of computational studies on 2-D and 3-D models of healing bones [25, 26, 33] showed that the FAS velocity increased during a simulated healing process. When the FAS wave corresponds to a lateral wave, its velocity is sensitive only to the properties of a small superficial region within the fracture gap. By making use of a broadband excitation that gives rise to multiple guided waves, it was made feasible to capture geometrical and material changes in the callus tissue during healing. However, it was demonstrated that the characteristics of the guided waves, such as the dispersion of velocity, are strongly affected by the irregular geometry and anisotropy of the cortical bone and callus, and by the boundary conditions induced by the soft tissues. Further computational studies on

2-D healing bones [21–23] revealed that the amplitude of the FAS is also sensitive to the fracture and can potentially be a good indicator for the changes in the mechanical properties of the callus due to the formation of connective tissue, cartilage and woven bone. Nevertheless, several issues need to be further addressed, such as more realistic bone geometries, material attenuation, microstructural effects [38], different types of fractures, accurate transducer modeling, etc. Therefore, the results from the simulation studies should be interpreted with care preferably in conjunction with clinical measurements from real fractures.

Quantitative ultrasound is low-cost, safe, easy to operate, and in some cases portable or even wearable when comparing with the alternative biomechanical methods that have also been proposed for fracture healing monitoring. Ultrasound is also preferable because it can be applied to practically all types of fractures in long bones independently of the existence of external fixation. Although ultrasound devices are currently available to assess osteoporosis and are gradually becoming an integrated part of the clinical practice, no similar progress has been made in the context of bone fracture healing monitoring. This is mainly attributed to the fact that few clinical studies have been reported and these do not involve large and homogenous group of patients. Another open issue is that the measurements have not been standardized and compared with normative data (e.g. bone densitometry) which would enable the validation of the diagnostic ability of ultrasound.

References

1. T. J. Blokhuis, J. H. de Bruine, J. A. Bramer, F. C. den Boer, F. C. Bakker, P. Patka, H. J. Haarman, and R. A. Manoliu, "The reliability of plain radiography in experimental fracture healing," Skeletal Radiol. **30**(3), 151–156 (2001).
2. L. E. Claes, and J. Cunningham, "Monitoring the mechanical properties of healing bone," Clin. Orthop. Relat. Res. **467**(8), 1964–1971 (2009).
3. J. L. Cunningham, J. Kenwright, and C. J. Kershaw, "Biomechanical measurement of fracture healing," J. Med. Eng. Technol. **14**(3), 92–101 (1990).
4. J. B. Richardson, J. L. Cunningham, A. E. Goodship, B. T. O'Connor, and J. Kenwright, "Measuring stiffness can define healing of tibial fractures," J. Bone Joint Surg. Br. **76**(3), 389–394 (1994).
5. Y. Nakatsuchi, A. Tsuchikane, and A. Nomura, "Assessment of fracture healing in the tibia using the impulse response method," J. Orthop. Trauma **10**(1), 50–62 (1996).
6. G. Nikiforidis, A. Bezerianos, A. Dimarogonas, and C. Sutherland, "Monitoring of fracture healing by lateral and axial vibration analysis," J. Biomech. **23**(4), 323–330 (1990).
7. Y. Hirasawa, S. Takai, W. C. Kim, N. Takenaka, N. Yoshino, and Y. Watanabe, "Biomechanical monitoring of healing bone based on acoustic emission technology," Clin. Orthop. Relat. Res. **402**, 236–244 (2002).
8. V. C. Protopappas, M. G. Vavva, D. I. Fotiadis, and K. N. Malizos, "Ultrasonic monitoring of bone fracture healing," IEEE Trans. Ultras. Ferroelectr. Freq. Control **55**(6), 1243–1255 (2008).
9. L. P. Floriani, N. T. Debervoise, and G. W. Hyatt, "Mechanical properties of healing bone by use of ultrasound," Surg. Forum **18**, 468–470 (1967).
10. W. F. Abendschein, and G. W. Hyatt, "Ultrasonics and physical properties of healing bone," J. Trauma **12**(4), 297–301 (1972).

11. P. J. Gill, G. Kernohan, I. N. Mawhinney, R. A. Mollan, and R. McIlhagger, "Investigation of the mechanical properties of bone using ultrasound," Proc. Inst. Mech. Eng. **203**, 61–63 (1989).
12. E. Maylia and L. D. Nokes, "The use of ultrasonics in orthopaedics – a review," Technol. Health Care **7**(1), 1–28 (1999).
13. S. Saha, V. V. Rao, V. Malakanok, and J.A. Albright, "Quantitative measurement of fracture healing by ultrasound," in Biomed. Engin. I: Recent Developments, Pergamon Press, New York, 247–249 (1982).
14. K. N. Malizos, A. A. Papachristos, V. C. Protopappas, and D. I. Fotiadis, "Transosseous application of low-intensity ultrasound for the enhancement and monitoring of fracture healing process in a sheep osteotomy model," Bone **38**(4), 530–539 (2006).
15. V. C. Protopappas, D. A. Baga, D. I. Fotiadis, A. C. Likas, A. A. Papachristos, and K. N. Malizos, "An ultrasound wearable system for the monitoring and acceleration of fracture healing in long bones," IEEE Trans. Biomed. Eng. **52**(9), 1597–1608 (2005).
16. G. T. Anast, T. Fields, and I. M. Siegel, "Ultrasonic technique for the evaluation of bone fractures," Am. J. Phys. Med. **37**, 157–159 (1958).
17. J. Saulgozis, I. Pontaga, G. Lowet, and G. Van der Perre, "The effect of fracture and fracture fixation on ultrasonic velocity and attenuation," Physiol. Meas. **17**(3), 201–211 (1996).
18. M. Gerlanc, D. Haddad, G. W. Hyatt, J. T. Langloh, and P. S. Hilaire, "Ultrasonic study of normal and fractured bone," Clin. Orthop. Relat. Res. **111**, 175–180 (1975).
19. N. Maffulli and A. Thornton, "Ultrasonographic appearance of external callus in long-bone fractures," Injury **26**(1), 5–12 (1995).
20. M. Risselada, B. H. van, M. Kramer, K. Chiers, L. Duchateau, P. Verleyen, and J. H. Saunders, "Evaluation of nonunion fractures in dogs by use of B-mode ultrasonography, power Doppler ultrasonography, radiography, and histologic examination," Am. J. Vet. Res. **67**(8), 1354–1361, (2006).
21. S. P. Dodd, J. L. Cunningham, A. W. Miles, S. Gheduzzi, and V. F. Humphrey, "An in vitro study of ultrasound signal loss across simple fractures in cortical bone mimics and bovine cortical bone samples," Bone **40**(3), 656–661 (2007).
22. S. P. Dodd, J. L. Cunningham, A. W. Miles, S. Gheduzzi, and V. F. Humphrey, "Ultrasound transmission loss across transverse and oblique bone fractures: an *in vitro study*," Ultrasound Med. Biol. **34**(3), 454–462 (2008).
23. S. P. Dodd, A. W. Miles, S. Gheduzzi, V. F. Humphrey, and J. L. Cunningham, "Modelling the effects of different fracture geometries and healing stages on ultrasound signal loss across a long bone fracture," Comput. Methods Biomech. Biomed. Eng. **10**, 371–375 (2007).
24. S. Gheduzzi, S. P. Dodd, A. W. Miles, V. F. Humphrey, and J. L. Cunningham, "Numerical and experimental simulation of the effect of long bone fracture healing stages on ultrasound transmission across an idealized fracture," J. Acoust. Soc. Am. **126**(2), 887–894 (2009).
25. V. C. Protopappas, I. C. Kourtis, L. C. Kourtis, K. N. Malizos, C. V. Massalas, and D. I. Fotiadis, "Three-dimensional finite element modeling of guided ultrasound wave propagation in intact and healing long bones," J. Acoust. Soc. Am. **121**(6), 3907–3921 (2007).
26. V. C. Protopappas, D. I. Fotiadis, and K. N. Malizos, "Guided ultrasound wave propagation in intact and healing long bones," Ultrasound Med. Biol. **32**(5), 693–708 (2006).
27. J. L. Rose, *Ultrasonic Waves in Solid Media* (Cambridge University Press, Cambridge, 1999).
28. G. Barbieri, C. Barbieri, P. de Matos, C. Pelá, N. Mazzer, "Ultrasonometric evaluation of bone healing: experimental study using a model of diaphyseal transverse osteotomy of sheep tibiae," Ultrasound Med. Biol. **32**(6), 875–882 (2006).
29. G. Lowet and G. Van der Perre, "Ultrasound velocity measurement in long bones: measurement method and simulation of ultrasound wave propagation," J. Biomech. **29**(10), 1255–1262, (1996).
30. E. Bossy, M. Talmant, and P. Laugier, "Effect of bone cortical thickness on velocity measurements using ultrasonic axial transmission: a 2D simulation study," J. Acoust. Soc. Am. **112**(1), 297–307 (2002).
31. C. F. Njeh, J. R. Kearton, D. Hans, and C. M. Boivin, "The use of quantitative ultrasound to monitor fracture healing: a feasibility study using phantoms," Med. Eng. Phys. **20**(10), 781–786 (1998).

32. J. J Kaufman, L. Gangming, and R. S. Siffert, "Ultrasound simulation in bone," IEEE Trans. Ultras. Ferroelectr. Freq. Control **55**(6), 1205–1218 (2008).
33. M. G. Vavva, V. C. Protopappas, L. N. Gergidis, A. Charalambopoulos, D. I. Fotiadis, and D. Polyzos, "The effect of boundary conditions on guided wave propagation in two-dimensional models of healing bone," Ultrasonics **48**, 598–606 (2008).
34. M. G. Vavva, V. C. Protopappas, D. I. Fotiadis, and K. N. Malizos "Ultrasound velocity measurements on healing bones using the external fixation pins: a two-dimensional simulation study," J. Serbian Soc. Comput. Mech. **2**(2), 1–15 (2008).
35. P. Moilanen, "Ultrasonic guided waves in bone" IEEE Trans. Ultras. Ferroelectr. Freq. Control **55**(6), 1277–1286 (2008).
36. I. Mirsky, "Wave propagation in transversely isotropic circular cylinders Part I: theory," J. Acoust. Soc. Am. **37**(6), 1016–1021 (1965).
37. X. Guo, D. Yang, D. Zhang, W. Li, Y. Qiu, and J. Wu, "Quantitative evaluation of fracture healing process of long bones using guided ultrasound waves: a computational feasibility study," J. Acoust. Soc. Am. **125**(5), 2834–2837 (2009).
38. M. G. Vavva, V. C. Protopappas, L. N. Gergidis, A. Charalambopoulos, D. I. Fotiadis, and D. Polyzos, "Velocity dispersion of guided waves propagating in a free gradient elastic plate: application to cortical bone," J. Acoust. Soc. Am. **125**(5), 3414–3427 (2009).

Chapter 15
Nonlinear Acoustics for Non-invasive Assessment of Bone Micro-damage

Marie Muller and Guillaume Renaud

Abstract This chapter presents the state of art in the field of nonlinear ultrasound applied to bone micro-damage assessment. An increasing number of groups have been conducting research in the past years on this particular topic, motivated by the particular sensitivity shown by nonlinear ultrasound methods in industrial materials and geomaterials. Some of the results obtained recently on bone damage assessment *in vitro* using various nonlinear ultrasound techniques are presented. In particular, results obtained with higher harmonic generation, Dynamic Acousto-Elastic Testing (DAET), Nonlinear Resonant Ultrasound Spectroscopy (NRUS), and Nonlinear Wave Modulation Spectroscopy (NWMS) techniques are detailed. All those results show a very good potential for nonlinear ultrasound techniques for bone damage assessment. They should benefit from a proper quantification of the relationship between micro-damage and nonlinear ultrasound parameters. This could be obtained through a thorough statistical study which remains to be achieved. A practical implementation of an *in vivo* setup also remains to be conducted.

Keywords Bone micro-damage · Fracture risk assessment · Nonlinear ultrasound · Harmonic generation · Dynamic Acousto-Elastic Testing · Nonlinear Resonant Ultrasound Spectroscopy · Nonlinear Wave Modulation Spectroscopy

M. Muller (✉)
Institut Langevin, Université Denis Diderot, 10 rue Vauquelin, 75005 Paris, France
e-mail: marie.muller@espci.fr

G. Renaud
Imagerie et Cerveau, UMR INSERM U930, CNRS ERL3106, Université François Rabelais, 10 boulevard Tonnelle, 37032 Tours, France
and
Université Pierre et Marie Curie,
Laboratoire d'Imagerie Paramétrique UMR CNRS7623, 15 rue de L'Ecole de Médecine, 75006 Paris, France
e-mail: renaud_gu@yahoo.fr

P. Laugier and G. Haïat (eds.), *Bone Quantitative Ultrasound*,
DOI 10.1007/978-94-007-0017-8_15,

15.1 Introduction

Cracks in solids were identified as sources of acoustic nonlinearity in industrial materials and geomaterials [1, 2]. These acoustical nonlinearities must be distinguished from elastic nonlinearity arising during irreversible plastic macroscopic deformation for strain of order 1% (see Chap. 1). Nonlinear acoustical techniques employ elastic waves with maximum strain amplitude of order 10^{-5}. Moreover it was suggested that microdamage initiates in bone tissue at strains of about 0.3%, below the apparent macroscopic yield strain of order 0.7% [3]. Consequently nonlinear acoustical techniques are non-destructive.

Promising results obtained in industrial non-destructive testing and geophysics motivated some research groups to apply these nonlinear acoustical methods to assess the level of microdamage in bone. On top of that, this motivation was supported by the growing interest in the role of microdamage in bone remodeling and bone biomechanics [4]. Finally the development of nonlinear acoustical techniques was also motivated by the failure of linear quantitative ultrasound to detect mechanical damage induced in trabecular bone [5].

Contrary to linear acoustics (see Chaps. 11 and 14), in the framework of nonlinear acoustics, the propagation velocity and the attenuation (or dissipation) of acoustic waves are amplitude dependent. Those peculiarities give rise to various phenomena called nonlinear acoustical effects. Some of those nonlinear phenomena were measured in bone and are presented in Sect. 15.2. Section 15.3 is dedicated to an introduction of the basic concepts employed to model the effect of cracks on the propagation of elastic waves.

15.2 Application of Nonlinear Acoustics to Experimental Assessment of Damage in Bone

In the context of nonlinear elasticity, the Hooke's law relating stress σ to strain ε is no more linear and additional terms are introduced to model nonlinear elastic phenomena. The following equation of state (15.1) is assumed in this experimental section to model nonlinear elasticity in bone, based on the results of both experimental and theoretical studies in micro-inhomogeneous media [1, 6]:

$$\sigma = M_0 \left(\varepsilon - \beta \varepsilon^2 - \delta \varepsilon^3 - \alpha \left[(\Delta\varepsilon)\, \varepsilon + sign(\dot{\varepsilon}) \frac{\varepsilon^2 - (\Delta\varepsilon)^2}{2} \right] \right), \qquad (15.1)$$

where M_0 is the linear elastic modulus, β and δ account for classical quadratic and cubic nonlinear elasticity, respectively, and α refers to nonclassical hysteretic quadratic nonlinearity. $\Delta\varepsilon$ is the maximum strain excursion, equal to the strain amplitude in the case of a constant-amplitude sinusoidal wave.

This section is devoted to the presentation of four experimental techniques applied to bone tissue in order to measure those three nonlinear elastic parameters.

15.2.1 Higher Harmonic Generation

The existence of elastic nonlinearity in a material induces a progressive distortion of an acoustic temporal waveform during propagation. When elastic nonlinearity can be modeled by a Taylor expansion of the elastic modulus, $M = M_0 + M_1\varepsilon + M_2\varepsilon^2 + \cdots$,[1] if the initial wave is monochromatic, the first order nonlinear interaction in the wave propagation equation gives rise to a solution containing new terms whose frequencies are higher multiples of the initial frequency $\omega/(2\pi)$ usually named higher harmonics [7].

Hence a classical experiment consists in propagating a monochromatic acoustic wave in the probed material over a distance L and measure the amplitude of second harmonic (at twice the fundamental or initial frequency) in the received acoustic wave.[2] The ratio between the amplitude of the second harmonic over the squared amplitude at the fundamental frequency quantifies the extent of the distortion of acoustic waveform, and consequently the magnitude of elastic nonlinearity in the medium. If diffraction and absorption (viscous and thermal) effects can be neglected over the propagation distance L and if phase velocity dispersion is sufficiently weak, a simple formula is obtained to evaluate the quadratic nonlinear elastic parameter β [7]:

$$\beta = \frac{4U_{2\omega}}{U_{\omega}^2 k^2 L}, \tag{15.2}$$

if the acoustic displacement U can be measured, where k, U_ω, and $U_{2\omega}$ are the wavenumber, the displacement amplitudes at the fundamental frequency and at twice the fundamental frequency, respectively,

$$\beta = \frac{2\rho_0 c_0^2 p_{2\omega}}{p_{\omega}^2 kL}, \tag{15.3}$$

if the acoustic pressure p is measured, where ρ_0, c_0, p_ω, and $p_{2\omega}$ are the linear density, the linear propagation velocity, the pressure amplitudes at the fundamental

[1] M_0 is the linear elastic modulus or the second-order (in energy) elastic constant, whereas M_1 M_2 are the third-order and fourth-order elastic constants, respectively, which account for nonlinear elasticity. M_1 and M_2 are negative for most of the materials.

[2] Practically, a burst containing at least ten acoustic periods is emitted to facilitate the extraction of the second harmonic amplitude in the frequency domain after the computation of the Fourier transform of the received acoustic signal.

frequency and at twice the fundamental frequency, respectively. Note that $M_0 = \rho_0 c_0^2$. This parameter includes two sources of nonlinearity: the kinematic or geometric nonlinearity, related to the small deviation from the linear relation between the strain and the particle displacement gradient, and the physical nonlinearity, associated with the small deviation from the linear Hooke's law[3] (15.1). In ordinary cases, for most of homogeneous fluids and solids, both sources of mechanical nonlinearity generally play a comparable role [8]. For fluids, β is usually expressed by:

$$\beta = 1 + \frac{B}{2A}, \tag{15.4}$$

where B and A are homogeneous to M_1 and M_0, respectively.

B/A is proportional to the first derivative of sound velocity with respect to the pressure under isentropic conditions [9]. This ratio B/A is indeed a measurement of the so-called acoustoelastic effect which is addressed in Sect. 15.2.2. Thus the quadratic elastic nonlinearity leads to a modulation of the propagation velocity: $c = c_0 + \beta v_{ac}$, where v_{ac} is the acoustic particle velocity. B/A varies between 2 and 15 for homogeneous liquids and solids[4] and ranges from 0.2 to 0.7 for gases [7]. Nonetheless, micro-inhomogeneous media like granular rocks, unconsolidated granular media (sand or sediment), cracked solids or liquids with gas bubbles, exhibit anomalously high acoustic nonlinearity and B/A can reach values up to 10^5 [1, 7, 10]. For these peculiar materials, kinematic nonlinearity can be neglected with respect to the nonlinearity of the equation of state.

Interestingly, the value of B/A assessed by the measurement of the second harmonic amplitude was shown to increase with the level of damage in metals. Thermal or mechanical damage was found to increase the value of β up to a few times [11–16].

The only reported *in vivo* study on the acoustic nonlinearity exhibited by bone tissue was precisely performed by the measurement of the second harmonic amplitude [17, 18]. An ultrasonic (US) burst containing 20 periods is transmitted through the heel bone. Because of huge ultrasonic attenuation in trabecular bone,[5] the fundamental frequency was chosen around 200 KHz. The acoustic pressure amplitude was of order a few hundreds of kPa. The authors conducted the experiment on five

[3] In other words, the nonlinearity in the equation of state of the material, relating stress to strain.

[4] In an isotropic solid, for a compressional plane wave, $\beta = -(3/2 + C_{111}/(2C_{11}))$, where C_{111} and C_{11} are elastic constants homogeneous to M_1 and M_0, respectively [7]. The value 3/2 instead of 1 in the expression of β is related to the difference between Lagrangian and Eulerian descriptions of particle motion. Moreover the negative sign arises from the difference in the definitions of the pressure and the stress. Besides, the reader has to pay attention to the definition of β when comparing values obtained by different studies. Indeed the parameter of quadratic nonlinear elasticity is sometimes defined as $\beta = -(3 + C_{111}/C_{11})$, twice the value usually employed in the "fluid" community.

[5] The heel bone or calcaneus contains 95% of trabecular surrounded by a thin cortical shell.

healthy volunteers and two osteopenic patients. For each subject, the T-score (see definition in Chap. 1) was measured by DXA (Dual energy X-ray Absorptiometry). Finally a substantial correlation was found out between the T-score and the ratio between the second harmonic amplitude and the fundamental amplitude. Thus this study suggests the ability of this nonlinear acoustical technique to distinguish between healthy and osteopenic subjects.

Nonetheless the physical origins of the increase of acoustic nonlinearity have to be clarified. Such a variation could be firstly attributed to an increase of the micro-crack density and/or the mean length of micro-cracks in osteopenic bone. Indeed a positive correlation between crack density and porosity was reported in other cortical and trabecular skeletal sites than heel but with various coefficients of determination ($R^2 = 0.1 - 0.7$) [19, 20]. Secondly the increase in the porosity also means the increase in the marrow volume fraction and consequently a decrease in the solid bone volume fraction. Calcaneal pores are mainly filled with yellow marrow which is in fact mostly fat. The nonlinear parameter B/A of fat is close to 10, in the same order of magnitude as the value for an homogeneous undamaged solid. Hence, for healthy solid bone tissue, B/A may be of order 10. Nevertheless, though this biphasic medium is made of a liquid and a solid whose B/A are similar, the nonlinear elastic effects will be more important in the fluid phase than in the solid phase. Indeed the relative importance of this acoustic nonlinearity can be evaluated by:

$$\frac{c - c_0}{c_0} = \beta \frac{v_{ac}}{c_0} = \beta \frac{p}{\rho_0 c_0^2} = \beta M_{ac}, \tag{15.5}$$

where M_{ac} is the acoustic Mach number. This allows to figure out that the relative magnitude is governed by β and M_{ac}. As a conclusion, for a given acoustic pressure amplitude, the nonlinear phenomena generated in healthy solid bone tissue may be weaker than in marrow because solids are denser and stiffer than liquids. Finally a simple increase in the marrow volume fraction (or porosity) may alternatively increase the level of acoustic nonlinearity. However if the presence of micro-cracks sufficiently increase the value of B/A in solid bone tissue, this could also lead to an increase of the global acoustic nonlinearity.

Besides, a rising number of experiments shows that the amplitude of the third harmonic (at three times the fundamental frequency) is more sensitive to the level of damage than the second harmonic. In an homogeneous undamaged material, the third harmonic is weaker than the second harmonic and its amplitude is proportional to the cube of the fundamental amplitude. On the contrary, the existence of inter-grain contacts or cracks in a solid enhances the third harmonic whose amplitude can even exceed the second harmonic amplitude [21]. Moreover the amplitude of the third harmonic is proportional to the square of the fundamental amplitude. Consequently the presence of "soft inclusions" embedded in a more rigid matrix modify the acoustic nonlinearity in qualitative and quantitative manners [2].

These effects were recently observed *in vitro* in trabecular human heel bone [22]. In this experiment, a 400 KHz burst is emitted by a focused transducer and received by a needle hydrophone after 45 mm of propagation. The measurement was

performed when propagation occurs in water only and when a 24 mm-thick slice of defatted (and saturated with water) calcaneal trabecular bone is inserted on the propagation path near the hydrophone (Fig. 15.1). The maximum acoustic amplitude used in the experiment is 110 kPa.

As expected, the propagation through water produces a third harmonic weaker than the second harmonic and whose amplitude is proportional to the cube of the fundamental amplitude (Fig. 15.2). On the contrary, despite high attenuation induced by trabecular bone at the third harmonic frequency (30 dB/cm), the third harmonic amplitude exceeds the second harmonic amplitude and is proportional to the square of the fundamental amplitude (Fig. 15.2) when the bone sample is inserted on the ultrasonic path. This anomalously high third harmonic amplitude may originate from the presence of cracks in the solid bone tissue, as reported for damaged solids [21].

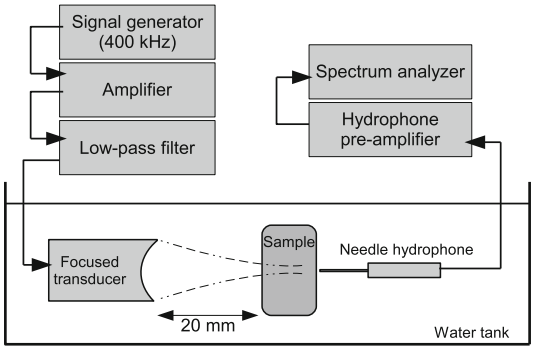

Fig. 15.1 Experimental setup for the harmonic distortion method

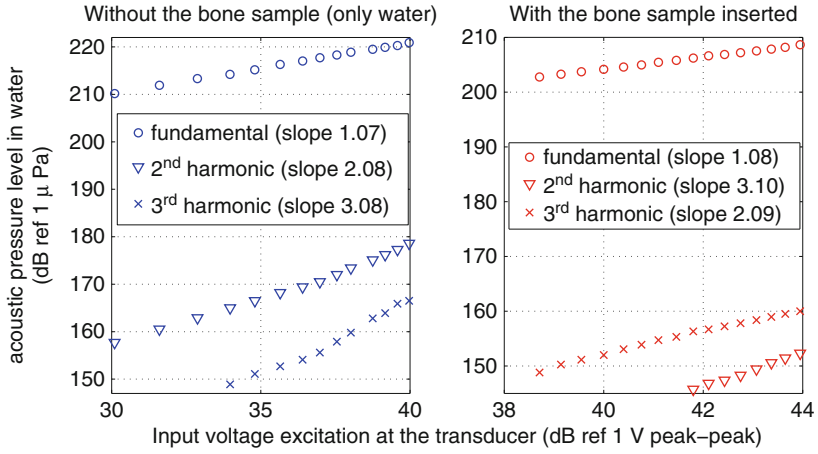

Fig. 15.2 Fundamental, second and third harmonics amplitudes (in dB) as functions of the input voltage amplitude measured after 45 mm propagation in water (*left*) and with a 24 mm-thick slice of calcaneal trabecular bone inserted in the propagation path (*right*). The bone sample is saturated with water

15.2.2 Dynamic Acoustoelastic Testing (DAET)

From the end of the nineteenth century, the primary measurements of elastic nonlinearity were performed by static methods leading to the thermodynamic p-v-T diagram, from which the pressure and temperature dependences of the bulk elastic modulus were deduced for fluids and solids [23]. In the beginning of the 20th century, dynamic resonant or interferometric techniques were developed to measure elastic moduli or sound velocity as functions of temperature and hydrostatic pressure [24–26]. Finally, with theoretical developments of the effect of a static stress field on the propagation of elastic waves [27,28], followed by the possibility of generating an ultrasound (US) pulse [29] and thus of measuring the sound velocity by the time-of-flight (TOF) determination, acoustoelastic testing became an alternative way to measure elastic nonlinearity. This technique consists in measuring changes in the US velocity induced by a hydrostatic [30,31] or uniaxial [32] stress. For metals and polymers, the relative variation in US velocity is of the order of 0.001 and 0.01%/MPa of the applied stress, respectively. Interestingly, in damaged or granular media, the presence of cracks or intergrain contacts can give rise to variations in US velocity exceeding 1%/MPa of applied stress [33], some orders of magnitude higher than in undamaged solids. Moreover, in these peculiar media, US attenuation is also affected by the application of a static stress as a result of the progressive closing of cracks when the external stress is increased [34,35]. Finally, the induced variations in the US velocity and attenuation can be related to acoustic nonlinear elasticity and dissipation, respectively.

15.2.2.1 Principle of Dynamic Acoustoelastic Testing

Close to the work of Ichida et al. [36] and Gremaud et al. [37], dynamic acoustoelastic testing (DAET) was firstly developed in a remotely manner [38, 39] for liquids, gels as well as porous and non-porous rather soft solids. In a water tank, the probed sample is simultaneously crossed by two acoustic waves propagating in perpendicular directions (Fig. 15.3):

- The probing wave: US pulses emitted from one side of the sample by an immersion transducer and received by another US transducer at the other side of the sample.
- The pumping wave: a low-frequency (LF) wave generated in water by a vibrating disk and received by a hydrophone placed near the sample.

Similar to quasi-static acoustoelastic testing, the LF acoustic pressure is expected to modulate the TOF and the attenuation of US pulses.

DAET needs the LF wave to be quasi-static over a US TOF and quasi-uniform in the probed volume. As a result, the LF period must be at least ten times higher than the US TOF. A quasi-uniform LF pressure amplitude in the probed volume is obtained if the LF wavelength is much higher than the characteristic size of the investigated volume. Moreover the diameter of the LF radiating disk is chosen so

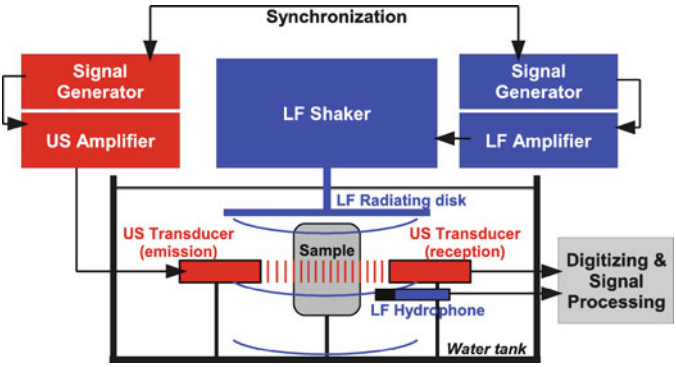

Fig. 15.3 Experimental configuration for DAET

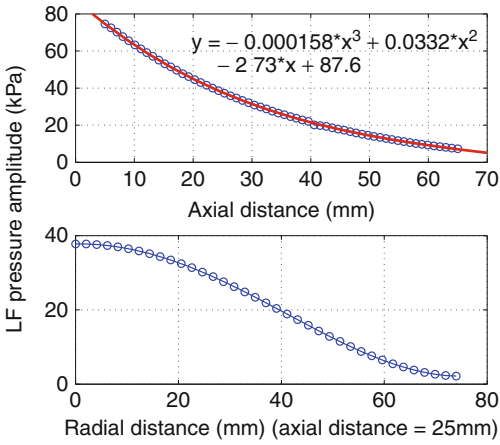

Fig. 15.4 Axial and radial LF diffraction patterns measured by the hydrophone, obtained for a 15 cm diameter glass disk at 2850 Hz

that the LF pressure amplitude is almost constant over the US propagation path. The diameter of the LF disk being smaller than the LF wavelength the LF diffraction pattern offers a soft decreasing profile for the LF pressure amplitude along the disk axis (Fig. 15.4). Consequently the pressure in the water surrounding the sample is quasi-uniform and sinusoidally modulated in time, inducing successively quasi-hydrostatic compression and expansion of the sample, when the LF acoustic pressure takes positive and negative values, respectively. Typically, the distance between US transducers equals a few centimeters, then the US TOF is of order 10 µs, so that the frequency of the pumping wave equals a few KHz. The LF pressure amplitude can not exceed 100 kPa because cavitation may occur during the expansion phase as soon as the acoustic pressure amplitude exceeds the ambient pressure.

Note that the dimensions of the water tank must be larger than the characteristic LF diffraction length $L_d = ka^2/2 \approx 3\,\text{cm}$, where k and a are the LF wavenumber and the LF disk radius, respectively. Indeed the walls must be approximately 30 cm away from the LF disk so that reflections from the wall are negligible. Plane or

focused US immersion transducers are used to generate and receive the US pulses. For a US frequency of order 1 MHz and 13 mm diameter plane transducers used to obtain the following results, the US beam is collimated over a few centimeters.

Thus DAET is capable of noninvasive (acoustic transducers are not bounded on the sample) and regional (region of interest is a cylindrical volume whose diameter equals the lateral resolution of the US beam) measurements of elastic and dissipative acoustic nonlinearities induced by dynamic tensile/compressive quasi-hydrostatic loading. It is worth noticing that if the sample is porous, it has to be saturated with water before performing DAET.

For each US pulse, the time-of-flight modulation (TOFM) and the relative energy modulation (REM), related to elastic and dissipative acoustic nonlinearities respectively, are computed [38, 39]. TOFM is determined by the time position of the interpolated maximum of the cross-correlation function between the current US pulse with index i and the first pulse ($i = 1$) which propagates through the medium with no LF perturbation [38]:

$$TOFM(i) = TOF(i) - TOF(1) \tag{15.6}$$

Furthermore, the Fourier transform of each US pulse with index i is computed to calculate its energy $E(i)$ as the integral of the power spectrum in the frequency bandwidth defined at -10 dB of the maximum amplitude. For the US pulse with index i, REM is given by:

$$REM(i) = [E(i) - E(1)]/E(1), \tag{15.7}$$

where $E(1)$ is the energy of the first US pulse that propagates through the medium without LF loading. Finally, each US pulse is associated with the mean value of the LF pressure during its TOF (Fig. 15.5).

The synchronization of the LF and US signals allows to plot TOFM and REM as functions of the LF pressure. Figure 15.6 represents the two diagrams obtained for a distance of 57 mm between the US transducers, without any sample (only water) and with a 52 mm thickness sample of PMMA (polymethyl methacrylate) inserted between the US transducers.

For water without any sample and with a PMMA sample inserted in the interaction area, no nonlinear dissipative effects are measured whereas the acoustoelastic effect leads to a linear relation between TOFM and the LF pressure (Fig. 15.6).

The relation between TOFM and the LF pressure can be related to elastic nonlinear parameters β[6] and δ, associated with quadratic and cubic nonlinearity, respectively [38, 39]. Because the propagation velocity equals $\sqrt{M/\rho}$, where M is the elastic modulus corresponding to the type of US propagation and ρ the density, TOFM is proportional to small variations of the elastic modulus ΔM_{sample} induced

[6] In the DAET configuration, the convective effect cannot occur because the LF and US beams propagate in perpendicular directions. In this section, we redefine β as $\beta = B/A$.

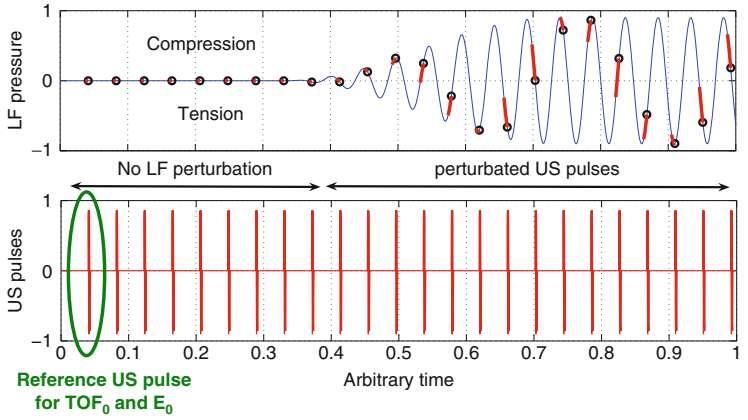

Fig. 15.5 Schematic representation of the raw LF and US time signals. *Top*: thin solid line is the LF pressure measured by the hydrophone, circles mark the value of the LF pressure when the US pulses reach the US receiver and thick solid lines show the slight variations of the LF pressure during a US TOF, averaged for each US pulse. *Bottom*: US pulses received by the US transducer after propagation through the sample and emitted with a repetition frequency slightly higher than the frequency of the pumping wave

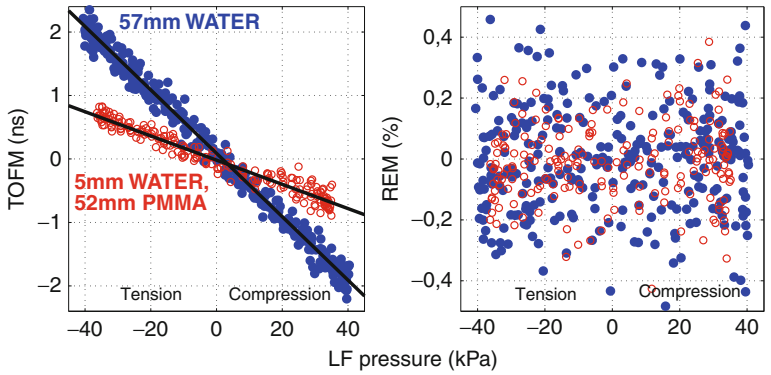

Fig. 15.6 TOFM and REM as functions of the LF pressure. *Filled circles*: 57 mm between US transducers without any sample. *Open circles*: with a 52 mm thick PMMA sample inserted between the US transducers. *Solid lines* are linear fits

by the LF pressure p_{LF}[7]:

$$TOFM_{sample} = -\frac{L_{sample}}{2\rho_{sample}\, c_{sample}^3}\Delta M_{sample},$$

[7] For most of materials, small relative variations of the density can be neglected compared to small relative variations of the elastic modulus.

$$\Delta M_{sample} = \beta p_{LF} - \delta \frac{p_{LF}^2}{M_0}, \tag{15.8}$$

where L_{sample}, ρ_{sample}, c_{sample} and $M_0 = \rho_{sample} c_{sample}^2$ are the propagation length in the probed medium, the density, the propagation velocity and the elastic modulus with no LF perturbation.

Using (15.8) and extracting the slope $\frac{\partial TOFM}{\partial p_{LF}}$ by linear fitting of the relation measured between TOFM and the LF pressure (Fig. 15.6), β equals 4.9 ± 0.3 and 11 ± 1 for water and PMMA, respectively. These values are in agreement with the literature [7].

After illustration and validation of the method in water and with a PMMA sample, results obtained for calcaneal human trabecular bone are now presented.

15.2.2.2 Results in Human Calcaneal Trabecular Bone

The acoustic nonlinearity exhibited by a human calcaneus whose lateral faces were sliced to obtain parallel surfaces is presented. The same 24 mm-thick slice of trabecular bone was investigated with the harmonic distortion method (Sect. 15.2.1). The marrow was removed by immersion in hot water and in trichloroethylene. Then the sample was saturated with water and placed in the experimental setup. Figure 15.7 illustrates the two investigated regions of interest (ROI): The upper part of the calcaneus (ROI 1) where the porosity is relatively low ($75\% \pm 5$) and trabeculae are plate-like shaped, the posterior part (ROI 2) where the porosity is higher ($89\% \pm 2$) and trabeculae are rather rod-like shaped [40].

Figures 15.8 and 15.9 show that the acoustic nonlinearities measured in the ROI 1 are an order of magnitude higher than the ROI 2. Whereas the ROI 2 does not change significantly the TOFM diagram measured in water without the sample, weak dissipative nonlinearities are observed in the ROI 2 while only noise is measured in the relation REM *vs.* LF pressure without the sample (Fig. 15.9). The corresponding quadratic nonlinear elastic parameter β equals 10. Interestingly the ROI 1 exhibits huge acoustic nonlinearity with tension-compression asymmetries and hysteresis for both TOFM and REM (Fig. 15.8). Using a quadratic fit, we obtain $\beta = 150$ and $\delta = 4.10^6$ for ROI 1. Consequently β is an order of magnitude higher than for undamaged solids and the value is in agreement with a previous study [41].

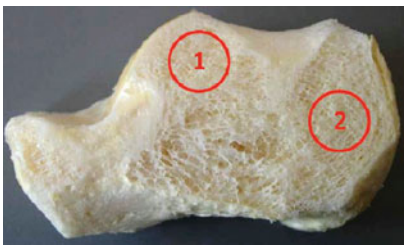

Fig. 15.7 Photography of a sample of human calcaneus. The two probed regions of interest are shown

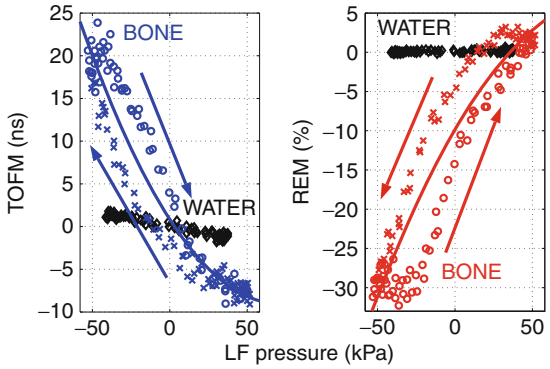

Fig. 15.8 TOFM and REM as functions of the LF pressure obtained in the ROI 1. Diamonds represent the measurement obtained in water without the sample. Open circles and crosses represent the results with the bone sample for increasing and decreasing LF pressure, respectively. The arrows show the way of variation of the LF pressure in the hysteresis. Solid lines are quadratic fits

Fig. 15.9 Same legend as Fig. 15.8 for the ROI 2

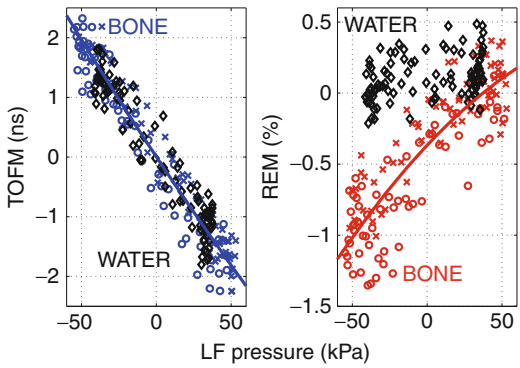

The fact that $\delta \gg \beta^2$ is another manifestation of non-classical elastic nonlinearity, was attributed to the presence of intergrain and/or cracks in granular rocks [42]. Tension-compression asymmetry and hysteresis were also observed by DAET in cracked pyrex [39], cracks are thereby again pointed out as being the source of acoustic nonlinearity investigated by DAET in trabecular bone. Note however that the bottom/anterior region of the calcaneus, which is highly porous (95.5±1.5%) [40], was also investigated but does not change the TOFM and REM measured in water without the sample, certainly because of too low solid bone volume fraction.

Aware that the treatment used to defat this bone sample induces a denaturation of the solid bone tissue, regional DAET scanning was conducted on 8 whole human calcanei defatted using the Supercrit© (BIOBank, France) technique[8] (supercritical CO_2 delipidation) ensuring minimum denaturation of bone tissue. Their lateral faces were also sliced to obtain parallel surfaces. The age of donors ranges 70–90 years old.

[8] http://www.biobank.fr/

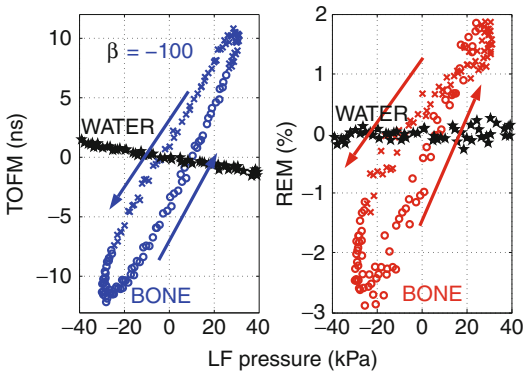

Fig. 15.10 DAET results obtained in ROI 1 of the sample defatted by supercritical CO_2 exhibiting the highest acoustic nonlinearities. *Stars*: measurement obtained in water without the sample. *Open circles*: measurement with the bone sample when the LF pressure increases. *Crosses*: measurement with the bone sample when the LF pressure decreases

Two samples out of 8 exhibited high acoustic nonlinearities in ROI 1 and weaker effects in ROI 2. The other six bone samples do not change significantly the results obtained in water without any sample. Figure 15.10 shows the DAET diagrams obtained for the sample exhibiting the highest acoustic nonlinearity. Quadratic nonlinear elasticity is high ($\beta = -100$) and a large hysteresis is observed in the relation between TOFM and the LF pressure. The anomalous negative sign of β requires further investigation to understand the responsible physical phenomenon. Moreover US energy modulation is also measured, REM reaches -3% in tension and 2% in compression with hysteresis as well. The reason why only two out of eight calcanei exhibited important acoustic nonlinearities may be the dispersion in the level of microdamage reported in histological studies [43].

In order to test the hypothesis that heterogeneity of the level of microdamage is responsible for weaker acoustic nonlinearities in ROI 2 than in ROI 1 in the "supposedly most damaged" sample, a histological quantification was recently reported by Moreschi et al. [44]. The sample exhibiting the highest acoustic nonlinearities was firstly bulk stained with 0.02% alizarin complexone (chelating fluorochrome) which bind to free calcium links so that cracks are labelled [45]. Secondly the sample is embedded in a polymeric resin and cut in 300 µm thick slices using a low-speed diamond saw. Cracks and split trabeculae were then counted under laser confocal microscopy in regions 1 and 2 (Fig. 15.11). Interestingly the crack density equals 0.2 ± 0.015 crack/mm^2 in ROI 1[9] and is half this value in ROI 2. Similarly the split trabeculae density equals 0.26 ± 0.047 crack/mm^2 in ROI 1 and reaches only 0.11 ± 0.039 in ROI 2.

[9] The crack density is expressed in cracks number per square mm of bone tissue.

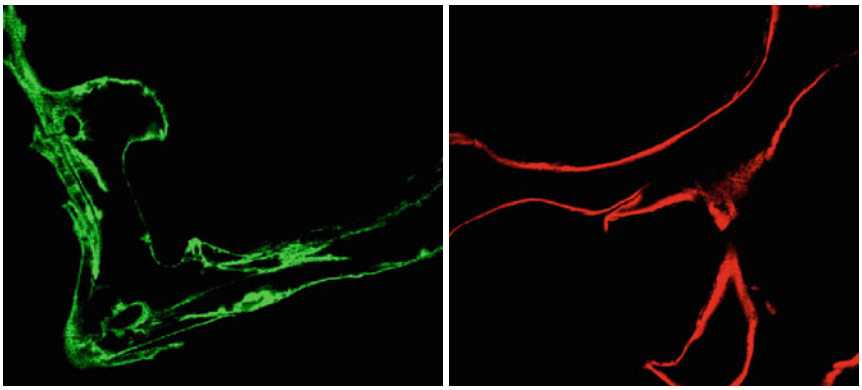

Fig. 15.11 Microdamage labelled by chelating fluorochrome and observed by Laser scanning microscopy. *Left*: the sample defatted by trichloroethylene shows multiple splits of the trabeculae. *Right*: an isolated split of a trabeculae in the sample defatted by supercritical CO_2

Consequently, this preliminary histological study supports the idea that the overall number of cracks is higher in ROI 1 than in ROI 2 for two reasons:

- The crack density is higher in region 1 than in region 2.
- The bone volume fraction is higher in region 1 than in region 2 (solid bone surface fraction equals 41.6% and 29% in ROI 1 and 2, respectively).

These may be the causes that give rise to acoustic nonlinearities higher in ROI 1 than in ROI 2. However the results indicate that DAET may not be able to detect microdamage if simultaneously the porosity is too high ($>\approx 85\%$) and the crack density is too weak ($<\approx 0.1$ crack/mm^2).

All these experimental findings put together suggest that DAET is a sensitive tool to assess the level of microdamage in trabecular bone. Moreover DAET allows noninvasive and regional measurement of elastic and dissipative acoustic nonlinearities, whose instantaneous effects can be plotted as a function of the LF pressure. Consequently a possible tension-compression asymmetry and hysteresis, which are signatures of the presence of cracks, can be observed.

Finally Moreschi et al. recently performed a study testing the correlations between acoustic nonlinearity measured by DAET, mechanical damage induced by fatigue [46] and histological quantification of microdamage by sequential labelling of the cracks using chelating fluorochromes of two different colors [47]. The quantification of the crack density before and after damaging mechanical testing is expected to provide quantitative relations between the level and the type of microdamage and the level and type of acoustic nonlinearity, as previously performed for rocks [48, 49] and carbon fiber reinforced plastic [50]. This current research is the necessary step before an *in vivo* application can be considered. Furthermore, DAET could also be applied to cortical bone using axial US transmission instead of transverse US transmission as presented here for trabecular bone.

15.2.3 Nonlinear Resonant Ultrasound Spectroscopy (NRUS)

Nonlinear Resonant Ultrasound Spectroscopy (NRUS) is a technique that has been developed as an extension of the Resonant Ultrasound Spectroscopy (RUS) technique [51], originally designed to assess the full linear elastic tensor of materials from their resonant behavior. The NRUS technique also exploits the resonant behavior of samples, but to retrieve the nonlinear elastic behavior of the material. As has been developed in the previous section, knowledge on the nonlinear elastic behavior of a sample, and especially on the nonlinear hysteretic behavior, can bring a relevant insight on its damage state. The NRUS technique has proved useful in various materials [21, 51–54], for non-destructive evaluation, and has been applied to bone [55, 56].

The purpose of this technique is precisely to assess the hysteretic behavior of a material sample. Micro-crack accumulation in a material sample is responsible for a softening of the material for increasing excitation amplitudes, leading to a decrease of the resonance frequency when excitation amplitude increases. From the expression of the nonlinear modulus in (15.1), it can be shown that, for a resonant mode, the resonance frequency shift expresses as a function of strain [57]:

$$\frac{f_0 - f}{f_0} = \frac{\alpha\varepsilon}{2} + \frac{\delta\varepsilon^2}{4} \tag{15.9}$$

The parameter α is called the nonlinear hysteretic parameter, and conveys information about the amount of hysteretic nonlinearity in a material. δ is the parameter describing the classical cubic nonlinearity. In bone, and particularly in damaged bone, the classical cubic nonlinearity is negligible compared to the hysteretic nonlinearity. Therefore, only the linear term of (15.10) remains, and the observed frequency shift is directly proportional to the nonlinear hysteretic parameter α. The NRUS technique is based on this approximation, and provides a very useful tool for the measurement of the parameter α.

$$\frac{f_0 - f}{f_0} \propto \frac{\alpha\varepsilon}{2} \tag{15.10}$$

As the classical nonlinearity is neglected compared to the hysteretic nonlinearity in bone, a linear decrease of the resonance frequency can be observed for increasing strain amplitudes. Therefore, measurement of the resonance frequency shift as a function of increasing strain amplitudes gives access to the hysteretic parameter in a straightforward manner.

The nonlinear hysteretic behavior of bone samples has been investigated using the NRUS method in a few studies in human and bovine femur [55, 56]. Frequency sweeps were applied to the bone samples for gradually increasing drive amplitudes, and the modal peak frequencies were measured at each drive amplitude (Fig. 15.12). The resonance modes were determined experimentally, and through finite elements

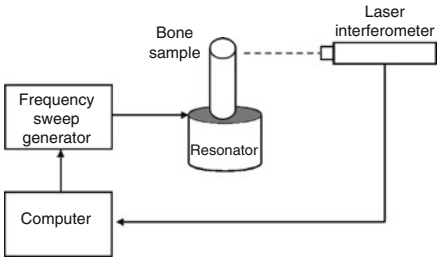

Fig. 15.12 Nonlinear Resonant Ultrasound Spectroscopy (NRUS) setup

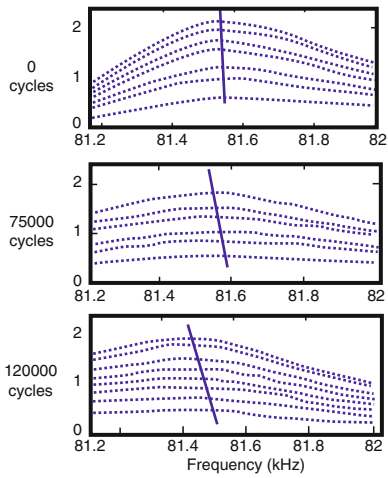

Fig. 15.13 Typical resonance spectra measured in one sample after 0, 75000, and 120000 cycles of mechanical testing. The resonance frequency shift significantly increases with damage accumulation

modeling methods, using a CT scan 3D image of the sample as an input. The nonlinear parameter was then simply derived from the resonance frequency shift as a function of strain, according to (15.10).

Samples were gradually damaged using compressive mechanical testing (with an INSTRON mechanical testing machine) and the nonlinear parameter α was assessed for each damage step using NRUS.

15.2.3.1 Influence of Damage Accumulation

Figure 15.13 shows typical resonance responses as an example from one sample at three different damage steps. It can be observed that, as damage accumulates, the resonance frequency shift for increasing excitation amplitude increases. For all the samples tested (around 30 samples), the nonlinear parameter derived from NRUS increased with the number of mechanical testing cycles and it started to increase as for the first few mechanical testing cycles. A similar behavior could have been expected for the hysteresis of the load/displacement curve, measured by the mechanical testing device, since it is the quasistatic equivalent of the dynamic nonlinear

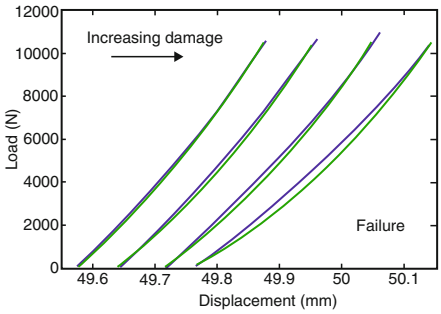

Fig. 15.14 Load/displacement curves for a single sample continuously cycled to failure. Just before failure, the hysteresis increases dramatically. Reprinted from Biomedical Applications of Vibration and Acoustics in Imaging and Characterizations, Mostafa Fatemi and A. El Jumaily (Editors), Copyright (2008), ASME Press

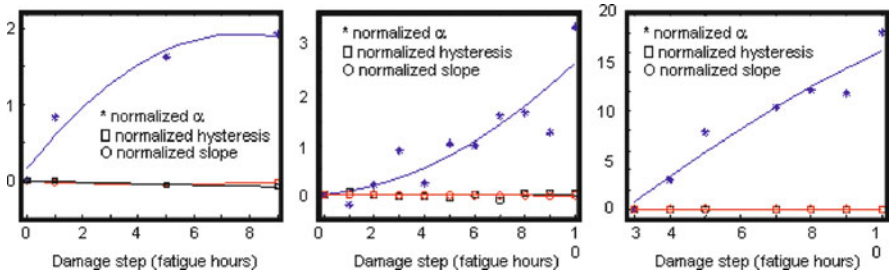

Fig. 15.15 Sensitivity of the nonlinear parameter α to fatigue cycling of bone. Comparison of the evolution of the nonlinear parameter α, the slope and the hysteresis of the load/displacement curve for three typical samples. Reprinted from Biomedical Applications of Vibration and Acoustics in Imaging and Characterizations, Mostafa Fatemi and A. El Jumaily (Editors), Copyright (2008), ASME Press

hysteretic parameter α [58, 59]. However, such behavior could not be observed in the quasistatic regime, where significant changes of the slope and hysteresis of the load/displacement curve were observable only just before failure, as can be seen on Fig. 15.14.

Figure 15.15 shows the evolution of $(\alpha/\alpha_0 - 1)$ derived from NRUS as a function of fatigue cycles, as an example for three samples. Here, α_0 is the nonlinear parameter α in the undamaged state, before mechanical testing. On the same figure are shown the behavior of the slope of the load/displacement curve, and of the damage parameter D, the parameter $(h/h_0 - 1)$, h being the hysteresis of the load/displacement curve obtained during mechanical testing. The nonlinear parameter α increases much more with accumulating damage than any other parameter that could be measured, which suggests a much stronger sensitivity. In addition, the measured nonlinear parameter α shows change immediately, after the first cycling in most cases, and changes significantly over the duration of cycling in most

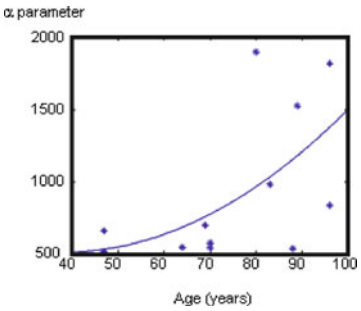

Fig. 15.16 Evolution of the nonlinear parameter α as a function age for all the tested samples. Reprinted from [56], Copyright (2008), with permission from Elsevier

cases, when other parameters start to change significantly just before failure. This suggests that the nonlinear parameter could be a potential tool for early damage detection in bone.

15.2.3.2 Influence of Donor Age

Figure 15.16 shows the evolution of the nonlinear parameter α with the age of donors. This curve can be approximated by an exponential, or second order relationship.

This second order behavior of the nonlinear parameter as a function of donor age is similar to direct measurements of damage in bone described in [60]. A larger scatter of α was observed in the region of the curve corresponding to older ages, and values tend to be larger with age in general. This observation is consistent with the distribution of damage accumulation across ages reported in [60]. The similarity of the behaviors of the nonlinear parameter and micro-damage accumulation as a function of age is an additional, qualitative indication that the nonlinear hysteretic parameter provides an relevant insight on the damage state of bone.

15.2.4 Nonlinear Wave Modulation Spectroscopy (NWMS)

The nonlinear wave modulation spectroscopy technique is based on the interaction of two waves with different frequencies f_0 and f_1 (typically $f_0 \ll f_1$) with amplitudes A_0 and A_1. Due to the presence of damage in the bone sample, the two waves interact, creating harmonic frequencies (e.g., $2f_0$, $3f_0$, etc. f_0 being the fundamental frequency) as well as sum and difference frequencies (sidebands), $f_1 \pm f_0$ and proportional in amplitude to the product of the primary wave amplitudes. This technique has been applied broadly in industrial materials and geomaterials [21, 54, 61, 62], and has proved to be efficient even in the presence of elastically linear scatterers [63]. The first attempt to use this technique is human bone was reported by Donskoy and Sutin (1997) [41], who retrieved the nonlinear parameter in trabecular bone in the 100 KHz frequency range, showing that it was an order

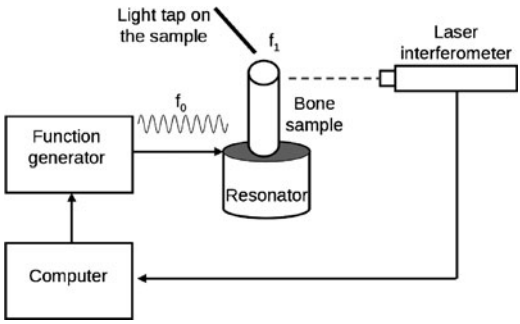

Fig. 15.17 Nonlinear Wave Modulation Spectroscopy (NWMS) setup

of magnitude stronger in bone than in nonporous media. Further NWMS measurements were performed, respectively in human cortical and trabecular femoral bone, by Ulrich et al. (2007) and Zacharias et al. (2009) [64, 65]. In the latter study, the technique has been used in both healthy and osteoporotic human trabecular bone, in the 50 KHz range, and the results exhibit a higher level of sidebands in the osteoporotic bone, potentially more micro-damaged. In the study by Ulrich et al., the technique was applied in the 200 KHz frequency range, on human cortical bone, progressively damaged using a mechanical testing device. Low-frequency vibrational modes of a human femur sample were simultaneously excited by a mechanical impulse (induced by a light tap on the sample) and a high frequency, continuous wave tone, in this case 223 KHz (Fig. 15.17). This frequency was selected as it was the frequency for which highest amplitude could be applied with the source transducers used. The vibrational modes mix (multiply) with the pure tone, producing multiple sidebands.

In Fig. 15.18 are shown some results obtained using the Nonlinear Wave Modulation Spectroscopy technique *in vitro* in human femur. The bone samples were subjected successively, to 45000 and 75000 mechanical testing cycles, inducing micro-damage to accumulate. The sidebands ($f_1 \pm f_0$ and $f_1 \pm 2f_0$) energy was found to increase with accumulating damage, visible on Fig. 15.18, *left*.

A new dynamic nonlinear parameter Γ, taking into account both the first order classical nonlinear parameter β and the hysteretic nonlinear parameter α (see (15.1)) was defined as the area below the linear frequency spectrum of the sample response, containing the first order ($f_1 \pm f_0$) and second order ($f_1 \pm 2f_0$) sidebands, here from 215–231 KHz, in order to include the effects of multiple sidebands simultaneously (Fig. 15.18, *left*). The evolution of this nonlinear parameter Γ is shown in Fig. 15.18 (*center*), along with the evolution of a quasistatic damage parameter D, derived from the slope of the stress-strain curves, obtained during the quasistatic mechanical testing experiments. Figure 15.18 shows that the dynamic nonlinear parameter Γ changes by about 700%, when the change in slope from the quasistatic experiment remains roughly the same until the last damage step, where a change of about 10% only is observable. This confirms the observations made by Muller et al. using the Nonlinear Resonant Spectroscopy technique [56]: the dynamic nonlinear parameters are far more sensitive than the quasistatic linear parameters, and are sensitive to earlier damage.

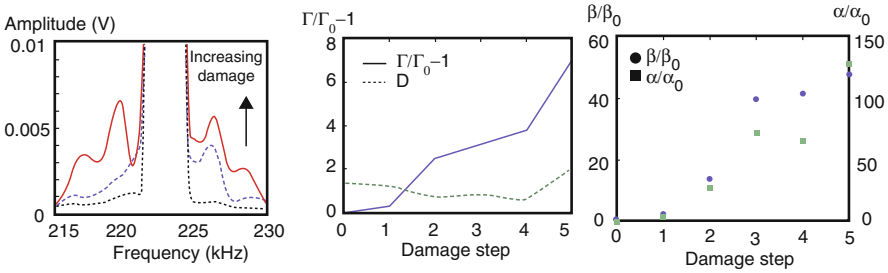

Fig. 15.18 *Left*: Power spectra of sideband frequency range for 3 damage steps (0, 30000, and 75000 cycles of mechanical testing). The increase in sideband energy as the fatigue damage increases is clearly visible. *Center*: Comparison of the relative changes of the nonlinear parameter Γ with the standard damage parameter D (extracted from linear elastic measurements). *Right*: Separate evolutions of the nonlinear parameters α and β, for increasing damage steps. Reprinted from Biomedical Applications of Vibration and Acoustics in Imaging and Characterizations, Mostafa Fatemi and A. El Jumaily (Editors), Copyright (2008), ASME Press, and from [64], Copyright (2007), with permission from the American Institute of Physics

It is also possible to isolate the two nonlinear parameters β and α by calculating the ratio of the first or second order sideband amplitudes respectively, to the drive amplitude. Figure 15.18 (*right*) shows the separate evolutions of the nonlinear parameters β and α as a function of accumulating damage (i.e. as a function of fatigue cycles), normalized to their respective values measured in the undamaged state. This normalization is important here, considering the fact that no absolute value could be obtained for the nonlinear parameters, since no calibration measurements have been performed that would link quantitatively the nonlinear parameters values to an amount of damage. It appears that both parameters significantly increase with increasing damage. However, the nonlinear parameter α seems to be more sensitive than the nonlinear parameter β, since the values of β are in a range of 0–60, while the values of α are in a range of 0–120, for the same sample.

15.3 Theoretical Modeling of Damage-induced Nonlinearity, Limitations of the Technique

15.3.1 Physical Origins of Nonlinearity in Damaged Bone

The previous section reviews different experimental nonlinear acoustic techniques that can be used for a noninvasive assessment of bone mechanics. Although ultrasound measurements give access to mechanical parameters strongly related to stress and strain, and to fracture risk, they do not allow their direct measurement. Experimental studies described in the previous section showed that the measurement of nonlinear ultrasound parameters can provide a straightforward access to damage

amount in bone. However, the use of appropriate models is required to fully characterize the nonlinear relationship between stress and strain in damaged bone. This full characterization could be useful for a better understanding of the nonlinearity induced by damage in bone. Indeed, the damage-induced nonlinearity that can be measured acoustically at the macroscopic level results from some nonlinear phenomena at the crack level and below, on a microscopic scale. A large amount of research has been conducted to establish the link between microscopic and macroscopic scales in terms of damage and nonlinearity. Different types of models are studied and used in the literature: phenomenological models and theoretical models.

15.3.1.1 Phenomenological Model

Phenomenological models used to describe micro-cracked solids are based on the observation that micro-damage induces a hysteresis in the stress-strain relation (Fig. 15.19). This phenomenon has been observed in a large class of materials, as well as in bone. In this paradigm, a microdamaged material is described as an ensemble of hysteretic units called hysterons, small structures at the microscopic level that are responsible for the hysteretic behavior of the stress-strain relationship. The strain response of each hysteron is modeled by the combination of a classical nonlinear term, and a nonclassical nonlinear contribution attributed to hysteretic behavior [1, 66]. In order to describe this phenomenon, a model has been established by Guyer and McCall [6, 67], inspired by the work of Preisach and Mayergoyz in magnetism [68, 69]. The nonclassical nonlinear contribution is obtained by stating that the hysteretic units can only be found in two equilibrium states: open or closed. Therefore, each hysteron can be fully described by two sets of parameter pairs: (σ_o, σ_c) and $(\varepsilon_o, \varepsilon_c)$, which respectively describe the stresses and strains necessary for the hysterons to be in open or closed states. Particular rheological relationships can be attributed to hysterons [70]. The hysterons can be arranged in the Preisach-Mayergoyz space (PM space, Fig. 15.19), that allows to keep track of the state (open or closed) of a whole distribution of hysterons. This arrangement in the PM space

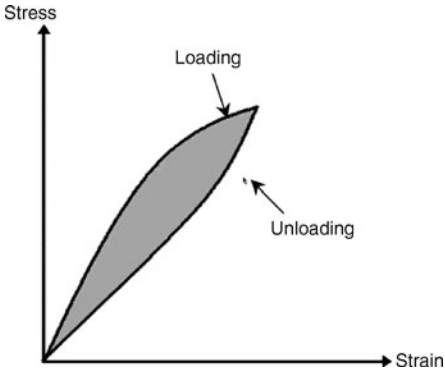

Fig. 15.19 Micro-cracked materials exhibit a very particular stress-strain relation, in which two different paths are taken, depending on the sign of the strain rate

constitutes the link between microscopic and mesoscopic scales. An equation of state (the stress/strain relation) is derived from the hysterons distribution density in the PM space. Note that it is possible to simplify this phenomenological model, in the case of small strains, by assuming a uniform density of the hysterons in the PM space. In this case, the nonclassical hysteretic nonlinearity can be described as having a quadratic dependence on strain, which qualitatively agrees with experimental results obtained with NRUS, and is shown in (15.1).

This phenomenological model can be numerically derived using various processes. Among them, the Local Interaction Simulation Approach (LISA) considers the hysteretic elements at the microscopic levels and models wave propagation in such media [70]. This modeling approach provides good results but is extremely demanding in terms of computational resources. Another numerical approach that has been used considers mesoscopic units, representing a statistical ensemble of hysterons (as opposed to the LISA method that considers each hysteron individually). These new units have a characteristic size smaller than the wavelength, exhibit hysteretic strain responses at the mesoscopic scale, and are used as elementary cells for finite differences simulations, using an elastodynamic finite integration technique (EFIT) [71, 72].

15.3.1.2 Theoretical Models

Some drawbacks can be pointed out regarding the phenomenological model described in the previous section. First, the numerical implementations of the model requires an *a priori* assumption about the distribution of hysteretic units, used as an input to the model. Secondly, the model does not describe an accurate picture of the physical phenomena responsible for the very typical nonlinear behavior of damaged solids. Some theoretical and experimental work has been conducted in various fields such as geophysics, non destructive evaluation, and granular materials physics, in order to depict the physical phenomena at stake. Although crack-induced nonlinearity is probably not fully understood and modeled yet, it appears that the observed phenomena (nonlinear modulation, hysteresis in the dynamic stress/strain relation...) are the consequences of various causes. One of these causes has been thoroughly studied over the years, and corresponds to the purely elastic nonlinearity, due for instance to Hertzian contacts, at the cracks inner contacts scale [73]. For this particular cause of crack-induced nonlinearity, the magnitude of the nonlinear effects is sensitive to the presence of weak, damaged regions in the material [74, 75]. In addition to these classical nonlinear elastic effects, more particular effects have been observed such as hysteretic nonlinearity. Some models have been derived [10, 62], based on the description of hysteresis as amplitude dependent dissipation. In these models, dissipation can be attributed to friction/adhesion hysteresis at the crack interface [76], or to locally enhanced thermoelastic coupling at the inner crack contacts. Note that in the case of friction/adhesion, a strain threshold is required to allow the phenomenon to occur. This threshold has never been

accurately calculated for bone, but corresponds to the ratio of the interatomic distance to the crack diameter [62], which would lead in bone to strains around 10^{-5}, in most cases higher than the strains used in the various experimental studies (from 10^{-6} to 10^{-5}). This could lead, as a first approximation, to the conclusion that the friction adhesion mechanisms in bone are unlikely to contribute significantly to the nonlinear hysteretic observed phenomenon, but only a thorough theoretical study of the possible mechanisms responsible for bone nonlinear behavior, taking into account bone peculiarities (heterogeneous, multiscale, micro-damaged with crack filled with a viscous fluid), could provide answers to these questions.

15.3.2 Limitations of the Techniques and Perspectives

The first limitation of the nonlinear ultrasonic techniques conducted until now for bone damage detection is that they still lack of a comparison to independent, quantitative evaluation of damage. A growing number of research groups are currently working on this subject and it appears clearly now that the next step in this research area will be to perform these validation measurements. A comparison to quasistatic measurements obtained using mechanical testing machine would have to be conducted carefully. In particular, one would have to keep in mind that time scales are a very important issue in this problem, since it deals with dissipation mechanisms. Therefore, a comparison between quasistatic and dynamic measurements would necessarily have some limitations. For instance, the thermal fluctuations, very likely to contribute to the hysteretic behavior of damaged bone subjected to a mechanical solicitation, will certainly be different for different strain rates. At very low frequency, for quasistatic solicitations, one can expect the system to have enough time to relax to its thermodynamic equilibrium within a period, whereas the characteristic time of the system could be longer than an excitation period at higher frequencies, leading to an increased hysteretic behavior [66]. A good candidate for the validation of the nonlinear acoustic measurements for damage characterization would be histological measurements. Histology is now considered as the gold standard for damage assessment *in vitro* in bone [77]. A quantitative comparison between nonlinear ultrasound parameters and the histologically measured damage could provide the quantitative relationship between damage and nonlinearity that is still needed, as long as it is statistically valid, *i.e.* conducted on a significant amount of samples. The derivation of this empirical relationship would be a huge progress in the field, especially in the context where a model still has to be developed for the damage-induced nonlinear behavior of bone. In terms of modeling, a lot of work has still to be done. The first step would be a proper identification of the different physical origins for the nonlinearity in damaged bone. Finer research has to be conducted in order to understand some of the observed phenomena such as the linear decrease of the resonance frequency shift as a function of amplitude in the NRUS measurements, or the fact that the measured nonlinear parameter β in trabecular bone is

significantly different in traction and in compression, when the Young's modulus does not change much in the two situations [78].

Another work that still remains to be conducted is the design of an *in vivo* setup, able to evaluate the nonlinear parameters β and α through a layer of soft tissue, in a clinical context. The choice of the anatomical site should correspond to an effective clinical fracture site such as the hip or the vertebrae. Again, some modeling, and some experimental trials would have to be conducted in order to circumvent the potential difficulties related to the presence of soft tissue around the bone.

15.4 Conclusion

A rising number of research groups has now reported essentially *in vitro* observations of acoustic nonlinearity in bone tissue. Four experimental techniques were applied to bone: harmonic distortion of a monochromatic wave, dynamic acoustoelastic testing, nonlinear resonant ultrasound spectroscopy and nonlinear wave modulation spectroscopy. It is worth noticing that these experimental findings attest the existence of non-classical acoustic nonlinearity because of anomalously high values of classical elastic nonlinear parameters β and δ and qualitative peculiarities like tension/compression asymmetry, hysteresis and resonance linear frequency shift, as was observed in damaged industrial materials and geomaterials.

The current research efforts now focus on the production of evidences that cracks embedded in the solid bone tissue are the origin of acoustic nonlinearity. Very few studies were conducted on a significant set of bone samples originating from different donors. Among these, NRUS and DAET showed a large dispersion in the level of acoustic nonlinearity, corroborating, if cracks are assumed to be sources of acoustic nonlinearity, the large dispersion in the level of microdamage reported in terms of crack density by histological studies [44, 47, 56].

The very recent trend in the research field is to conduct both progressively damaging mechanical testing and histological quantification of microdamage by fluorescence microscopy together with the measurement of acoustic nonlinearity [44, 47]. Controlled mechanical testings are used as a tool to increase progressively the level of microdamage in bone samples and to monitor the associated reduction of the macroscopic mechanical integrity. This *in vitro* objectivation of the relation between the actual level of microdamage and the level and type of acoustic nonlinearity is essential before the development of an *in vivo* nonlinear acoustical technique is addressed. Depending on the *in vivo* sensitivity of these nonlinear acoustical methods, the measurement of the acoustic nonlinearity exhibited by bone tissue may be a powerful non-invasive tool to assess the level of microdamage generated in bone and to improve our comprehension of the role of cracks in bone remodeling and bone biomechanics.

References

1. V.E. Nazarov, L.E. Ostrovsky, I.A. Soustova, A. Sutin.: Nonlinear acoustics of micro-inhomogeneous media. Phys. Earth Planet. Inter. **50**, 65–73 (1988)
2. R.A. Guyer and P.A. Johnson.: Nonlinear mesoscopic elasticity: Evidence for a new class of materials. Phys. Today **52**, 30–35 (1999)
3. E.F. Morgan, O.C. Yeh, and T.M. Keaveny.: Damage in trabecular bone at small strains. Eur. J. Morphol. **42(1–2)**, 13–21 (2005)
4. D. Vashishth.: Hierarchy of bone microdamage at multiple length scales. Int. J. Fatigue **29**, 1024–1033 (2007)
5. P.H. Nicholson and M.L. Bouxsein.: Quantitative ultrasound does not reflect mechanically induced damage in human cancellous bone. J. Bone Miner. Res. **15(12)**, 2467–2472 (2000)
6. K.R. McCall and R.A. Guyer.: Equation of state and wave-propagation in hysteretic nonlinear elastic-materials. J. Geophys. Res. Solid Earth **99(B12)**, 23887–23897 (1994)
7. M.F. Hamilton and D.T. Blackstock.: Nonlinear Acoustics, Theory and Applications. Academic Press, New York (1998)
8. M.F. Hamilton and D.T. Blackstock.: On the coefficient of nonlinearity β in nonlinear acoustics. J. Acoust. Soc. Am. **83(1)**, 74–77 (1988)
9. R.T. Beyer.: Parameter of nonlinearity in fluids. J. Acoust. Soc. Am. **32(6)**, 719–721 (1960)
10. V.Y. Zaitsev, A. Dyskin, E. Pasternak, and L. Matveev.: Microstructure-induced giant elastic nonlinearity of threshold origin: Mechanism and experimental demonstration. Europhys. Lett. **86(4)**, 44005 (2009)
11. W.L. Morris, O. Buck, and R.V. Inman.: Acoustic harmonic generation due to fatigue damage in high-strength aluminium. J. Appl. Phys. **50(11)**, 6737–6741 (1979)
12. J.Y. Kim, L.J. Jacobs, J. Qu, and J.W. Littles.: Experimental characterization of fatigue damage in a nickel-base superalloy using nonlinear ultrasonic waves. J. Acoust. Soc. Am. **120(3)**, 1266–1273 (2006)
13. J. Herrmann, J.Y. Kim, L.J. Jacobs, J. Qu, J.W. Littles, and M.F. Savage.: Assessment of material damage in a nickel-base superalloy using nonlinear rayleigh surface waves. J. Appl. Phys. **99(12)**, 124913, 1–8 (2006)
14. C.S. Kim, I.K. Park, and K.Y. Jhang.: Nonlinear ultrasonic characterization of thermal degradation in ferritic 2.25Cr-1Mo steel. NDT&E Int **42**, 204–209 (2009)
15. S. Baby, B.N. Kowmudi, C.M. Omprakash, D.V.V. Satyanarayana, K. Balasubramaniam, and V. Kumar.: Creep damage assessment in titanium alloy using a nonlinear ultrasonic technique. Scripta Mater. **59(8)**, 818–821 (2008)
16. K.Y. Jhang.: Nonlinear ultrasonic techniques for nondestructive assessment of microdamage in material: A review. Int. J. Precis. Eng. Manuf. **10(1)**, 123–135 (2009)
17. L. Hoff, K.G. Oygarden, E.K. Hagen, and J.-A. Falch.: Diagnosis of osteoporosis using nonlinear ultrasound. Ultrasonics IEEE Symp. **1**, 1010–1013 (2003)
18. H.E. Engan, K.A. Ingebrigtsen, K.G. Oygarden, E.K. Hagen, and L. Hoff.: Nonlinear ultrasound detection of osteoporosis. Ultrasonics IEEE Symposium, Vancouver 2096–2099 (2006)
19. T.L. Norman, T.M. Little, and Y.N. Yeni.: Age-related changes in porosity and mineralization and in-service damage accumulation. J. Biomech. **41(13)**, 2868–2873 (2008)
20. M.E. Arlot, B. Burt-Pichat, J.P. Roux, D. Vashishth, M.L. Bouxsein, and P.D. Delmas.: Microarchitecture influences microdamage accumulation in human vertebral trabecular bone. J. Bone Miner. Res. **23(10)**, 1613–1618 (2008)
21. L. Ostrovsky and P. Johnson.: Dynamic nonlinear elasticity in geomaterials. Rivista del Nuovo Cimento. **24**, 1–46 (2001)
22. G. Renaud, S. Callé, J.-P. Remenieras, and M. Defontaine.: Non-linear acoustic measurements to assess crack density in trabecular bone. Int. J. Nonlinear Mech. **43(3)**, 194–200 (2008)
23. P.W. Bridgman.: Water, in the liquid and five solid forms, under pressure. Proc. Am. Acad. Arts Sci. **47**, 441–558 (1912)
24. J.C. Swanson.: Pressure coefficients of acoustic velocity for nine organic liquids. J. Chem. Phys. **2**, 689–693 (1934)

25. F. Birch.: The effect of pressure on the modulus of rigidity of several metals and glasses. J. Appl. Phys. **8**, 129–133 (1937)
26. J.M. Ide.: The velocity of sound in rocks and glasses as a function of temperature. J. Geol. **45**, 689–716 (1937)
27. M.A. Biot.: The influence of initial stress on elastic waves. J. Appl. Phys. **11**, 522–530 (1940)
28. R.A. Toupin and B. Bernstein.: Sound waves in deformed perfectly elastic materials. acoustoelastic effect. J. Acoust. Soc. Am. **33(2)**, 216–225 (1961)
29. J.R. Pellam and J.K. Galt.: Ultrasonic propagation in liquids: I. Application of pulse technique to velocity and absorption measurements at 15 megacycles. J. Chem. Phys. **14(10)**, 608–614 (1946)
30. D. Lazarus.: The variation of the adiabatic elastic constants of KCl, NaCl, CuZn, Cu, and Al with pressure to 10,000 bars. Phys. Rev. **76**, 545–553 (1949)
31. G. Holton.: Ultrasonic propagation in liquids under high pressures: Velocity measurements on water. J. Appl. Phys. **22(12)**, 1407–1413 (1951)
32. D.S. Hughes and J.L. Kelly.: Second-order elastic deformation of solids. Phys. Rev. **92(5)**, 1145–1149 (1953)
33. G.A. Gist.: Fluid effects on velocity and attenuation in sandstones. J. Acoust. Soc. Am. **96**, 1158–1173 (1994)
34. T. Bourbié, O. Coussy, and B. Zinszner.: Acoustics of porous media. Institut Français du Pétrole publications, Ed TechniP, Paris (1987)
35. K.W. Winkler and W.F. Murphy.: Acoustic velocity and attenuation in porous rocks. In T.J. Ahrens (ed.) Rock Physics and Phase relations, A Handbook of Physical Constants, American Geophysical Union, Washington, DC, 20–34 (1995)
36. N. Ichida, T. Sato, and M. Linzer.: Imaging the nonlinear parameter of the medium. Ultrason. Imaging **5**, 295–299 (1983)
37. G. Gremaud, M. Bujard, and W. Benoit.: The coupling technique: A two-wave acoustic method for the study of dislocation dynamics. J. Appl. Phys. **61(5)**, 1795–1805 (1987)
38. G. Renaud, S. Callé, J.-P. Remenieras, and M. Defontaine.: Exploration of trabecular bone nonlinear elasticity using time-of-flight modulation. IEEE Trans. UFFC **55(7)**, 1497–1507 (2008)
39. G. Renaud, S. Callé, and M. Defontaine.: Remote dynamic acoustoelastic testing: Elastic and dissipative acoustic nonlinearities measured under hydrostatic tension and compression. Appl. Phys. Lett. **94(1)**, 011905 (2009)
40. M. Rupprecht, P. Pogoda, M. Mumme, J.M. Rueger, K. Pschel, and M. Amling.: Bone microarchitecture of the calcaneus and its changes in aging: A histomorphometric analysis of 60 human specimens. J. Orthop. Res. **24(4)**, 664–674 (2006)
41. D. Donskoy and A. Sutin.: Nonlinear acoustic parameter of trabecular bone. J. Acoust. Soc. Am. **102(5)**, 3155 (1997)
42. R.A. Guyer and P.A. Johnson.: Nonlinear Mesoscopic Elasticity. Wiley, New York (2009)
43. N.L. Fazzalari, J.S. Kuliwaba, and M.R. Forwood.: Cancellous bone microdamage in the proximal femur: Influence of age and osteoarthritis on damage morphology and regional distribution. Bone **31(6)**, 697–702 (2002)
44. H. Moreschi, S. Callé, S. Guerard, D. Mitton, G. Renaud, and M. Defontaine.: Monitoring of trabecular bone induced microdamage using a nonlinear wave-coupling technique. In Proceedings of the IEEE-UFFC Ultrasonics Symposium, Rome (2009)
45. T.C. Lee, S. Mohsin, D. Taylor, R. Parkesh, T. Gunnlaugsson, F.J. O'Brien, M. Giehl, and W. Gowin.: Detecting microdamage in bone. J. Anat. **203**, 161–172 (2003)
46. T.L.A. Moore and L.J. Gibson.: Fatigue microdamage in bovine trabecular bone. J. Biomech. Eng. **125**, 769–776 (2003)
47. H. Moreschi, S. Callé, S. Guérard, D. Mitton, G. Renaud, and M. Defontaine.: Monitoring trabecular bone microdamage using Dynamic AcoustoElastic Testing method. Proc. IMechE vol. 225, Part H: J. Eng. Med. (2010)
48. K. Hadley.: Comparison of calculated and observed crack densities and seismic velocities in westerly granite. J. Geophys. Res. **81(20)**, 3484–3494 (1976)
49. S. Peacock, C. McCann, J. Sothcott, and T.R. Astin.: Seismic velocities in fractured rocks: An experimental verification of Hudson's theory. Geophys. Prospect. **42(1)**, 27–80 (1994)

50. K. Van Den Abeele, P.Y. Le Bas, B. Van Damme, and T. Katkowski.: Quantification of material nonlinearity in relation to microdamage density using nonlinear reverberation spectroscopy: Experimental and theoretical study. J. Acoust. Soc. Am. **126(3)**, 963–972 (2009)
51. W.M. Visscher, A. Migliori, T.M. Bell, and R.A. Reinert.: On the normal-modes of free-vibration of inhomogeneous and anisotropic elastic objects. J. Acoust. Soc. Am. **90(4)**, 2154–2162 (1991)
52. K. Van Den Abeele, J. Carmeliet, J.A. Tencate, P.A. Johnson.: Nonlinear wave modulation spectroscopy (NWMS) techniques to discern material damage, Part II: Single-mode nonlinear resonance acoustic spectroscopy. Res. Nondestr. Eval. **12**, 31–42 (2000)
53. R.A. Guyer, K.R. McCall, G.N. Boitnott, L.B. Hilbert, and T.J. Plona.: Quantitative use of Preisach-Mayergoyz space to find static and dynamic elastic moduli in rock. J. Geophys. Res. **102**, 8105–8120 (1997)
54. P.A. Johnson, B. Zinszner, P. Rasolofosaon, F. Cohen-Tenoudji, and K.V.D. Abeele.: Dynamic measurements of the nonlinear elastic parameter in rock under varying conditions. J. Geophys. Res. **109**, B02202 (2004)
55. M. Muller, A. Sutin, R.A. Guyer, M. Talmant, P. Laugier, and P.A. Johnson.: Nonlinear resonant ultrasound spectroscopy (NRUS) applied to damage assessment in bone. J. Acoust. Soc. Am. **118**, 3946–3952 (2005)
56. M. Muller, A. D'Hanens, D. Mitton, M. Talmant, P. Laugier, and P.A. Johnson.: Nonlinear ultrasound can detect accumulated damage in human bone. J. Biomech. **41(5)**, 1062–1068 (2008)
57. P.A. Johnson, B. Zinszner, and P.N.J. Rasolofosaon.: Resonance and nonlinear elastic phenomena in rock. J. Geophys. Res. **101(B5)**, 11553–11564 (1996)
58. W.E. Caler and D.R. Carter.: Bone creep-fatigue damage accumulation. J. Biomech. **22**, 625–635 (1989)
59. D.R. Carter, W.E. Caler, D.M. Spengler, and V.H. Frankel.: Fatigue behaviour of adult cortical bone: the influence of mean strain and strain range. Acta Orthop. Scand. **52**, 481–490 (1981)
60. M.B. Schaffler, K. Choi, and C. Milgrom.: Aging and matrix microdamage accumulation in human compact bone. Bone **17**, 521–525 (1995)
61. K. Van Den Abeele, J. Carmeliet, J.A. Tencate, and P.A. Johnson.: Nonlinear wave modulation spectroscopy (NWMS) techniques to discern material damage, Part I: Nonlinear wave modulation spectroscopy (NWMS). Res. Nondestr. Eval. **12**, 17–30 (2000)
62. V. Zaitsev, V. Nazarov, V. Gusev, and B. Castagnede.: Novel nonlinear-modulation acoustic technique for crack detection. NDT&E Int. **30**, 184–194 (2006)
63. V.V. Kazakov, A. Sutin, P.A. Johnson.: Sensitive imaging of an elastic nonlinear wave-scattering source in a solid. Appl. Phys. Lett. **81(4)**, 646–648 (2002)
64. T.J. Ulrich, P.A. Johnson, M. Muller, D. Mitton, M. Talmant, P. Laugier.: Application of nonlinear dynamics to monitoring progressive fatigue damage in human bone. Appl. Phys. Lett. **91**, 213901 (2007)
65. K. Zacharias, E. Balabanidou, I. Hatzokos, I.T. Rekanos, and A. Trochidis.: Microdamage evaluation in trabecular bone based on nonlinear ultrasound vibro-modulation (NUVM). J. Biomech. **42**, 581–586 (2009)
66. V.E. Gusev, V. Tournat.: Amplitude- and frequency-dependent nonlinearities in the presence of thermally induced transitions in the Preisach model of acoustic hysteresis. Phys. Rev. B **72**, 054104 (2005)
67. R.A. Guyer, K.R. McCall, G.N. Boitnott.: Hysteresis, discrete memory, and nonlinear-wave propagation in rock – A new paradigm. Phys. Rev. Lett. **74(17)**, 3491–3494 (1995)
68. F. Preisach.: Uber die magnetische Nachwirkung. Z. Phys. **94**, 277–302 (1935)
69. I.D. Mayergoyz.: Hysteresis models from the mathematical and control theory points of view. J. Appl. Phys. **57**, 3803–3805 (1985)
70. M. Scalerandi, P.P. Delsanto, V. Agostini, K. Van Den Abeele, P. A. Johnson.: Local interaction simulation approach to modelling nonclassical, nonlinear elastic behavior in solids. J. Acoust. Soc. Am. **113**, 3049–3059 (2003)
71. K. Van Den Abeele, F. Schubert, V. Aleshin, F. Windels, and J. Carmeliet.: Resonant bar simulations in media with localized damage. Ultrasonics **42**, 1017–1024 (2004)

72. P. Fellinger, R. Marklein, K.J. Langenberg, and S. Klaholz.: Numerical modeling of elastic-wave propagation and scattering with EFIT – Elastodynamic finite integration technique. Wave Motion **21**, 47–66 (1995)
73. L.D. Landau, and E.M. Lifshitz, Theory of Elasticity, 3rd edn. Pergamon, New York (1986)
74. V. Tournat, V.E. Gusev, V.Y. Zaitsev, V.E. Nazarov, and B. Castagnède.: Probing granular media via nonlinear acoustic effects. Reviex Progress in QNDE. **24**, 369–376 (2005)
75. I.Y. Belyaeva, L.A. Ostrovsky, V.Y. Zaitsev.: Microstructure indiced nonlinearity of unconsolidated rocks as related to seismic diagnostics problems. Nonlinear Process. Geophys. **4**, 4–10 (1997)
76. R.B. Gordon and L.A. Davis.: Velocity and attenuation of seismic waves in imperfectly elastic rock. J. Geophys. Res. **73**, 3917–3935 (1968)
77. T.C. Lee, E.R. Myers, and W.C. Hayes.: Fluorescence aided detection of microdamage in compact bone. J. Anat. **193(2)**, 179–184 (1998)
78. E.F. Morgan, O.C. Yeh, W.C. Chang, and T.M. Keaveny.: Nonlinear behavior of trabecular bone at small strains. J. Biomech. Eng. **123**, 1–9 (2001)

Chapter 16
Microscopic Elastic Properties

Kay Raum

Abstract Several high frequency ultrasound techniques have been developed during the last decade with the intention to assess elastic properties of bone at the tissue level. In this chapter three major principles are described with exemplary measurements in the frequency range from 50 MHz to 1.2 GHz. The methods are compared and their application potentials and limitations are discussed with respect to the hierarchical structure of cortical bone. While highly focused transducers with frequencies between 50 and 200 MHz are suitable for the assessment of microscale elastic properties, frequencies in the gigahertz range are dedicated to the investigation of the anisotropic lamellar bone structure. The relations between tissue mineralization, acoustic properties and anisotropic elastic coefficients at the micro- and nanoscales will be summarized.

Keywords Acoustic impedance · Acoustic lens · Analogue-to-digital (A/D) · Anisotropy · Aperture · Numerical aperture · N.A. · Attenuation · Bandpass · Beam axis · Beam width · Bone matrix · Collagen · Compressional wave · Confocal · Cortical bone · C-scan · Degree of mineralization of bone · Depth of focus · Elastic coefficient · Elasticity · Embedding · Fast Fourier transformation (FFT) · Femur · Fibril · Filter · Focal plane · Focal point · Group velocity · Haversian canal

16.1 Introduction

Mechanical properties of bone depend on a multiplicity of material and structural properties at several hierarchical length scales (Fig. 16.1). Bone tissue matrix predominantly consists of three elementary constituents: mineral (mostly

K. Raum (✉)
Julius-Wolff Institute and Berlin-Brandenburg School for Regenerative Therapies,
Charité – Universitätsmedizin Berlin, Augustenburger Platz 1, 13353 Berlin, Germany
e-mail: Kay.Raum@charite.de

P. Laugier and G. Haïat (eds.), *Bone Quantitative Ultrasound*,
DOI 10.1007/978-94-007-0017-8_16,

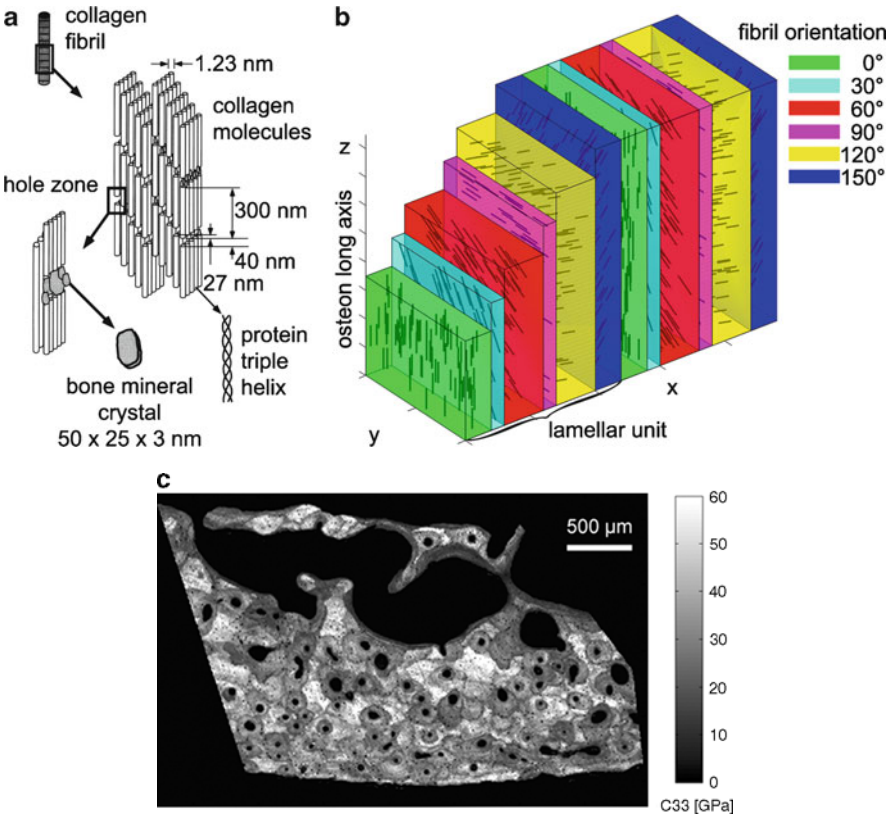

Fig. 16.1 Hierarchical structure of cortical bone. (**a**) A schematic diagram illustrating the assembly of collagen Type I molecules into fibrils with a specific tertiary structure having a 67 nm periodicity and 40 nm gaps or holes between the ends of the molecules. Plate-like apatite crystals of bone occur within the discrete spaces within the collagen fibrils (Reprinted from Rho et al. [2] copyright (1998), with permission of Elsevier). (**b**) Model of the lamellar unit, which is composed of six individual layers. One layer consists of a variable number of parallel oriented mineralized fibrils. The fibrils of adjacent layers are tilted by a fixed angle (30°). (**c**) The cortical structure of mature large mammals is mainly composed of a network of secondary osteons (*darker regions*) with Haversian canals and osteocyte lacunae, and of interstitial tissue (*brighter regions*)

hydroxyapatite), collagen and water, which are arranged in mineralized collagen fibrils with a diameter of less than 0.2 µm (see Chap. 2 for more information on bone biomechanics). The fibrils aggregate to form structural units, e.g. woven type, plexiform or lamellar bone [1]. The peripheral skeleton of mature mammals and humans consists of a highly ordered system of Haversian and Volkmann canals with typical diameters in the range between 10 and 200 µm, canaliculi (diameter: 0.2–0.3 µm) and other pores, e.g. osteocyte and resorption lacunae with diameters in the order of 2–8 µm, and up to about 200 µm, respectively.

Another important feature of bone tissue is the capacity of regeneration, which is most evident as an endogeneous healing after a traumatic fracture, but also occurs permanently and throughout the entire skeleton in a process called

remodelling. These characteristics lead to a tissue compound that is not only highly heterogeneous and anisotropic at all hierarchy levels as a result of perfect adaptation to external and intrinsic loading conditions, but also dynamic with respect to tissue resorption, synthesis, and maturation. Mineralization of the collagen fibrils is a process that can be divided into two phases: *primary mineralization* of the nonmineralized osteoid occurs within a few days and leads to a mineralization of about 70% of the final value; *secondary mineralization* is a slow process that is associated with further intra- and interfibrillar mineral deposition, crystal growth and maturation over a time period of several years [3].

Low frequency ultrasound has been used successfully for decades for the assessment of macroscopic anisotropic elastic properties of cortical bone [4–7] (see Chap. 13). The properties measured at this scale are determined by both the elastic properties of the bone matrix and by the porous structure. However, a thorough understanding of tissue maturation, ageing, adaptation to mechanical loading, or divergence from normal bone remodelling in the course of bone pathologies, genetic regulations, or fracture healing can only be achieved at the cellular and at the tissue level.

Acoustic methods have received increasing attention in the last decade, because (i) the volume of interaction of the ultrasound wave with the material can be adjusted to the hierarchical level of organization over three orders of magnitude, i.e. from the millimeter-range at 500 kHz to the micrometer-range at 1.5 GHz, (ii) the inherent contrast mechanism arises from the elastic interaction of the acoustic wave with the interrogated material, and (iii) the combination with imaging approaches allow the assessment of structural and elastic features, which are both essential for the macroscopic function, e.g. biomechanical stability and resistance to fracture.

16.1.1 Definition of Hierarchy Levels

Up to seven hierarchical levels of organization have been proposed for mineralized musculoskeletal tissues [1]. According to the levels of experimental assessment and numerical homogenization approaches described in Chap. 9, four levels of hierarchy (Table 16.1) are used hereinafter.

16.1.2 Principle of Scanning Acoustic Microscopy

16.1.2.1 Major Hardware Components

Scanning Acoustic Microscopy (SAM) with frequencies between 50 MHz and 2 GHz is adapted to the investigation of local *nano-* and *microscale* elasticity of the bone tissue matrix. However, in this frequency range, only single element transducers are currently available. Therefore acoustic microscopes usually require mechanical scanning for the translation of the transducer. The other major components are illustrated in Fig. 16.2.

Table 16.1 Definition of characteristic length scales

Length scale	Composition	Compound	Nomenclature
1–200 nm	Hydroxyapatite, collagen, water, other	Mineralized collagen fibril	Nanoscale
200 nm to ∼10 µm	Mineralized collagen fibrils, pores	Mineralized tissue matrix (woven, plexiform, or lamellar structures)	Microscale
10 µm to ∼1 mm	Mineralized tissue matrix, pores	Cortical or trabecular tissue	Mesoscale
>1 mm	Various tissue types, cavities	Organs	Macroscale

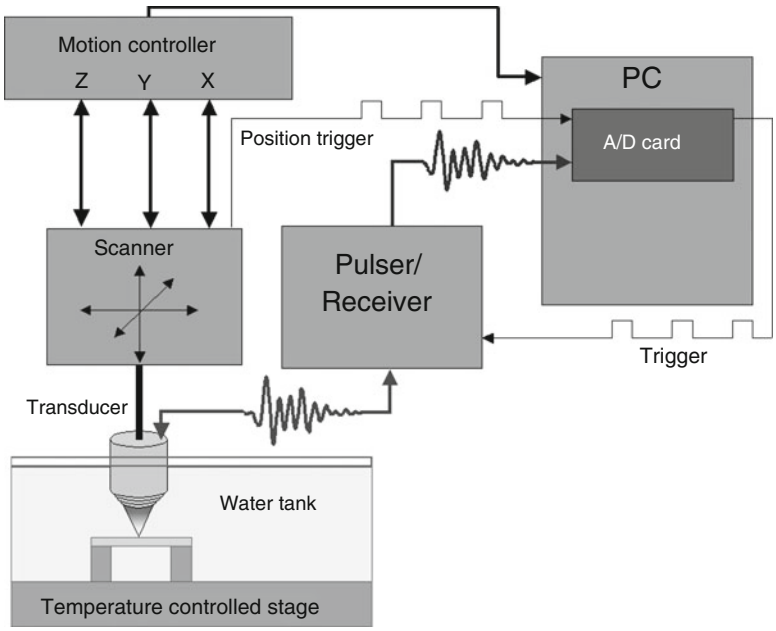

Fig. 16.2 Schematic diagram of a Scanning Acoustic Microscope. The major components are: single element transducer, temperature controlled water bath with tilt control and sample mount, three-axis scanning stage, pulser-receiver unit, analogue-to-digital (A/D) data acquisition card, control computer

16.1.2.2 The Acoustic Lens

A high spatial resolution at the sample surface, but no subsurface information is required in most applications. Therefore, spherically focused sound fields with a

Table 16.2 Wavelength, lateral resolution and depth of focus for characteristic transducer frequencies and aperture angles of 60° and 100° (in parenthesis)

Frequency	Wavelength (μm)	Lateral resolution (μm)	Depth of focus (μm)
50 MHz	29.8	30.7 (20.0)	211.3 (90.0)
200 MHz	7.5	7.7 (5.0)	52.8 (22.5)
400 MHz	3.7	3.8 (2.5)	26.4 (11.2)
1 GHz	1.5	1.5 (1.0)	10.6 (4.5)

Water at 25°C ($v_0 = 1492\,\mathrm{m/s}$) was assumed as a coupling fluid

high numerical aperture $(N.A.)$ are frequently applied. The lateral resolution $D_{lateral}$ is determined by the −6-dB transmit-receive beam width in the focal plane:

$$D_{lateral} = 1.028 \cdot \lambda \cdot \frac{ROC}{2a} \tag{16.1}$$

whereas λ is the acoustic wavelength, ROC is the transducer's radius of curvature and a is the radius of the transducer, respectively. The semi-angle θ_0 of the lens-aperture is [8]:

$$\sin\theta_0 = N \cdot A \cdot = \frac{a}{ROC}. \tag{16.2}$$

The depth of focus F_z, defined as the distance between points along the beam axis where the intensity is 3 dB less compared to the focal point is [8]:

$$F_z = 7.08 \cdot \lambda \left(\frac{ROC}{2 \cdot a}\right)^2. \tag{16.3}$$

The values in Table 16.2 demonstrate that for increasing frequencies the lateral resolution is improved on the expense of depth of focus.

The majority of ultrasound based microelastic studies of bone have used pulse-echo configurations for the measurement of

- The acoustic impedance
- Surface acoustic wave velocities
- Compressional and shear wave velocities in thin sections

The underlying principles will be described in the following sections.

16.1.2.3 Acoustic Impedance

It has been shown in Chaps. 2 and 13 that the velocities of various wave propagation modes (compressional, shear quasi-shear, quasi-compressional waves) are directly linked to the elastic coefficients c_{ij}. The reflected amplitude of a plane wave incident

at a boundary between a fluid and a homogeneous isotropic elastic materials is proportional to the angular dependent reflectance function $R(\theta)$ [9]:

$$R(\theta) = \frac{Z_P \cos^2 2\theta_S + Z_S \sin^2 2\theta_S - Z_1}{Z_P \cos^2 2\theta_S + Z_S \sin^2 2\theta_S + Z_1}, \tag{16.4}$$

$$Z_1 = \frac{\rho_1 v_1}{\cos\theta}, Z_P = \frac{\rho_2 v_P}{\cos\theta_P}, Z_s = \frac{\rho_2 v_S}{\cos\theta_s}, \tag{16.5}$$

Z_1 is the acoustic impedance value of the coupling fluid. Z_P and Z_S in the solid material are related to the product of mass density ρ and compressional (v_P) and shear (v_s) velocities [9]. The characteristic acoustic impedance Z of a material is defined as the ratio of tensile stress σ_T to particle displacement velocity $\partial\overrightarrow{u}/\partial t$:

$$Z = -\frac{\sigma_T}{\partial\overrightarrow{u}/\partial t}, \tag{16.6}$$

and is usually expressed in Mrayl $(1\,\text{rayl} = 1\,\text{kgm}^{-2}\,\text{s}^{-1})$. Under the condition of normal incidence, i.e. the surface of the sample is perpendicular to the sound beam axis, the generation of shear waves is not possible and the reflectance function can be replaced by the reflection coefficient R:

$$R = \frac{Z_2 - Z_1}{Z_2 + Z_1}. \tag{16.7}$$

Z_1 and Z_2 are the acoustic impedance values of the coupling fluid and the material under investigation, respectively.

The transmission and reflection of plane waves at plane boundaries of anisotropic materials is described by the acoustic impedance Z^n, which relates traction force T_{in} to particle velocity v_j [10–12]:

$$\begin{aligned} -T_{in} &= (Z^{\hat{n}})_{ij} v_j, \\ i, j &= x, y, z, \end{aligned} \tag{16.8}$$

where $\hat{n}$ is the direction in which the impedance is measured. Equation 16.8 can be written in matrix notation:

$$-T_{in} = \frac{n_{iK} c_{KL} k_{Lj}}{\omega} v_j, \tag{16.9}$$

where

$$n_{iK} = \begin{bmatrix} n_x & 0 & 0 & 0 & n_z & n_y \\ 0 & n_y & 0 & n_z & 0 & n_x \\ 0 & 0 & n_z & n_y & n_x & 0 \end{bmatrix}, \tag{16.10}$$

and

$$k_{Lj} = \begin{bmatrix} k_x & 0 & 0 \\ 0 & k_y & 0 \\ 0 & 0 & k_z \\ 0 & k_z & k_y \\ k_z & 0 & k_x \\ k_y & k_x & 0 \end{bmatrix}. \tag{16.11}$$

The acoustic impedance matrix elements for the direction $\hat{n}$ are:

$$(Z^n)_{ij} = \frac{n_{iK} c_{KL} k_{Lj}}{\omega}, \tag{16.12}$$

where c_{KL} are the components of the stiffness tensor C. For a compressional wave propagation in the x-direction with $k_x = (\omega / v_{Px})$, $k_y = k_z = 0$, $n_x = 1$, $n_y = n_z = 0$, v_{Px} is the phase velocity of the longitudinal wave, (16.12) becomes

$$\omega (Z^{n_x})_{xx} = c_{11} k_x, \tag{16.13}$$

which can be written in the form

$$(Z^{n_x})_{xx} = \sqrt{c_{11} \cdot \rho}. \tag{16.14}$$

Similarly, the impedance for a compressional wave propagating in the z-direction is

$$(Z^{n_z})_{zz} = \sqrt{c_{33} \cdot \rho}. \tag{16.15}$$

Equations 16.14 and 16.15 show that if the wave propagation direction and particle displacement are normal to the interface and the propagation direction is parallel to the direction i, the acoustic impedance normal to the surface $(Z^{n_i})_{ii}$ is directly proportional to the elastic coefficient c_{ii} and the mass density ρ. The impedance for the propagation not parallel to the elastic symmetry axes can easily be obtained by rotation of the elastic stiffness tensor [10]. For the transverse isotropic case rotation in the xz plane yields [13]:

$$c(\theta) = c_{33} \cos^4 \theta + 2(c_{13} + 2c_{44}) \sin^2 \theta \cos^2 \theta + c_{11} \sin^4 \theta, \tag{16.16}$$

where θ is the rotation angle. $c(\theta)$ is the elastic coefficient c_{33} of the rotated tensor. It can be seen that $c(0^\circ) = c_{33}$ and $c(90^\circ) = c_{11}$. Combining (16.15) with (16.16) gives:

$$(Z^{n_\theta})_\theta = \sqrt{c(\theta) \cdot \rho}, \tag{16.17}$$

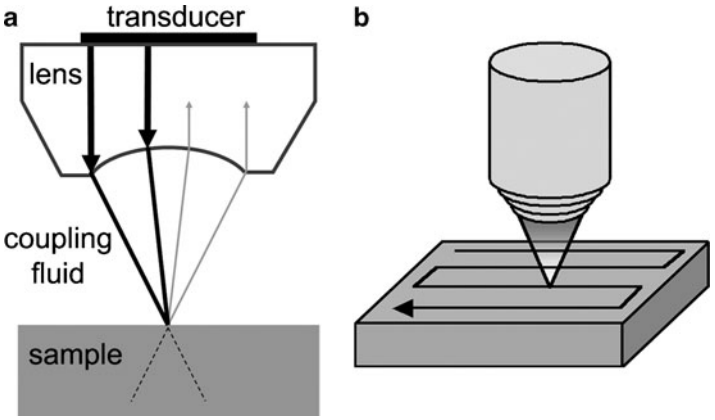

Fig. 16.3 (**a**) If the waves of a spherically focused transducer are reflected in the focal plane, an acoustic impedance map can be derived from the echo amplitudes by 2D scanning (**b**)

hereinafter simply referred to as $Z(\theta)$. For spherically focused sound fields the condition of plane wave propagation can be approximated in the focal point [14, 15]. At this point the incoming waves from the transducer are in phase and all shear wave components are diminished. Therefore, if the boundary between a liquid and an anisotropic material is placed in the focal plane normal to the sound beam axis, the acoustic impedance in the direction normal to the boundary is determined by (16.17) and the reflection coefficient becomes

$$R = \frac{Z(\theta) - Z_1}{Z(\theta) + Z_1}. \tag{16.18}$$

Thus by measuring the confocal reflection amplitude with a scanning system, $Z(\theta)$ can be mapped in two dimensions (Fig. 16.3). The main limitation of (16.18) is the assumption that the solid material is homogeneous within the interrogated boundary area.

16.1.2.4 Surface Acoustic Waves

When the sound field is focused inside a stiff material (negative defocus) surface acoustic waves (SAW) can be generated (Fig. 16.4a). These waves excite waves back into the coupling fluid and can eventually be detected by the transducer. Rayleigh wave and surface skimming compressional wave (SSCW) velocities can easily be measured in homogeneous stiff biomaterials, e.g. dentin and tooth enamel, either with quasi-monochromatic burst excitation using the well-established $V(z)$ technique [16–18] or with broad-band excitation and time-resolved $V(z,t)$ acquisition and spectral analysis [19] (Fig. 16.5).

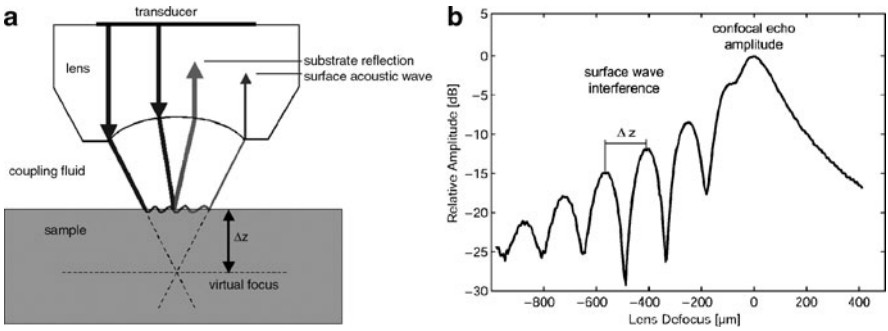

Fig. 16.4 (**a**) Principle of the SAW measurement; (**b**) a typical 50-MHz spectral component of a V(z) measurement in quartz glass (Reprinted from Raum et al. [19] copyright (2007), with permission from Elsevier)

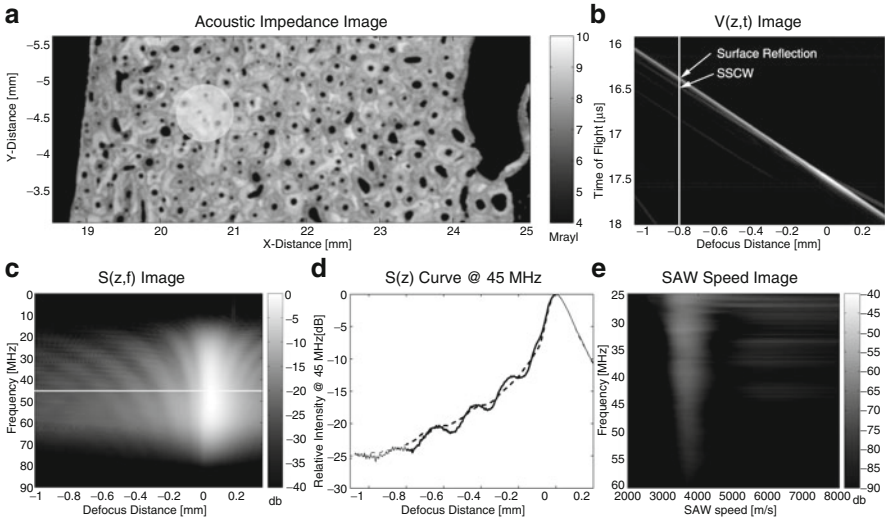

Fig. 16.5 50-MHz acoustic impedance image (**a**) with a circular bright spot indicating the region for a V(z, t) measurement (**b**–**e**). The acoustic impedance was determined from the confocal reflection amplitude (z = 0 mm) measured in x and y directions. The V(z, t)-image (**b**) shows the Hilbert-transformed signals for all measured defocus distances at the center of the bright spot in (**a**). The vertical line corresponds to one pulse-echo measured at a defocus of 800 µm. Frequency domain representation (**c**) of the V(z, t) data in (**b**). SAW speed evaluation at 45 MHz (**d**). The dashed line is from the reference signal measured in teflon. The bold sections were used for the estimation of the SAW velocities. In the SAW speed image (**e**) a surface skimming compressional wave can be identified (Reproduced with authorization from Raum [12], © 2008 IEEE)

Only one echo with the maximum intensity is obtained, when the focal plane coincides with the sample surface (Fig. 16.5b). By moving the transducer towards the sample eventually one or more additional echoes from the generated SAW can

be observed. With increasing defocus distance Δz the phase difference $\Delta\phi$ between the surface reflection and leaking surface wave is successively increasing:

$$\frac{\Delta\phi}{\Delta z} = 2k(1-\cos\theta_{SAW}), \tag{16.19}$$

whereas $k = 2\pi/\lambda$ is the wave number, λ is the acoustic wavelength and θ_{SAW} is the critical angle for the generation of a surface wave [20]. In a quasi-monochromatic system the interference between SAW and reflected waves results in characteristic oscillations of the detected reflection amplitude in a so-called $V(z)$ measurement (Figs. 16.4b and 16.5d).

The spatial oscillation frequency due to this interference is:

$$\frac{1}{\Delta z} = \frac{2\cdot f}{v_0}(1-\cos\theta_{SAW}). \tag{16.20}$$

f denotes the ultrasound frequency and v_0 is the compressional wave velocity in the coupling fluid. The surface wave velocity v_{SAW} is obtained by Snell's law:

$$v_{SAW} = \frac{v_0}{\sin\theta_{SAW}}. \tag{16.21}$$

In a broadband system the time delay Δt between surface reflection and the leaky surface wave depends on defocus distance Δz and the SAW velocity:

$$v_{SAW} = \left[\frac{\Delta t}{v_0\cdot\Delta z} - \frac{1}{4}\left(\frac{\Delta t}{\Delta z}\right)^2\right]^{-\frac{1}{2}}. \tag{16.22}$$

If Δt is larger than the pulse duration of the pulses, the individual pulses are separated (Fig. 16.5b). The precise estimation of the time delay is difficult, if more than one surface wave is generated or if the material is highly attenuating. However, the use of broadband pulses allows to determine phase velocities as a function of the frequency [12, 19]. Briefly, the pulse echo signals $V_z(t)$ at each defocus position z are Fourier-transformed to obtain the power spectra $S(z,f)$, as shown in Fig. 16.5c. Each vertical line corresponds to the measured magnitude of the power spectrum $S_z(f)$ of a pulse-echo sequence $V_z(t)$ at a specific defocus z. A horizontal line $S_f(z)$ in turn is equivalent to a monochromatic $V(z)$ measurement at a single frequency. For example, the $V(z)$ curve in Fig. 16.5d was obtained from the $S(z,f)$ image at $f = 45\,\text{MHz}$. For each $S_f(z)$ curve a spatial frequency domain analysis [12, 19, 21] can be applied to estimate multiple SAW velocities from the oscillation frequencies in $S_f(z)$. In the example of Fig. 16.5 the multi-frequency $S_f(z)$ curves were analysed within a defocus range from 0 to $-800\,\mu\text{m}$ and in the frequency range from 25 to 60 MHz. A convenient way for a graphical illustration is to convert the

spatial frequency data into a velocity domain via (16.20) and (16.21), to obtain a frequency dependent SAW-speed image (Fig. 16.5e). The vertical bright line indicates the occurrence of a SSCW wave.

Finally, the group velocity of broadband pulse is given by:

$$v_{SSCW(gr)} = \frac{\delta\omega}{\delta k} \tag{16.23}$$

where $\omega = 2\pi f$ is the angular frequency. The phase velocities were determined in the frequency range from 30 to 50 MHz and within this frequency range the group velocity $v_{SSCW(gr)} = 3832\,\mathrm{ms}^{-1}$ was derived from the linear slope of $\omega(k)$ according to (16.23). It should be noted that the derived velocity corresponds to the velocity averaged over all propagation directions parallel to the interrogated surface.

However, a drawback of the necessary defocusing is that the interrogated surface area is increased and the spatial resolution is lost. The radius of the illuminated surface area r_{max} is:

$$r_{\max} = -z_{\max} \tan\theta_0, \tag{16.24}$$

whereas θ_0 is the semi-aperture angle of the transducer and z_{max} is the maximum defocus position used for the analysis. The surface diameter contributing to the SAW measurement in Fig. 16.4 was approximately 670 µm. It can be seen that bone tissue is neither isotropic nor homogeneous within this area. Indeed, an important feature of cortical bone at the peripheral skeleton of mature large mammals is its heterogeneous microstructure with greatly varying tissue properties. Even with a 2 GHz lens (and a typical aperture of 100°), for which the maximum defocus is approximately 20 µm the corresponding sampled surface diameter would be about 40 µm.

16.1.2.5 Measurement of Compressional and Shear Wave Velocities

Turner and co-workers have measured the compressional wave velocity with a 50-MHz pulse-echo microscope that provided a spatial resolution of approximately 60 µm [22–28]. By measuring the time-of-flight difference (ΔTOF) of front and back side reflections in 500-µm thick sections (Fig. 16.6) the compressional wave velocity v_p was calculated as twice the sample thickness d divided by average delay time:

$$v_P = \frac{2d}{\Delta TOF}. \tag{16.25}$$

The elastic coefficient C was obtained using the relation

$$C = \rho v_p^2, \tag{16.26}$$

whereas ρ is the mass density. In principle, the sample thickness has to be thick enough, that front and back side echoes can be separated (i.e., approximately twice

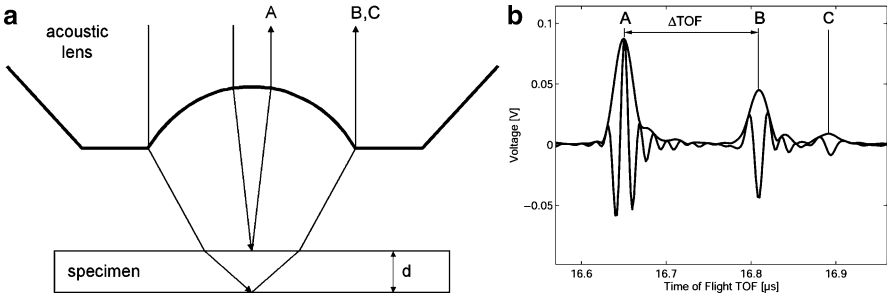

Fig. 16.6 (**a**) Principle of the measurement of compressional and shear wave velocities in thin tissue sections. (**b**) The time delay between waves reflected at the front (A) and back side (B and C) of a thin specimen can be used to calculate the wave velocities. Mode conversions can result in the generation of compressional (B) and shear waves (C). Because of the lower sound velocities, shear waves have larger time delays compared to compressional waves

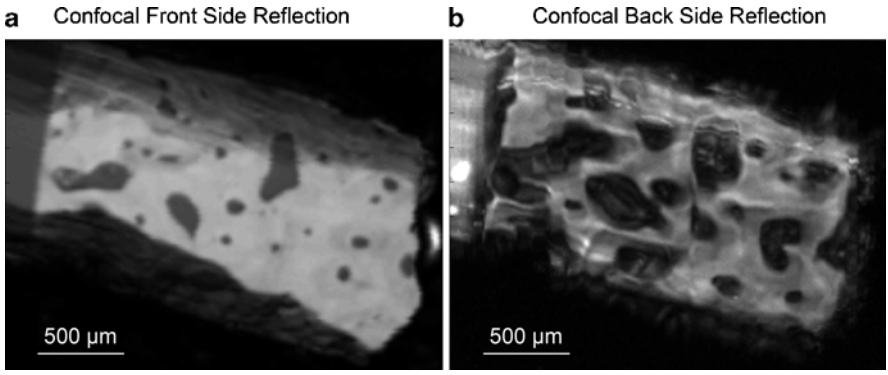

Fig. 16.7 50-MHz images of a thin embedded cortical bone cross section (thickness: 150 µm) with sound focused on the front side (**a**) or on the back side (**b**) of the sample (Reprinted with authorization from Raum [12], © 2008 IEEE)

the wavelength).On the other hand the spatial resolution degrades, if front and back side echoes cannot be placed within the depth of focus of the transducer. Figure 16.7 shows exemplary 50-MHz measurements of a 150 µm thick bone sample focused either at the front or at the back side of the sample ($\lambda_{bone} \sim 80\,\mu m$). The measurement has been done with a highly focused transducer (V605, Valpey Fisher, Hopkinton, MA, USA) that provides a confocal lateral resolution of 23 µm. While the Haversian canals are precisely separated from the tissue in the confocal front side image, they cause a remarkable image distortion and loss of resolution, when the sound field is focused on the back side of the sample. Although systems operating with center frequencies up to 2 GHz are available, the high attenuation in bone tissues limits the applicable frequency bandwidth for these measurements. Therefore this method has only been applied with frequencies up to 50 MHz and is limited to tissue regions sufficiently far away from structural boundaries, like Haversian canals.

16.2 Material and Methods

16.2.1 Sample Preparation

A flat smooth surface is mandatory for high frequency acoustic inspection. Scratches and local inclinations result in a change of the propagation direction of the incident waves, if the irregularities are comparable to or larger than the wavelength. Therefore the surface roughness after preparation should be much less than the used wavelength. The way of surface preparation depends on the type of sample preparation. While tissue embedding has the advantages of long term tissue fixation and hence sample durability as well as easy sample preparation using standard metallographic techniques, the replacement of water by the embedding material may alter the elastic properties of the tissue. On the other hand the preparation of the necessary surface smoothness in native samples is not straightforward, but can provide elastic tissue properties similar to in vivo conditions.

16.2.1.1 Native Samples

For native samples grinding and polishing is not suitable, since the abrasive particles can be pressed inside the bone cavities (Haversian and Volkmann canals, osteocyte lacunae) and the matrix, which may cause artefacts in the acoustic image. An alternative is ultramilling using a fast rotating diamond knife. Other artefacts arise from fat bubbles escaping from the cavities during the measurement. Therefore the tissue sections should be cleaned and defatted prior to acoustic inspection. The preparation steps we have established in our laboratory are as follows: Fresh sections are cut using a diamond saw (Exakt – Trennschleifsystem Makro, Exakt Apparatebau, Norderstedt, Germany). The sections are then rinsed in phosphate buffered saline (PBS), defatted for up to 12 h in dichloromethane (CH_2Cl_2) solution, and fixed with Technovit® 3040 resin (Heraeus Kulzer, Hanau, Germany) on special thick polypropylene sample holders. After shock freezing of sample and holder in liquid nitrogen flat tissue surfaces are prepared using an ultra milling machine (Reichert Jung Ultrafräse, Leica GmbH, Bensheim, Germany). Three to four freeze-milling cycles are necessary to produce the necessary surface flatness without thawing the sample during the milling process.

16.2.1.2 Embedded Samples

For the embedding it has to be ensured that (i) water is completely replaced by the embedding monomer, (ii) excessive heat production during the polymerization and gas bubble generation at or near the tissue is avoided, and (iii) the material properties of the embedding resin are suitable for high quality grinding and polishing. The bone specimens are fixed and dehydrated in a graded series of ethanol

(70%, 96% and 100%, immersion for 24 h in each solution) and defatted in Histoclear (National Diagnostics, Atlanta, GA) for 12 h. The embedding material is then infiltrated by immersing the samples in pure methylmethacrylate (MMA) for 24 h at 4°C and in a mixture of 94% MMA, 5% dibuthylphtalate (softener) and 1% benzoylperoxide (activator) for 24 h. For the polymerization solution the activator concentration is slightly higher (93% MMA, 4% dibutylphtalate, 3% benzoylperoxide). A slow polymerization without considerable temperature rise is ensured by placing the embedding molds in a temperature-controlled water bath at 24°C. With this procedure the water content in the tissue can be assumed to be almost completely replaced by the resin without considerable shrinking or other alteration of the tissue structure.

The necessary surface smoothness depends on the desired ultrasonic evaluation frequency. The required surface preparation steps were evaluated in embedded bone samples by (i) visual observation of surface scratches and (ii) comparison of the mean reflection amplitude after each preparation step. The preparation was considered to be sufficient, if no preparation scratches were visible and no significant change of the reflection amplitude in comparison to the higher preparation step was observed. For low frequencies ($\leq$50 MHz) grinding with successively decreasing grain size (SiC paper #2400 and #4000; Struers GmbH, Willich, Germany) yields a sufficient surface smoothness. For higher frequency evaluations the surfaces were polished using a Logitech WG2 (Struers GmbH, Willich, Germany) polishing system with a hard synthetic cloth, ethyleneglycol suspension and diamond particles as abrasive. For intermediate frequencies (50–200 MHz) one polishing step was applied after grinding (cloth: Microtex 500, Struers GmbH, Willich, Germany; abrasive: 3-µm diamond particles; time: 10 min). For frequencies above 200 MHz a second polishing step was necessary (cloth: MD-Dur, Struers GmbH, Willich, Germany; abrasive: 1-µm diamond particles; time: 5 min).

It should be noted that immersion of the embedded samples in water during the acoustic inspection causes diffusion of water into resin and tissue. The resulting swelling can be neglected even at investigations with GHz frequencies, if the sample was embedded properly, and if the duration of the exposure to water is short (e.g. $<$30 min for GHz measurements, $<$2 h for 50 MHz measurements). However, it should be noted that repetitive wet-dry cycles result in a remarkable increase of the surface roughness.

16.2.2 Acoustic Impedance Mapping

Crucial prerequisites for the estimation of the acoustic impedance from the confocal reflection amplitude are stable measurement conditions and a sophisticated calibration. All influences that potentially have an effect on the measured voltage in addition to the variations caused by the reflection coefficient have to be excluded or compensated. A summary of the most prominent effects are summarized in Table 16.3.

Table 16.3 Potential influences on the measured confocal surface reflection amplitude

Influence	Primary effects	Effects on amplitude measurement	Compensation
Temperature variation in the sound propagation path	Alteration of sound velocity, density, acoustic impedance and attenuation in transducer, coupling fluid and sample	Change of confocal pulse echo time and amplitude	Ensure stable temperature by a large, slightly stirred coupling fluid reservoir Measure temperature at least before and after acquisition Include the effects in your calibration
Sample tilt	Oblique sound incidence	Change of confocal pulse echo time and reduced amplitude	Align the sample surface before measurement Time-of-flight-based defocus compensation Measure a series with variable sample-transducer distance
Nonlinearities in the receive electronics	Saturation for higher reflection coefficients	Nonlinear relation between reflection amplitude and reflection coefficient	Determine linear range prior to system calibration
Instable electronics	Variable amplification	Change of confocal pulse echo amplitude	Always use the same cable Calibrate the system for each measurement
Surface roughness	Partial deflection away from the transducer	Reduction of confocal pulse echo time reduced amplitude	Improve surface preparation
Surface not in focal plane	Reflected waves are not in phase	Change of confocal pulse echo time and reduced amplitude	Align the sample surface before measurement Time-of-flight-based defocus compensation Measure a series with variable sample-transducer distance

16.2.2.1 Time-Resolved Measurements

The analysis of time-resolved pulse-echo data has several advantages compared to measurements with amplitude detected signals. The major benefit is that the entire information is kept in the signal and can be used for analysis. However, some pre-processing steps are necessary for reliable amplitude estimation:

- Bandpass filtering
- Amplitude detection
- Time-of-flight based defocus correction

Bandpass filtering, e.g. phase preserving forward and backward filtering with a type II Chebyshev filter is necessary to remove DC and high frequency components outside of the transducer bandwidth. The amplitude can then be detected from the Hilbert-transformed envelope signal. However, if the sampling frequency of the digitized signal is close to the Nyquist limit, this approach can be become considerably inaccurate. In this case, the signal should be upsampled using an FFT-based interpolation prior to the Hilbert transformation or the square root of the integrated spectral intensity (*ISI)* from the power spectrum $S(f)$ should be used.

$$ISI = \int_{f_1}^{f_2} S(f)df, \tag{16.27}$$

where f_1 and f_2 are the -6 dB bandwidth limits. Time of flight (*TOF*) can either be determined from the position of the maximum of the Hilbert transformed envelope signal (see Fig. 16.8), or from the slope of the unwrapped phase spectrum within the bandwidth of the transducer:

$$TOF = t_0 + t_{ph} = t_0 + \frac{\partial \phi}{\partial \omega} = t_0 + \frac{\partial N}{\partial f}, \tag{16.28}$$

where ϕ is the phase, $\omega = 2\pi f$ is the angular frequency and t_{ph} is the time relative to the start time t_0 of the digitized sequence, and N is the number of phase rotations [29].

TOF is a measure of the two-way pulse travel time from the transducer towards the reflecting surface. If the surface is located in the focal plane, the maximum amplitude is obtained. For a given combination of transducer, coupling fluid and temperature the confocal time-of flight (TOF_{focus}) is invariant. Therefore, the *TOF* of a measured pulse echo can be used to estimate the distance of the surface from the focal plane (defocus) and to estimate the relative decrease of the reflection amplitude relative to the confocal reflection amplitude (Fig. 16.9).

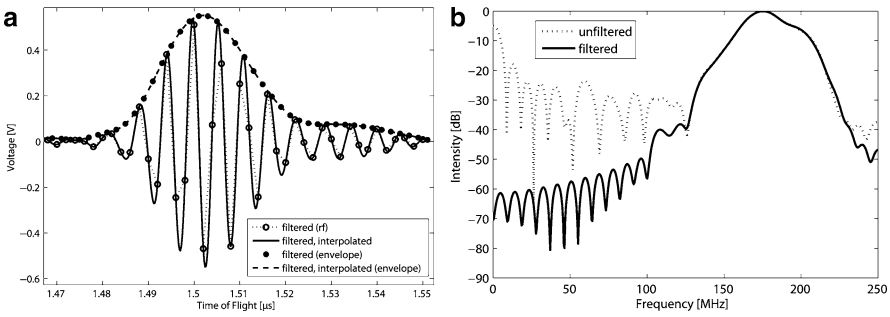

Fig. 16.8 Time-resolved signal processing. Confocal pulse echo (**a**) and power spectrum (**b**)

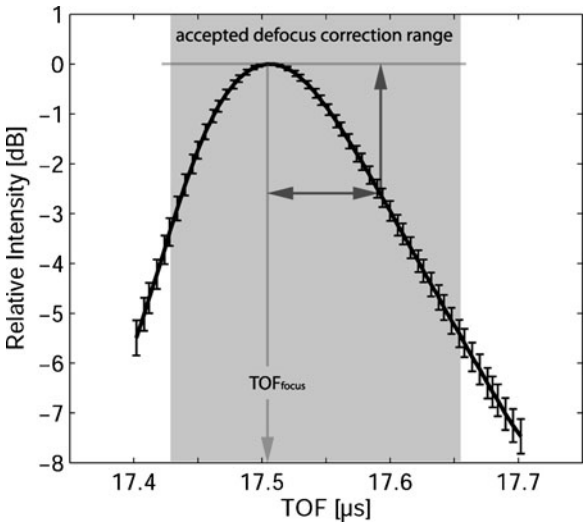

Fig. 16.9 Defocus correction function for a 50-MHz transducer. Mean and standard error of the normalized intensity as a function of *TOF*. The accepted *TOF* range corresponds to a defocus range from -58 to $+91\,\mu$m

16.2.2.2 Measurements with Time-Gated Amplitude Detection

Acoustic impedance mapping above 200 MHz has often been performed with systems that use burst excitation and time-gated amplitude detection. With these systems, the radio-frequency data are usually not accessible. Therefore, a careful adjustment of all hardware settings is mandatory for a reliable assessment of the reflection coefficient. In addition to the points summarized in Table 16.3 proper selections of excitation frequency and time-gate position are mandatory for good signal sensitivity and the exclusion of signal artefacts.

The confocal reflection amplitude is determined by a 2D $V(z)$ analysis, which requires the acquisition of a set of digital C-scan images at successively decreasing transducer-sample distances [30]. Starting from a z-position, where the focus of the lens is well above the sample surface (positive defocus), images are captured with a successively decreasing lens-surface distance. The image acquisition is stopped, when the focus is well below the surface everywhere in the scanned image (negative defocus). The increment between two adjacent C-scans should be small enough to fulfill the Nyquist limit, i.e. the sampling frequency in the z direction should be at least two-times of the highest oscillation frequency in the $V(z)$ curve. This three dimensional data set $V(x,y,z)$ allows a $V(z)$ analysis in two dimensions, i.e. for each x,y-coordinate. The confocal position at each xy-scan point corresponds to the position of the maximum signal amplitude in the z-direction. While the value of the maximum is proportional to the reflectivity, the position is a measure of the distance between an arbitrary xy-scan plane and the sample surface. These values

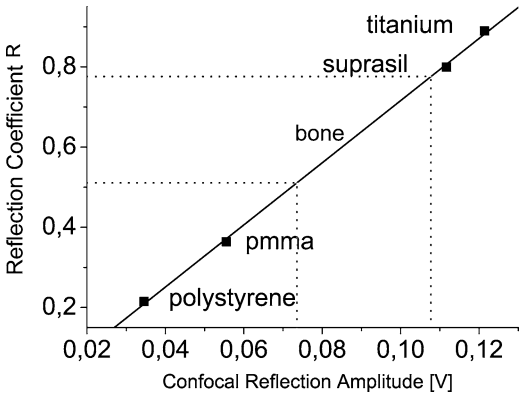

Fig. 16.10 Impedance calibration. For homogeneous reference materials the amplitude of the confocal reflection is correlated with the known reflection coefficients. The range of values measured in bone tissue is marked with dotted lines

are used to compute the two-dimensional surface topography and a topographically corrected amplitude map. For each point of the topography map the gradients in x and y directions are determined, which allows an estimation of the local inclination angles.

16.2.2.3 Calibration

The confocal reflection amplitudes can be converted to values of the reflection coefficient by calibration with homogeneous isotropic and non-dispersive materials. Speed of sound and mass density of these materials and the coupling fluid should be determined by a low frequency substitution method and by Archimedes' principle, respectively. From Eq. 16.7 the corresponding reflection coefficients can be calculated and the relation between reflection coefficient R and the measured voltage is obtained by linear regression (Fig. 16.10).

Exemplary impedance images of human cortical bone measured with 50 MHz to 1.2 GHz are shown in Fig. 16.11.

16.3 Results

16.3.1 Relations Between Mass Density, Acoustic Impedance, and Elastic Properties at the Microscale

Figure 16.12 shows the relation of Z and ρ with the elastic coefficient c over a broad range of materials [12]. It can be seen that Z is generally a better predictor for the elastic properties of a material than the mass density. However, (16.7) implies that the relation between the amplitude of the reflected wave and the acoustic material property is not linear. A good discrimination of varying acoustic properties is only

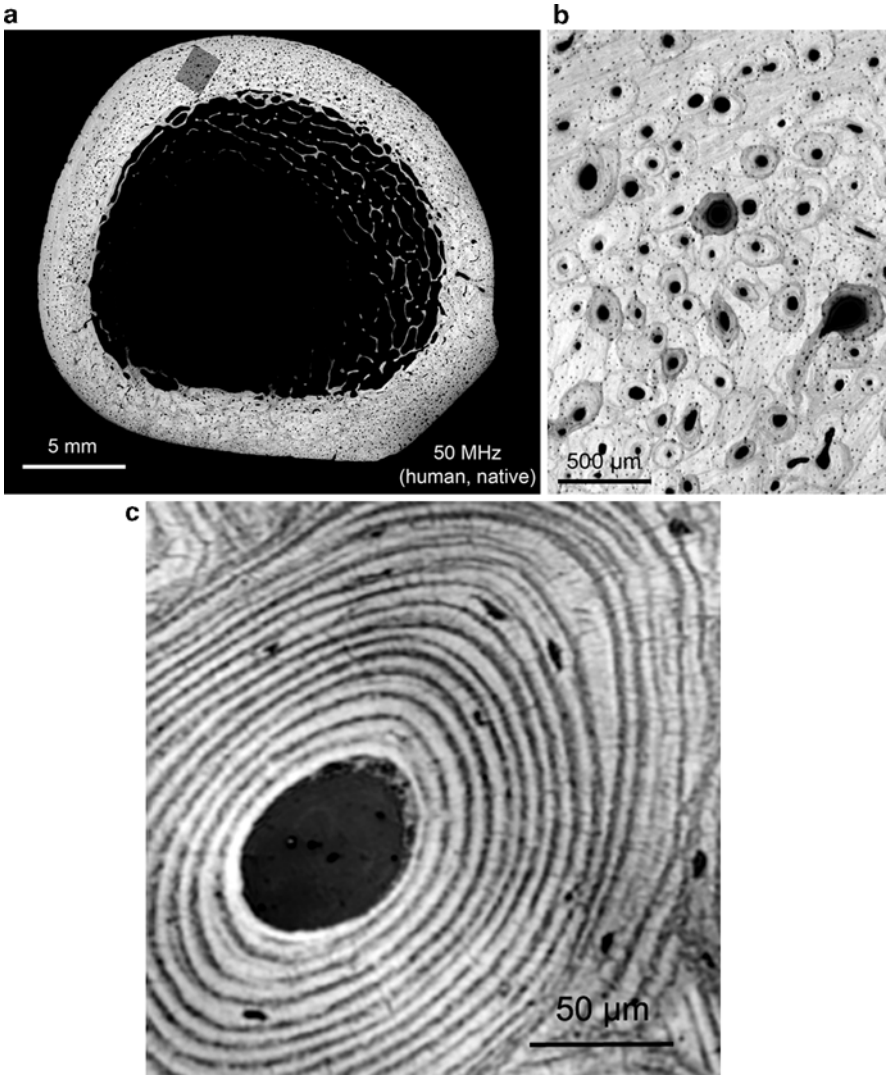

Fig. 16.11 Acoustic impedance images of human cortical bone cross-sections from the femoral mid-diaphysis. (**a**) 50 MHz: the Haversian canals can be distinguished from the mineralized tissue. The indicated rectangular area was measured again with a 200-MHz transducer (Reprinted with authorization from Raum [12], © 2008 IEEE). (**b**) Remnants of circumferential tissue in the upper left part of the image can be well distinguished osteonal and interstitial tissue. The large dark spots are Haversian canals and the small spots correspond to osteocyte lacunae. The latter are not resolved at this frequency and the size of the spots is larger than the actual size of the lacunae (Reprinted with authorization from Raum [12], © 2008 IEEE). (**c**) 900 MHz: the anisotropic lamellar tissue structure of an osteon with a central Haversian canal and osteocyte lacunae are clearly visible

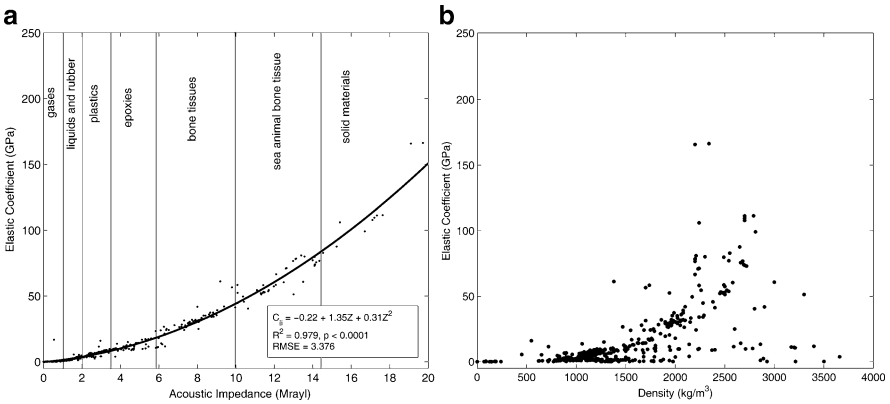

Fig. 16.12 Relationships between acoustic impedance, mass density, and elastic stiffness for different materials (Reprinted with authorization from Raum [12], © 2008 IEEE)

obtained for materials with intermediate or low acoustic impedance values. As the impedance increases, the reflection coefficient converges towards one and the confocal image contrast decreases. Within the typical impedance range of bone tissue (5–12 Mrayl) the average variation of the reflection coefficient R is approximately 3.3% Mrayl^{-1}.

Bone can be assumed to consist of three basic components: hydroxyapatite, collagen and water. The total mass density of the tissue is therefore given by:

$$\rho_{tissue} = vf_{HA}\rho_{HA} + vf_{col}\rho_{col} + vf_{H_2O}\rho_{H_2O}, \tag{16.29}$$

where vf_j is the volume fraction of the component j and ρ_j is the density. The subscript is HA for mineral, col for collagen and H_2O for water. The mass densities for the three components are $\rho_{HA} = 3.0\,\mathrm{g\,cm^{-3}}$, $\rho_{col} = 1.41\,\mathrm{g\,cm^{-3}}$, $\rho_{H2O} = 1.0\,\mathrm{g\,cm^{-3}}$.

Quantitative microradiography (qMR), quantitative backscattered electron imaging (qBEI) and synchrotron radiation micro computed tomography (SRμCT) may be utilized to measure tissue mineralization [31]. Depending on the experimental method tissue mineralization has been expressed either as weight percent of calcium (e.g. 39.86 wt% Ca for pure hydroxyapatite) or as tissue degree of mineralization of bone (DMB):

$$DMB = vf_{HA}\rho_{HA}. \tag{16.30}$$

The relation between weight percent of calcium and mass fraction mf_{HA} is:

$$\frac{39.86wt\%}{wt\%} = \frac{1}{mf_{HA}}. \tag{16.31}$$

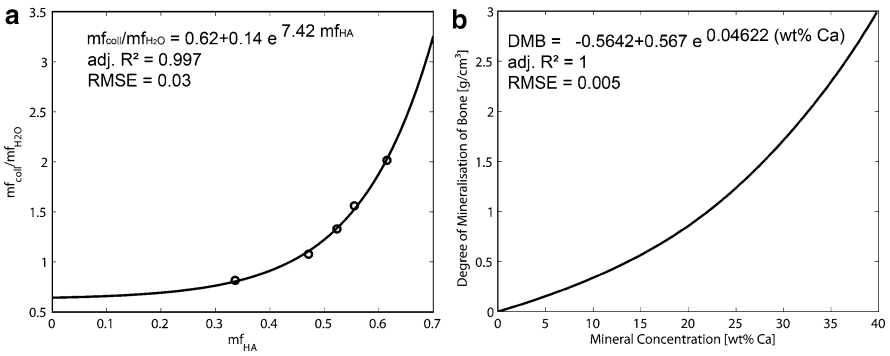

Fig. 16.13 (**a**) Mass fraction ratio mf_{col}/mf_{H_2O} as a function of vf_{HA} as derived from data published by Broz et al. (1995) (Reprinted from Raum et al. [29] copyright (2006), with permission from IOP Publishing Ltd.). (**b**) Conversion from wt% Ca to *DMB*

Raum et al. [32] have shown that the ratio of collagen to water volume fractions is determined by vf_{HA}. This relation can also be expressed in terms of mass fractions and allows the conversion between wt% Ca and *DMB* (Fig. 16.13).

The relations of *DMB* and wt% Ca with mass density can be approximated with second order polynomials:

$$\rho_{tissue} = 1.12\,g\,cm^{-3} + 0.73 \cdot DMB - 0.033\,cm^3\,g^{-1} \cdot DMB^2, \tag{16.32}$$

$$\rho_{tissue} = 1.153\,g\,cm^{-3} + 0.01094 \cdot (wt\%\,Ca) + 8.865 \cdot 10^{-4} cm^3\,g^{-1} \cdot (wt\%\,Ca)^2. \tag{16.33}$$

Numerous site-matched investigations of tissue mineralization and acoustic impedance have been conducted at the microscale, i.e. with acoustic frequencies between 50 and 200 MHz. By means of Eqs. 16.32, 16.33 and 16.17 c_{11} and c_{33} have been derived. Table 16.4 summarizes the average microscale properties measured in various species, tissue types and anatomical sites. In addition to the studies in mature tissues the data from Kotha et al. [33] and from Leicht et al. [34] provide information about partially demineralized tissue and nonmineralized cartilage, respectively.

Over the entire range of mineralization *DMB* shows a good correlation with the acoustic impedance, which is consistent with the assumption that the elastic stiffness in bone tissue is predominantly achieved by the deposition of mineral in the collagen matrix (Fig. 16.14a). As a result, all parameters exhibit a reasonable correlation with tissue elastic properties (Table 16.5). However, it can be seen that the regression curves of *DMB* with Z_1 and Z_3 are different. The divergence of the acoustic impedance values measured in the directions perpendicular and parallel to the bone long axis indicate a characteristic elastic anisotropy that is not depicted in the scalar quantities representing tissue mineralization. Moreover, the prediction accuracy is much better for the acoustic impedance than for *DMB* or mass density.

Table 16.4 Microscale tissue properties of various species and measurement sites

Species	Tissue	Tissue type	Z_1 (Mrayl)	Z_3 (Mrayl)	DMB (g/cm^3)	Po (%)	c_{11} (GPa)	c_{33} (GPa)	Study
Human	Femur^e	Cortical	7.5	8.5	–	4.1	27.3	35.0	Raum et al. [35]
Human	Femur^e	Haversian cortical	6.7	7.8	1.1	10.8	21.9	29.9	Rohrbach et al. [36]
Bovine	Femur^n	Plexiform cortical		8.1	1.1	–	31.7	–	Kotha et al. [33]
Bovine	Femur^n	Plexiform cortical (partially demineralized)		7.1	0.93	–	24.9	–	Kotha et al. [33]
Bovine	Femur^n	Plexiform cortical (partially demineralized)		6.3	0.81	–	19.4	–	Kotha et al. [33]
Mice (B6)	Femur^e	Cortical	6.5	–	1.28	–	21.7	–	Raum et al. [37]
Mice (B6)	Femur^e	Epiphysis	6.7	–	1.22	–	22.7	–	Raum et al. [37]
Mice (B6)	Femur^e	Trabecular	5.8	–	1.13	–	17.3	–	Raum et al. [37]
Mice (C3H)	Femur^e	Cortical	7.8	–	1.33	–	30.1	–	Raum et al. [37]
Mice (C3H)	Femur^e	Epiphysis	7.4	–	1.23	–	28.1	–	Raum et al. [37]
Mice (C3H)	Femur^e	Trabecular	6.9	–	1.27	–	23.8	–	Raum et al. [37]
Human	Radius^n	Haversian cortical (near periost)	6.6	8.0	1.14	2.3	21.4	31.0	Raum et al. [38], Saïed et al. [39]
Human	Radius^n	Haversian cortical (1-mm region from periost)	6.7	8.1	1.13	3.6	22.0	31.7	Raum et al. [38], Saïed et al. [39]
Human	Radius^n	Haversian cortical (central to endosteum)	6.7	8.2	1.13	6.2	22.0	32.5	Raum et al. [38], Saïed et al. [39]
Human	Radius^n	Haversian cortical (osteonal tissue)	–	7.2	1.06	–	–	25.2	Raum et al. [29]
Human	Radius^n	Haversian cortical (interstitial tissue)	–	9.3	1.16	–	–	41.5	Raum et al. [29]
Human	Tibia plateau^n	Subchondral bone	6.3	–	–	–	19.5	–	Leicht et al. [34]
Human	Tibia plateau^n	Cartilage	2.1				3.0		Leicht et al. [34]

All measurements have been conducted with frequencies between 50 and 200 MHz. Po is the tissue porosity. The superscript letters n and e stand for native and embedded tissues, respectively

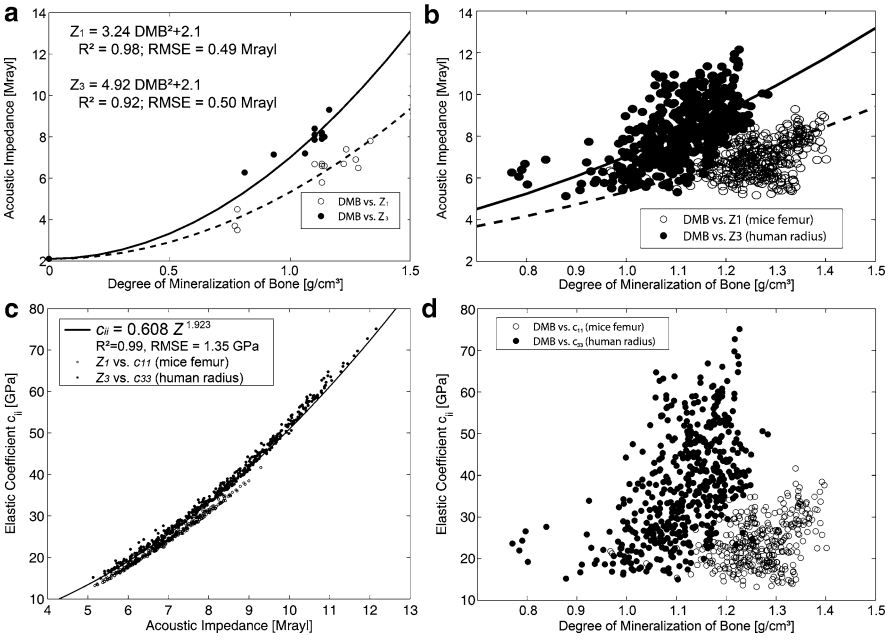

Fig. 16.14 (**a**) Relation between acoustic impedance Z and *DMB* over the full range of mineralization (Data from Table 16.4). (**b**) The strong dependence of Z on *DMB* disappears after the primary mineralization phase. (**c**) c_{ii} is directly proportional to the square of Z_i. (**d**) *DMB* has only a marginal correlation with c_{ii} for $DMB > 0.7\,\mathrm{g/cm}$ (The data in (**b–d**) are compiled from Raum et al. [29, 32, 37])

The situation is quite different for tissue after completion of the *primary mineralization* process, i.e. for $DMB > 0.7\,\mathrm{g/cm^3}$ (Fig. 16.14b). Figure 16.14b–d shows the results of two studies on mature human radius [32] and mice femur [37] samples. In both studies no or only weak correlations of *DMB* with Z_i and c_{ii} were observed (R^2 : 0.13–0.31), while the correlations between Z_i and c_{ii} remained highly significant ($\mathrm{R}^2 > 0.99$).

Lakhsmanan et al. [11] have measured $c(\theta)$ in small cylindrically shaped cortical bone sections from a human femur (Fig. 16.15). This method allowed direct assessment of c_{33}, c_{11}, and $c^* = 2(c_{13} + 2c_{44})$ from $c(\theta)$. The remaining elastic coefficients of a transverse isotropic stiffness tensor were derived using continuum micro-mechanical model constraints [40]. The means and standard deviations of the derived elastic coefficients were: $c_{33} = 29.9 \pm 5.0\,\mathrm{GPa}$, $c_{11} = 21.9 \pm 2.1\,\mathrm{GPa}$, $c_{12} = 9.2 \pm 1.5\,\mathrm{GPa}$, $c_{13} = 9.7 \pm 1.6\,\mathrm{GPa}$, and $c_{44} = 6.7 \pm 1.2\,\mathrm{GPa}$, and the corresponding engineering constants, i.e. Young moduli and Poisson ratios were: $E_3 = 23.8 \pm 3.7\,\mathrm{GPa}$, $E_1 = 16.8 \pm 1.1\,\mathrm{GPa}$, $\nu_{12} = 0.32 \pm 0.02$, $\nu_{13} = 0.22 \pm 0.01$, and $\nu_{31} = 0.31 \pm 0.01$.

Table 16.5 Conversion rules for the estimation of the elastic coefficients c_{11} and c_{33} from acoustic impedance, *DMB* and mass density for the data summarized in Table 16.4

	Z_1 (Mrayl)	Z_3 (Mrayl)	c_{11} (GPa)	c_{33} (GPa)
Z_1 (Mrayl)	–	$1.29Z_1 - 0.55$ $R^2 = 0.98$ RMSE $= 0.29$ GPa	$0.91Z_1^{1.70}$ $R^2 = 0.99$ RMSE $= 0.49$ GPa	$0.97Z_1^{1.87}$ $R^2 = 0.99$ RMSE $= 0.91$ GPa
Z_3 (Mrayl)	$0.76Z_1 + 0.54$ $R^2 = 0.98$ RMSE $= 0.22$ Mrayl	–	$0.97Z_3^{1.49}$ $R^2 = 0.95$ RMSE $= 1.44$ GPa	$0.59Z_3^{1.90}$ $R^2 = 0.99$ RMSE $= 0.88$ GPa
DMB(g/cm^3)	$3.24\,DMB^2 + 2.1$ $R^2 = 0.92$ RMSE $= 0.49$ Mrayl	$4.92\,DMB^2 + 2.1$ $R^2 = 0.92$ RMSE $= 0.50$ Mrayl	$16.89\,DMB^{1.84}$ $R^2 = 0.84$ RMSE $= 3.10$ GPa	$26.38\,DMB^{1.73}$ $R^2 = 0.89$ RMSE $= 3.10$ GPa
ρ(g/cm^3)	$1.02\rho^{2.83}$ $R^2 = 0.90$ RMSE $= 0.52$ Mrayl	$1.64\rho^{2.51}$ $R^2 = 0.95$ RMSE $= 0.39$ Mrayl	$0.99\rho^{4.74}$ $R^2 = 0.85$ RMSE $= 3.07$ GPa	$2.75\rho^{3.99}$ $R^2 = 0.88$ RMSE $= 3.41$GPa

It should be noted that these relations have been calculated over the full range of mineralization. The RMSE values for the DMB based correlations indicate that elastic predictions using *DMB* or ρ are not very accurate

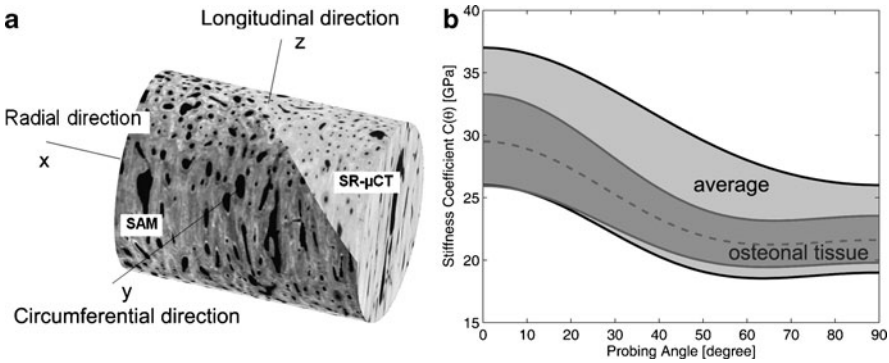

Fig. 16.15 (**a**) Site-matched evaluation of *DMB* and $Z(\theta)$ in small cylindrically shaped cortical bone tissue sections (human femur: diameter: 4.4 mm) [11, 36]. (**b**) The typical course of $c(\theta)$ averaged over the entire mineralized matrix (osteonal and interstitial tissue) and separately for osteonal tissue

The conversion between elastic coefficients and engineering constants is straightforward, if all independent coefficients are known. For example, the conversion between c_{33} and E_3 is:

$$E_3 = \frac{(1+\nu_{12})(1-\nu_{12}-2\nu_{13}\nu_{31})}{1-\nu_{12}^2} \cdot c_{33}, \tag{16.34}$$

where ν_{12} is the Poisson's ratio in the cross-sectional plane (x_1x_2 – plane) and $\nu_{13} = \nu_{23}$ and $\nu_{31} = \nu_{32}$ are the Poisson ratios in the longitudinal section (i.e., x_1x_3– and x_1x_2–) planes [32]. With the commonly used assumption of an isotropic Poisson ratio $\nu_{iso} = 0.3$ [41–43] (16.34) becomes

$$E_3 = 0.7429 \cdot c_{33}. \tag{16.35}$$

Using the Poisson ratios reported by Lakshmanan et al. [11] the scaling factor becomes considerably higher (0.80 ± 0.01) than in (16.35). However, these data measured in the femur of a 72-year old female human donor may not be representative for other bone tissues, but rather demonstrates that Eq. 16.35 should be used with caution.

Experimentally, the impact of the Poisson ratio has been investigated by site-matched analyses of the acoustic impedance and Young's modulus in human femoral cortical bones [44, 45]. Young's modulus E_{IT} is usually derived from nanoindentation measurements. Interestingly, in all studies consistent, but rather moderate correlations between Z and E_{IT} ($0.61 \leq R^2 \leq 0.67$) have been observed. Although at least some of the unexplained variances have to be attributed to experimental artefacts, e.g. caused by surface roughness, viscous and contact effects, not perfectly matched interaction volumes, a considerable amount has been suggested to be caused by variations of the Poisson ratios. Indeed, Rupin et al. [45] have recently suggested that a site-matched analysis of Z and E_{IT} may be used to assess the Poisson ratios experimentally. They reported isotropic Poisson ratios in the range between 0.18 and 0.46 (mean and standard deviation: 0.41 ± 0.04). However, a rigorous incorporation of the anisotropic theory has to be established in future analyses.

16.3.2 Relations Between Mineralization, Acoustic Impedance, and Elastic Properties at the Nanoscale

With frequencies in the gigahertz range a characteristic lamellar pattern with alternating impedance values between adjacent lamellae is usually observed (Figs. 16.11c and 16.16a–b). However, since the diameter of a single mineralized fibril ($\sim 0.1\,\mu m$) is still approximately one order of magnitude smaller than the wavelength, the individual fibrils are not resolved. Therefore, interpretation of the data obtained in the gigahertz range requires some ultrastructural model assumptions. Hofmann et al. [44] have evaluated osteonal tissue by site-matched SAM at

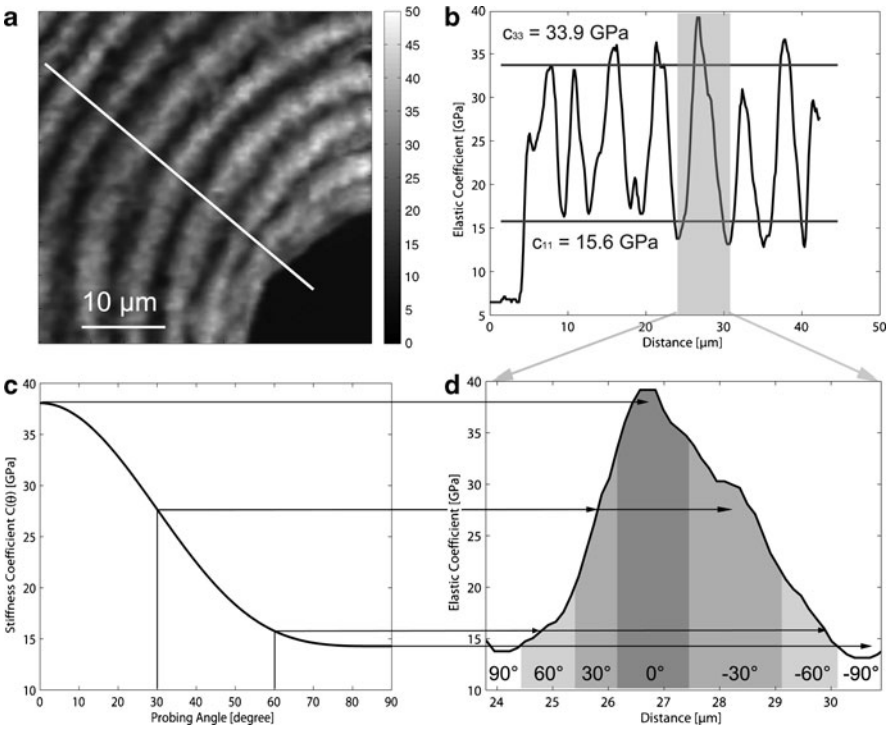

Fig. 16.16 (**a**) Typical alterations of the elastic coefficient in osteonal lamellae. 1.2 GHz image, image plane perpendicular to the osteonal long axis, one quarter of an osteon. The Haversian canal is in the lower right part of the image. (**b**) Elastic coefficient measured along the line in (**a**). The mean maxima and minima correspond to c_{33} and c_{11} of the individual fibrils, respectively. A representative lamellar unit is highlighted in the gray box. (**c**) Theoretical $c(\theta)$ with estimated remaining coefficients: $c_{12} = 5.2\,\text{GPa}$, $c_{13} = 8.8\,\text{GPa}$, $c_{44} = 3.4\,\text{GPa}$; (**d**) Schematic illustration of a six-layer lamellar unit. The different gray scales indicate fibril layers with parallel alignment and variable thickness, but distinct orientations (0°: parallel to the osteon long axis)

911 MHz, nanoindentation and 2D Raman spectroscopy. They found that the relative mineral concentration within individual osteons is relatively homogeneous and concluded that the alternating impedance pattern observed with gigahertz ultrasound arises from mineralized collagen fibrils with relatively equal transverse isotropic elastic properties (with c_{33} parallel and c_{11} perpendicular to the fibril long axis; $c_{33} > c_{11}$) that are arranged in an asymmetric twisted plywood structure [46, 47]. According to this model fibril bundles are tilted progressively layer by layer with an angle of rotation between adjacent layers of around 30° (Fig. 16.1b). One layer consists of a variable number of parallel fibrils and a lamellar unit is composed of six layers with fibril orientations from 0° to 180°. For example, the thickness of a lamellar unit in Fig. 16.16 can be considered as the space between two adjacent low-impedance regions. The average lamellar unit thickness can be estimated from the oscillation period along the line drawn in Fig. 16.16, to be $6.9 \pm 0.1\,\mu\text{m}$.

It is reasonable to argue that the fibrils oriented perpendicular to the osteon long axis are located in the low-impedance regions (corresponding to c_{11}), while the fibrils oriented parallel to the osteon long axis are located in the high impedance regions (corresponding to c_{33}). The layers with orientations of 30° and 60° should exhibit impedance values corresponding to the rotated elastic coefficients $c(30°)$ and $c(60°)$ of the fibrils (Fig. 16.16c). Apparently, due to the spatial resolution limit of approximately 1 µm at 1.2 GHz the six individual sublayers of the lamellar unit in Fig. 16.16d cannot be distinguished. Hofmann et al. [48] hypothesized that layers with a fibril orientation close to or parallel to the osteon axis appear as single thick and high reflective lamellae in acoustic cross-sectional images. Similarly, the layers with fibril orientations close to or perpendicular to the osteon axis may be observed as single thin low reflective lamellae. This asymmetric arrangement of individual layer thicknesses within a lamellar unit causes the tissue anisotropy at the next level of organization.

In a first attempt Hofmann et al. [48] have evaluated the average area fractions and impedance values of low reflective (thin) and high reflective (thick) regions for osteons cut at various angles relative to the osteon long axis. By fitting the data separately to a transverse isotropic model they found similar mean elastic properties (E_1 : 23.4–24.1 GPa, E_2 : 26.5–28.0 GPa, G_{12} : 9.1–10.4 GPa) but different symmetry orientations. They concluded that the effective orientations of the long axis of the collagen fibrils in the low and high reflective regions were 90° and 27°, respectively. However, a drawback of this study was that the data were obtained from different osteons. According to the twisted plywood model all possible fibril orientations can be observed in a single cross-sectional image (Fig. 16.16d). Future work should therefore aim to fit the data measured in a single cross-sectional image to an asymmetric twisted plywood model.

16.4 Conclusion

Ultrasound offers various possibilities for the evaluation of bone. The acoustic wavelength can be varied over more than four orders of magnitude. Acoustic parameters, e.g. acoustic impedance and sound velocities are directly linked with elastic parameters of the material interrogated by the acoustic wave. Due to the hierarchical organization of bone the elastic properties at each level are determined by the compound properties of the preceding level. The mechanical function and resistance to fracture of cortical bone are predominantly determined by the intrinsic elastic properties of the mineralized collagen matrix and by the porous microstructure. While the porous microstructure can be assessed with high accuracy in three dimensions with other imaging modalities, e.g. µCT, the target of ultrasound with frequencies between 50 MHz and 2 GHz is to assess the heterogeneous anisotropic elastic properties of the mineralized collagen matrix. Because of the small spatial dimensions of the characteristic structural units, e.g. osteonal and interstitial tissue, lamellar units with rapid alterations of fibril composition and orientation the requirements on the

spatial resolution are demanding. The measurement of the sound velocity in thin samples or the surface acoustic waves in thick samples requires defocusing of the sound field, and consequently, to increase the interrogated sample volume. Therefore, the applicability of these methods is limited to relatively homogeneous tissue regions that are sufficiently away from structural boundaries.

Two-dimensional mapping of the confocal reflection amplitude has emerged from a semi-quantitative method to the modality of choice for ultrasonic investigations of bone at the tissue level. A reliable estimation of the confocal reflection amplitude with defocus correction and surface tilt control is possible with time-resolved or amplitude detection microscopes. By adjusting the ultrasound frequency rapid scans can be performed either with large scan fields to map the effective elastic coefficient of the tissue matrix, or with small scan fields and frequencies in the gigahertz range to map the anisotropic tissue properties at the lamellar level. In addition to that the high resolution imaging capability allows a precise estimation of microstructural properties.

The potential of a combined assessment of structural and tissue elastic properties in musculoskeletal research has already been demonstrated in several studies. Raum et al. [38] have used 50-MHz impedance maps in conjunction with synchrotron radiation μCT data to predict the velocity of the first arriving signal measured with diagnostic ultrasound (bi-axial transmission) in human radius sections. In the low megahertz range ultrasonic propagation in cortical bone depends on anisotropic elastic tissue properties, porosity, and on the cortical geometry, e.g. thickness. Based on the SAM data a new model was derived that accounts for the nonlinear dispersion relation with the cortical thickness and predicts the velocity of the first arriving signal by a non-linear combination of fracture determining parameters, i.e. porosity, cortical thickness and tissue impedance ($R^2 = 0.69, p < 10^{-4}, RMSE = 52\,m/s$). Two-dimensional impedance maps are particularly suitable for investigations of tissue de- and regeneration or pathologies in animal models. For example, Hube et al. [3] have shown that the combined assessment of structural and anisotropic elastic tissue properties in a callus distraction model (sheep) by 50-MHz SAM allowed the prediction of the fracture force of distracted tibiae with a very high accuracy ($R^2 = 0.86,\ p < 0.0005$). On the other hand, genetic influences on the elastic bone phenotype have been determined using 200-MHz time-resolved scanning acoustic microscopy [37,44]. These findings may lead to the establishment of pathology specific treatment and regeneration monitoring strategies.

High resolution acoustic impedance maps in combination with the locally derived average elastic stiffness tensor are perfectly suited for numerical deformation or sound propagation analyses on “real-life” models [49]. Such models are crucial for the development and validation of new non-invasive diagnostic tools dedicated to the prediction of an individual fracture risk. Moreover, assessment of changes of local tissue anisotropy at the lamellar level with ultrasound in the gigahertz range may provide new insight in studies of bone remodeling, e.g. in the course of fracture healing, bone pathologies, ageing, or adaptation to modified loading conditions at the bone-implant interface after endoprothetic surgeries.

Acknowledgments This work has been conducted within the European Associated Laboratory "Ultrasound Based Assessment of Bone" (ULAB) and was supported by the Deutsche Forschungsgemeinschaft (grants Ra1380/1 and Ra1380/7).

References

1. S. Weiner and H. D. Wagner, "The material bone: Structure mechanical function relations," Annual Review of Materials Science **28**, 271–298 (1998).
2. J. Y. Rho, L. Kuhn-Spearing, and P. Zioupos, "Mechanical properties and the hierarchical structure of bone," Medical Engineering and Physics **20**(2), 92–102 (1998).
3. D. Ruffoni, P. Fratzl, P. Roschger, K. Klaushofer, and R. Weinkamer, "The bone mineralization density distribution as a fingerprint of the mineralization process," Bone **40**(5), 1308–1319 (2007).
4. R. B. Ashman, S. C. Cowin, J. Y. Rho, W. C. Van Buskirk, and J. C. Rice, "A continous wave technique for the measurement of the elastic properties of cortical bone," Journal of Biomechanics **17**(5), 349 (1984).
5. S. Lees, "A model for the distribution of HAP crystallites in bone – an hypothesis," Calcified Tissue International **27**(1), 53 (1979).
6. J. Y. Rho, "An ultrasonic method for measuring the elastic properties of human tibial cortical and cancellous bone," Ultrasonics **34**(8), 777 (1996).
7. W. C. VanBuskirk, S. C. Cowin, and R. N. Ward, "Ultrasonic measurement of orthotropic elastic constants of bovine femoral bone," Journal of Biomechanical Engineering **103**, 67 (1981).
8. K. Raum and W. D. O'Brien, "Pulse-echo field distribution measurement technique for high-frequency ultrasound sources," IEEE Transactions on Ultrasonics Ferroelectrics and Frequency Control **44**(4), 810 (1997).
9. G. A. Briggs and G. A. Briggs, *Acoustic Microscopy* (Clarendon Press, Oxford, 1992).
10. B. A. Auld, *Acoustic Fields and Waves in Solids* (Krieger Publishing Company, Malabar, 1990).
11. S. Lakshmanan, A. Bodi, and K. Raum, "Assessment of anisotropic tissue elasticity of cortical bone from high-resolution, angular acoustic measurements," IEEE Transactions on Ultrasonics Ferroelectrics and Frequency **54**(8), 1560–1570 (2007).
12. K. Raum, "Microelastic imaging of bone," IEEE Transactions on Ultrasonics Ferroelectrics and Frequency Control **55**(7), 1417–1431 (2008).
13. R. M. Jones, *Mechanics of Composite Materials* (McGraw-Hill, New York, 1984).
14. S. Hirsekorn, S. Pangraz, G. Weides, and W. Arnold, "Measurement of elastic impedance with high spatial resolution using acoustic microscopy" Applied Physics Letters **67**(6), 745 (1995).
15. S. Hirsekorn, S. Pangraz, G. Weides, and W. Arnold, "Erratum: Measurement of elastic impedance with high spatial resolution using acoustic microscopy," Applied Physics Letters **69**(14), 2138 (1996).
16. S. D. Peck and G. A. Briggs, "A scanning acoustic microscope study of the small caries lesion in human enamel," Caries Research **20**, 356 (1986).
17. S. D. Peck and G. A. Briggs, "The caries lesion under the scanning acoustic microscope," Advances in Dental Research **1**, 50 (1987).
18. S. D. Peck, J. M. Rowe, and G. A. Briggs, "Studies on sound and carious enamel with the quantitative acoustic microscope," Journal of Dental Research **68**(2), 107 (1989).
19. K. Raum, K. Kempf, H. J. Hein, J. Schubert, and P. Maurer, "Preservation of microelastic properties of dentin and tooth enamel in vitro–a scanning acoustic microscopy study," Dental Materials **23**(10), 1221–1228 (2007).
20. K. Raum and T. Kundu, "Ultrasonic characterization of hard tissues," in T. Kundu (ed.) *Ultrasonic Nondestructive Evaluation: Engineering and Biological Material Characterization* (CRC Press, Boca Raton, 2003), p. 761.

21. C. S. Jorgensen and T. Kundu, "Measurement of material elastic constants of trabecular bone: a micromechanical analytic study using a 1 GHz acoustic microscope," Journal of Orthopaedic Research **20**(1), 151 (2002).
22. K. Hasegawa, C. H. Turner, and D. B. Burr, "Contribution of collagen and mineral to the elastic anisotropy of bone," Calcified Tissue International **55**(5), 381 (1994).
23. R. M. Pidaparti and D. B. Burr, "Collagen fiber orientation and geometry effects on the mechanical properties of secondary osteons," Journal of Biomechanics **25**(8), 869 (1992).
24. R. M. Pidaparti, A. Chandran, Y. Takano, and C. H. Turner, "Bone mineral lies mainly outside collagen fibrils: predictions of a composite model for osteonal bone," Journal of Biomechanics **29**(7), 909 (1996).
25. Y. Takano, C. H. Turner, and D. B. Burr, "Mineral anisotropy in mineralized tissues is similar among species and mineral growth occurs independently of collagen orientation in rats: results from acoustic velocity measurements," Journal of Bone and Mineral Research **11**(9), 1292 (1996).
26. Y. Takano, C. H. Turner, I. Owan, R. B. Martin, S. T. Lau, M. R. Forwood, and D. B. Burr, "Elastic anisotropy and collagen orientation of osteonal bone are dependent on the mechanical strain distribution," Journal of Orthopaedic Research **17**(1), 59 (1999).
27. C. H. Turner, K. Hasegawa, W. Zhang, M. Wilson, Y. Li, and A. J. Dunipace, "Fluoride reduces bone strength in older rats," Journal of Dental Research **74**(8), 1475 (1995).
28. C. H. Turner, J. Y. Rho, Y. Takano, T. Y. Tsui, and G. M. Pharr, "The elastic properties of trabecular and cortical bone tissues are similar: results from two microscopic measurement techniques," Journal of Biomechanics **32**(4), 437 (1999).
29. K. Raum, I. Leguerney, F. Chandelier, M. Talmant, A. Saied, F. Peyrin, and P. Laugier, "Site-matched assessment of structural and tissue properties of cortical bone using scanning acoustic microscopy and synchrotron radiation muCT," Physics in Medicine and Biology **51**(3), 733–746 (2006).
30. K. Raum, K. V. Jenderka, A. Klemenz, and J. Brandt, "Multilayer analysis: Quantitative scanning acoustic microscopy for tissue characterization at a microscopic scale," IEEE Transactions on Ultrasonics Ferroelectrics and Frequency Control **50**(5), 507 (2003).
31. P. Roschger, E. P. Paschalis, P. Fratzl, and K. Klaushofer, "Bone mineralization density distribution in health and disease," Bone **42**(3), 456 (2008).
32. K. Raum, R. O. Cleveland, F. Peyrin, and P. Laugier, "Derivation of elastic stiffness from site-matched mineral density and acoustic impedance maps," Physics in Medicine and Biology **51**(3), 747–758 (2006).
33. S. P. Kotha, C. A. DePaula, A. B. Mann, and N. Guzelsu, "High frequency ultrasound prediction of mechanical properties of cortical bone with varying amount of mineral content," Ultrasound in Medicine and Biology **34**(4), 630–637 (2008).
34. S. Leicht and K. Raum, "Acoustic impedance changes in cartilage and subchondral bone due to primary arthrosis," Ultrasonics **48**(6–7), 613–620 (2008).
35. K. Raum, J. Reisshauer, and J. Brandt, "Frequency and resolution dependence of the anisotropic impedance estimation in cortical bone using time-resolved scanning acoustic microscopy," Journal of Biomedical Materials Research A **71**(3), 430–438 (2004).
36. D. Rohrbach, S. Lakshmanan, F. Peyrin, and K. Raum, "Spatial distribution of tissue mineralization and anisotropic tissue elastic constants in human femoral cortical bone," presented at the WC 2009, IFMBE Proceedings, Munich, 2009.
37. K. Raum, T. Hofmann, I. Leguerney, A. Saied, F. Peyrin, L. Vico, and P. Laugier, "Variations of microstructure, mineral density and tissue elasticity in B6/C3H mice," Bone **41**(6), 1017–1024 (2007).
38. K. Raum, I. Leguerney, F. Chandelier, E. Bossy, M. Talmant, A. Saied, F. Peyrin, and P. Laugier, "Bone microstructure and elastic tissue properties are reflected in QUS axial transmission measurements," Ultrasound in Medicine and Biology **31**(9), 1225–1235 (2005).
39. A. Saied, K. Raum, I. Leguerney, and P. Laugier, "Spatial distribution of anisotropic acoustic impedance assessed by time-resolved 50-MHz scanning acoustic microscopy and its relation to porosity in human cortical bone," Bone **43**(1), 187–194 (2008).

40. C. Hellmich, F. J. Ulm, and L. Dormieux, "Can the diverse elastic properties of trabecular and cortical bone be attributed to only a few tissue-independent phase properties and their interactions? Arguments from a multiscale approach," Biomechanics and Modeling Mechanobiology **2**(4), 219 (2004).
41. J. Y. Rho, P. Zioupos, J. D. Currey, and G. M. Pharr, "Microstructural elasticity and regional heterogeneity in human femoral bone of various ages examined by nano-indentation," Journal of Biomechanics **35**(2), 189 (2002).
42. J. Xu, J. Y. Rho, S. R. Mishra, and Z. Fan, "Atomic force microscopy and nanoindentation characterization of human lamellar bone prepared by microtome sectioning and mechanical polishing technique," Journal of Biomedical Materials Research **67A**(3), 719 (2003).
43. P. K. Zysset, X. E. Guo, C. E. Hoffler, K. E. Moore, and S. A. Goldstein, "Elastic modulus and hardness of cortical and trabecular bone lamellae measured by nanoindentation in the human femur," Journal of Biomechanics **32**(10), 1005 (1999).
44. T. Hofman, K. Raum, I. Leguerney, A. Saied, F. Peyrin, L. Vico, and P. Laugier, "Assessment of bone structure and acoustic impedance in C3H and BL6 mice using high resolution scanning acoustic microscopy," Ultrasonics **44** (Suppl 1), e1307–1311 (2006).
45. F. Rupin, A. Saied, D. Dalmas, F. Peyrin, S. Haupert, E. Barthel, G. Boivin, and P. Laugier, "Experimental determination of Young modulus and Poisson ratio in cortical bone tissue using high resolution scanning acoustic microscopy and nanoindentation," Journal of the Acoustical Society of America **123**(5), 3785–3786 (2008).
46. M. M. Giraud-Guille, "Twisted plywood architecture of collagen fibrils in human compact bone osteons," Calcified Tissue International **42**(3), 167 (1988).
47. M. M. Giraud-Guille, L. Besseau, and R. Martin, "Liquid crystalline assemblies of collagen in bone and in vitro systems," Journal of Biomechanics **36**(10), 1571 (2003).
48. T. Hofmann, F. Heyroth, H. Meinhard, W. Franzel, and K. Raum, "Assessment of composition and anisotropic elastic properties of secondary osteon lamellae," Journal of Biomechanics **39**(12), 2282–2294 (2006).
49. Q. Grimal, K. Raum, A. Gerisch, and P. Laugier, "Derivation of the mesoscopic elasticity tensor of cortical bone from quantitative impedance images at the micron scale," Computer Methods in Biomechanics and Biomedical Engineering **11**(2), 147–157 (2008).

Chapter 17
Ultrasonic Computed Tomography

Philippe Lasaygues, Régine Guillermin, and Jean-Pierre Lefebvre

Abstract Ultrasonic Computed Tomography (UCT) is a full digital imaging technique, which consists in numerically solving the inverse scattering problem associated to the forward scattering problem describing the interaction of ultrasonic waves with inhomogeneous media. For weakly inhomogeneous media such as soft tissues, various approximations of the solution of the forward problem (straight ray approximation, Born approximation, etc.), leading to easy-to-implement approximations of the inverse scattering problem (back-projection or back-propagation algorithms) can be used. In the case of highly heterogeneous media such as bone surrounded by soft tissues, such approximations are no more valid. We present here two non-linear inversion schemes based on high-order approximations. These methods are conceived like the prolongation of the methods implemented in the weakly inhomogeneous case for soft tissues. The results show the feasibility of this UCT approach to bones and its potential to perform measurements in vivo.

Keywords Acoustical impedance · Adult thighbone · Algebraic inversion · Artificial resin · Back-projection · Back-propagation · Born approximation · Childhood fibula · Circular arrays · Compound quantitative ultrasonic tomography · Computed tomography · Conjugated-gradient method · Constant background · Cortical bone · Cross-sectional imaging · Diffraction measurements · Distorted Born diffraction tomography · Electronic steering · Far field asymptotic method · Filtered back-projection algorithm · Geometrically-mimicking phantom · Green function · High impedance contrast · High-order approximations · Integral equation · Inverse problem · Inverse scattering · Iterative method · Linear arrays · Lippmann-Schwinger equation · Low-contrasted tissues · Lumbar vertebrae · Mechanical scanning · Mechanical steering · Neukadur ProtoCast 113^{TM} · Non-linear inversion · Osteoporosis · Papoulis deconvolution · Prototypes · Reflection measurements · Regularization process · Resolution · Scattered field · Snell-Descartes

P. Lasaygues (✉), R. Guillermin, and J.-P. Lefebvre
Laboratoire de Mécanique et d'Acoustique, UPR CNRS 7051 31, chemin Joseph Aiguier, 13402 Marseille cedex 20 – France
e-mail: lasaygues@lma.cnrs-mrs.fr; guillermin@lma.cnrs-mrs.fr; lefebvre@lma.cnrs-mrs.fr

P. Laugier and G. Haïat (eds.), *Bone Quantitative Ultrasound*,
DOI 10.1007/978-94-007-0017-8_17,

laws · Spatial Fourier transforms · Toroidal arrays · Transducers · Transmission measurements · Variable background · Wave attenuation · Wave velocity · Wavelet analysis

17.1 Introduction

Clinical ultrasound, which was developed for soft biological tissues, i.e., weakly inhomogeneous media, is not suitable for studying hard tissues such as bone because of the high acoustical properties contrast existing between the bone and the surrounding soft tissues. Some promising attempts were achieved by combining the mechanical displacement of mono-element ultrasonic probes with numerical processing of B-mode images, known as ultrasonic echo-tomography, for example on the brain [1] and long bones [2]. All these methods result in qualitative images of the internal structure of the imaged media, but they fail to provide quantitative estimates of relevant physical parameters, such as the velocity or the attenuation of the ultrasonic wave, or the acoustical impedance of the medium. Ultrasonic Computed Tomography (*UCT*), which combines *X*-ray Computed Tomography (*CT*) reconstruction procedures (back-projection or back-propagation algorithms) and ultrasonic waves, is expected to yield parametric cross-sectional images, i.e., images of wave velocities, wave attenuations or acoustical impedances. *UCT* has been developed by several authors to study soft tissues [3–6], using approaches such as the straight rays approximation [7] or the Born approximation [8], the latter consisting in assuming that the total field is equal to the incident field in every internal point of the scatterer, and which is accurate when the scattered field is much smaller than the incident field (typical case of soft tissues). The use of powerful computers makes it possible nowadays to introduce highly complex algorithms [9, 10], and many experimental devices have been developed based on linear, circular and/or toroidal arrays, and on mechanical and/or electronic steering and scanning [11–15]. When *UCT* is applied to hard tissues like bones, the problems involved become more complex, mainly because of the high contrast existing between bone and the surrounding soft tissues [16]. However, several authors have developed algorithms by simply linearizing the inverse problem [17–22] using both straight ray or Born approximations. However, difficulties arise with respect to quantitative tomography, i.e., for mapping the velocity or the attenuation of the ultrasonic waves, or the acoustical impedance of the medium. Finding solutions in these cases involves either using non-linear schemes [23] and/or performing extensive studies on the limitation of the approximations [24, 25].

In this chapter, we describe two iterative *UCT* methods based on the use of Born approximation. In both cases, the general scheme consists in estimating, at step n, a small deviation from a previously estimated configuration of the medium at step n–1. At each step, the field deviation, induced by the medium inhomogeneity (also called the perturbation), is indeed related to that previous one by a linear relationship. For weakly inhomogeneous media, starting from a homogeneous reference

(also called constant background) having properties near the mean acoustical properties of the medium, the strategy to solve the inverse problem necessitates only one iteration, and a first-order approximation is generally sufficient. Since in that case the field deviation (the perturbation) from the reference field (field in absence of the perturbation) is linearly related to the medium deviation (the medium perturbation) by a simple spatial Fourier transform, the inversion results in a simple inverse spatial Fourier transform which can be easily implemented by a filtered back-projection algorithm [26] like ones commonly used in X-ray *CT* scanners. For more contrasted media several iterations are necessary.

When the problem can be reduced to the study of a fluid-like cavity (like marrow) buried in an elastic hollow cylinder (like bone) surrounded by fluid (like muscle), we propose an iterative method, based on broken straight rays taking into account the wave refraction at the bone-soft tissue interface [7, 25]. This approach, called Compound Quantitative Ultrasonic Tomography (*CQUT*), is purely experimental and consists in performing reflection and transmission measurements, using an iterative correction procedure, which compensates for refraction effect arising at the boundary between bone and the surrounding tissues. The reflected/scattered waves provide information about the bone's geometrical properties, and the transmission waves, within a refracted straight ray approach, provide the local wave velocities. The tomographic reconstruction procedure is based on Born iterative method, and successive inverse spatial Fourier transforms. The main limitation of the *CQUT* method is the heavy experimental-costs involved (multiple iterative experiments).

The other *UCT* method presented in this chapter is based on an iterative algorithm using successive high-order Born approximations. The tomographic method in this case is known as Distorted Born Diffraction Tomography (*DBDT)* [27]. In comparison with the previous upgrade, *DBDT* combines diffraction measurements with a purely numerical non-linear inversion algorithm. This second approach is then more general than *CQUT*. It is not restricted to the case of a fluid-like cavity buried in an elastic hollow cylinder. Its main drawback is a heavy computational cost.

The performances and the limitations of these two tomographic methods applied to quantitative bone imaging problems are presented, and the results obtained using these methods are compared with experimental data.

17.2 Ultrasonic Computed Tomography

The aim of *UCT* is to reconstruct the geometry and the spatial distribution of acoustical parameters of an object from scattered ultrasonic measurements.

UCT measurements are carried out using variably densely spaced sets of transmitter and receiver positions as illustrated in Fig. 17.1. The reconstruction of the object (geometry and acoustical properties) requires first a accurate model to solve the forward scattering problem, i.e. predicting the pressure field when the scattering medium and the incident field are assumed to be known, and second, solves the inverse scattering problem, i.e. determines the parameters of the medium from

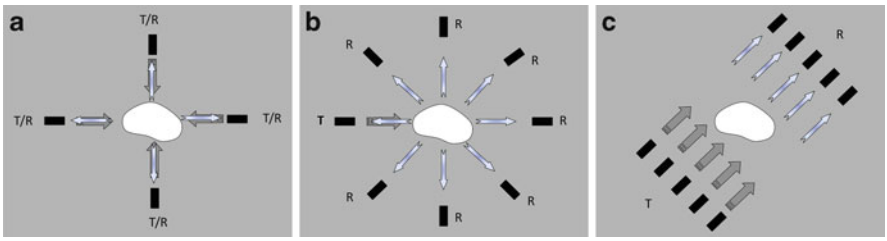

Fig. 17.1 Operating modes in Ultrasonic Computed Tomography. (**a**) A single transmitter/receiver in the reflection mode, (**b**) "n" transmitters/receivers in the diffraction mode, and (**c**) two paired transducers, one transmitter and one receiver in the transmission mode, are translated (the number of displacements corresponding to the points on the projections) and rotated around the tested body

measurements of the incident and scattered fields on some surface. Inverse scattering problems are non-linear and ill posed. No single solution exists and it is necessary to find a way of eliminating the solutions that do not correspond to reality.

Basic *UCT* principles have been clearly established in the case of weakly varying media such as low-contrasted tissues.

The forward scattering problem can be then solved with the Lippmann-Schwinger integral equation [23, 28], using the Green function [29] of the unperturbed problem (the homogeneous reference medium or constant background). Various approximations like straight ray approximation, for propagation measurements, or the first-order Born approximation, for scattering measurements, can be used in order to linearize the integral representation. This leads to a linear relation between the object function, which is related to the characteristics (dimensions, shape or acoustical parameters) of the reconstructed object, and the scattered field. Then, one possible way to solve this inverse problem consists in performing a far field asymptotic development [23], and 2-*D* or 3-*D* Fourier transforms, which makes it possible in principle to reconstruct the object function in almost real time based on a sufficiently large set of scattering data ("classical" tomographic algorithm) [26].

However, if the contrast between the media increases, the first-order Born approximation is no longer valid and other strategies will be considered. The first strategy adopted in this case consists in iteratively correcting the experimental data acquisition procedure, depending on the reflection and refraction behavior of the waves propagating through the soft/hard tissue interface. This strategy, which is known as Compound Quantitative Ultrasonic Tomography *(CQUT)*, makes it possible to use the first-order Born approximation, correcting at each iteration, i.e. in each experiment, the refraction of the propagating wave due to the impedance contrast between the surrounding medium and the bone. The disadvantage of this procedure is that as many experiments as iterative steps have to be carried out.

A second strategy involves the algebraic inversion of the scattered field, based on the distorted Born iterative method, using iterative numerical steps and performing only one experiment.

17.2.1 Modeling and Linearization

Let A be the operator that describes acoustic propagation or scattering phenomena in the heterogeneous medium that is to be imaged (including boundary and/or Sommerfeld radiation condition at infinity [23]). Let S be the acoustic sources, which are assumed to be known. All operators are time and space dependants. The variable φ, which denotes the resulting acoustic field, satisfies the equation:

$$A\varphi = S \tag{17.1}$$

Let us assume the medium to be composed of a known part, related to the reference medium, resulting in an operator A_0, and an unknown part, related to the perturbation of the reference medium and identified by the object function, resulting in an operator A' such that:

$$A = A_0 + A' \tag{17.2}$$

Assuming that φ_0, the solution of the non-perturbed problem, is known:

$$A_0\varphi_0 = S \tag{17.3}$$

Let φ' be the difference between φ and φ_0 ($\varphi' = \varphi - \varphi_0$), that is the field perturbation induced by the perturbation of the reference medium. Therefore φ' is the solution of

$$A_0\varphi' = -A'(\varphi_0 + \varphi') \tag{17.4}$$

If the Green function G_0 of the unperturbed problem is given [8], we obtain

$$\varphi' = G_0A'(\varphi_0 + \varphi') \tag{17.5}$$

The latter equation is the well-known Lippmann-Schwinger equation [23, 28], and the so-called inverse problem is therefore the solution of this non-linear equation. A solution can be found by using a perturbation scheme, based on successive linear approximations. The "Born series" is one of these schemes introducing different development orders [23, 30]. Within the first-order Born approximation, the field perturbation φ' is neglected in every internal point of the scatterer. The correspondent solution φ'_1 can be written:

$$\varphi'_1 = G_0\,A'\varphi_0 \tag{17.6}$$

In the frequency range (>3 MHz) of classical *UCT* of weakly heterogeneous soft tissues, the reference medium is considered to be constant in first approximation, leading to an Inverse Born Approximation (*IBA*) method with a "constant background". The final objective is to obtain suitable images from scattered measurements $(\varphi')^m$, where the subscript m stands for "measurements". Rotating the transducers around the object and transmitting broadband pulses at each position can be handled using the same approach as in *X*-ray tomography [31]: it provides

a slice-by-slice spectral coverage of the object spectrum (*2-D*-spatial Fourier transform, F_{2D}):

$$A' = (F_{2D}^{-1})(\varphi')^m \tag{17.7}$$

where F_{2D}^{-1} designates the inverse *2-D*-spatial Fourier transform. A reconstruction can therefore be performed using a classical algorithm of the summation of filtered back-projections [31].

17.2.2 Limitations in the Case of Bone Imaging

Since the acoustic impedance of bone is highly contrasted with that of the surrounding medium, the ultrasound propagation is perturbed by wave refraction, attenuation and scattering. This results in the propagation of more complex waves, such as those occurring in elastic volumes (compressional and shear waves). The weak scattering hypothesis is therefore not realistic.

However, by adopting some assumptions, the field of application of *UCT* can be extended to bone imaging. If the object to be imaged can be modeled by a set of concentric isotropic homogeneous noncircular "fluid-like" media representing the homogenized surrounding tissues, bone and marrow, only compressional waves are taken into account. In the diagnostic frequency range of bone *QUS* ($<$3 MHz), the wavelength of compressional wave (propagating at velocities ranging between 2000 and 4000 $m\,s^{-1}$) in cortical bone is typically greater than 1 mm, which remains much larger that the typical size of bone microstructures. Therefore bone itself in the cortical shell can be assimilated to a weakly heterogeneous medium, and the ultrasonic wave propagation will be minimally disturbed. So, the Born approximation is satisfied in this area. The *IBA* with a "variable background" can be used here; the background here being the set consisting of the homogeneous solid cylinder and the homogeneous fluid surrounding medium.

On the other hand, the wavelength in water ranges between 0.5 and 6 mm, which remains smaller than the mean diameter ($\approx 10 \pm 2$ mm) of the bone. The product *ka*, where "*k*" is the wave number and "*a*" is the mean radius of the bone, ranges between 2 and 47, and the configuration is therefore non-resonant. The background can be defined in terms of the following two parts: a solid part (bone) without any hollow and the surrounding water (or soft tissue), and the perturbed part, i.e. the object to be reconstructed, namely the cavity (marrow-filled medullary canal). The algorithm of summation of the filtered back-projections can then be used with some signal processing refinements. Despite the artifacts and biases affecting the assessment of the shell thickness, the main result obtained will be a qualitative tomogram of the cavity, where the gray or color level sets are not referenced to a physical parameter.

17.2.3 Compound Quantitative Ultrasonic Tomography (CQUT)

The main difficulties, however, arise when attempting to provide quantitative tomographic images of acoustical wave parameters. Finding solutions in this case

involves either using non-linear schemes or performing extensive studies on the limitation of the Born series. Following the same approach than in the Sect. 17.2.1, we can write:

$$\varphi_1' = G_b A' \varphi_b \tag{17.8}$$

where G_b is the appropriate Green function of the "variable background". φ_b and A_b are respectively the corresponding field and the corresponding operator such that:

$$A_b \varphi_b = S \text{ and } G_b A_b = -I \tag{17.9}$$

where I is the identity operator. This strategy can be applied iteratively:

$$\varphi_n' = G_b^{n-1} A_n' \varphi_b^{n-1} \tag{17.10}$$

where G_b^n is the inhomogeneous Green function of the "variable background" distorted/adapted for every iteration step n. This non-linear inversion scheme is called the distorted Born iterative (*DBI*) method. The reconstruction algorithm is therefore the same as the previous classical one, and the solutions are iteratively determined using Eq. 17.7. *UCT* based on the *DBI* method yields quantitative images.

Experimentally, the approach was designed first, to cancel out the refraction effects by using a specific set-up in order to impose straight ray propagation inside the shell, and second, to use the Born iterative method. Based on a priori knowledge of the geometrical properties and the acoustical properties, after calculating the incident and refracted angles using the Snell-Descartes laws, a compensation procedure has to be performed to determine the most suitable positions and orientations of the paired transducers (Fig. 17.2).

Reflection measurements and transmission measurements give, respectively and successively, the boundaries of the shell and the quantitative values of the velocity of the wave along the whole path. A quantitative image obtained after experiment n is used as the a priori information for the following procedure $n+1$. The initial guess is the image obtained without any angular corrections, and the stop criterion of this iterative process is when the difference between the mean velocities calculated at two different steps is less than $5\,\mathrm{m\,s^{-1}}$.

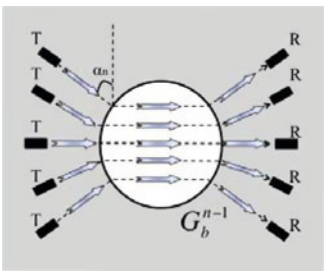

Fig. 17.2 Compensatory operating procedure in *CQUT* – α_n is the incident angle determined at the step n using the Snell-Descartes laws; G_b^{n-1} is the Green function adapted to a variable background (homogeneous cylinder plus homogeneous surrounding medium) at each iteration

Our initial attempts along these lines have been improved using signal and image processing methods [32]. This iterative experimental method, known as Compound Quantitative Ultrasonic Tomography (*CQUT*), has been described in detail in Ouedraogo et al. [33,34]. Despite limitations due to heavy data processing requirements and complex acoustical signals resulting from multiple physical effects involved (various pathways into the shell, roughnesses of the water/bone interfaces etc. [35]), *CQUT* gives images that are quantitatively related to the compressional wave velocities in a cross-section of a cortical shell, and the error remains within reasonable limits (about 7%).

17.2.4 Distorted Born Diffraction Tomography (DBDT)

A second non-linear inversion method, which is also based on the *DBI* method, was investigated. With this approach, the medium is modeled without any a priori knowledge by performing a simple geometrical discretization of the object. The algorithm involves successive linearizations of the Lippmann-Schwinger representation. The initial guess in the iterative process is provided by the first-order Born approximation. If the solution is known with the order (n–1), the n-order solution A'_n will satisfy [36]:

$$\left[(\varphi')^m - \varphi'_{n-1}\right] = G_b^{n-1}\left[A'_n - A'_{n-1}\right]\varphi_b^{n-1} \tag{17.11}$$

At each iteration, the algorithm numerically solves a forward diffraction problem in order to calculate the appropriate inhomogeneous Green function G_b^{n-1} and the internal field φ_b^{n-1}. Contrary to what occurs with the *CQUT*, the *DBDT* requires only a single series of experimental data. However, this technique is computational time consuming because it involves inversion of huge, full and complex matrix. The matrix inversion procedure is the key point with this method. Generally non-square ill-conditioned matrixes have to be inverted. A mean-square solution can be calculated using a conjugated-gradient method associated with a regularization procedure [37]. To make use of the broadband frequency content of the impulse signal used, the idea is to begin with the low frequencies, which carry overall information, and to gradually inject the high frequencies to simultaneously improve both the qualitative aspects (the resolution) and the quantitative aspects (the characterization).

17.3 The UCT-Scanner

These methods were tested on data obtained with a mechanical scanner, on bone-mimicking phantoms and real human bones. Whenever possible, *UCT* images of bones were compared with *X*-ray tomography images obtained at the same cross-section levels. Details of the imaging conditions are systematically presented below.

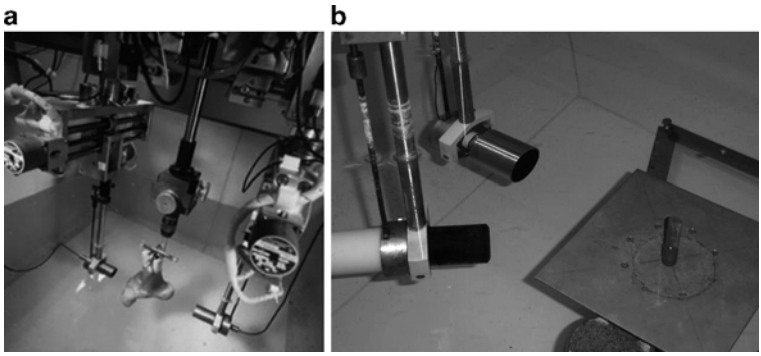

Fig. 17.3 The *UCT*-scanner, (**a**) transmission configuration, (**b**) reflected (only one transducer is used) and diffracted (two transducers are used) configurations

The general architecture of this mechanical system is that of a first generation ultrasonic scanner (Fig. 17.3): the main symmetrical arm holds two transversal arms with which two transducers can be translated in parallel. By rotating either the main arm or the object holder, angular scanning can be performed. Six stepping motors sequentially driven by a programmable translator-indexer device fitted with a power multiplexer control all the movements. The object to be imaged is placed in the presumed geometrical center of the bench so that the distance between the transducers and the center is limited to 150 mm. The surrounding fluid-like medium is water at a temperature of 18.6° ($\rho_o = 1000\,\mathrm{kg\,m^{-3}}$, $c_o = 1480\,\mathrm{m\,s^{-1}}$). The transducers used for data acquisition are broadband piezo-composite transducers with nominal frequencies of 250 kHz to 1 MHz. The transducers are driven using a pulse/receiver, and are positioned automatically as required around the object, and the data stored are then used to determine the time-of-flight between the source, the object and the receiver. The reconstruction algorithm and some signal processing algorithms were implemented on a personal computer.

17.4 Results

17.4.1 2D and 3D Qualitative Tomography

Contrast tomographic images of bone were obtained using the linearized (first-order Born approximation) *UCT* algorithm based on reflected and diffracted measurements (no transmission measurements were used at this stage). Except for the processing of the input signals, no compensatory procedures or changes in the wave paths were made.

17.4.1.1 Lumbar Vertebrae

The first example focuses on the analysis of a L2 lumbar human vertebra without any articular or transversal apophysis, having a visible external spinal body diameter of approximately 30 mm (Fig. 17.4a). A 4-mm circular metallic rod was placed inside the specimen, perpendicular to its upper surface.

The nominal frequency of the transducer (Fig. 17.4b) was 500 kHz ($\lambda = 3$ mm in water) and the reflected sinogram consisted of 180 projections (through 360°), each including 1024 samples. The sampling frequency was 20 MHz. The size of the image was 255×255 pixels. The resolution was improved using Papoulis deconvolution of the signal measured by the transfer function of the apparatus, with a frequency threshold of -15 dB in the (330–760) kHz frequency range [38]. Under these signal-processing conditions, the resolution of the image was about 0.375 mm ($\lambda/8$ in water).

The *X*-ray tomography device (Fig. 17.4c) was a Philips MG 450 radiation source, with a high intensity tube receiving a 80 keV beam with an intensity of 10 mA. The focal size was 4.5 mm. The distance from source to object was 3 m. A Thalès Flashscan 35 was used as the scintillator-imaging device. The resolution was 127 µm, and the image size was 2304×3200 pixels.

The dimensions and the shape of the bone sample could be readily distinguished on the *UCT* image. The dimensions and the location of the rod were also visible and well reconstructed. This means that on the one hand, the ultrasonic wave propagated into the center of the body despite the attenuation of the wave due to the porosity and/or the anisotropy, and that on the other hand, it was then possible to discriminate and to size a metallic implant placed inside the bone specimen. But it was impossible to discriminate between the trabecular zone and the cortical zone. In addition, *UCT* does not give the same quality of image resolution as *X*-ray tomography. This is a serious limitation, as it makes it difficult to determine some characteristic parameters precisely from *UCT* images, such as the bone volume fraction.

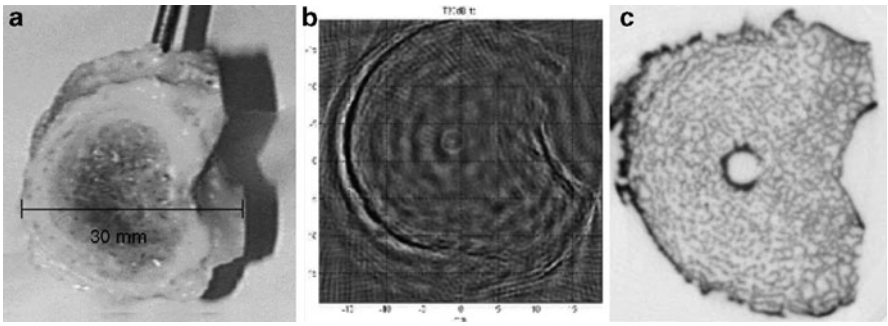

Fig. 17.4 L2 -Lumbar vertebra. (**a**) Sample picture, (**b**) *2-D-UCT* obtained from the reflected sinogram, 180 projections with 1024 samples, Nominal frequency Fc = 500 kHz, resolution 375 µm, image size 255×255 pixels (**c**) corresponding X-ray tomography, resolution 127 µm, image size 2304×3200 pixels (Reproduced from [38], 2001. Permission granted from Dynamedia, Inc)

17.4.1.2 Diaphysis of an Adult Thighbone

In the second example, a *3-D UCT* of adult human female thighbone was obtained from diffracted sinograms. The first sample (Fig. 17.5) was obtained from a post-menopausal 78-year old woman with osteoporosis, and the second (Fig. 17.6) from a 81-year-old woman without any bones pathology (healthy bones).

The nominal frequency of the transducers was 1 MHz. The resolution and the size of the image were 0.75×0.75 mm and 512×512 pixels, respectively. The diffracted sinograms included 2048 projections, each including 8256 samples, involving 32 angular transmitter positions combined with 64 angular receiver positions covering an angle of 360°. The sampling frequency used was 40 MHz.

A signal-processing tool [22, 39] was used to determine cortical thickness. This tool was based on a segmentation of the final image and a size correction of the inner boundaries, using a priori information on physical parameters (in this case, mean compressional wave velocity in bone $= 3500 \pm 100\,\mathrm{m\,s^{-1}}$, bone mass density $= 1700\,\mathrm{kg\,m^{-3}}$).

Figures 17.5a and 17.6 show the *3-D UCT* images of the pathological and healthy thighbones. These reconstructions were obtained by superimposing sequential *2-D*

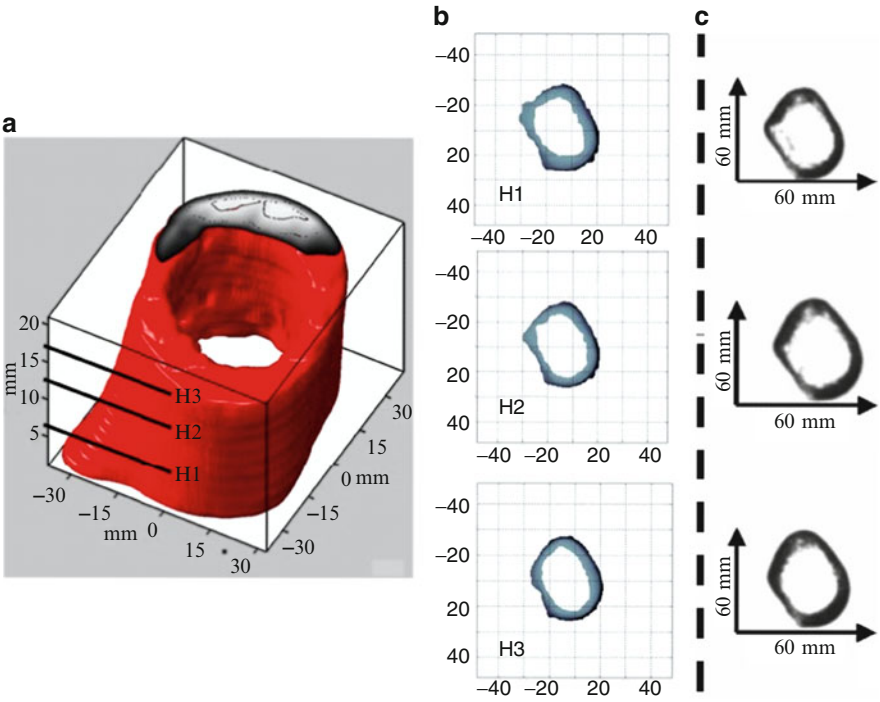

Fig. 17.5 Diaphysis of an adult thighbone with osteoporosis. (**a**) Qualitative image obtained with *3-D UCT*, (**b**) cross-sections, H1 = 8 mm, H2 = 14 mm and H3 = 18 mm, (**c**) corresponding X-ray tomographies

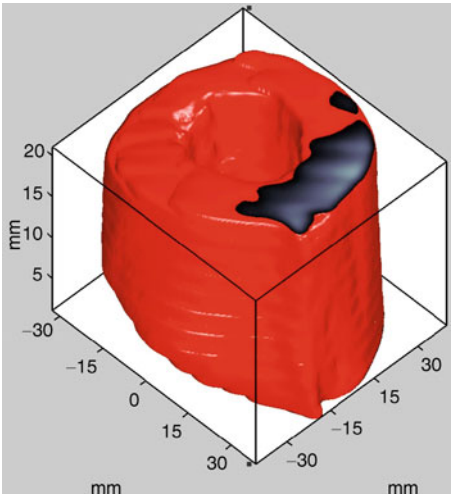

Fig. 17.6 *3-D-UCT* of a healthy thighbone

UCT images (80 cross-sections). The step between two cross-sections was 0.25 mm. The interpolation scheme used for a given *3-D* image was the shape-based method (Matlab®, MathWorks™). In Fig. 17.5b and c, three *2-D UCT* spaced 6 and 4 mm apart (H1 = 8 mm, H2 = 14 mm and H3 = 18 mm) are compared with the corresponding *X*-ray tomographic images of the unhealthy bone.

The *X*-ray device was a clinical General Electric® device (*CE 12000*). The thickness of the cross-section was 1 mm. The resolution was 0.25×0.25 mm and the image size was 512×512 pixels.

17.4.1.3 Childhood Fibula

In the third example (Fig. 17.7), the same experimental configuration was used as previously (see Sect. 17.4.1.2). The sample was a fresh fibula from a 12-year old child containing no marrow in the inner cavity. The mean dimensions of the bone sample were 17 ± 2 mm on the outside and 6 ± 2 mm in the inner cavity. Twenty sequential cross-sections were performed in this case with a 1-mm step.

These results obtained with human specimens show that it is possible to characterize the size and shape of bones using Ultrasonic Computed Tomography. Focusing on well-contrasted images obtained using *UCT*, and comparison with *X*-ray, show that this method provide efficient means of assessing the cortical thickness, which is known to be an important indicator of bone strength.

17.4.2 Quantitative Assessment

The aim of the second experiment was to obtain a quantitative assessment of the ultrasonic wave velocity in bone using *UCT* methods.

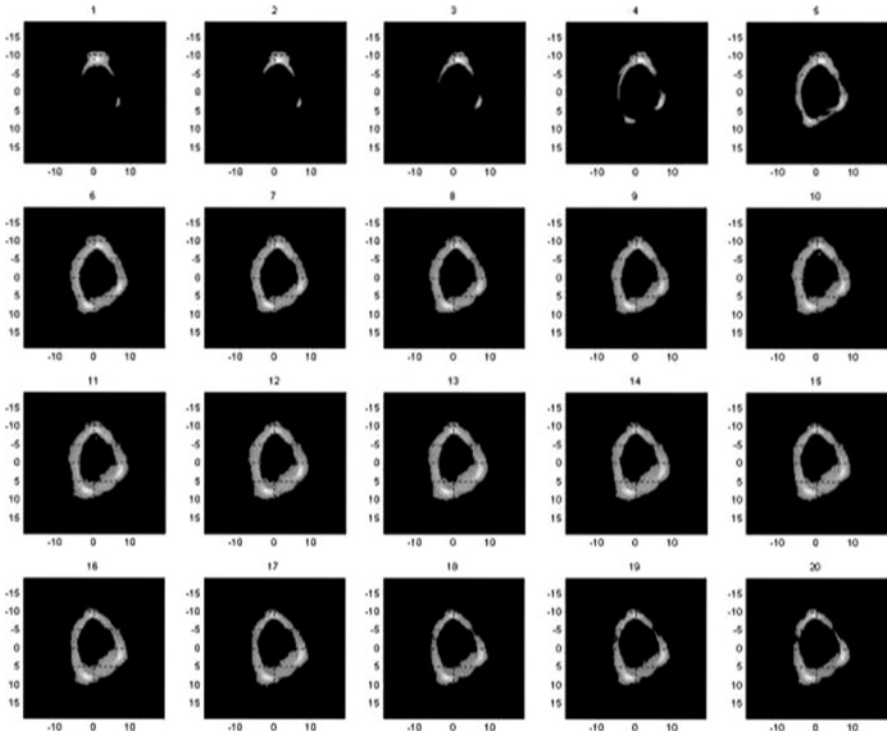

Fig. 17.7 *3-D UCT* image of a child's fibula

17.4.2.1 Compound Quantitative Ultrasonic Tomography (CQUT)

CQUT was tested first on circular Plexiglas cylinders and results were excellent because of the weak errors and the fast convergence of the algorithm (only two iterations) [34]. Because long bones look like more non-cylindrical elastic hollow tubes, the number of iterations (about five here) is higher and the convergence is slower than with academic objects [33].

The bone sample tested here was a human femoral diaphysis with an external diameter of about 32 ± 5 mm and an internal diameter of 16 ± 2 mm. The initial velocity of the compressional wave propagating into the bone was set at $3400\,\mathrm{m\,s^{-1}}$.

In the *UCT,* the backscattered sinogram consisted of 90 signals covering an angle of 360°. The transmitted sinogram consisted of 90 projections with 128 transverse displacements in steps of 330 µm. The time-of-flight was calculated with several algorithms (zero-crossing, cross-correlation, etc.). The *X*-ray device used was that described above in Sect. 17.4.1.1.

From the qualitative (contrast) point of view, the *UCT* image was similar to the *X*-ray image (Fig. 17.8). *X*-ray tomography, which estimates the mass density, is the main method currently used to determine the structural characteristics of bone, and

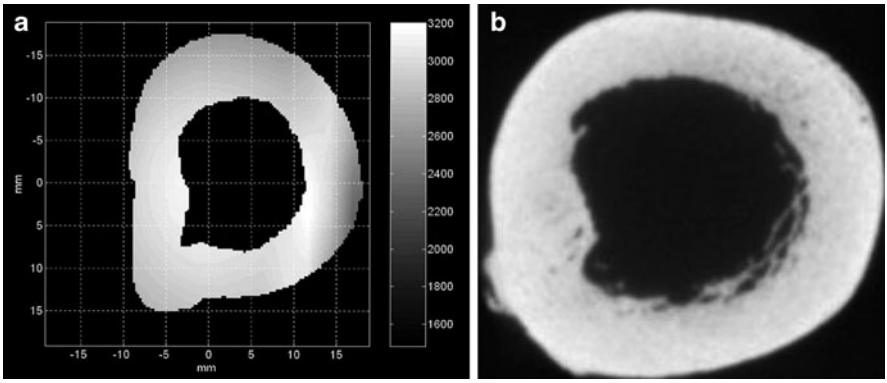

Fig. 17.8 Human thighbone (**a**) *CQUT* (90 projections, 128 translation samples; resolution 0.75×0.75 mm, size 256×256 pixels), (**b**) corresponding *X*-ray tomography (80 keV, 10 mA, 4.5 mm, resolution 127 µm, size 2304×3200 pixels) (Reproduced from Lasaygues, [19] copyright 2005. Permission granted from IOP Publishing limited)

the present reconstruction was more detailed than that obtained with *UCT*. However, the ultrasonic image represents a quantitative map of the velocity of the compressional wave into the cortical shell. The speed of sound of the fluid contained in the inner cavity was accurately reconstructed with a mean wave velocity close to $1500\,\mathrm{m\,s^{-1}}$, and the diameter of the inner cavity was found to be 15–17 mm. The external diameter was found to be in the 30–34 mm range, which is close to the actual values. Mean wave velocity in the shell was $3150 \pm 50\,\mathrm{m\,s^{-1}}$. This value seems to be lower than the mean wave velocity in cortical bones usually reported in literature (see Chap. 13 for more details). However, experimental studies were performed in parallel on small cubic samples taken from the same femur, and similar values with only a slight dispersion ($<0.5\,\mathrm{m\,s^{-1}}$) were obtained.

17.4.2.2 Distorted Born Diffraction Tomography (DBDT)

The performances obtained with *DBDT* were then assessed with a set of experimental data. The sample used here was a geometrically-mimicking phantom of a child's bone. The phantom was a non-circular homogeneous isotropic tube made of artificial resin (Neukadur ProtoCast 113^{TM}) with maximum internal and external diameters of 6 and 12 mm, respectively. The volumetric mass density of the resin was $\rho_1 \approx 1150\,\mathrm{kg\,m^{-3}}$, and the mean velocity of the compressional wave was $c_1 \approx 2400 \pm 50\,\mathrm{m\,s^{-1}}$. The transmitter and receiver were placed 17.5 cm to the right of the center of the bench. The diffraction sinograms were assessed with two transducers, which were placed in 72 by 72 positions around the object with a 5° step. The transducers had a nominal frequency of 250 kHz and their -6 dB frequency bandwidth was 135–375 kHz. The initial frequency was chosen so that the fist-order Born solution, that provides the initial guess of the iterative process,

does not include too many artifacts. Previous studies [36,40] have shown that if the phase shift resulting from the presence of the scatterer is greater than π, the reconstruction will present important artifacts. We therefore chose an initial frequency such as:

$$f < \frac{c_0 c_l}{2d|c_l - c_0|} \approx 150\,\text{kHz} \tag{17.12}$$

where d is the largest dimension of the scatterer. Because of the small frequency range available, the image resolution rather limited. The scattered field was obtained by subtracting the incident field (measured without the scatterer) from the total field. The frequency data were obtained by computing the Fast Fourier Transform of the temporal signals and no other corrections or signal processing steps were carried out.

Figure 17.9a shows the first-order diffraction tomography of the scatterer. Since the wavelength of the wave in water was similar to the size of the object, the image resolution is poor and the assessment of the shell thickness is not possible.

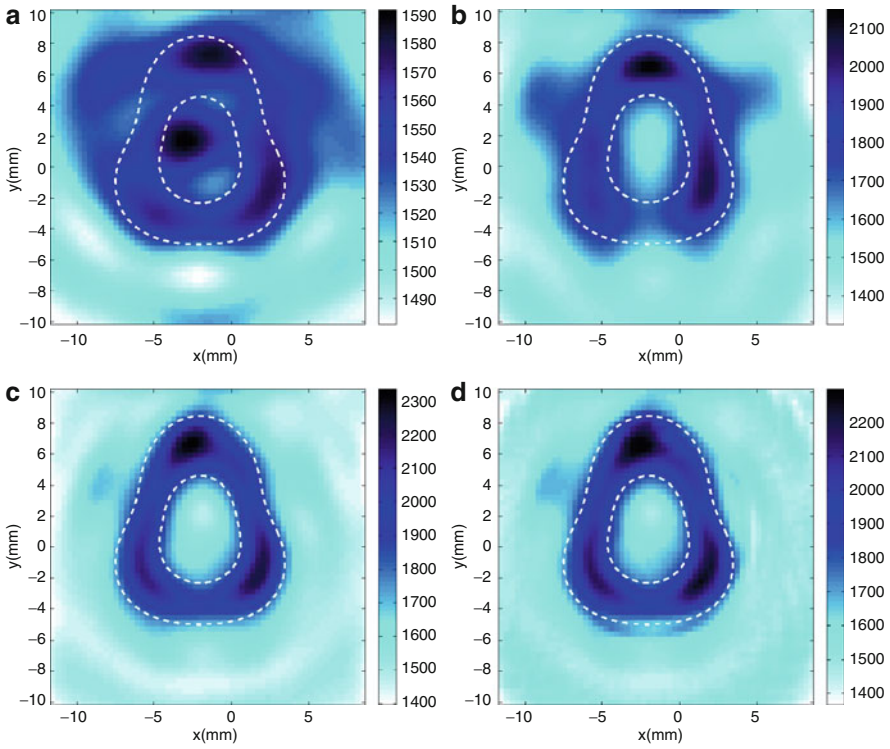

Fig. 17.9 Quantitative *UCT* of a geometrically-mimicking phantom of a child's bone. (**a**) Initial solution of the *DBDT* at 150 kHz (first-order Born approximation), (**b**) iterations at 150 kHz, (**c**) iterations at 350 kHz, (**d**) iterations at 1 MHz

Figure 17.9b–d show three sequential iterations of the distorted Born diffraction tomography. It can be seen that with *DBDT*, the resolution and the quality of the contrast gradually improved. The final result of the iteration process was satisfactory. The geometry was fairly accurate (position and dimensions reconstructed with mean relative error of the order of 5%), whereas the velocity was estimated with a rather large relative error of about 10%.

17.5 Conclusion

This chapter deals with 2-D and 3-D imaging of human long bones using Ultrasonic Computed Tomography (*UCT*). The scope of *UCT* methods was thus extended here from low impedance and velocity contrast media such as soft tissues (the classical domain) to higher contrast domains such as cortical bone structures, using non-linear and correction schemes with the following features: the wave field and the associated Green function of the reference background medium were determined iteratively at the various steps. Due to the mismatch between the acoustical impedance of bone and that of the surrounding soft tissues, the higher the frequency, the lower the proportion of the energy transmitted through bone and the lower the resolution of the resulting ultrasonic image. The ultrasonic propagation is greatly perturbed by the contrast between the media, which generates large artifacts. Two strategies were used to solve this problem.

The first strategy, named Compound Quantitative Ultrasonic Tomography (*CQUT*), was based on the Born iterative method with a corrected experimental data acquisition procedure. Bone was assumed to be equivalent to an internally weakly contrasted object immersed in a homogeneous reference medium (water). The results obtained with *CQUT* were satisfactory, and both the reconstructed geometries and wave velocities were close to the actual values. The main limitations of the *CQUT* are the number of measurements required, which involve multiple iterative experiments and heavy data processing.

The second method tested here was also a non-linear inversion method with higher-order levels of approximation, but in this case, the iterations were performed numerically, based on a single experimental measurement. The so-called Distorted Born Diffraction Tomography (*DBDT*) strategy gave reasonably accurate results without requiring any a priori information about the object.

The methods presented in this chapter were tested so far using bone mimicking phantoms as well as real bones, including vertebrae, femurs and fibulas, with a non-canonical homogeneous shape. In comparison with classical *X*-ray tomography, *UCT* methods were found to be promising, and the geometrical and physical parameters of the object were accurately reconstructed with these methods.

It is now proposed to investigate various ways of improving these methods. Work is in progress, for instance, on the matrix inversion procedure involved in *DBDT* method and particularly on the regularization process, which is an extremely important aspect of the inversion scheme, especially with high-contrast targets.

Signal processing and image processing studies on how to handle the heavy experimental data are also in progress (wavelet analysis, blind deconvolution, segmentation etc.).

In conclusion, in situ measurements of the acoustic properties of long bones in various parts of the skeleton must be sufficiently accurate for the results to be of use in the diagnosis and/or treatment of bone diseases. Once the requisite degree of accuracy has been achieved, it will be possible to start developing prototypes for in vivo applications.

Acknowledgment The authors are grateful for medical assistance from Dr P. Petit and Dr. J.-L. Jouve at Public Assistance Hospitals in Marseille and the "*Timone*" Children's Hospital. The *X*-ray tomographies were performed by V. Kaftandjian at the Laboratory for Nondestructive Testing using Ionizing Radiation, INSA, Lyon.

References

1. S. W. Smith, O. T. Von Ramm, J. A. Kisslo, and F. L. Thurstone, "Real time ultrasound tomography of the adult brain," Stroke 9, 117–122 (1978).
2. B. Migeon and P. Marche, "3D surfacing representation of limb long bones using ultrasound tomography," ITBM 15(6), 693–706 (1994).
3. M. P. Andre, P. J. Martin, G. P. Otto, L. K. Olson, and T. K. Barrett, A new consideration of diffraction computed tomography for breast imaging: studies in phantoms and patients, *Acoustical Imaging* (Plenum Press, New York, 1995), Vol. 21, pp. 379–390.
4. J. F. Greenleaf, Introduction to computer ultrasound tomography, *Computed Aided Tomography and Ultrasonics in Medicine* (North-Holland, Amsterdan, 1970).
5. J. P. Lefebvre, Acoustic impedance tomography: two reconstructions procedure, *Acoustical Imaging* (Plenum Press, New York, 1985), Vol. 14, pp. 719–723.
6. S. J. Norton and M. Linzer, "Ultrasonic reflectivity imaging in three dimensions: reconstruction with spherical transducer arrays," Ultrasonic Imaging 1, 210–231 (1979).
7. A. H. Anderson and A. C. Kak, The application of ray tracing towards a correction for refracting effects in computed tomography with diffracting sources, *School of Electrical Engineering*, TR-EE 84–14 (Perdue University, Ind, West Lafayette, 1984).
8. M. Born and E. Wolf, *Principles of Optics* (Pergamon Press, Oxford, 1964).
9. E. Franceschini, S. Mensah, L. Le Marrec, and P. Lasaygues, "An optimization method for quantitative impedance tomography," IEEE Transactions on Ultrasonics Ferroelectrics and Frequency Control 54(8), 1578–1588 (2007).
10. S. Mensah and L. J. P., "Enhanced compressibility tomography," IEEE Transactions on Ultrasonics Ferroelectrics and Frequency Control 44(66), 1245–1252 (1997).
11. M. P. André, H. S. Janée, P. J. Martin, G. P. Otto, B. A. Spivey, and D. A. Palmer, "High-speed data acquisition in diffraction tomography system employing large-scale toroidal arrays," International Journal of Imaging Systems and Technology 8(1), 137–147 (1997).
12. N. Duric, P. Littrup, A. Babkin, D. Chambers, S. Azevedo, K. Arkady, R. Pevzner, M. Tokarev, and E. Holsapple, "Development of ultrasound tomography for breast imaging: technical assessment," Medical Physics 32(5), 1375–1386 (2005).
13. S. A. Johnson, D. T. Borup, J. W. Wiskin, F. Natterer, F. Wubbling, Y. Zhang, and O. C., "Apparatus and method for imaging with wavefields using inverse scattering technique," US patent n°6, 005, 916 (1999).
14. P. Lasaygues, D. Tanne, S. Mensah, and J. P. Lefebvre, "Circular antenna for breast ultrasonic diffraction tomography," Ultrasonic Imaging 24, 135–146 (2002).

15. R. C. Waag and R. J. Fedewa, "A ring transducer system for medical ultrasound research," IEEE Transactions on Ultrasonics Ferroelectrics and Frequency Control 53(10), 1707–1718 (2006).
16. J. P. Lefebvre, P. Lasaygues, and S. Mensah, Born ultrasonic tomography: some limits and improvements, *Acoustical Imaging* (Plenum Press, New York, 2000), Vol. 25, pp. 79–86.
17. P. L. Carson, T. V. Oughton, and W. R. Hendee, Ultrasound transaxial tomography by reconstruction, in D. N. White and R. W. Barnes (eds.) *Ultrasound in Medicine II* (Plenum Press, New York, 1976).
18. P. L. Carson, T. V. Oughton, W. R. Hendee, and A. S. Ahuja, "Imaging soft tissue through bone with ultrasound transmission tomography by reconstruction," Medical Physics 4(4), 302–309 (1977).
19. P. Lasaygues, E. Ouedraogo, J. P. Lefebvre, M. Gindre, M. Talmant, and P. Laugier, "Progress toward in vitro quantitative imaging of human femur using compound quantitative ultrasonic tomography," Physics in Medicine and Biology 50(11), 2633–2649 (2005).
20. H. Merk, "Ultrasonic tomography in the diagnosis of diseases of the skeletal system in childhood," Diagnostic Radiology 29(2), 269–278 (1988).
21. C. M. Sehgal, D. G. Lewallen, J. F. Greenleaf, R. A. Robb, and J. A. Nicholson, "Ultrasound transmission and reflection computerized tomography for imaging bones and adjoining soft tissues," presented at the IEEE Ultrasonics Symposium, San Diego, CA, 1988.
22. G. Ylitalo, J. Koivukangas, and J. Oksman, "Ultrasonic reflection mode computed tomography through a skullbone," IEEE Transactions on Biomedical Engineering 37(11), 1059–1066 (1990).
23. W. C. Chew, *Waves and Fields in Inhomogeneous Media* (IEEE Press, New York, 1995).
24. M. Slaney, A. C. Kak, and L. Larsen, "Limitations of imaging with first-order diffraction tomography," IEEE Transactions on Microwave Theory and Techniques 32, 860–874 (1984).
25. X. Teng, "Application of ultrasonic tomography in industrial materials," Ph.D. thesis (The John Hopkins University, 1993).
26. J. P. Lefebvre, A linearized inverse problem: acoustic impedance tomography of biological media, in C. Bourelly et al. (eds.) *Electromagnetic and Acoustic Scattering: Detection and Inverse Problem* (World Scientific, Singapore, 1988).
27. C. Lu, J. Lin, W. C. Chew, and G. Otto, "Image reconstruction with acoustic measurement using distorted Born iteration method," Ultrasonic Imaging 18(2), 140–156 (1996).
28. A. Ishimaru, *Electromagnetic Wave Propagation, Radiation, and Cattering* (Prentice-Hall, Englewood Cliffs, NJ, 1991).
29. P. M. Morse and K. U. Ingard, *Theoretical Acoustics* (McGraw-Hill, New York, 1968).
30. P. M. Morse and H. Feshbach, *Methods of Mathematical Physics* (McGraw-Hill, New York, 1953).
31. A. C. Kak and M. Slaney, *Principles of Computerized Tomographic Imaging* (Society for Industrial and Applied Mathematics, Philadelphia, PA, 2001).
32. P. Lasaygues, J. P. Lefebvre, and S. Mensah, Deconvolution and wavelet analysis on ultrasonic reflection tomography, *Advances in Signal Processing for NDE of Materials* (ASNT, 1998), Vol. 3, pp. 27–32.
33. E. Ouedraogo, P. Lasaygues, J. P. Lefebvre, M. Gindre, M. Talmant, and P. Laugier, Multistep compensation technique for ultrasound tomography of bone, *Acoustical Imaging* (Plenum Press, New York, 2001), Vol. 26, pp. 153–160.
34. E. Ouedraogo, P. Lasaygues, J. P. Lefebvre, M. Gindre, M. Talmant, and P. Laugier, "Contrast and velocity ultrasonic tomography of long bones," Ultrasonic Imaging 24, 135–146 (2002).
35. P. Lasaygues, Compound quantitative ultrasonic tomography of long bones using wavelets analysis, *Acoustical Imaging* (Plenum Press, New York, 2007), Vol. 28, pp. 223–229.
36. O. S. Haddadin, "Ultrasound inverse scattering for tomographic imaging self-focusing array," Ph. D. (University of Michigan, 1998).
37. P. Lasaygues, R. Guillermin, and J. P. Lefebvre, "Distorted Born diffraction tomography applied to inverting ultrasonic field scattered by noncircular infinite elastic tube," Ultrasonic Imaging 28(4), 211–229 (2006).

38. P. Lasaygues and J. P. Lefebvre, “Cancellous and cortical bone imaging by reflected tomography,” Ultrasonic Imaging 23, 55–68 (2001).
39. P. Lasaygues, “Assessing the cortical thickness of long bone shafts in children, using two-dimensional ultrasonic diffraction tomography,” Ultrasound in Medicine and Biology 12(8), 1215–1227 (2006).
40. O. S. Haddadin and E. S. Ebbini, “Imaging strongly scattering media using a multiple frequency distorted Born iterative method,” IEEE Transactions on Ultrasonics Ferroelectrics and Frequency Control 45, 1485–1496 (1998).

Index

A

AA. *See* Average attenuation (AA)
Absorption, 40, 41, 105, 106, 116, 129, 136, 138, 139, 164, 173, 193, 217, 267, 268, 273, 298, 308, 322, 334, 348, 383
Acoustical impedance, 442, 456
Acoustic lens, 412–413
Acoustoelasticity, 383, 386, 387, 390
Adult thighbone, 451–452
AIB. *See* Apparent integrated backscatter (AIB)
Algebraic inversion, 444
Analogue-to-digital (A/D), 412
Angle-dependent Biot's model (stratified Biot's model), 299
Angle-dependent structural parameter, 298
Anisotropic medium, 147, 161, 167, 333
Anisotropy, 10, 11, 20, 31, 35, 88, 89, 91, 95, 96, 99–101, 104–105, 110, 111, 113, 130, 140, 160, 191, 194–196, 217–219, 292, 295, 296, 299, 305, 314, 333, 334, 340, 341, 353, 375, 376, 429, 434, 436, 450
Aperture, 326, 327, 413, 419
Apparent backscatter coefficient, 131
Apparent integrated backscatter (AIB), 266, 269, 271, 272, 278–280
Archimedes principle, 20, 97, 134, 336, 426
Arrays, 55, 56, 61, 62, 136, 158, 162–166, 280, 326, 442
Artifact, 201, 212, 323, 326, 327, 446, 455, 456
Artificial models of trabecular structures, 310
Artificial resin, 454
Attenuation, 30, 48, 73, 84, 124, 182, 243, 266, 293, 319, 332, 363, 381, 420, 442
Attenuation coefficient, 31, 39–42, 51, 52, 91, 99–110, 112, 125, 139, 220, 268, 271, 272, 274–277, 294, 296, 298, 299, 301, 306, 321, 324, 334, 337, 338, 341–343, 353–355, 365
Attenuation compensation, 135, 270, 271
Attenuation, role of scattering, 124, 138–139
Autocorrelation, 129, 134
Average attenuation, 273
Average attenuation (AA), 273
Averaged trabecular length, 302, 303
Axial transmission, 48, 60–65, 148, 149, 159, 161–168, 172, 174, 191, 192, 210, 216, 217, 219, 220, 223, 267, 332, 348, 350, 362–364, 370–372, 375, 436

B

Backcatter, 132
Back-projection, 442, 443, 446
Back-propagation, 442
Backscatter, 49, 65, 124–140, 216, 243, 266–272, 275, 276, 278, 280, 281, 283, 428, 453
Backscatter coefficient measurement, 133, 138, 140
Bandpass, 423, 424
Bayesian, 291, 319, 323
Bayesian probability theory, 311, 323–326
Beam axis, 336, 413, 414, 416
Beam width, 128, 130, 313, 413
Bidirectional axial transmission, 61
Binary Mixture Model, 129
Biomechanics, 2, 6, 381, 404
Biot-Allard model, 104
Biot, M.A., 87, 88, 91–93, 102, 106, 107, 111–113, 115, 223, 230, 235, 255
Biot's theory, 37, 58, 84, 94–96, 99, 103, 107, 114, 116, 137, 194, 220, 230, 292, 296, 314
Biot's wave equations, 305
Biot-Willis elastic constants, 97

Bone characterization, 163, 181–224, 332
Bone composition, 17
Bone marrow, 3, 20, 33, 41, 43, 58, 124, 219, 279, 293–296, 372
Bone matrix, 5, 94, 194, 220, 229, 266, 279, 345, 348, 411
Bone mechanics, 400
Bone mineral density (BMD), 18, 19, 22–24, 48, 59, 64, 65, 73–77, 107, 132, 136–138, 171, 172, 229, 243, 266, 273, 274, 278, 280–283, 312–314, 335, 341, 344–347, 349, 351, 355
Bone phantoms, 277, 300
Bone quality, 21, 23, 181, 283, 319, 320, 323, 333, 355
Bone strength, 2, 17, 18, 23, 48, 65, 74, 75, 77, 140, 219, 223, 230, 278, 280, 452
Bone structure, 36, 48, 95, 192, 201, 215, 219–221, 278–282, 300, 304, 305, 314, 322, 332, 333, 346, 456
Born approximation, 127, 442–446, 448, 449, 455
Boundary conditions, 86–87, 149, 183, 187–190, 199, 203–205, 244, 249, 372, 374, 376
Broadband ultrasonic attenuation, 48, 49, 219, 332, 342, 346, 352–355
Broadband ultrasound attenuation (BUA), 54, 273, 274, 282, 293, 296
Broadband ultrasound backscatter (BUB), 132, 266
BUA. *See* Broadband ultrasound attenuation
BUB. *See* Broadband ultrasound backscatter
Bulk modulus, 10–11, 33, 87, 251, 258

C

Calcaneus, 3, 31, 48, 49, 51, 53, 55, 56, 60, 76–79, 97–99, 104, 106, 107, 110, 125–128, 130–133, 137, 138, 266, 280, 296, 319, 332, 390–392
Callus tissue, 362, 363, 371, 372, 376
Canaliculi, 5, 410
Cancellous bone, 3, 31, 48, 84, 125, 194, 230, 290–314, 319–327, 332, 371
Cancellous bone phantoms, 300
CFL. *See* Courant, Friedrichs and Levy (CFL)
Characteristic size of pore space, 92
Childhood fibula, 452
Circular arrays, 442
Circumferential waves, 60, 96, 303
Clinical application, 48, 73–79, 137–138, 219, 310–314
Clinical devices, 31, 54, 136, 172, 266, 273
Collagen, 4, 22, 43, 279, 332, 341, 410, 411, 428, 429, 434, 435
Collagen fibers, 2, 5, 11, 17, 20, 36, 333
Compound Quantitative Ultrasonic Tomography, 443, 444, 446–448, 456
Compressional wave, 95, 105, 217, 230, 256, 322, 323, 413, 415–420, 446, 448, 451, 453, 454
Compression wave, 30, 31, 33, 36, 62
Computed tomography, 16, 18–22, 59, 137, 173, 193, 215, 219, 283
Confocal, 58, 96, 393, 416, 417, 420, 422–426, 436
Conjugated-gradient method, 448
Constant background, 443–445
Cortical bone, 2, 31, 48, 130, 146–174, 182, 259, 267, 293, 331–355, 364, 394, 410, 446
Courant, Friedrichs and Levy (CFL), 200–203, 211
Cross-sectional imaging, 435, 442
Crystals, 1
C-scan, 425

D

Damage, 8–15, 362, 381–404
Darcy flow, 88, 91
Degree of anisotropy (DA), 35, 95, 113, 160, 217, 296, 302, 314
Degree of mineralization of bone, 65, 428
Densitometry, 18, 74, 369, 377
Density, 17, 30, 48, 73, 85, 124, 148, 182, 229, 266, 312, 336, 363, 383, 414, 451
Depth of focus, 413, 420
Diagnosis, 2, 22–24, 73, 75–76, 174, 223, 266, 457
Diffraction, 21, 41, 50, 51, 103, 127, 131, 273, 319–327, 337, 341, 383, 388, 443, 444, 448, 454–456
Diffraction measurements, 443
Diphasic, 229
Discretization, 184, 189, 196, 200–202, 206–207, 210, 212, 214, 222, 448
Dispersion, 31, 52, 84, 124, 148, 201, 302, 318–327, 337, 363, 383, 454
Dispersive medium, 31, 334, 338
Distorted Born Diffraction Tomography, 443, 448, 454–456
3-D segmentation, 451
Dual frequency ultrasound, 274–277
3-D visualization, 303
Dynamic acoustoelastic testing, 386–394
Dynamic coupling, 88

E
Effective properties, 221, 254
Elastic anisotropy, 429
Elastic coefficients, 11–12, 35, 36, 149, 194–196, 333, 413, 415, 419, 426, 431–435
Elasticity, 2, 6, 8–17, 23, 24, 33, 37, 42, 59, 87, 89, 93, 116, 173, 184, 195, 196, 212, 220, 223, 251, 267, 308, 312, 340, 365, 382, 383, 386, 392, 411
Elastic modulus, 32, 37, 171, 365, 382, 390
Elastic properties, 16, 17, 30, 33, 34, 36, 65, 98, 107, 148, 168, 171, 182, 194–196, 218, 223, 333, 340, 341, 409–436
Elastic solid, 33–37, 105, 296
Electronic steering, 442
Embedding, 96, 421, 422
Erosion/dilation procedure, 217, 219, 305, 310
Estimated bone density, 59, 312

F
Failure load, 6–7, 172, 282
Faran Cylinder Model, 126–132, 139
Far field asymptotic method, 444
Fast and slow waves, 110
Fast FDUA, 310
Fast Fourier transformation (FFT), 348, 424
Fast wave, 58, 94, 95, 98–101, 103–105, 108–110, 112, 115, 217, 223, 230, 293, 294–299, 301–303, 305, 307–312, 314, 323, 325
Fatigue, 14, 17, 394, 396, 397, 399
FDTD. *See* Finite-difference time domain (FDTD)
FEM. *See* Finite-element methods (FEM)
Femur, 2, 3, 6–8, 19, 48, 49, 60, 74, 76, 95, 97–99, 104, 106, 124, 130, 131, 133, 134, 174, 182, 192, 215, 223, 255, 266, 268, 274, 276, 280–283, 304–306, 326, 334, 346, 395, 398, 431, 433, 454
Fibril, 4
Filter, 62, 97, 138, 170, 269, 423, 424, 443
Filtered back-projection algorithm, 443, 446
Finite-difference time domain (FDTD), 169, 183, 184, 187, 196–202, 208–222, 292, 303, 304, 306, 310
Finite element, 375
Finite-element methods (FEM), 184, 187, 188, 196, 201–209, 213–218, 220–222, 248, 250, 292, 305, 306
First-arriving signals (FAS), 61, 62, 64, 65, 163, 168–174, 215, 348, 364–367, 369–372, 374–377
Focal plane, 413, 416, 417, 424
Focal point, 58, 413, 416
Focused (concave) transmitters, 306
Forearm, 49, 58–59, 61, 64, 163, 168, 169
Fracture healing, 362, 364
Fracture risk, 2, 23, 24, 48, 59, 63, 65, 73–75, 77, 79, 133, 138, 139, 174, 266, 283, 332, 400, 436
Fracture risk assessment, 24, 74–75
Frequency-dependent ultrasound attenuation (FDUA), 302, 310, 311
Frequency slope of apparent backscatter (FSAB), 266, 271
Friction loss at the interface between solid and liquid, 308
FSAB. *See* Frequency slope of apparent backscatter (FSAB)

G
Gaussian random field distributions, 310
Geometrically-mimicking phantom, 454, 455
Green function, 444, 445, 447, 448, 456
Group velocity, 31, 104, 156, 168, 170, 320, 337, 338, 348, 374, 418
Guided waves, 32, 35, 36, 48, 56, 57, 64, 65, 147–174, 192, 215, 216, 218, 267, 348, 363, 364, 370, 374–376

H
Harmonic distortion, 385, 390, 403
Haversian canal, 3, 5, 36, 410, 420, 427
Haversian structure, 345, 346, 348, 351
Heel, 48, 50, 52, 54–56, 60, 64, 65, 74, 75, 77, 78, 127, 182, 223, 266, 268, 274, 281, 283, 292, 384, 385
Heterogeneous, 36, 124, 184, 196, 200, 208, 333, 352, 355, 402, 410, 435, 445, 446
Heterogeneous medium, 200, 352, 445, 446
Hierarchical level, 411–420
Hierarchy, 411
High-order approximations, 197
High-resolution synchrotron radiation microcomputed tomography (SR-μCT), 216, 293
Hilbert-transformation, 417, 424
Hip, 19, 21–23, 48, 49, 60, 64, 74–77, 137, 138, 174, 266, 267, 281, 283, 403
Homogeneous, 33–37, 40, 85, 87, 90, 104, 148, 161, 169, 173, 174, 187, 188, 190, 191, 198, 199, 201, 208, 212, 235, 371, 383–385, 414, 416, 419, 426, 434, 436, 442, 444, 446, 447, 454, 456

Homogenization, 37, 195, 196, 229–259, 411
Homogenized mechanical properties, 339–340
Hydroxyapatite, 3, 4, 11, 20–22, 26, 333, 410, 428

I
Image processing technique, 303, 309, 448
Image resolution, 193, 450, 455
Impedance, 39, 41, 102, 124, 155, 188, 189, 414, 415, 426, 428, 429, 432–436, 444, 456
Individualized model, 183, 195, 196, 221
Inhomogeneous, 36–37, 154, 292, 300, 371, 382, 442, 447, 448
Initial values, 190, 191, 198, 241
In-silico approach, 304
Instrumentation, 47–65
Integral equation, 206, 444
Integrated reflection coefficient (IRC), 266, 269, 276–280
Interaction force, 85, 87–89, 91–93, 105
Interstitial tissue, 5, 348, 410, 427, 432, 435
Inverse problem, 103, 129, 130, 136, 223, 229–259, 298, 324, 442–443, 445
Inverse scattering, 443, 444
IRC. *See* Integrated reflection coefficient (IRC)
Isotropy, 10, 11, 88–89, 105, 135, 194, 302, 375
Iterative method, 443, 444, 447, 456

J
Johnson-Koplik-Dashen model, 103, 113, 258, 259

K
Kelvin-Voight viscoelastic material, 243
Kramers-Kronig relationships, 320–322, 327, 353–355
Kramers-Krönig relationships, 31

L
Lacuna, 3, 5, 36, 410, 421, 427
Lamb waves, 35, 148, 150, 155, 156, 158, 171, 215, 218, 374
Lamellae, 4, 5, 11, 16, 344, 345, 348, 433–435
Lamellar bone, 5, 6, 410
Lamellar unit, 410, 434, 435
Lateral resolution, 388, 413, 420
Lateral wave, 64, 169, 211, 215, 216, 218, 365, 370–372, 374–376
LD-100, 312–314
Lens, 412–413, 419, 425
Linear acoustics, 126, 265–284, 381
Linear elastic wave equations, 304
Lippmann-Schwinger equation, 444, 445
Literature review, 194, 214–222, 331, 337
Llead-zirconate-titanate (PZT), 295
Long cortical bone, 148, 168–172
Low-contrasted tissues, 444
Lumbar vertebrae, 266, 450

M
Macrocontinual Biot's model, 300
Macroscale, 341
Macroscopic trabecular orientation, 301
Mass density, 30, 32–34, 37, 85, 86, 148, 154, 159, 171, 173, 174, 185, 194–196, 212, 213, 243, 312, 336, 339–341, 347, 351, 355, 414, 415, 419, 426–433, 453, 454
Mass fraction, 428, 429
Material characterization, 148
Material properties, 2, 6, 37, 48, 58, 134, 168, 172, 182, 183, 189, 191, 194–196, 212, 213, 215, 219, 222, 230, 267, 332–334, 339, 341, 371, 421, 426
Mechanical properties, 8, 11, 15, 17, 23, 102, 133, 138, 140, 172, 194–196, 222, 278–282, 333, 339–340, 362, 363, 368, 409
Mechanical scanning, 411, 442
Mechanical steering, 442
Mesoscale, 412
Methylmethacrylate (MMA), 422
Microarchitecture, 65, 134, 309
Microcontinual cellular model, 300
Microcracks, 5, 13, 17, 21, 22
Microdamage, 65, 381–404
Microscale, 249, 411, 426–433
Microstructure, 22, 124, 129, 130, 134, 136, 243, 249, 250, 253–255, 259, 267, 292, 300, 302, 303, 333, 335, 341, 345–348, 350–355, 419, 435, 446
Mineralization, 5, 20, 22, 65, 171, 332, 371, 411, 428, 429, 432–435
Mineralized fibril, 4, 410
Mode conversion of the incident acoustic wave to shear waves, 308
Modified Biot-Attenborough (MBA) model, 102, 103, 298
Modified Biot's models, 107, 113
Monitoring, 48, 64, 77, 78, 223, 361–377, 436
Multi component signal, 148
Multi-layer model, 84, 104

Multiple scattering, 124, 126, 127, 132, 135–138, 322, 353
Multi-scale, 3–6, 24, 185, 220–221, 248, 250, 333, 402
Multiscale medium, 333

N
N.A. *See* Numerical aperture (N.A.)
Nanoindentation, 16, 196, 433, 434
Nanoscale, 4, 433–435
Native, 421
Navier-Stokes, 244, 254
Negative dispersion, 101, 105–106, 115, 319–327, 351–353
Neukadur ProtoCast 113^{TM}, 454
Nominal model, 183, 192, 194, 215, 221
Nonlinear dissipation, 386
Nonlinear elasticity, 382, 383, 386
Non-linear inversion, 443, 447, 448, 456
Nonlinear resonant ultrasound spectroscopy (NRUS), 394–397, 399, 401, 403
Nonlinear ultrasound, 400
Nonlinear wave modulation, 398–399, 403
Non-Newtonian fluid, 243–248
Non-union, 362, 363, 365, 369, 376
Normalized broadband ultrasound attenuation (nBUA), 269, 273, 274, 277, 279, 332, 342–348, 353, 354
Numerical aperture (N.A.), 413
Numerical simulations, 105, 169, 171, 173, 182–187, 191, 193, 216–223, 267, 279, 292, 303, 308, 314, 323, 376
Numerical upscaling, 248–254
Nyquist, 424, 425

O
Order of approximation, 197, 322, 443–445, 448, 449, 455, 456
Osteoblasts, 5
Osteoclasts, 5
Osteocyte, 3, 5, 36, 410, 421, 427
Osteons, 3, 5, 16, 36, 333, 343, 344, 348, 410, 427, 434, 435
Osteoporosis, 2, 21–24, 48, 73–77, 132, 172, 174, 182, 219, 223, 229, 230, 250, 257, 266, 283, 284, 292, 332, 364, 371, 377, 451
Overlapping fast and slow waves, 51, 96, 105, 217, 302, 305
Overlapping of the two waves, 310

P
Papoulis deconvolution, 450
Partial waves, 150–152, 154, 157, 160
Perfectly matched layers (PML), 189, 199
Peripheral quantitative CT (pQCT), 21, 22, 173, 313, 314
Permeability, 88, 93, 97, 107, 111–115, 256, 258
Phalanges, 48, 56–58, 64, 74, 174, 214
Phase cancellation, 51, 103, 115, 125, 319–327, 355
Phase spectrum, 53, 163, 173, 424
Phase velocity, 31, 36, 53, 62, 91, 99–109, 115, 127, 148, 151–154, 160, 161, 163, 168–170, 173, 201, 279, 319–327, 334, 337, 338, 348, 349, 352–355, 383, 415
Plexiform, 335, 341, 345–348, 351, 352, 410
Plexiform bone, 410
PML. *See* Perfectly matched layers (PML)
Poissonφs coefficient, 9–10
Poissonφs ratio, 9–11, 33, 103, 152, 431, 433
Polymethylmethacrylate (PMMA), 389, 390
Poly(vinylidence fluoride) (PVDF) transducers, 293
Pores, 37, 84–88, 91, 92, 96, 98, 100, 101, 103, 106, 107, 110, 112–115, 137, 194, 195, 220, 230, 233, 235–243, 254, 255, 258, 293, 296, 298, 300, 304, 310, 335, 344, 345, 347, 348, 384, 410
Pore size in cancellous bone, 298
Poro-elasticity, 37, 91
Poromechanical modelling, 91–94
Porosity, 3, 5, 17, 20, 22, 36, 37, 62, 65, 85–87, 89, 96–100, 102–104, 113, 124, 129, 137, 171, 173, 195, 196, 254, 257, 258, 310, 332, 333, 345, 384, 385, 390, 393, 436, 450
Power spectrum, 131, 311, 388, 418, 424
Propagation velocity, 30, 31, 34, 65, 172, 363–366, 368, 381, 383, 390
Prototypes, 56, 60, 62, 64, 127, 457
Pseudo-attenuation image, 313
Pseudo-SOS image, 313
Pulse-echo, 37, 148, 164, 266, 267, 269, 278–281, 283, 413, 417–419, 423

Q
Quality control, 78, 79
Quantitative ultrasound (QUS) imaging, 23, 29, 48, 55, 56, 65, 76, 174, 182, 266
Quasi-compressional wave, 413

Quasi-shear wave, 413
QUS imaging
QUS imaging. *See* Quantitative ultrasound (QUS) imaging

R
Radiological methods, 313
Radius, 7, 21, 48, 49, 58, 59, 61, 63–65, 75, 96, 113, 132, 155, 157–160, 170–172, 174, 182, 192, 215, 312, 313, 332, 338, 388, 413, 419, 431, 436, 446
Radius of curvature (ROC), 159, 192, 413
Random distribution of pores, 230, 235–243
Rayleigh wave, 153, 154, 416
Reflectance function, 414
Reflection, 35, 37–42, 49, 58, 59, 63, 65, 86, 103, 105, 110–113, 130, 150, 169, 188–190, 209, 210, 257, 267, 269–276, 280, 336, 388, 414, 416–419, 422–426, 428, 436, 443, 444, 447
Reflection coefficient, 38, 110, 414, 416, 422, 425, 426, 428
Reflection measurements, 59, 447
Refraction, 37–41, 104, 190, 267, 303, 443, 444, 446, 447
Regularization process, 456
Representative volume element (RVE), 248–250, 253
Rigidity, 6–7, 186, 199
RVE. *See* Representative volume element (RVE)

S
Saturating fluid, 84, 95, 106–110, 114, 134
Scalogram, 311
Scanning acoustic microscopy (SAM), 3, 411–420, 433, 436
Scattered field, 126, 442, 444, 455
Scattering, 21, 37, 40–43, 65, 103, 106, 107, 116, 123–140, 188, 201, 217, 267, 268, 271, 273, 298, 300, 303, 305, 308, 322, 344, 345, 347, 348, 353, 371, 443–446
Schoenberg model, 105, 298
Shape function, 203–208, 252
Shear modulus, 11, 33, 98, 251, 255, 258
Shear waves, 30, 31, 34, 35, 39–41, 90, 91, 110, 116, 128, 130, 135, 138, 139, 150, 154, 155, 159, 187, 209, 256, 303, 308, 337, 413, 414, 416, 420, 446, 517
Short-time Fourier transform, 310
Signal processing, 55, 60, 62, 65, 106, 115, 140, 148, 149, 161–167, 172, 173, 182, 223, 310, 312, 348, 424, 446, 449–451, 455, 457
SimSonic, 200, 213, 304
Singular value decomposition (SVD), 62, 164, 166, 167, 170, 173
Slip effect, 87
Slow FDUA, 310
Slow wave, 51, 58, 59, 94–96, 99–101, 104, 105, 108, 110, 111, 115, 217, 220, 230, 256, 292–303, 305, 307, 309–314, 323–326
Snell-Descartes laws, 447
Snell's law, 38, 40, 150, 156, 159, 162, 418
SOS. *See* Speed of sound (SOS)
Spatial Fourier transforms, 129, 214, 443, 446
Speckle, 42, 131, 135, 137, 140
Spectrograms, 310, 311
Spectrum, 41, 49, 51, 53, 131, 138, 149, 152, 155, 163, 164, 173, 270, 272, 273, 275–277, 281, 310, 311, 337, 341, 388, 399, 418, 424, 446
Spectrum centroid shift, 138, 272
Speed of sound (SOS), 30–37, 40, 48, 49, 51–54, 56–59, 61–65, 76, 78, 95, 106, 109, 134, 137, 198, 219, 266, 267, 271, 273, 274, 277, 279, 281, 282, 293, 296, 319, 320, 332, 338, 344, 345, 347, 348, 426, 454
Spherical pores, 220, 310
Squirt flow, 91, 92
Stage of propagation, 308
Stiffness, 11, 12, 17, 32, 33, 35, 37, 59, 65, 159–161, 171, 173, 174, 195, 206, 208, 332, 362, 365, 376, 415, 428, 429, 431, 436
Stiffness tensor, 11, 12, 33, 415, 431, 436
Strain, 8–9, 11, 12, 14, 15, 30, 33, 34, 87, 150, 159, 160, 186, 248–250, 362, 381–383, 394, 395, 400–402
Strain tensor, 34, 87, 159, 186, 248, 249
Stratified model, 95, 104, 105, 298–300, 322
Strength, 2, 6–15, 17, 18, 23, 24, 48, 65, 74, 75, 77, 130, 133, 140, 155, 171–172, 219, 223, 229, 230, 267, 268, 278–280, 283, 362, 368, 369, 376, 452
Stress, 2, 8, 9, 11–15, 31, 33, 34, 36, 85–87, 89, 92, 93, 105, 110, 111, 148–150, 152, 155, 157, 159, 185–190, 199, 206, 209, 232, 243, 244, 247, 248, 250, 255, 305, 346, 382, 383, 386, 400, 401, 414
Stress tensor, 31, 34, 85–87, 89, 93, 105, 185, 186, 243, 247, 248, 255
Structure, 2, 3, 5–7, 11, 17, 24, 36, 37, 48, 84, 88, 93–95, 98, 103–107, 112, 114, 116,

124, 125, 127, 130, 135, 148, 182, 192–194, 199, 201, 215, 216, 219–221, 236, 248, 257, 266, 278–283, 292, 293, 296, 299–305, 308–310, 314, 322, 332, 333, 335, 343–347, 352, 355, 372, 375, 400, 410, 411, 422, 427, 434, 442, 456
Surface acoustic waves (SAW), 413, 416–419, 436
Surface skimming compressional wave (SSCW), 416, 417, 419
Synchrotron radiation μCT (SR-μCTp, 20, 21, 293, 428, 436

T
Thin cylinder model, 126–128
Three-dimensional (3-D), 3, 18, 95, 129, 134, 168, 191, 192, 215, 255, 292, 304, 306
Through-transmission, 137, 221, 266–268, 271, 273–274, 277, 281–283
Tibia, 3, 22, 48, 63, 95, 98, 99, 102, 104, 132–134, 171–173, 268, 274, 332, 343, 365–368, 375, 436
Time-frequency analysis, 302, 348
Time integration, 203, 206
Time-of-flight (TOF), 52, 53, 57, 61, 64, 163, 273, 275, 320, 338, 348, 386–389, 419, 423–425, 449, 453
Time of flight modulation (TOFM), 388–392
Time-resolved, 416, 423–425, 436
Time slope of apparent backscatter (TSAB), 266, 271, 272
Tissue level, 195, 411, 436
Tomography, 16–19, 21, 22, 59, 97, 113, 137, 173, 193, 215, 219, 220, 255, 283, 293, 428, 441–457
Toroidal arrays, 442
Tortuosity, 88, 98, 103, 104, 107–115, 258
Toughness, 2, 15, 17
Trabeculae, 3, 43, 84, 124, 192, 230, 267, 295, 390
Trabecular bone, 3, 33, 77, 123, 182, 254, 265, 332, 381
Trabecular microstructure, 95, 136, 300, 302
Trabecular orientation, 95, 98, 104, 106, 128, 292, 295, 296, 298–304
Trabecular thickness, 20, 116, 127, 128, 132–135, 139, 140, 278, 309, 310
Transducers, 32, 41, 48–50, 53–60, 62–65, 78, 96, 125, 127, 129–132, 137, 148, 150, 155, 156, 158, 159, 162–164, 173, 190–192, 267–269, 272, 274, 277, 279, 293–295, 304, 306, 308, 323, 326, 336–338, 349, 352, 355, 363–370, 373, 374, 376, 377, 385–389, 398, 411–413, 416, 417, 419, 420, 424, 425, 427, 444, 445, 447, 449–451, 454
Transmission, 38, 48–65, 74, 78, 86, 105, 110–113, 115, 124, 125, 134, 136, 137, 148, 149, 159, 161–168, 172, 174, 191, 192, 210, 214–217, 219–221, 223, 266, 267, 277, 282, 296, 332, 336, 342, 348, 350, 362–364, 370–373, 375, 394, 414, 436, 443, 444, 447, 449
Transmission coefficient, 38, 51, 110–113, 277, 342
Transmission measurements, 48–52, 57, 59, 61–62, 125, 137, 162, 165, 217, 220, 370, 375, 443, 447, 449
Transverse isotropy, 88–89, 105, 375
Transverse transmission, 48–60, 64, 65, 74, 191, 214, 296, 332
Treatment, 23, 73, 76–77, 79, 212, 314, 362, 392, 436, 457
TSAB. *See* Time slope of apparent backscatter (TSAB)
Twisted plywood, 5, 434, 435
Two-axis scanning, 59
Two-dimensional (2-D), 164, 191–192, 220, 255, 326, 426, 436
Two-phase model, 85
Two-scale convergence, 231–235, 237–243, 246, 259
Two-wave phenomenon, 303–306, 310–314

U
Ultrasound velocity, 243, 363–365, 367, 370, 376
Unfocused transducers, 32, 41, 54, 55, 304

V
Variable background, 446, 447
Velocity dispersion, 31, 43, 52, 101, 105, 106, 136, 148, 163, 217, 302, 338, 348, 349, 351–353, 355, 363, 374, 383
Virieux, 199, 200, 211–213, 304
Virtual specimens, 303
Viscoelastic, 12, 30, 40, 110, 116, 194, 243, 248, 256, 259, 333, 334, 345, 347, 348, 355
Viscoelasticity, 12–13, 91, 256, 348
Viscosity (of the saturating fluid), 108–110
Viscous characteristic length, 103, 112–115, 258
Viscous coupling, 88

Viscous friction, 41, 298
Visual dynamic images, 308
Volkmann canal, 5, 410, 421
Volume fraction, 58, 59, 98–100, 102, 104, 106, 132, 134, 138, 217, 219, 274, 278–280, 292–295, 301, 307, 312, 314, 341, 353, 384, 385, 392, 393, 428, 429, 450
V(z)-scan, 416–418, 425
V(z,t)-scan, 416, 417
V(z) technique, 416

W
Waveguide, 149, 157, 161, 174
Wave attenuation, 103–105, 108–110, 113, 115, 297, 308, 309, 442
Wavelength, 30–31, 33, 35–37, 42, 49, 62, 94, 107, 116, 127, 128, 130, 132, 148, 154–156, 160, 162, 169–171, 194, 201, 210–213, 215, 254, 267, 298, 337, 339, 340, 365, 370, 371, 387, 401, 413, 418, 420, 421, 433, 435, 446, 455
Wavelet analysis, 173, 457
Wavelet transform analysis, 311
Wave number, 90, 149, 150, 152, 164, 418, 446
Wave separation techniques, 310–312
Wave velocity, 40, 98–102, 104–106, 115, 149, 154, 160, 163, 172, 186, 200, 332, 336–341, 418, 419, 451, 452, 454
Weak scattering model, 126, 128–135
Woven type bone, 5, 6, 377, 410

X
X-ray μCT, 21, 293, 306, 308
XR-QCT, 18, 193

Y
Young's modulus, 2, 9–12, 14–17, 33, 98, 102–104, 133, 154, 172, 221, 340, 369, 376, 403, 431, 433